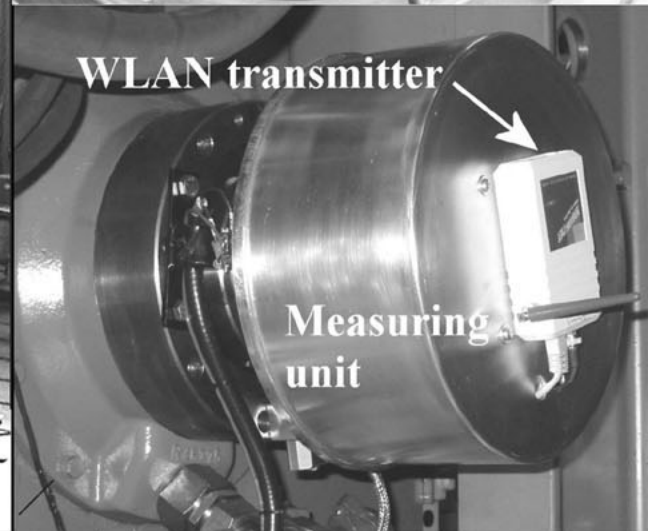
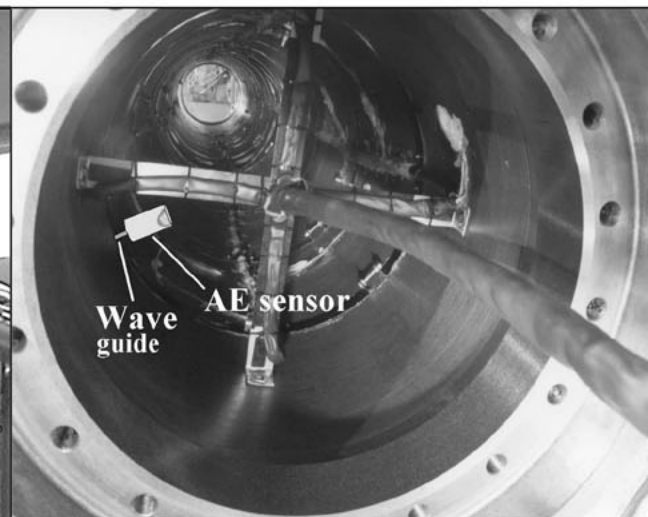
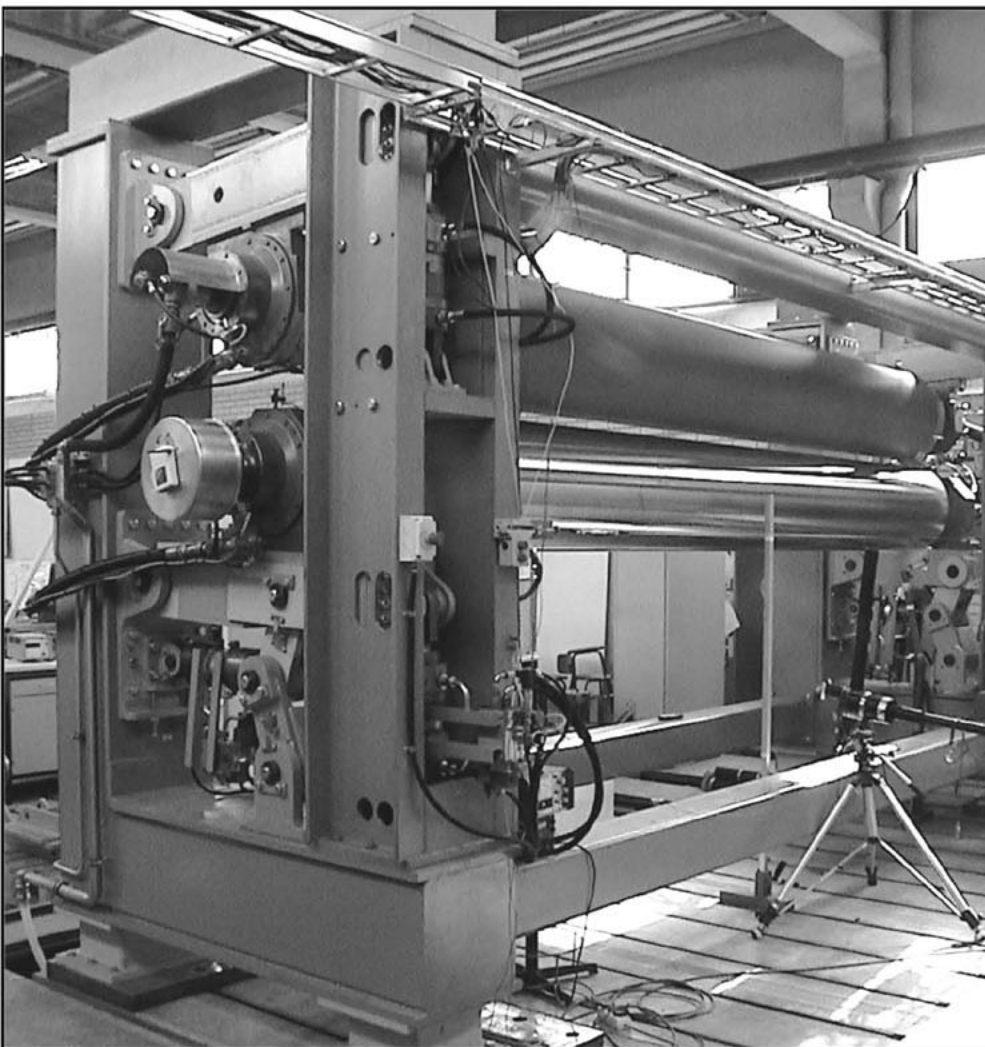


An International
Forum For
The AE Science
and Technology

JOURNAL OF ACOUSTIC EMISSION

Vol.21/January-December 2003



AE Monitoring of Paper Roll with WLAN

Endorsed by
AEWG
and
EWGAE

Published by
Acoustic Emission Group
Encino, CA USA

JOURNAL OF ACOUSTIC EMISSION

VOLUME 21, 2003

VIEWING AN ARTICLE

You need a software that can read a pdf-file. Two folders are provided for Windows 95/98/ME/2000/XP and for Macintosh. Each contains **Adobe Acrobat Reader®** Installer for respective OS. Install one first before going further. You can also download the latest version from www.adobe.com. Use of Adobe Acrobat ® (not provided) allows one to utilize the Search function. This gives the power to search for a name or a word in the entire volume and is highly recommended.

PDF Files: Contents are listed below. Individual papers have file names of **21-xxx.pdf**, with xxx as their first page number.

ISSN 0730-0050

Copyright©2003 Acoustic Emission Group

Coden JACEDO

Contents

21-001	Identifying Acoustic Emission Sources in Aging Bridge Steel Takao Kobayashi and Donald A. Shockey	1
21-014	Analysis of Source Location Algorithms, Part I: Overview and Non-Iterative Methods Maochen Ge	14
21-029	Analysis of Source Location Algorithms, Part II: Iterative Methods Maochen Ge	29
21-052	Wavelet Transform Signal Processing to Distinguish Different Acoustic Emission Sources K. S. Downs, M. A. Hamstad and A. O’Gallagher	52
21-070	Practical Aspects of Acoustic Emission Source Location by a Wavelet Transform M. A. Hamstad, K. S. Downs and A. O’Gallagher	70
Appendix	Practical Aspects of Acoustic Emission Source Location by a Wavelet Transform - Appendices M. A. Hamstad, K. S. Downs and A. O’Gallagher	A1
21-095	Acoustic Emission Monitoring of a High Pressure Test of a Steel Reactor Containment Vessel Model A. G. Beattie	95
21-112	Micro-Cracking and Breakdown of Kaiser Effect in Ultra High Strength Steels Hideo Cho, Kenzo Fukaura and Kanji Ono	112

21-120	Acoustic Emission from the Fracture of Atmospheric Rust M. Takemoto, T. Sogabe, K. Matsuura and K. Ono	120
21-131	Acoustic Property of CVD-Diamond Film and Acoustic Emission Analysis for Integrity Evaluation R. Ikeda, Y. Hayashi and M. Takemoto	131
21-142	Evaluation of Coated Film by Laser-Based AE-UT Technique M. Enoki and T. Kusu	142
21-149	Acoustic Emission from Micro-Fracture Processes of Bio-Ceramics in Simulated Body Environment Shuichi Wakayama, Teppei Kawakami, Satoshi Kobayashi, Mamoru Aizawa and Akira Nozue	149
21-157	Corrosion Monitoring in Reinforced Concrete by Acoustic Emission Masayasu Ohtsu and Yuichi Tomoda	157
21-166	Evaluation of Bond Behavior of Reinforcing Bars in Concrete Structures by Acoustic Emission K. Iwaki, O. Makishima, H. Tanaka, T. Shiotani and K. Ozawa	166
21-176	Development of a Novel Optical Fiber Sensor for AE Detection in Composites Isamu Ohsawa, Kazuro Kageyama, Yukiya Tsuchida and Makoto Kanai	176
21-187	Acoustic Emission Evaluation of Corrosion Damages in Buried Pipes of Refinery S. Yuyama and T. Nishida	187
21-197	New Concept of AE Standard: JIS Z 2342-2002 “Method for Acoustic Emission Testing of Pressure Vessels during Pressure Tests and Classification of Test Results” Y. Mori, M. Shiwa, M. Nakano and K. Iwai	197
21-206	Acoustic Emission Caused by Environmental Embrittlement of an Al-Mg-Si Alloy Keitaro Horikawa, Kenichi Yoshida, A. Ohmori and Kiyoshi Sakamaki	206
21-213	Quantitative Study of Acoustic Emission Due to Leaks from Water Tanks K. Morofuji, N. Tsui, M. Yamada, A. Maie, S. Yuyama and Z. W. Li	213
21-223	Effect of Pinhole Shape with Divergent Exit on AE Characteristics during Gas Leak K. Yoshida, Y. Akematsu, K. Sakamaki and K. Horikawa	223
21-230	Operation Monitoring of Roll Cover by Acoustic Emission Juha Miettinen and Pekka Salmenperä	230
Contents21.pdf	Contents of Volume 21 (2003)	I-1 - I-3
AuIndex21.pdf	Authors Index of Volume 21	I-4
AusNotes.pdf	Policy/Author’s Notes/Meeting Calendar/Subscription Information	I-5 - I-7
IAES16.pdf	IAES16, 16-th International Acoustic Emission Symposium	

APPENDICES (Available on CD-ROM only)

AGU-Vallen Wavelet Transform Freeware and Introduction by M. Hamstad

e-Mail Addresses of Selected Authors

A. G. Beattie	agbeattie@worldnet.att.net
Hideo Cho	cho@me.aoyama.ac.jp
Karyn S. Downs	ksdowns@excite.com
Manabu Enoki	enoki@rme.mm.t.u-tokyo.ac.jp
Maochen Ge	mug10@psu.edu
M.A. Hamstad	mhamstad@du.edu
Takao Kobayashi	takao.kobayashi@sri.com
Yasuhiko Mori	mori@cit.nihon-u.ac.jp
Koichi Morofuji	morofuji@tokyo-gas.co.jp
Isamu Ohsawa	ohsawa@giso.t.u-tokyo.ac.jp
Masayasu Ohtsu	ohtsu@gpo.kumamoto-u.ac.jp
Kanji Ono	ono@ucla.edu
Tomoki Shiotani	shiotani@df7.so-net.ne.jp
M. Takemoto	takemoto@me.aoyama.ac.jp
Shuichi Wakayama	wakayama@ecomp.metro-u.ac.jp
Juha Miettinen	juha.s.miettinen@tut.fi
Kenichi Yoshida	yoshida@me.tokushima-u.ac.jp
Shigenori Yuyama	yuyama@pacjapan.com

Authors Index of Volume 21 (2003)

Mamoru Aizawa	149	M. Nakano	197
Y. Akematsu	223	T. Nishida	187
A. G. Beattie	95	Akira Nozue	149
Hideo Cho	112	A. O’Gallagher	52, 70, A1
K. S. Downs	52, 70, A1	A. Ohmori	206
M. Enoki	142	Isamu Ohsawa	176
Kenzo Fukaura	112	Masayasu Ohtsu	157
Maochen Ge	14, 29	Kanji Ono	112, 120
Y. Hayashi	131	K. Ozawa	166
M. A. Hamstad	52, 70, A1	Kiyoshi Sakamaki	206, 223
Keitaro Horikawa	206, 223	Pekka Salmenperä	230
R. Ikeda	131	T. Shiotani	166
K. Iwai	197	M. Shiwa	197
K. Iwaki	166	Donald A. Shockey	1
Kazuro Kageyama	176	T. Sogabe	120
Makoto Kanai	176	M. Takemoto	120, 131
Teppei Kawakami	149	H. Tanaka	166
Satoshi Kobayashi	149	Yuichi Tomoda	157
Takao Kobayashi	1	Yukiya Tsuchida	176
T. Kusu	142	N. Tsui	213
Z. W. Li	213	Shuichi Wakayama	149
A. Maie	213	M. Yamada	213
O. Makishima	166	Kenichi Yoshida	206, 223
K. Matsuura	120	S. Yuyama	187, 213
Juha Miettinen	230		
Y. Mori	197		
K. Morofuji	213		

JOURNAL OF ACOUSTIC EMISSION

Editor: Kanji Ono

Associate Editors: A. G. Beattie, T. F. Drouillard, M. Ohtsu and W. H. Prosser

1. Aims and Scope of the Journal

Journal of Acoustic Emission is an international journal designed to be of broad interest and use to both researcher and practitioner of acoustic emission. It will publish original contributions of all aspects of research and significant engineering advances in the sciences and applications of acoustic emission. The journal will also publish reviews, the abstracts of papers presented at meetings, technical notes, communications and summaries of reports. Current news of interest to the acoustic emission communities, announcements of future conferences and working group meetings and new products will also be included.

Journal of Acoustic Emission includes the following classes of subject matters;

A. Research Articles: Manuscripts should represent completed original work embodying the results of extensive investigation. These will be judged for scientific and technical merit.

B. Applications: Articles must present significant advances in the engineering applications of acoustic emission. Material will be subject to reviews for adequate description of procedures, substantial database and objective interpretation.

C. Technical Notes and Communications: These allow publications of short items of current interest, new or improved experimental techniques and procedures, discussion of published articles and relevant applications.

D. AE Literature section will collect the titles and abstracts of papers published elsewhere and those presented at meetings and conferences. Reports and programs of conferences and symposia will also be presented.

E. AE Program and Data Files: Original program files and data files that can be read by others and analyzed will be distributed in CD-ROM.

Reviews, Tutorial Articles and Special Contributions will address the subjects of general interest. Non-technical part will cover book reviews, significant personal and technical accomplishments, current news and new products.

2. Endorsement

Acoustic Emission Working Group (AEWG), European Working Group on Acoustic Emission (EWGAE), and Committee on Acoustic Emission from Reinforced Composites (CARP) have endorsed the publication of Journal of Acoustic Emission.

3. Governing Body

The Editor and Associate Editors will implement the editorial policies described above. The Editorial Board will advise the editors on any major change. The Editor, Professor Kanji Ono, has the general responsibility for all the matters. Associate Editors assist the review processes as lead reviewers. Mr. Thomas F.

Drouillard is responsible for the AE Literature section. The members of the Editorial Board are selected for their knowledge and experience on AE and will advise and assist the editors on the publication policies and other aspects. The Board presently includes the following members:

P. Cole	(UK)
L. Golaski	(Poland)
M.A. Hamstad	(USA)
H.R. Hardy, Jr.	(USA)
T. Kishi	(Japan)
O.Y. Kwon	(Korea)
J.C. Lenain	(France)
P. Mazal	(Czech Republic)
S.L. McBride	(Canada)
C.R.L. Murthy	(India)
A.A. Pollock	(USA)
F. Rauscher	(Austria)
I. Roman	(Israel)
C. Scala	(Australia)
C. Scruby	(UK)
P. Tscheliesnig	(Austria)
H. Vallen	(Germany)
P. J. Van de Loo	(Netherlands)
M. Wevers	(Belgium)
B.R.A. Wood	(Australia)

4. Publication

Journal of Acoustic Emission is published annually in CD-ROM by Acoustic Emission Group, PMB 409, 4924 Balboa Blvd, Encino, CA 91316. It may also be reached at 6531 Boelter Hall, University of California, Los Angeles, California 90095-1595 (USA). tel. 310-825-5233. FAX 818-990-1686. e-mail: ono@ucla.edu

5. Subscription

Subscription should be sent to Acoustic Emission Group. Annual rate for 2004 and 2005 is US \$111.00 including CD-ROM delivery, by priority mail in the U.S. and by air for Canada and elsewhere. For additional print copy, add \$40. Print only +shipping is \$140. Overseas orders must be paid in US currencies with a check drawn on a US bank. VISA/MC accepted. Inquire for individual (with institutional order) and bookseller discounts.

6. Advertisement

No advertisement will be accepted, but announcements for books, training courses and future meetings on AE will be included without charge.

Notes for Contributors

1. General

The Journal will publish contributions from all parts of the world and manuscripts for publication should be submitted to the Editor. Send to:

Professor Kanji Ono, Editor - JAE
6531 Boelter Hall, MSE Dept.
University of California
Los Angeles, California 90095-1595 USA
FAX (1) 818-990-1686
e-mail: ono@ucla.edu

Authors of any AE related publications are encouraged to send a copy for inclusion in the AE Literature section to:

Mr. T.F. Drouillard, Associate Editor - JAE
11791 Spruce Canyon Circle
Golden, Colorado 80403 USA

Only papers not previously published will be accepted. Authors must agree to transfer the copyright to the Journal and not to publish elsewhere, the same paper submitted to and accepted by the Journal. A paper is acceptable if it is a revision of a governmental or organizational report, or if it is based on a paper published with limited distribution.

Compilation of annotated data files will be accepted for inclusion in CD-ROM distribution, so that others can share in their analysis for research as well as training. ASCII or widely accepted data formats will be required.

The language of the Journal is English. All papers should be written concisely and clearly.

2. Page Charges

No page charge is levied. One copy of CD-ROM will be supplied to the authors free of charge.

3. Manuscript for Review

Manuscripts for review need only to be typed legibly; preferably, double-spaced on only one side of the page with wide margins. The title should be brief. An abstract of 100-200 words is needed for Research and Applications articles. Except for short communications, descriptive heading should be used to divide the paper into its component parts. Use the International System of Units (SI).

References to published literature should be quoted in the text citing authors and the year of publication. These are to

be grouped together at the end of the paper in alphabetical and chronological order. Journal references should be arranged as below. Titles for journal or book articles are helpful for readers, but may be omitted.

H.L. Dunegan, D.O. Harris and C.A. Tatro (1968), Eng. Fract. Mech., 1, 105-122.

Y. Krampfner, A. Kawamoto, K. Ono and A.T. Green (1975), "Acoustic Emission Characteristics of Cu Alloys under Low-Cycle Fatigue Conditions," NASA CR-134766, University of California, Los Angeles and Acoustic Emission Tech. Corp., Sacramento, April.

A.E. Lord, Jr. (1975), Physical Acoustics: Principles and Methods, vol. 11, eds. W. P. Mason and R. N. Thurston, Academic Press, New York, pp. 289-353.

Abbreviations of journal titles should follow those used in the ASM Metals Abstracts. In every case, authors' initials, appropriate volume and page numbers should be included. The title of the cited journal reference is optional.

Illustrations and tables should be planned to fit a single page width (6.5"). For the reviewing processes, these need not be of high quality, but submit glossy prints or equivalent electronic files with the final manuscript. Lines and letters should be legible.

4. Review

All manuscripts will be judged by qualified reviewer(s). Each paper is reviewed by one of the editors and may be sent for review by members of the Editorial Board. The Board member may seek another independent review. In case of disputes, the author may request other reviewers.

5. Electronic Media

This Journal will be primarily distributed electronically by CD-ROM. In order to expedite processing and minimize errors, the authors are requested to submit electronic files or floppy disk copy of the paper. We can read Macintosh and IBM PC formats. On the INTERNET, you can send an MS Word file or the text portion to "ono@ucla.edu".

6. Color Illustration

We can process color illustration needed to enhance the technical content of an article. With the new format, authors are encouraged to use them.

MEETING CALENDAR:

The 47-th Meeting of AEWG

The next meeting of AEWG will be at Pennsylvania State University on July 19-22, 2004. The primer will be held on July 19, 2004. Send inquiry to Maochen Ge at mug10@psu.edu. Registration forms, as well as other information regarding this conference, can be found at:

<http://www.egee.psu.edu/AEWG47/>

EWGAE2004

26th European Conference on Acoustic Emission Testing will be held on September 15-17, 2004, in Berlin, Germany. The meeting is sponsored by EWGAE and DGZfP – Deutsche Gesellschaft für Zerstörungsfreie Prüfung e.V. (German Society for Non-Destructive Testing). Details can be found at:

<http://www.ewgae2004.de/>

IAES17, The 17th International AE Symposium

The upcoming IAES-17 will be held at Tokyo Metropolitan University at Tokyo, Japan on November 9-12, 2004 sponsored by Japan Society for Non-Destructive Inspection. The venue is the TMU's Minami Ohsawa campus, located at the city of Hachioji in western Tokyo. Information can be found at:

<http://www.eng.metro-u.ac.jp/iaes/>

2004/2005 SUBSCRIPTION RATE

Base rate (CD-ROM) for one year	\$ 103.00
Add Postage of U.S. - Priority rate	\$ 8.00
All others - Air mail rate	\$ 8.00
CD-ROM + printed copy, US Media mail: add	\$ 40.00
Print copy only with priority/air shipping	\$140.00
For countries without Global Priority Service,	\$160.00

Payment must be in U.S. dollars drawn on a U.S. bank. Bank transfer accepted at California Bank and Trust, San Fernando Valley Office (Account No. 080-03416470) 16140 Ventura Blvd, Encino, CA 91436 USA

Back issues available; Inquiry and all orders should be sent to (or Fax 1-818-990-1686):

Acoustic Emission Group
PMB 409, 4924 Balboa Blvd. Encino, CA 91316 USA

For inquiry through Internet, use the following address:

Editor-Publisher

Publication Date of This Issue (Volume 21):

ono@ucla.edu

Kanji Ono Tel. (310) 825-5233

30 April 2004.

IDENTIFYING ACOUSTIC EMISSION SOURCES IN AGING BRIDGE STEEL

TAKAO KOBAYASHI and DONALD A. SHOCKEY
Center for Fracture Physics, SRI International, Menlo Park, CA 94025

Abstract

Specific microfracture events responsible for acoustic emission (AE) signals in a failing bridge steel were identified. Resonant AE sensors attached to tensile specimens of aged A7 steel recorded signals as a function of applied strain. After the tests, an advanced fractographic technique, FRASTA, was applied to the fracture surfaces to determine the specimen strain, at which individual microcracks nucleated. A one-to-one correlation between AE signals and cleavage cracks was found for certain cases, identifying the microstructural origins of AE in this bridge steel. Such correlations improve understanding and interpretation of AE signals and promote application of AE technology.

Key Words: A7 Steel, Bridge integrity, Microcrack formation, Acoustic emission, Fracture surface topography, FRASTA

1. Introduction

A long-standing goal of the Federal Highway Administration (FHWA) and bridge engineers responsible for the integrity of bridge structures is a technique for reliably detecting early signs of cracking in steel bridge members (NDE Conference, 1993). Currently, periodic visual inspections or inspections using ultrasonic and other flaw detection techniques are conducted to determine the presence of flaws that can grow slowly under service conditions to a critical size and suddenly result in catastrophic failure of the member and even the entire structure.

Unfortunately, the current detection techniques are often not able to detect dangerous, integrity-threatening flaws. Moreover, these procedures are labor intensive and, hence, expensive to implement. To circumvent these drawbacks, researchers are attempting to develop acoustic emission (AE) technology for monitoring bridges (Prine, 1997; Livingston, et. al., 1996). This technology uses transducers attached to bridge members to record the tiny bursts of sound emitted by microfailure events at the front of a slowly growing crack. The potential advantages of acoustic emission are that monitoring is continuous, it is not labor intensive, and it indicates when failure processes are occurring.

In its present state of development, AE technology can often indicate *if* something is happening, *when* it is happening, and, via triangulation from outputs of several transducers, approximately *where* it is happening. However, workers knowledgeable in AE physics (e.g., Huang et al., 1998), know that AE is capable of indicating much more about *what* is happening inside the failing material. Emissions from nucleating microcracks are possibly distinguishable from emissions from growing cracks, so that if the AE signals can be adequately detected and analyzed, useful information regarding damage severity and rate of damage growth can be obtained. To this end, wideband sensors are being engineered to record AE waveforms (Hamstad and Fortunko, 1995), high bandwidth digital signal acquisition and storage systems are being developed and software and strategies are being created to process and interpret the enormous

quantities of data. To detect AE signals, however, the current sensitivity of wideband sensors must be increased by about an order of magnitude.

For AE to be practical, a way must be found to discriminate between irrelevant signals (signals associated with vibration from traffic and the like) and relevant signals (signals produced by micro-failure events occurring within a bridge member), as well as to interpret relevant signals in terms of micro-failure activity and macrocrack growth rates. Moreover, ways must be found to manage the very large amount of data generated by continuous monitoring.

Whereas the data management problem can be solved by online data processing and discarding of irrelevant information, achieving a physical interpretation of AE signals requires a mathematical description of the source and resulting surface motion. For geometries where a theoretical computation of Green's function is impossible, an experimental transfer function can be obtained (Fukaura and Ono, 2001). These researchers used resonant sensors and a laser-induced impulse to verify a crack-opening type AE source (carbide cracking in a tool steel) and its resultant waveform.

The work reported here is aimed at solving the former concern; i.e., the interpretation of AE signals produced by material micro-failure. Although considerable effort has been directed at understanding AE signals from resonant sensors, little success has been achieved in relating AE signals to micro-failure events associated with flaw growth. A significant limitation has been the lack of a way to observe in detail micro-failures occurring in the interior of a specimen or component. This paper describes the application of state-of-the-art fracture analysis technology to the problem of deducing micro-failure activity from AE signals.

2. Materials, Specimen Geometry, and Fracture Test Method

To investigate fracture mechanisms responsible for acoustic emission and identify AE sources, we machined circumferentially fatigue-pre-cracked, round-bar tensile specimens (Fig. 1) from modern bridge steels A36 and A572, and from an older A7 steel obtained from an I-bar of the decommissioned Pasco-Kennewick Bridge built in 1922 across the Columbia River in Oregon. This specimen geometry produces a high three-dimensional constraint at the crack front (Giovanola, et al., 1997) and encourages micro-fracture by cleavage.

Fatigue pre-cracking was accomplished by rotating the specimen in a lathe and applying a bending moment. Pre-crack depth was controlled by fatiguing in steps. After a certain number of load cycles, the stiffness of the sample was measured in tension and compared with a calibration curve relating stiffness with ligament diameter. The stiffness of the sample was measured by dividing the applied load of 11.12 kN by the displacement in a 25-mm gauge length.

To determine the point of origin of AE signals, two AE sensors were used. Signals generated at the pre-crack plane were analyzed; signals that initiated outside of this plane were not. The sensors (150-kHz Model R15 resonant type from Physical Acoustics Corp.) were attached to 45-degree waveguides placed an equal distance from the plane of the fatigue pre-crack, as shown in Fig. 2. An AE couplant (Dow Corning 200 silicone fluid) was used to improve acoustic wave transmission at the interfaces of the AE sensors and the waveguides and also at the waveguide/specimen interface. The preamplifier gain and LOCAN gain were 40 dB and 20 dB, respectively. The preamplifier bandwidth was 100-300 kHz and the threshold level was 60 dB (1 mV at the sensor) in reference to 0 dB as 1 μ V at the pre-amplifier input.

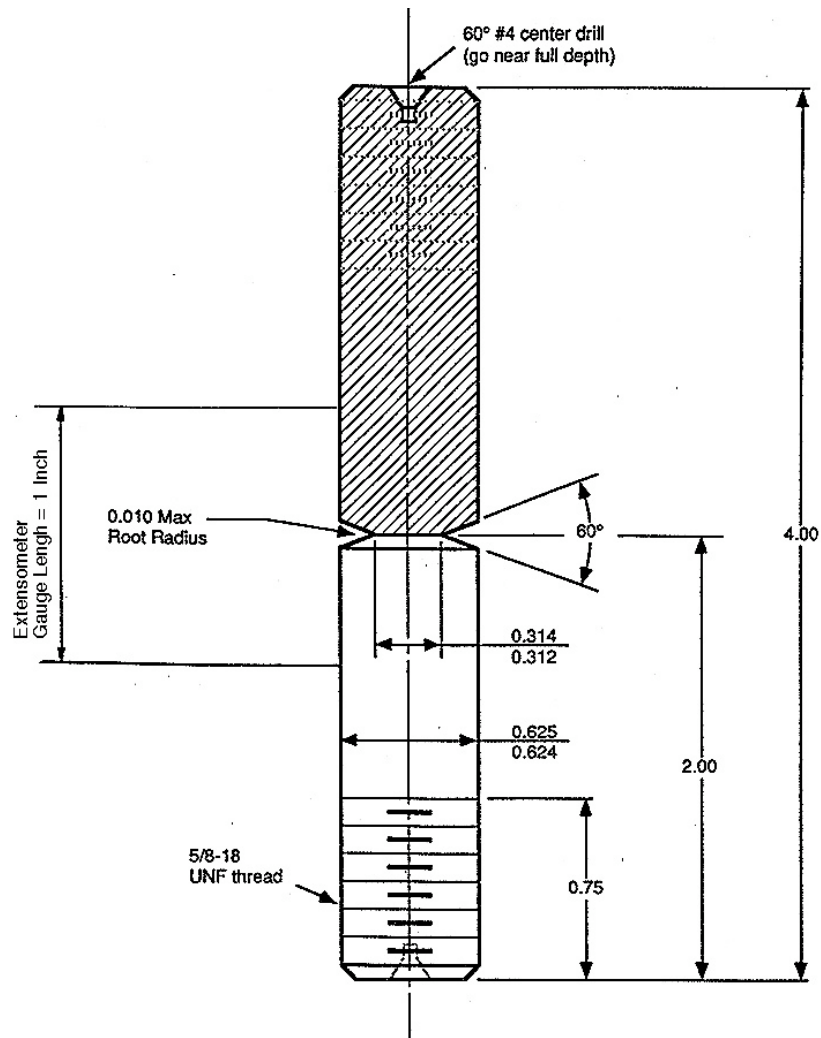


Fig. 1. Geometry of circumferentially notched and fatigue pre-cracked round-bar specimen (dimensions in inches).

Load and specimen elongation were recorded during the fracture tests. The specimen elongation was measured by two extensometers of 50 mm gauge length mounted on opposite sides of the specimens. The displacement of the fatigue pre-crack faces was computed from the elongation of the gauge section by subtracting the elastic elongation of the test specimen outside the notched section. The J-integral value was calculated using the opening displacement of the fatigue pre-crack face.

3. Test Results

Tests on the modern bridge steels A36 and A572 produced no acoustic emission, except at very low temperatures (-50°C or below). In contrast, clear AE signals were recorded in A7 specimens, even at room temperature. Thus, we focused our analysis on A7 steel.

Three tests were performed on A7 steel specimens. In all cases the loading rate was 4.17×10^{-6} m/s and the temperature was 23°C , and in each specimen AE signals were recorded well before rupture. Figure 3 shows the variation of load and J-integral with displacement for one of these specimens. The J-integral value at rupture was 30 kJ/m^2 . The fatigue pre-cracked ligament shape was elliptical (major axis of 5.056 mm vs. minor axis of 4.895 mm).

NEW 45°-SLANT ALUMINUM ACOUSTIC EMISSION WAVEGUIDES TO USE WITH EXISTING SENSORS AND 0.625"-DIAMETER ROUND-BAR SPECIMENS

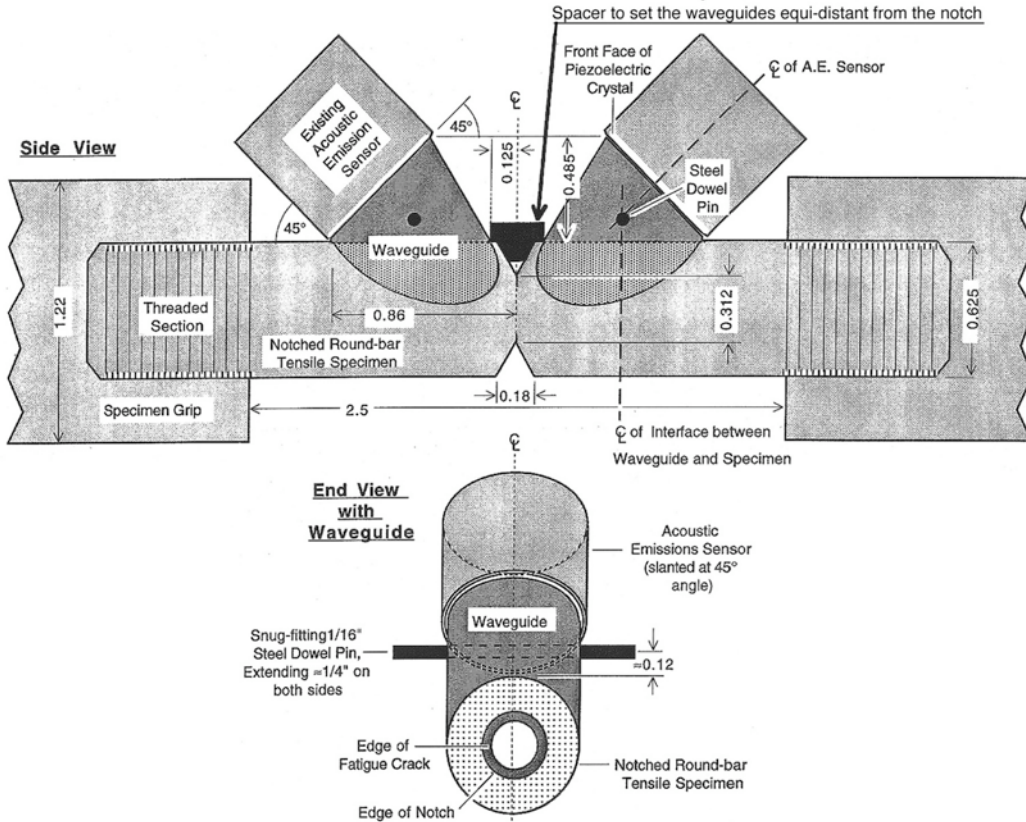


Fig. 2. Specimen setup and method of mounting AE sensors. (dimensions in inches).

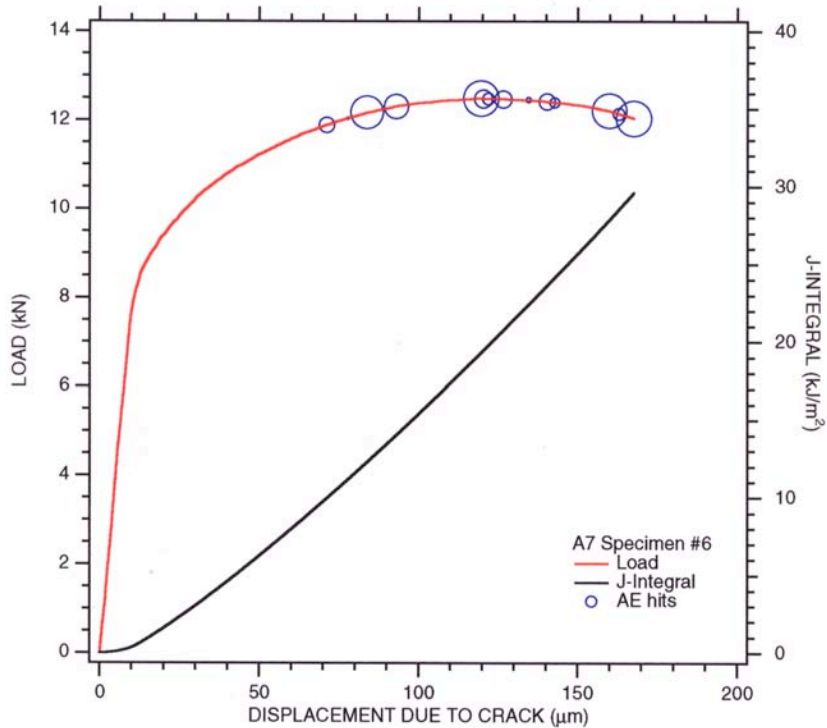


Fig. 3. Load and J-integral value as a function of fatigue pre-cracked surface displacement for A7 steel specimen tested at 23°C. The acoustic emission events are also shown. (Size of the circles indicates magnitude of AE signals.)

All A7 steel samples exhibited uneven fatigue pre-cracking around the notch circumference, resulting in elliptical ligament shapes. This suggests directionality in material properties not observed in the other bridge steels A36 and A572. Furthermore, the J-integral values at rupture showed significant scatter (30 to 265 kJ/m²). A plausible reason would be non-uniform microstructure and variations in the micro-fracture features that generate acoustic emission. Further studies are needed to investigate material variability in A7 steel.

4. FRASTA Examination

To identify the fracture mechanisms responsible for acoustic emission, we applied an advanced fractographic technique, FRASTA, to the fracture surfaces (Kobayashi and Shockey, 1991a and 1991b or <http://www.sri.com/poulter/frasta/fracture.html>). Topographic maps of the surfaces were made with a confocal optics scanning laser microscope coupled with a computer-controlled precision x-y stage. The conjugate fracture surface topographs were positioned in the relative configuration of the fracture surfaces during the fracture test and viewed at various crack face displacements. Local areas of surface mismatch are indications of differences in the amount of inelastic deformation that occurred during crack growth, and this information is used to reconstruct microfracture processes.

The results are presented graphically in three ways. A series of *fractured area projection plots* (FAPPs) was generated to identify locations of microcrack initiation and indicate how the microcracks grew. A series of *cross sectional plots* (XSPs) was generated to observe the crack opening profiles. Finally, the fractured area increase rate was indicated by plotting the fractured area as a function of conjugate surface spacing. This curve is useful for identifying the onset of micro-fracturing, changes in crack growth rate, and initiation of rapid crack propagation. The curve is also sensitive to changes in loading conditions. More detailed discussion of the FRASTA method and its results can be found in Kobayashi and Shockey (1991a and 1991b).

Fractography

Figure 4 is a scanning electron micrograph of the fracture surface of the specimen whose load-deflection curve is shown in Fig. 3. Three distinct zones are evident on the fracture surface:

- (1) the fatigue pre-cracked area,
- (2) a ductile fracture zone in advance of the fatigue pre-crack tip, and
- (3) the interior area populated by cleavage facets.

In addition, a series of small cracks perpendicular to the fatigue pre-crack surface exist in some areas of the ductile fracture zone. The planes of these secondary cracks are parallel, suggesting planes of weakness produced by the fabrication process.

Figure 5 shows gray-scale topographic images of the conjugate fracture surfaces. Darker areas are lower; lighter areas are higher. The image of Surface B was flipped horizontally to facilitate comparison with Surface A.

Fracture Reconstruction

We used FRASTA to show the evolution of micro-failures in the fracturing specimen. Conjugate topographs were positioned in the configuration of the opposing fracture surfaces during the fracture test and then displaced in the direction normal to the nominal surface. Since the topographs do not match perfectly when juxtaposed, gaps appear and grow and join one another as the conjugate topographs are displaced. Mismatches in the conjugate fracture surfaces occur because the surfaces are produced by nucleation, growth, and coalescence of micro-failures.

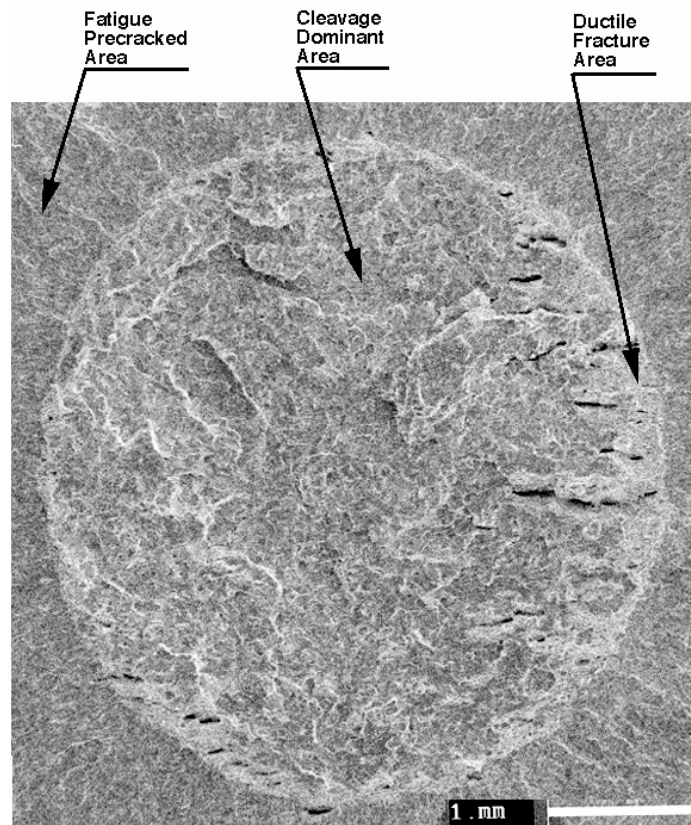


Fig. 4. Scanning electron micrograph of A7 steel fracture surface.

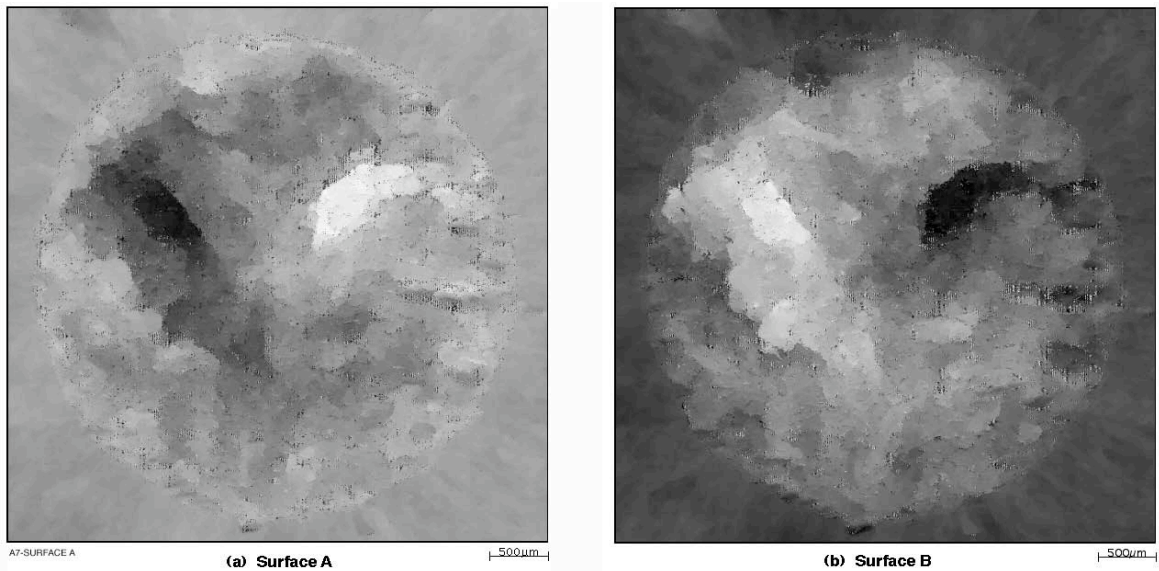


Fig. 5. Grayscale topography images of fracture surface.

These processes require plastic flow around and between cleavage cracks as the specimen displacement increases. Thus the appearance, growth, and coalescence of gaps between conjugate topographs portray the nucleation, growth, and coalescence of micro-failures.

Therefore, the FRASTA technique reconstructs the fracture process in microscopic detail. Figure 6 shows a series of FAPPs, in which black areas indicate topograph overlap (representing

intact material) and white areas are the gaps between the topographs and indicate fractured areas. The figures show the evolution of micro-failures and the formation of the fracture surface.

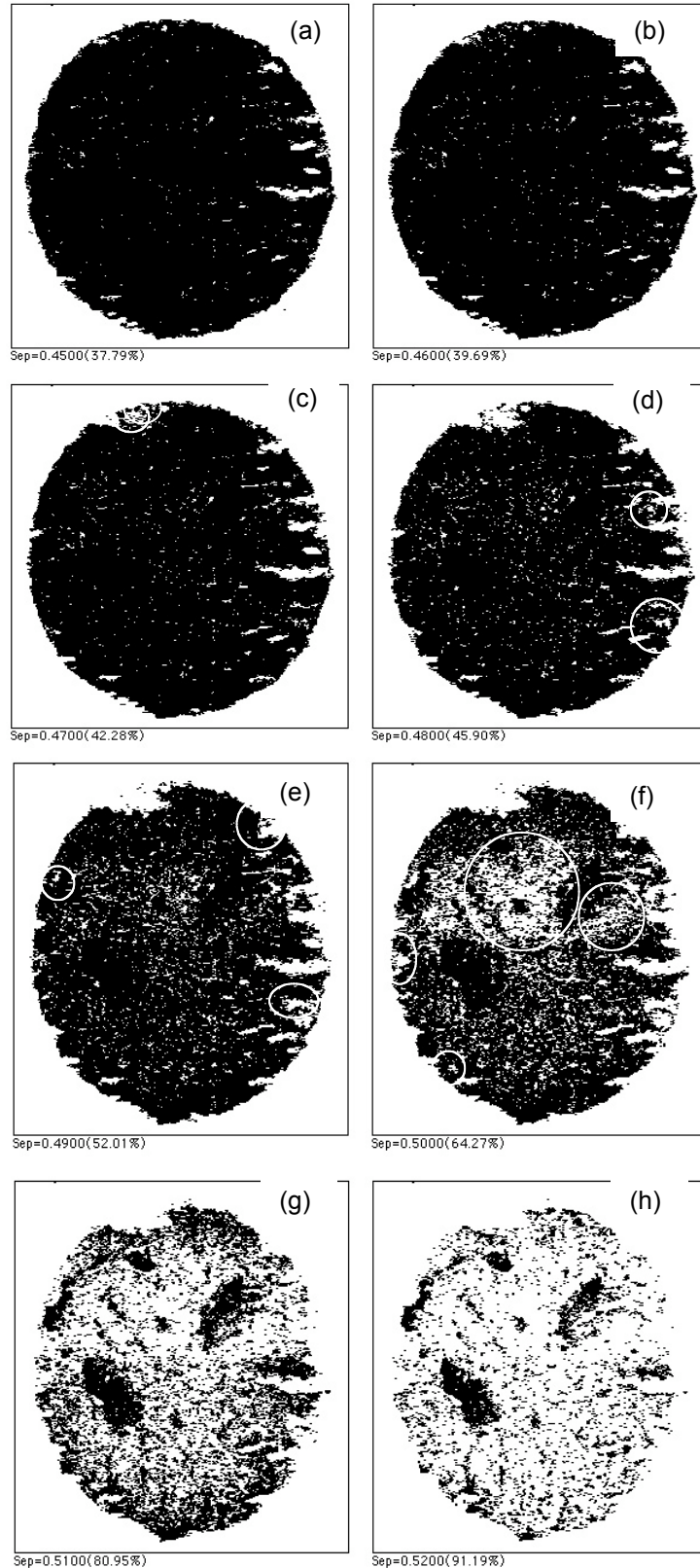


Fig. 6. A series of FAPPs showing microfracture processes in A7 Specimen 6 and details of fracture surface development.

The resolution of FRASTA depends on the roughness of the specific surfaces. The confocal optical microscope determines the elevation to better than $\pm 0.2\%$ of the full elevation range. For our specimen, the elevation range was $990\ \mu\text{m}$ for one surface and $943\ \mu\text{m}$ for the other; thus, the FRASTA resolution was about $\pm 4\ \mu\text{m}$.

Tiny white spots in the FAPPs are noise that results from the topographic data fluctuation within the error band, and from steep areas (insufficient reflection) or areas where significant in-plane deformation occurred. Since FRASTA considers only out-of-plane deformation and neglects in-plane deformation, the in-plane deformation around the secondary cracks results in permanent gaps and white islands in the FAPPs. For example, the parallel secondary cracks evident in Fig. 4 appear in Fig. 6 as white islands from the beginning. Thus, it requires care to distinguish white areas associated with cleavage cracks from areas resulting from errors in topography data.

Since cleavage failure of a grain is expected to be sudden, cleavage cracks were identified by careful examination of closely spaced FAPPs. Areas in which a gap appeared within a small displacement increment are circled in Fig. 6. Further expansion of these areas is equivalent to crack growth, and shows that growth is more gradual than nucleation. Wideband sensors and waveform analyses will allow more accurate location and size determination of cleavage crack nucleation. Since the fracture surface topography suggests that growth occurred by plastic flow and void coalescence, AE technology may not be effective in monitoring macrocrack expansion.

Assistance with AE signal-microcrack correlation was obtained from the failure progression curve shown in Fig. 7, which was obtained by summing the white (fractured) areas in individual FAPPs in a series and plotting the data as a function of the conjugate surface spacing. The curve has four major segments. The first linear segment with the steep slope (below a conjugate surface displacement of $797\ \mu\text{m}$) corresponds to the fatigue pre-cracking phase. The steep slope indicates that the deformation involved in fatigue pre-cracking was small; the linearity indicates that the fatigue crack growth rate was nearly constant.

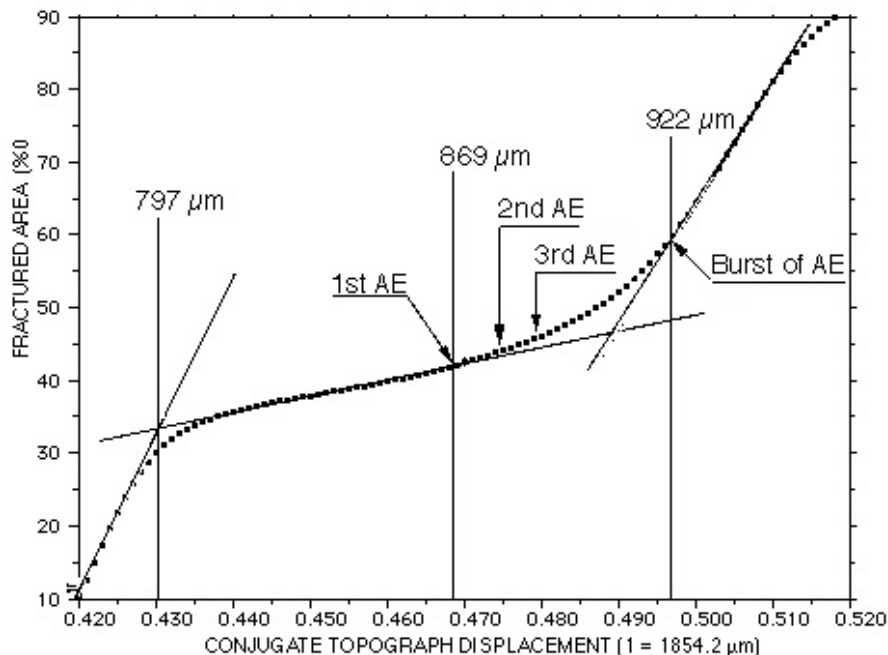


Fig. 7. Area increase as a function of conjugate surface spacing.

The second region corresponds to the period from when monotonic loading began to the beginning of microcracking. Initially the slope of the curve is nearly flat and linear. A small area increase resulted from the blunting of the fatigue pre-crack tip and the associated small crack extension. At a conjugate surface displacement of about 869 μm , the curve deviates from linearity, because of microcrack formation at the blunting fatigue pre-crack tip. This corresponds to the state shortly before the FAPP at 0.470 shown in Fig. 6c. The displacement from the onset of the monotonic loading is 72 μm .

Within Region 2 the fractured area increase gradually accelerated until at a conjugate surface displacement of 922 μm the slope became steep and constant. At this point the crack propagated rapidly, leading to specimen rupture. The total displacement from the onset of loading to onset of rapid crack propagation was 125 μm .

The microcrack nucleation displacements determined by FRASTA can be compared with the displacements at which AE signals were recorded. Figure 3 shows that the first AE signal occurred at a fatigue pre-crack surface displacement of 70 μm , which corresponds with the onset of nonlinearity indicating the beginning of Region 3. The white area developing at the 11 o'clock position on the periphery of Fig. 6c was the first to rapidly expand and, moreover, occurs at a displacement range consistent with the AE signal. Thus, the cleavage crack responsible for that white area is the source of the initial AE signal. Figure 3 also shows that the maximum load and multiple AE signals occurred at the displacement of about 125 μm . Since the maximum load and intense AE activity correspond to the onset of crack instability and rapid crack propagation, the end of Region 3 in Fig. 7 also agrees with the AE result. The state of specimen during rupture is shown in Figs. 6f and 6h.

The second and third AE signals in Fig. 3 agree with the FAPPs shown in Fig. 6d. A considerable increase in topograph displacement was required for the white areas to achieve the size of a cleavage facet. One would expect the white areas to develop more quickly, since cleavage cracking occurs suddenly. The neglect of elastic deformation by FRASTA may affect the rate indicated by the reconstruction. Despite the uncertainty, these findings show that FRASTA can identify AE sources and begin to interpret the meaning of AE signals in terms of microcracking behavior.

Local Fracture Surface Analysis

We obtained a detailed look at cleavage crack nucleation by applying FRASTA to a small area of the fracture surface containing a cleavage facet. Figure 8 shows a characteristic cleavage facet: relatively flat, smooth, and planar, with a distinct boundary surrounded by a fibrous surface characteristic of ductile void coalescence.

Figure 9 is a series of FAPPs portraying the evolution of the fracture surface area. Little indication of the impending cleavage crack is given in Figs. 9a through 9d. The first sign is in Fig. 9e, where a few isolated gaps appear within the facet area at a topograph separation of 0.500. At a separation of 0.510, Fig. 9f, the gap area is continuous over most of the facet area. Thus, this cleavage facet formed at a displacement increment of 13 μm . Figures 9f through 9h show the cleavage crack joining the fatigue crack and penetrating into the specimen interior. Figure 10 superimposes a FAPP at 0.515 on the micrograph of the fracture surface and shows the correspondence of the gap generated by FRASTA with the cleavage crack.

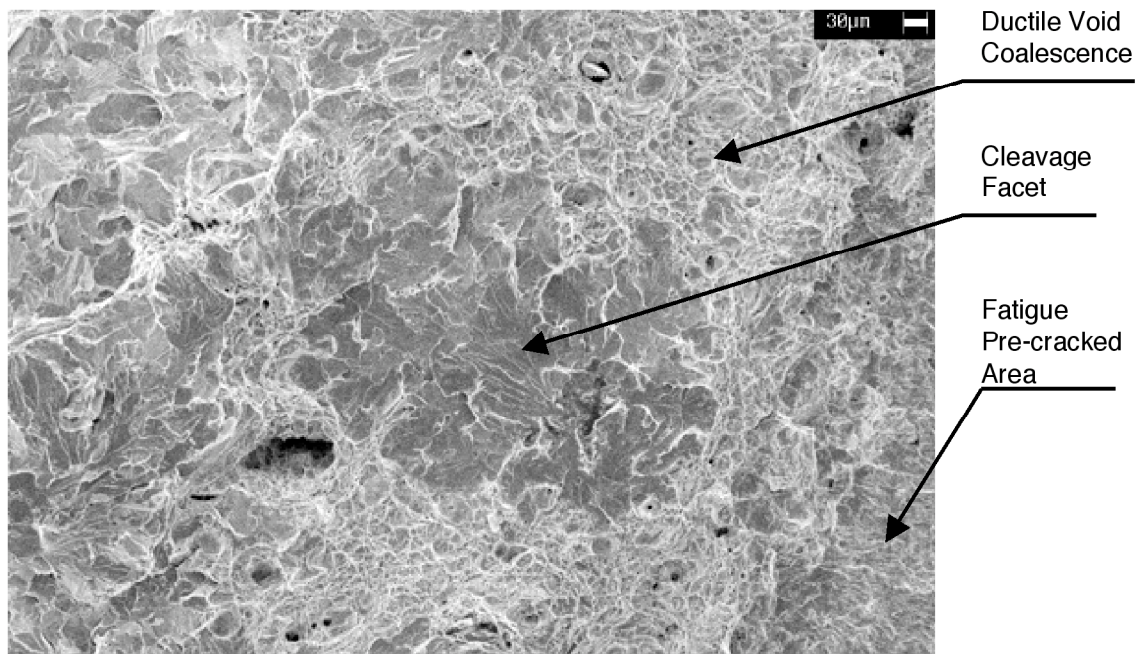


Fig. 8. SEM image of cleavage facet in A7 fracture surface.

5. Discussion

The modern structural steels, A36 and A572, obviously more homogeneous and clean, did not generate AE at room temperature. Acoustic emission could be detected only when these steels were tested at extremely low temperatures. A7 steel, on the other hand, generated AE easily even at room temperature, suggesting that the microstructure possesses internal weak spots that initiate micro-failure. The large variation in toughness measured on the three specimens of A7 steel (J-integral values ranged from 30 kJ/m² to 265 kJ/m²) is consistent with a non-uniform microstructure. Thus, bridges made from older steels are more likely to crack and fail, and are therefore more in need of monitoring.

More precise definition of the microcracks (white areas in Figs. 6e and 6f) can be achieved with a higher resolution microscope system. The confocal optics scanning laser microscope used to characterize the elevation was an 8-bit system, which divided the elevation range of about 1 mm (for the samples we analyzed) into 256 divisions. Thus, the elevation data step increment was large (approximately 4 μm spacing). Since the microscope determines the elevation at each step with the accuracy of 0.2% of full range, the error band of each step was about ±2 μm on one surface. This broad error band was responsible for the fuzziness of the micro-fractured areas in the FAPPs. A 16-bit confocal optics scanning laser microscope would improve the capability of FRASTA significantly and might permit the determination of microcrack initiation sites even in A36 steel tested at -50°C.

To achieve AE monitoring capability for bridges, further studies should be carried out on steels such as A7 to develop AE detection and signal interpretation methods and to develop alerting protocols for impending failure of aging bridge components. Because bridges are subjected to cyclic strains, as opposed to the monotonically increasing strains of the tensile tests performed here, the studies should be carried out under fatigue loading conditions.

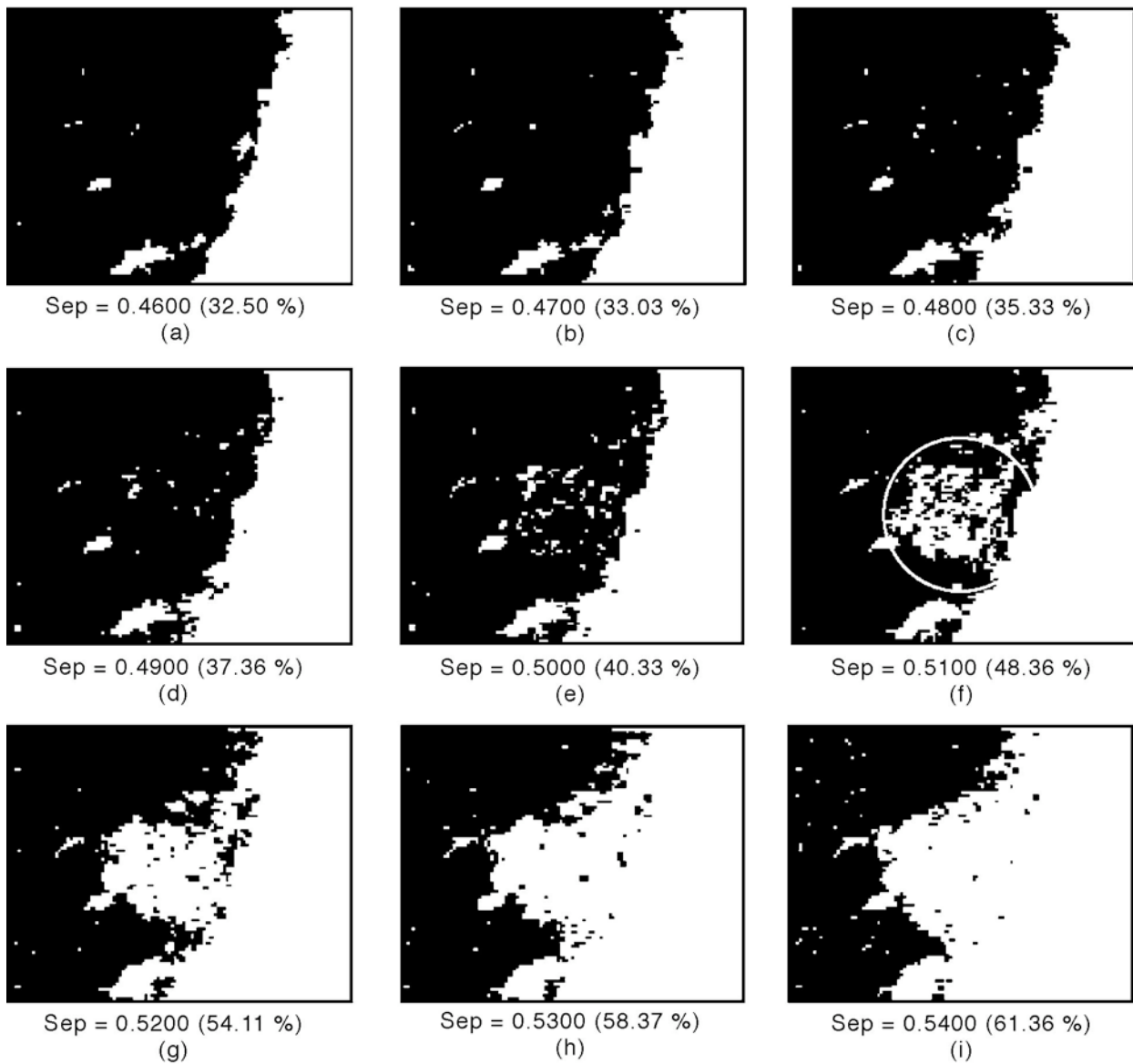


Fig. 9. A series of FAPPs showing sudden appearance of a cleavage crack (circled) near the fatigue pre-crack front.

To assess remaining life and to develop active strategies for preventing catastrophic failure, more needs to be known about damage accumulation kinetics. Information on microcrack coalescence and crack growth rates should be sought in the shape of AE signals. Needed are broadband sensors with improved sensitivity capable of recording acoustic waveforms and high bandwidth digital signal acquisition and storage systems.

6. Summary

Tensile tests were performed on three bridge steels. AE transducers were attached to record AE signals as the steel strained. The more modern bridge steels, A36 and A572, did not produce AE at ambient temperatures. However, specimens of older A7 steel taken from a decommissioned bridge produced AE signals well before the maximum load was reached.

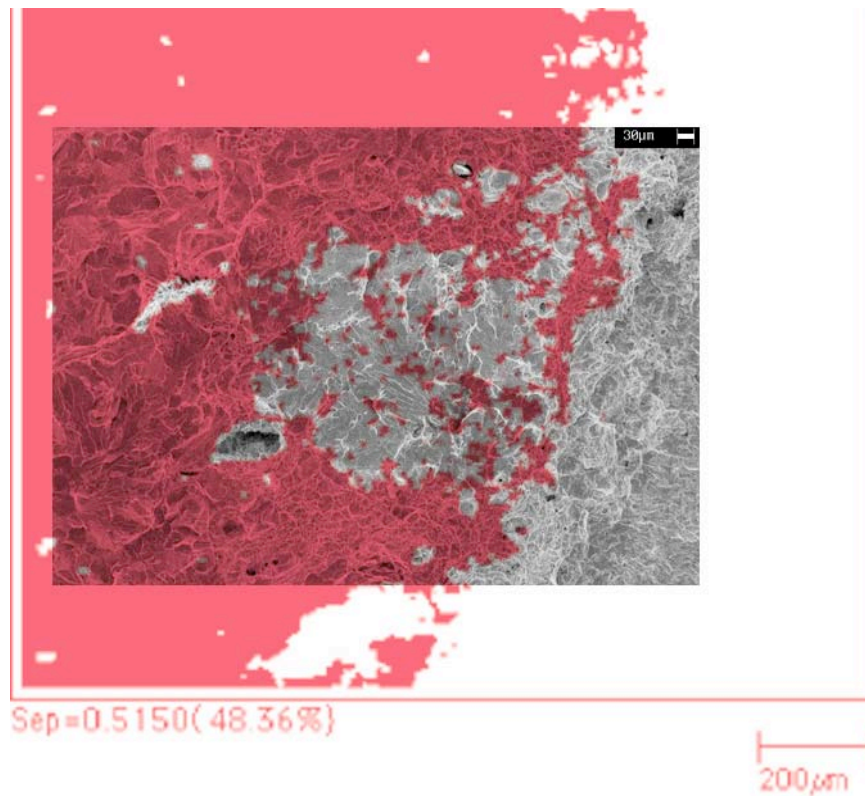


Fig. 10. FAPP at Sep = 0.515 superimposed on the SEM photograph, showing that the gap corresponds to the cleavage facet.

Details of the microcracking occurring in the interior of the A7 specimens were determined with an advanced fractographic procedure. In certain cases individual cleavage crack events could be correlated with AE signals, thus identifying the source of AE and enhancing the prospect of using AE sensors to monitor the structural integrity of older bridges. Additional investigations are needed to confirm these findings and to extract mechanisms and rates of damage from AE waveform data. A7 steel is an attractive material for further studies because of its practical importance and the opportunity it provides to advance interpretability of AE signals.

Acknowledgments

This work was supported by Contract DTFH61-95-X-00043 with the Federal Highway Administration. The authors thank Richard Livingston for providing technical guidance, identifying sources of sample materials, and putting us in touch with people in the bridge industry and with AE researchers. We thank Professor Marvin Hamstad of the University of Denver for guidance in the AE work, and David McColsky at the NIST in Boulder, Colorado for providing specimens and performing ancillary fracture tests.

References

K. Fukaura and K. Ono (2001), "Acoustic Emission Analysis of Carbide Cracking in Tool Steels", *J. Acoustic Emission*, **19**, 91-99.

J.H. Giovanola et al. (1997), "Using Small Cracked Round Bars to Measure the Fracture Toughness of a Pressure Vessel Steel Weldment: A Feasibility Study," *Small Specimen Test Tech*

niques, ASTM STP 1329, W. R. Corwin, S.T. Rosinski and E. van Walle, eds., American Society for Testing and Materials.

M. A. Hamstad and C. M. Fortunko (1995), "Development of Practical Wideband High-Fidelity Acoustic Emission Sensors, "Nondestructive Evaluation of Aging Bridges and Highways," S. Chase, ed., SPIE-The International Society for Optical Engineering, Bellingham, WA. pp. 281-288.

M. Huang, L. Jiang, P. K. Liaw, C. R. Brooks, R. Seeley, and D. L. Klarstrom (1998), "Using Acoustic Emission in Fatigue and Fracture Materials Research," *Journal of Materials*, **50** (11).

T. Kobayashi and D.A. Shockey (1991a), "FRASTA: A New Way to Analyze Fracture Surfaces, Part 1: Reconstructing Crack Histories," *Advanced Materials & Processes*, **140**(5), 28-34.

T. Kobayashi and D.A. Shockey (1991b), "Fracture Analysis Via FRASTA, Part 2: Determining Fracture Mechanisms and Parameters," *Advanced Materials & Processes*, **140**(6), 24-32.

R. A. Livingston, C. M. Fortunko, M. A. Hamstad, T. Kobayashi, D. McColsky, and D. A. Shockey (1996), "Digital Waveform-Based Acoustic Emission System for Nondestructive Testing of Steel Bridges," *Proceedings, 3rd Conference on Nondestructive Evaluation of Civil Structures and Materials*, ed. M. P. Schuller and D. B. Woodham, Atkinson-Noland and Associates, Boulder, CO.

D. W. Prine (1997), "Application of Acoustic Emission and Strain Gauge Monitoring to Bridge Retrofit Evaluation," presented at ASNT Spring Conference, Houston, Texas, March.

Proceedings of the Conference on Nondestructive Evaluation of Bridges (1993), FHWA-RD-93-040A, National Technical Information Service, Springfield VA.

ANALYSIS OF SOURCE LOCATION ALGORITHMS

Part I: Overview and non-iterative methods

MAOCHEN GE

Pennsylvania State University, University Park PA 16802

Abstract

This article and the accompanying one discuss the source location theories and methods that are used for earthquake, microseismic and acoustic emission studies. The present paper provides an overview of the principles of source location methods as well as a detailed analysis of several principal approaches, including triaxial sensor method, zonal location technique and non-iterative algorithms. The accompanying paper is devoted entirely to the iterative methods because of their particular importance. A thorough and in-depth analysis is provided for the derivative and Simplex methods in order to develop a fundamental understanding of the mechanics of these methods.

1. Introduction

An accurate acoustic emission (AE) source location depends on many factors and a suitable source location method is one of them. To have a proper knowledge on source location methods is not just essential for operational reasons, such as data gathering, processing and interpretation. It is probably more significant for monitoring planning. When the event location is a primary concern, a key issue for success is how to achieve the required location accuracy. In order to answer this question, the role of the location method has to be determined. One has to be able to select the most suitable algorithm(s) for the given condition and to be able to evaluate its capability of resolving the anticipated problems.

The goal of this and the accompanying papers is to help readers to establish a perspective view on source location methods. In addition to the detailed analysis of the algorithms themselves, the emphasis is the location principles and mechanics. The present paper discusses how a source location method may be viewed and a simple classification is presented to characterize the hierarchy of location approaches and methods. A detailed analysis is then given to several principal approaches, including triaxial sensor method, zonal location technique and non-iterative algorithms.

The accompanying paper is devoted entirely to the iterative methods because of their particular importance. The focus of the discussion is the derivative and Simplex methods. In order to develop a fundamental understanding for these methods, an in-depth analysis is carried out for a number of problems that are of both theoretical and practical importance. These problems are: concept of nonlinear location, mechanics of iterative methods, stability of location systems, and optimization method and error analysis.

2. An Overview of Source Location Methods

A source location method in this article refers to a mathematical procedure that deduces the data from physical observations to the information of the event origin expressed as hypocenter parameters.

Triaxial sensor approach

A source location method can be viewed in many different ways. In terms of physical information that is utilized, there are two distinctive approaches: the triaxial sensor approach and the arrival time approach. The triaxial sensor approach makes use of two types of physical data: amplitude and arrival time. With this approach an event location is defined by its relative distance and azimuth to the sensor, which are determined by P- and S-wave arrival time difference and the amplitude information in three orthogonal directions. It is called the triaxial sensor approach since 3-component transducers have to be used.

Arrival time approach

The arrival time approach utilizes only arrival time information. While this information is not restricted to specific wave types, P- and S-waves are the ones mostly used. The major advantage of the arrival time approach over the triaxial sensor approach is the reliability of the physical data that it is utilized. Arrival time information is considered much more stable than amplitude information as travel times are less sensitive to the change of the medium properties. It is because of this reason the approach has been used in most location cases.

Point and zonal location

Arrival time methods primarily refer to the algorithms that are designed for the pin-point location accuracy. Because of the extensive use of this type of algorithms, the focus of this article is the representatives of these algorithms. Zonal location, which also uses only arrival times, may be considered a special case of the arrival time approach. Zonal location refers to those methods that are used to identify whether an event is from a predefined zone based on primarily the first-hit sensor location.

The location principle of the arrival time approach is relatively simple. With this approach a number of single-element transducers are needed. These transducers are installed at suitable positions where acoustic emission/microseismic (AE/MS) activity can be effectively detected. The arrival time function is then established for each transducer in terms of observed arrival time, velocity model, and sensor coordinates. The following is the simplest form of this function:

$$\sqrt{(x_i - x)^2 + (y_i - y)^2 + (z_i - z)^2} = v(t_i - t) \quad (1)$$

where, the unknowns, x , y , and z are the coordinates of the source; t is the origin time of the event, x_i , y_i and z_i are the coordinates of the i th transducer, t_i is the arrival time at the i th transducer, v is stress wave propagation velocity, and $i=1, 2, \dots, N, \dots, M$. Here, N denotes the number of unknowns and M denotes the number of equations. In order to solve for the unknowns, it is clear that the condition $M \geq N$ must be satisfied. When $M = N$, we can determine the unknown precisely; when $M > N$, the problem becomes over determined and a regression method has to be used for the optimum solution. Eq. (1) represents arrival time functions that assume a constant velocity model.

Non-iterative algorithms

A set of nonlinear equations as defined by Eq. (1) can be solved either iteratively or non-iteratively. Non-iterative methods refer to those algorithms that solve the source location problem defined by Eq. (1) without invoking any numerical approach.

The non-iterative methods are, in general, simple and easy to apply. Users do not have to worry about many computational problems that they would otherwise have to face, such as choosing the guess solution, setting the convergency criterion, and, especially, handling the problem of divergence. These methods are also quick because of the non-iterative nature. The major shortcoming of these methods is their inflexibility in dealing with velocity models. Eventually, they have to assume the same velocity for all stations. With the consideration of the complexity of arrival types, this assumption severely limits the meaningful applications of these methods. The Inglada's method and the USBM method are representative in this category and will be discussed in this paper.

Iterative algorithms

The iterative approach, on the other hand, is much more flexible in handling arrival time functions. As this capability is essential in dealing with a wide range of practical problems, the iterative approach is of primary importance in source location.

The iterative approach covers a large array of algorithms, from empirically based sequential searching methods to highly sophisticated derivative methods. Geiger's method and the Simplex method are considered most important ones with this approach. These methods will be discussed in the accompanying paper which is entirely devoted on the subject of iterative methods.

A classification of the source location methods based on the above discussion is presented in Fig. 1 and our discussion will closely follow the logic shown by the flow chart. It has to be emphasized that this classification is developed mainly for the convenience of the discussion and should not be interpreted as a serious effort to classify the source location methods.

The detailed discussion on the location algorithms will be split into two papers. The present paper covers the triaxial sensor method, zonal location technique and two non-iterative algorithms: Inglada method and USBM method. The second paper deals exclusively with the subject of iterative algorithms.

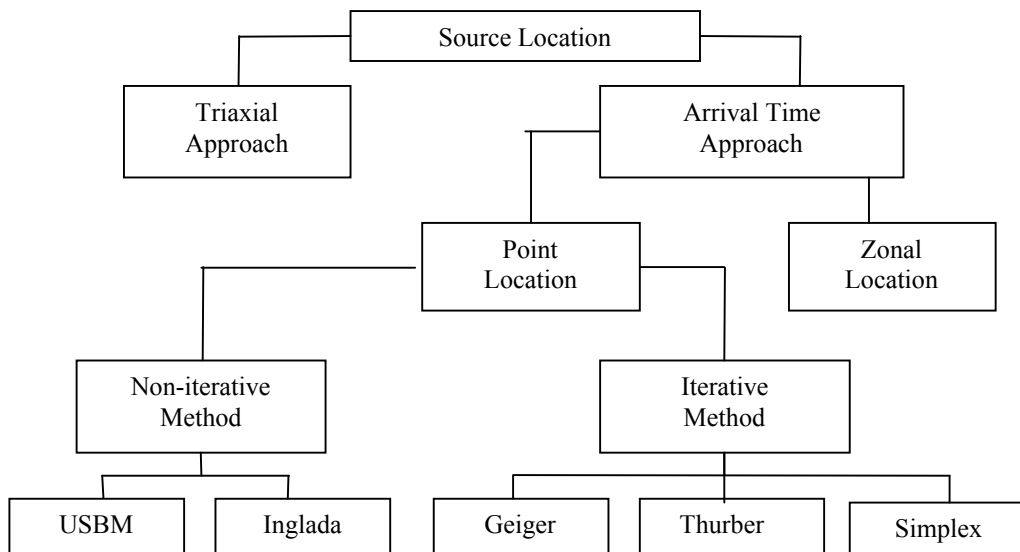


Fig. 1. Classification of AE/MS source location methods.

3. Triaxial Sensor Approach

The triaxial sensor approach is based on the idea that if the spatial position of a point is known, then the spatial position of any other point can be expressed in terms of its relative distance and azimuth to the known point. The unique advantage of this approach is that the source location can be carried out from a single location. The approach is therefore critical for those deep level applications where long drill holes are required for the sensor installation. The approach has been utilized for various deep level applications, such as rockburst study (Brink and Mountfort, 1984), stability of petroleum reserve site (Albright and Pearson, 1979), and geothermal engineering (Albright and Pearson, 1979; Baria and Batchelor, 1989; Niitsuma et al., 1989).

3.1 Location principle

The geometry of the triaxial sensor approach is illustrated in Fig. 2. Here the location of a triaxial sensor, TR, is known. Source S is to be determined in terms of its relative distance, d , and its azimuth (α, β, γ).

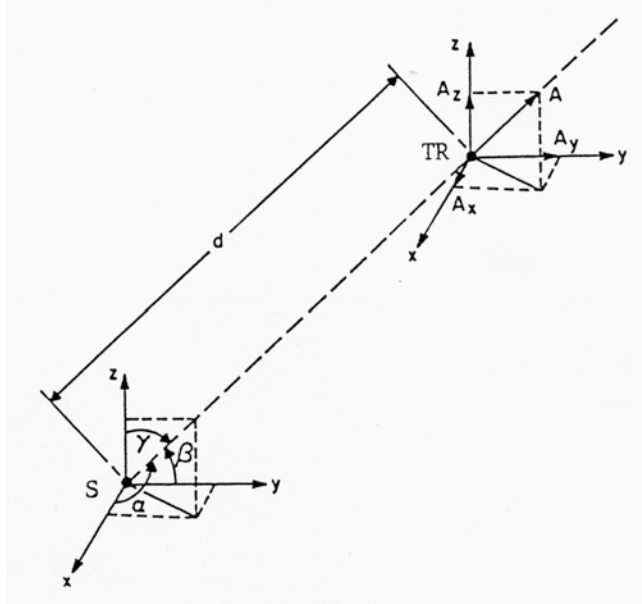


Fig. 2. The geometry associated with triaxial sensor approach (After Hardy, 1986).

Based on the P- and S-wave arrival times, the relative distance can be expressed as

$$d = \frac{v_p v_s}{v_p - v_s} (t_s - t_p) \quad (2)$$

where d is the distance from the source to the sensor, v_p and v_s are the velocities of P- and S-waves, and t_p and t_s are the arrival times of P- and S-waves.

The relative azimuth (α, β, γ) can be determined by the amplitude of the received signals. Assuming that A_x, A_y and A_z are the amplitudes of three mutually orthogonal components of the signal. The direction cosines of this signal relative to the sensor are

$$l = A_x / A \quad m = A_y / A \quad p = A_z / A \quad (3)$$

and

$$A = \sqrt{A_x^2 + A_y^2 + A_z^2} \quad (4)$$

where l , m and p are the direction cosines of the signal relative to the sensor. The relative azimuth is simply

$$\begin{aligned}\alpha &= \cos^{-1}(l) \\ \beta &= \cos^{-1}(m) \\ \gamma &= \cos^{-1}(p)\end{aligned}\tag{5}$$

Using signal amplitudes to determine the relative azimuth is based on the fact that, for a compressional wave, the first particle motion is in the direction of propagation (Hardy, 2003).

3.2 Least squares solution for azimuth

When there are n sets of observations, such as

$$\begin{aligned}l_i &= A_{xi} / A_i, \\ m_i &= A_{yi} / A_i, \\ p_i &= A_{zi} / A_i,\end{aligned}\quad i = 1, 2, \dots, n$$

the best solution defined by the least squares method is:

$$\begin{aligned}\frac{\partial}{\partial l} \left(\sum_{i=1}^n (l - A_{xi} / A_i)^2 \right) &= 0 \\ \frac{\partial}{\partial m} \left(\sum_{i=1}^n (m - A_{yi} / A_i)^2 \right) &= 0 \\ \frac{\partial}{\partial p} \left(\sum_{i=1}^n (p - A_{zi} / A_i)^2 \right) &= 0.\end{aligned}$$

where l , m , and p are the best fit for l_i s, m_i s and p_i s. Solving the above equations, we have

$$\begin{aligned}l &= \frac{\sum_{i=1}^n (A_{xi} / A_i)}{n} \\ m &= \frac{\sum_{i=1}^n (A_{yi} / A_i)}{n} \\ p &= \frac{\sum_{i=1}^n (A_{zi} / A_i)}{n}\end{aligned}\tag{6}$$

3.3 Discussion

Triaxial sensor approach is found extremely useful for those deep level applications where borehole drilling is required for the sensor installation. Since borehole drilling is a very expensive operation, it has to be minimized. With the triaxial sensor approach, the required location accuracy may be achieved with a single or few sensors which effectively reduces the request for borehole drillings.

In addition to its cost benefit for deep level applications, there are two technical advantages associated with the triaxial sensor approach. First, it improves the stability of the source location solutions for those outside array events as the approach uses both P- and S- wave arrivals. Second, it allows one to analyze the status of the ground motion at the sensor location, which is critical for studying event magnitude and source mechanism.

The major technical problem associated with the triaxial sensor approach is the stability of the azimuthal angles as amplitudes are much more sensitive to material properties and structures than travel times. A technique that could improve the problem is called hodogram (Doebelin, 1975). With this technique, amplitude data from two components are cross-plotted and an elliptical figure is obtained. The major axis of the ellipse is considered the direction of wave propagation in the plane. Figure 4 shows the hodogram of particle motions detected by two horizontal sensors.

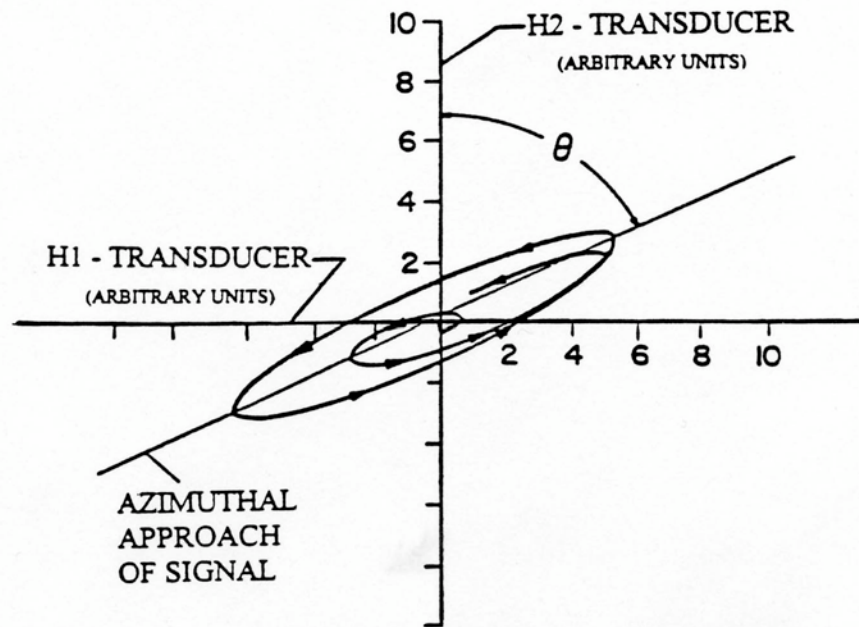


Fig. 3. Hodogram of particle motions detected by two horizontal sensors (after Hardy, 2003).

4. Zonal Source Location

Zonal location is a source location technique that identifies a predefined zone as the event location based on, primarily, the location of the first triggered sensor. It is the simplest form to use arrival times for source location. If the network is relatively dense with a good coverage, the technique offers a quick and reliable idea on the general area where the event took place.

The concept of zonal location and its application to large structures originated from AE studies in material science (Arrington, 1984; Fowler, 1984; Tiede and Eller, 1982; and Hutton and Storpik, 1976). The idea of the zonal location is demonstrated in Figure 4. Here the monitoring region is divided into a number of primary zones, and each zone is associated with a particular station which is the first one to be triggered when the source is located within the area. Based on the locations of the later triggered stations, the primary zone is further divided into smaller ones, such as the second-hit sub-zone and the third-hit sub-zone as illustrated in the figure.

The sub-zones provide the better idea on the relative azimuth position of the source in the primary zone, but offers no improvement in the radial direction. The problem may be overcome by two simple techniques. The first one is to compare the observed arrival time difference between the first and the later triggered stations with the associated theoretical limit. The theoretical limit is the distance between two sensors divided by the velocity. The ratio of the

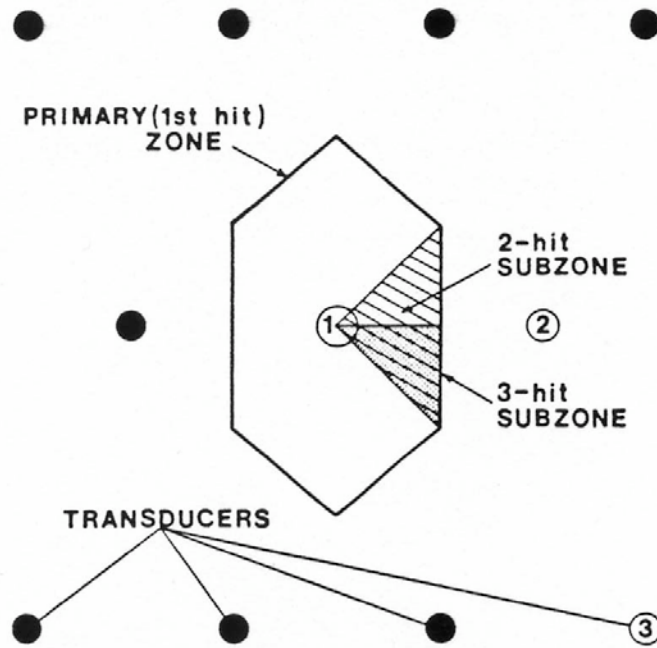


Fig. 4 The geometry associated with the zonal location method (after Hardy, 2003).

observed arrival time difference to the theoretical limit is an indication of the event location. The larger the ratio, the closer the source to the first triggered station. If the ratio reaches to one, the source is at or behind the first triggered station. If it is zero, the source is on the central line between the two stations, or on the board of the primary zone. The second technique is to use the P- and S-wave arrival time difference to estimate the distance from the first station, which can be done by using Eq. (2).

In comparison with the methods designed for the pin-point location purpose, the zonal location approach has two distinctive advantages. First it does not need to determine the precise ray trace, which is often very difficult when the structure under the study is complicated. It is largely because of this reason that the zonal location becomes one of the primary methods used in the non-destructive testing industry. The other advantage of the method is that it posts no request on the minimum number of stations to be triggered. Lack of the sufficient stations for precise source location is a frequently observed problem. When this is the case, the zonal location becomes the only alternative.

An important assumption made with the zonal location approach is that all stations are triggered by the same wave type, presumably by P-waves. This, however, may not necessarily be the case. In fact, AE systems are often triggered by S-waves instead of P-waves. This is because amplitudes of P-waves are often much lower than that of S-waves, and this phenomenon is shown in Figure 5 by an AE signal recorded by a triaxial sensor.

In addition to the S-wave triggering, experimental conditions may also play an important role. For instance, it was observed by the author in the test of a water-filled tank car that the sensor at the opposite side of the calibrated source was triggered instead of those closer ones on the same side. This is because the water-borne P-wave that triggered the sensor at the opposite side was less attenuated while the metal-borne waves that had supposedly triggered the nearby sensors were largely absorbed by the water.

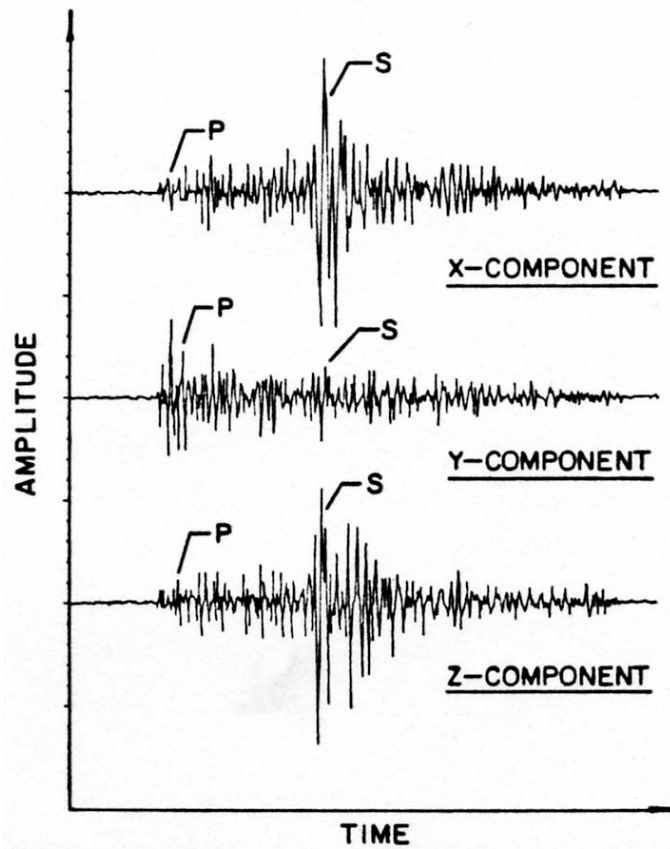


Fig. 5. AE signals detected using a triaxial monitoring transducer (after Hardy, 2003).

It is understood from the above discussion that the zonal location technique, as any other source location methods, is subject to errors and the causes for the error are not uncommon. Therefore, the solution by the zonal location should not be automatically assumed correct and should be examined if it is possible.

5. Inglada's Method

We now begin our discussion on non-iterative methods. Non-iterative methods are an important category in the family of location algorithms. They are simple and easy to use, and, in fact, the basic ones used by AE practitioners. Inglada's method and USBM method are considered the representatives in this category and we discuss Inglada's method first.

5.1 Algorithm

Inglada's method (Inglada, 1928) is a non-iterative, analytical solution of the source location problem defined by Eq. (1). The method is best suited for simple source location problems where the number of sensors used is minimum and a constant velocity model can be assumed.

Inglada method starts with squaring Eq. (1):

$$(x_i - x)^2 + (y_i - y)^2 + (z_i - z)^2 = v^2(t_i - t)^2 \quad (7)$$

for $i = 1, 2, 3$, and 4 and then linearizes the system by subtracting the first equation from three remaining ones, which yields:

$$a_i x + b_i y + c_i z = e_i + f_i t \quad (8)$$

where

$$a_i = x_i - x_1$$

$$b_i = y_i - y_1$$

$$c_i = z_i - z_1$$

$$e_i = 0.5(R_i^2 - R_1^2 - v^2(t_i^2 - t_1^2))$$

$$f_i = v^2(t_i - t_1)$$

and

$$R_i^2 = x_i^2 + y_i^2 + z_i^2$$

$$R_1^2 = x_1^2 + y_1^2 + z_1^2$$

for $i = 2, 3$, and 4 .

Three linear equations defined in (8) can be solved for x , y and z in terms of t by using Cramer's rule. The solution is as follows:

$$\begin{aligned} x &= \frac{M_1 + N_1 t}{D} \\ y &= \frac{M_2 + N_2 t}{D} \\ z &= \frac{M_3 + N_3 t}{D} \end{aligned} \quad (9)$$

where D is the determinant given by

$$D = \begin{bmatrix} a_2 & b_2 & c_2 \\ a_3 & b_3 & c_3 \\ a_4 & b_4 & c_4 \end{bmatrix}.$$

M_j and N_j , for $j = 1, 2, 3$, are also the determinants. They are similar to D , but with the j th column of D replaced by (e_2, e_3, e_4) and (f_2, f_3, f_4) , respectively.

Substitute three equations defined in (9) back to one of the equations defined in (7). Since x , y and z in (9) are all expressed in terms of t , this back substitution yields a second order equation of t with the form

$$At^2 + Bt + C = 0 \quad (10)$$

where A , B and C are constants.

Eq. (10) is a quadratic function of t and there are two solutions, say, t_{01} and t_{02} . Substituting t_{01} and t_{02} into Eq. (9), the corresponding solutions are $(x_{01}, y_{01}, z_{01}, t_{01})$ and $(x_{02}, y_{02}, z_{02}, t_{02})$, respectively.

5.2 Identifying non feasible solution

Usually, one of these solutions will not be physically feasible and can be easily identified. For instance, the solution can be immediately eliminated if its calculated origin time is later than

the observed arrival time(s). Otherwise, a further check is necessary in order to determine the true source location. This is usually done by substituting the solutions back into the nonlinear system defined in Eq. (1). There is, however, the possibility that both the solutions satisfy those nonlinear equations, which are called multiple solutions. When the problem of multiple solutions is encountered, the arrival time data from an additional sensor is required to identify the true source.

5.3 Multiple solutions

The problem of multiple solutions is not caused by the Inglada's method. Rather, it is due to the non-linear nature of the location formulas. It can be shown that the problem will occur only when the minimum number of sensors is utilized for location computation (Ge, 1988). Figure 6 illustrates the multiple solutions associated with a 2-dimensional array.

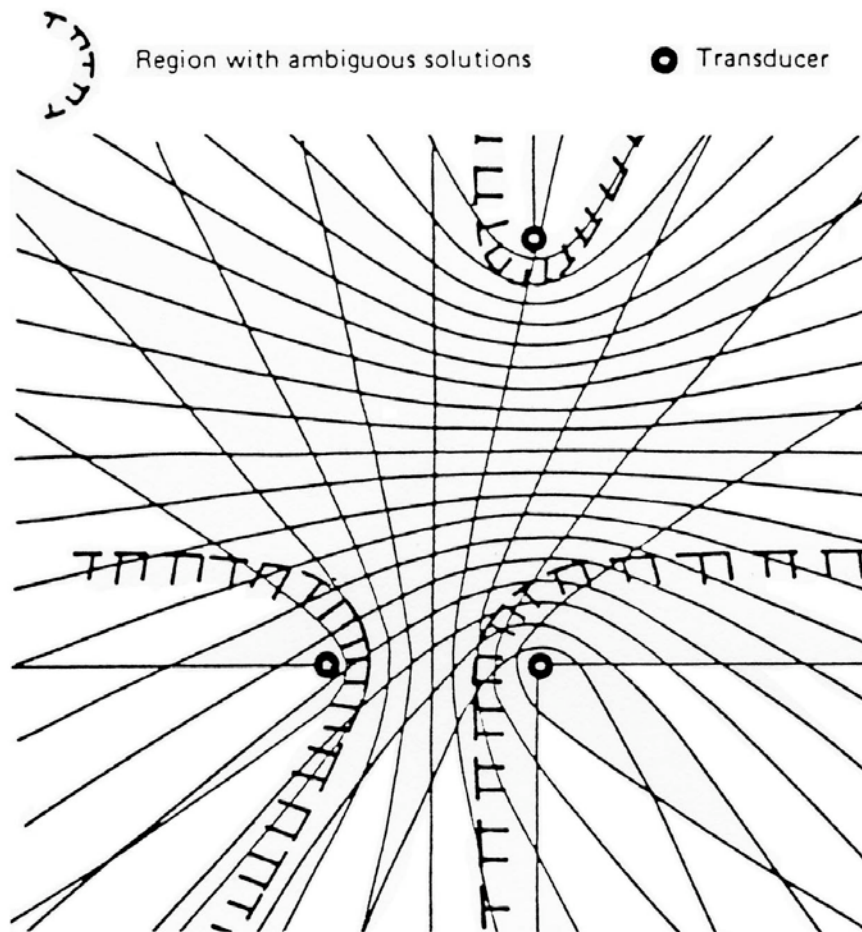


Fig. 6. Distribution of multiple solutions (After Rindorf, 1981)

5.4 Application conditions

Inglada's method is simple and easy to use. In fact, it is probably the simplest algorithm for solving a set of equations defined by Eq. (1). Users however need to be aware of its operational conditions. First, it is understood from the deriving process that the algorithm assumes the same velocity for all stations. This assumption may restrict the meaningful use of the method in many cases and should be validated before its application.

Second, the algorithm uses only a minimum number of sensors that is mathematically required for the pin-point location, that is, the number of equations is equal to the number of unknowns. Because of this requirement, no optimization method can be applied to the algorithm.

From an error control point of view, one should use as many sensors as possible. There are two important reasons. First, the location accuracy is fundamentally determined by the sensor array geometry (Ge, 1988). Using more sensors in general will lead to the better array geometry. Second, the data set is statistically more reliable when more sensors are used. Christy (1982) demonstrated that the algorithm incorporated with the least squares method would yield the better source location accuracy than Inglada method. For these reasons, one should consider to use the algorithms with the optimization capability if the location data is available from sensors that are more than the minimum.

6. The USBM Method

The USBM method is a non-iterative algorithm for the source location problem defined by Eq. (1). It was developed in the early 1970s by the researchers at the United States Bureau of Mines (USBM). The development of this method was part of the Bureau of Mines' effort to make the acoustic emission/microseismic (AE/MS) technique an effective engineering tool for determining the stability of rock structures. The method was first published in 1970 and was further modified in 1972 (Leighton and Blake, 1970; Leighton and Duvall, 1972). Since then it has become the major mine-oriented AE/MS source location method used in North America.

6.1 Algorithm

Let D_i represent the distance from the source to the i th transducer,

$$D_i = \sqrt{(x_i - x)^2 + (y_i - y)^2 + (z_i - z)^2} \quad (11)$$

and rewrite Eq. (1) as

$$D_i = v(t_i - t) \quad (12)$$

Subtract the first equation from the rest which are all defined by Eq. (12),

$$D_i - D_1 = v(t_i - t_1) \quad (13)$$

where, $i = 2, 3, \dots, m$. Squaring and simplifying the above equation, this yields

$$d_i + \frac{e_i}{d_i} - \frac{2(a_i x + b_i y + c_i z)}{d_i} = -2D_1 \quad (14)$$

where

$$a_i = x_1 - x_i$$

$$b_i = y_1 - y_i$$

$$c_i = z_1 - z_i$$

$$d_i = v(t_i - t_1)$$

$$e_i = x_1^2 + y_1^2 + z_1^2 - (x_i^2 + y_i^2 + z_i^2)$$

The non-linear system defined by (14) can be linearized by subtracting the 2nd equation from the rest of them. This process yields

$$f_{i,1}x + f_{i,2}y + f_{i,3}z = h_i + g_i v^2 \quad (15)$$

where

$$\begin{aligned}
 f_{i,1} &= 2\left(\frac{a_2}{t_2} - \frac{a_i}{t_i}\right) \\
 f_{i,2} &= 2\left(\frac{b_2}{t_2} - \frac{b_i}{t_i}\right) \\
 f_{i,3} &= 2\left(\frac{c_2}{t_2} - \frac{c_i}{t_i}\right) \\
 g_i &= t_2 - t_i \\
 h_i &= \frac{e_2}{t_2} - \frac{e_i}{t_i} \\
 & \quad i = 3, 4, \dots, m.
 \end{aligned}$$

Eq. (15) defines a linear system.

In matrix notation, the linear system defined by Eq. (15) can be written as

$$\mathbf{Ax} = \mathbf{b} \quad (16)$$

where

$$\mathbf{A} = \begin{bmatrix} f_{3,1} & f_{3,2} & f_{3,3} \\ \vdots & & \vdots \\ f_{m,1} & f_{m,2} & f_{m,3} \end{bmatrix}, \quad \mathbf{x} = \begin{bmatrix} x \\ y \\ z \end{bmatrix}, \quad \mathbf{b} = \begin{bmatrix} h_3 + g_3 v^2 \\ \vdots \\ h_m + g_m v^2 \end{bmatrix}.$$

6.2 The least squares solution

It is important to note that the USBM method requires the arrival times from at least $(n + 1)$ stations, where n is the number of unknowns. For instance, if there are five stations, \mathbf{A} is a 3 by 3 matrix and unknowns, x , y and z , can be solved exactly. If there are arrival times from more than five stations, the source location has to be defined statistically. With the USBM method, the error is conventionally defined as the sum of squares of residuals and the corresponding least squares solution is (Strang, 1980):

$$\mathbf{A}^T \mathbf{Ax} = \mathbf{A}^T \mathbf{b} \quad (17)$$

or

$$\mathbf{x} = (\mathbf{A}^T \mathbf{A})^{-1} \mathbf{A}^T \mathbf{b}$$

The origin of time is not given in \mathbf{x} ; but it can be obtained by substituting \mathbf{x} back into (1).

6.3 Velocity as an unknown

The velocity can be estimated by the USBM method and this can be done by considering v^2 as an unknown variable in Eq. (15) and moving $g_i v^2$ from the right hand side of the equation to the left, such as:

$$f_{i,1}x + f_{i,2}y + f_{i,3}z - g_i w = h_i \quad (18)$$

where $w = v^2$.

While it is an additional freedom to treat the velocity as an unknown, an extra caution should be exercised to use this feature. The main reason is the errors and uncertainties associated with the arrival time information. If the velocity is treated as an unknown, we have the less chance to isolate the arrival time errors to the places where they occur. Instead, they may be “accommodated” by a false velocity value, creating an even worse situation.

6.4 Discussion

The USBM method is a fairly straight forward algorithm for solving a set of non-linear equations defined by (1). With this method the origin time is eliminated by subtracting the first equation from the rest. The resulting equations are then linearized and form a linear system.

There are two basic conditions to use the USBM algorithm. First the method assumes the same velocity for all stations, and second it requires at least one more equation than the number of unknowns, that is, the condition $m \geq n + 1$ must be satisfied, where m and n denote the number of equations and unknowns, respectively. For instance, we need the arrival time information from at least 5 stations in order to solve a problem of 4 unknowns, such as x , y , z , and t .

The major advantage of the USBM method over the Inglada’s method is that all available arrival time information can be used simultaneously for the source location calculation. This allows the statistic analysis to be carried out, an important approach to improve the location accuracy.

There is another similar algorithm which is called the ISA Mine's method, and readers may refer to Godson and McKavanagh (1980) for details.

7. Conclusions

In terms of the physical data utilized for source location, we have two distinctive approaches: the triaxial sensor approach and the arrival time approach. The importance of the triaxial sensor approach may be viewed from two perspectives. First, the source location can be carried out from a single sensor location, which becomes a particular important advantage when sensor installation is expensive. Second, it provides the data that allows one to characterize the status of stress wave at the point, which is critical for the further study of the source mechanism and source parameters.

The limited use of the triaxial sensor approach is primarily due to the two practical reasons. First, the amplitude data is more susceptible to material structures and properties, and therefore, the method is less stable than the one that uses only arrival times. Second, three single-element sensors with spread locations in general give the much better data for source location than a triaxial sensor. Therefore, the arrival time approach is normally the choice from a cost-benefit point of view unless there are some other special considerations.

Zonal location technique is considered a special case of the arrival time approach since all other methods in this category are for pin-point location purpose. Zonal location technique is simple and easy to use. Users, however, still should pay attention to arrival types. The technique is based on the assumption that all sensors are triggered by the same type of wave. As it was discussed in the paper, this might not be the case.

There are two major branches within the arrival time approach: non-iterative and iterative. The “ Δt ” algorithms that are conventionally called and used by AE practitioners are non-iterative. Inglada and USBM methods are the representatives in this category. Non-iterative methods are simple and easy to use in that they require little interaction from users. The major difference between these two methods is that Inglada method is limited to the minimum number of sensors while USBM method does not subject to this limitation. A common problem with these two methods is the assumption of a single velocity, which severely restricts their valid applications.

The solution to the problem of the single velocity assumption is to use the iterative methods, which are discussed in the accompanying paper: *Analysis of source location algorithms Part II: iterative methods*.

Acknowledgments

I am grateful to Dr. Kanji Ono for his encouragement to write my research experience in the area. I thank Dr. R. Hardy for his thorough review and the anonymous reviewer for his comments and suggestions to improve the manuscript.

References

Albright, J. N. and C. F. Pearson (1979). Microseismic monitoring at Byran Mound strategic petroleum reserve, Internal Report, Los Alamos Scientific Laboratory, Los Alamos, March 1979.

Albright, J. N. and C. F. Pearson (1982). Acoustic emission as a tool for hydraulic fracture location: experience at the Fenton Hill hot dry rock site, *Society Petroleum Engineering Journal*, August 1982, 523-530.

Arrington, M., (1984). In-situ acoustic emission monitoring of a selected node in an offshore platform, Proc. 7th International Acoustic Emission Symposium, Sendai, Japan, October 1984, 381-388.

Baria, R. K. and A. S. Batchelor (1989). Induced seismicity during the hydraulic stimulation of a potential hot dry rock geothermal reservoir, *Proc. 4th Conference on Acoustic Emission/Microseismic activity in geologic structures and materials*, The Pennsylvania State University, October 1985, Trans Tech Publications, Clausthal-Zellerfeld, Germany 327-325.

Doebelin, E. O., (1975). Measurement systems, McGraw-Hill Book Company, New York, 591-593.

Christy, J. J., (1982). A comparative study of the “Miner” and least squares location technique as used for the seismic location of trapped coal miners, M.S. Thesis, The Pennsylvania State University, College of Earth and Mineral Sciences, University Park, Pennsylvania, August 1982.

Fowler, T. J., (1984). Acoustic emission testing of chemical process industry vessels, Proc. 7th International Acoustic Emission Symposium, Sendai, Japan, October 1984, 421-449.

Ge, M., (1988). Optimization of transducer array geometry for acoustic emission/ microseismic source location, Ph.D. Thesis, The Pennsylvania State University, College of Earth and Mineral Sciences, University Park, Pennsylvania, August 1982.

- Godson, R. A., M. C. Gridges and B. M. Mckavanagh (1980). A 32-channel rock noise source location system, *Proc. 2nd Conference on Acoustic Emission/Microseismic activity in geologic structures and materials*, The Pennsylvania State University, November 1978, Trans Tech Publications, Clausthal-Zellerfeld, Germany 117-161.
- Hardy, H. R. (1986). Source location velocity models for AE/MS field studies in geologic materials, *Proc. 8th International Acoustic Emission Symposium*, Tokyo, Japan, October 1986, Japanese Society for Non-Destructive Testing, Tokyo, 365-388.
- Hardy, H. R. (2003). *Acoustic emission/microseismic activity*, A.A. Balkema, Lisse, Netherlands.
- Hutton, P. H. and J. R. Skorpik (1976). A simplified approach to continuous AE monitoring using digital memory storage, *Proc. 3rd International Acoustic Emission Symposium*, Tokyo, Japan, September 1976, 152-166.
- Inglada, V., (1928). Die berechnung der herdkoordinaten eines nahbebens aus den eintrittszeiten der in einigen benachbarten stationen aufgezeichneten P-oder P-wellen, *Gerlands Beitrage zur Geophysik* 19, 73-98.
- Leighton, F. and W. Blake (1970). Rock noise source location techniques, USBM RI 7432.
- Leighton, F. and W. I. Duvall (1972). A least squares method for improving rock noise source location techniques, USBM RI 7626.
- Niitsuma, H., K. Nakatsuka, N. Chubachi, H. Yokoyama, and M. Takanohashi (1989). Downhole AE measurement of a geothermal reservoir and its application to reservoir control, *Proc. 4th Conference on Acoustic Emission/Microseismic activity in geologic structures and materials*, The Pennsylvania State University, October 1985, Trans Tech Publications, Clausthal-Zellerfeld, Germany 327-325.
- Rindorf, H. J., (1981). Acoustic emission source location, Bruel & Kjaer, *Technical Review*, No. 2.
- Strang, G. (1980). *Linear algebra and its applications*, Academic Press Inc., New York, New York.
- Tiede, D. A. and E. E. Eller (1982). Sources of error in AE location calculations, *Proc. 6th International Acoustic Emission Symposium*, Susono, Japan, October/November 1982, 155-164.

ANALYSIS OF SOURCE LOCATION ALGORITHMS

Part II: Iterative methods

MAOCHEN GE

Pennsylvania State University, University Park PA 16802

Abstract

Iterative algorithms are of particular importance in source location as they provide a much more flexible means to solve nonlinear equations, which is essential in order to deal with a wide range of practical problems. The most important iterative algorithms are Geiger's method and the Simplex method. This article provides an overview of iterative algorithms as well as an in-depth analysis of several major methods.

1. Introduction

In Part I, we discussed the non-iterative location methods. A restriction that severely limits the application of these methods is the assumption of a single velocity for all channels. This assumption is not arbitrary or just for convenience; it is necessary in order to keep the source location equations in the simplest form so that they can be solved non-iteratively. In other words, the assumption is a reflection of an inherent difficulty associated with non-iterative location methods. If a single velocity model is not suitable, as in most cases, we have to turn to an iterative method.

While the associated searching strategies may vary significantly, iterative methods in general refer to those algorithms that start from an initial solution, commonly called a guess or trial solution. This trial solution is tested by the given conditions, and then updated by the predefined schemes, which subsequently forms a new trial solution. Therefore, iterative methods, in essence, are a process of testing and updating trial solutions.

An iterative method is distinguished by its updating scheme, which determines its efficiency as well as its other major characters. While there are many different schemes, the ones that are truly significant both theoretically and practically are few for the purpose of source location. The object of this article is to provide an in-depth analysis of these methods. But first we will give a brief review on the basic searching approaches.

2. An Overview on Basic Searching Approaches

The iterative methods used for source location fall into several basic categories, which are derivative, sequential, genetic and Simplex. A brief discussion of these approaches is given as follow.

Derivative approach

Derivative approach refers to those methods that use the derivative information to update trial solutions. Derivative approach is a classical means in mathematics for solving nonlinear problems and is probably one of the most widely used numerical approaches for this purpose. "Root finding" by derivatives, an elementary topic in calculus, is such an example.

Derivative methods update their trial solutions based on the nonlinear behavior information at the trial solution as given by derivatives. This searching mechanism makes derivative methods far more efficient than any other iterative methods.

The derivative algorithms used for source location include Geiger's method (Geiger, 1910, 1912) and Thurber's method (Thurber, 1985). The difference between these two methods is that the Geiger's method uses the first order derivatives while the Thurber's method uses both the first and second order derivatives. Mathematically, Geiger's method is an application of Gauss-Newton's method (Lee and Stewart, 1981) and Thurber's method an application of Newton's method (Thurber, 1985).

Geiger's method is probably the most important source location method, and has been used almost exclusively for local earthquake locations. Understanding this method is important for both theoretical and practical reasons and we will give a detailed discussion on this method. We will also discuss Thurber's method. In addition to the fact that Thurber's method constitutes a significant derivative approach, the discussion of this method will help us understand the derivative approach as a whole.

Sequential searching algorithms

Sequential searching algorithms here refer to those methods that partition the monitoring volume into smaller blocks and study these blocks sequentially. With these methods, each block, which is represented by either the center of the block or other feature locations, is considered as a potential AE source. The block may be further refined in the searching process. While the approach is extremely simple, easy to use, and easy to modify, the main problem is inefficiency, which essentially blocks its application potential for problems requiring the good location accuracy. For instance, if we would like to achieve 1 mm location accuracy on a 1 cubic meter block, the points that to be searched are in the order of one billion. In contrast, it may take only a few iterations for Geiger's method to achieve this accuracy.

Simplex algorithm

A notable problem with high efficiency derivative algorithms is divergence, which could become very severe if the associated system is not stable. Sequential searching algorithms, on the other hand, exhibit very stable solution process, although they are just too slow. A method that comes in between is the Simplex algorithm, which is quite efficient while showing very stable characteristics.

The Simplex algorithm is a robust curve fitting technique developed by Nelder and Mead (1965). It was introduced for the source location purpose in late 1980s by Prugger and Gendzwill (Prugger and Gendzwill, 1988; Gendzwill and Prugger, 1989). The mathematical procedures and related concepts in error estimation for this method were further discussed by Ge (1995). Because of the rare combination of efficiency and stability, the Simplex algorithm is suited for a wide range of problems and has rapidly become a primary source location method. We will give a detailed discussion on this method.

Genetic Algorithm

The genetic algorithm was developed by Holland (1975). It is an optimization technique that simulates natural selection in that only the "fittest" solutions survive so that they can create even better answers in the process of reproduction. The algorithm was applied by a number of researchers for earthquake locations (Kennett and Sambridge, 1992; Sambridge and Gallagher,

1993; Billings et al., 1994, Xie et al., 1996). While the algorithm seems very flexible for incorporating various source location conditions, it is less conclusive on its efficiency and accuracy. The viability of the algorithm for source location will largely depend on how these questions are answered.

3 Geiger's Method

Geiger's method, developed at the beginning of the last century (Geiger, 1910, 1912), is the classical source location method by all accounts. In addition to its long history, the method is the best known and most widely used source location method. In seismology, it is used almost universally for local earthquake locations.

3.1 Algorithm

Geiger's method (Geiger, 1910, 1912) is an example of the Gauss-Newton's method (Lee and Stewart, 1981), a classical algorithm for solving nonlinear problems. The method is discussed here in terms of the first-degree Taylor polynomials and the least-squares solution to an inconsistent linear system.

Let $f_i(\mathbf{x})$ represent the arrival time function associated with the i th sensor, where \mathbf{x} denotes the hypocenter parameters:

$$\mathbf{x} = (x, y, z, t)^T. \quad (1)$$

The unknowns, x , y and z , are the coordinates of an event and t is the origin time of this event.

Expand $f_i(\mathbf{x})$ at a nearby location, \mathbf{x}_0 , and express the expansion by the first-degree Taylor polynomial:

$$f_i(\mathbf{x}) = f_i(\mathbf{x}_0 + \delta\mathbf{x}) = f_i(\mathbf{x}_0) + \frac{\partial f_i}{\partial x} \delta x + \frac{\partial f_i}{\partial y} \delta y + \frac{\partial f_i}{\partial z} \delta z + \frac{\partial f_i}{\partial t} \delta t \quad (2)$$

where

$$\mathbf{x} = \mathbf{x}_0 + \delta\mathbf{x},$$

$$\mathbf{x}_0 = (x_0, y_0, z_0, t_0)^T,$$

and

$$\delta\mathbf{x} = (\delta x, \delta y, \delta z, \delta t)^T. \quad (3)$$

Eq. (2) may also be expressed in vector notation:

$$f_i(\mathbf{x}) = f_i(\mathbf{x}_0 + \delta\mathbf{x}) = f_i(\mathbf{x}_0) + \mathbf{g}_i^T \delta\mathbf{x} \quad (4)$$

where \mathbf{g}_i^T is the transpose of the gradient vector \mathbf{g}_i and is defined by

$$\mathbf{g}_i^T = \nabla f_i(\mathbf{x}) = \left(\frac{\partial f_i}{\partial x}, \frac{\partial f_i}{\partial y}, \frac{\partial f_i}{\partial z}, \frac{\partial f_i}{\partial t} \right) \quad (5)$$

In source location, the nearby location, \mathbf{x}_0 , is conventionally called *guess* or *trial* solution. Since the trial solution is either assigned by users or generated from the previous iteration, it is always known at the beginning of each iteration. As such, $f_i(\mathbf{x}_0)$ is also a known quantity and is called *calculated arrival time*. The term *calculated arrival time* reflects the fact that this quantity is obtained by calculation, assuming the trial solution, \mathbf{x}_0 , as the hypocenter.

The term on the left hand side of Eq. (2), $f_i(\mathbf{x}_\theta + \delta\mathbf{x})$, represents the arrival time recorded at the i th sensor, which is conventionally termed *observed arrival time*. As such, the physical meaning of Eq. (2) is that an observed arrival time is expressed by the arrival time calculated from a nearby location, and by

$$\frac{\partial f_i}{\partial x} \delta x + \frac{\partial f_i}{\partial y} \delta y + \frac{\partial f_i}{\partial z} \delta z + \frac{\partial f_i}{\partial t} \delta t,$$

a correction factor, which is a function of the partial derivatives of the hypocenter parameters. All the partial derivatives of the arrival time function are known quantities here as they can be numerically evaluated based on the trial solution.

In solving a system of the equations defined by Eq. (2), our goal is to find an \mathbf{x}_θ , such that the calculated arrival times will best match the observed arrival times so that \mathbf{x}_θ can be considered as the hypocenter of the event. This is done in a self correction process: the trial solution is updated at the beginning of each iteration by adding $\delta\mathbf{x}$, known as the correction vector, obtained from the previous iteration.

For the convenience of the solution for $\delta\mathbf{x}$, we rearrange Eq. (2) into the form:

$$\frac{\partial f_i}{\partial x} \delta x + \frac{\partial f_i}{\partial y} \delta y + \frac{\partial f_i}{\partial z} \delta z + \frac{\partial f_i}{\partial t} \delta t = \gamma_i \quad (6)$$

where

$$\gamma_i = t_{oi} - t_{ci}, \quad (7)$$

$$t_{oi} = f_i(\mathbf{x}),$$

and $t_{ci} = f_i(\mathbf{x}_\theta)$.

Here, γ_i is known as *channel residual*.

In matrix notation, a system defined by Eq. (6) can be written:

$$\mathbf{A}\delta\mathbf{x} = \boldsymbol{\gamma} \quad (8)$$

where

$$\mathbf{A} = \begin{bmatrix} \frac{\partial f_1}{\partial x} & \frac{\partial f_1}{\partial y} & \frac{\partial f_1}{\partial z} & \frac{\partial f_1}{\partial t} \\ \vdots & \vdots & \vdots & \vdots \\ \frac{\partial f_m}{\partial x} & \frac{\partial f_m}{\partial y} & \frac{\partial f_m}{\partial z} & \frac{\partial f_m}{\partial t} \end{bmatrix} \quad \delta\mathbf{x} = \begin{bmatrix} \delta x \\ \delta y \\ \delta z \\ \delta t \end{bmatrix} \quad \boldsymbol{\gamma} = \begin{bmatrix} \gamma_1 \\ \vdots \\ \gamma_m \end{bmatrix}$$

The least squares solution to the system defined by Eq. (8) satisfies (Strang, 1980)

$$\mathbf{A}^T \mathbf{A} \delta\mathbf{x} = \mathbf{A}^T \boldsymbol{\gamma} \quad (9)$$

or

$$\delta\mathbf{x} = (\mathbf{A}^T \mathbf{A})^{-1} \mathbf{A}^T \boldsymbol{\gamma}$$

The total effect of the mismatch between the observed and calculated arrival times is called the event residual or simply residual. The event residual that is defined by the least-squares solution is (Ge, 1985):

$$Res = \sqrt{\frac{\boldsymbol{\gamma}^T \boldsymbol{\gamma}}{m - q}} \quad (10)$$

where m is the number of equations and q is the degree of freedom. For the number of hypocenter parameters defined by Eq. (1), the degree of freedom is 4.

Now the correction vector, $\boldsymbol{\delta x}$, has been found and it can be added to the previous trial solution to form a new trial solution. This process is repeated until the given error criterion is fulfilled, and the final trial solution is then regarded as the true source.

3.2 Implementation

The algorithm of Geiger's method discussed in the previous section was developed for general arrival time functions, that is, we can use this algorithm for any arrival time functions as far as the functions and their partial derivatives can be evaluated. To further enhance our understanding of this algorithm, we now discuss the implementation of Geiger's method through examples.

The implementation of Geiger's method is a three-step process:

- establishing arrival time functions,
- data preparation, and
- solving a system of simultaneous equations.

Establishing arrival time functions

The first task in implementing the Geiger's method is establishing arrival time functions. Arrival times are affected by many factors. Categorically, there are three major ones: structure and composition of media where stress waves propagate, source mechanism and relative orientation of the source and sensors, and the shape and geometry of the structure under study. While real travel time models are complicated in nature, the arrival time functions that are used to describe a model have to be simplified for either theoretical and/or practical reasons. As an example, the following is an arrival time function for a homogeneous velocity model:

$$f_i(\mathbf{x}) = f_i(x, y, z, t) = t + \frac{1}{v_i} \sqrt{(x_i - x)^2 + (y_i - y)^2 + (z_i - z)^2} \quad (11)$$

where the unknowns, x , y and z , are the coordinates of an AE event; t is the origin time of this event; x_i , y_i and z_i , are the coordinates of the i th sensor, and v_i is the velocity of the stress wave.

We note the difference of the velocity model used here and the velocity model assumed for those non-iterative methods discussed in the preceding paper. For those non-iterative methods, we have to assume a single velocity for all arrival time data. With the homogeneous velocity model used in this example, each equation can have its own velocity. This allows us to assign the velocity based on the arrival type, which is critical for accurate source location.

The arrival time functions used for Geiger's method can be much more complicated than the one used in this example. In fact, Geiger's method posts no restrictions on the velocity model to be utilized as far as arrival time functions can be established and their first-order derivatives can be evaluated.

Data preparation

Once arrival time functions are established, the next step is preparing data. It is known from Eq. (2) that there are four types of data that we have to prepare, which are: trial solution, observed arrival time, calculated arrival time, and partial derivatives.

Trial solution At the beginning of the iteration process, a trial solution has to be assigned manually by users or generated automatically by the location code. After this, it is updated automatically by adding the new correction vector.

A question that is frequently asked is: is it necessary for the trial solution to be very close to the true event location? While it would never hurt to have a close guess, it may not be achievable in many cases, especially in the situation where source location is carried out automatically. Fortunately, the answer to this question is “no”. In general, it will be good enough if a trial solution is within the monitoring area. A practice that is frequently adopted by the author is to use the location of the first triggered sensor as the trial solution if we do not have any prior knowledge on event locations.

There is a perception, however, that the choice of the trial solution is important. While it is possible that one has to “play” the initial trial solutions in order to get the right answer, it usually indicates that the associated system is unstable, a far more serious problem than the choice of the trial solution. When this is the case, the confidence that one can put on the final solution is significantly diminished.

Observed arrival time The observed arrival times are the data provided externally. Since the physics of source location is to find a location that its associated arrival times best match the observed arrival times, the accuracy of the observed arrival times has to be compatible with the required accuracy. For instance, if the required location accuracy is 1 mm and the travel velocity of the stress wave under study is 1 km/sec, then the allowed timing error is $1/1000000 = 1 \mu\text{s}$.

Calculated arrival time The calculated arrival times are obtained by substituting the trial solution into the arrival time functions, such as Eq. (11).

Partial derivatives The partial derivatives defined by A in Eq. (8) have to be fulfilled. This is a two-step procedure: deriving the general expressions of the partial derivatives and numerical evaluation of these partial derivatives in terms of the trial solution. As a demonstration, the following are the general expressions of the partial derivatives of the arrival time function given by Eq. (11):

$$\frac{\partial f_i}{\partial x} = -\frac{x_i - x_0}{v_i R}$$

$$\frac{\partial f_i}{\partial y} = -\frac{y_i - y_0}{v_i R}$$

$$\frac{\partial f_i}{\partial z} = -\frac{z_i - z_0}{v_i R}$$

$$\frac{\partial f_i}{\partial t} = 1$$

$$R = \sqrt{(x_i - x_0)^2 + (y_i - y_0)^2 + (z_i - z_0)^2}$$

Solving a system of simultaneous equations

The least squares solution to an inconsistent system is given by Eq. (9). Usually, the size of correction vector, $\delta\mathbf{x}$, will decrease rapidly and reach a prescribed accuracy within a few iterations. However, it is possible that $\delta\mathbf{x}$ will not converge: it may oscillate or even increase beyond control. The problem of the divergence is a sign of the instability of the associated mathematical system, which is usually the result of poor array geometry.

3.3 Mechanics of iteration by first order derivatives

Although Geiger's method is relatively straight forward from a computational point of view, conceptually, the method is still quite confusing despite its enormous popularity and long history. For instance, it is a generally accepted perception in seismology that Geiger's method is a linear approximation of nonlinear source location problems (Thurber, 1985). The implication of this perception is that the method is unable to take into account of the nonlinear behavior of arrival time functions. This is a serious mistake. It affects not only our theoretical understanding of the method, but also its applications.

While the confusions that surround Geiger's method may be attributed to many causes, fundamentally, it is the lack of the correct understanding of the mechanics of derivative methods. In order to solve this problem, there are two issues we have to discuss further: Taylor's theorem and the function of first-order derivatives

Taylor's theorem and formulation principle

The key element in developing Geiger's method is the expansion of arrival time functions into the first-degree Taylor polynomials, and we begin our discussion with Taylor's theorem. The focus of this discussion is whether the expansion of a function by the Taylor polynomials is an approximation of that function.

The Taylor's theorem states that a function at a point may be evaluated by the Taylor polynomial of the function at its neighboring point and the error for this approximation can be evaluated by the associated error function. The key here is that, when the Taylor polynomials are used for the function evaluation at the location by its neighbors, the accuracy of this approximation is the function of the size of this neighborhood and, unless demonstrated otherwise, it has to be assumed very small. Therefore, the Taylor polynomial in general is a highly localized function in that it changes with each neighboring point that is being chosen and there is no unique Taylor polynomial that can represent a function for its entire domain.

Furthermore, the Taylor polynomials used for the purpose of numerical computations are mostly associated with a very low degree, typically first or second. Under this condition, it is virtually impossible to approximate a function by polynomials. If we consider the fact that Geiger's method only uses the first order derivatives, it is impossible to represent arrival time functions by these polynomials.

When an arrival time function is expanded in the form of the Taylor polynomial, the resulting equation, such as Eq. (2), no longer represents the original arrival time function. The original arrival time function is the function of hypocenter parameters and the new equation is the function of a correction vector. With this new equation, the observed arrival time is represented by the arrival time calculated for a nearby point and a correction factor. As it has been discussed earlier, the calculated arrival time is the result of the evaluation of the original arrival time function in terms of the trial solution, which eventually represents the hypocenter. The correction factor

determines how the trial solution is to be changed in the next iteration. As such, none of these terms can be regarded as the linear portion of the original arrival time function.

It is understood from the above analysis that the first-degree Taylor polynomials used in Geiger's method are not the approximation of original arrival time functions and, therefore, this expansion process cannot be characterized by linearization. The analysis of the components of the expanded function also shows that there is no physical evidence to characterize this process by linearization.

So far we have demonstrated that the Taylor polynomials used in Geiger's method are not the approximations of arrival time functions, and, therefore, linearization is not an appropriate term to characterize the formulation of Geiger's method. We now discuss the question whether the searching process can be termed as linear because Geiger's method uses only first order derivatives.

The answer to this question is actually quite simple: any derivative method is a nonlinear searching method. This is because derivatives, regardless of their orders, are used to catch up with the nonlinear behavior of functions at trial locations and correction vectors are determined by this information. Therefore, the question with a derivative method is not whether it is a nonlinear searching method; the question is the type of the nonlinear behavior that is utilized. We now demonstrate the geometric meaning of the searching process associated with Geiger's method.

Consider the general form of a nonlinear system:

$$\mathbf{F}(\mathbf{x}) = \mathbf{0},$$

where

$$\mathbf{F}(\mathbf{x}) = (f_1(\mathbf{x}), f_2(\mathbf{x}), \dots, f_m(\mathbf{x})),$$

$$f_1(\mathbf{x}) = 0, f_2(\mathbf{x}) = 0, \dots, f_m(\mathbf{x}) = 0,$$

$$\text{and } \mathbf{x} = (x_1, x_2, \dots, x_n)^T.$$

The solution of this system is to find the common intersection of the functions of $\mathbf{F}(\mathbf{x})$ at $\mathbf{F}(\mathbf{x}) = \mathbf{0}$. Because of the inherent difficulty to solve a nonlinear system analytically, it is usually done numerically, and the corresponding process is commonly known as root finding. One of the best known methods for this purpose is the Gauss-Newton's method, and Geiger's method is an application of this method (Lee and Stewart, 1981). The Gauss-Newton's method uses the first-order derivative information to determine the correction vector.

Gradient vectors, such as the one given by Eq. (5), represent the directions of the steepest slopes. The key to understand the Gauss-Newton's method, and therefore Geiger's method, is how these first order derivatives are used to determine correction vectors. Although it is impossible to demonstrate the geometrical meaning of gradient vectors for problems with more than two independent variables, it is fortunate that the mechanics remains the same for all dimensions. As such, we will use the Newton-Raphson method, the Gauss-Newton's method in one variable, to illustrate how first order derivatives are used to determine correction vectors.

Newton-Raphson method

The Newton-Raphson method is one of the most powerful numerical methods for finding a root of $f(x) = 0$, and, yet, both the concept and the procedure are extremely simple. The method begins with the first-degree Taylor polynomial for $f(x)$, expanded about x_0 ,

$$f(x) = f(x_0) + (x - x_0)f'(x_0)$$

Since we are finding the root of f , so that $f(x) = 0$ and the above equation becomes:

$$0 = f(x_0) + (x - x_0)f'(x_0)$$

Solving for x in this equation gives:

$$x = x_0 - \frac{f(x_0)}{f'(x_0)}$$

where x should be a better approximation of the root. This sets the stage for the Newton-Raphson method, which involves generating the sequence $\{x_n\}$ in an iteration process:

$$x_{n+1} = x_n - \frac{f(x_n)}{f'(x_n)}.$$

The geometry of the Newton-Raphson method is shown in Fig. 1. At each iteration stage, we determine the first-order derivative of the function at the trial solution. Geometrically, it represents the tangent line of the function at this location. The intersection of this line with the x-axis defines the new trial solution, x_{n+1} . The corresponding correction vector is $\delta x = x_n - x_{n+1}$. From the figure, it is easy to verify the relation:

$$f'(x_n) = \frac{f(x_n)}{x_n - x_{n+1}}.$$

The above equation is another form of the preceding equation, but with much clearer geometrical meaning: the slope of the tangent line represented by $f'(x_n)$ on the left-hand side of the equation is the ratio of the function value at the trial solution and the correction vector.

In summary, the Newton-Raphson method can be viewed as a procedure that we use the intersection of the tangent line at the x -axis to approximate the root of the function and the direction of the tangent line is defined by the first order derivative of the function at the trial solution.

3.4 Stopping criteria

When an iterative method is used, the calculation has to be stopped at a certain point. There are three commonly used stopping criteria for derivative methods, and their applicability for the problem of source location is discussed next.

Residual as stopping criterion

When residual is utilized as the stopping criterion, we stop the calculation soon after the residual is smaller than a pre-defined tolerance, such that:

$$\text{Res} < \epsilon, \quad \text{for } \epsilon > 0,$$

where Res is the event residual and ϵ is the tolerance. The event residual is a measurement of the location error in terms of the total effect of the mismatch between the observed and calculated arrival times. Mathematically, it is defined by the regression method being used. For the least-squares method, the event residual is (Ge, 1996) given by Eq. (10):

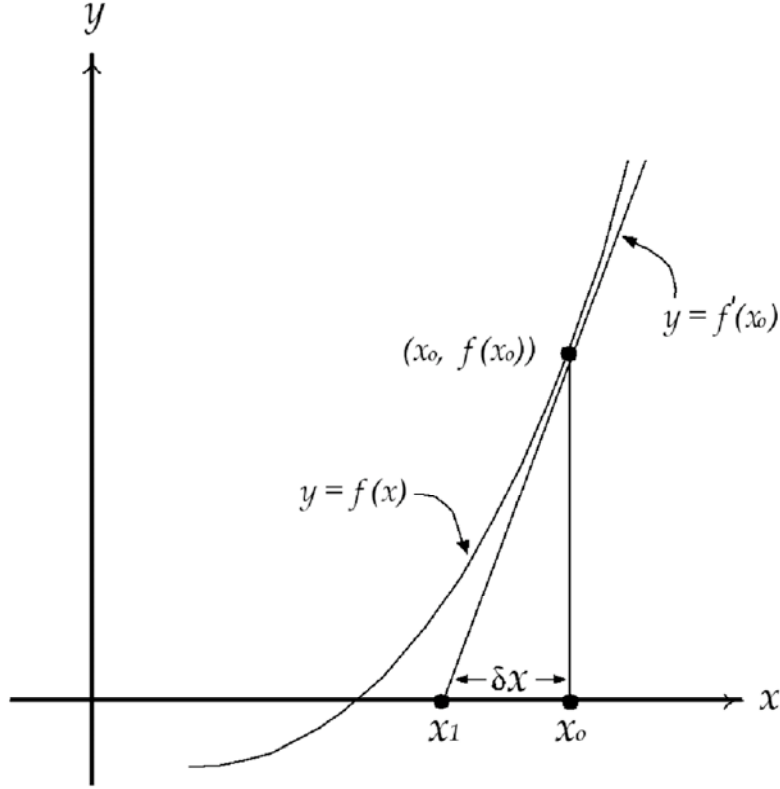


Fig. 1 Geometry of Newton-Raphson method

$$Res = \sqrt{\frac{\boldsymbol{\gamma}^T \boldsymbol{\gamma}}{m - q}} \quad (10)$$

as defined previously.

Although the approach appears quite natural for many applications as the residual is a mathematical measurement of the computational error, the problem in the case of source location is that it may vary in a very wide range for events under similar conditions, say, covered by the same array. If the tolerance is set too low, many solutions may never be able to reach that level. If it is set too high, we lose the accuracy. Therefore, it is difficult to implement this approach for source location problems.

Size of correction vector as stopping criterion

The second criterion is the size of correction vectors, $\boldsymbol{\delta x}$. In the case of source location, correction vectors include both spatial and time components. This creates a problem for calculating the size of $\boldsymbol{\delta x}$ because of the difference in units. A solution to this problem is to represent the size of correction vectors by $\boldsymbol{\delta d}$, the size of the spatial components only, such as

$$\boldsymbol{\delta d} = \sqrt{\delta x^2 + \delta y^2 + \delta z^2}$$

and the corresponding stopping criterion is:

$$\boldsymbol{\delta d} < \varepsilon$$

When the size of correction vectors is used as a stopping criterion, the underlying assumption is that it is a sign of the convergency when $\boldsymbol{\delta d} \rightarrow 0$ as the number of iterations increases to infinity.

Relative size of correction vector as stopping criterion

The third criterion is the relative size of correction vectors. Again, if we only consider the spatial components, this third criterion can be expressed:

$$\frac{\delta d}{\sqrt{x^2 + y^2 + z^2}} < \varepsilon$$

where x , y and z are the coordinates of the event location determined at the current iteration. The relative error is a better measurement for many applications, although it has two serious drawbacks in the case of source location. First, the relative error would be the function of the coordinate system. For instance, the relative error for an array described by three digits would be drastically larger than the same array that is described by five digits. Secondly, the approach would make the error as the function of event locations. If we consider the fact that the size of an array is normally much larger than the location error, typically of the order of 2 or higher, the event location will significantly affect the outcome of this approach. For these reasons, relative size is not a suitable stopping criterion.

In comparison of these three criteria, the size of correction vectors appears most suitable for the purpose of source location. In any case another stopping criterion is always necessary: the number of iterations. This is especially true for derivative methods, with which divergence may occur.

3.5 Problem of divergence

The major problem associated with the Geiger's method is divergence. Divergence is a common problem associated with many iterative algorithms. The cause of divergence is complex and a detailed discussion of the problem is beyond the scope of this article. However, there are two points we wish to make. First, although divergence can be caused by many different technical reasons, it is fundamentally governed by the stability of the associated mathematical system. In the case of source location, this stability is determined by the sensor array geometry relative to the actual event location. For instance, because of the inherent difficulty to spread the seismographs in the vertical direction, the location accuracy of local earthquakes in the depth direction is in general poorer than in the other directions. Therefore, the best means to alleviate the divergence problem is to optimize the sensor array geometry, if it is possible. The second point is that divergence is a phenomenon closely related to the convergence rate. For those methods with a very high convergence rate, such as the Geiger's method, the chances to develop the divergence problem is also considerably higher.

Many research studies were carried out in seismology on the improvement of the convergence character of the source location algorithm, and some remedial measures were proposed (Smith, 1976; Buland, 1976; Lee and Stewart, 1981; Anderson, 1982; Lienert and Frazer, 1983; Thurber, 1985). In general, the efficiency of these remedial measures is very limited as none of them could fundamentally address the two inherent difficulties discussed earlier.

4. Thurber's Method

Geiger's method uses the first order derivatives to catch up the nonlinear behavior of arrival time functions at the trial solutions. We now discuss another significant derivative approach, Thurber's method (Thurber, 1985), which uses the information of both the first and second derivative to determine correction vectors.

4.1 Algorithm

Similar to our discussion on Geiger's method, let $f_i(\mathbf{x})$ be the general form of the arrival time function associated with the i th sensor, where \mathbf{x} denotes the hypocenter parameters defined by Eq. (1). Expand $f_i(\mathbf{x})$ at a nearby location, \mathbf{x}_0 , and express the expansion by the second-degree Taylor polynomial:

$$f_i(\mathbf{x}) = f_i(\mathbf{x}_0 + \delta\mathbf{x}) = f_i(\mathbf{x}_0) + \mathbf{g}_i^T \delta\mathbf{x} + \frac{1}{2} \delta\mathbf{x}^T H_i \delta\mathbf{x} \quad (12)$$

where \mathbf{g}_i^T is the transpose of the gradient vector \mathbf{g}_i defined by Eq. (5) and H_i is the Hessian matrix:

$$H_i = \begin{bmatrix} \frac{\partial^2 f_i}{\partial x^2} & \frac{\partial^2 f_i}{\partial x \partial y} & \frac{\partial^2 f_i}{\partial x \partial z} & \frac{\partial^2 f_i}{\partial x \partial t} \\ \frac{\partial^2 f_i}{\partial y \partial x} & \frac{\partial^2 f_i}{\partial y^2} & \frac{\partial^2 f_i}{\partial y \partial z} & \frac{\partial^2 f_i}{\partial y \partial t} \\ \frac{\partial^2 f_i}{\partial z \partial x} & \frac{\partial^2 f_i}{\partial z \partial y} & \frac{\partial^2 f_i}{\partial z^2} & \frac{\partial^2 f_i}{\partial z \partial t} \\ \frac{\partial^2 f_i}{\partial t \partial x} & \frac{\partial^2 f_i}{\partial t \partial y} & \frac{\partial^2 f_i}{\partial t \partial z} & \frac{\partial^2 f_i}{\partial t^2} \end{bmatrix} \quad (13)$$

The physical meanings of $f_i(\mathbf{x}_0 + \delta\mathbf{x})$ and $f_i(\mathbf{x}_0)$ in Eq. (12) remains the same as in Eq. (2), which are the observed and calculated arrival times, respectively.

Eq. (12) is a quadratic function of the correction vector. With the partial differentiation of the equation and setting the resulting equation to zero, we have

$$\mathbf{g}_i + H_i \delta\mathbf{x} = 0. \quad (14)$$

For convenience, the hypocenter notation given by Eq. (1) may also be expressed as

$$\mathbf{x} = (x_1, x_2, x_3, x_4)^T. \quad (15)$$

With the hypocenter notation given by Eq. (15), an alternative form of Eq. (14) is

$$\frac{\partial f_i(x)}{\partial x_k} + \sum_{j=1}^4 \delta x_j \frac{\partial^2 f_i(x)}{\partial x_j \partial x_k} = 0, \quad k = 1, 2, 3, 4, \quad (16)$$

which gives us a detailed view of the content of Eq. (14).

The least squares solution for the system defined by Eq. (14) is (Thurber, 1985):

$$\Delta\mathbf{x} = (\mathbf{A}^T \mathbf{A} - (\nabla \mathbf{A}^T) \mathbf{r})^{-1} \mathbf{A}^T \mathbf{r} \quad (17)$$

where both \mathbf{A} and \mathbf{r} are defined in Eq. (8). If we use \mathbf{N} to represent $(\nabla \mathbf{A}^T) \mathbf{r}$ in Eq. (17), such that

$$\mathbf{N} = (\nabla \mathbf{A}^T) \mathbf{r}, \quad (18)$$

and the entry N_{ij} of this 4 x 4 matrix is given by

$$N_{ij} = \sum_{k=1}^m \frac{\partial^2 f_k}{\partial x_i \partial x_j} \gamma_k \quad i, j = 1, 2, 3 \quad (19)$$

$$N_{ij} = 0 \quad i, j = 4$$

The step that holds the key to understand Newton's method, and therefore Thurber's method, is the transition from Eq. (12) to Eq. (14). Eq. (12) is a quadratic function. By the partial differentiation of this equation and setting the resulting equation to zero, Eq. (14) defines the extreme of this quadratic function. This extreme in Newton's method is regarded as the optimum correction vector for the trial solution, and therefore, the solution for Eq. (12).

4.2 Mechanics of iteration by first and second order derivatives

Following the approach that the Newton-Raphson's method was used to illustrate the geometric meaning of the first order derivatives, we now use Newton's method in one variable to demonstrate geometrically how the first and second order derivatives are used to determine the correction vector.

Finding the root with first and second derivatives

Consider the second-degree Taylor polynomial for $f(x)$, expanded about x_0 ,

$$f(x) = f(x_0) + (x - x_0)f'(x_0) + \frac{1}{2}(x - x_0)^2 f''(x_0) \quad (20)$$

Our goal is to determine x so that $f(x) = 0$. Note that $f(x)$ in this case is expressed by a quadratic function of x and the best approximation of $f(x) = 0$ is to find the minimum of the function and this can be done by taking the first derivative of the function with respect to x ,

$$\begin{aligned} \frac{df(x)}{dx} &= \frac{df(x_0)}{dx} + \frac{d((x - x_0)f'(x_0))}{dx} + \frac{1}{2} \frac{d((x - x_0)^2 f''(x_0))}{dx} \\ &= f'(x_0) + (x - x_0)f''(x_0) \end{aligned}$$

and let the resulting equation equal to zero,

$$f'(x_0) + (x - x_0)f''(x_0) = 0$$

Solving the equation for x ,

$$x = x_0 - \frac{f'(x_0)}{f''(x_0)}$$

the final solution can be approached iteratively by the sequence $\{x_i\}$ defined by

$$x_{i+1} = x_i - \frac{f'(x_i)}{f''(x_i)} \quad i \geq 0 \quad (21)$$

The geometry of this solution process is illustrated in Fig. 2. The second-degree Taylor polynomial, denoted by $p(x_0)$ in the figure, is used to represent the function at the neighborhood of x_0 . The extreme of this polynomial, x_I , is considered by Newton's method as the optimum solution which becomes the new trial solution. Eq. (21) is a mathematical definition of this extreme.

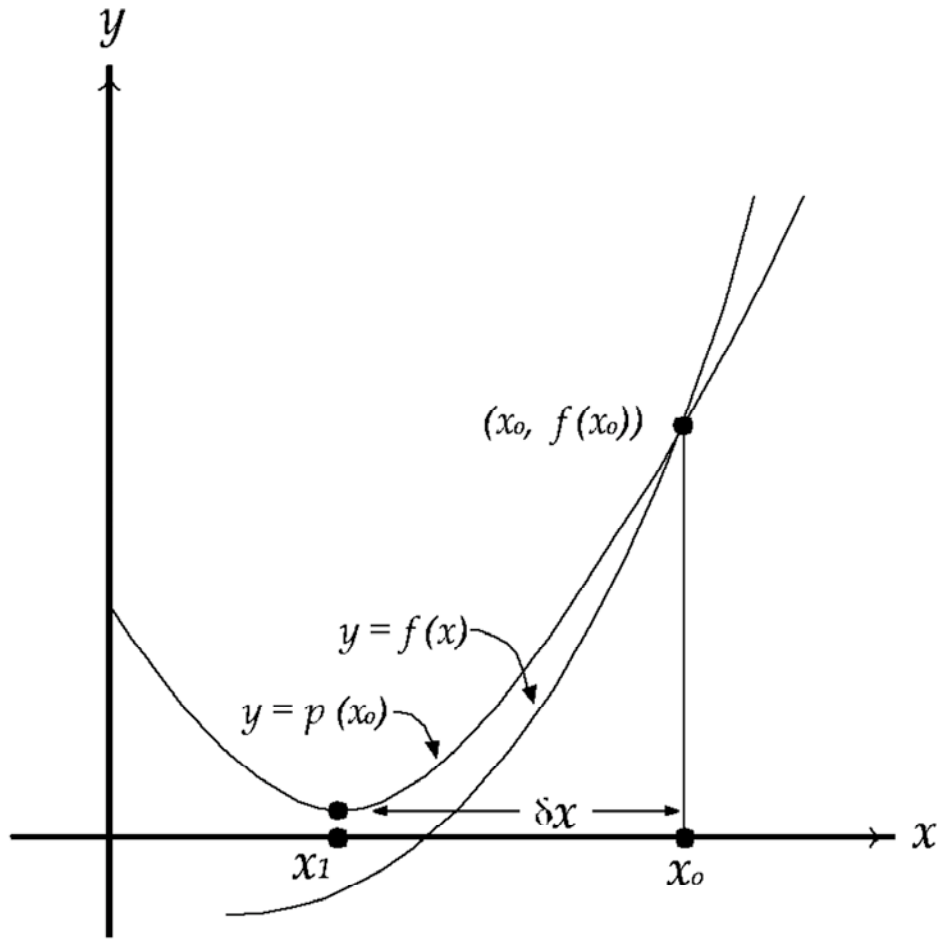


Fig. 2 Geometry of Newton's method in one variable.

A very interesting point shown by Fig. 2 is the difference between $f(x)$, the original function, and $p(x_0)$, the second-degree Taylor polynomial, which clearly demonstrates that the Taylor polynomial is not the approximation of that function.

4.3 Discussion

The essence of derivative methods is using nonlinear characters of functions at the trial solution, described by derivatives, to determine correction vectors. The difference among derivative methods is hence the type of nonlinear characters that are used. The simplest derivative method is Geiger's method. The nonlinear character used by this method is gradient, or the steepest slope at the trial solution, which are represented by first order derivatives. Thurber's method uses both the first and second order derivatives and its solution is geometrically represented by the extreme of a quadratic function.

Thurber's method is a more sophisticated derivative method than Geiger's method in that it utilizes the quadratic model for optimization. Although the method was demonstrated with the improved stability in several cases (Thurber, 1985), it is not clear whether it can be regarded as a general solution to the problem. A major uncertainty associated with the quadratic model based methods is whether the model is positive definite. While it is not a requirement, an underlying assumption for these methods is that the model is positive definite. If the assumption is not fulfilled, the performance of these methods is much more difficult to predict.

5. Simplex Method

The Simplex method is a relatively new method developed by Nelder and Mead (1965). It searches the minimums of mathematical functions through function comparison. The method was introduced for the source location purpose in late 1980s by Prugger and Gendzwill (Prugger and Gendzwill, 1988; Gendzwill and Prugger, 1989). The mathematical procedures and related concepts in error estimation for this method were further discussed by Ge (1995). Readers should be aware that the Simplex method discussed here is different from the one used in linear programming where it refers an algorithm for a special type of linear problems.

5.1 Method concept

The Simplex method starts from the idea that, for a given set of arrival times associated with a set of sensors, an error can be calculated for any point by comparing the observed and the calculated arrival times. An error space is thus the one in which every point is defined by an associated error, and the point with the minimal error is the event location.

The process of searching for the minimal point with the Simplex method is unique. The solution is said to be found when a Simplex figure falls into the depression of the error space. The Simplex is a geometric figure which contains one more vertex than the dimension of the space in which it is used. A simplex for a two dimensional space is a triangle, a simplex for a three dimensional space is a tetrahedron, etc.

The search for the final solution with the Simplex source location method involves four general steps:

- i) setting an initial Simplex figure;
- ii) calculating errors for vertices;
- iii) moving Simplex figures; and
- iv) examining the status of convergency.

At the beginning of search, an initial Simplex figure has to be set, which is then rolling through the error space, expanding, contracting, shrinking and turning towards the minimal error point of the space. The movement of the Simplex figure is governed by the error distribution at its vertex, which is calculated each time when the Simplex figure is reshaped.

5.2 Simplex figure and its initial setting

It is understood from the earlier discussion that the Simplex is a geometric figure that contains one more vertex than the dimension of the space in which it is used. Because a source location problem is spanned by not only its geometric dimensions, but also time dimension, the Simplex figure will be tetrahedron and five-vertices for two and three geometrical problems, respectively, if we apply the Simplex method directly to our source location problems.

A more convenient approach is to consider spatial coordinates and origin time “separately” in that error spaces are already optimized in terms of origin time. With this treatment, the dimension of the Simplex figures is solely determined by the geometric dimension of the source location problems: a triangle for two-dimensional problems and a tetrahedron for three-dimensional problems. We will discuss the mathematical procedure of this approach in the next section.

There is no rigid guideline regarding how to set the initial Simplex figure. For the purpose of efficiency, one may want to set it near the potential location with a reasonable size. Care must

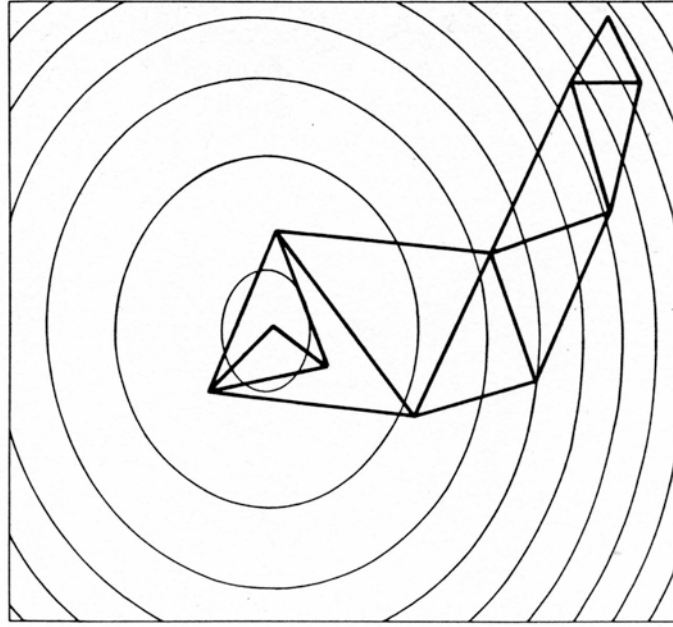


Fig. 3 An example of the Simplex moving on the error space contour plot (after Caceci and Cacheris, 1984).

be taken that the figure is not dimensionally reduced. A practice by the author is to set the initial Simplex figure near the first triggered sensor with the size about one third to one half of the monitoring array. Because of the very robust nature of the Simplex method, the size, shape and location of the initial figure can be quite arbitrary.

5.3 Error calculation and origin time

The location errors are defined by the associated optimization method. Two most popularly employed such methods are the least squares method (L2 norm) and the absolute value method (L1 norm) method. The implementation of these methods for the Simplex source location method is discussed as follows.

Error estimation by the Least squares method

Assume that the observed arrival time at the i th station is t_{oi} and the calculated arrival time at this station is t_{ci} , the station residual as given by Eq. (7) is

$$\gamma_i = t_{oi} - t_{ci}, \quad (7)$$

where γ_i is station residual. A calculated arrival time consists of two parts: origin time, t , and travel time from the vertex under concern to the i th station, tt_i , which are related by the following equation:

$$t_{ci} = tt_i + t. \quad (22)$$

It is noted that origin time is a source parameter, and hence an unknown here. Substituting Eq. (22) into Eq. (7), we express the station residual as a function of origin time:

$$\gamma_i = t_{oi} - (tt_i + t), \quad (23)$$

Now the goal is to find the best estimate of the origin time such that the total error will be minimized. With the least squares method, the total error is defined by

$$\sum \gamma_i^2$$

and it is minimized when the origin time is determined by the equation

$$\frac{d(\sum \gamma_i^2)}{dt} = 0$$

Solving the above equation, the best estimate of the origin time is

$$t = \frac{\sum t_i}{n} - \frac{\sum tt_i}{n} \quad (24)$$

By substituting Eq. (24) into Eq. (23), we express the station residual in terms of observed arrival time and calculated travel time:

$$\gamma_i = (t_i - \frac{\sum t_i}{n}) - (tt_i - \frac{\sum tt_i}{n}) \quad (25)$$

The event residual is

$$Res = \sqrt{\frac{\sum \gamma_i^2}{m - q}} \quad (26)$$

Eq. (26) is the equation that is used for the error calculation for each vertex if the least squares method is used. Note that the origin time with this approach is given by Eq. (24).

Error estimation by the absolute value method

For the absolute value method, the total error is defined by

$$\sum |\gamma_i|.$$

The best estimate of the origin time has to satisfy the objective function

$$\text{Minimize } (\sum |\gamma_i|).$$

Substituting Eq. (23) into the above expression, we have

$$\text{Minimize } (\sum |t_i - (tt_i + t)|).$$

For a set of linear equations with the form of

$$x = b_i,$$

where x is the variable to be estimated and b_i is a constant, the analytical solution of the best fit for x defined by the L1 misfit norm is the median of b_i s (Chavatal, 1983). Accordingly, the best fit of the origin time is the median of all $(t_i - tt_i)$. Let us denote it as t_m . The station residual defined by the absolute value method is therefore

$$\gamma_i = t_i - tt_i - t_m \quad (27)$$

and the total error is

$$\sum |\gamma_i| = \sum |t_i - tt_i - t_m|. \quad (28)$$

Eq. (28) is the equation that is used for the error calculation for each vertex if the absolute value method is used. Note that the origin time with this approach is the median of all $(t_i - tt_i)$.

5.3 Rules for moving Simplex figures

The movement of Simplex figures is realized by deformation. There are four deformation mechanisms: reflection, expansion, contraction, and shrinkage, which are explained in Fig. 4.

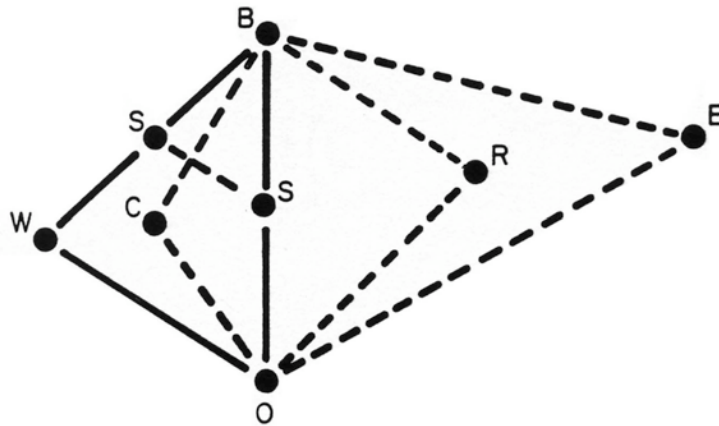


Fig. 4 An illustration of four deformation mechanisms: reflection, expansion, contraction and shrinkage. BWO = the Simplex figure prior to deformation, B = best vertex, W = worst vertex, E = expanded vertex, C = contracted vertex, and S = shrunken vertexes (after Caceci and Cach-eris, 1984).

Triangle BWO in the figure represents a two-dimensional Simplex figure. Assuming that W and B represent the worst and best vertex, respectively. R is then called reflected vertex, a mirror image of W about the midpoint of all the other vertexes. E is expanded vertex, which doubles the image distance. C is contracted vertex, located a halfway from W to the midpoint. S represents shrunken vertexes, the middle locations between the best vertex and the others.

The logic to apply these mechanisms is illustrated in the flow diagram in Fig. 5. The following is a summary of this logic:

- i) calculating the location error for each vertex,
- ii) determining the vertices with the maximum and minimum errors,
- iii) locating the reflected vertex and calculating its location error,
- iv) if this error is less than the old maximum but more than the minimum, a new Simplex figure is formed by replacing the old maximum by the reflected vertex, and go back to i) to restart the process.
- v) if the error at the reflected vertex is less than the minimum, locating the expanded vertex and calculating its location error. If the error is less than the minimum, a new Simplex figure is formed by replacing the old maximum by the expanded vertex, and go back to i) to restart the process. If the error is larger than the minimum, a new Simplex figure is formed by replacing the old maximum by the reflected vertex, and go back to i) to restart the process,
- vi) if the error at the reflected vertex is larger than the old maximum, locating the contracted vertex and calculating its location error. If this error is less than the old maximum, replacing the old maximum by the contracted vertex. Otherwise, shrinking the Simplex figure by moving all vertices other than the old minimum to the shrunken vertices. Go back to i) to restart the process.

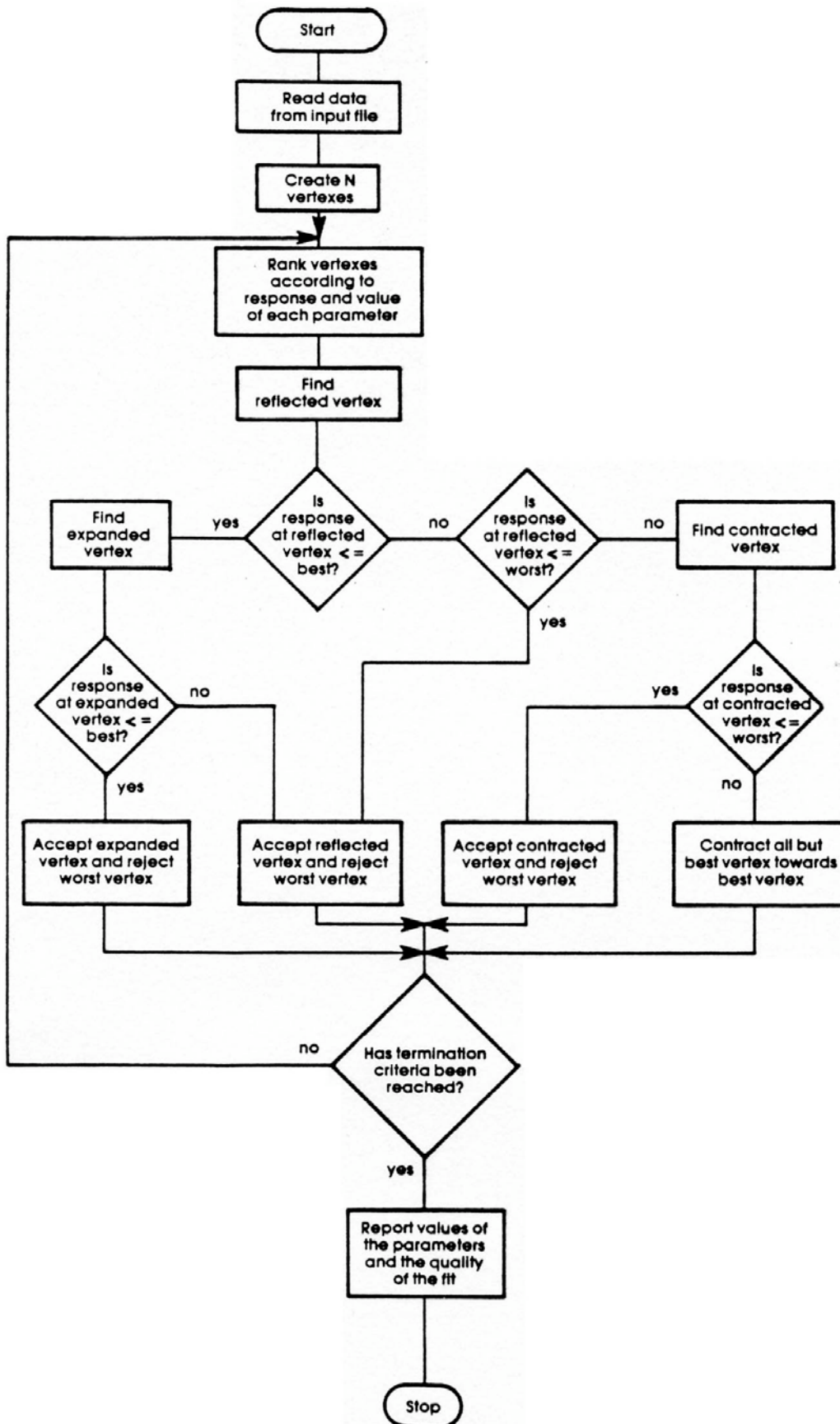


Fig. 5. Flowchart of the Simplex algorithm (after Caceci and Cacheris, 1984).

5.5 Examining the status of convergency

In section 3.4 we discussed the stopping criterion for derivative methods and determined that the size of correction vectors would be most appropriate for the purpose of source location. It is for the same reason that we use the size of Simplex figures as the measurement of the convergency status of Simplex solutions. We accept the solution if the size of the Simplex figure is less than the tolerance. The size may be defined differently. For instance, the average distance from a vertex to others would be a convenient and representative measurement of the size.

5.6 Discussion

The Simplex method offers several distinctive advantages over derivative methods. The most important one is that divergence is impossible. The author manually examined several thousands of location data by the Simplex method and did not observe a single divergence case. In fact, the same Simplex code developed by the author has been installed at a numerous mine sites for the continuous monitoring for many years and there has been no divergence problems ever reported. The reason for this robust performance is that the Simplex figure will not leave the lowest error point which has been found unless a better one is located. Therefore, the Simplex method will always keep the best solution that has been found, whereas for others it may be lost in iteration processes. This character is especially important for the automated monitoring.

The other important advantage of the method is its flexibility. Unlike derivative methods, with which arrival time functions have to be established prior to the analysis, arrival time functions used in the Simplex method can be established during the data processing, which is a necessary condition in order to handle many sophisticated problems.

A frequently mentioned advantage of the Simplex method is that we avoid many computational problems associated with partial derivatives and matrix inversions. It is, however, important to understand that this is not equivalent to say that the underlying problems are also gone. For instance, an ill-conditioned matrix in source location is a reflection of the instability of the associated mathematical system. It would be a serious mistake to expect the disappearance of the problem by using the Simplex method. The truth is that the problem is physical; its existence is independent of the solution methods.

6. Conclusions

Iterative methods are of primary importance in source location methods. This is because of their flexibility in dealing with arrival time functions, which is essential for realistically approaching a great majority of source location problems. Non-derivative methods have to assume a single velocity for all channels, which severely limits their application.

The best known group of iterative methods is derivative algorithms. With derivative methods, we approach the final solution through a continuous updating process of trial solution, and this is done by adding the correction vector found from the previous iteration at each stage. The correction vector is determined by the assessment of nonlinear behavior of arrival time functions at the trial solution. The difference among derivative methods is therefore the type of the nonlinear behavior that is utilized.

The nonlinear behavior used by Geiger's method is the gradient of arrival time functions, or the steepest direction of these functions, represented by the first-order derivatives. The one util

ized by Thurber's method is the extreme of the quadratic functions, which is the second-degree of Taylor polynomials, including both the first- and second-order derivatives..

Because the nonlinear behaviors are used decisively for the calculation of correction vectors, derivative methods, such as Geiger's method and Thurber's method, are inherently efficient, and offer superior performance to other iterative methods. The final solutions are usually approached within a few iterations if the associated systems are stable.

A shortcoming of derivative methods is divergence. While the cause of divergence is complex and a detailed discussion of the problem is beyond the scope of this article, it is important to know that divergence, in general, reflects the problem of instability, which, in turn, is largely governed by the sensor array geometry.

The Simplex method is the most important source location method emerged in recent years. Because of its unique iteration approach, divergence is impossible. This has given the method a huge advantage over derivative methods. The other major advantage of the method is its flexibility to deal with complicated velocity models. Unlike derivative methods, with which arrival time functions have to be established prior to the analysis, arrival time functions used in the Simplex method can be established during the data processing, which is a necessary condition in order to handle many sophisticated problems.

Finally, we would like to emphasize that source location is a subject affected by many factors and the location algorithm is only one of them. In order to use a location algorithm efficiently, we need not only a good understanding of the algorithm itself, but also a perspective view on how the algorithm relates to other factors. The two most important factors are sensor array geometry and errors associated with input data.

Sensor array geometry and system stability

The importance of the sensor array geometry in AE source location lies on the fact that we would never be able to eliminate input errors completely and the impact of these initial errors on the final location accuracy is controlled by the sensor array geometry (Ge, 1988). Good array geometry can effectively limit the impact of initial errors while a poor one will maximize the impact. In other words, the stability of the associated mathematical system is determined by the sensor array geometry. Therefore, the sensor array geometry is fundamental for an accurate and reliable AE source location.

Understanding the relation between sensor array geometry and system stability is important from two perspectives. First, the stability of an event location is independent of the location algorithm being used; that is, we can not change the degree of the sensitivity of a solution to initial errors by switching the location algorithm. If we want to improve the reliability of event locations, the only means is to improve the sensor array geometry. There is no other way around.

Second, a phenomenon that is closely associated with an unstable system is divergence. It is more difficult to approach the solution numerically when the associated system is unstable. It is, however, important to note that the convergence character does differ from method to method. We can reduce the risk of divergence by choosing an algorithm with the better convergence character, and Simplex method is such an example.

Errors associated with input data

There are a number of error sources for AE source location data. The obvious ones are timing, velocity model and sensor coordinates. The one that is often not recognized but may cause most damages is misidentification of arrival types.

An assumption that is frequently made in AE source location is P-wave triggering. In reality, many arrivals are due to S-waves or even not related signals called outlier. An outlier may be caused by either culture noises or the interference of other events. The analysis of AE data shows that S-wave arrivals may account for as much as more than 50% of total arrivals (Ge and Kaiser, 1990). As S-wave velocity is typically half of the P-wave velocity, mixing of P- and S-wave arrivals immediately introduces a large and systematic error to the location system. This has been the primary reason responsible for the poor AE source location accuracy in the past.

Although there are means to reduce the impact of input errors, such as optimization of the sensor array geometry and statistical analysis, one should not expect that any of these methods would be able to deal with large and systematic errors. These errors have to be detected and eliminated before the location process starts.

Acknowledgments

I am grateful to Dr. Kanji Ono for his encouragement to write my research experience in the area, and his detailed review of the manuscript and comments. I thank Dr. Hardy for his thorough review and the anonymous reviewer for his comments and suggestions to improve the manuscript.

References

- Anderson, K. R., (1982). Robust earthquake location using M-estimates, *Phys. Earth and Planet Int.*, **30**, 119-130.
- Billings, S. D., B. L. N. Kennett, and M. S. Sambridge, (1994). Hypocentre location: genetic algorithms incorporating pro lem-specific information, *Geophys. J. Int.* **118**, 693-700.
- Buland, R., (1976). The mechanics of locating earthquakes, *Bull. Seism. Soc. Am.* **66**, 173-187.
- Burden, R. L., J. D. Faires and A. C. Beynolds (1981). *Numerical analysis*, Prindle, Weber & Schmidt, Boston, Massachusetts.
- Caceci, M. S. and W. P. Cacheris (1984). Fitting curves to data (the Simplex algorithms is the answer), *Byte* **9**, 340-362.
- Ge, M., (1988). Optimization of Transducer array geometry for acoustic emission/microseismic source location. Ph.D. Thesis, The Pennsylvania State University, Department of Mineral Engineering, 237 p.
- Ge, M. and P. K. Kaiser (1990). Interpretation of physical status of arrival picks for microseismic source location. *Bull. Seism. Soc. Am.* **80**, pp. 1643-1660.

- Ge, M. (1995). Comment on "Microearthquake location: a non-linear approach that makes use of a Simplex stepping procedure" by A. Prugger and D. Gendzwil, *Bull. Seism. Soc. Am.* **85**, 375-377.
- Geiger, L. (1910). Herbsetimmung bei Erdbeben aus den Ankunftszeiten, *K. Gessell. Will. Goett.* **4**, 331-349.
- Geiger, L. (1912). Probability method for the determination of earthquake epicentres from the arrival time only, *Bull. St. Louis. Univ.* **8**, 60-71.
- Gendzwil, D. and A. Prugger (1989). Algorithms for micro-earthquake location, in *Proc. 4th Conf. Acoustic emission/Microseismic Activity in Geologic Structures*, Trans Tech. Publications, Clausthal-Zellerfeld, Germany, 601-605.
- Holland, J. H. (1975). *Adaption in Natural and Artificial Systems*, The University of Michigan Press, Ann Arbor.
- Kennett, B. L. N. and M. S. Sambridge, (1992). Earthquake location – genetic algorithms for teleseisms, *Phys. Earth and Planet Int.*, **75**, 103 -110.
- Lee, W. H. K. and S. W. Stewart (1981). Principles and applications of microearthquake networks, *Adv. Geophys. Suppl.* **2**.
- Lienert, B. R. and L. N. Frazer (1983). An improved earthquake location algorithm, *EOS, Trans. Am. Geophys. Union*, **64**, 267.
- Nelder, J. A. and R. Mead (1965). A simplex method for function minimization, *Computer J.* **7**, 308-313.
- Prugger, A. and D. Gendzwil (1989). Microearthquake location: a non-linear approach that makes use of a Simplex stepping procedure, *Bull. Seism. Soc. Am.* **78**, 799-815.
- Sambridge, M., K. Gallagher, (1993). Earthquake hypocenter location using genetic algorithms, *Bull. Seism. Soc. Am.* **83**, 1467-1491.
- Smith, E. G. C., (1976). Scaling the equations of condition to improve conditioning, *Bull. Seism. Soc. Am.* **66**, 2075-2076.
- Strang, G. (1980). *Linear algebra and its applications*, Academic Press Inc., New York, New York.
- Thurber, C. H. (1985). Nonlinear earthquake location: theory and examples, *Bull. Seism. Soc. Am.* **75**, 779-790.
- Xie, Z, T. W. Spencer, P. D. Rabinowitz, and D. A. Fahlquist, (1996). A new regional hypocenter location method, *Bull. Seism. Soc. Am.* **86**, 946-958.

WAVELET TRANSFORM SIGNAL PROCESSING TO DISTINGUISH DIFFERENT ACOUSTIC EMISSION SOURCES

K. S. DOWNS¹, M. A. HAMSTAD^{2,3} and A. O'GALLAGHER²

¹ Contractor to National Institute of Standards and Technology, Boulder, CO 80305-3328

² National Institute of Standards and Technology, Materials Reliability Division (853),
325 Broadway, Boulder, CO 80305-3328

³ Department of Engineering, University of Denver, Denver, CO 80208

Abstract

A database of wideband acoustic emission (AE) modeled signals was used to continue to examine the use of wavelet-transform (WT) results to accomplish identification of AE sources. The AE signals in the database were created by use of a validated three-dimensional finite-element code. These signals represented the out-of-plane displacements from buried dipole sources in aluminum plates 4.7 mm thick with large lateral dimensions. The surface displacement signals at three distances (60, 120, and 180 mm) were filtered with a 40 kHz high-pass filter prior to applying the WT. The WTs were calculated with a freeware software program. The WT peak magnitudes were calculated at three key frequencies (i.e., 60, 270, and 522 kHz) for all the signals generated by three different source types (i.e., in-plane dipole, microcrack initiation, and balanced shear). The signal database covered seven different radiation angles (from 0° to 90°) and six or seven depths for each source type. The fundamental Lamb modes that corresponded to the WT peak magnitudes were also determined. It was concluded that the variation of the normalized peak WT magnitudes as a function of the radiation angles was effectively constant for the various source depths. This effective independence of source depth was demonstrated for a fixed source type, propagation distance, and key frequency-mode combination. The fact that the radiation-angle dependence varied among source types for particular frequency-mode combinations allowed ratios of the WT peak magnitudes at different radiation angles to be used to uniquely distinguish the different source types.

Keywords: Acoustic emission; Acoustic emission modeling; AE; Finite-element modeling; Source identification; Wavelet transform; Wideband acoustic emission.

Contribution of the U.S. National Institute of Standards and Technology; Not subject to copyright in the United States. Trade names in this paper are included for information only; endorsement is neither intended nor implied.

1. Introduction

A previous attempt by two of the authors to use results from a wavelet transform (WT) to distinguish different acoustic emission (AE) sources types was not fully successful [1]. The previous effort examined only two frequency-mode combinations, namely the fundamental anti-symmetric mode (A_0) at 50 kHz and the fundamental symmetric mode (S_0) at 522 kHz. A ratio of the peak WT magnitude of the A_0 mode at 50 kHz to the peak WT magnitude of the S_0 mode at 522 kHz successfully distinguished different source types based on far-field AE signals originating from sources at the same depth, for AE signals propagating only in the 0°, x-axis direction. (Note: throughout this paper, the term "far-field" implies that the Lamb modes have developed in the recorded AE signals.) However, when the depth of the AE sources below the plate

surface was changed, the technique was no longer successful. Specifically, the mixed-mode A_0/S_0 ratios of the WT magnitudes changed as the source depth changed, thus resulting in ratio values that overlapped for the different source types [1].

In this current research, it was also found that the inclusion of data from multiple radiation angles did not eliminate the problems encountered when using the mixed-mode A_0/S_0 ratio approach to determine source types for multiple different source depths. Thus, it was desired to create a different analytical approach for source type identification free from the effects of variations in source depths.

It was noted that Buttle and Scruby [2, 3] successfully identified different sources with a radiation-pattern approach in the near field, and the present authors observed that the different AE source types studied here have different radiation patterns [4, 5]. Thus the present authors used these radiation patterns successfully to develop a single-mode WT ratio technique (incorporating ratios of WTs for a single mode at various radiation angles) to distinguish different AE source types from far-field AE signals (even having various source depths) when the source location is already known.

Some key differences in the present work versus the authors' previous effort are as follows: (a) the present effort used data from multiple radiation directions for a given AE event, whereas the prior work used only data from the 0 degree propagation direction; (b) the present effort examined data and associated ratios of WT magnitudes for only a single mode at a time (either the A_0 or S_0) for two different angles, versus the approach in the prior effort using a mixed-mode A_0/S_0 ratio for a single angle; and, (c) the present effort examined six frequency-mode combinations (i.e., A_0 at 60 kHz; A_0 at 270 kHz; A_0 at 522 kHz; S_0 at 60 kHz; S_0 at 270 kHz; and S_0 at 522 kHz) versus only two combinations in the prior effort.

The AE source-identification approach that was successfully developed used AE signals in the far-field, which were generated by finite-element modeling (FEM) in a plate of large lateral dimensions. Since the FEM technique created a definitive knowledge of the modeled AE sources, the signal processing results could be related to the different source types in an unambiguous fashion.

To the authors' knowledge, no other comprehensive study has been published where the results of forward modeling have been used to develop and validate an AE source identification methodology for far-field signals. Work published by Buttle and Scruby [2, 3] used forward modeling to develop signal-processing techniques to distinguish source types in the near-field. In their case, the AE signals (bulk waves) were obtained from the direct path to the sensors located at different radiation angles. Their approach is in contrast to the work reported here in which the AE signals propagate into the far-field so that the various Lamb modes are present.

2. Brief Description of the FEM-based AE Signal Database

A detailed description of the development of an extensive AE signal database was given previously [1]; a subset of this database was used in the present effort. Hence, only certain key or additional aspects are highlighted here. The FEM signals were generated in an aluminum plate (1 m x 1 m x 4.7 mm). The signals represent the out-of-plane top surface displacement as recorded by a flat-with-frequency point-contact sensor. Each FEM signal calculation started at the beginning of the operation of the source (rise time of 1.5 μ s) and continued for 200 μ s; the

displacement signals were calculated at time increments of 44.6 ns. Due to the lateral size of the plate, plate-edge reflections did not superimpose on the direct arrival of the signals. More specifically, the edge-reflected signals typically appear from about 150 μs to the calculation end (at 200 μs) for signals with a propagation distance of 180 mm. At shorter propagation distances, the edge reflections occur at later times. The AE signals were modeled for three in-plane propagation distances (60 mm, 120 mm, 180 mm) and seven in-plane radiation angles (0° , 12° , 22.5° , 45° , 67.5° , 78° , and 90°). Also, a total of three AE source types composed the database subset used here: (a) a single in-plane dipole in 0° direction (x-axis); (b) a microcrack initiation with major axis in 0° direction (x-axis); and, (c) a shear about the y-axis with the shear directions at 45° to the x-axis with no net moment. The depths from the top of the plate surface of the modeled sources were 2.35, 2.037, 1.723, 1.41, 1.097, and 0.783 mm for all three source types. Additionally, the in-plane dipole had one more source depth of 0.47 mm.

Figure 1 shows the three source types and their orientation relative to the x-y-z plate coordinate system. This figure also shows reference 0° and 90° directions used for the seven radiation directions. The assumption of the relevance of these sources to real AE experiments is based on assuming the real plate is being stressed in the x-direction. Thus, the dominant dipole for the microcrack initiation is oriented in that direction. Also, the shear (without a resultant moment) at 45° about the y-axis represents the case of a dislocation type source on the planes of maximum shear for axial loading. Finally, the in-plane dipole in the x-direction could approximately represent the fracture of a fiber aligned in that direction for an aluminum metal-matrix composite with a low fiber volume. All the dipoles had 1 N force except for the microcrack initiation source dipoles in the y and z directions, where the forces were 0.52 N. The centers of the sources were located at six or seven depths (z-axis) below the top surface of the plate. Only six depths are available in some cases, since the authors have determined that locating one of the monopoles (which make up the dipoles) as a body force in a FEM cell adjacent to the plate surface alters the results in a small but observable way. The authors believe this effect is due to a “mixing” of the plate surface boundary conditions as a result of the structure of the finite-element program. In essence, the body force interferes with the assumption of a stress-free plate surface at this cell for the intended internal dipole.

3. Description of Signal Processing and Feature Extraction

All the FEM-calculated AE signals were processed in the following fashion. Prior to performing the WT, the FEM-calculated signals were all numerically filtered with a 40 kHz four-pole Butterworth high-pass filter. Then the signals were re-sampled from their original time increment of 44.6 ns to a time increment of 0.1 μs , and the signal was extended with zeroes beyond 200 μs , for a total of 8192 points in each signal.

Each adjusted FEM signal had a wavelet transform performed upon it using a software program called AGU-Vallen Wavelet version R2002.0703 [6]. For each WT computation, a number of processing parameters must be specified. The following Wavelet Transformation Settings were used: maximum frequency = 700 kHz; frequency resolution = 3 kHz; wavelet size = 600 samples. The following Wavelet Time Range Settings were used: number of samples (i.e., points) = 800 for 60 mm distances, 1200 for 120 mm distances, and 1500 for 180 mm distances; offset samples = 0. By this choice of number of samples, all edge reflections were eliminated from consideration.

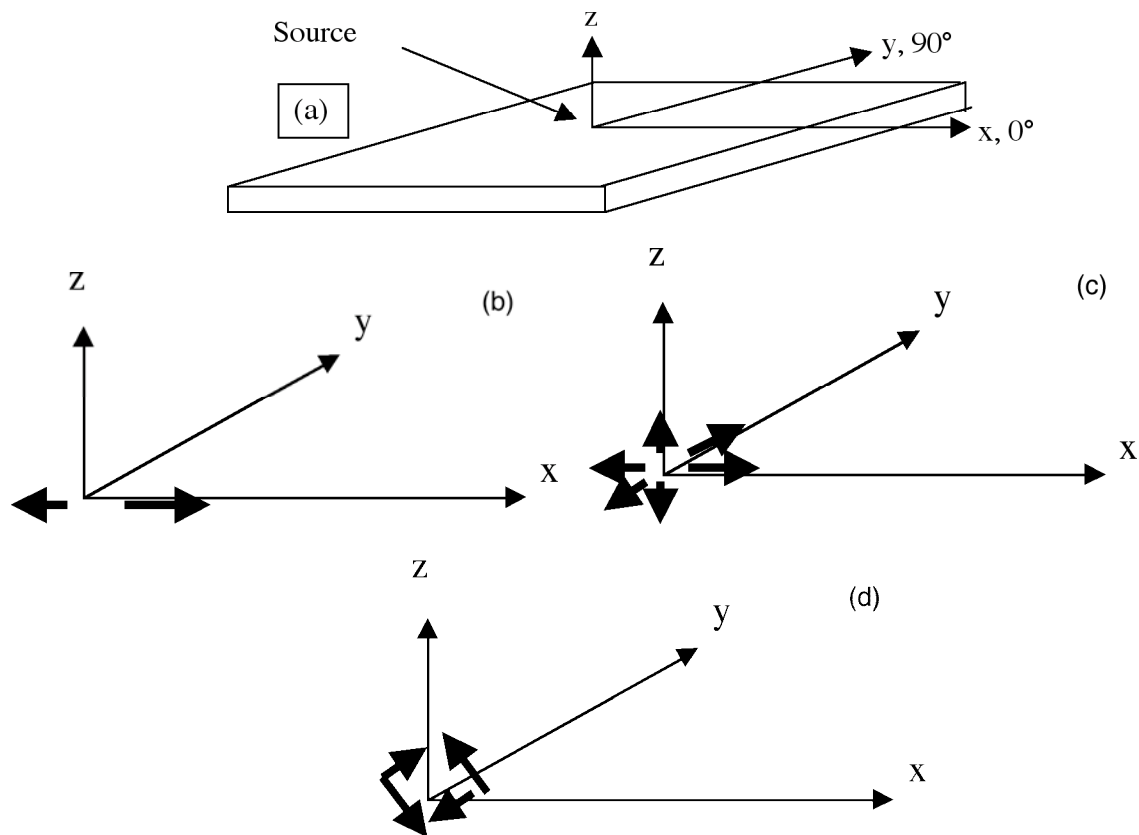


Fig. 1 Coordinate systems: (a) used with source propagation plate and radiation angles; (b) in-plane dipole source; (c) microcrack initiation source; (d) balanced shear (zero moment) 45° about y-axis.

The resulting output for each wavelet transform consists of numerical values for the WT magnitude as a function of both time and frequency. This output can be viewed numerically in a spreadsheet format, or in a more qualitative, graphic format where various colors are used to indicate the WT magnitude on a time-vs.-frequency plot. A software feature also allows superposition of the Lamb-wave group velocities onto the graphical WT result; however, knowledge of the propagation distance is required to correctly superimpose the group velocity curves. See WT examples (with superimposed group-velocity curves) and further processing details in references [7] and [8; Fig. 2].

For each WT, several features were extracted and recorded. First, the absolute maximum WT magnitude for the entire time-frequency continuum examined was noted. Next, the predominant mode (A_0 or S_0) was determined and recorded at the 60 kHz frequency using the superimposed group-velocity curves. Additionally, the peak WT magnitude at 60 kHz was recorded. The process was repeated, and similar peak WT magnitudes and their associated modes were recorded for the 270 and 522 kHz frequencies for each WT. These features as extracted at the three key frequencies were studied extensively as described later in this paper.

4. Terminology and Related Discussion

To discuss the background research and the new approach presented here for source type identification, it is necessary to introduce some concepts and terminology detailed in a related companion paper on WT-based source location [8]. In that related research, a much larger data

base of AE signals was used encompassing eight various dipole-based AE sources at various source depths and radiation angles in a 4.7 mm thick aluminum plate. The three source types that were examined in the effort described in this paper are a subset of this larger database. After manually examining WTs for the entire, larger database of eight source types, it was determined that three “key” frequencies and their associated modes at those frequencies could characterize all the potentially most energetic regions that could appear in the WTs of the larger database. It would be most accurate to further explain that each of the key frequencies is actually a band 3 kHz wide across which the WT magnitude was effectively averaged by the 3 kHz resolution chosen for the WT computation. These three “key” frequencies were 60 kHz, 270 kHz, and 522 kHz. A more detailed discussion of the process used to identify these three key frequencies can be found in reference [8].

As noted earlier, the peak WT magnitude was determined at each of the three key frequencies for each AE signal. For each WT examined, each of the three frequencies of interest was given one of three labels based on their peak WT magnitudes. The frequency having the greatest peak WT magnitude as a function of time was defined as the “primary” frequency for that particular WT; in a similar fashion, the other two frequencies examined were ranked with respect to their peak WT magnitudes (in descending order) as “secondary” and “tertiary.” The frequency-labeling process was repeated for each WT.

Several noteworthy observations were made when the frequency-labeling results of the WTs for the FEM AE signals were examined and combined with the already recorded modes and WT magnitudes for the key frequencies. The peak WT magnitude for the primary frequency was typically quite close in value to the absolute maximum WT magnitude for the entire signal examined, and the theoretical arrival time for its associated portion of the fundamental Lamb mode (A_0 or S_0) corresponded closely to the arrival time of the peak WT magnitude for that frequency. It was further observed that when a primary frequency occurred at 60 kHz, the mode that corresponded to the arrival time of the peak WT magnitude was always A_0 , whereas when the primary frequency occurred at 270 kHz or 522 kHz, its actual mode was always S_0 . Thus, the term “principal mode” was defined as the A_0 mode for 60 kHz, and as the S_0 mode for 270 and 522 kHz. In summary, each primary frequency WT peak magnitude always represented the principal mode for that frequency, whereas the WT peak magnitudes of secondary and tertiary frequencies may have represented either the principal mode or an alternate mode for that frequency.

Additionally, for secondary or tertiary frequencies, the plot of WT magnitude versus time could be used to determine the arrival time of a particular fundamental mode at the frequency of interest even if a non-principal (i.e., alternate) mode were present. The ability to determine the arrival times of modes other than that of the WT peak at a certain frequency was also enhanced by the knowledge of the signal propagation distance and the known theoretical group velocity curves.

For a given source type and as a function of source depth, certain frequencies no longer appeared as the primary frequency. In fact, the WT magnitude of the mode at these frequencies can become quite small. For example, when source depths were very near the plate surface, the WT for the S_0 mode peak at 522 kHz no longer had significant magnitude. In a similar fashion, when source depths were quite near the mid-plane of the plate, the WT for the A_0 mode peak at 60 kHz no longer had significant magnitude.

5. Single-Mode WT Ratio Approach for Source Identification

Based upon these concepts and the terminology described above, the authors propose an alternate source identification methodology based on single-mode WT ratios as follows. Each combination of a given source type and source depth was considered separately. Specifically, each of the peak WT magnitudes (at the three frequencies of interest, i.e., 60 kHz, 270 kHz, and 522 kHz), for all the radiation angles was normalized using the zero-degree peak WT magnitude at that source depth and frequency, as long as the zero-degree data had the same mode as for the angle being normalized. In a few cases, the peak mode at a given frequency for various non-zero radiation angles differed from the zero-degree peak mode; in those cases, the non-zero degree data were normalized using a lower magnitude WT peak from the zero-degree data for the proper mode. In other words, two different modes (i.e., both A_0 and S_0 modes) were occasionally present in a signal (for a given source type and depth) at the frequency of interest; sometimes the relative magnitudes of these two peaks gradually shifted as the radiation angle changed. The peak WT magnitude of the A_0 mode at 0° was used to normalize the data from other radiation angles where the A_0 mode predominated; similarly the peak WT magnitude of the S_0 mode at 0° was used to normalize the data from other radiation angles where the S_0 mode predominated. In a few cases, the predominant mode at a non-zero radiation angle was of a mode that had no localized peak WT magnitude for the 0° -angle data; thus, no normalized WT value could be computed for that particular non-zero radiation angle.

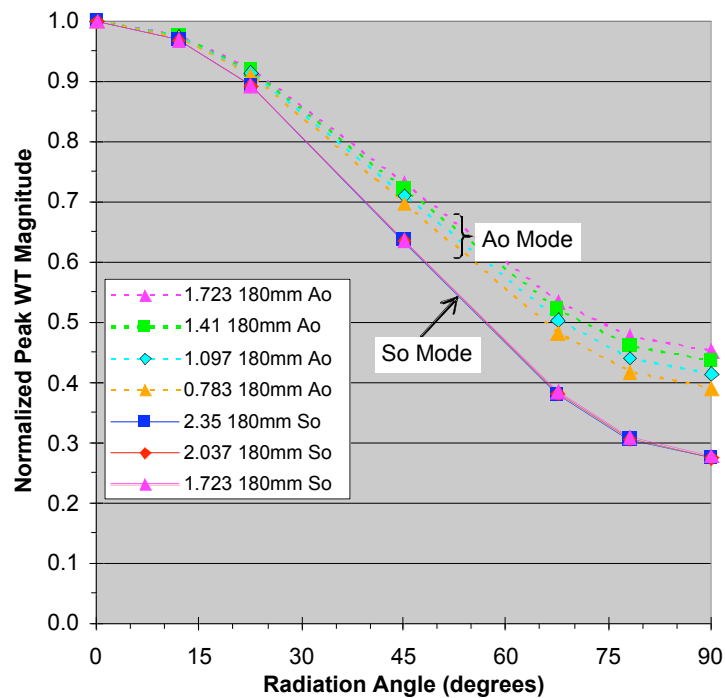


Fig. 2 Normalized peak WT magnitudes for microcrack source at 270 kHz; legend lists source depth (mm), propagation distance (mm), and mode.

Figure 2 plots normalized WT magnitude values versus radiation angle for a series of source depths for a microcrack source, frequency: 270 kHz, propagation distance: 180 mm; the figure includes both A_0 and S_0 modes. While this plot displays data for only a single combination of source type, frequency, and propagation distance, it is representative of many trends that were observed for all the data. First, A_0 data are often (although not always) significantly different from S_0 data; thus it was decided to treat and consider results from each mode separately in all

Table 1 Source depths of the normalized peak WT magnitudes that were averaged for A_0 mode for each combination of frequency, source type, and radiation angle.

Frequency (kHz)	Source Type	Radiation Angles (°)	Depths for which normalized peak WT magnitudes were averaged for each angle shown	
			Propagation Distance	
			60 mm	180 mm
60	In-plane dipole	0, 12, 22.5, 45, 67.5, 78	2.037, 1.723, 1.41, 1.097, 0.783, 0.47	2.037, 1.723, 1.41, 1.097, 0.783, 0.47
		90	none	2.037, 1.723, 1.41, 1.097, 0.783, 0.47
	Micro-crack	0, 12, 22.5, 45, 67.5, 78, 90	2.037, 1.723, 1.41, 1.097, 0.783	2.037, 1.723, 1.41, 1.097, 0.783
	Shear	0, 12, 22.5, 45, 67.5, 78, 90	2.037, 1.723, 1.41, 1.097, 0.783	2.037, 1.723, 1.41, 1.097, 0.783
270	In-plane dipole	0, 12, 22.5, 45, 67.5	1.41, 1.097, 0.783, 0.47	1.41, 1.097, 0.783, 0.47
		78	1.097, 0.783, 0.47	1.41, 1.097, 0.783, 0.47
		90	0.783, 0.47	1.41*, 1.097*, 0.783, 0.47
	Micro-crack	0, 12, 22.5	1.41, 1.097, 0.783	1.723*, 1.41, 1.097, 0.783
		45, 67.5, 78, 90	1.41, 1.097, 0.783	1.723, 1.41, 1.097, 0.783
	Shear	0, 12, 22.5, 45	1.097, 0.783	1.41*, 1.097, 0.783
67.5, 78, 90		1.097, 0.783	1.097, 0.783	
522	In-plane dipole	0, 12, 22.5, 45, 67.5, 78	0.47	0.47
		90	0.47*	0.47*
	Micro-crack	0, 12, 22.5, 45, 67.5, 78, 90	none	0.783
	Shear	0, 12, 22.5, 45, 67.5, 78, 90	none	none

* Indicates that the WT magnitude for this depth (for the angles indicated) was normalized by a *localized* peak WT magnitude of the proper mode for 0° radiation angle data, (since the *maximum* WT peak at 0° had a different mode)

further analysis. Next, it is clear that the normalization does in fact eliminate significant effects due to source depths, as long as data results are considered for any one source type, one frequency, one particular mode (A_0 or S_0), and one propagation distance. Although each of the six different source depths for each mode is represented by a separate line on Fig. 2, the lines overlap so much for the S_0 mode that many of the lines cannot be seen individually. Because of the great similarity in results across the depths, it was decided to average the information for all source depths that overlapped or nearly overlapped for each combination of source type, frequency, propagation distance, and radiation angle. It is important to note that for each possible combination, the information for A_0 modes was averaged separately from the information for S_0 modes. Since a given depth for a given signal case and frequency usually represented either the A_0 or S_0 mode (but not both), only certain depths were averaged for each mode. Also, if the results at a certain depth did not sufficiently overlap, that depth was not included in the average.

Tables 1 and 2 summarize which depths were averaged for each mode, radiation angle, frequency, source type, and propagation distance.

Table 2 Source depths of the normalized peak WT magnitudes that were averaged for S₀ mode for each combination of frequency, source type, and radiation angle.

Frequency (kHz)	Source Type	Radiation Angles (°)	Depths for which normalized peak WT magnitudes were averaged for each angle shown	
			Propagation Distance	
			60 mm	180 mm
60	In-plane dipole	0, 12, 22.5, 45	2.35	2.35
		67.5, 78, 90	none	none
	Micro-crack	0, 12, 22.5, 45, 67.5, 78, 90	2.35	2.35
	Shear	0, 12, 22.5, 45, 67.5, 78, 90	2.35	2.35
270	In-plane dipole	0, 12, 22.5, 45, 67.5, 78	2.35, 2.037, 1.723	2.35, 2.037, 1.723, 1.41*, 1.097*
		90	2.35, 2.037, 1.723	2.35, 2.037, 1.723, 1.41, 1.097
	Micro-crack	0, 12, 22.5	2.35, 2.037, 1.723	2.35, 2.037, 1.723
		45	2.35, 2.037, 1.723*	2.35, 2.037, 1.723*
		67.5, 78, 90	2.35, 2.037	2.35, 2.037, 1.723*
	Shear	0, 12, 22.5, 45	2.35, 2.037, 1.723, 1.41	2.35, 2.037, 1.723, 1.41
		67.5, 78, 90	2.35, 2.037, 1.723	2.35, 2.037, 1.723, 1.41
	522	In-plane dipole	0, 12, 22.5, 67.5, 78	2.35, 2.037, 1.723, 1.41, 1.097, 0.783
45, 90			2.35, 2.037, 1.723, 1.41, 1.097, 0.783	2.35, 2.037, 1.723, 1.41, 1.097, 0.783*
Micro-crack		0, 12, 22.5	2.35, 2.037, 1.723, 1.41, 1.097	2.35, 2.037, 1.723, 1.41, 1.097
		45	2.35, 2.037, 1.723, 1.41	2.35, 2.037, 1.723, 1.41
		67.5	2.35, 2.037, 1.723	2.35, 2.037, 1.723*
		78, 90	none	none
Shear		0, 12, 22.5, 45	2.35, 2.037, 1.723, 1.41, 1.097, 0.783	2.35, 2.037, 1.723, 1.41, 1.097, 0.783
		67.5, 78, 90	2.35, 2.037, 1.723, 1.41, 1.097	2.35, 2.037, 1.723, 1.41, 1.097

* Indicates that the WT magnitude for this depth (for the angles indicated) was normalized by a *localized* peak WT magnitude of the proper mode for 0° radiation angle data, (since the *maximum* WT peak at 0° had a different mode)

Figure 3 shows a plot of averaged normalized values of peak WT magnitudes as a function of radiation angle for an in-plane dipole source; separate curves are shown for propagation distances of 60 mm and 180 mm. It should be noted here that the data for all three propagation distances (60, 120, and 180 mm) were initially examined in a preliminary fashion. For efficiency purposes only, it was then decided to focus upon the two extreme distances, namely 60 and 180 mm. Figures 4 and 5 show similar results for a microcrack and balanced shear source, respec-

tively. The main point to be gained from these figures is that the curves for propagation distances of 60 mm and 180 mm are very similar to each other, and often times are directly overlapping.

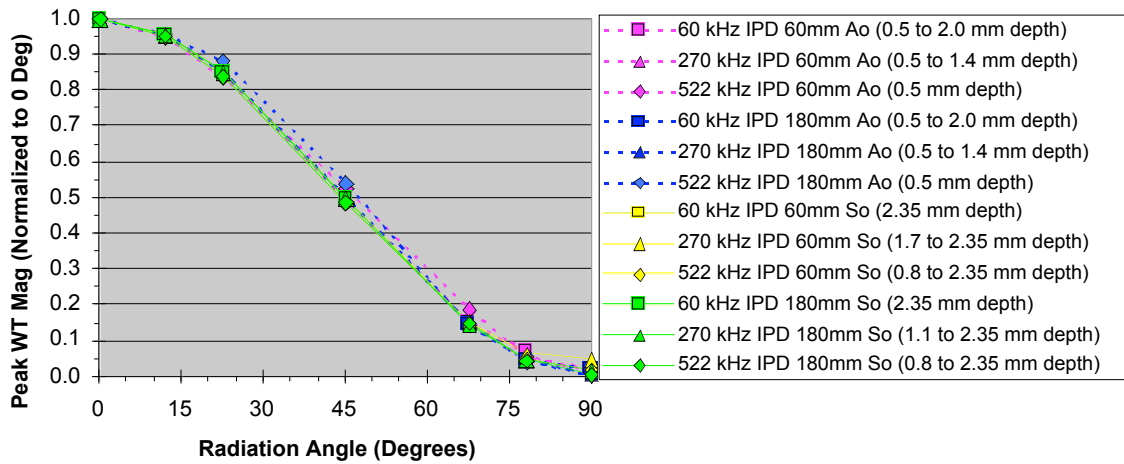


Fig. 3 Averaged results for 60 mm versus 180 mm propagation distance for in-plane dipole source.

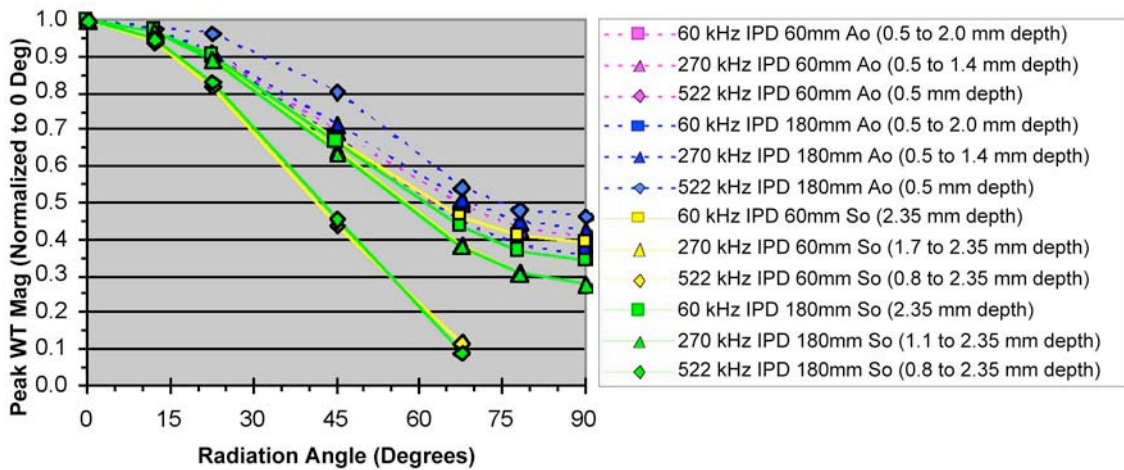


Fig. 4 Averaged results for 60 mm versus 180 mm propagation distance for microcrack initiation source.

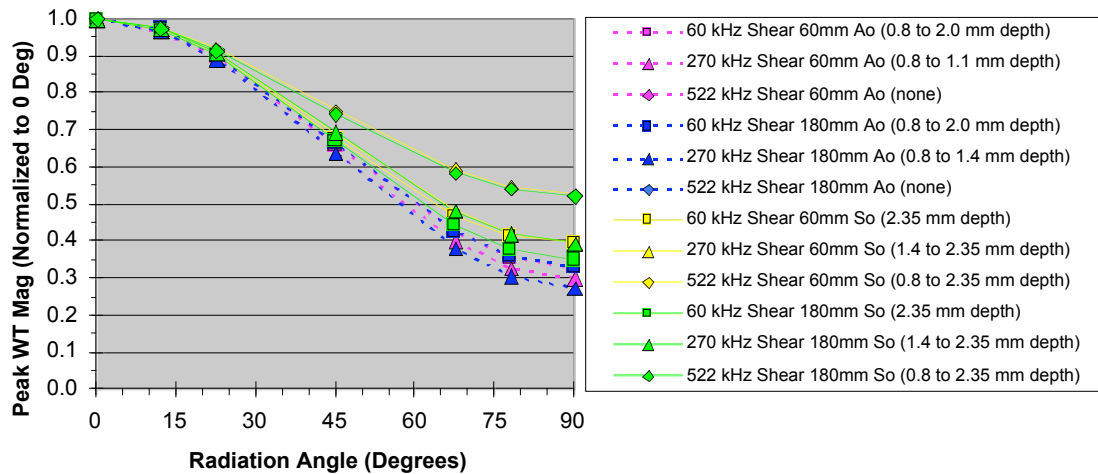


Fig. 5 Averaged results for 60 mm vs. 180 mm propagation distance for balanced shear source.

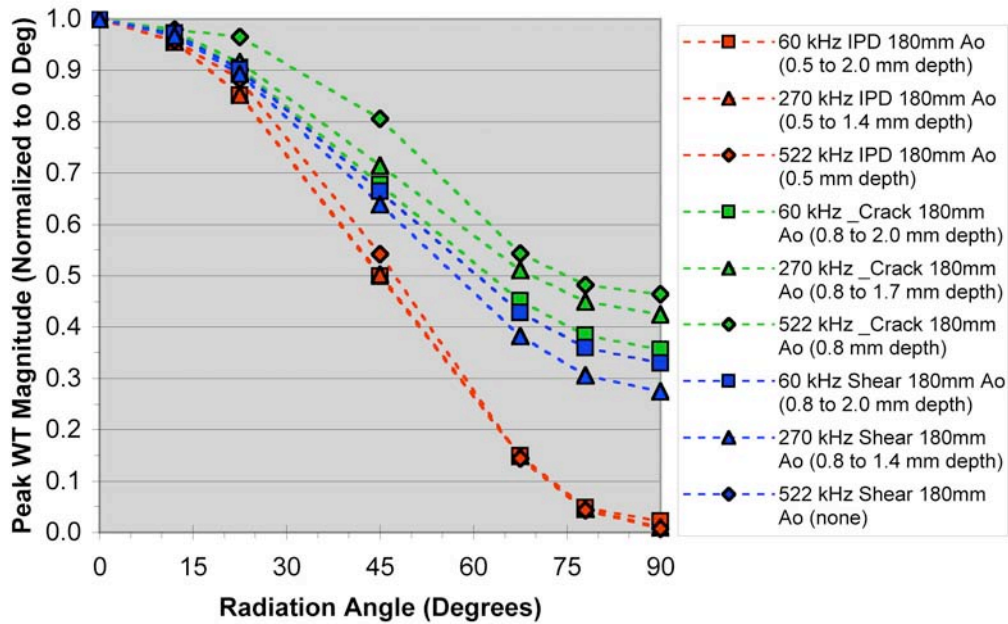


Fig. 6 Normalized peak WT magnitudes for A_0 mode (averaged for multiple depths) for all three source types for 180 mm propagation distance.

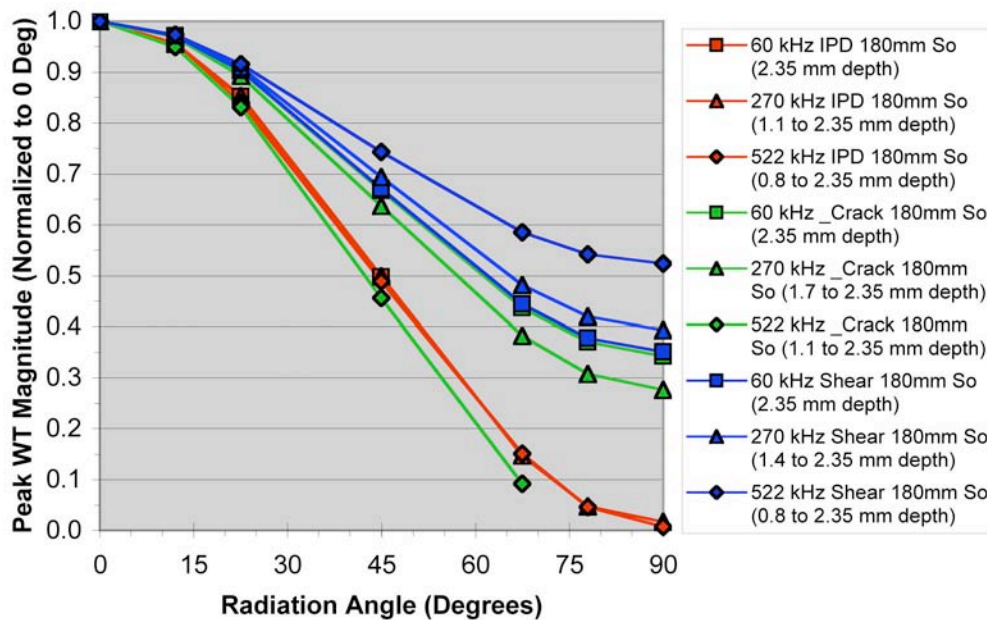


Fig. 7 Normalized peak WT magnitudes for S_0 mode (averaged for multiple depths) for all three source types for 180 mm propagation distance.

Because of the great similarity in the normalized results for all three source types for the two extreme propagation distances of 60 and 180 mm, all further analysis in this paper focused upon data from only the 180 mm propagation distance. Discussion later in this paper examines in more detail the effects of different propagation distances on WTs. It is worth briefly noting here that in some cases there are two different modes that have nearly the same arrival time in the 60 mm data; however, in the 180 mm data, the dispersion effects of the signals over the greater

propagation distance result in a separation in arrival times of the two modes, thus making the 180 mm data more useful for the development and application of a source-identification scheme.

Figures 6 and 7 show plots for all three source-types of the averaged normalized peak WT magnitudes versus radiation angle for the A_0 and S_0 modes, respectively. For these plots, the curves have been color coded as follows: red indicates an in-plane dipole source; green indicates a microcrack initiation source; and, blue indicates a balanced-shear source. One can readily see in both Figs. 6 and 7 that for certain curves the different source types are distinct, and the differences in normalized peak WT magnitudes generally become greater as the radiation angle increases (with almost no difference in normalized peak WT values at very small angles); such trends imply that one can uniquely distinguish source types for an event of unknown source. Because the curves in Figs. 6 and 7 are not linear, it was hoped that further data manipulation could enhance the source differences already evident in Figs. 6 and 7. Thus, a set of 21 ratios was created for each curve (i.e., for each combination of a given frequency, source type, and mode) shown on Figs. 6 and 7. The ratios were created by comparing normalized WT magnitude data for one radiation angle to another radiation angle for the same curve. For example, the ratios compared data for 90° to 78° ; 90° to 67.5° ; 90° to 45° ; 90° to 22.5° ; 90° to 12° ; 90° to 0° ; 78° to 67.5° ; etc., for all 21 possible ratio combinations for the seven different radiation angles.

Figures 8 through 11 summarize four examples of these ratio results, which use the same red-green-blue color coding for the three source types. These four examples were chosen because they are the frequency-mode combinations that occur most often in the frequency-based WT peak magnitudes for the whole database. The authors note that the S_0 mode results pertain most often to source depths nearer the plate midplane, and the A_0 mode results pertain most often to source depths nearer the plate surfaces. Also, in Fig. 9 there are no ratios shown that include data for the angles of 78° or 90° for the microcrack source having S_0 mode at 522 kHz because the signal had insufficient energy to define a correct mode arrival time.

Ideally one would wish to identify a ratio in which all three source types have a significant normalized peak WT magnitude (to allow for concerns presented by the presence of electronic noise in empirically recorded AE signals), yet in which there are also the greatest differences among the three source types. It is worth noting that, for all four examples examined, the greatest distinctions among source types are apparent for ratios including greater radiation angles, and the ratios using only smaller angles show almost no distinction between source types. From this observation, one might be tempted to rely heavily on the data from these greater radiation angles to identify source types. However, a discussion of peak WT magnitudes is first warranted.

Figures 12-14 show the absolute peak WT magnitudes (without regard to frequency) for the various source types and source depths as a function of radiation angle. An examination of the underlying data shows that as the source depth increases toward the mid-plane, the significant amplitude of the antisymmetric mode decreases and the symmetric mode amplitude increases (albeit at a rate slower than that at which the antisymmetric mode amplitude changes). A minor exception to this trend occurs for the in-plane dipole and microcrack sources, which show a slight increase in the symmetric-mode amplitude near the plate surface; this exception might be accounted for due to reduced constraint because of the presence of a nearby free surface. The net overall effect of the antisymmetric-mode and symmetric-mode trends is that the greatest peak WT magnitudes occur for AE sources near the plate surface for all three source types, with decreasing peak WT magnitudes at greater source depths.

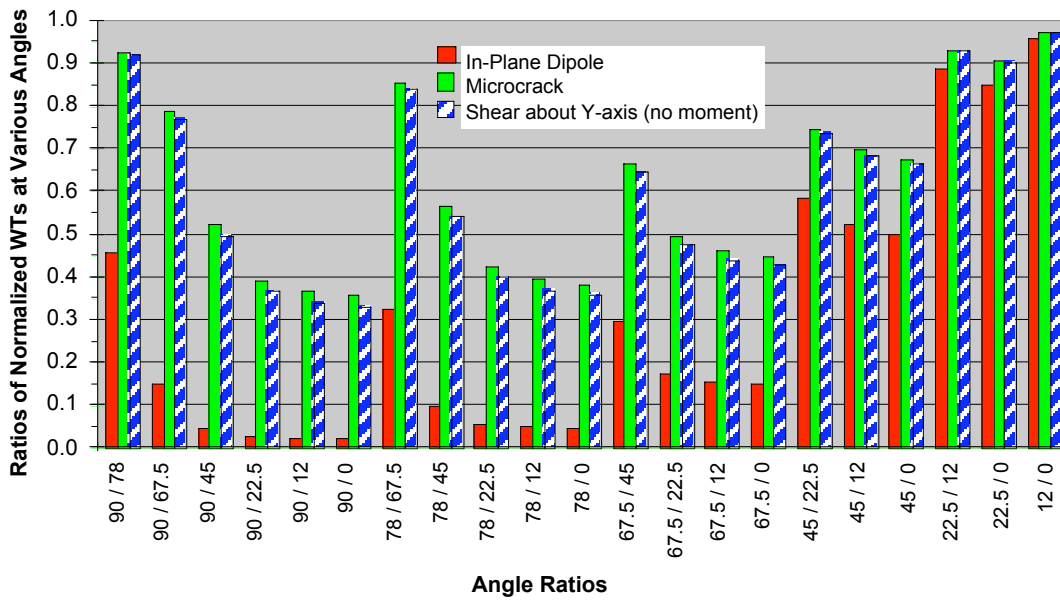


Fig. 8 Ratios of normalized peak WT magnitudes for A₀ mode at 60 kHz at various radiation angles for all three source types.

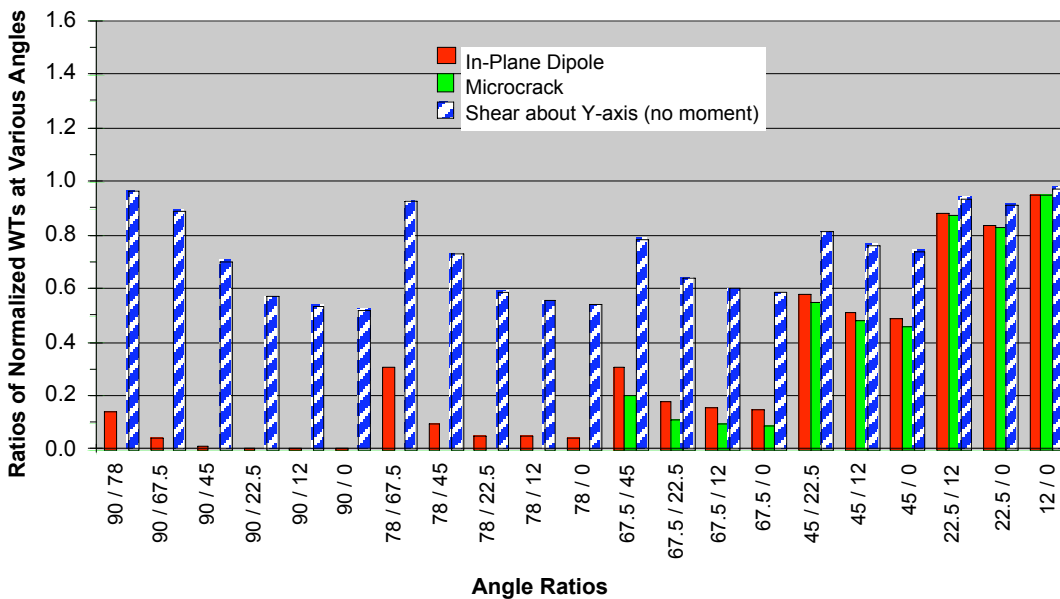


Fig. 9 Ratios of normalized peak WT magnitudes for S₀ mode at 522 kHz at various radiation angles for all three source types.

More importantly, one should note that the absolute peak magnitudes of the WT signals fall off (sometimes dramatically) at greater radiation angles. For all three source types, the rate at which the WT signal falls off is most dramatic for sources nearest the plate surface. Of the WT magnitudes for the three source types, the in-plane dipole falls off most dramatically overall (with its 90° magnitude generally being only about 2% of its original 0° degree magnitude); microcrack WT magnitudes are the least for the three source types at 0°, but they fall off much more moderately (with their 90° magnitude being about one-third of their original 0° magnitude); the shear source has the greatest 0° WT magnitudes of the three source types, and also falls off moderately (with its 90° magnitude being about one-third to one-half of its 0° magnitude).

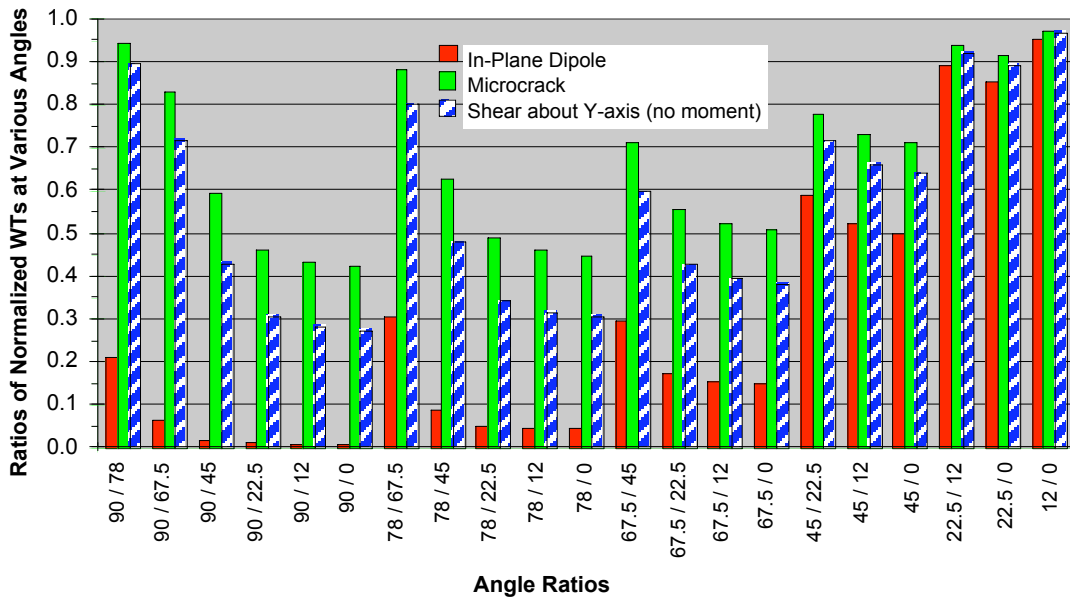


Fig. 10 Ratios of normalized peak WT magnitudes for A₀ mode at 270 kHz at various radiation angles for all three source types.

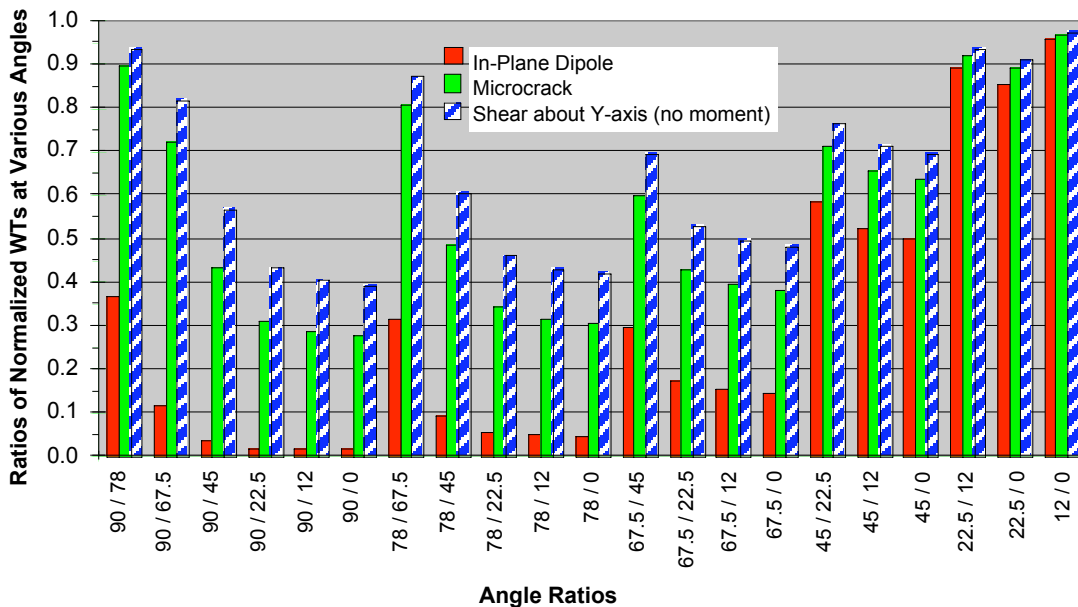


Fig. 11 Ratios of normalized peak WT magnitudes for S₀ mode at 270 kHz at various radiation angles for all three source types.

Thus, the data curves and ratios (in Figs. 6 through 14) show two opposing trends: the greatest distinctions between source types are at the greatest radiation angles, but these greater radiation angles have peak WT magnitudes that have fallen off significantly from the original 0° values, and perhaps are so small as to be not usable, particularly for some sources near the mid-plane of the plate. If one wishes to choose the most appropriate ratio to use in distinguishing the three source types from each other, one must therefore make a compromise choice that leans toward using data from moderate radiation angles (perhaps 22° to 67.5° or so in the numerator, and 0° to 45° or so in the denominator) to ensure that the signal magnitude and source-type distinctions are both sufficient.

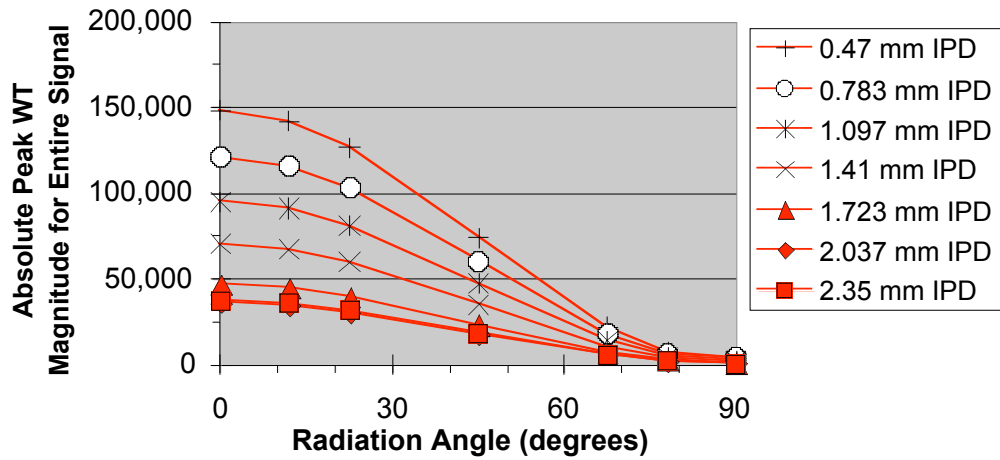


Fig. 12 Absolute peak WT magnitudes vs. radiation angle for various source depths for in-plane dipole source at 180 mm propagation distance.

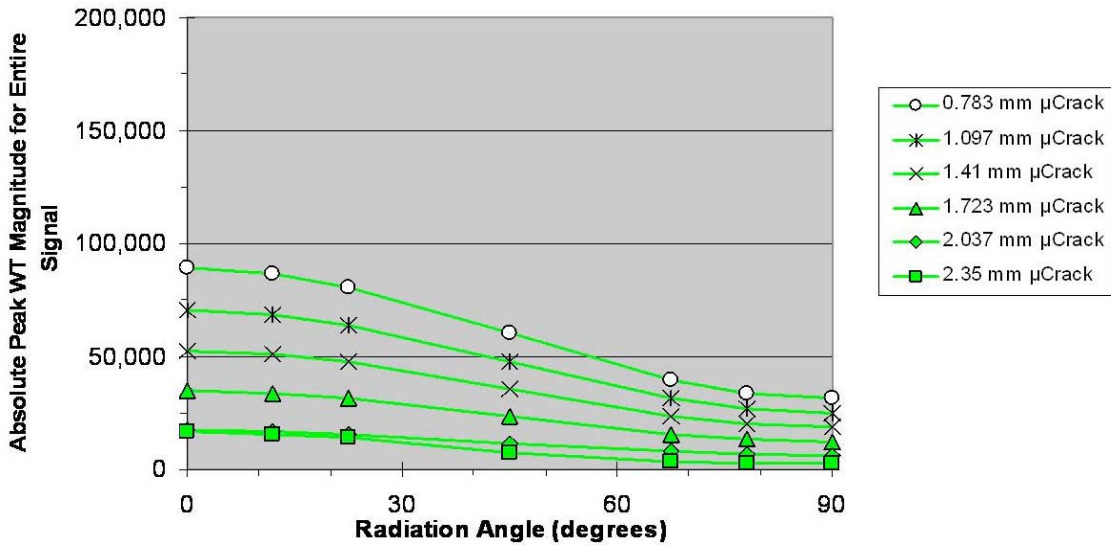


Fig. 13 Absolute peak WT magnitudes vs. radiation angle for various source depths for microcrack initiation source at 180 mm propagation distance.

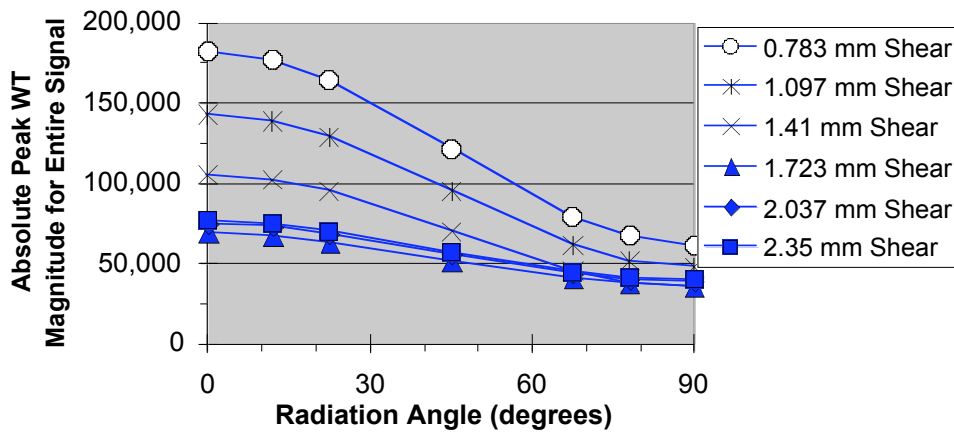


Fig. 14 Absolute peak WT magnitudes vs. radiation angle for various source depths for balanced shear source at 180 mm propagation distance.

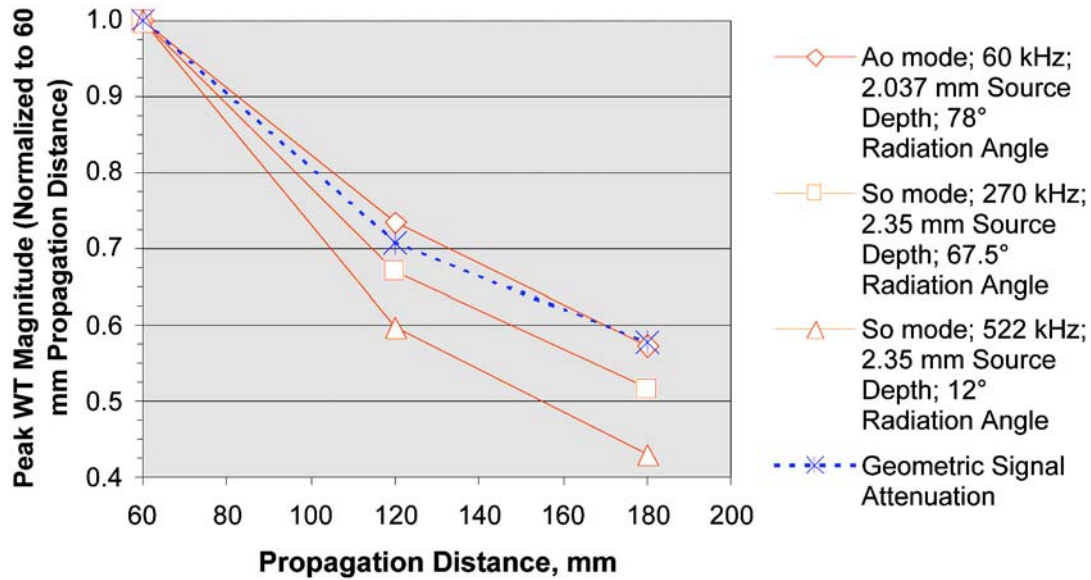


Fig. 15 Attenuation of peak WT magnitudes for microcrack initiation source for various combinations of mode, frequency, source depth, and radiation angle.

For the A_0 mode ratios for 60 kHz (Fig. 8), the in-plane dipole source is readily distinguished from the other two source types by any ratio of WT magnitudes in which at least one of the angles in the ratio is 45° or greater (e.g., WT magnitude for 45° / WT magnitude for 0°). None of the A_0 at 60 kHz ratios is particularly effective in distinguishing the microcrack from the shear source, although it can be noted that the microcrack ratio is always slightly less than the shear ratio for A_0 at 60 kHz.

The S_0 mode for 522 kHz (Fig. 9), readily distinguishes the shear source from the other two source types when at least one angle in the ratio is 45° or 67.5° . The ratio of the WT magnitude for 67.5° / WT magnitude for 45° has more moderate distinctions between the in-plane dipole and microcrack, yet also likely still maintains a reasonable peak WT magnitude.

Figures 10 and 11 display ratios for A_0 at 270 kHz and S_0 at 270 kHz, and one can see significant differences between the source types. These differences are similar in nature to those pointed out in figures 8 and 9. Upon closer examination of all 19 cases in the current database (i.e., three source types and six or seven source depths for each source type), the source type for eight of the 19 cases could be determined by using only primary WT angle ratios of the WT magnitude for 45° / the WT magnitude 0° at either A_0 at 60 kHz or S_0 at 522 kHz, as appropriate. But to uniquely identify the other 11 cases, it was additionally necessary to use secondary ratios from one of the following frequency-mode combinations: A_0 at 270 kHz, S_0 at 522 kHz, A_0 at 270 kHz, or S_0 at 270 kHz.

Successfully analyzing empirical AE data using the analysis approach described will obviously require giving greater consideration to various practical issues such as signal-to-noise ratios; however, the specific considerations necessary to account for noise issues are beyond the scope of this paper. In the present scenario (which used FEM AE signals without any noise), clearly the ability to uniquely identify the current set of three source types was possible using the angle-based ratio of WT magnitudes. Additional source types could likely also be identified using the same approach. For example, an out-of-plane dipole is an axisymmetric source, hence the angle ratios of WT magnitudes would all be equal to one.

6. Discussion of the Use of Normalized Single-Mode WT Magnitude Ratios for Various Radiation Angles for Source Identification

The technique described above does provide a means for the identification of the AE source type among the three source types considered. Due to symmetries in radiation patterns, the results from this study (which examined radiation angles from 0 to 90°) are directly applicable to radiation angles from 0 to 360°. The technique is successful because the radiation pattern of a particular mode and frequency is largely independent of the source depth over the range of depths for which the frequency-mode combination has a reasonable presence in the signal. However, developing the technique for use with experimental data will require additional research to resolve several issues.

The first issue to consider is the fact that when experimental data are recorded by multiple sensors located at various radiation angles from the source, it is highly unlikely that the propagation distances from the source to the various sensors will be equal. An approach to account for this scenario would be to use attenuation data such as those shown in Fig. 15 to correct the peak WT magnitudes at the different sensors to a common propagation distance. Straightforward research would need to confirm the success of such a basic approach.

A second issue regarding signal-to-noise (S/N) ratio is potentially more difficult to resolve. Electronic noise magnitudes in recorded AE signals are similar for all radiation angles and propagation distances. Thus, when one recalls that the peak WT magnitudes for AE signals do fall off (sometimes greatly) at larger radiation angles (see Figs. 12-14), it becomes apparent that the contributions of electronic noise may overwhelm the AE displacements for signals recorded at certain radiation angles from the source (perhaps 60 to 90°, and angles related to these by radiation symmetry). Thus, at larger radiation angles, the noise may be sufficiently great (compared to the AE signal) that the peak WT magnitude and/or its arrival time for the selected mode could be determined at best only inaccurately (or not at all). Such inaccuracy could result in the value of peak WT magnitude recorded as being greater or lesser than the actual value (caused by additive or negative reinforcement of the AE signal by the noise), or the arrival time of the WT peak may not correctly correspond to the mode of interest. Either type of error may give a peak WT magnitude not associated with or representative of the actual mode of the AE signal. Even for those events in which the signal magnitudes are quite large for the primary frequency, it is still desirable for the magnitudes from a secondary frequency also to be sufficiently large to be usable (for cases when the secondary frequency information is necessary to distinguish between source types), which may not be possible if the secondary S/N ratios are too low, as may occur even at moderate radiation angles.

The aspect of S/N ratios and their effect on the ability to perform source identification will be studied in detail in future research. Such a study can be done by use of a technique in which recorded electronic noise signals are numerically added in various amounts to finite-element-modeled AE signals; a study using a similar technique has already been completed, and has made a significant first step in examining the effect of S/N ratios on the accuracy of determined WT-based arrival times for calculating source locations [9].

Finally, it is not necessary to normalize the WT peak magnitudes by the 0° magnitudes, since direct ratios of WT peak magnitudes at two different angles yield the same numeric result as ratios of normalized WT values, assuming the propagation distance is the same for both WT peak magnitudes. The normalization was useful, however, to compare the WT peak magnitude results

at different depths as a function of the radiation angle (as shown in figures 2 to 7) prior to taking ratios at two different angles.

7. Conclusions

The following conclusions apply to the results for the 4.7 mm thick aluminum plate. For other materials and/or plate thicknesses, appropriate changes in key frequencies and associated modes will be necessary. These changes could likely be predicted using modeled AE signals.

A primary benefit of WTs versus other potential analysis techniques for AE signals is that magnitude information is created as a function of both time and frequency, thus allowing a focused examination at specific frequencies of particular interest and determination of arrival times of various modes. Wideband AE data is thus necessary to take advantage of the frequency information produced by the WT.

The exploration of energetic combinations of fundamental modes and frequencies of interest that are present in wideband AE data is made possible by the use of WT information in conjunction with group velocity curves.

The radiation pattern of the peak WT magnitudes (as normalized by the 0° value) for a fixed frequency and mode is almost totally independent of source depth. For particular frequencies and modes, this radiation pattern changes as a function of the AE source type.

For the three source types studied (in-plane dipole, microcrack initiation, and 45° shear without a moment) and the six or seven depths considered, the source type can be uniquely identified by certain simple single-mode ratios of peak WT magnitudes because of the differences in radiation patterns among different source types. Specifically, the ratios must be based on data for the same AE propagation distance at two selected radiation angles by the use of the primary frequency-mode combination, and in some cases supplemented by the inclusion of secondary frequency-mode information. The choice of radiation angles must be given some care to ensure both that the peak WT magnitudes are sufficiently large (they are greatest at angles in the range of 0° to 60° , and related symmetric angles) and that the differences in the source types ratios are maximized (which occurs at angles in the range of 45° to 90° , and related symmetric angles).

For the plate studied, the key frequency-mode combinations that are necessary for unique source identification are A_0 at 60 kHz, S_0 at 522 kHz, A_0 at 270 kHz, and S_0 at 270 kHz.

Acknowledgements

This work was partially supported by NASA Langley Research Center. We also acknowledge the original development of the finite element code by John Gary (retired) of NIST, Boulder, Colorado. We wish to express our gratitude to Prof. M. Takemoto, who released the source code of the wavelet transform that his group had developed; this wavelet transform source code was utilized in the creation of the AGU-Vallen Wavelet software. We also thank Dr. Y. Mizutani and Mr. Jochen Vallen for making the AGU-Vallen Wavelet software into a highly usable form. The contributions of all the above people have significantly advanced the field of acoustic emission.

References

1. M.A. Hamstad, A. O’Gallagher and J. Gary, “Examination of the Application of a Wavelet Transform to Acoustic Emission Signals: Part 1. Source Identification”, *J. of Acoustic Emission*, **20**, 2002, 39-61.
2. D.J. Buttle and C.B. Scruby, “Characterization of Fatigue of Aluminum Alloys by Acoustic Emission – Part I: Identification of Source Mechanism,” *J. of Acoustic Emission*, **9**, (4), 1990, 243-254.
3. D.J. Buttle and C.B. Scruby, “Characterization of Fatigue of Aluminum Alloys by Acoustic Emission – Part II: Discrimination Between Primary and Secondary Emissions,” *J. of Acoustic Emission*, **9**, (4), 1990, 255-269.
4. C.B. Scruby, “Quantitative Acoustic Emission Techniques,” *Research Techniques in Nondestructive Testing*, Chap. 4, Vol. 8, ed. R. S. Sharpe, Academic Press Inc., London, 1985, pp. 141-210.
5. M. Ohtsu, “Radiation Pattern of Acoustic Emission,” *Zairyo*, **32**, (356) (Japanese), 1983, 577-583.
6. Vallen-Systeme GmbH, München, Germany, <http://www.vallen.de/wavelet/index.html>, 2001, software version R2002.0703.
7. M.A. Hamstad, “An Illustrated Overview of the Use and Value of a Wavelet Transformation to Acoustic Emission Technology,” <http://www.vallen.de/zdownload/pdf/hamstad.pdf>.
8. M.A. Hamstad, K.S. Downs, and A.O’Gallagher, “Practical Aspects of Acoustic Emission Source Location by a Wavelet Transform”, *Journal of Acoustic Emission*, **21**, 2003, xxx.
9. M.A. Hamstad, A. O’Gallagher and J. Gary, “Examination of the Application of a Wavelet Transform to Acoustic Emission Signals: Part 2. Source Location”, *Journal of Acoustic Emission*, **20**, 2002, 62-81.

PRACTICAL ASPECTS OF ACOUSTIC EMISSION SOURCE LOCATION BY A WAVELET TRANSFORM

M. A. HAMSTAD^{1,2}, K. S. DOWNS³ and A. O'GALLAGHER¹

¹ National Institute of Standards and Technology, Materials Reliability Division (853)
325 Broadway, Boulder, CO 80305-3328

² University of Denver, Department of Engineering, Denver, CO 80208

³ Contractor to National Institute of Standards and Technology, Boulder, CO

Abstract

An algorithmic approach to improve the accuracy of acoustic emission (AE) source location was demonstrated by using a large database of wideband-AE-modeled signals and wavelet-transform (WT) results. The AE-signal database was created by a three-dimensional, finite-element code. These signals represented the out-of-plane displacements from buried dipole AE sources in aluminum plates of 4.7 mm thickness and large lateral dimensions. The AE signals included eight different source types, six or seven source depths (below the plate surface), and seven different radiation angles (0° to 90°). The surface displacement signals were measured at three propagation distances (i.e., 60, 120, and 180 mm) and were filtered with a 40 kHz high-pass filter. The WT results consisted of WT magnitudes (i.e., WT coefficients) as a function of both time and frequency. The regions of greatest WT magnitude were found to occur at or very near three key frequencies (60, 270, and 522 kHz), and these regions were typically representative of the first fundamental antisymmetric mode (A_0) or the first fundamental symmetric mode (S_0). Additionally, a plot of the signal-propagation distances as a function of the WT-peak-based arrival times created slope-based velocities that corresponded quite closely to the relevant theoretical group velocities for the A_0 or S_0 modes. It was determined that the key frequency having the greatest WT peak magnitude always corresponded to a known mode having a known group velocity. The remaining two key frequencies had their associated modes determined by means of a newly devised algorithm (which could be computer-automated) that considers the arrival times of the WT peak magnitudes but requires knowledge of neither the propagation distance nor the AE-source-operation time. The algorithm also computed a range (i.e., linear distance) from a measured signal to the AE source.

Key Words: Acoustic emission; Acoustic emission modeling; Finite element modeling; Source location; Wavelet transform; Wideband acoustic emission.

Contribution of the U.S. National Institute of Standards and Technology; Not subject to copyright in the United States. Trade names are included for information only; endorsement is neither intended nor implied.

1. Introduction

In a recent publication [1], some initial promising results were presented on the use of a wavelet transform (WT) to enhance the accuracy of the location of acoustic emission (AE) sources. The results showed that accurate signal arrival times could be extracted from peak magnitudes of wavelet transform results for key frequencies. These arrival times correspond to known group velocities from dominant energy regions of the fundamental Lamb modes present in the signals. Since that reference pointed out the difficulties with the standard AE location

technique (i.e., penetration of fixed voltage thresholds to determine the arrival times), the discussion is not repeated here. For the same reason, alternate source location (arrival time determination) approaches, including some based on the use of a WT, are not discussed and referenced here. The unique aspect of the previous publication [1] and the research presented in this paper is the use of an AE signal database that was created by finite-element modeling (FEM) techniques. Both the experiments to validate this FEM technique and some of the results of the application of the FEM approach have been previously published [2-6]. The fundamental advantage of the use of the modeled signals is that the exact three-dimensional location (relative to the sensors) of the AE sources is known along with the source origination time. Hence, all of the current research results can be quantitatively examined with respect to the exact location of the realistic dipole-type sources.

The research reported here had two basic objectives. The first was to extend the limited study [1] to a much broader AE signal database that included multiple AE source types and multiple radiation angles as well as multiple source depths (below the surface of the plate samples). The second objective was to develop a methodology that would allow automatic determination of the Lamb mode and consequently the group velocity associated with an arrival time obtained from a WT. To be useful for the practical application of AE source location, this methodology must function when the source operation time and the propagation distance are unknown. For an unknown propagation distance and source operation time, the group velocity curves cannot be accurately and automatically superimposed on the WT result. Thus, the correct mode and associated group velocity must be determined in some other fashion.

2. Description of the FEM-based Signal Database and WT Signal Processing

The description of the generation of the AE signal database was given previously [7]. Hence, only certain key or additional aspects are highlighted here. The FEM signals were generated in an aluminum plate (1 m x 1 m x 4.7 mm). The signals represent the out-of-plane top surface displacement from a flat-with-frequency point-contact sensor. Each FEM signal calculation started at the beginning of the operation of the source (rise time of 1.5 μ s) and continued for 200 μ s. Due to the lateral size of the plate, plate-edge reflections did not superimpose on the direct arrival of the signals. The AE signals were calculated for three in-plane propagation distances (60 mm, 120 mm, 180 mm) and seven in-plane radiation angles (0°, 12°, 22.5°, 45°, 67.5°, 78°, and 90°). Also, a total of eight AE source types composed the database as follows, where the plate surface is parallel to the x and y axes:

- (1) single in-plane dipole in 0° direction along x-axis;
- (2) microcrack initiation, with the major axis in x-direction;
- (3) single out-of-plane dipole along the z-axis;
- (4) dilatation aligned with coordinate axes;
- (5) in-plane shear (x-axis direction) about the y-axis with a net moment;
- (6) out-of-plane shear (z-axis direction) about the y-axis with a net moment;
- (7) shear (x-axis and z-axis) about y-axis with no net moment; and,
- (8) shear (about y-axis) inclined at 45° to x-axis with no net moment.

The depths (z-axis) from the top of the plate surface of the centers of the modeled sources were 2.35, 2.037, 1.723, 1.41, 1.097, and 0.783 mm for all eight source types. Additionally, two sources (i.e., the single in-plane dipole and the out-of-plane shear) had one more source depth of 0.47 mm.

All the FEM-calculated AE signals were processed in the following fashion. Prior to performing the WT, the FEM-calculated signals were all numerically filtered with a 40 kHz four-pole Butterworth high-pass filter. Then the signals were re-sampled from their original time increment of 44.6 ns to a time increment of 0.1 μ s, and the signals were extended with zeroes beyond 200 μ s, for a total of 8192 points in each signal.

Each adjusted FEM signal had a wavelet transform performed upon it by use of a software program called AGU-Vallen Wavelet version R2002.0703 [8]. For each WT computation, a number of processing parameters must be specified. The following Wavelet Transformation Settings were used for the first part of this work (with only one exception, when a frequency resolution of 2 kHz was used): maximum frequency = 700 kHz; frequency resolution = 3 kHz; wavelet size = 600 samples. The following Wavelet Time Range Settings were used: number of samples (i.e., points) = 800 for 60 mm distances, 1200 for 120 mm distances, and 1500 for 180 mm distances; offset samples = 0.

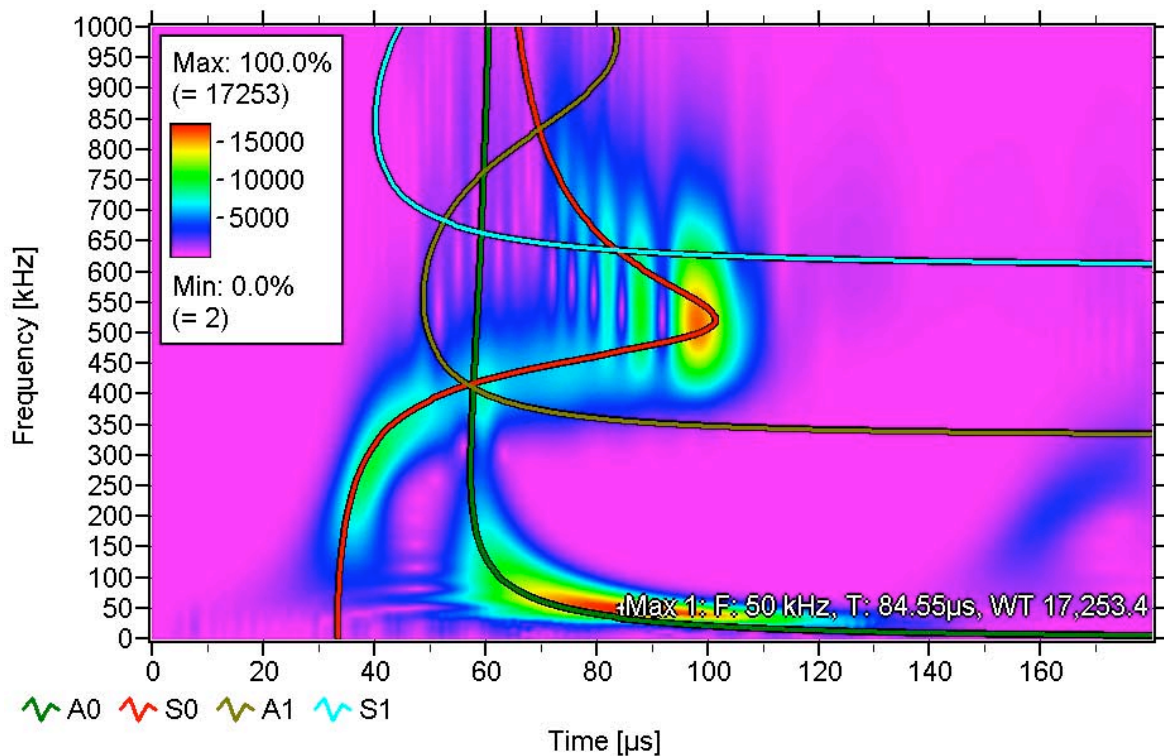


Fig. 1 Typical WT result with superimposed group velocity curves. The maximum WT magnitude is located at the + sign at 50 kHz, 84.5 μ s, magnitude of 17,253 and A_0 mode.

The resulting output for each wavelet transform consists of numerical values for the WT magnitude (i.e., WT coefficients) as a function of both time and frequency. This output can be viewed numerically in a spreadsheet format, or in a more qualitative graphic format where various colors are used to indicate the WT magnitude on a time-vs.-frequency plot. A software feature also allows superposition of the theoretical Lamb-wave group velocities onto the graphical WT result; however, knowledge of the propagation distance and the source origination time are required to correctly superimpose the group-velocity curves. Figure 1 shows a typical WT result with superimposed group-velocity curves along with the location of the absolute peak magnitude and its associated frequency and arrival time.

3. Preliminary Examination of WT Database

It was desired to review the overall data first in a preliminary fashion and note general trends regarding the regions of significant WT magnitude. Thus fifty signal cases for the 0° propagation direction (i.e., eight source types with six or seven depths each for a single propagation distance of 180 mm) were each examined to find and characterize the three most highly energetic regions of the WTs (i.e., noting the frequency regions and associated modes having the greatest WT magnitudes). Note that some WTs only had one or two highly energetic regions. Additionally, the absolute maximum WT magnitude along with its associated mode and frequency were noted.

4. Analysis Terminology and Preliminary Observations

As a result of the preliminary study, a total of three “key” frequencies (60, 270, and 522 kHz) were selected to be examined for each WT signal. These specific frequencies were chosen because in all of the WT cases examined the most energetic regions of the WTs were located at or very near one or more of these three frequencies. In choosing 60 kHz as the lowest key frequency, consideration was given to ensure that signal arrival times would not be distorted by the 40 kHz high-pass filter. Specifically, the authors examined the linearity of the arrival times for several known signal cases at the three propagation distances over a series of frequencies starting at 54 kHz.

Of the three “key” frequencies examined, the one having the greatest peak WT magnitude was defined as the “primary” peak (or “primary” frequency), and the next two frequencies in descending order of peak WT magnitude were called the secondary and tertiary.

It was noted that certain modes were very often associated with these “key” frequencies; thus the authors defined the following “principal modes” for the “key” frequencies: the A_0 mode at 60 kHz, the S_0 mode at 270 kHz, and the S_0 mode at 522 kHz. When the entire database was more thoroughly examined (as described in more detail below), a critical observation was made. Namely, the associated mode for the primary frequency was *always* the “principal mode”; this observation held true even when radiation directions other than 0° were considered (as discussed much later in this article). However, the associated mode for the secondary and tertiary frequencies was not necessarily the same as the “principal mode” for that frequency. For example, in some cases the peak at 522 kHz was found to be associated with the A_0 mode (or in just a few cases the A_1 mode) rather than with the S_0 mode.

A term called “WT fraction” was defined as the peak WT magnitude at a given frequency divided by the greatest value from among the peak WT magnitudes for 60 kHz, 270 kHz, and 522 kHz for a particular signal case. The frequency (60, 270 or 522 kHz) for which the WT fraction equaled 1 corresponds to the previously defined primary frequency; similarly, the frequency with the second greatest WT fraction corresponds to the secondary frequency; the frequency with the least WT fraction corresponds to the tertiary frequency. Thus, the definition of the term “principal mode” can be restated as follows: the principal mode for each of the key frequencies is the only mode at that frequency for which the WT fractions equaled 1 when the whole signal database was examined.

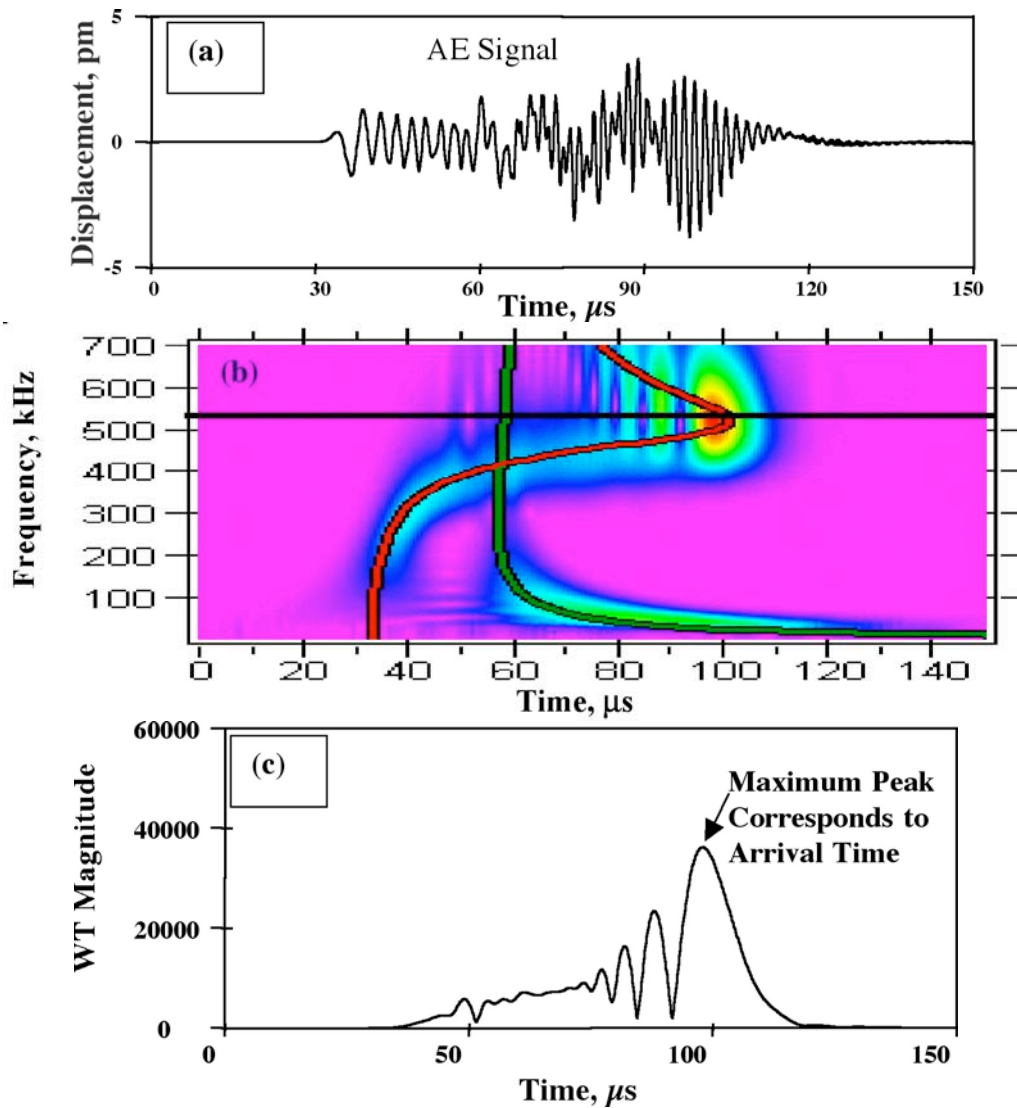


Fig. 2 Process of using wavelet transform (WT): (a) start with AE displacement signal; (b) perform WT and identify mode of high intensity region at frequency of interest; (c) examine WT magnitude values at particular frequency of interest to find peak magnitude and its associated arrival time (current software does this automatically upon selection of frequency).

5. Determination of Arrival Times and Associated Group Velocities for 0° Radiation Direction

A thorough examination was made of the WTs of each of the 150 cases in the signal database for the propagation direction of 0°. For each WT, the primary frequency and the peak WT magnitudes and their arrival times for each of the three key frequencies were determined. This process is shown graphically in Fig. 2. Since data for three propagation distances were available for each of the 50 unique cases (i.e., source type and source depth), a computed group velocity (slope) could be determined from a linear analysis of propagation distance versus arrival time. Table 1 gives key information about the primary WT peaks for each of the 50 modeled cases in the 0° propagation direction, including the primary frequency (at its associated principal mode) as well as the slope-based and theoretical group velocities. Table 1 also includes a column called

Table 1 Primary WT results for different source types and depths for 0° radiation angle

Source Type	Source Depth (mm)	Primary Frequency (kHz), Mode	Slope-based group velocity (mm/ μ s)	Theoretical group velocity (mm/ μ s)	Y-axis intercept (mm)	r ² value
In-plane dipole	2.35	522, S ₀	1.82	1.78	2.19	1.0000
	2.037	522, S ₀	1.82	1.78	2.30	1.0000
	1.723	60, A ₀	2.51	2.55	-15.18	0.9999
	1.41	60, A ₀	2.52	2.55	-15.74	0.9999
	1.097	60, A ₀	2.52	2.55	-16.04	1.0000
	0.783	60, A ₀	2.53	2.55	-16.24	1.0000
	0.47	60, A ₀	2.54	2.55	-16.66	1.0000
Microcrack initiation	2.35	522, S ₀	1.81	1.78	2.84	1.0000
	2.037	522*, S ₀	1.80	1.78	3.19	1.0000
	1.723	60, A ₀	2.52	2.55	-15.65	0.9999
	1.41	60, A ₀	2.52	2.55	-15.95	0.9999
	1.097	60, A ₀	2.53	2.55	-16.24	1.0000
	0.783	60, A ₀	2.53	2.55	-16.45	1.0000
Out-of-plane dipole	2.35	522, S ₀	1.83	1.78	1.34	1.0000
	2.037	522, S ₀	1.83	1.78	1.34	1.0000
	1.723	522, S ₀	1.83	1.78	1.58	1.0000
	1.41	522 ⁺ , S ₀	1.83	1.78	1.58	1.0000
	1.097	60, A ₀	2.53	2.55	-16.66	0.9999
	0.783	60, A ₀	2.53	2.55	-16.87	1.0000
Dilatation	2.35	270, S ₀	4.82	4.84	-5.62	1.0000
	2.037	60, A ₀	2.51	2.55	-15.61	0.9997
	1.723	60, A ₀	2.54	2.55	-16.63	0.9999
	1.41	60, A ₀	2.55	2.55	-17.31	0.9999
	1.097	60, A ₀	2.55	2.55	-17.4	1.0000
	0.783	60, A ₀	2.54	2.55	-17.03	1.0000
In-plane shear about y-axis with moment	2.35	60, A ₀	2.59	2.55	-19.78	1.0000
	2.037	60, A ₀	2.59	2.55	-19.78	1.0000
	1.723	60, A ₀	2.59	2.55	-19.78	1.0000
	1.41	60, A ₀	2.59	2.55	-19.53	1.0000
	1.097	60, A ₀	2.59	2.55	-19.53	1.0000
	0.783	60, A ₀	2.59	2.55	-19.14	1.0000
Out-of-plane shear about y-axis with moment	2.35	60, A ₀	2.59	2.55	-18.79	1.0000

Out-of-plane shear about y-axis with moment	2.35	60, A ₀	2.59	2.55	-18.79	1.0000
	2.037	60, A ₀	2.59	2.55	-18.79	1.0000
	1.723	60, A ₀	2.59	2.55	-18.79	1.0000
	1.41	60, A ₀	2.59	2.55	-18.79	1.0000
	1.097	60, A ₀	2.59	2.55	-19.01	1.0000
	0.783	60, A ₀	2.59	2.55	-19.01	1.0000
	0.47	60, A ₀	2.59	2.55	-18.79	1.0000
Shear 0° about y-axis with no moment	2.35	60, A ₀	2.59	2.55	-17.24	1.0000
	2.037	60, A ₀	2.59	2.55	-17.24	1.0000
	1.723	60, A ₀	2.59	2.55	-17.24	1.0000
	1.41	60, A ₀	2.58	2.55	-17.03	1.0000
	1.097	60, A ₀	2.58	2.55	-17.03	1.0000
	0.783	60, A ₀	2.58	2.55	-17.12	1.0000
Shear 45° about y-axis with no moment	2.35	522, S ₀	1.83	1.78	1.34	1.0000
	2.037	522, S ₀	1.82	1.78	1.70	1.0000
	1.723	522, S ₀	1.82	1.78	1.70	1.0000
	1.41	60, A ₀	2.52	2.55	-16.09	0.9999
	1.097	60, A ₀	2.52	2.55	-16.45	0.9999
	0.783	60, A ₀	2.53	2.55	-16.70	1.0000
* Primary frequency changed to 60 kHz at 180 mm. Since the 522 kHz peak at 180 mm was less than 1 % below that for 60 kHz (the maximum), 522 kHz was selected as the primary frequency for the three propagation distances.						
+ Primary frequency changed to 60 kHz at 180 mm. Since the 522 kHz peak at 180 mm was less than 3 % below that for 60 kHz (the maximum), 522 kHz was selected as the primary frequency for the three propagation distances.						

the “y-axis intercept, mm”. (See appendix A for a more detailed discussion of y-intercepts.) This is the standard intercept that corresponds to zero time for the straight line that fits the three data points in the plot of distance versus arrival time.

Of the 150 slopes calculated, only six slope values did not correspond reasonably well to the expected theoretical group velocities. These six slopes had correlation coefficients (i.e., r^2 values for a straight-line fit) that were low (i.e., less than 0.999). Closer examination of the individual WTs (with superimposed group velocity curves) for these cases revealed that these poor velocities could be explained by the fact that the mode was not consistent for all three propagation distances (e.g., the mode associated with the frequency-based WT peak changed from S₀ to A₀ or A₁, or vice versa, for different propagation distances). Hence, the arrival times and the resulting computed velocities were not consistent with one particular mode, thus yielding a poor value for r^2 .

Three other slope values are noteworthy. They had accurately determined velocities (i.e., r^2 values of 1.000), but were confirmed to be for the A₁ mode rather than the A₀ or S₀ modes. Figures 3 and 4 demonstrate the contrast between cases in which the WT magnitude at 522 kHz has a peak corresponding to the A₀ mode (Fig. 3) versus the A₁ mode (Fig. 4). In all three cases, these slope values were not from the primary frequency.

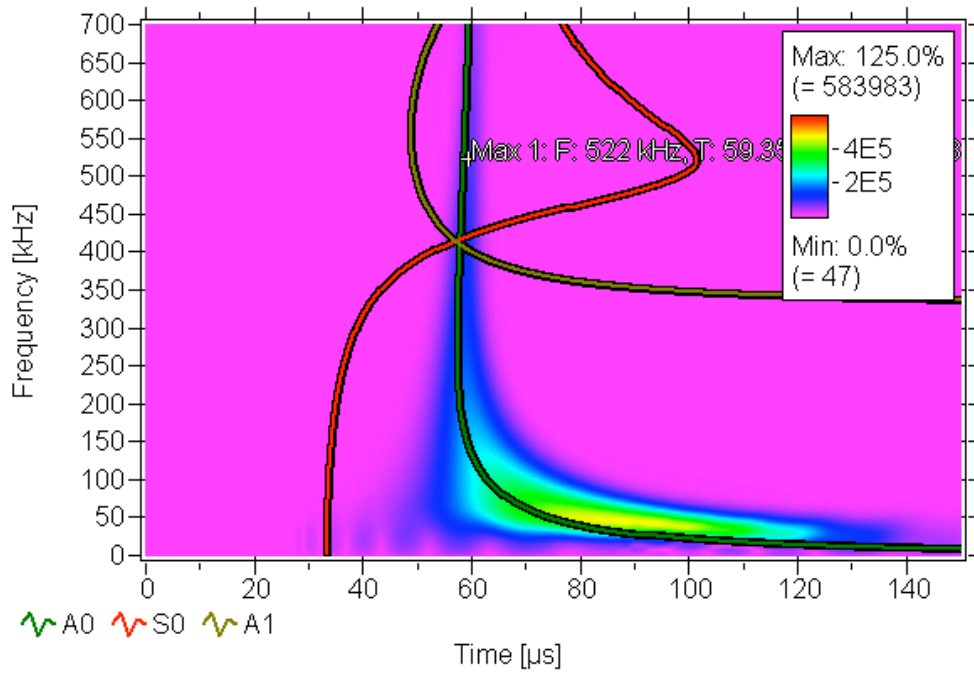


Fig. 3 Wavelet transform in which peak WT magnitude at 522 kHz corresponds to A_0 mode (out-of-plane shear source about y-axis, with moment; 2.35 mm source depth; 180 mm propagation distance).

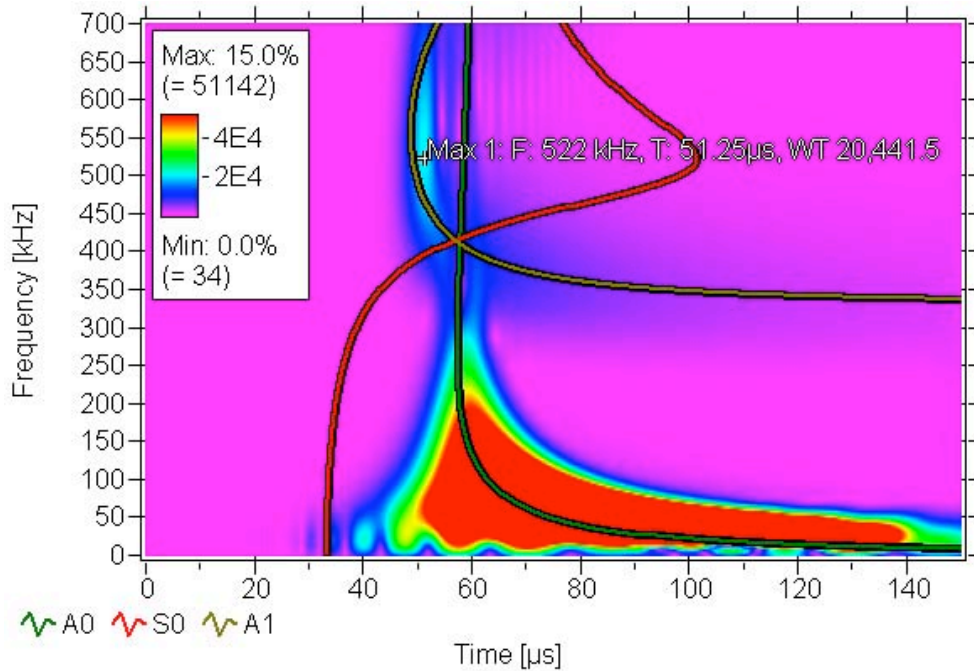


Fig. 4 Wavelet transform in which peak WT magnitude at 522 kHz corresponds to A_1 mode (in-plane shear source about y-axis, with moment; 2.35 mm source depth; 180 mm propagation distance).

As Table 1 indicates, the combination of A_0 at 60 kHz was most often the dominant peak (38 times). The S_0 at 522 kHz combination was the dominant peak eleven times, and S_0 at 270 kHz

was dominant only once. This table also indicates the typically high values of the correlation coefficient (r^2). The value was 0.9999 or greater, except for one case where it was 0.9997. Also, the table shows very good correspondence between the slope-based group velocities and the theoretical group velocities. The maximum difference between the slope-based and theoretical group velocities was only 2.8 %, and the range (maximum to minimum) of slope-based velocities for a given frequency-mode combination was 3.2 % or less of the average.

6. Description of Algorithm Created to Determine Modes at Key Frequencies and Determine Source Location Ranges

The practical implementation of the use of WT-peak-magnitude arrival times for AE source location determination depends upon being able to identify the correct mode associated with the arrival time obtained at a key frequency. Once the mode is known, the correct group velocity can be selected. Then with multiple sensor arrival times for a single AE event, standard source location algorithms can be used along with this group velocity. This procedure is very straightforward when the primary frequency at each hit (from a single AE event) is the same. In this case, the mode of the primary frequency has always been found to be the principal mode within the extensive database examined to date. For the radiation direction of 0° , a total of 150 cases (consisting of eight source types; six or seven source depths for each source type; and three propagation distances for each source type and depth) have been examined, with the result that the mode of the primary frequency was always the principal one. In addition for the six other radiation directions, (each having three important source types with six or seven depths each, and three propagation distances) a total of 342 additional cases have been examined with the same result. These three important source types are an in-plane dipole, a microcrack initiation, and a balanced shear at 45° about the y-axis. Further, due to the known symmetries of radiation patterns, the results for 0° to 90° indicate that the results for 0° to 360° will yield the same conclusion. Thus, all available evidence from the modeled AE signals indicates that the mode of the primary frequency is *always* the principal mode.

As will be discussed later in this article, for a given source type and source depth, the primary frequency can change as a result of different radiation directions and/or different propagation distances. In all such cases, only two different primary frequencies have been observed (at different propagation distances or radiation angles) for a given source type and depth. Thus, one is concerned with two important frequencies in these cases. At each sensor location, one frequency will be the primary, and the other one will be call the “non-primary” frequency. The term “non-primary” frequency was adopted since (contrary to expectations) the “non-primary” one of the two remaining frequencies is not always the secondary frequency and can in fact be the tertiary frequency. Further, in these cases, when the modes associated with the WT-magnitude peaks of these two frequencies were examined, it was found that the mode of the non-primary frequency was also the principal one at all propagation distances and/or radiation angles for which data were available. Thus, in these cases, it is necessary only to add an additional step to the source location calculation. In this step, a choice is made as to which key frequency (called the working frequency) will be used to select arrival times. Due to signal-to-noise considerations, it makes the most sense to select as the working frequency the primary frequency at the last hit sensor. Then, with the group velocity associated with the working frequency, the source location calculation can proceed in a normal fashion with the WT-based arrival times associated with the working frequency.

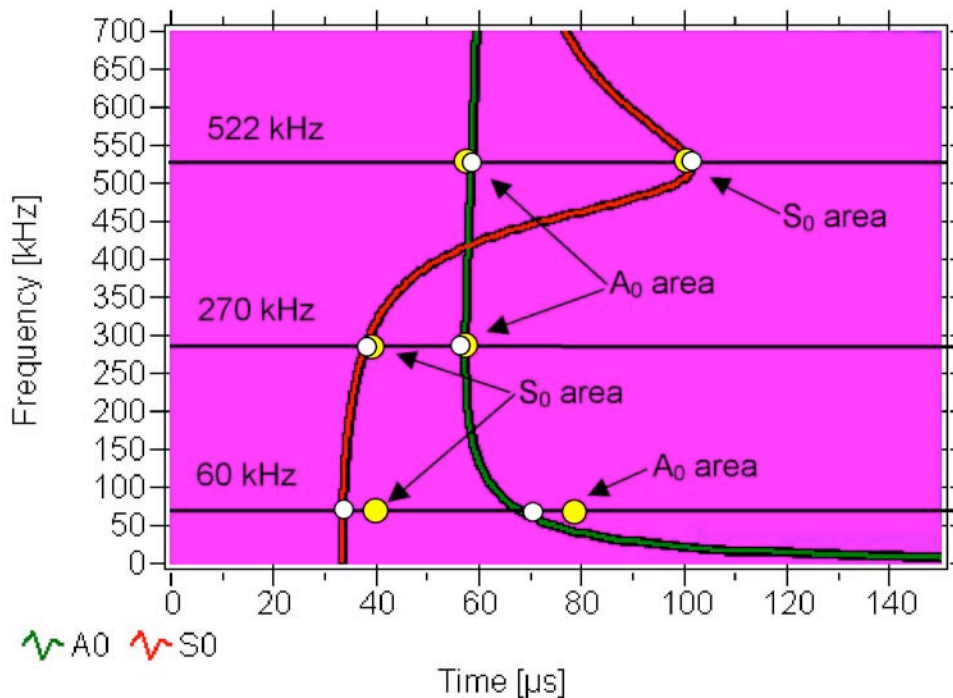


Fig. 5 Frequencies of interest (60, 270, and 522 kHz) and where they correspond to theoretical group-velocity curves for example at 180 mm propagation distance; note that small white circles (theoretical values) show literal intersection of velocity curves with frequencies of interest, whereas larger yellow circles (FEM data) show typical areas of peak WT magnitudes most nearly corresponding to intersection of velocity curves with frequencies of interest.

Since the signal-processing approach with three key frequencies results in three arrival times for each signal, there would be potential opportunities to make more than one calculation of the source location (for a multiple-sensor array); for single-sensor hits, the range to the source location could be calculated. These opportunities could be exploited only if the proper modes of the WT-based arrival times can be identified for the secondary and tertiary frequencies. To be useful for typically large experimental AE data files, the identification of these modes needs to be determined by an automated algorithm (by appropriate software) rather than a trial-and-error process of assuming propagation distances and then superimposing the group velocity curves onto a WT result and visually determining when a match occurs [9]. Thus, the authors made a first attempt to develop and test such an algorithm that could be fully automated. Since the modes corresponding to the WT peaks at the key frequencies were the fundamental modes S_0 and A_0 (except for a very few cases where the 522 kHz non-primary peak magnitude corresponded to the A_1 mode), it was assumed that only the S_0 and A_0 fundamental modes would be associated with the peaks. Thus for the algorithm development, cases where the A_1 mode corresponded to the 522 kHz peak were eliminated.

The algorithm first determines the primary, secondary, and tertiary frequencies (at this point without the determination of associated modes) based upon the ranking of the WT fractions of the peak magnitudes for 60, 270 and 522 kHz. Then, as has already been stated, the mode of the primary frequency peak is known since it is always the principal mode (i.e., A_0 for 60 kHz; S_0 for 270 kHz; S_0 for 522 kHz). The next step in the algorithm was based upon the information shown in Fig. 5. This figure shows the relative relationship in time of the typical locations of the frequency-based peak WT magnitudes corresponding to the two fundamental modes. The figure

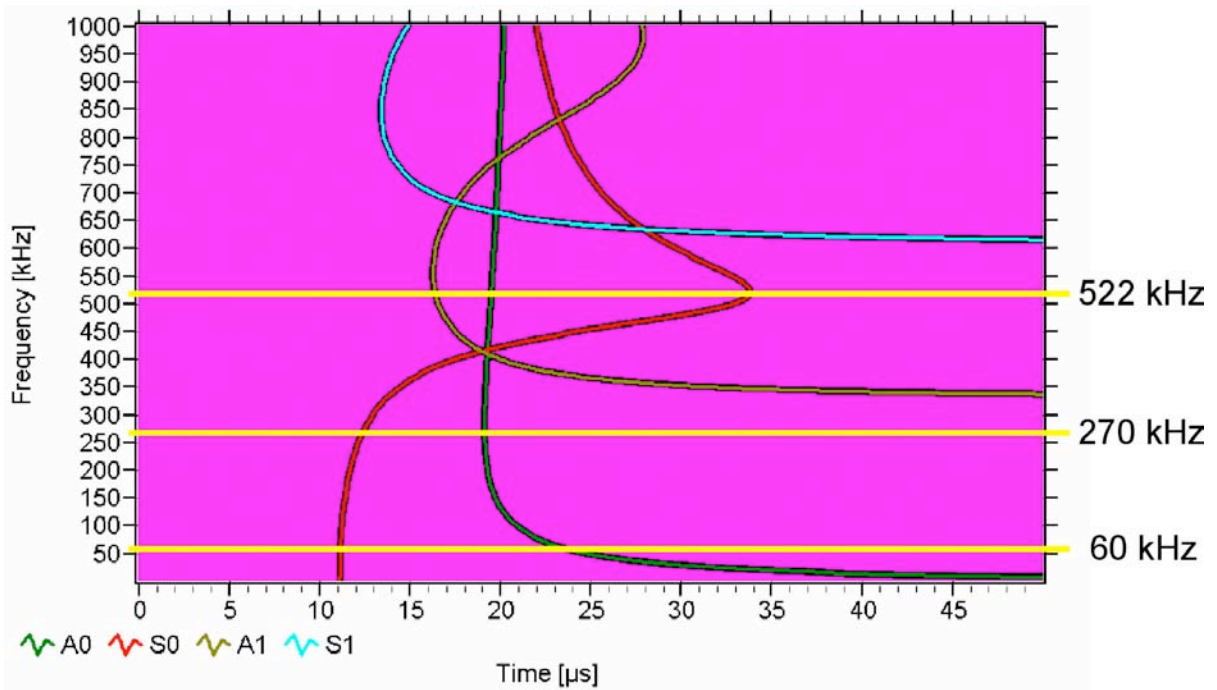


Fig. 6 WT which shows the potential of overlap of WT results for multiple modes at 60 mm propagation distance.

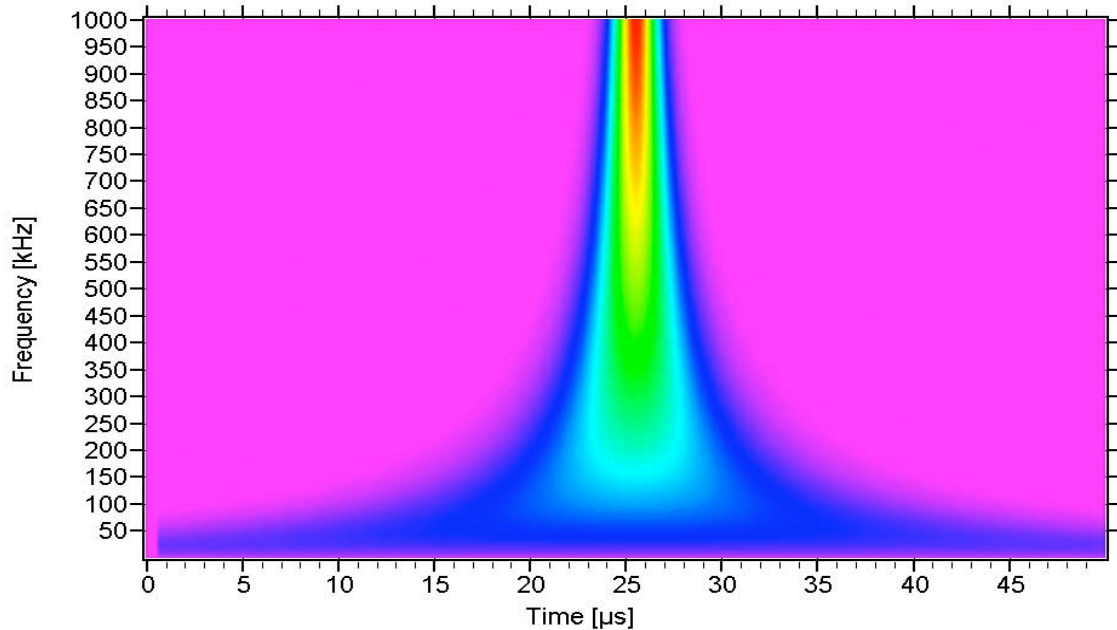


Fig. 7 WT which shows the “smear” at lower frequencies of WT of Dirac delta function at 25.5 μ s.

also shows the intersections for the key frequencies and the theoretical group-velocity curves for a propagation distance of 180 mm. The relative location in time of the actual WT-peak locations as a function of the key frequency and mode provides for much of the motivation and basis for the mode determination approach described below. Later results will be presented based on a test of the algorithm with a test database that did not include cases involving the A_1 mode at 522 kHz.

For cases where the primary frequency is 270 kHz (and the mode of its peak WT magnitude is thus S_0), one may use the following approach to determine the modes of the peak WT magnitudes at the two other frequencies of interest, 60 kHz and 522 kHz.

Determine the mode of the peak WT magnitude at 60 kHz (regardless of whether it is the secondary or tertiary frequency) as follows.

If the arrival time for 60 kHz occurs within $\pm 5\%$ of the arrival time for 270 kHz, then the mode of the peak WT magnitude at 60 kHz is S_0 . (*The 5 % value was selected based on reviewing the test-case database, described later; it may be desirable to adjust this value somewhat after seeing the results of applying this logic to a more extensive test database.)

Otherwise, the mode of the peak WT magnitude at 60 kHz is A_0 .

If the mode of the peak WT magnitude at 60 kHz has been determined as S_0 , then the mode of the peak WT magnitude at 522 kHz can be assumed to be S_0 also (since it is highly unlikely that any real AE signal would have S_0 character at 60 kHz and 270 kHz, but A_0 character at 522 kHz; not a single instance of this behavior was observed in the entire FEM database of known signals, and thus the authors believe that the physics dictates this behavior is unlikely).

If the mode of the peak WT magnitude at 60 kHz has been determined as A_0 , then the mode of the peak WT magnitude at 522 kHz can be determined as follows.

If the arrival time for 522 kHz occurs before the arrival time for 60 kHz, then the mode of the peak WT magnitude at 522 kHz is A_0 .

Otherwise, the mode of the peak WT magnitude at 522 kHz is S_0 .

For cases where the primary frequency is 522 kHz (and the mode of its peak WT magnitude is thus S_0), one may use the following approach to determine the modes of the peak WT magnitudes at the two other frequencies of interest, 60 kHz and 270 kHz.

Determine the mode of the peak WT magnitude at 60 kHz (regardless of whether it is the secondary or tertiary frequency) as follows.

If the arrival time for 60 kHz occurs within $\pm 5\%$ of the arrival time for 270 kHz, then the mode of the peak WT magnitude at 60 kHz is S_0 and the mode of the peak WT magnitude at 270 kHz is also S_0 .

If the arrival time for 60 kHz occurs more than 5% before the arrival time for 270 kHz, then the mode of the peak WT magnitude at 60 kHz is S_0 and the mode of the peak WT magnitude at 270 kHz is A_0 .

Otherwise, if the arrival time for 60 kHz occurs more than 5% after the arrival time for 270 kHz, then the mode of the peak WT magnitude at 60 kHz is A_0 and the mode of the peak WT magnitude at 270 kHz is not yet determined.

*The 5 % value was selected based on reviewing the test case database; it may be desirable to adjust this value somewhat after seeing the results of applying this logic to a more extensive test database.

If the mode of the peak WT magnitude at 60 kHz has been determined as A_0 , then the mode of the peak WT magnitude at 270 kHz *cannot* be immediately determined (regardless of whether it is the secondary or tertiary frequency). One approach to resolving this situation is to compute ranges assuming both A_0 and S_0 modes for 270 kHz, then determine which mode assumption gives the most consistent results for a computed range. The methodology used for range calculations is described in detail in appendix B of this paper.

For cases where the primary frequency is 60 kHz (and the mode of its peak WT magnitude is thus A_0), one may use the following approach to determine the modes of the peak WT magnitudes at the two other frequencies of interest, 270 kHz and 522 kHz.

Determine the mode of the peak WT magnitude at 522 kHz (regardless of whether it is the secondary or tertiary frequency) as follows.

If the arrival time for 522 kHz occurs before the arrival time for 60 kHz, then the mode of the peak WT magnitude at 522 kHz is A_0 .

Otherwise, the mode of the peak WT magnitude at 522 kHz is S_0 .

If the mode of the peak WT magnitude at 522 kHz has been determined as A_0 , then the mode of the peak WT magnitude at 270 kHz can be immediately determined (regardless of whether it is the secondary or tertiary frequency).

If the arrival time for 522 kHz occurs within $\pm 5\%$ * of the arrival time for 270 kHz, then the mode of the peak WT magnitude at 270 kHz is A_0 . (*The 5% value was selected based on reviewing the test case database; it may be desirable to adjust this value somewhat after seeing the results of applying this logic to a greater test database.)

Otherwise, the mode of the peak WT magnitude at 270 kHz is S_0 .

If the mode of the peak WT magnitude at 522 kHz has been determined as S_0 , then the mode of the peak WT magnitude at 270 kHz *cannot* be immediately determined (regardless of whether it is the secondary or tertiary frequency). One approach to resolving this situation is to compute ranges (see appendix B) assuming both A_0 and S_0 modes for 270 kHz, then determine which mode assumption gives the most consistent results for a computed range.

7. Use of Secondary and Tertiary Arrival Times

The WT results provide three arrival times for each signal (one for each frequency); thus it is of interest to consider the possible use of the secondary- and tertiary-based arrival times for either source range calculations and/or alternative source location (for multi-sensor applications) calculations. Since the r^2 values for the slope-based group velocity were typically high (greater than 0.999, as was already discussed), data for the 0° radiation direction were examined as to whether the group velocities determined from the secondary and tertiary frequencies differed significantly from those determined from the primary frequency.

Table 2 shows the data that were used for this examination. The data cover 94 cases for the secondary and tertiary frequencies. The other six cases had mixed modes (for the fixed frequency) as a function of propagation distance. The examination was based upon the range (minimum to maximum) of group velocities determined for the secondary and tertiary frequency-mode combinations. To provide a basis for comparison, the table includes the ranges of group velocities determined from the primary frequency-mode (i.e., the principal mode). The table indicates some increase in the ranges of group velocity that were determined from the secondary and tertiary frequencies, but in most cases the deviation from the theoretical group velocity is relatively small.

The frequency-mode combinations with the largest deviations were S_0 at 270 kHz and A_0 at 270 kHz. Upon closer examination of these cases, it was determined that the larger deviations from the theoretical group velocity were related directly to the closeness (with respect to time) of the arrival of more than one mode at a given frequency. To better understand the reasons for the velocity variations, the arrival times for these cases were studied for the three propagation distances. This study revealed that the arrival time of the WT peak for the 60 mm propagation distance was in error by a few percent compared to what it was for the same mode for cases when the group velocity was nearer to the theoretical value. Since the arrival time at propagation distances of 120 mm and 180 mm were right at the expected values, it was concluded that the error

Table 2 Ranges of group velocities determined from non-primary (i.e., secondary and tertiary frequencies) versus those from primary frequency for 0° radiation angle.

Frequency (kHz)	Mode (* indicates principal mode at this frequency)	Theoretical group velocity (mm/μs)	Non-primary group velocity range (mm/μs)	Non-primary group velocity range (± % from theory)	Non-primary number of cases	Primary group velocity range (± % from theory)	Primary number of cases
60	A ₀ *	2.550	2.48 to 2.52	-2.6 to -1.2	7	-1.6 to +1.6	38
60	S ₀	5.383	5.26 to 5.48	-2.9 to +1.7	5	--	--
270	S ₀ *	4.841	4.76 to 5.23	-1.6 to +7.9	15	na (only 1 case)	1
270	A ₀	3.138	2.92 to 3.13	-7.1 to -0.2	33	--	--
522	S ₀ *	1.776	1.70 to 1.86	-4.0 to +4.8	16	+1.4 to +3.0	11
522	A ₀	3.077	3.05 to 3.12	-1.0 to +1.3	15	--	--
522	A ₁	3.664	3.59 to 3.60	-1.9 to -1.7	3	--	--

Table 3 Comparison of theoretical versus average slope-based values for group velocities (including most of data for 0° radiation angle)

Frequency (kHz)	Mode (* indicates principal mode at this frequency)	Theoretical group velocity (mm/μs)	Calculated average group velocity (mm/μs)	Coefficient of sample dispersion (%)	Number of cases
60	A ₀ *	2.550	2.55	1	45
60	S ₀	5.383	5.33	2	6
270	S ₀ *	4.841	4.88	3	16
270	A ₀	3.138	3.09	2	33
522	S ₀ *	1.776	1.81	2	27
522	A ₀	3.077	3.07	0.7	15
522	A ₁	3.664	3.60	0.2	3

for the 60 mm distance was due to the interaction of both the A₀ and S₀ modes in the calculated WT results. At the increased distances, the effect of dispersion results in a wider separation in time between the two modes. This wider separation seems to be sufficient to keep the WT peak from being biased in time towards the adjacent mode.

Figure 6 with superimposed theoretical group velocity curves shows that, at 270 kHz for a propagation distance of 60 mm, the difference in time between the arrivals of S₀ and A₀ is only about 6.5 μs. Thus, the potential for interaction of the WT energy from the two modes is relatively high. The time interval between the arrivals of A₀ and S₀ at 60 kHz is considerably larger,

at about 12.5 μ s. At higher frequencies, such as 522 kHz, the time interval between the arrivals of A_0 and S_0 is large. However, the time interval between the arrivals of A_0 and A_1 is small, at about 3 μ s. The database does not indicate that this close proximity in arrival time for 522 kHz is a problem. The authors conclude this observation is due to the fact that the WT does not “smear” out at higher frequencies in the same fashion as at lower frequencies. Figure 7 illustrates WT results (calculated with the same parameters) for a Dirac delta function at a time of 25.5 μ s. This figure shows that the WT “smearing” out at higher frequencies is not as large as at lower frequencies.

Based upon the above results, the entire database for the 0° radiation direction was used (with a few exceptions) to calculate average group velocities and the sample coefficient of dispersion for each of the frequency-mode combinations present in the 0° radiation angle database. The exceptions were to eliminate the six cases with mixed modes at different propagation distances. Table 3 gives the results along with a comparison with the theoretical group velocities as determined from theoretical group-velocity curves.

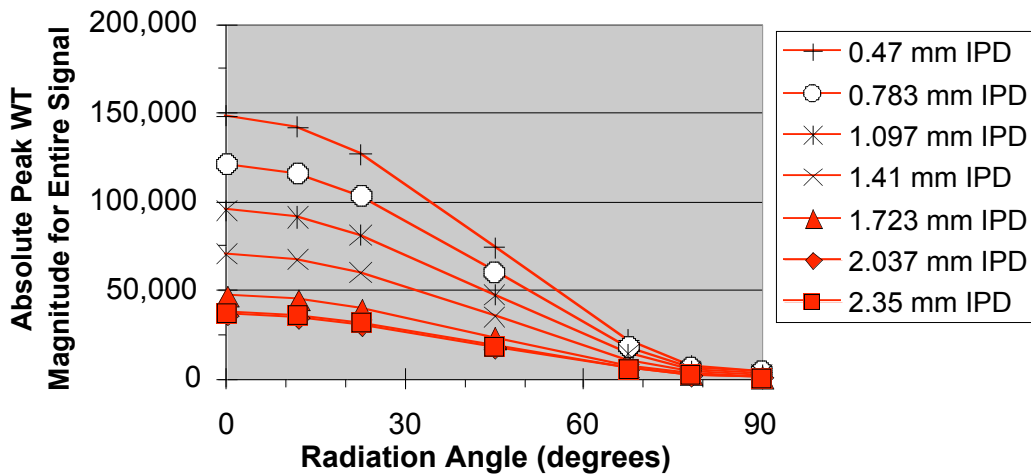


Fig. 8 Absolute peak WT magnitudes for various source depths for in-plane dipole source at 180 mm propagation distance.

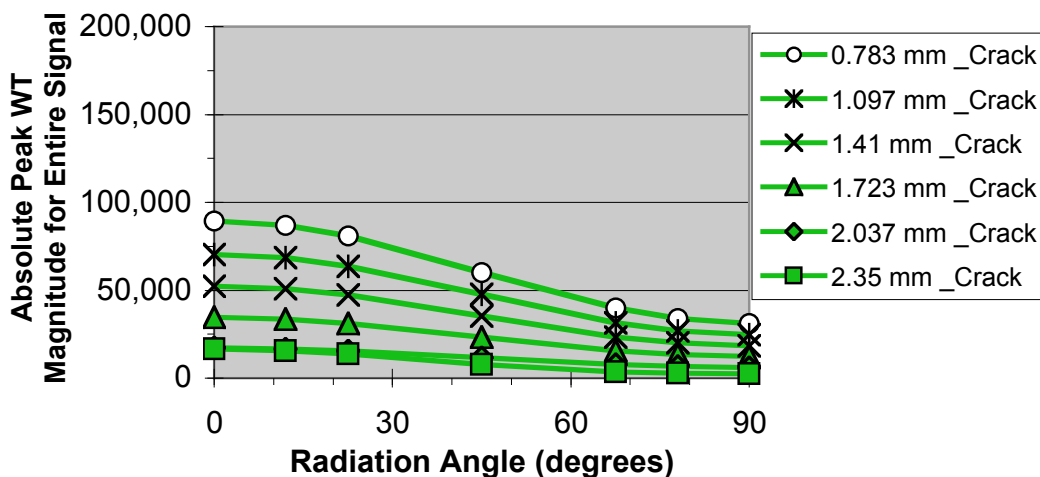


Fig. 9 Absolute peak WT magnitudes for various source depths for microcrack initiation source at 180 mm propagation distance.

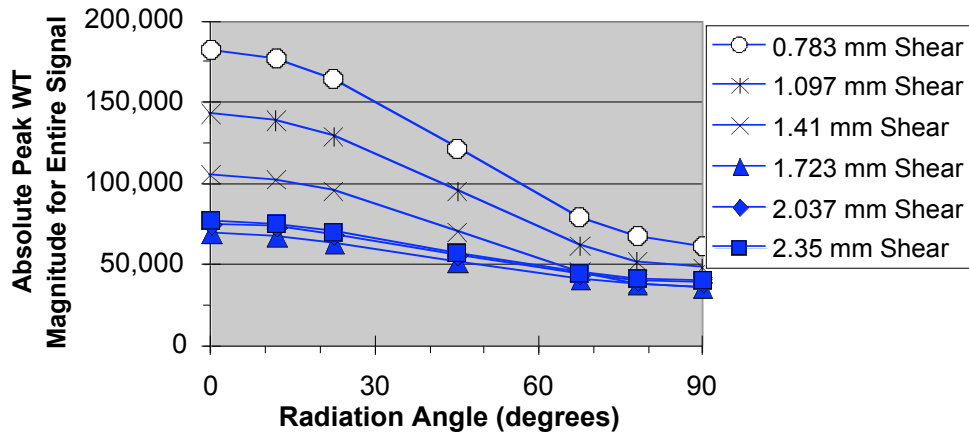


Fig. 10 Absolute peak WT magnitudes for various source depths for balanced shear source (45° about y-axis) at 180 mm propagation distance.

8. Effects of Radiation Angles (Other Than 0°) on Determination of Arrival Times for Peak WT Magnitudes

Nearly all of the above aspects considered only the 0° (x-axis) radiation direction. Prior to a discussion of the group velocity results in other radiation directions, it is useful to characterize the changes in the absolute WT peak magnitude as a function of radiation angle and source depth. Figures 8, 9, and 10 show for three important source types (i.e., in-plane dipole, microcrack initiation, and shear at 45° about the y-axis without a moment) that the absolute peak WT magnitudes decrease as the radiation angle increases from 0° (x-axis) to 90° (y-axis). The fall-off with increasing angle is very dramatic for the in-plane dipole (nearly 100%), and it is least for the microcrack initiation, except for a source at the mid-plane, where the 45° shear has the least fall-off. These three figures also demonstrate that the WT absolute peak magnitudes have their greatest values when the source is close to the surface and have their lowest values when the source is located at or near the mid-plane. The above observations with respect to radiation angle and source depth were generally true for all of the source types considered in this reported research. The only exceptions were the out-of-plane dipole and the dilatation sources, which have axisymmetric radiation patterns. However, these two sources did show the typical effect of source depth on the WT peak magnitude.

The examination of the effects of radiation angle on WT-based determination of arrival times of particular frequency and mode combinations took place in two stages. First, WTs were calculated (using the same setup as before) for each signal at a propagation distance of 180 mm in the complete database of different source types, depths, and radiation angles. After superimposing the relevant group velocity curves on these results, it was determined that the three key frequencies (60, 270, and 522 kHz) with their associated principal modes (A_0 , S_0 , and S_0 , respectively) were sufficient to represent the peak WT magnitude regions regardless of the source type, depth, and radiation angle. Also this examination demonstrated (as already described) that, regardless of the radiation angle, the mode associated with the primary frequency WT peak was always the principal mode.

The second stage centered around a detailed examination of peak-WT-magnitude-based arrival times at the three selected frequencies for three important source types (namely, in-plane

dipole, microcrack initiation, and balanced shear at 45° about the y-axis) for radiation angles other than 0°. Similar to the study with 0° data, the approach taken was to use the arrival times for the primary frequency at the three propagation distances to calculate a group velocity, correlation coefficient (r^2) and y-intercept. (See appendix A for a detailed discussion of the y-intercepts.) The group velocities were calculated for a total of 133 cases. For three cases, the primary frequency changed with propagation distance. In these cases, the group velocity was determined for the frequency that was the primary one at two of the three propagation distances. This necessitated the use of the secondary frequency at one of the distances, but in all cases, the WT peak magnitude at the secondary frequency always corresponded to the principal mode of that frequency. Out of the 133 cases, the primary frequency-mode was A_0 at 60 kHz for 89 cases, S_0 at 522 kHz for 41 cases and S_0 at 270 kHz for 3 cases.

Upon study of the data, it was observed that the primary frequency for a particular source type and source depth also may change with the radiation direction. For example, the primary frequency of the microcrack initiation source at a depth of 2.35 mm (i.e., mid-plane) is 522 kHz at 0°, 22.5°, and 45°, and is 270 kHz at 67.5°, 78°, and 90°, at all three propagation distances. At a depth of 2.037 mm, the primary frequency is 522 kHz at 0° and 12° at propagation distances of 60 and 120 mm; it is 60 kHz at 0° and 12° at propagation distances of 180 mm; and it is 60 kHz at 22.5°, 45°, 67.5°, 78°, and 90° at all these distances.

Table 4 summarizes the radiation-angle-based changes at the relevant source depths, and it also includes the WT fractions of the primary and a non-primary, alternative frequency. As indicated in the table footnotes, the mode of the non-primary frequency for these cases was always the principal mode. However, when a frequency changed to a non-primary frequency as a result of changes in radiation angle, it was not always secondary and could in fact be tertiary. For some particular combinations of source type and depth, the specific frequency that is primary for most radiation angles may have very small WT fractions (hence poor signal-to-noise ratios) at a few other angles. Using such low-magnitude, noisy data could introduce greater potential for errors in the determined arrival times. The authors note that this could happen primarily at larger first-quadrant radiation angles, but it could also occur at low first-quadrant radiation angles. The data indicate that as much as 10 dB in WT peak magnitude could be lost by having to use a non-primary frequency. At present, standard source location software that uses different group velocities (determined at *different* frequencies and modes) at different sensors is not available. This status forces the use of a single frequency-mode combination for the arrival times as determined by peak WT magnitudes at all the sensors for a given AE event. It is clear (due to radiation pattern symmetries) that in the general experimental case all four quadrants would experience this situation in certain cases.

An additional important piece of information from AE signals measured at various radiation angles is the possibility of significant changes in the WT-based group velocities from different radiation directions. In theory, the group velocity does not change with direction in isotropic materials. Most AE source types have radiation patterns of bulk waves that change with radiation direction. Since these bulk waves lead to Lamb waves, the proportions of different Lamb modes vary with the radiation angle. These proportion changes could potentially result in changes in the WT-based group velocities in different directions due to the characteristics of a particular WT. Further, this potential effect could be complicated by the already-demonstrated effect of source depth on the relative proportions of the symmetric and antisymmetric Lamb waves [1].

Table 4 Summary of changes⁺ in WT fractions (thus primary frequency) with radiation angle

Source type, depth (mm)	Radiation angle (°)	WT fractions at various angles, frequencies, and propagation distances					
		60 mm	120 mm	180 mm	60 mm	120 mm	180 mm
In-plane di- pole, 2.35		522 kHz			270 kHz		
	0	1	1	1	0.33	0.37	0.39
	12	1	1	1	0.33	0.37	0.40
	22.5	1	1	1	0.33	0.39	0.40
	45	1	1	1	0.33	0.38	0.40
	67.5	1	1	1	0.33	0.36	0.38
	78	1	1	1	0.43	0.39	0.39
	90	1	1	0.98	0.83	0.96	1
In-plane di- pole, 2.037 * Tertiary, not secondary frequency		522 kHz			60 kHz		
	0	1	1	1	0.46	0.56	0.6
	12	1	1	1	0.46	0.56	0.6
	22.5	1	1	1	0.47	0.56	0.61
	45	1	1	1	0.46	0.56	0.61
	67.5	1	1	1	0.44	0.55	0.59
	78	1	1	1	0.69	0.66	0.62
	90	0.6	0.51	0.51*	1	1	1
Microcrack initiation, 2.35		522 kHz			270 kHz		
	0	1	1	1	0.48	0.54	0.58
	12	1	1	1	0.50	0.56	0.59
	22.5	1	1	1	0.52	0.59	0.62
	45	1	1	1	0.69	0.76	0.79
	67.5	0.65	0.51	0.44	1	1	1
	78	0.45	0.3	0.31	1	1	1
	90	0.84	0.56	0.51	1	1	1
Microcrack initiation, 2.037 * Tertiary, not secondary frequency		522 kHz			60 kHz		
	0	1	1	0.99	0.77	0.92	1
	12	1	1	0.97	0.79	0.95	1
	22.5	1	0.99	0.91	0.84	1	1
	45	0.86	0.72	0.68	1	1	1
	67.5	0.35*	0.25*	0.21*	1	1	1
	78	0.24*	0.18*	0.16*	1	1	1
	90	0.43*	0.26*	0.24*	1	1	1
Balanced shear at 45° about y-axis, 1.41		522 kHz			60 kHz		
	0	0.8	0.65	0.61	1	1	1
	12	0.81	0.66	0.61	1	1	1
	22.5	0.82	0.67	0.62	1	1	1
	45	0.91	0.74	0.68	1	1	1
	67.5	1	0.9	0.83	0.9	1	1
	78	1	0.99	0.91	0.81	1	1
	90	1	1	0.97	0.78	0.96	1

+ For all cases listed in table, mode of non-primary frequency was always the principal mode

Finally, as discussed above, the very low signal levels for some sources at angles near 90° could result in inaccurate arrival times. Thus, the dependence of the WT-based group velocities was studied as a function of source type, depth, radiation angle and *primary* frequency. For each important source type over the series of depths, the largest ranges in the WT-based group velocities over the seven radiation directions and all available source depths were 6.7 % (89 cases) at

A_0 at 60 kHz, 2.7 % (40 cases) at S_0 at 522 kHz, and 0.4 % (3 cases) for S_0 at 270 kHz. These changes are relatively small in the context of what is essentially experimental data. Further, in the case of the 6.7 % variation, nearly half of the range comes from one case (in-plane dipole, 2.037 mm source depth, 90° radiation angle). If this case is ignored, the velocity based on radiation angle changes from a minimum of 2.50 mm/ μ s to a maximum of 2.59 mm/ μ s (A_0 at 60 kHz; 3.7 %) that is nearly centered on the theoretical group velocity. In only one case (in-plane dipole, 2.037 mm source depth, 90° radiation angle) was an arguably poor group velocity obtained. In this case, the calculated velocity of 2.43 mm/ μ s was 4.7 % below the theoretical group velocity for A_0 at 60 kHz. This result at 90°, as can be seen in Fig. 8, occurred when the signal is very small compared to that radiated in the 0° direction. Thus, the authors conclude that WT-based arrival times will generally be independent of radiation direction, and source locations can be calculated with minimal effects on accuracy of the results.

In summary, as was stated earlier when only data for 0° were considered, WT-based arrival times can be used to improve source location accuracy regardless of the radiation angle to the sensors. The key addition needed for AE hardware is a wideband sensor. The key change for AE location software is a step to determine which key frequency-mode gives the best signal-to-electronic-noise ratio, and an additional step to select the corresponding group velocity.

9. Evaluation of the Algorithm Created to Determine Modes at Key Frequencies and Source Location Ranges

Description of Test Signal Database

A subset of 23 FEM-calculated AE signals from the larger FEM database was selected to create a smaller, testing database for evaluating the previously described analysis algorithm. Two additional “difficult” signals were added to the subset for a total of 25 test signals. The 25 signals were slightly modified to be more representative of actual AE signals (which have unknown source operation times). Specifically, each signal had an arbitrary (but documented) time increment added to its data file, thus altering the signal initiation time such that it no longer corresponded to the source operation time. The database was made up of various types of typical AE signals covering a wide variety of scenarios intended to test the algorithm’s capabilities. At one extreme, some cases had solely the A_0 mode throughout the signal (e.g., #6, 14, 16, and 17), whereas cases at the other extreme had entirely S_0 mode behavior (e.g., #1, 3, 7, 8, 10, 11, 15, 18, 21, and 22). In between these two extremes were some cases (e.g., #2, 4, 5, 9, 12, 13, 23, 24, and 25) with both A_0 and S_0 modes among the three key frequencies. The database also included signals from all three available propagation distances. Two purposely difficult test cases were also included in the database. One of these cases (#20) had no AE signal (which was modeled via a certain source type at a certain radiation angle that resulted in no AE signal); the only recorded “signal” for this case was essentially ultra-small-amplitude numerical noise that was present long after the time period when a real direct-path signal would normally have arrived. The other difficult test case (#19) had a small-amplitude, direct AE signal with a discrete reflection (from the edge of the large plate) of larger amplitude than the direct signal; the reflection occurred well after the main amplitude of the direct signal had ended (i.e., about 76 μ s later). The segments of time containing the signal reflections within the unknown signals were beyond the segments of time that were examined for the known signals.

Implementation of Algorithm for Unknown Signal Analysis

The algorithm described earlier was mathematically implemented within a simple spreadsheet. The inputs required to the spreadsheet for each signal were as follows: test signal file

name; overall peak WT magnitude for the entire signal; the peak WT magnitude and its associated arrival time for each of the frequencies 60 kHz, 270 kHz, and 522 kHz.

These inputs were calculated using a version of the WT software that automatically provides the required values. Empirical waveform-based acoustic emission signals typically are recorded with a preset, fixed number of data points that is 2^x , where x can be one of several integer values; typical choices might be $2^{10} = 1024$ points, or $2^{11} = 2048$ points, or $2^{12} = 4096$ points, $2^{13} = 8192$ points, etc. For this analysis effort, a typical experimental test file of 4096 points was assumed, although the approach devised would also be compatible with files of fewer or greater numbers of points. The data for this effort had $0.1 \mu\text{s}$ per point, thus each file was equivalent to a signal $409.6 \mu\text{s}$ in length.

Wavelet transforms were performed on the 25 finite-element-based modified test signal cases. For each WT computation, the following Wavelet Transformation Settings were used: maximum frequency = 700 kHz; frequency resolution = 3 kHz; wavelet size = 600 samples. The following Wavelet Time Range Settings were used: number of samples (i.e., points) = 4096; offset samples = 0.

Using only the algorithm inputs listed earlier, the spreadsheet calculations were able to compute the following items: primary, secondary, and tertiary frequencies; modes for primary, secondary, and tertiary frequencies; a best computed range (i.e., averaging the two most consistent of the three computed range values). Three warning flags (described later) were included in the algorithm to highlight cases where computed results may need closer examination.

Appendix tables C-1 and C-2 give selected results of the spreadsheet algorithm used to analyze the data from the 25 test cases. The logic of these tables for each horizontal row moves from left to right from table C-1 and continues on to C-2. The description of this logic flow follows in several sections below. Although the cases had known source operation times, they were analyzed as though the source operation times were unknown (i.e., no use was made of the source operation times during the algorithm, and no superposition of dispersion curve information upon the WT data was performed) as would be the situation for analyzing the large number of AE hits in real experimental AE signal cases. Generally speaking, the algorithm was quite successful in meeting the objectives described above, although a few minor errors were produced by either the WT software (as currently configured) or the analysis algorithm that interprets the WT information.

WT Results for Test Signals

First, the accuracy of the arrival times as calculated by the WT software was examined by comparing them to the actual known times. All of the WT-computed arrival times for all three frequencies of interest matched the known arrival times perfectly (i.e., a time difference of $0.0 \mu\text{s}$) except for markedly wrong times computed for the 60 kHz frequency peak of case #18, and all three frequencies for the difficult cases #19 and 20. The problems with these signals arose in part due to the use of a WT signal length of 4096 points (i.e., $409.6 \mu\text{s}$) when computing the WT. This choice for WT signal length resulted in data being included in the overall WT that were not associated with the direct AE signals. For example, edge-reflected signals typically appear after about $150 \mu\text{s}$ until the FEM-calculation end (at $200 \mu\text{s}$) for signals with a propagation distance of 180 mm. At shorter propagation distances, the edge reflections occur at later times.

It should be noted that the WT software (as currently configured) was not intended to recognize and disregard aberrant signals; thus any WT magnitudes greater than zero (even those values caused by any type of noise) will be mathematically considered when determining the peak WT magnitudes (and their associated arrival times) at the three frequencies of interest. In test case #20, the peak WT magnitudes at the frequencies of interest were due solely to numerical noise, and not surprisingly resulted in meaningless computed arrival times.

In test case #19 (which contained a reflection of significant amplitude late in the signal), the peak WT magnitudes for all three frequencies of interest occurred in the reflection portion of the signal. Thus, while the arrival times computed by the WT software for all three frequencies of this test case were mathematically correct (in that they did correspond to the peak WT magnitudes present), the computed times were completely wrong conceptually in that they corresponded to the reflection rather than to the lower-amplitude, direct-path AE signal. Consequently, all three computed arrival times for test case #19 significantly differed from the known arrival times for the signal. A similar problem happened for test case #18, where the peak WT magnitude for 60 kHz (but not for 270 or 522 kHz) occurred in a distinct reflection late in the signal; thus, the computed arrival time for 60 kHz was markedly wrong.

In summary, the WT software generally produced very accurate arrival times except for three cases that had significant signal aberrations. Unfortunately, the WT software presently is not intended to automatically and selectively disregard aberrant information that may not correspond to a meaningful portion of a digitized AE signal; however, future research could possibly develop such features for the WT software. To attempt to respond to this aspect, some algorithm warning flags were implemented as described below.

Algorithm Warning Flags

Three warning flags were added to the analysis algorithm to help prevent any problematic or erroneous information from the WT software being unwittingly used as input to the analysis algorithm. Observations of known signal cases showed that the WT peak of the primary frequency was not significantly less energetic than the overall WT peak of the signal, provided that the signal was, in fact, a real AE signal without significant distortions added from noise or reflections, etc. To warn of signals containing such significant distortions (as happened in test case #19), the first flag returns a result of “Disregard signal” if the peak WT magnitude of the primary frequency is less than 70 % of the overall peak WT magnitude for the entire signal; otherwise it returns an “Okay” result. The value of 70 % was chosen somewhat arbitrarily; users of the algorithm may later determine that the criterion value needs to be adjusted somewhat once the algorithm has been tested on a much larger set of unknown cases. A “Disregard signal” result implies that the most energetic region is very atypical in its location with respect to time and frequency compared to usual AE signals (i.e., not located near the primary frequency WT peak); hence one could expect that any arrival times computed from such a signal might be erroneous or meaningless.

A second flag considers whether the entire signal is of low amplitude, thus implying that the case may be a noise signal or perhaps a real signal but of amplitude sufficiently small that it cannot be distinguished from background noise. The flag returns a result of “Low Amplitude” if the overall peak WT magnitude for the signal is less than 1000; this value of 1000 was also chosen somewhat arbitrarily and may need to be further adjusted after the algorithm is tested more extensively on a larger set of data, and when consideration is given to particular experimental factors such as signal gain, background electronic noise, etc.

The third flag pertains to the computed ranges for each signal (i.e., linear in-plane distance from AE sensor to AE source epicenter). Each computation of range requires using information from two of the three frequencies of interest, as described in appendix B equations B-7, B-8, and B-9. Assuming that a mode has been determined for each of the three frequencies of interest, three different ranges can be computed for each signal case. In a perfect world, these three values should be identical, and none of them should be negative. However, observation of the test data results showed that usually at least two of the three of the computed range values were reasonable, with the third value sometimes being markedly wrong. The authors expect that the errors in the range calculation are due in part to a lack of preciseness in y-intercept values (see further discussion in appendix A). As a practical matter, it was assumed that both of the following conditions would be met for reasonable range values: (a) the two most similar of the three computed range values should be nearly identical in value (i.e., the population coefficient of dispersion is the smallest for this pair of computed range values, and it should be less than 0.3); and, (b) none of the three computed ranges should be negative. If both of these conditions are successfully met, then the third flag returns a result of “Okay”; if either of the two conditions is not met, the flag returns a result of “Range Consistency Concern”. Such a result warrants a closer look at the computed values to determine whether there is a reason to disregard the computed ranges, and/or to question the validity of the mode determinations.

The three warning flags were applied to all 25 test cases. Not surprisingly (and consistent with the previous discussion above), case #20 with its low-amplitude noise signal triggered the flags for low amplitude and range consistency, and case #19 (with its late reflection) triggered the flags for disregarding the signal and range consistency. Additionally, case #18 was flagged for range concerns.

Algorithm Mode Determinations

Using the approach described earlier in this paper, the algorithm was used to determine the modes of the arrival times as determined by peak WT magnitudes. The implementation was straightforward except for the test cases in which determination of the mode for the 270 kHz peak required a range consistency step based on assuming both S_0 and A_0 modes. Selected results are given in appendix C tables C-1 and C-2. There were 10 cases where the mode determination required assuming that the 270 kHz peak corresponded to the A_0 and then the S_0 mode. For each of these cases, two ranges ($R_{60/270}$ and $R_{522/270}$) were calculated using the two noted frequencies. Then using the $R_{60/522}$ -based range, for each set of three ranges the coefficient of dispersion (population) was calculated twice, once each for the S_0 assumption and the A_0 assumption for the 270 kHz peak. Then the mode for 270 kHz was automatically selected based upon the assumption that produced the lowest coefficient of dispersion. The algorithm was successful in determining the appropriate modes for all test cases in which the arrival times were correctly determined by the WT software, i.e., for all test cases except #18, and 20. The modes were correctly determined for case #19, but this was likely due to mathematical happenstance because all the arrival times for #19 were wrong.

Algorithm Range Computations

As described earlier, three range computations were made for each signal, with each computation using data from two of the three frequencies of interest. As noted earlier, a cursory examination of the ranges for the test cases showed that often there seemed to be a single outlier value among the three computed range values. For this reason, the following practical approach was devised, even though from a theoretical standpoint all three range values should be

consistent. The two range values with the smallest coefficient of dispersion were selected (as already described); next, these two range values were averaged, thus creating a final “best computed range” value. The range results are also shown in appendix C tables C-1 and C-2.

The algorithm was moderately successful in determining a relatively accurate “best computed range.” For each of the test cases in which the arrival times were correctly determined by the WT software (i.e., all test cases except #18, 19, and 20), the relative difference between the best computed range and the actual range was quite reasonable. On average, the best computed range was within 5 % of the actual range value, although several values had about a 9 % difference, and the difference for case #5 in particular was more than 15 %. It is not immediately obvious whether the error percentages would stay constant, get worse, or perhaps improve for longer sensor ranges. However, these authors suggest that perhaps the relative difference between the best computed and the known ranges might decrease for greater ranges. This suggestion is made for the following reason: the average difference between the best computed and actual range values for 60 mm cases was 11.2 %; for 120 mm cases, 3.9 %; and, for 180 mm cases, 3.3 %. These results (while admittedly based on a very small database) are encouraging for empirical applications of much greater distances.

A further consideration may be worthwhile to note for real-world AE testing. Because the original AE bulk waves must propagate some distance (i.e., up to 10 plate thicknesses) to fully develop into Lamb waves [10], it should be recognized that AE signals measured at short distances can have a significant portion of their travel distance occurring where the Lamb waves are still developing. This effect seems to be more pronounced for lower-frequency Lamb waves (which have longer wavelengths), based upon the fact that the y-intercept values for group velocities are larger for the lower frequencies (see further discussion in appendix A and table A-1).

10. Conclusions

The conclusions presented here refer specifically to an aluminum plate that is 4.7 mm thick. In addition, the AE signals are plate Lamb waves. But the conclusions presented here can be expected to extend to thin plates of other thicknesses and/or other isotropic metals when appropriate changes in the key frequencies are made.

One or more of three key frequencies were found to always represent the most energetic regions of an extensive, finite-element-modeled AE database. These three frequencies are 60, 270, and 522 kHz. A “principal mode” was associated with each key frequency as follows: the A_0 mode at 60 kHz, the S_0 mode at 270 kHz, and the S_0 mode at 522 kHz.

For three different propagation distances, AE signal arrival times were defined by the time of peak WT magnitude at the primary key frequency (i.e., the key frequency having the greatest peak WT magnitude). These arrival times accurately corresponded to a single group velocity that was close to the theoretical velocity for the corresponding mode. The accuracy applies for eight different source types over a full range of source depths and radiation angles. Further, similarly defined arrival times for the secondary and tertiary frequencies have these same characteristics. But, in these non-primary cases, the modes can be either the A_0 or S_0 mode for each frequency. In a few cases (where 522 kHz is the tertiary frequency), the mode is A_1 .

Since the primary frequency (largest WT peak magnitude) for any signal is always associated with the principal mode at that frequency, the relevant group velocity is known. Then source

location calculations can proceed in the usual fashion for experimental data when the source origination time and the propagation distances are unknown. Further, in all cases (in the current extensive database) where for a given source type and depth the primary frequency alternates between two different key frequencies at different radiation angles and/or propagation distances, both of these frequencies are always associated with their principal modes. Thus, upon choosing one working frequency from the two frequencies that are each primary at different sensors in the array for a particular event, the appropriate group velocity is known and the source location calculation can proceed.

An algorithm that can be computer automated has been developed to identify the modes of the peak WT magnitudes for secondary and tertiary frequencies. The result of having these two mode identifications (along with the knowledge that the primary frequency is always associated with the principal mode) is that range calculations can be made using just one signal from an AE event using the arrival times for the primary, secondary, and tertiary frequency WT magnitude peaks and y-intercept values. In addition, once the modes are identified, the group velocities of the arrival times associated with these key frequencies are also known.

For a specific source type and source depth, the primary frequency can change with the radiation angle and/or the propagation distance.

11. Practical Aspects of Conclusions to Empirical AE Testing

The implementation of these results for actual AE testing requires the selection of AE sensors with frequency sensitivity in the necessary ranges. The best sensor would be a wideband, flat-with-frequency sensor with high signal-to-electronic-noise sensitivity. A sensor like this has been developed at NIST, Boulder, CO [11, 12]. This sensor can effectively cover the key frequencies of the highly energetic portions of the AE signals (in this case 60 kHz, 270 kHz, and 522 kHz). The authors note that the often-used resonant AE sensor with a resonance at 150 kHz would lose a significant portion of potential sensitivity advantage for the current plate since its highest sensitivity is far from some of the actual energetic frequency regions of the AE signals that are generated by the various source types at different source depths. For example, a commercial sensor (characterized as a 150 kHz resonant sensor by ASTM standard E976) when calibrated by the ASTM standard E1106 (which is relevant for Lamb wave signals) is quite insensitive at two of the three frequencies of interest. In particular, a typical sensor had a peak sensitivity of 65 dB (referenced to 1 V/ μm) at 78 kHz. At the three frequencies of interest in the current 4.7 mm plate, its sensitivity was down by 5 dB, 12 dB and 32 dB at 60 kHz, 270 kHz and 522 kHz, respectively [13].

Acknowledgements

This work was partially supported by NASA Langley Research Center. We also acknowledge the original development of the finite-element code by John Gary (retired) of NIST, Boulder, Colorado. We also express our gratitude to Prof. M. Takemoto, who released the source code of the wavelet transform that his group had developed; this wavelet transform source code was utilized in the creation of the AGU-Vallen Wavelet software. We also thank Dr. Y. Mizutani and Mr. Jochen Vallen for making the AGU-Vallen Wavelet software into a highly usable form. The contributions of all the above people have significantly advanced the field of acoustic emission.

References

1. Hamstad, M.A., A.O’Gallagher and J. Gary, “Examination of the Application of a Wavelet Transform to Acoustic Emission Signals: Part 2. Source Location”, *J. Acoustic Emission*, **20**, 2002, 62-82.
2. Hamstad, M.A., A. O’Gallagher and J. Gary, "Modeling of Buried Acoustic Emission Monopole and Dipole Sources With a Finite Element Technique," *J. Acoustic Emission*, **17** (3-4), 1999, 97-110.
3. Gary, John and Marvin Hamstad, "On the Far-field Structure of Waves Generated by a Pencil Break on a Thin Plate," *J. Acoustic Emission*, Vol. 12, Nos. 3-4, 1994, pp. 157-170.
4. Prosser, W. H., M. A. Hamstad, J. Gary and A. O’Gallagher, "Reflections of AE Waves in Finite Plates: Finite Element Modeling and Experimental Measurements," *Journal of Acoustic Emission*, **17** (1-2), 1999, 37-47.
5. Hamstad, M.A., J. Gary and A. O’Gallagher, "Wideband Acoustic Emission Signals as a Function of Source Rise-Time and Plate Thickness," *Progress in Acoustic Emission IX*, Acoustic Emission Working Group and Acoustic Emission Group, Los Angeles, CA, pp. IV-48 to IV-57, 1998. Also in *J. Acoustic Emission*, **16**, (1-4), 1998, S251 to S259.
6. Guo, Dawei, Ajit K. Mal and Marvin A. Hamstad "AE Wavefield Calculations in a Plate," *Progress in Acoustic Emission IX*, Acoustic Emission Working Group and Acoustic Emission Group, Los Angeles, CA, pp. IV-19 to IV-29, 1998. Also in *J. Acoustic Emission*, **16**, (1-4), 1998, S222 to S232.
7. Hamstad, M.A., A. O’Gallagher and J. Gary, “Examination of the Application of a Wavelet Transform to Acoustic Emission Signals: Part 1. Source Identification”, *J. Acoustic Emission*, **20**, 2002, 39-61.
8. Vallen-Systeme GmbH, Munich, Germany, <http://www.vallen.de/wavelet/index.html>, 2001, AGU-Vallen Wavelet software version R2002.0703.
9. Holland, Stephen, Tadej Kosel, Richard Weaver, and Wolfgang Sachse, “Determination of Plate Source, Detector Separation from One Signal,” *Ultrasonics*, **38**, 2000, 620-623.
10. Sachse, Wolfgang and Yih-Hsing Pao, “Signals in the far-field of an AE source”, *Ultrasonics International 1981: Conference Proceedings*, IPC Science and Technology Press, Guildford, Surrey, UK, 1981, pp. 116-122.
11. Hamstad, M.A., and C.M. Fortunko, "Development of Practical Wideband High Fidelity Acoustic Emission Sensors," *Nondestructive Evaluation of Aging Bridges and Highways*, Steve Chase, Editor, Proc. SPIE 2456, Published by SPIE – The International Society for Optical Engineering, Bellingham, WA, 1995, pp. 281-288.
12. Hamstad, M.A., "Improved Signal-to-Noise Wideband Acoustic/Ultrasonic Contact Displacement Sensors for Wood and Polymers," *Wood and Fiber Science*, **29** (3), 1997, 239-248.
13. Physical Acoustics Corporation, Princeton, New Jersey, USA, R-15 Top-Connector, S/N AA02, calibrated 4/8/97.

Appendix A –C: Supplied in the CD-ROM in the form of a file, Hamstad-Appendix.pdf.

PRACTICAL ASPECTS OF ACOUSTIC EMISSION SOURCE LOCATION BY A WAVELET TRANSFORM - Appendices

M. A. HAMSTAD, K. S. DOWNS and A. O’GALLAGHER

Appendix A: Discussion of Y-intercept Values for Computed Slope-based Group Velocities

Table 1 in the main article body includes a column called the “y-axis intercept, mm”. This is the standard intercept that corresponds to zero time for the straight line that fits the three data points in the plot of distance versus arrival time. As is apparent from the table, this value is not zero for the 0° radiation angle data. A previous publication [1] associated this non-zero intercept with the fact that Lamb waves do not start instantaneously at the dipole source, but instead these waves can be distinguished only after the bulk waves have propagated a distance of some ten or more plate thicknesses from the source position [10]. Thus, the authors believe that the non-zero intercept arises from the need for propagation over a certain distance to develop the Lamb modes, which then can be observed to propagate at their associated group velocities. Table 1 indicates much wider variations in the y-intercept values as compared to the group velocities for the primary WT results. For example, the range of the slope-based intercept for A₀ at 60 kHz is about 30 % as compared to only about 3.2 % for the group velocities.

Additional observations can be made when considering the data for radiation angles other than 0°. Since the slope-based group velocities from the secondary and tertiary frequencies data were nearly the same as those from the primary frequency data, the y-intercept values from these data were also compared to the primary-based intercept values. In general, the comparison was not as favorable, even where data for $r^2 < 0.9997$ were eliminated. For example, the range of y-intercepts for the secondary and tertiary values for A₀ at 522 kHz varied from -1.7 to 4.5 mm (for 16 values). This wider range contrasts with the primary y-intercept values of 1.3 to 3.2 (for 11 values). Upon closer examination, it was found that the biggest contributor to this wider range was the tertiary-based values. If only the secondary-based values were used, the range was

Table A-1 Average y-intercept values and coefficients of sample dispersion for two greatest of three WT fractions for selected cases for radiation angles other than 0°

Frequency (kHz)	Mode (* indicates principal mode at this frequency)	Calculated average y-intercept (mm)	Coefficient of sample dispersion (%)	Number of cases
60	A ₀ *	17	9	43
60	S ₀	na	na	na
270	S ₀ *	-6.5	23	3
270	A ₀	-3.1	-- (all intercept values are equal)	6
522	S ₀ *	2.0	30	15
522	A ₀	-1.3	15	6

reduced to 2.0 to 3.2 mm (for 8 values). Thus, since even the primary-based y-intercept values had a wider percentage range than the associated group velocity values, we chose to reduce the database before calculating average values. Table A-1 gives the results when at least 2 of the 3 WT fractions for a case were greater than 0.5. Taking note of the rather large coefficients of sample dispersion (expressed as a percentage) in table A-1 in comparison to those in table 3, it is clear that the y-intercept values are not as certain for radiation angles other than 0° as are the velocities. Thus, if these values are used in calculations, the potential for errors is present.

Appendix B: Computation Approach for Signal Ranges

One may use standard algebra to compute a slope for a given set of x,y data pairs. The standard form for such an equation is

$$y = mx + b, \quad (\text{B-1})$$

where m is the slope and b is the y-axis intercept at $x = 0$.

In AE signal scenario, y is the range (or distance, mm); x is the arrival time of the signal ($_s$); m is the group velocity (mm/ $_s$); and b is the group velocity y-intercept (mm). The following equation applies in those cases where the “real arrival time” (i.e., equivalent to a clock starting at the source operation time) is precisely recorded:

$$R = VT + B, \quad (\text{B-2})$$

where R is the range, V is the group velocity, T is the real arrival time, and B is the y-intercept. The reason that B is typically not equal to zero is that an AE signal must travel a linear distance usually up to 10 plate thicknesses before Lamb waves and the associated group velocity behavior fully develops [10].

However, the typical AE measurement and waveform recording system does not record a signal until a signal magnitude threshold is crossed, and it also records a certain amount of pretrigger information for each signal, hence the source operation time is not necessarily at the very beginning of the stored waveform. Therefore, the recorded arrival time (i.e., the “measured arrival time”) differs from the “real arrival time” by some time offset (i.e., an arbitrary time amount that varies for each recorded signal but which is the same for all frequencies within a given signal, and which could be either negative or positive in value). In other words, the real arrival time equals the measured arrival time ($T_{measured}$) plus a time offset (T_{offset}). Thus, the equation below is a more generalized form for measured AE signals.

$$R = V_x (T_{measured@x} + T_{offset}) + B_x, \quad (\text{B-3})$$

where R is the range, V is the group velocity, B is the y-intercept, and x is any particular frequency of interest.

To assist the reader in gaining a greater understanding of T_{actual} versus $T_{measured}$ and T_{offset} , Figure B-1 shows a timeline for (a) the unknown test signals used in section 10, and (b) a typical measured experimental AE signal. In it, one may see scenarios in which T_{offset} can have either a negative or positive value.

Since this effort has used three frequencies of interest, one could compute three range values for each signal (assuming one knew the proper T_{offset} for each signal), e.g., one value of R based on the velocity and arrival time information for each of the three frequencies of interest. In an

ideal case, these three range values would be identical, and in the empirical case, they should be quite consistent with each other. One can use equation B-3 and solve for the arrival time, $T_{\text{measured}@x}$, (using the shortened notation $T_x = T_{\text{measured}@x}$) for each of the frequencies of interest, thus creating equations B-4, B-5 and B-6.

$$T_{60} = T_{\text{offset}} + \frac{R - B_{60}}{V_{60}} \quad (\text{B-4})$$

$$T_{270} = T_{\text{offset}} + \frac{R - B_{270}}{V_{270}} \quad (\text{B-5})$$

$$T_{522} = T_{\text{offset}} + \frac{R - B_{522}}{V_{522}} \quad (\text{B-6})$$

Since it is not easily possible to determine the proper T_{offset} for each signal, one may eliminate T_{offset} algebraically by combining equations for two different T_x values for the same signal (equations B-4, B-5 and B-6). Subtracting equation B-5 from equation B-4 and solving for R yields the following expression, where $R_{60/270}$ is defined as the range computed using information from the 60 kHz and 270 kHz frequencies. $R_{60/522}$ and $R_{270/522}$ are defined in a similar fashion.

$$R_{60/270} = \frac{(T_{60} - T_{270}) + \left(\frac{B_{60}}{V_{60}} - \frac{B_{270}}{V_{270}} \right)}{\frac{1}{V_{60}} - \frac{1}{V_{270}}} \quad (\text{B-7})$$

Similarly, combining equations B-4 and B-6 results in equation B-8.

$$R_{60/522} = \frac{(T_{60} - T_{522}) + \left(\frac{B_{60}}{V_{60}} - \frac{B_{522}}{V_{522}} \right)}{\frac{1}{V_{60}} - \frac{1}{V_{522}}} \quad (\text{B-8})$$

Similarly, combining equations B-5 and B-6 results in equation B-9.

$$R_{270/522} = \frac{(T_{270} - T_{522}) + \left(\frac{B_{270}}{V_{270}} - \frac{B_{522}}{V_{522}} \right)}{\frac{1}{V_{270}} - \frac{1}{V_{522}}} \quad (\text{B-9})$$

In attempting to compute ranges described above, one could use the theoretical values of group velocity, but that approach would not produce the most appropriate computed values. One must recognize that there is not a single absolute wavelet transform; in fact, different mother wavelets used in a WT software approach, or different choices in certain of the wavelet settings can result in different values for the peak WT magnitudes (and hence different arrival times) at the frequencies of interest for any given signal. Therefore, the most appropriate manner found

for choosing values of group velocity was to use data from known signals that were processed in a WT fashion identical to that which would be used for unknown signals. Consequently, the WT data from the 150 cases of signals at the zero-degree radiation direction with known source operation times (i.e., 50 types with three distances per signal type) were used to compute average group velocities and average y-intercepts for both A_0 and S_0 modes at the three frequencies of interest. This database was used since it included more source types than the database for non-zero radiation angles. Only those instances where at least two out of the three different distances for a given signal type had WT fractions of 0.5 or greater were used to compute the averages (except for values for S_0 at 60 kHz, where all available values were necessarily used). These results are summarized in appendix table B-1.

Table B-1 Summary of average group velocities and y-axis intercepts (where signals for at least two of three distances had WT fractions of 0.5 or greater)

Mode	Frequency	Average Group Velocity (mm/_s)	# of Values Used to Compute Average Group Velocity	Std. Deviation (sample) of Group Velocity	Average Group Velocity y-axis Intercept (mm)	# of Values Used to Compute Average y-axis Intercept	Std. Deviation (sample) of y-axis Intercept
A_0	60 kHz	2.551	43	0.03	-17.2	43	1.5
A_0	270 kHz	3.133	6	0.00	-3.1	6	0.0
A_0	522 kHz	3.049	6	0.004	-1.3	6	0.2
S_0	60 kHz	5.352*	5	0.07	-27.2*	5	3.6
S_0	270 kHz	4.819	3	0.04	-6.5	3	1.5
S_0	522 kHz	1.811	15	0.03	2.0	15	0.6

*average of all available values, even those with WT fractions less than 0.5.

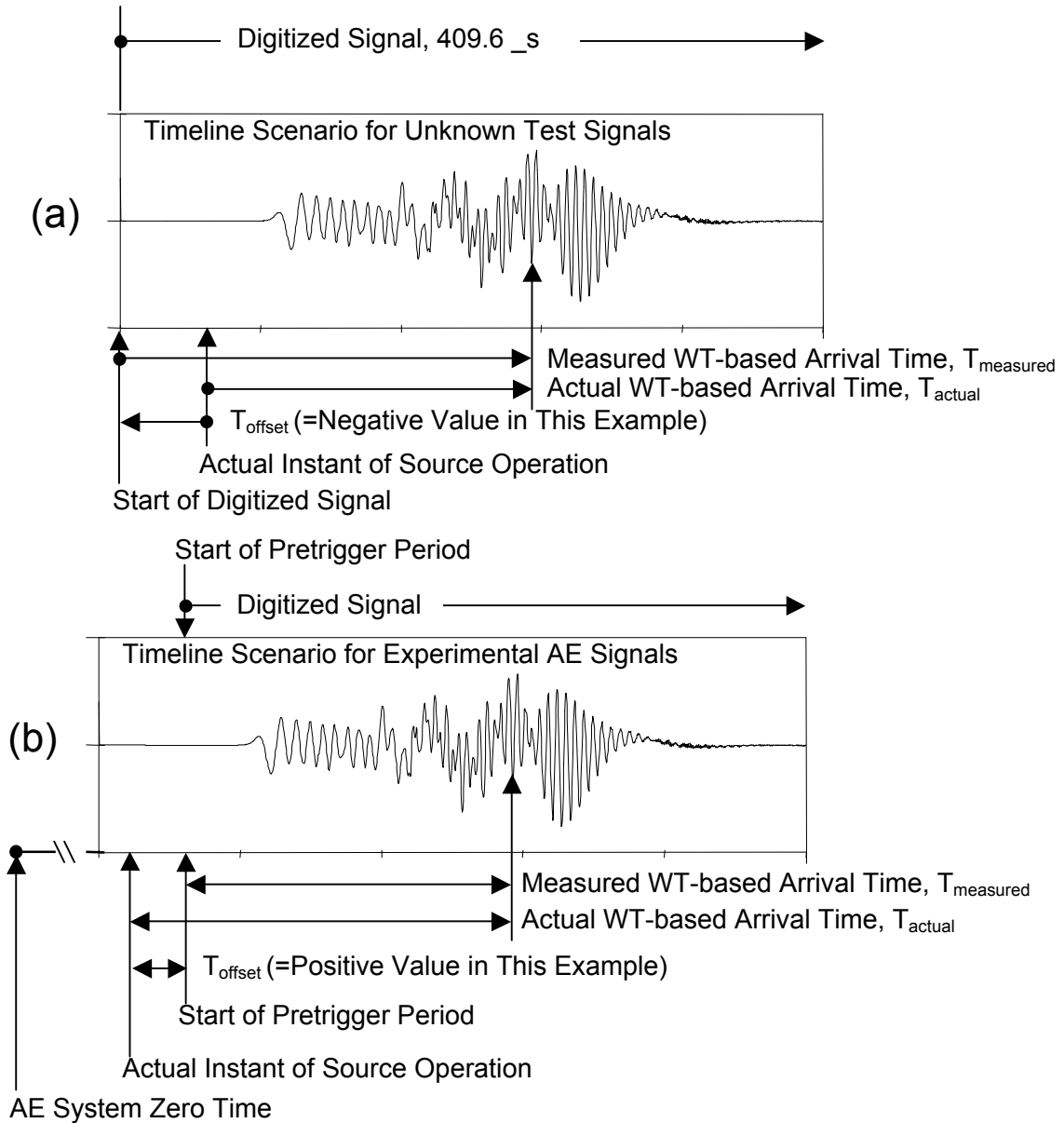


Fig. B-1 Timeline for AE signal: (a) for unknown test signals; (b) for experimental AE signals.

Appendix C: Selected Results for Algorithm Applied to Test Cases

Table C-1 Selected frequency and mode results determined by algorithm for test cases.

Test File Name	Primary Frequency (kHz), Mode	Secondary Frequency, WT Fraction, Mode	Tertiary Frequency, WT Fraction, Mode	Ranges for Known Modes (mm)		
				R _{60/522}	R _{60/270}	R _{522/270}
1	522, S ₀	270, 0.48, S ₀	60, 0.10, S ₀	57	26	59
2	522, S ₀	60, 0.77, A ₀	270, 0.52, UK*	58	-	-
3	270, S ₀	522, 0.85, S ₀	60, 0.26, S ₀	63	21	66
4	522, S ₀	60, 0.44, A ₀	270, 0.22, UK	57	-	-
5	60, A ₀	522, 0.8, S ₀	270, 0.29, UK	59	-	-
6	60, A ₀	270, 0.33, A ₀	522, 0.18, A ₀	117	117	121
7	522, S ₀	270, 0.54, S ₀	60, 0.12, S ₀	119	128	118
8	522, S ₀	270, 0.39, S ₀	60, 0.08, S ₀	179	186	178
9	60, A ₀	270, 0.16, UK	522, 0.09, S ₀	175	-	-
10	522, S ₀	270, 0.58, S ₀	60, 0.13, S ₀	179	181	179
11	270, S ₀	522, 0.52, S ₀	60, 0.28, S ₀	195	142	198
12	60, A ₀	522, 0.76, S ₀	270, 0.33, UK	173	-	-
13	522, S ₀	60, 0.84, A ₀	270, 0.56, UK	59	-	-
14	60, A ₀	270, 0.85, A ₀	522, 0.60, A ₀	54	54	53
15	522, S ₀	270, 0.68, S ₀	60, 0.15, S ₀	58	26	60
16	60, A ₀	270, 0.37, A ₀	522, 0.10, A ₀	58	72	178
17	60, A ₀	270, 0.94, A ₀	522, 0.71, A ₀	106	111	144
18	270, S ₀	522, 0.84, A ₀	60, 0.35, A ₀	2353	929	172
19	270, S ₀	60, 0.68, S ₀	522, 0.27, S ₀	39	486	13
20	60, A ₀	522, 0.79, S ₀	270, 0.36, UK	88	-	-
21	270, S ₀	522, 0.52, S ₀	60, 0.28, S ₀	195	142	198
22	270, S ₀	522, 0.98, S ₀	60, 0.92, S ₀	176	108	180
23	60, A ₀	522, 0.43, S ₀	270, 0.26, UK	175	-	-
24	60, A ₀	522, 0.46, S ₀	270, 0.28, UK	58	-	-
25	60, A ₀	522, 0.33, S ₀	270, 0.26, UK	117	-	-

*UK = Unknown at this point

Table C-2 Selected range calculation results for test cases.

Test File Name	Range (mm) assuming A ₀ mode for 270 kHz		Range (mm) assuming S ₀ mode for 270 kHz		Population coefficient of dispersion (all 3 samples)		Range-based mode selection for 270 kHz	Lowest Population Coefficient of dispersion for 3 pairs of computed ranges examined	Best Computed Range (mm)	% Difference of “best computed range” to known range
	R _{60/270}	R _{522/270}	R _{60/270}	R _{522/270}	Assume A ₀ mode for 270 kHz	Assume S ₀ mode for 270 kHz				
1	-	-	-	-	-	-	-	0.016	58	2.6
2	141	84	57	58	0.364	0.007	S ₀	0.004	58	3.9
3	-	-	-	-	-	-	-	0.020	64	7.5
4	149	86	61	59	0.394	0.024	S ₀	0.014	60	0.2
5	117	77	48	53	0.288	0.083	S ₀	0.050	51	15.4
6	-	-	-	-	-	-	-	0.002	117	2.3
7	-	-	-	-	-	-	-	0.002	118	1.5
8	-	-	-	-	-	-	-	0.001	179	0.8
9	174	175	70	119	0.003	0.352	A ₀	0.001	175	2.8
10	-	-	-	-	-	-	-	0.000	179	0.6
11	-	-	-	-	-	-	-	0.008	196	9.0
12	461	263	184	179	0.401	0.024	S ₀	0.013	181	0.7
13	142	85	58	58	0.364	0.008	S ₀	0.004	58	2.9
14	-	-	-	-	-	-	-	0.001	54	9.4
15	-	-	-	-	-	-	-	0.016	59	1.7
16	-	-	-	-	-	-	-	0.112	65	8.1
17	-	-	-	-	-	-	-	0.021	108	9.8
18	-	-	-	-	-	-	-	0.434	1641	2635
19	-	-	-	-	-	-	-	0.514	26	78.3
20	-102	29	-38	20	15.940	2.209	S ₀	0.624	54	69.7
21	-	-	-	-	-	-	-	0.008	196	9.0
22	-	-	-	-	-	-	-	0.011	178	1.1
23	185	178	75	121	0.024	0.330	A ₀	0.009	176	2.1
24	83	66	35	45	0.153	0.206	A ₀	0.064	62	3.0
25	119	118	49	81	0.006	0.340	A ₀	0.002	117	2.2

*UK = Unknown at this point

ACOUSTIC EMISSION MONITORING OF A HIGH PRESSURE TEST OF A STEEL REACTOR CONTAINMENT VESSEL MODEL

A. G. BEATTIE

Dept. 9742, Sandia National Laboratories, Albuquerque NM 87185-0615; Now affiliated with Physical Acoustics Corporation, Princeton Junction, New Jersey

Abstract

A mixed-scale steel model of a boiling water reactor (BWR) containment vessel was pressurized to failure in December 1996. The instrumentation included an acoustic emission (AE) source location system in addition to strain and displacement gauges. Post-test analysis showed general agreement between the location of AE sources and the regions of distortion and failure. The analysis also gives the pressure dependence of the different emitting regions. The general location plot of the emission shows that much of the emission was located around the stiffening ring on the conical shell section.

This paper was originally published as appendix H of NRC NUREG/CR-5679 and Sandia National Laboratories SAND 98-2701, "Design, Instrumentation, and Testing of a Steel Containment Vessel Model".

1. Introduction

A program to investigate the response of nuclear containment structures to pressure loading beyond their design loads is being conducted at Sandia National Laboratories. This program is sponsored by the Nuclear Power Engineering Corporation of Japan and the U.S. Nuclear Regulatory Commission, Office of Nuclear Regulatory Research. In the test described in this report, a mixed-scale model representative of a steel containment vessel (SCV) for an Improved Mark II Boiling Water Reactor was used. The geometric scale is 1:10. The same materials were used for the model as for the actual plant and the scaling on the wall thickness was set at 1:4. A steel contact structure was placed over the SCV model to simulate some of the features of the reactor shield building in an actual plant.

The instrumentation for the test included over 800 data channels consisting of strain gauges, displacements sensors, temperature and pressure gauges and video monitoring. It also included an acoustic emission (AE) source location system operating independently of the other data channels. This system monitored the entire surface of the SCV above the ring support girder. The purpose of the acoustic monitoring was to detect and approximately locate emission sources that occurred in the shell of the vessel during the pressure test in real time and then to try to gain additional information by a more sophisticated post test analysis. This real time monitoring could not give accurate locations because the available commercial real time programs were not designed to accommodate the complex geometry of the model.

2. Acoustic Emission Testing

Acoustic emissions are acoustic waves produced by materials subjected to a stress. (1, 2) There are many mechanisms, which can generate such waves but almost all involve a relatively rapid rearrangement of the internal structure of the material on a microscopic level. In a large structure, such as the SCV, the important sources of emission will be crack initiation and flaw growth. Other sources, which may be seen, are spallation or fracture of corrosion particles, rubbing of adjacent surfaces due to expansion of the structure with increased stress and, in the case of pressure vessels, gas flow. The emissions generated by these sources travel as bulk acoustic waves until they reach the surface of the structure where they change acoustic mode and become surface or plate waves. These waves will propagate along the surface of the structure where they can be detected by piezoelectric sensors. For structures with low to moderate acoustic attenuation, an emission of moderate amplitude can excite most of the sensors on the structure. This enables an AE test to monitor an entire structure with a reasonable number of sensors. When the structure is stressed, only flaws, which are affected by the applied stress field will generate emission. Flaws in regions which are not stressed or do not grow under the applied stress will not generate emission. The absence of AE during the stressing of a structure is the sign of a sound structure. Thus an AE test is a negative test, which puts stringent requirements on the knowledge that the AE system is functioning normally.

Acoustic emissions are unfortunately not simple waves. They are produced by discrete events in the material and are transient, not continuous, waves. By the time that they reach a sensor, they have become a combination of different acoustic propagation modes and may contain both bulk and surface bounded modes as well as reflected waves from different surfaces and discontinuities in the structure. The acoustic velocities differ for different acoustic modes and some of the bounded modes have frequency dependent velocities. To add to the complexity, the events that produce AE occur semi-randomly in time and stress level. One is never able to predict the exact time (or location) at which an event will occur. This is in contrast to ultrasonic testing where a signal with a known waveform is introduced into a known location on the structure at a known time. While there is no physical difference between an ultrasonic and an AE wave, the differences in generation of the waves result in quite different methods of analysis.

Growing cracks in a material produce readily detectable AE. However, other types of flaws may not. Any emissions produced by creep are extremely low amplitude and appear to be usually below the equipment noise level. Ductile tearing appears to produce some emission but much less and of lower amplitude than does a crack. On the other hand, a flake of rust spalling off a surface can produce very large amplitude emission. In testing pressurized vessels, the most prevalent source of extraneous acoustic noise is flowing gas, either from pressurizing the vessel or from a leak. The one thing working to the testers advantage is that the gas flow noise seems to be strongly dependent upon the internal pressure in the vessel. In the SCV, flow noise dropped below the sensitivity of the system (the threshold was set at 175 microvolts out of the sensor) at about an internal pressure of 0.35 MPa (50 psi).

A single emission, either detected by one sensor or detected by enough sensors to have its source located, is mainly an indication that something happened. A growing flaw will generate a

series of emissions as the stress level increases. Unstable crack growth generates a rapidly increasing number of emissions. A steady rate of emissions from one region generally indicates stable flaw growth. A region where the emissions stop as the stress level increases either has arrested flaw growth or the emissions are not from a stress driven flaw. Because of the random occurrence of acoustic emissions, a small gap in the emissions as the stress increases means nothing but a total cessation of emissions indicates a source, which is not detrimental to the integrity of the structure.

Several terms unique to AE testing will be used in this paper and will be defined here. When an acoustic wave passes underneath a sensor and the amplitude of the wave detected by the sensor exceeds a preset threshold, the system is triggered and records the time and other parameters of the wave. This is called a hit. When several sensors are triggered by the same acoustic wave at times consistent with travel from a single point on the structure, the data set is called an event. If the time data from an event is used to calculate a location on the structure and the calculated location is consistent with acoustic travel times to at least the first six sensors hit, the event is called a located event. The term event is also used to describe the physical occurrence of some phenomena in the structure, which generates the acoustic wave. A data set event can be generated by waves from several events in the structure and thus not result in a located event.

3. Experimental Details

An elevation drawing of the SCV model and contact structure is given in Fig. 1. The design pressure of the prototype containment vessel is 0.31 MPa (45 psig) while the design pressure for the SCV model is 0.78 MPa (113 psig). The model consists of sections with different geometries and wall thicknesses. The first section above the ring support girder is a short cylindrical shell. This is joined to a section of a conical shell. Attached to the conical shell is a section of a spherical shell, which is joined by the knuckle section to another cylindrical shell. A thick steel ring welded to this cylindrical shell represents the flange to which the top head is bolted on the actual vessel. The top head is a cylinder with a flattened sphere as a top. Several stiffener rings representative of the actual vessel are on the inside of the SCV model. A representation of an equipment hatch is welded to the conical shell section. The thickness of the structure varies at different heights. A typical thickness in the conical section is 9.6 mm. The bell-shaped steel contact structure installed over the model was made of 38 mm thick steel. The nominal gap between the contact structure and the SCV was 18 mm and the SCV was expected to close this gap and come into contact with the contact structure around 3.5 MPa.

The acoustic emission (AE) system used was a 24 channel Physical Acoustics Corp. (PAC) Spartan AT source location system. The sensors were PAC R15I sensors, which have a maximum sensitivity around 150 kHz. These sensors feature an integral 40 dB preamplifier powered from the main AE system through the signal cable. Twenty-four sensors were applied to the model with magnetic hold-downs and acoustically coupled with silicone vacuum grease. The paint on the model surface was removed and the metal ground smooth before the sensor was mounted. Locations of the sensors are given in Table 1. The "vertical distances" listed are the measured distances along the interior or exterior surface of the vessel, starting from the ring

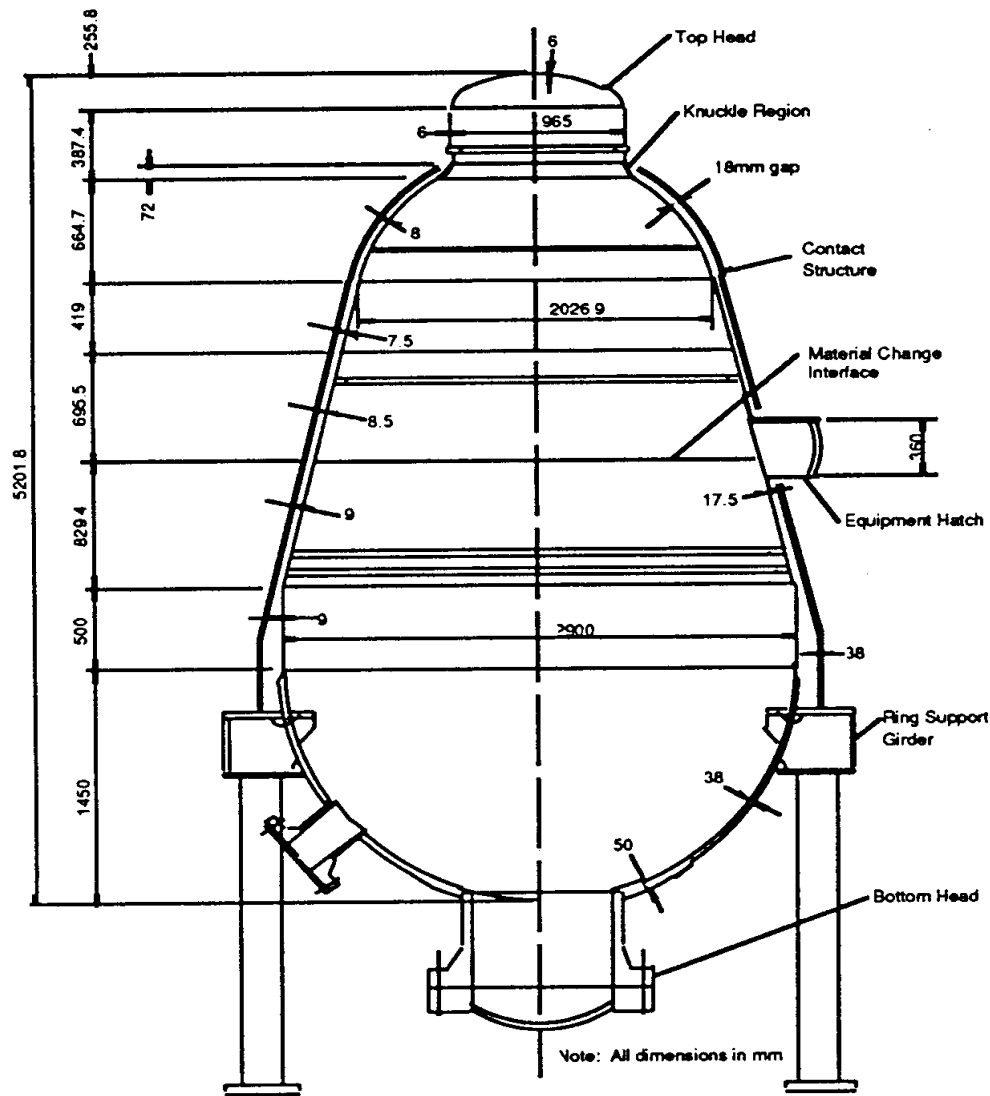


Fig. 1. Schematic of the SCV and contact structure assembly.

support girder. Sensors 1 through 16 and 22 and 23 were mounted inside the model because the contact structure prevented their placement on the outside. A schematic of the sensor locations is given in Fig. 2. The cables to these sensors ran through pressure tight coaxial feed throughs located in the bottom head. Sensors 17 through 21 were mounted on the outside of the model above the contact structure. Sensor 24 was mounted in the middle of the equipment hatch on the outside. The computer for the AE system was located in the control center and connected to the system electronics by approximately 900 m of fiber optic cable.

The Spartan system collects a full set of analog AE parameters. A test time for the detection of each AE signal is assigned to the data set. The accuracy of the time measurement is 0.25 μ s. The pressure inside the model was also recorded on each data set. Each set was immediately written to the hard disk before any analysis was performed. This allows the use of post-test analysis programs, which are completely independent of any programs built into the AE system. The maximum data collection rate is around 2000 hits/s. Several built-in location programs for

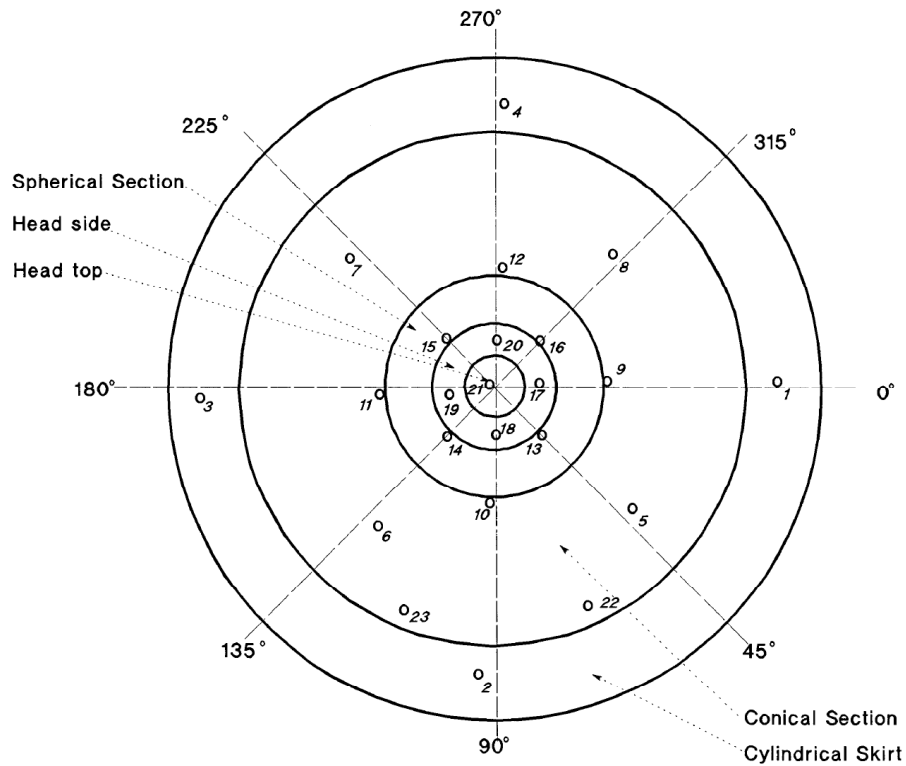


Fig. 2. Schematic representation of the sensor layout on the SCV

Table 1 Sensor Locations

Sensor	"Vertical" Distance - mm	Azimuth Angle - Degrees	Sensor	"Vertical" Distance - mm	Azimuth Angle - Degrees
1	510	357	13	3400	45
2	515	94	14	3400	135
3	515	177	15	3400	225
4	510	274	16	3400	315
5	1650	41	17 *	3805	351
6	1670	131	18 *	3805	90
7	1670	221	19 *	3805	171
8	1670	311	20 *	3805	270
9	2690	356	21 *	37 mm from top head center	225
10	2690	96	22	1210	67
11	2675	176	23	1215	113
12	2665	276	24 *	center of eq. hatch	

* located on outside of model

different geometries are contained within the system to analyze data in real time. None of these programs included a conic section, which is the underlying geometry of the SCV model. The best approximation for real time location was to divide the representation of the model into two parts, a cylinder with the average diameter of the cylindrical, conic and spherical sections and a separate short cylinder with a spherical cap to represent the top head. These two graphs resulting from this representation showed approximate source locations and were capable of indicating a tight clustering of located events during the test. The major problem with this set up was that the low acoustic attenuation allowed a large AE event to excite most of the sensors on the model. The computer considered the bottom and top arrays to be completely separate and therefore often plotted two locations, one on each graph, for a single event.

When the sensors were installed, each sensor was tested by breaking a 0.5-mm-diameter lead near the sensor on the surface of the model. The output waveforms from the sensors were digitally recorded and the few sensors, which had low output amplitude, were re-coupled or had the surface under them reground until all sensors had approximately equal sensitivity. After the model was closed, lead breaks on the outer surface were made to insure that all sensors were working and that the locations on the real time maps were reasonably accurate. More checks were made on the sensors and the programs during the low-pressure tests.

The SCV model was pressurized with nitrogen gas. This gas was generated by evaporating liquid nitrogen and heating the gas to room temperature. Gas was introduced into the model through a pipe into the bottom head. The pressurization schedule for the high-pressure test called for the gas pressure inside the vessel to be raised in steps with pressure holds between the steps. The holds were to last for approximately 15 minutes each. The pressure increment started at 0.137 MPa (20 psi) and decreased in size toward the end of the test. Each pressure step took

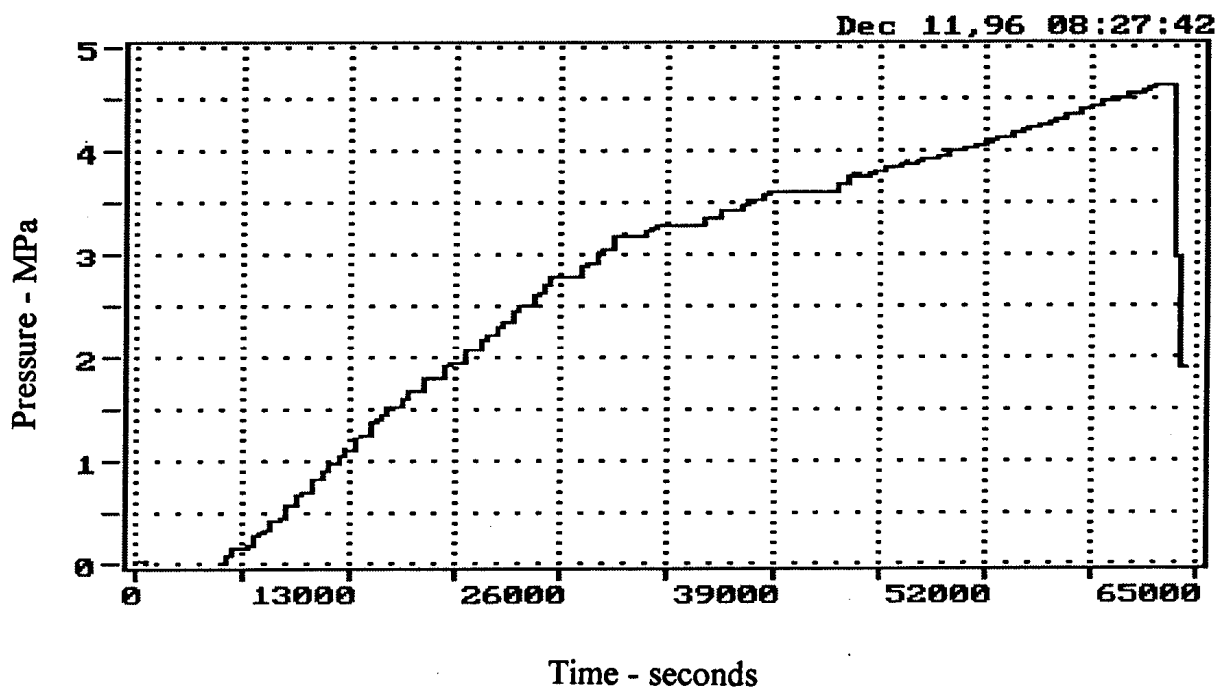


Fig. 3 Pressure as a function of time in the SCV.

about a minute and a half to complete. There was always a small decrease in the pressure during the holding period due to cooling of the gas. This pressurization schedule was continued with a few longer holds until the SCV model failed.

4. Real Time Tests

One of the preliminary low-pressure tests of the SCV model was conducted with the AE system operating. In this test the model was subjected to the maximum pressure, which it saw before the high-pressure test, 1.26 MPa (183 psig). From the start of the pressurization, large amounts of AE were produced by the flow noise from the pressurizing gas. The noise did not diminish until after an extended hold at 0.21 MPa (30 psig). When the pressurization resumed, the noise level rapidly decreased. During the rest of the pressurization, only seven located events were seen by the system. These occurred between 0.78 MPa (113 psig) and 1.26 MPa. There was no clustering of the event sources, and all were located in different triangles formed by the three nearest sensors to the source.

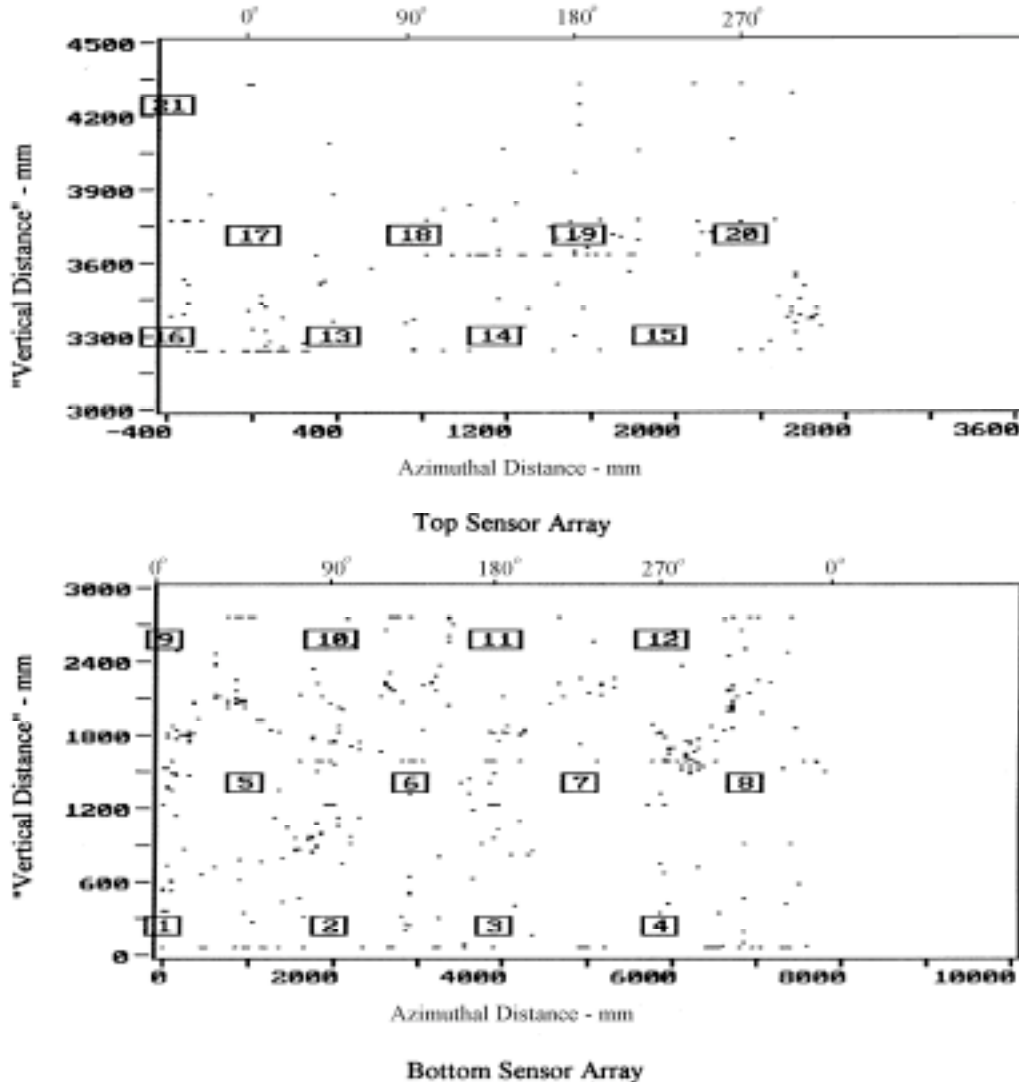


Fig. 4 Total event locations seen in the real time test.

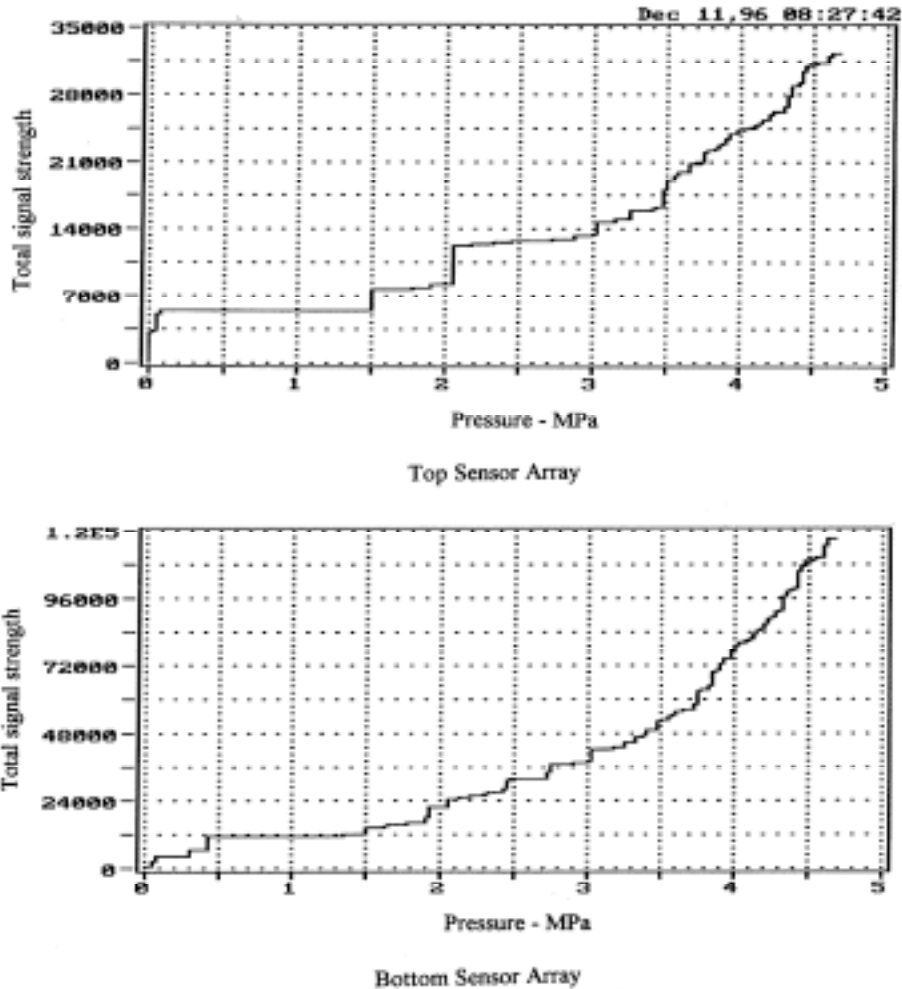


Fig. 5 Total signal strength of located events vs. pressure top and bottom arrays.

The pressurization curve for the high-pressure test is shown in Fig. 3. During the initial gas flow, there was again excessive AE. The gas flow noise stopped at about 0.35 MPa and the first located emission was seen at 0.44 MPa (64 psi). Figure 4 shows the events located by the bottom and the top sensor arrays during the test. There are some areas that appear suspicious but nothing that would indicate imminent failure. Figure 5 shows curves of the total signal strength from the located events versus the pressure for the two arrays. There is an apparent change in the slope of the curves around 3.5 MPa (508 psi) but again nothing that suggested that the vessel was about to fail. There was certainly an increase in the AE rate above 3.5 MPa and this was communicated to the test director but nothing appeared serious right up to the appearance of a major leak at 4.62 MPa (672 psi). After the leak started, no more located events were seen. However, the leak produced large amounts of AE. Figure 6 is a graph of the total signal strength from all of the hits during the test as a function of pressure. The fill noise during the start of pressurization and the leak noise at the end of the test are quite obvious. These two regimes generated most of the AE seen during the test. The test was terminated when the leak prevented further increases in the pressure in the vessel. Post-test examination of the interior showed a tear in the wall near the equipment hatch.

The AE system did detect activity from the area near this tear. It can be seen in Fig. 4 as the group of events in the center of the triangle formed by sensors 2, 5 and 6. However, this activity did not appear any worse than several other areas seen in Fig. 4. Metallographic examination of the tear showed that it was primarily ductile in nature. Ductile tears produce fewer and lower amplitude emissions than do growing cracks. The real time AE monitoring did detect an increase in the damage rate in the vessel, located the region that failed and immediately indicated a serious leak. While it did not predict the failure of the vessel it should be noted that catastrophic failure did not occur.

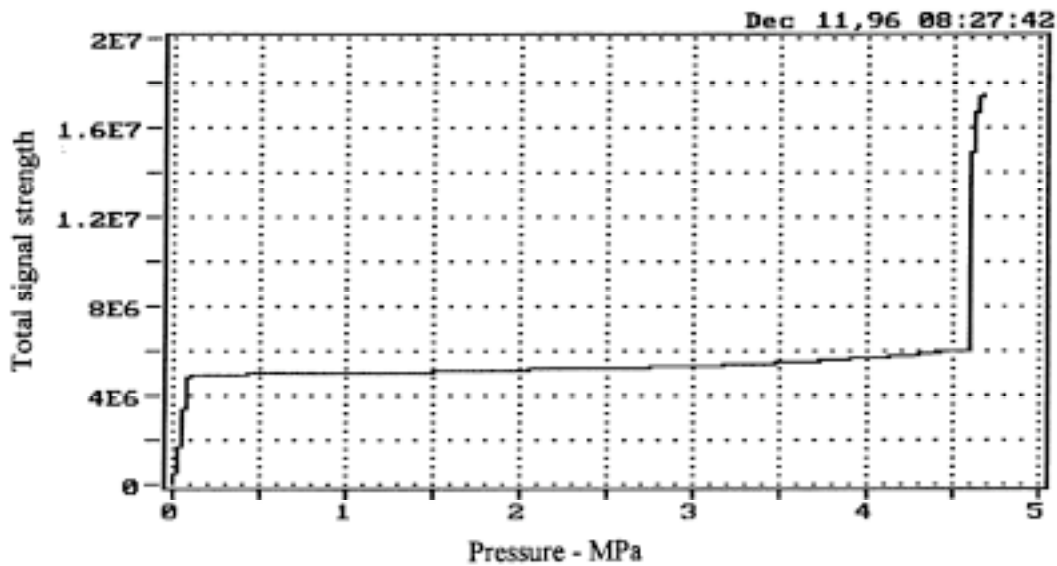


Fig. 6 Total hit signal strength for entire test showing gas inflow noise and leak noise.

5. Post-Test Analysis

Post-test analysis of the AE data from this test was done for several reasons. An accurate calculation of the locations of the AE sources allows the use of a clustering algorithm to determine locations where serious damage might be occurring. It also allows a determination of the pressure dependence of the AE from each one of the clusters. For possible future tests, it tells whether the highly approximate location set up used in real time is sufficiently valid to be worth using again or whether the locations calculated in real time from such a distorted set up are meaningless.

The first problem to be faced in the post-test analysis was the determination of which collections of hits constituted an event. The data file consisted of a sequence of hits ordered according to their time of occurrence. The question is, how does one take this data set and decide which hits belong to an event. An event definition time must be chosen. This is the time interval between the detection of the first and the last hit in an event. It will depend, in part, upon the attenuation of the material in the structure. The low attenuation of the steel in the SCV model allowed a moderate amplitude emission to travel over the whole surface of the model, exciting almost every sensor. For a flexural wave, an emission would take about 1.8 ms to travel the distance between a

sensor on the bottom on one side of the model to one on the top on the other. An event definition time much shorter than this would define multiple events where only one actually occurred and a time much longer could combine several real events into one. The most important point in determining an event is to find the first sensor hit. This sensor defines the starting time for the event. Missing the first sensor makes the calculated location for that event almost meaningless as there is an unknown interval, which must be added to each travel time. For the SCV model, an event definition time of 2.0 ms was chosen and a manual search of the data and the selected hits for each event showed this to be a reasonable value.

Location on a plane requires that a minimum of three sensors be hit. The three unknowns are the initial time of the event and the x and y coordinates of the source. For accurate data, this is all that is needed. Unfortunately, in the real world, AE data is very seldom highly accurate. Attenuation and dispersion of the waves in the plate cause the waveform to vary at different sensors on a uniform plate. Different acoustic modes travel at quite different velocities. The mode, which is detected, depends in part on the geometry of the crack and in part of the geometry of path that the acoustic wave takes to the detecting sensor. Reflections from discontinuities (including welds) in the plate and surface attachments to the plate can greatly affect the waveform for some acoustic paths. For these reasons, a fixed trigger level (which is used in this and most AE source location systems) will produce uncertainties in the measured time of arrival at the sensor. Two methods of alleviating some of these uncertainties were used in this analysis. First an over determined data set was used when possible. The arrival times at the first six sensors on the cone to be excited comprised the event data set. If six sensors were not hit, data from as few as three was used. A non-linear least squares fitting program was used to calculate the most probable location of the source. This program also calculated a goodness of fit parameter (one minus the ratio of the average deviation between the calculated and the measured times over the average standard deviation of the time data) for the calculated answer. Data sets which had a goodness of fit parameter of less than 0.85 and those whose calculated location was more than 1400 mm away from the center of the triangle formed by the first three sensors hit were not included in the set of located events.

The second method of reducing the uncertainty in the locations was to use a simple procedure developed by Ge and Kaiser (3) to determine what acoustic velocity should be used for the travel time from the source to each sensor hit. The dispersion curves for steel plates at frequencies between 120 and 150 kHz show an extensional wave velocity around 5.2×10^6 mm/ μ s and a flexural wave velocity of 3.3×10^6 mm/ μ s. Similar wave speeds were roughly measured in the vessel so these figures were used in the post-test analysis. To partially determine whether a sensor in an event data set was triggered by an extensional wave or a flexural wave, the distances between the first and subsequent sensors hit were calculated. Ge showed that if the measured time difference between the excitation of two sensors was greater than the time it would take for an extensional wave to travel between the two sensors, the wave from the source could not be traveling at the extensional velocity. If the time difference is greater than the time it would take for a flexural wave to travel between the two sensors, in this experiment, the system probably triggered on a waveform that was distorted by dispersion, scattering or multiple paths. The following procedure was thus used. Initially an extensional velocity was assumed for the waves to all sensors. The sensors, which could not have had an extensional velocity, were assigned the flexural veloc-

ity. Those whose arrival times were later than 10% greater than the flexural velocity would have allowed were dropped from the data set. If the calculation with these velocities did not have a goodness of fit parameter that exceeded 0.85, a flexural velocity was assumed for all sensors. If the parameter still did not exceed 0.85 with all flexural velocities, that event was not included in the set of located events.

The SCV model is primarily a thin metal shell. The shell thickness can be considered only as contributing a small uncertainty in the time measurements. To simplify the problem to location on a plane, the conical section was theoretically cut down the zero-degree longitude and the surface unrolled onto a plane. This can be done without distortion of a conical surface. The cylindrical surface below the cone was also treated as lying on the same plane as the cone. The distortion produced by this procedure was not thought to have a significant effect on the location of the events on the cylindrical surface. The intention had been to treat spherical surface above the conical section as a cone, if possible or a slice of a sphere if necessary. The head of the vessel was to be treated as a cylinder with a hemisphere on top of it. These latter two calculations proved unnecessary because of the small number of widely scattered events originating on these surfaces. The events on these surfaces were calculated using a planar approximation of a surface within the triangle formed by the three first hit sensors.

A total of 446 events out of 650 data sets on the conical section met all the criteria and were kept in the set of located events. Many of the discarded events were either of very low amplitude or appeared to have another event mixed in with them. The accuracy of the location calculations were approximately plus or minus 50 mm. This uncertainty is produced primarily by the uncertainties in the triggering points on the individual waveforms. The uncertainty due to a finite thickness of the shell is 10 mm or less.

In order to determine what AE was produced by possibly serious damage and what was of a more benign nature, a cluster-seeking program was written. A cluster was defined as a collection of located events located within a confined area. The definition of a cluster is quite arbitrary. A crude estimate of the area of the conical plus cylindrical sections divided by the number of located events gave a rough density of one event per 7000 mm². It was decided that a cluster should have at least ten times that density. Also with the uncertainty in the location accuracy, the smallest area that made much sense was a circle with a 100 mm radius. The criteria for the existence of a cluster was then set as four or more events within a circle of radius 100 mm (an 8-inch diameter circle). As each point was calculated, the program checked to see if it were within 100 millimeters of any previous point. Two points within this distance form the nucleus of a cluster. The center of the cluster is then calculated. Each succeeding point is checked to see if it is either within 100 mm of a cluster center or if it starts another cluster with another solitary point. If it is within the 100 mm, it is added to the cluster and a new center calculated. A growing flaw will show a steady or increasing emission rate as the stress field is increased. A source, which does not emit with increasing stress field, is either a flaw that has arrested or an event that does not affect the structures integrity, such as a corrosion particle flaking off. Therefore, if the cluster did not contain at least one event at a pressure greater than 90% of the failure pressure, it was defined as not a significant cluster.

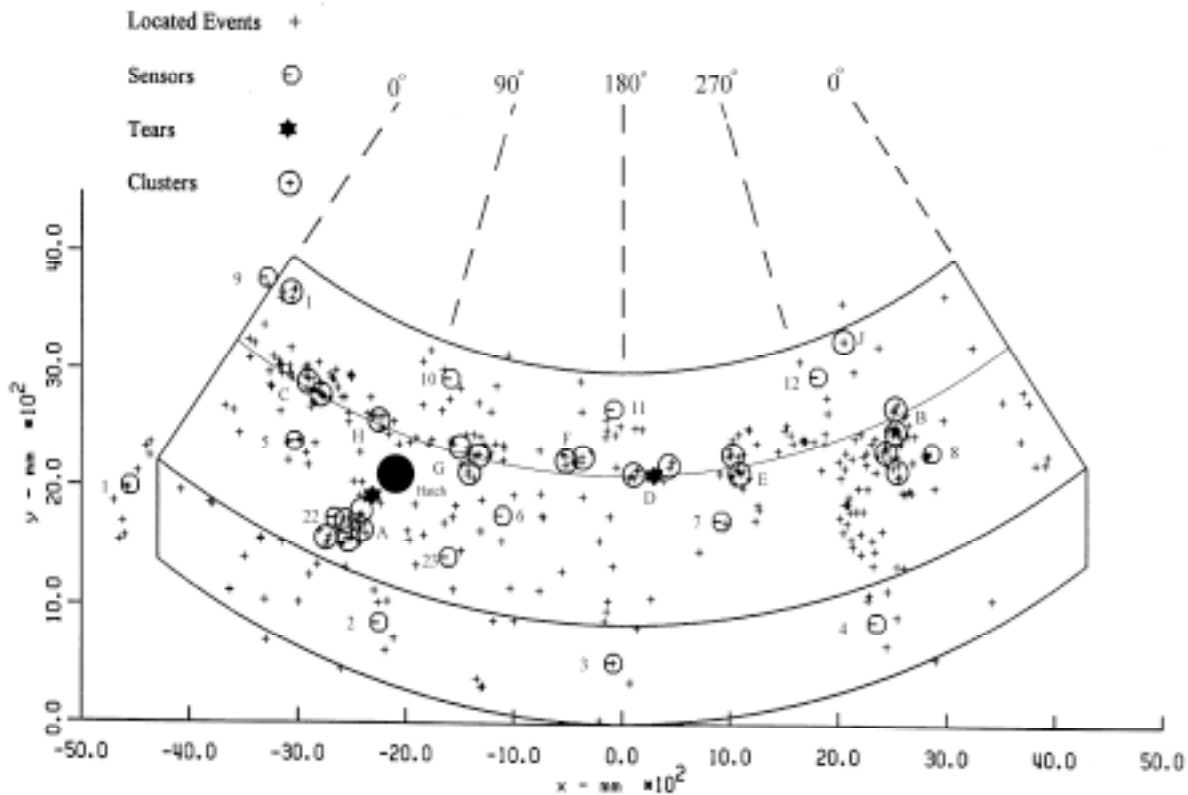


Fig. 7 Map of the flattened conical section and cylindrical skirt.

Figure 7 shows the locations of all located events and the significant clusters superimposed over the events. It is a map of the flattened conical section with the cylindrical skirt attached. Included are the positions of the sensors, the two visible tears in the SCV model and the stiffener ring. A group of overlapping clusters is counted as one cluster and all clusters are identified with a letter. In cluster D, the two clusters do not touch but both appear associated with the crack lying between them.

In Fig. 5, the total signal strength was shown as a function of pressure for the entire test. Figure 8 shows the total signal strength as a function of pressures for clusters A, B, C and D. These were the largest clusters, and all are graphed on the same scale. The curves for clusters E, F and G were very similar to that for D. The curve for H had about half the envelope strength of D and the curves for I and J were each composed of four very small events around 4.5 MPa. These curves show the severity (from an AE standpoint) of the clusters and allow one to determine at what pressure flaw growth started for each. Finally, the number of located events in each 50 mm high slice of the conical section and skirt is shown Fig. 9. The peak of this curve corresponds very well to the position of the strengthening ring.

The nine events located on the spherical slice were well scattered. No two events were close enough to form a cluster under the definition given above. Only one occurred above 4.4 MPa.

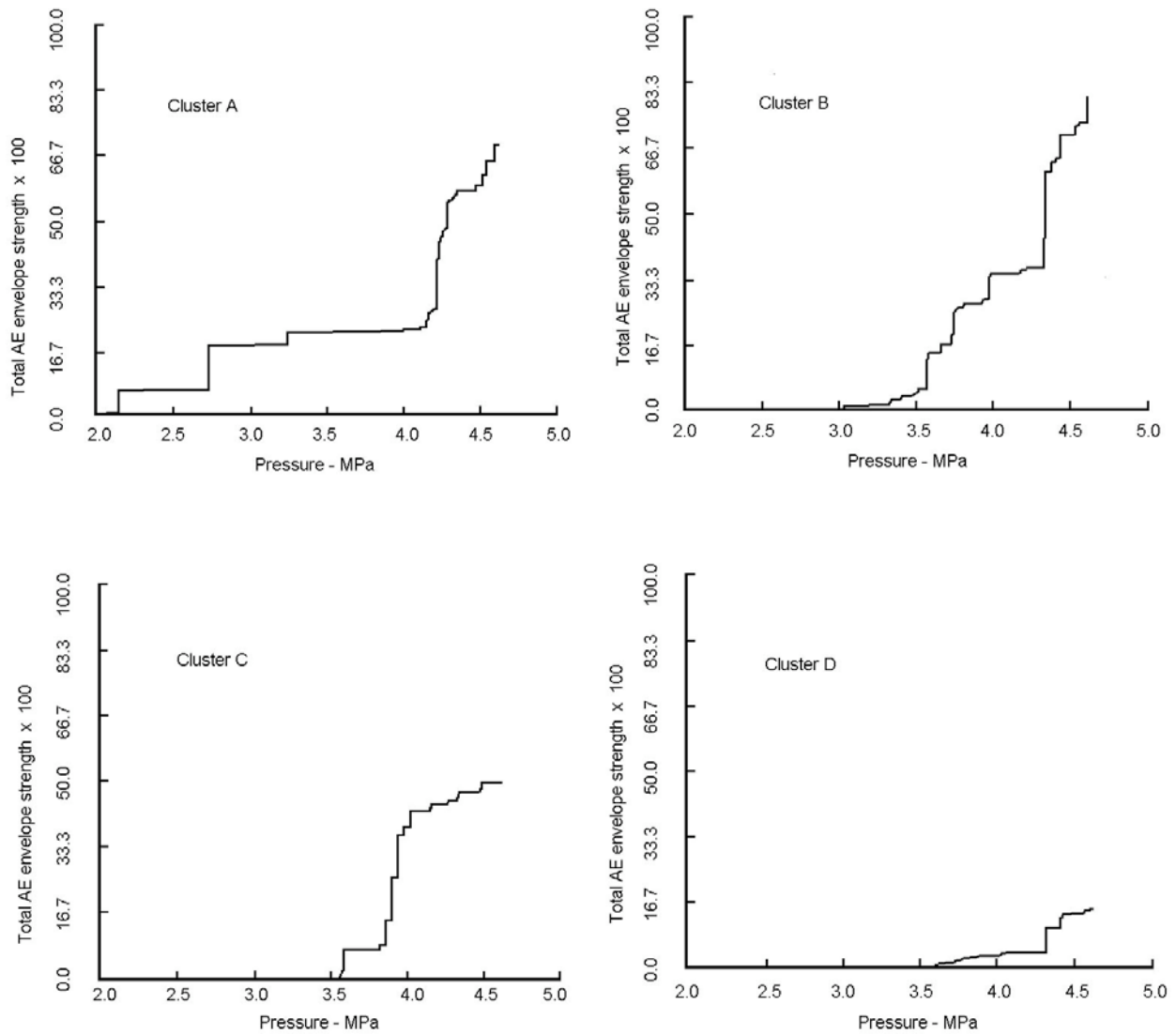


Fig. 8 Total signal strength as a function of pressure.

The 21 events detected from the top head were scattered over seven of the triangles formed by the sensors on the head. Three triangles had four or more events in them. In two of these triangles, the events were well scattered, both in space and pressure. In the third triangle, formed by sensors 13-17-18, there were four events located within a cluster radius of 20 mm (essentially all at the same point to the accuracy of this calculation). However, the highest-pressure event in this cluster occurred at 3.65 MPa (530 psig). So the cluster was not caused by any structural problems.

6. Discussion

The only significant AE occurred in the conical section and to a lesser extent, the cylindrical skirt. The top cap, the spherical slice, the knuckle region and their attendant welds gave no signs of any serious problem. Examination of Fig. 7 shows that most of the clustering of the emission sources borders the location of the stiffening ring, about two thirds of the way up the conical

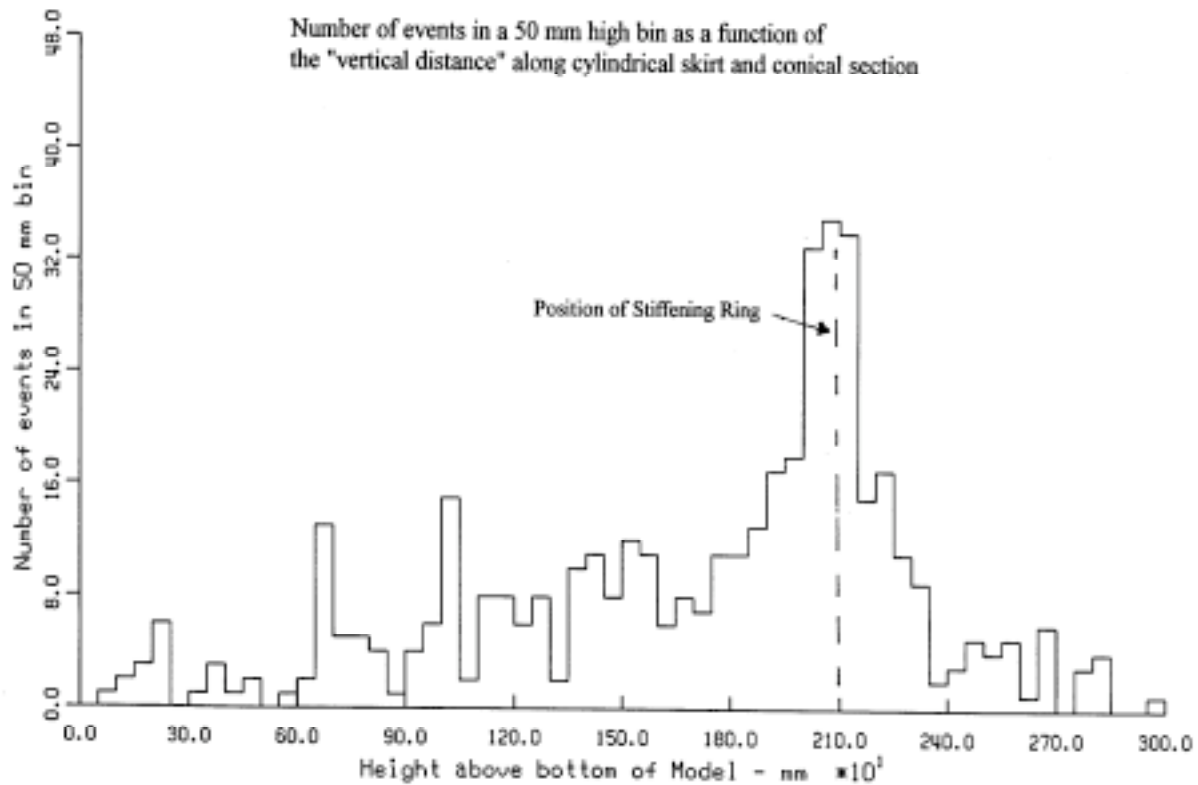


Fig. 9 Distribution of located events as a function of "vertical distance" above the ring support girder.

section. Figure 9 shows that the highest density for all located events was also at the locus of the stiffening ring. The only serious cluster not located near this ring was A which was associated with the flaw that terminated the test. Clusters I and J are each comprised of four events, with all events in each having a very low signal strength. They are not considered of any significance, at least below the failure pressure.

The large tear in the SCV model occurred just above cluster A on Fig. 7. It was located in an area near the equipment hatch. This region had been ground smooth and was somewhat thinner than the rest of the conical shell. The tear was roughly 250 mm in length. Most of the events in this cluster are located below the locus of the tear. It is thought that they were produced by the tear and that this offset was caused by acoustic path distortions produced both by the hatch opening and by the tear itself. The plot of the signal strength as a function of pressure for cluster A (seen in Fig. 8) shows several well-spaced events below 4.0 MPa but most of the events appear above 4.2 MPa. Emission continued until the test was stopped. The events which appeared at lower pressure may have been produced by minor flaws in the weld joining the hatch to the conical section. It should be noted in the graph for cluster A in Fig. 8 that there is no emission immediately prior to the leak. The last located event in cluster A occurred 3 minutes and 36 seconds before the acoustic leak signal was seen. This shows clearly that the opening, which stopped the test, was a ductile tear and not a propagating crack.

The cluster at B, whose activity plot is also shown in Fig. 8, extends down the model from the stiffening ring. No flaw was visible on the structure in this region. However, the paint on the outside of the model (which had been hidden by the contact structure) showed many vertical parallel cracks, Fig. 10. Laboratory tests showed that fracture of a paint chip from the vessel could produce very large AE signals. Unfortunately, visual examination of the paint cannot determine whether the cracks occurred by paint fracture or by slow tearing. There were at least two other areas on the vessel, which had similar paint cracks but they did not produce a strong cluster at



Fig. 10. Paint cracks on outside of SCV at cluster B. The curved line encloses cluster B.

high pressures. The best interpretation would appear to be that the upper emission locations were associated with the stiffener ring with at least some of the lower emissions produced by paint cracks.

The clusters at B, C, D, E, F, G and H all appear to be associated with the stiffening ring. This ring was welded to the inside of the conical section shell. The ring was a complete circle, but the weld was omitted and two small holes cut on the inside portion of the ring 180 degrees apart. One of these holes was situated at the position of the tear in cluster D. The metal of the conical shell stretched and tore underneath the ring where the weld had been omitted. The other hole was located just at the end of cluster C. Here the metal of the shell deformed but did not tear. Metallographic sections from around the tear at D did not show any cracking. However, strain gauge data from the test showed large deformations in the conical shell around the stiffening ring. It appeared that the ring prevented the expansion of the shell in its immediate vicinity but had no effect on the expansion of the rest of the shell. This caused a distortion of the shell in the form of a trough along the ring. The small gaps in the weld, a few centimeters wide, allowed the unrestrained shell in that region to try to follow the rest of the shell, resulting in ductile deformation and tearing. It is interesting to note that the cluster at D is actually two clusters with a gap

in the middle, exactly at the position of the ductile tear. This may be a coincidence but varying fitting parameters in the location program never placed any emission locations just at the tear. This is consistent with the tear being ductile and not a propagating crack.

The question then becomes what produced the AE in the vicinity of the stiffening ring. There was elastic distortion of the metal shell at the ring during the test but elastic distortion does not produce AE. The answer came when sections of the ring were cut out. The ring was welded to the shell from the top and bottom. However there was not full penetration of these welds, leaving a void between the shell and ring between the welds. This void varied from the shell and ring being in actual contact to gap of a millimeter or more. This type of weld geometry leaves portions of the weld-base metal intersection with very sharp intersection angles. These can act as starter points for micro cracking. In addition, any weld flux trapped in this void can crack with small changes in the void geometry. Both micro-cracks and flux cracking produce AE. The best explanation for the concentration of the located events around the stiffener ring is that they were produced by micro cracking in the weld root driven by the elastic distortion of the shell produced by the ring.

It had been expected that when the contact structure and the conical shell touched, AE would be produced. Such emission would be generated by the two surfaces sliding against each other. This emission would be characterized very long events. No such events or hits were seen. However, examination of the contact regions showed that wiring running between the two structures was flattened. This wiring, and to a lesser extent, the thick paint on the outside of the conical shell would tend to prevent direct contact of the metal structures. The only evidence of the effect of the contact structure is seen in Fig. 8, the curve for cluster C. Here, while there is emission all the way to the failure pressure, the rate drops off suddenly at 4.0 MPa. This could be explained by the contact structure reducing the amount of elastic expansion in the conical shell in this region above 4.0 MPa.

7. Conclusions

The real time AE monitoring of the high-pressure test of the SCV model showed that damage in the model was increasing above 3.5 MPa. It also located the general area where the tear occurred which stopped the pressurization. Furthermore, it showed a large gas leak at 4.62 MPa. It did not predict failure of the vessel but catastrophic failure of the vessel did not occur. The lack of a real time program, which could be adapted to the exact geometry of the SCV model prevented accurate location of the AE sources but gave enough information to indicate the general condition of the vessel throughout the test.

The post-test AE analysis showed two regions on the SCV model, which suffered damage during the high-pressure test. Cluster A is located approximately at the site of the ductile tear that ended the test. The AE data in Fig. 8 indicates that major damage occurred between 4.20 and 4.30 MPa. However, Fig. 6 shows that the large gas leak did not start until 4.62 MPa. This leads to the conclusion that some cracking in the metal occurred from 4.2 to 4.3 MPa at this site but that ductile tearing did not open the large leak path until 4.62 MPa. The other damaged region was the area on the conical shell lying along the strengthening ring. This includes clusters B

through H. The lack of penetration of the upper and lower welds attaching this ring to the conical shell created both a void between the ring and the shell and many possible crack initiation sites. AE activity curves for the clusters along the ring indicate that some micro cracking started at the base of this ring around 3.5 MPa. This cracking was driven by the distortion in the expanding conical shell caused by the local restraint produced by the ring. It does not appear that the ductile deformation and tearing in the shell metal caused by two gaps in the welds along the ring produced any AE. The conclusion drawn is that ductile tearing and not crack propagation produced the leak paths in SCV model. The ductile tearing did not generate detectable AE at the threshold of detection used (the trigger threshold was 45 dB - 180 μ V out of the sensor).

The overall conclusions of this report are that this model showed no significant damage at pressures up to 3.5 MPa. The region where the large ductile tear occurred produced enough emissions to locate it before it occurred. The design and construction of the stiffening ring on the conical section produced detectable damage starting at 3.5 MPa.

Acknowledgments

The author is grateful to Jean Sena and David Schulze for taking the data for this test while he was out of the country. Their dedication and competence allowed him to make the trip without worry. The entire project team gave him outstanding and cheerful support during the design and installation of the AE set up. Constructive criticism by Vincent Luk has greatly improved this report and conversations with Jim Van Den Avyle has aided in understanding the data.

References

1. A. G. Beattie, "Acoustic Emission, Principles and Instrumentation", *J. of Acoustic Emission*, **2**, (1/2), 1983, 95-128.
2. R.K. Miller and P. McIntire, *Non Destructive Testing Handbook, Vol. 5, Acoustic Emission Testing*, ASNT, Inc. Columbus, OH 1987.
3. M. Ge and P.K. Kaiser, "Interpretation of Physical Status of Arrival Picks for Microseismic Source Location", *Bulletin of the Seismological Society of America*, **80**, (6), 1990, 1643-1660.

MICRO-CRACKING AND BREAKDOWN OF KAISER EFFECT IN ULTRA HIGH STRENGTH STEELS

HIDEO CHO, KENZO FUKAURA¹ and KANJI ONO²

Department of Materials Processing, Tohoku University, Sendai, Miyagi 980-8579 Japan;
now at Aoyama Gakuin University, Sagamihara, Kanagawa, Japan.

¹ University of Hyogo, Shosha, Himeji 671-22, Japan

² University of California, Los Angeles CA 90095, USA

Abstract

This study investigates the progression of mechanical damage in ultra high strength steels during tensile testing using acoustic emission technique. We prepared samples from two steels, whose chemical composition are 1.4C-11Cr-0.8Mo-0.23V (JIS SKD11) and 0.8C-8.1Cr-1.9Mo-0.52V (modified SKD11), respectively. We heat-treated the samples to obtain peak secondary hardening. The mean and maximum diameter of primary M_7C_3 carbide inside the samples was 5.3 μm and 26 μm for SKD11, and 2.5 μm and 14.4 μm for modified SKD11. In SKD11 steel, we detected the AE events starting from 0.6 GPa having the amplitude of 23 - 40 dB. AE events were continuously detected as load increased. Above 1.2 GPa, we also detected many stronger AE events of 40 to 65 dB. In the second or later loading, we observed AE events at higher than 1.1 GPa, and AE persisted even when load was kept constant. Kaiser effect was not observed and AE typically started at 90% of the previous load after the second loading. In modified SKD11, the process of AE generation is similar to that in SKD11 steel. However, the AE initiation stress was higher and the amplitude of almost all the AE events was below 40 dB. The difference in amplitude of AE events between SKD11 and modified SKD11 reflects the size of carbide particles. These findings suggest that detected AE events were classified into two fracture types. One is, in lower stress ranges, AE signals caused by carbide cracking, as reported previously. The other is, in higher stress ranges, AE signals caused by micro-cracking, which propagated from fractured carbides. These micro-crack AE events are responsible for the breakdown of Kaiser effect when these steels are highly stressed. They are also indicative of slow crack growth as the loading approaches fracture criticality.

Keyword: Ultra high strength steel, Kaiser effect, Carbide cracking, Micro-cracks

1. Introduction

Cold-work tool steels form a class of ultra-high strength steels and derive their strength properties from high-carbon martensite with secondary hardening. Another attribute arises from the presence of primary carbide particles, imparting high wear resistance [1-3]. Previously, we showed that acoustic emission (AE) of two such steels (JIS SKD11 and its modification) originates mostly from the fracture of primary carbides and demonstrated by the use of laser-induced impulse method that observed AE signals correspond to the crack-opening mode of fracture in hour-glass tensile sample [4]. These fracture events also have fast rise time of $\sim 1 \mu\text{s}$. In connection to the fracture and fatigue strength of the steels examined, AE-start stress was substantially higher for a modified SKD11 steel, which had improved strength properties from the reduction of the average size of the primary carbides [5]. The peak amplitude of AE signals also indicated that the modified steel samples had a lower median value from smaller carbides.

The AE study verified its worth in characterizing the fracture initiation. It is possible that the subsequent progression of fracture and improvement of fatigue properties can be attained with better AE analysis.

In this study, we have extended AE analysis of the same two ultra-high strength steels. Because the modified SKD11 steels produced few or no AE with wide-band 40-dB preamplifiers, even at the stress levels of 1 to 2.5 GPa, we utilized narrow-band instrumentation and captured low-amplitude (20-40 dB) AE activities and analyzed them in detail. We have altered loading schemes and separated AE due to micro-cracking from those of carbide fracture. The breakdown of Kaiser effect was observed once micro-cracking appears to initiate. This points to the progression of fracture although the final fracture is not preceded by any precursor. Amplitude distribution analysis, load holding and brine exposure were also utilized in this study.

2. Materials and Experimental Procedures

A conventional tool steel (1.4C-11Cr-0.8Mo-0.23V, JIS SKD11) and its modification are used in this study. The modification reduced Cr and C content and increased Mo and V, resulting in the optimized composition of 0.8C-8.1Cr-1.9Mo-0.52V (modified SKD11). The chemical composition, heat treatment and other details are given in reference [4]. We heat-treated the samples to obtain peak secondary hardening effects (tempering at 773 K for SKD11 and 793 K for modified SKD11). The mean and maximum diameter of primary M_7C_3 carbide inside the samples was 5.3 μm and 26 μm for SKD11, and 2.5 μm and 14.4 μm for modified SKD11. The shape of specimens was hour-glass type. The specimen has the reduced section of 5-mm minimum diameter with the radius of 30 mm. The stress concentration factor is 1.406. It has shoulder flat on both side of the reduced section. Tensile tests utilized a floor-model Instron and the crosshead speed was 0.01"/min. We typically conducted the loading-unloading cyclic test. AE instrumentation is basically identical to that used in the previous study with AET MAC375L sensors, except the bandwidth was reduced to 250-500 kHz and 60-dB preamplifiers (AET 160) were used. This allowed us to set the threshold level at 23 dB (equivalent to 14 μV at the pre-amplifier input).

Two parallel data acquisition systems were used. Both are based on PAC Mistras boards, running Mi-LOC or Mi-TRA software. The latter was set to trigger from either of 2 channels synchronously. Since the sensitivity of the two sensors (AET MAC375L) was unmatched, Mi-LOC system recorded about ten times less events. This produced unintentional down-sampling and was useful in rapid data analysis when the hit counts were high. The main part of AE data was obtained from Mi-TRA recordings. All the recognized AE events were visually waveform-matched by viewing the waveforms in "group replay" mode and each set had had less than 5 μs arrival time difference. Signal features of only these events were extracted and subsequently analyzed. This is tedious, time-consuming practice, but produces highly reliable results.

3. Results and Discussion

Tensile and AE test results for modified SKD11 steel (tempered 773 K) are shown in Fig. 1. The sample was loaded to 2.75 GPa and held for 80 s. Two cumulative AE event count plots are given. One is from Mi-TRA (marked syn) and the other from Mi-LOC (ind). The load-displacement curve is essentially linear and no plastic yielding was recognized. AE events started at 1.2 GPa (the fifth event at 1.6 GPa) and the event rates continually increased until reaching the maximum stress

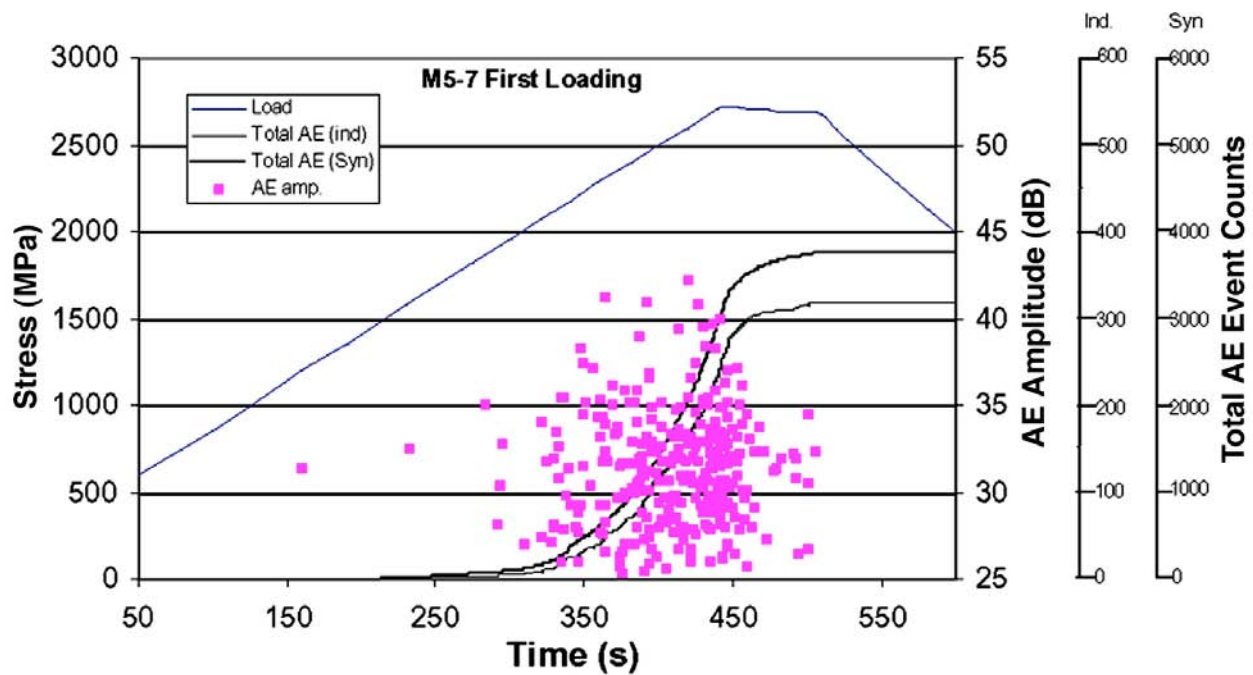


Fig. 1 AE test results for modified SKD11 steel during the first tensile loading.

of 2.75 GPa. The total AE event count was 3100 plus 700 counts during load hold. The waveform was essentially unchanged throughout the test from that reported previously [4]. In Fig. 1, the peak amplitude of independently triggered events is shown by squares. Initial events had a range of 30-35 dB, which broadened later to 25 to 43 dB. Only a few events were detected for similar tests when the threshold was set at 40 dB and after careful noise discrimination.

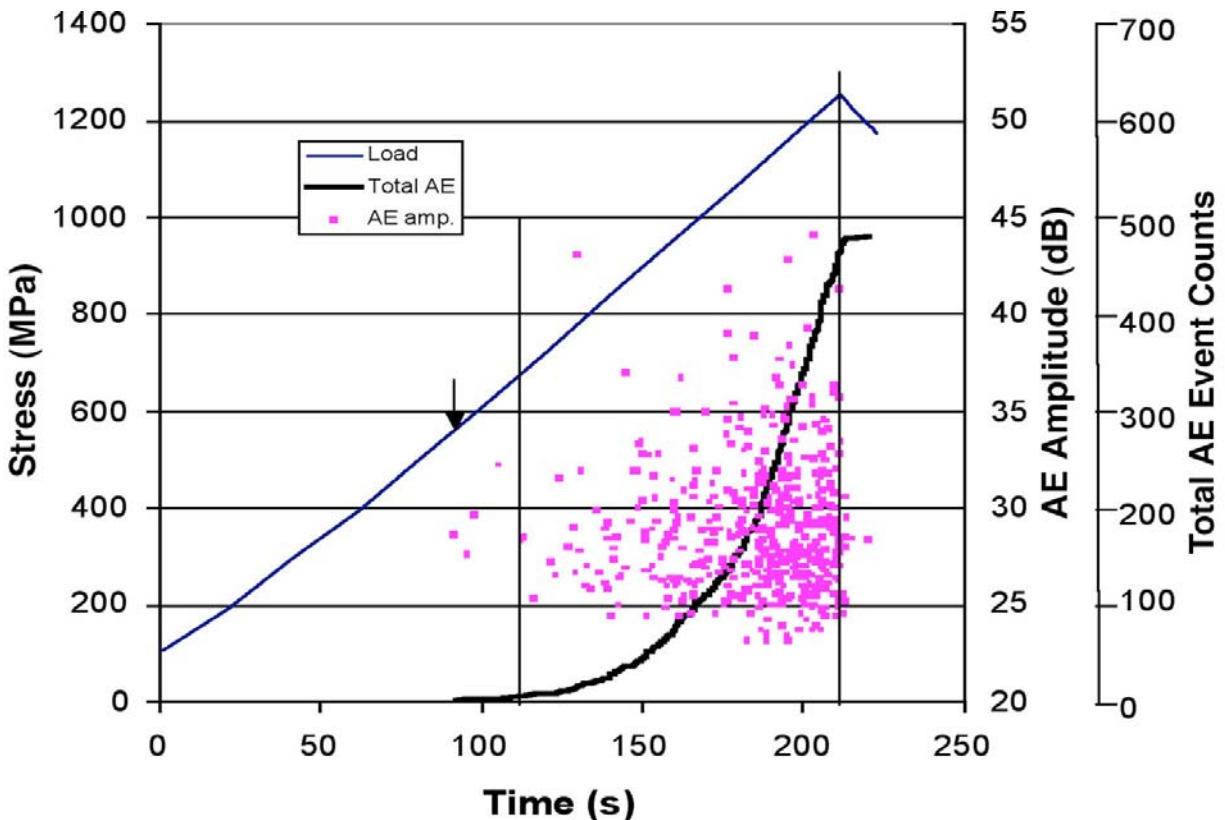


Fig. 2 AE test results for SKD11 steel during the first tensile loading.

For SKD11 steel tempered at 793 K, tensile and AE test results are given in Fig. 2 for its first loading. AE events started at a much lower stress of 550 MPa (the fifth event at 680 MPa). About 300 AE events were detected before 1.2 GPa, when the first event was recorded in the m-SKD11 test shown in Fig. 1. The peak amplitude of the observed events, again shown by squares, had comparable range of 23 to 44 dB, as in Fig. 1. Initial events had the amplitude range slightly higher than that of later events. Load hold at 1.25 GPa generated a limited number of AE events. The next loading to the same stress started to generate AE at ~95% of the previous maximum stress; the number of AE events was low or 5% of the previous total. See Fig. 3. Several events were detected during the initial part of unloading.

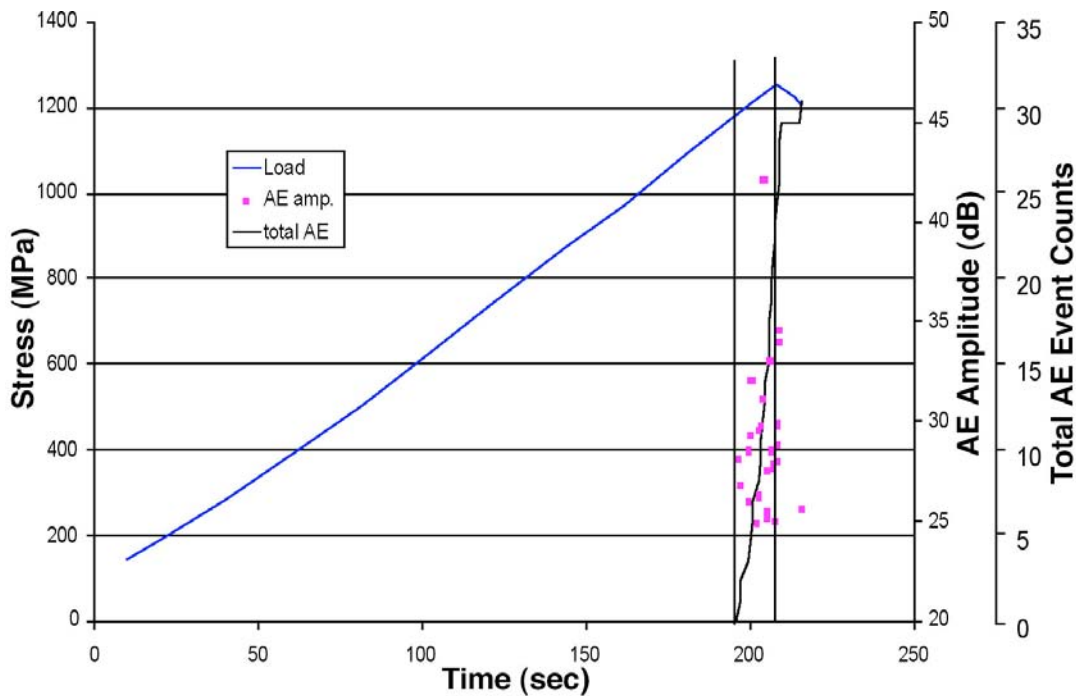


Fig. 3 AE test results for the same SKD11 steel sample during the second tensile loading.

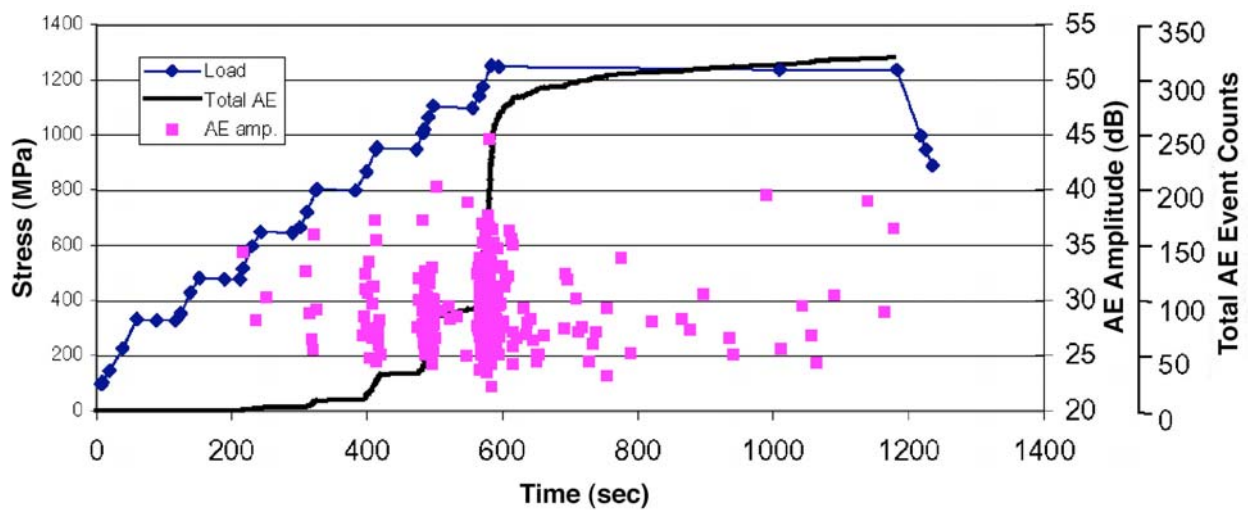


Fig. 4 AE test results for SKD11 steel during tensile testing with load holds.

Figure 4 shows the results of loading with intermittent load holds. Overall AE behavior in this test is comparable to Fig. 2 without load hold. It is shown, however, that AE during load hold be

gins at 1.1 GPa. Load hold AE continues beyond 10 min at 1.25 GPa. In this test, the first AE was recorded at 530 MPa. Figure 5 summarizes another series of cyclic-load testing with 40-dB threshold setting and 2.1 GPa maximum stress. Kaiser effect breakdown is shown initially with the Felicity ratio of 0.95, but it approaches unity by the fifth loading cycle. AE counts during each cycle are reduced 300-folds. Figure 6 shows similar test results, except during the fourth cycle, the sample was wrapped with cotton cloth saturated with 0.5% brine solution. The first AE was detected at 1.8 GPa or at the Felicity ratio of 0.85 and the total AE counts exhibited 4-fold increase over the previous cycle. This indicated hydrogen-induced cracking. Premature fracture occurred after 15 second load hold.

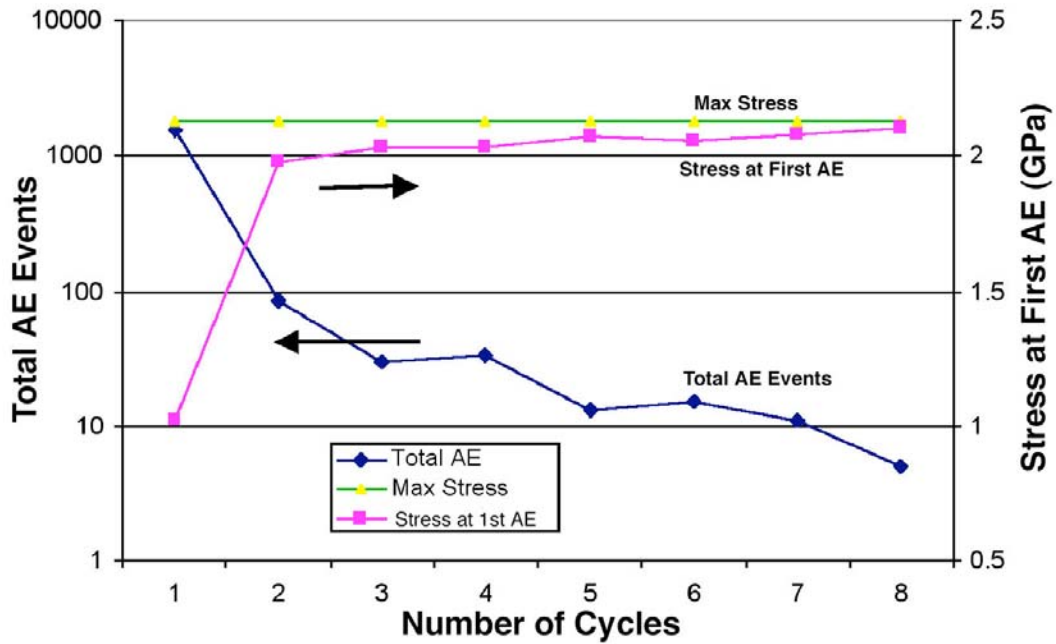


Fig. 5 Cyclic loading to 2.1 GPa, showing AE start stress and total AE events for each cycle.

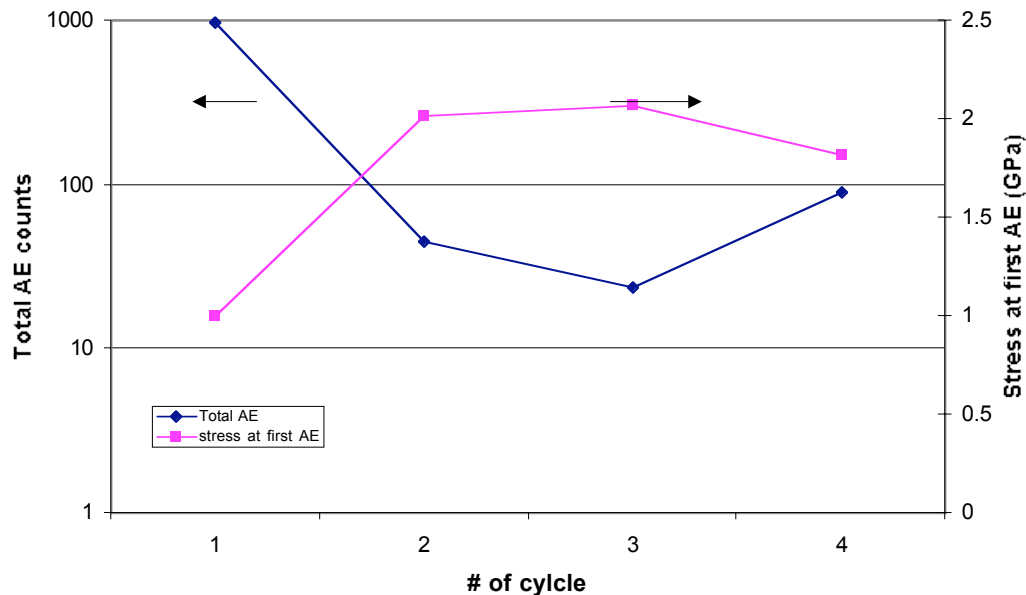


Fig. 6 Cyclic loading results (to 2.1 GPa) showing AE start stress and total AE events for each cycle. For the fourth cycle, this sample was exposed to 0.5%-brine, reducing the Felicity ratio to 0.85.

The peak amplitude distribution of observed (and discriminated) AE events has been analyzed. All the results can best be modeled by Weibull-type distribution function as shown in Figs. 7-9. Only poor power-law approximation is possible because of systematic curvature exhibited. Here, Weibull-type distribution function for the cumulative event count is given by

$$N_{\text{cumulative}} = A \exp(-B (V_p)^q),$$

where A and B are constants, V_p is the peak amplitude (in μV), and q is the Weibull coefficient. Figure 7 is the distribution plot for the entire event data of test shown in Fig. 4. Squares indicate observed data points, while triangles show a Weibull distribution; in this case, $q = 0.48$. Differential distribution curve is also plotted. Choice of the constant B affects q-values and so B is taken as unity in all the present analyses. These AE events were detected from an SKD11 sample at stress below 1.25 GPa with 20 dB threshold. Figure 8 shows the distribution plot for the AE event data of the same steel, but at stresses of 1 to 2.1 GPa with 40 dB threshold. Even when the low-amplitude data between 20 and 40 dB is absent, a similar Weibull distribution function with $q = 0.395$ can model the observed data. Figure 9 is a plot for AE when a sample was exposed to brine. The event data represents both during load increase and load hold. This distribution is almost identical to that in Fig. 8 with $q = 0.38$. These show that the peak amplitude distribution is essentially unchanged.

The Weibull distribution with $q = 0.35 - 0.5$ was used to describe burst emission data from high-strength low-alloy steels [6,7]. These emissions originated in the decohesion of MnS inclusions, flattened on planes parallel to the hot-rolling plane. The amplitude distribution was correlated to the inclusion size distribution, using a simplified model of source function response [6]. In the case of AE from carbide cracking, a similar modeling may be validated once detailed carbide size distribution is obtained. If micro-cracks in SKD11 steels have fractured carbides as their origin, the same distribution also is likely.

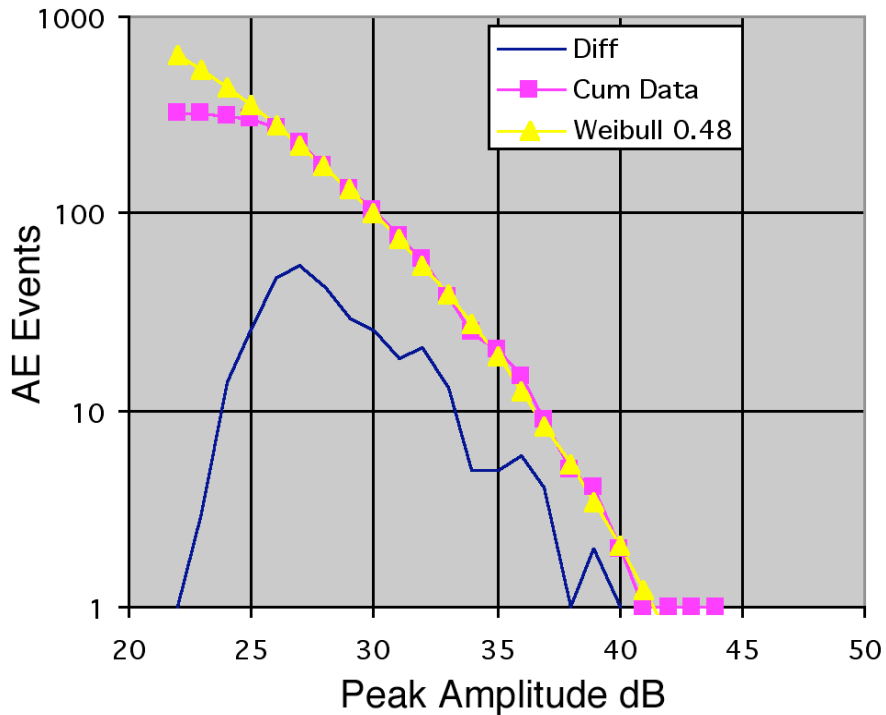


Fig. 7 Peak amplitude distribution for the entire event data of test shown in Fig. 4. Differential data and calculated Weibull distribution curve are also shown.

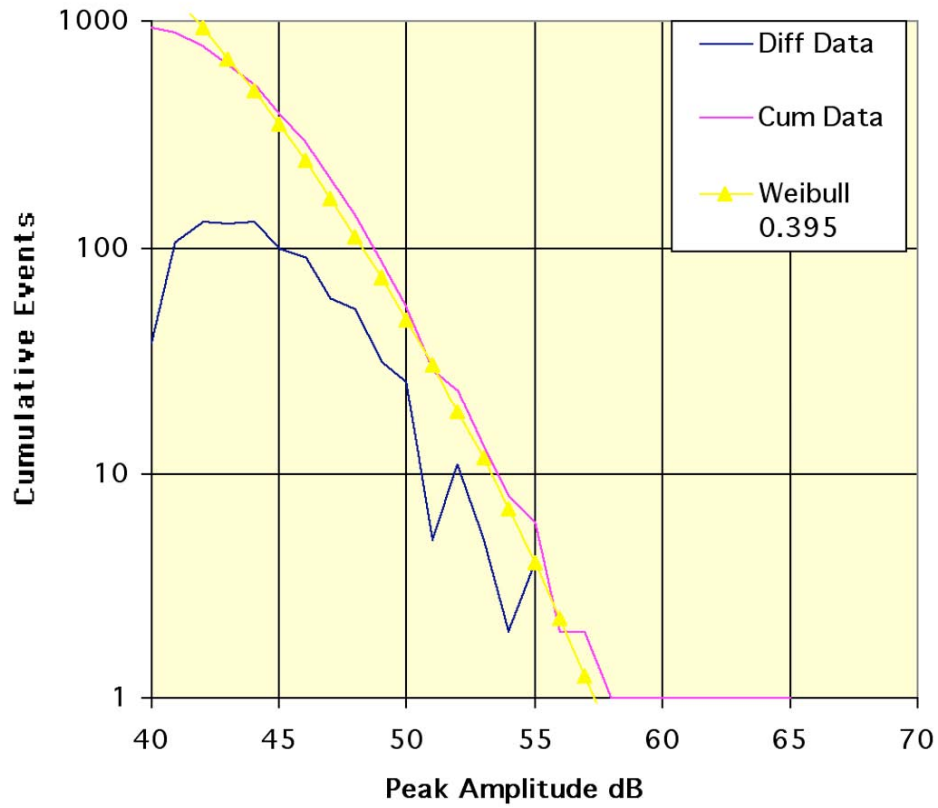


Fig. 8 Peak amplitude distribution for the event data of SKD11 test with 40 dB threshold stress of at 1 to 2.1 GPa.

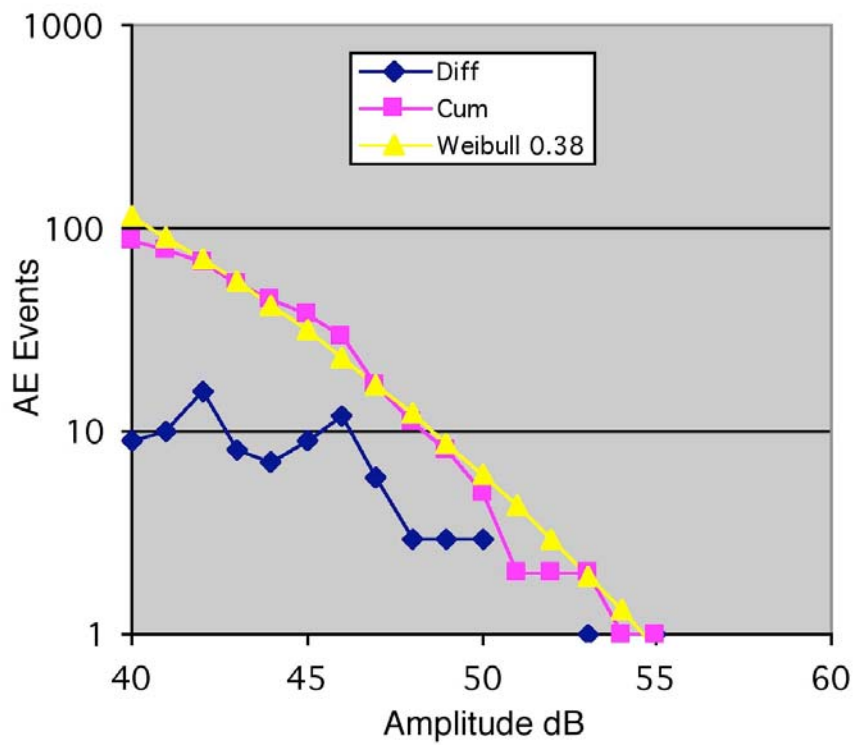


Fig. 9 Peak amplitude distribution of the fourth loading of SKD11 with brine exposure. This is expected to indicate the distribution of micro-cracking AE.

The results of this study demonstrate the presence of two types of AE. One type is observed starting at low stresses (0.5-0.7 GPa for SKD11 and 0.7 to 1.6 GPa for m-SKD11), having amplitude of 20 to 45 dB. This is consistent with the carbide fracture origin, as previously postulated [4]. The other type is detected during load hold above 1.1 GPa in SKD11 and at 1.8-2.1 GPa in m-SKD11, with higher amplitude events and the sensitivity to brine environment. These emissions also do not exhibit Kaiser effect. This appears to be originated from micro-cracking. Internal carbides cannot be affected by short-term brine exposure. In SKD11 steel, many emissions have 40-55 dB amplitude, as shown in Fig. 8. Very few emissions of such amplitude were found in m-SKD11. Thus, micro-crack size appears to be related to carbide size.

One aspect is puzzling. All the elasticity calculations predict larger energy release when a micro-crack or carbide fracture occurs at a higher stress [8]. No apparent correlation between the stress level and observed AE amplitude is evident. This needs to be explored further.

4. Conclusions

1. Carbide fracture and micro-cracking produce detectable AE in the ultra-high-strength steels examined.
2. Peak AE amplitude, however, is relatively low, in the range of 20-65 dB.
3. No significant distinction in signal waveforms exists. Weibull-type amplitude distribution was found for the two types of AE. However, the amplitude range for carbide fracture is 20-45 dB, while micro-crack AE ranges up to 65 dB.
4. Micro-crack AE is associated with the breakdown of Kaiser effect, load-hold AE, and sensitivity to brine exposure.

References

- 1) F. K. Krik, Metal Tech., **49** (1982) 198.
- 2) Y. Murakami, S. Kodera and S. Konuma, Trans. Japan Soc. Mechanical Eng., **A54** (1987) 688.
- 3) A. M. El-Rakayby and B. Mills, J. Mater. Sci., **23** (1968) 4340.
- 4) K. Fukaura and K. Ono, J. Acoustic Emission, **19** (2001) 91.
- 5) K. Fukaura, Y. Yokoyama, D. Yokoi, N. Tsujii and K. Ono (to be published).
- 6) K. Ono, R. Landy and C. Ouchi, Proc. 4th Acoustic Emission Symp., Int. Tech. Exchange Center, Tokyo, (1978) pp. 4/33-4/45.
- 7) H.B. Teoh and Kanji Ono, J. Acoustic Emission, **6**, (1987) 1-12.
- 8) E.g., R. Kant and D.G. Bogy, Trans. ASME., J. Applied Mechanics, **47**, (1980) 545-50.

ACOUSTIC EMISSION FROM THE FRACTURE OF ATMOSPHERIC RUST

M. TAKEMOTO¹, T. SOGABE¹, K. MATSUURA¹ and K. ONO²

¹ Faculty of Science and Engineering, Aoyama Gakuin University,
Fuchinobe 5-10-1, Sagamihara, Kanagawa, 229-8558 JAPAN

² Department of Materials Science and Engineering, UCLA, Los Angeles, CA, U.S.A.

Abstract

Corrosion damages of tank bottom steel plates are recently diagnosed by in-situ AE monitoring. It is generally suggested that AE is produced by two types of fracture of hard rust; i.e., self-fracture and/or spallation of the rust due to volumetric-expansion during growth and mechanical fracture of grown rust by external forces. However, reliable information on the rust-induced AE is absent. This study examines the characteristics of AE signals produced by rust fractures. Three kinds of AE monitoring were conducted; 1) Lamb-wave AE monitoring during accelerated wet-and-dry rust growth test of steel plate (laboratory testing up to 30 days), 2) AE monitoring during four-point bending of steel plate with rust grown by in-laboratory acceleration and out-door exposure and 3) AE monitoring from rusting of a model tank bottom plate with source location.

Strong Lamb-wave AE signals with frequencies of 100 to 600 kHz were frequently produced by rust growth above 100 μm thickness, and event counts increased with rust thickness up to 400 μm (test 1). Emission rate increased when magnetite (Fe_3O_4) layer was formed underneath the surface hematite (Fe_2O_3) rust. AE event counts during four-point bending of corroded plate (test 2) increased with an increase of rust thickness. Hard magnetite rust, major component of the rust produced by out-door exposure, appears to increase AE activities at lower surface strain of the substrate plate. Due to the extremely long crack of rust fracture, crack opening volume of thin rust is million times larger than those estimated for delayed fracture of high strength steel. Crack extension rate is estimated to be ten times longer than those for the delayed fracture (test 3). Accelerated atmospheric corrosion of bottom plate of water-loading model tank of 850 mm diameter produced strong P-wave AE signals via water detectable by AE sensors on the side wall. Propagation path of AE signals in liquid loading tank and source location method were discussed in last section.

Keywords: Atmospheric rust, Volumetric expansion, Self fracture, Magnetite, Hematite, Crack opening volume,

1. Introduction

Monitoring of corrosion damage of storage tanks (1,2), buried pipelines, steel bridges and concrete reinforcements is becoming important problems. Integrity diagnosis of these steel structures exposed to atmospheric corrosion must be performed periodically over several tens of years. AE monitoring cannot estimate the reduction of wall thickness, but possibly it can monitor whether the corrosion and wall reduction is progressing. This concept is based on an assumption that AE signals are produced during rust growth and by fracture of grown rust. AE is advantageous for monitoring the corrosion occurrence and progression on hidden structures and

structural members such as the bottom plate of storage tank and the buried pipeline, to which conventional NDT method is difficult to apply. However, little is known whether AE signals are produced by corrosion. Corrosion covers a variety of material damage, such as wet and dry corrosion. Wet corrosion involves general and localized corrosion and sometimes causes corrosion-assisted fractures such stress corrosion cracking (SCC) and delayed fracture. Among these corrosion morphologies, delayed fracture of high strength steel is well known to produce strong AE signals.

Mechanism of wet corrosion of steel depends on the environmental condition. For instance, active corrosion or anodic dissolution of the steel immersed in an acidified solution ($\text{pH} < 3.0$) does not produce AE since iron dissolves as cation. However, processes accompanying cathodic reaction, such as hydrogen gas evolution, may produce secondary AE when gas bubbles leave the metal surface. In slightly acidified or neutral solution ($\text{pH} > 4$), steel produces rust composed of oxides and hydroxides. In the mostly wet condition, loose and soft hydroxide rust, generally $\text{Fe}(\text{OOH})_x$, are produced on the surface. This kind of rust and reduction of dissolved oxygen at cathode do not produce AE. We once monitored AE from the steel plate immersed in $\text{pH}=4$ sulfuric acid solution saturated with air, and no AE signals were detected even by 80 dB amplification. Contrary to this, at alternate wet-and-dry condition, steel produces hard and thick rust dominated by oxides such as Fe_3O_4 (magnetite) and Fe_2O_3 (hematite). These oxides are most common black and red rusts on steel structures exposed to natural atmosphere and generally hard. Hard rusts are likely to crack (self cracking) due to the volumetric expansion during rust growth. Underneath such rusts, localized reduction of wall thickness, generally proportional to rust thickness, was clearly observed. Therefore, AE monitoring of rust formation and/or rust crack leads to integrity diagnoses. However, no scientific evidence of AE generation from rust fracture has been reported so far.

In this paper we first studied whether the rusting of steel produces AE signals. Four types of AE monitoring or rusting tests were conducted. Next we studied the characteristics of AE produced by mechanical fracture of grown rust. Finally, we monitored AE from accelerated rusting of a model tank bottom plate by AE sensors mounted on sidewall and identified their location. Location accuracy and sensor setting method are also discussed.

2. AE Signals during Atmospheric Rust Growth by Wet-Dry Acceleration Test

Using the equipment and AE sensor layout shown in Fig. 1, AE signals during rust growth by accelerated wet-and-dry test were monitored. Low-carbon steel plates (JIS SPC-C for cold drawing) of 1 mm thick, 150 mm wide and 200 mm long were exposed to alternate wet-and-dry rust growth test. Surface of the plate was coated with silicone grease except the rust growth area or the inside of 40 mm diameter O-ring, and irradiated by an infrared lamp to keep the O-ring area at 40°C . Five kinds of corrodants shown in Table 1 were sprayed into the O-ring area for 5 s at 1.8 ks (30 min) interval, and dried at 40°C .

These tests were also used to prepare the specimens used for next section (fracture test of grown rust). AE in this section was monitored for samples 11 to 15 using 7 sensors (PAC, Type-PICO). Three sensors (#5,6,7) mounted on the plate monitored the Lamb wave AE signals produced by self-fracture of the rust. As these sensors monitored the So-Lamb packet, source locations were identified using the sheet velocity (5400 m/s). Outputs of sensors were amplified by 40 dB and then digitized by an A/D converter. Digital data were analyzed by using the software developed in-house.

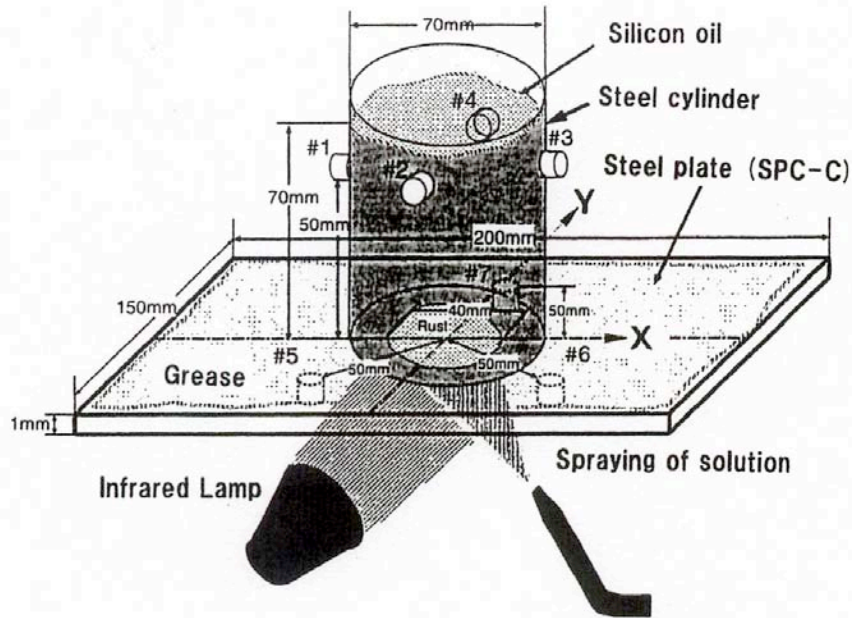


Fig. 1 AE monitoring from rusting of steel plate by accelerated atmospheric rust growth.

Table 1 Specimen number exposed to accelerated rust growing test for maximum 30 days.

Solution	Exposure time		
	864ks(10dyas)	1.728Ms(20 days)	2.592Ms(30days)
1% NaCl	Test No.1	6	11
pH=2 H ₂ SO ₄	2	7	12
pH=2 H ₂ SO ₄ with 1% NaCl	3	8	13
pH=3 H ₂ SO ₄	4	9	14
pH=3 H ₂ SO ₄ with 1% NaCl	5	10	15

We also monitored AE signals using four sensors mounted on a 70 mm diameter cylindrical cell with silicon oil in it. This intended to study whether AE signals can be monitored as the P-wave via liquid in tank, as being utilized in TANK-PAC method (1). The cell was adhered to the plate by high-damping silicon gum to reduce the propagation of Lamb wave to the cell wall. Four sensors (#1 to #4) were mounted on the cell wall at 50 mm height. Both the silicon gum and sensor at high position can eliminate the Lamb and mode-converted P-wave from Lamb wave, and makes it possible to monitor the P-wave through liquid (direct P-wave). Indeed, arrival time difference between the direct P-wave and the mode-converted P-wave is less than 1 μ s, when the source is at the center of the cell. The arrival time of the direct P-wave to sensors on cell wall is 25 μ s later than that of the fastest Ao-Lamb wave (3300m/s) to sensors on the plate. This time difference is effectively utilized to determine whether the sources are in the corroding area.

Figure 2 shows cumulative AE counts with exposure time for sample No. 13, exposed to (pH=2; H₂SO₄ + 1% NaCl) solution. Another solid line “from loaded steel plate” indicates AE data when the plate was subjected to wet-dry-rusting test at being bucked (0.1 % compression strain on the rusting surface) by a vise.

AE signals increased with exposure time or thickness of the rust. Sources of most AE events are located inside the O-ring. X-ray diffraction analysis of dried rust showed Fe₃O₄, α -Fe₂O₃ and

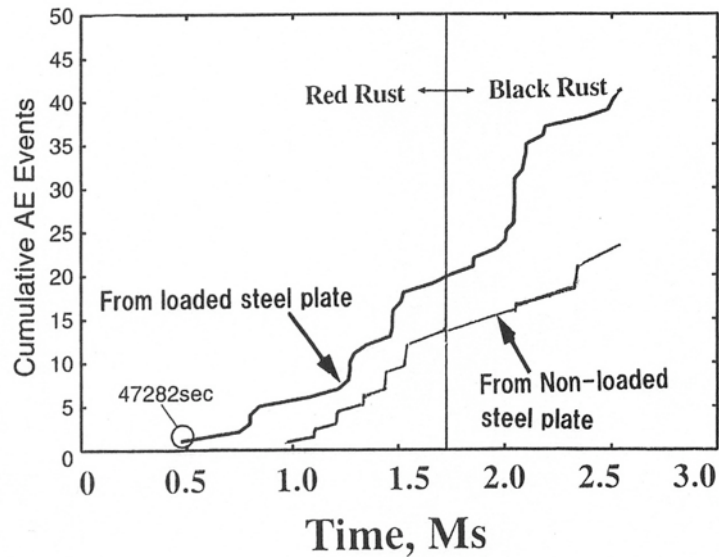


Fig. 2 Cumulative AE counts with exposure time for sample No. 13 exposed to pH=2 H₂SO₄ + 1% NaCl corrodant.

γ -FeOOH, but no NaCl crystal. We observed many cracks on the rust surface after the test. These results strongly demonstrate that the atmospheric rust produces AE signals during their growth, due to self-cracking by volumetric expansion.

Figure 3 show typical AE waves for sample No. 13. Sensors #5, #6 and #7 detected large amplitude Lamb waves of a few tens of mV as well as small So waves. Outputs of sensor #1 to #4 are P-wave via oil and their arrival times are 25 μ s later than these of #5 - #7 sensors. This demonstrates that atmospheric hard rusts produce the P-waves detectable by AE sensors on the shell wall. Power spectra of these signals (mainly A₀ mode wave) showed strong components from 300 to 600 kHz, close to the resonant frequency of the PICO sensor.

Figure 4 shows a relation between AE event counts and rust thickness measured by transverse SEM observation after the test. AE can be produced by the formation of only 100 μ m thick rust. Severe corrodants such as pH=2 H₂SO₄ with or without small amount of NaCl accelerated AE generation.

3. AE Signals due to Mechanical Fracture of Grown Atmospheric Rust

AE monitoring during four-point bending of the steel plate with grown rust (specimen 1 to 15 in Table 1) was conducted using the method shown in Fig. 5. AE event counts were monitored as a function of surface tensile strain measured by the strain gage at the center of inner span. Figure 6 shows relations between the cumulative AE counts and surface strains as a function of exposure times. Sources of all the AE events are located inside of the O-ring.

Frequent AE signals are produced from relatively small surface strains of 0.35% for specimens exposed to severe corrodants such as pH=2 H₂SO₄ with or without 1% NaCl solutions. Specimens 9, and 10, exposed to mild corrodants; pH=3 H₂SO₄ and with 1% NaCl produced small events due to thin rust. Lamb waveform and wavelet contour map of AE detected for No. 15 specimen is shown in Fig. 6.

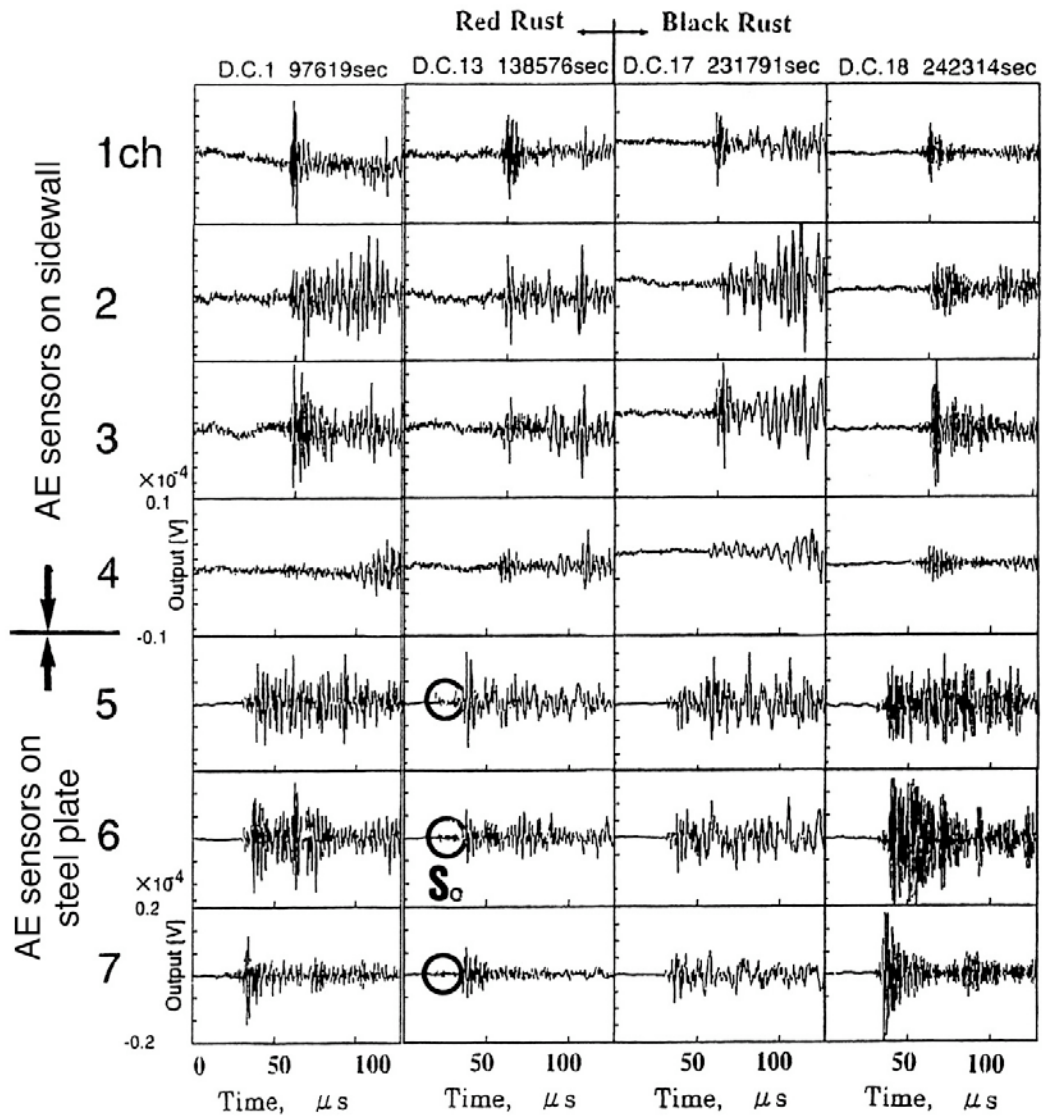


Fig. 3 AE events detected during rust growth on sample No. 13.

In the four-point bend test, large Ao Lamb waves with 0.1 V output as well as weak So packet were monitored, indicating a fast and large crack opening (Fig. 7). In spite of large attenuation of Ao components by silicone grease on the plate (3), waves are remarkably strong and this demonstrates a large crack opening of rust. Frequency components of the Ao packet are ranging from 0.4 to almost 1 MHz, close to those of the Lamb waves produced by pencil-lead breaking. Long cracks of 1 mm to 3 mm length were observed on the rust surface after the test. Longer cracks were often observed for the thinner rust produced by mild corrodants. Crack opening volumes are estimated to be million times larger than those estimated for delayed fracture of high strength steel (4,5). Crack opening times, estimated from the rise time of first-arriving So-mode wave, are from 2 μs to 4.2 μs , and ten times smaller than those estimated for delayed fracture.

In order to study how the naturally grown atmospheric rust produces AE signals, we exposed 50 steel plates for 400 days at our campus: Setagaya, Tokyo. Specimen has the same dimension as that in Fig. 1, but coated with coal tar except a 30 mm diameter center circle. Four kinds of samples exposed for 100, 200, 300 and 400 days were submitted to four-point bending. Yellow-

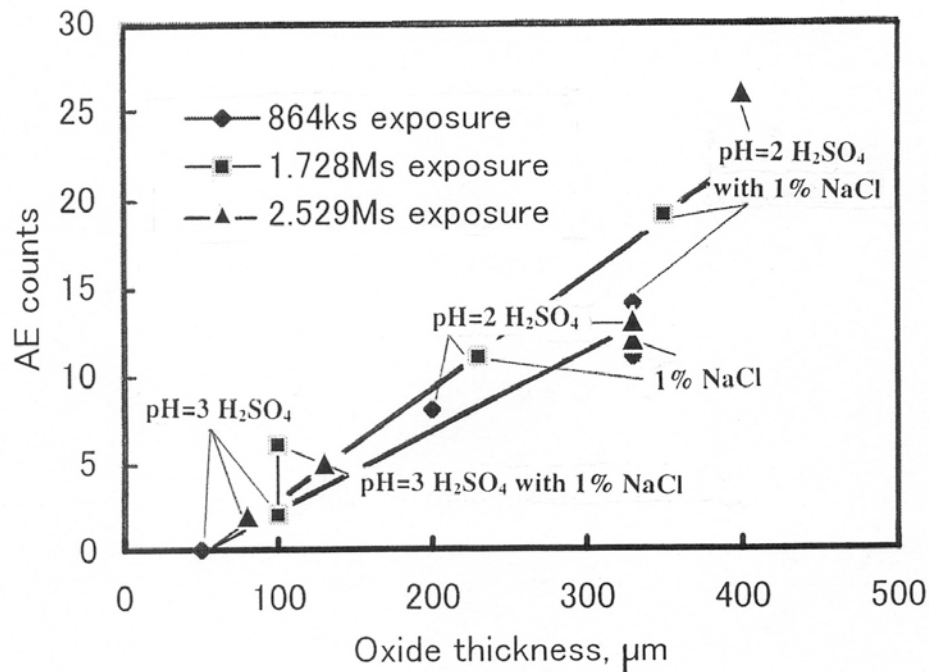


Fig. 4 Relation between rust thickness on steel plate and cumulative AE counts

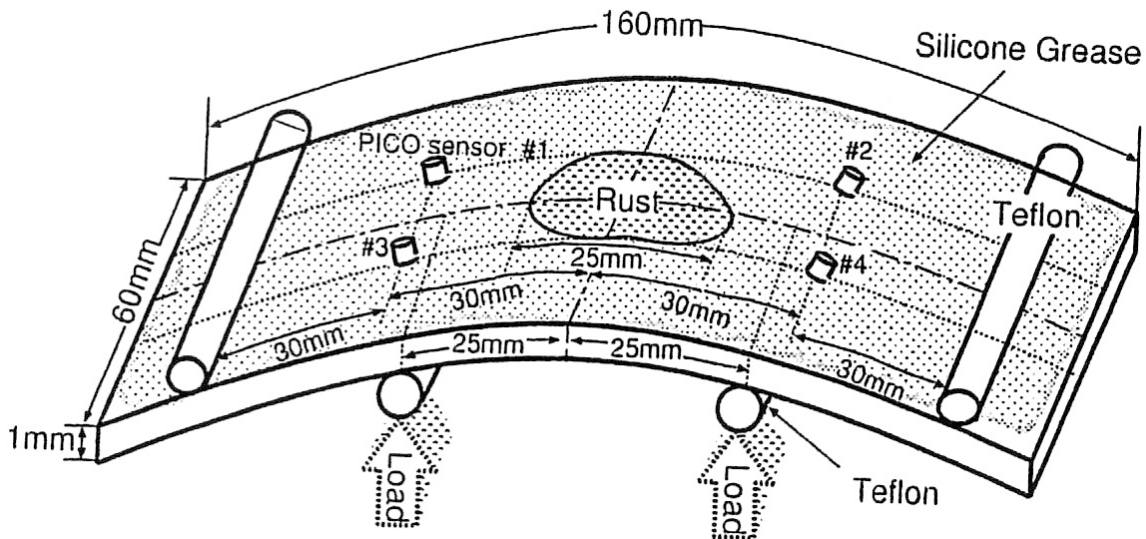


Fig. 5 AE monitoring during four point bending of the steel plates with grown rust.

red rust was formed over the exposed area after 2-week exposure and gradually changed to black-red rust after 30 days. Average rust thickness of 200 and 400 days exposed steel were measured as 100 μm and 180 μm , respectively. Compared to the relatively uniform rust thickness prepared by accelerated wet-dry test in laboratory, thickness of natural rust was non-uniform. In the thick part, the rust pegged into the substrate steel and produced uneven surface. AE signals were detected for four specimens from elastic strain (0.1%) of the steel substrate. Figure 8 represents AE event counts vs. applied strain of steel plate exposed 400 days. Event counts increased exponentially with strain. This behavior is different from those observed for the rusts prepared by accelerated laboratory tests.

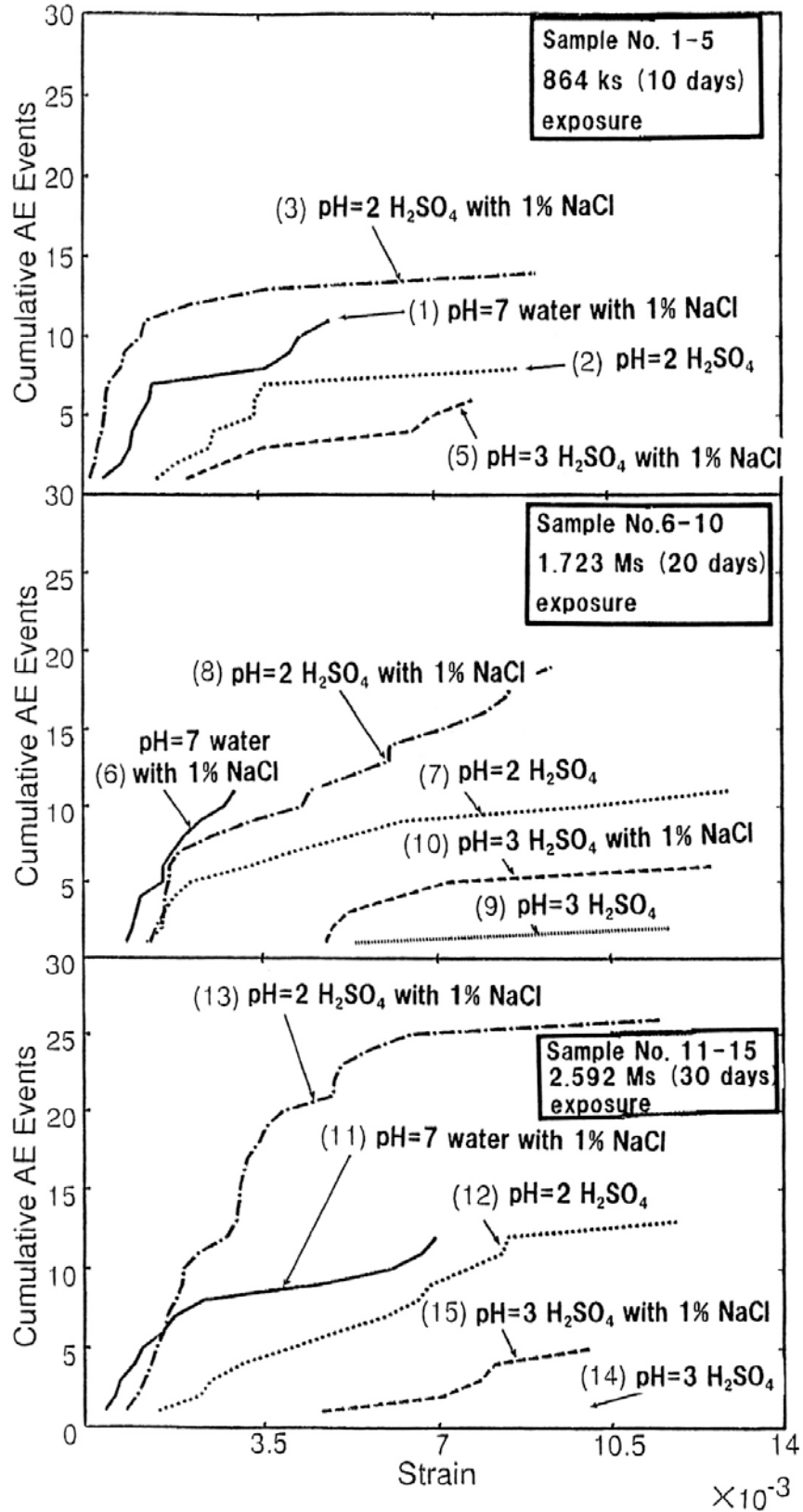


Fig. 6 Cumulative AE counts as a function of tensile strain of steel plates exposed to wet-dry acceleration test for 10, 20 and 30 days.

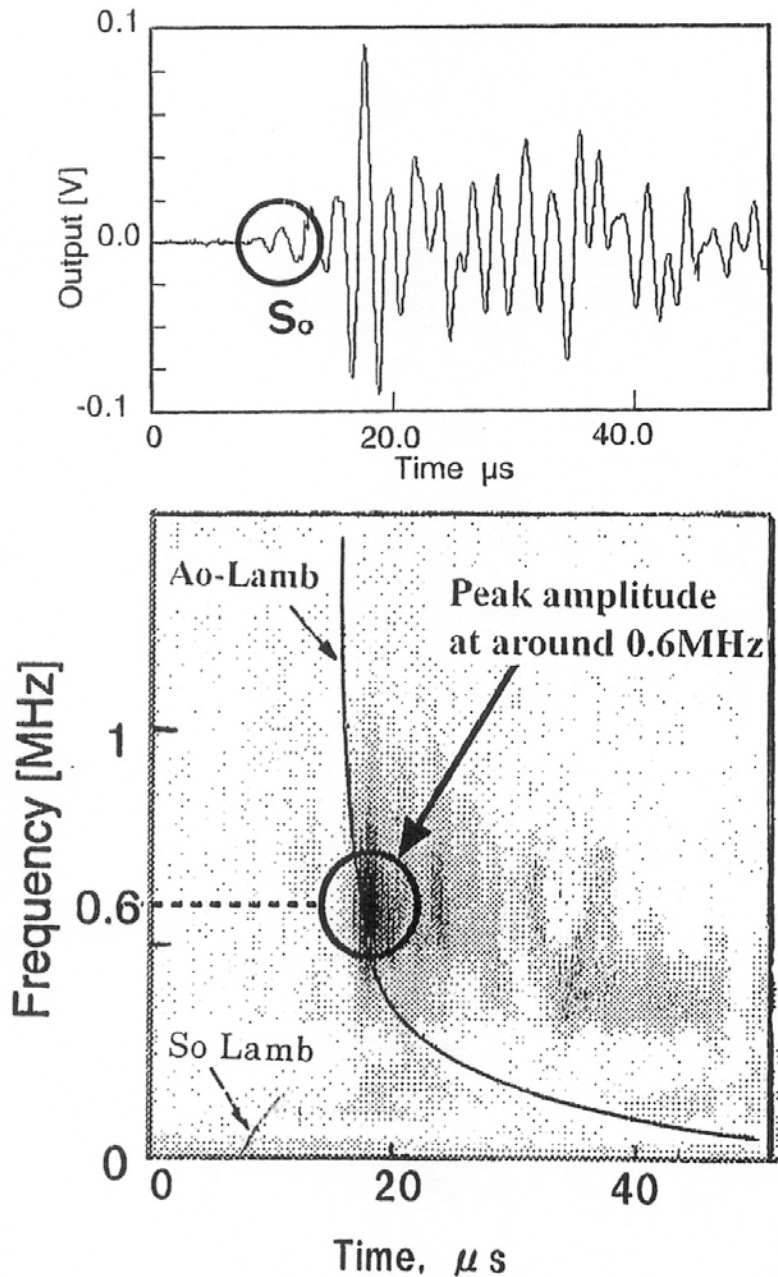


Fig. 7 Lamb waveform detected during four point bending test of steel plates with grown rust.

4. AE Signals from Bottom Plate Rusting of a Model Tank

We studied how we can monitor AE signals and identify their sources from rusting of bottom plate of water-filled tank. We used an 820-mm diameter water-filled cylindrical tank of steel (Fig. 9). Three resonant AE sensors (PAC R6I) were mounted on shell wall at height of 100 mm. Rusting were produced by wet-dry test of pH=3 H_2SO_4 solution at two locations (in 40 mm diameter area at center #1 and annular position #2) of the bottom plate by separate corrosion test. We also monitored AE signals from rusting using AE sensors mounted at 30 mm height, but could not determine the arrival time due to small amplitude and continuous-type waveform. Taking the radiation pattern (6) of P-wave in water into account, sensor height was changed to 100 mm so that it can capture much stronger signals. This height corresponds to 8 m height for 50 m diameter tank, and far higher than the sensor height used for TANK-PAC (1).

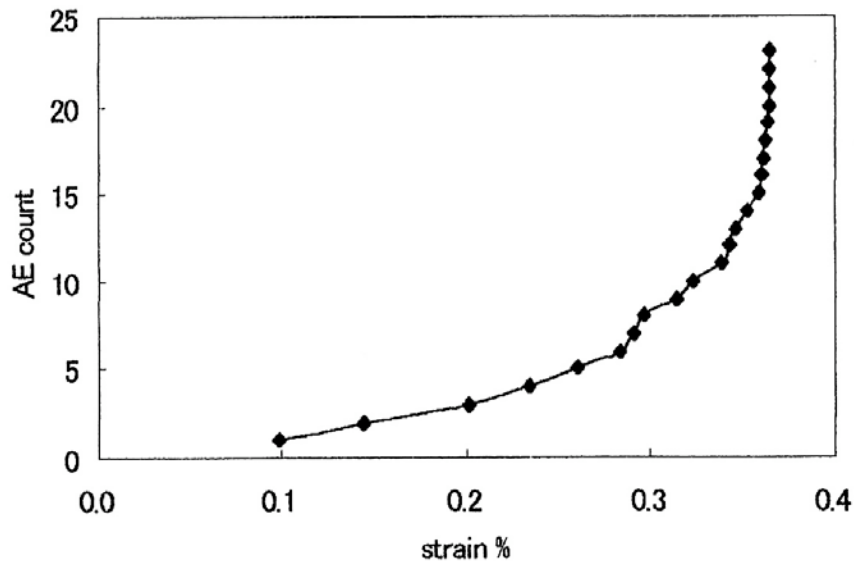


Fig. 8 Cumulative AE counts as a function of tensile strain of steel plates exposed to weathering test for 400 days.

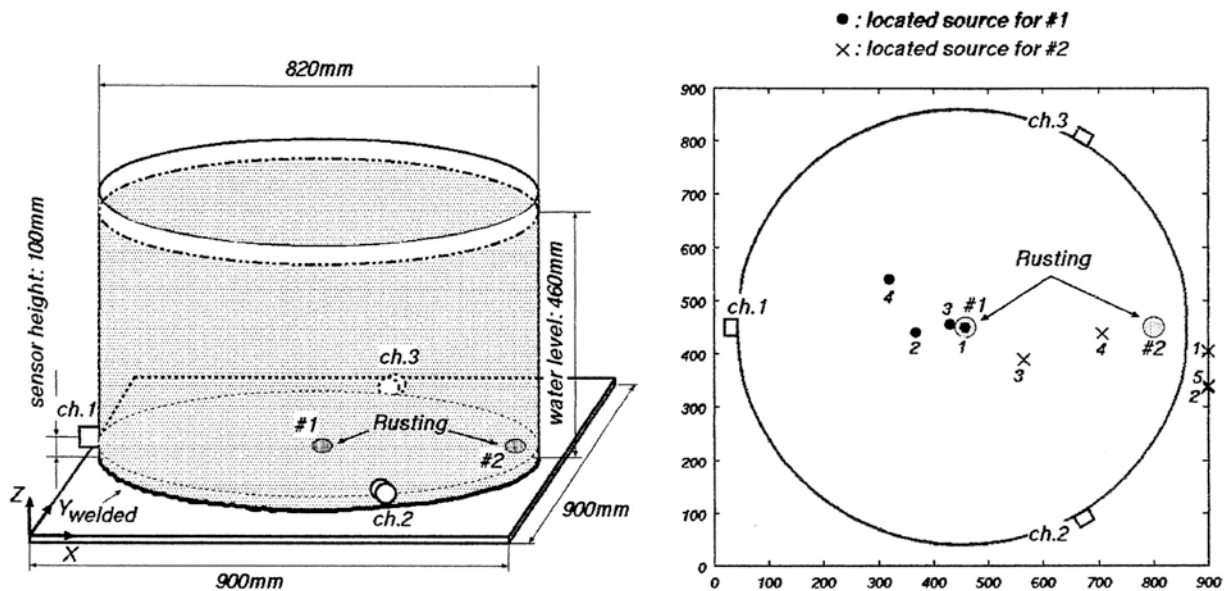


Fig. 9 Setup for AE monitoring from rusting at #1 and #2 on the outer surface of bottom steel plate of water-filled cylindrical tank and estimated source location of AE events.

About one hundred AE events were detected from 60 to 100 hr duration. Source location was possible only for four events in central rusting (#1) and five events for annular rusting (#2). The positions are shown in Fig. 9 as filled circles (#1) and x (#2). For the latter, three events were located outside the cylinder.

Figure 10 shows two typical waveforms and wavelet transform coefficients (WT) at 75 kHz for #1 and #2 rust. AE waveform due to rust fracture is complicated and looks like a continuous-type AE, due to successive arrival of fastest Ao Lamb wave (3000 m/s), P-wave in water converted from Ao Lamb wave, and direct P-wave in water. Source location of pencil-lead breaking on bottom plate of this tank was successfully determined by using the arrival time of WT at 70 to

90 kHz and P-wave velocity in water (1500 m/s). Therefore, we located AE source using WT at 75 kHz. Results are shown on the right of Fig. 9.

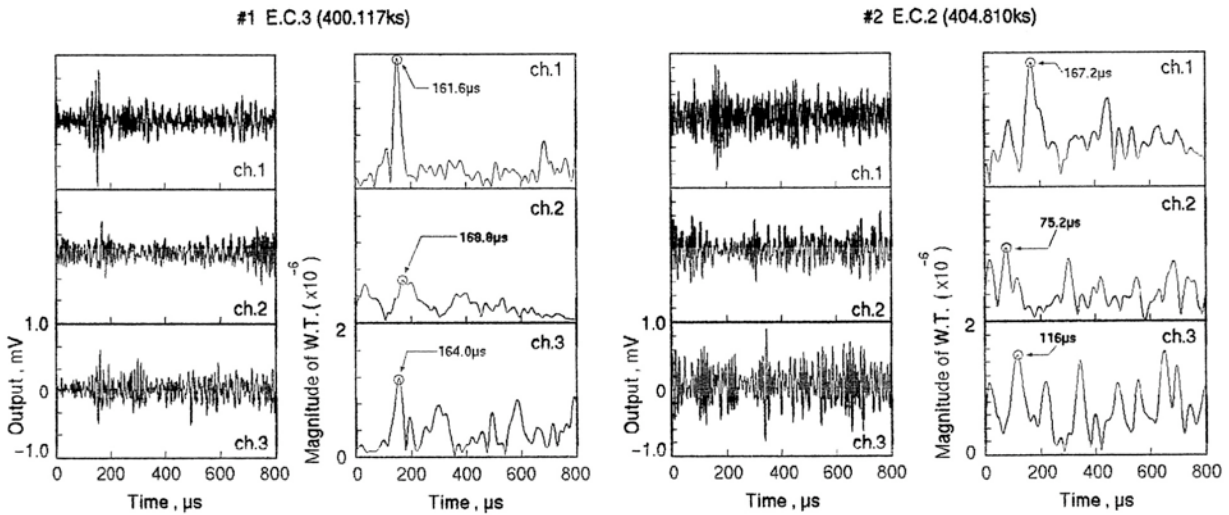


Fig. 10 Typical waveforms and their time transient of wavelet coefficients at 75kHz from rusting at #1 and #2 positions

Location accuracy is poor for both #1 and #2 rust sources. This suggests that the AE signals should not be monitored by sensors on shell wall, but should be monitored as Lamb waves by sensors mounted on the bottom plate.

5. Conclusion

Scientific evidence for AE generation by self-fracture and mechanical fracture of hard atmospheric rust is presented by conducting three types of AE monitoring. Results are summarized below.

- 1) Wet-dry acceleration rusting test of steel plate demonstrated AE generation from self-fracture of growing hard rust. AE signals were produced by formation of rust thicker than 100 μm and total event counts increased with the rust thickness. Lamb wave AE signals, monitored on the corroding plate, contained S_0 -component as well as A_0 mode, suggesting large and fast crack opening. Frequency components of A_0 -Lamb waves by rust self-fracture extend higher ranges than those by pencil-lead break.
- 2) Mechanical fracture of hard rust composed of magnetite and hematite produced strong AE due to extremely long crack length with large crack opening. Source volumes were one million times larger than that estimated in the delayed fracture of high strength steel. Total event counts increased with an increase of rust thickness.
- 3) Using an 820-mm diameter cylindrical tank filled with water, AE from bottom plate rusting was monitored by three AE sensors (PAC, R6I) mounted on sidewall. AE sensors mounted at lower height (30 mm) detected continuous-type signals and source location was impossible. AE sensors mounted at 100 mm height monitored burst-type signal from self-fracture of rust growth. Location accuracy, estimated by utilizing the arrival times of wavelet coefficients at 75 kHz and P-wave velocity in water, was poor, possibly due to misreading of in-water P-wave arrival time. AE for tank integrity evaluation should be monitored as the Lamb wave by AE sensor mounted on the bottom plate.

Acknowledgement

This research was performed under project on “The Reliability Assessment Technology for the Petroleum Refining Facilities” by the research fund from NEDO (New Energy and Industrial Technology Development Organization) and PEC (Petroleum Energy Center). The authors wish to express our appreciation to colleagues who contribute the project

References

- 1) P.T. Cole and P.J. Van de Loo, Acoustic Emission Beyond the Millennium, Elsevier Sci, (2000) 169.
- 2) Report on the research project on “The Reliability Assessment Technology for the Petroleum Refining Facilities” by NEDO, (2002).
- 3) S. Fujimoto, M. Takemoto and K. Ono, J. Acoustic Emission, **19** (2001) 63.
- 4) R. Masaki, M. Takemoto and K. Ono, Acoustic Emission Working Group Meeting, Princeton, (1999).
- 5) O. Tamura and M. Takemoto, Tetsu to Hagane, (J. Iron and Steel Inst. Japan), **83** (1999) 532.
- 6) F. J. Fahy, Foundations of Engineering Acoustics, Academic Press, 1987, p. 126.

ACOUSTIC PROPERTY OF CVD-DIAMOND FILM AND ACOUSTIC EMISSION ANALYSIS FOR INTEGRITY EVALUATION

R. IKEDA¹, Y. HAYASHI² and M. TAKEMOTO²

¹R and D Div., Asahi Diamond Co., Ltd, 787, Tabi, Ichihara, Chiba, 290-0515, JAPAN,

²Faculty of Science and Engineering, Aoyama Gakuin University
Fuchinobe 5-10-1, Sagamihara, Kanagawa, 229-8558, JAPAN

Abstract

The authors determined the acoustic properties of CVD-diamond film using a laser ultrasonic system. Three elastic stiffness coefficients, i.e, C_{11} , C_{12} , C_{44} for cubic structure, were estimated by inverse processing of Lamb waves detected for a free-standing diamond film. Two stiffness coefficients; C_{11} (1026 GPa) and C_{12} (250 GPa), estimated from sheet velocity and velocity dispersion of Ao-Lamb wave, agreed well with those reported for natural diamond, but C_{44} (388 GPa) was estimated to be 80 % that of natural diamond. Residual stress of diamond film deposited on WC-Co substrate was measured as 2.2 to 2.4 GPa in compression by the Raman spectroscopy.

We analyzed the Lamb-wave AE signals from two kinds of diamond film deposited in different area on a 1-mm thick WC-Co substrate during four-point bending. No AE was detected for the specimen with small area diamond film (Type-A) under tensile and compressive bending. We also detected no AE for the specimen with large area diamond (Type-B) when it is subjected to tensile bending. Diamond film suffered damages (fragmentation and decohesion) when the substrate suffered macroscopic unstable fractures at +1.56 GPa. In contrast, we detected frequent AE signals from compressive surface stress (-0.58 GPa) when Type-B specimen was subjected to compressive bending. AE events rapidly increased above the surface stress of -0.58 GPa. Most AE signals with small peak amplitudes were located outside the sensors and their fracture types were not classified. A few AE signals with low amplitude and fast rise time of So-mode, detected at around -0.60 GPa, were classified to the Mode-I cleavage fracture of the film. Though fragmentary diamond film exfoliated from the substrate, we could not monitor the AE events due to the film spalling. Fracture mechanism of diamond film under tensile and compressive loading was discussed in relation to the compressive residual stress.

Key Words: CVD-diamond, Acoustic property, Residual stress, Four-point bending, Decohesion, Cleavage fracture

1. Introduction

Diamond film was first synthesized by chemical vapor deposition (CVD) method almost 20 years ago. Since then diamond film has been expected to become new functional material in tools and machinery as hard coating, SAW devices and so on. Diamond is the hardest material and shows high thermal conductance but good electrical insulation. It is brittle and shows low fracture toughness. Utilization of the hardest diamond as cutting tools has been the most succeeding industrial practice, but it is still limited on the market due to poor reliability against fracture and decohesion of the film during machining. Interpretation of decohesion mechanism and effective countermeasure against it are indispensable for further expansion of the diamond as

a cutting-tool material. Driving force of decohesion damages are the residual, thermal and applied (cutting) stresses. Cutting stress is often dynamic or impact. As the diamond film is deposited on hard substrate material such as WC-Co at temperatures higher than 1073K, extremely high residual stresses exist in the film. Interfacial quality or bond strength of the diamond film depends on the area, thickness, deposition condition and so on. Estimation of the interfacial quality is particularly important for establishing countermeasures against decohesion damages, but has not been studied much.

We first estimated the elastic properties of polycrystalline CVD-diamond utilizing laser generated ultrasonics. We estimated elastic stiffness coefficients for isotropic cubic structure and compared with those reported for natural diamond. Both the zero-th order symmetric (S_0) and anti-symmetric (A_0) mode Lamb waves detected for free-standing diamond film were analyzed. Residual stress was estimated by Raman spectroscopy.

We studied effects of residual stress and film area on the film damage by monitoring AE during four-point bending. Diamond films with different deposition area on WC-Co plates were subjected to compressive and tensile bending. Threshold stress to cause film or substrate fracture under tension and compression were determined by AE monitoring. Next, we studied fracture types of the film and progression of fractures by waveform analysis of S_0 component of Lamb AE signals.

2. Acoustic Properties And Residual Stress Of Cvd-Diamond Film

Two kinds of polycrystalline diamond film were prepared by hot-filament CVD method of methane and hydrogen gas mixture. One is a free standing film with average grain size of $\sim 50 \mu\text{m}$, mechanically exfoliated after being deposited on 5.4 mm thick sintered SiC substrate (denoted hereafter as 50FSD). Film surface and transverse structure of 50FSD film are shown in Fig. 1. Surface of the diamond film was polished and coated with gold, depending on the purpose. Another specimen is a film deposited on 1 mm thick WC-Co substrate with average grain size of about $3 \mu\text{m}$ (denoted hereafter as 3MD). This one is submitted to the residual stress measurement by Raman spectroscopy.

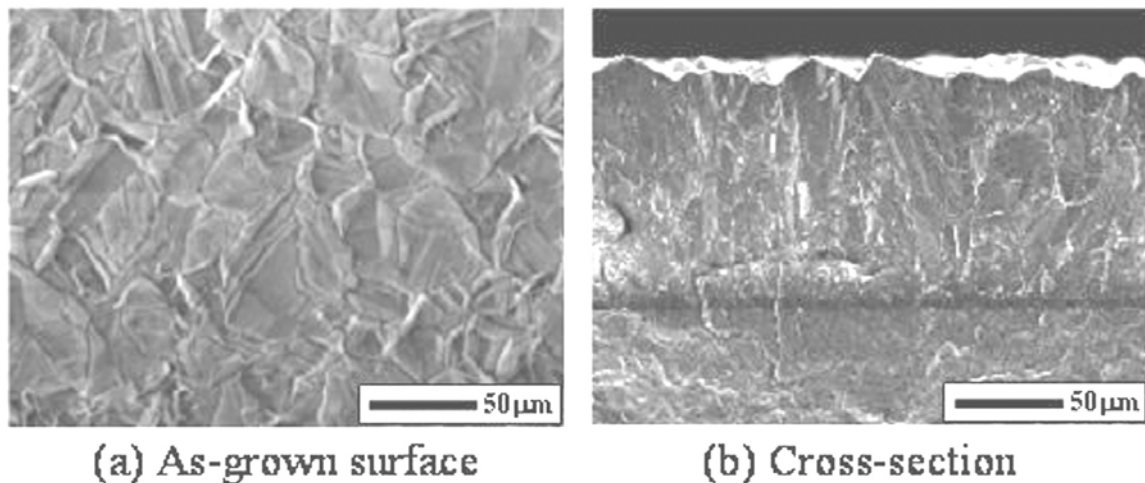


Fig. 1 SEM images of as-grown surface (a) and cross-section (b) of CVD-diamond with average grain size of $50 \mu\text{m}$ (50SFD).

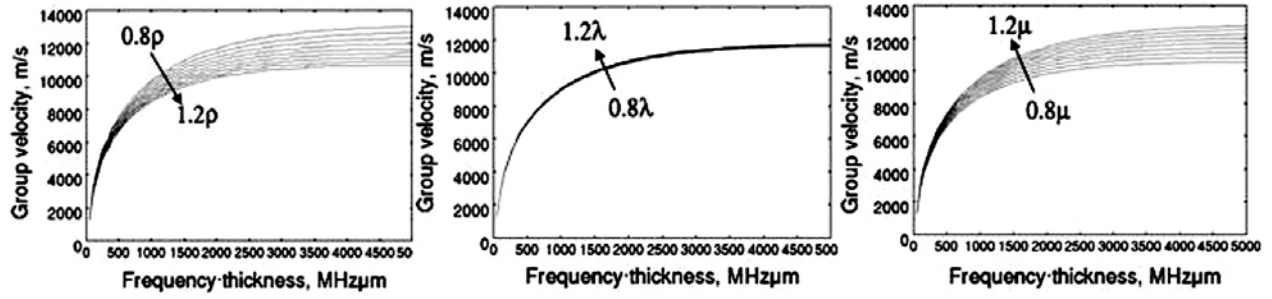


Fig. 2 Effects of density (ρ) and Lamé's constants (λ) and (μ) on the group-velocity dispersion of Ao-mode Lamb waves for free-standing diamond film.

We estimated elastic stiffness coefficients of the diamond film from the sheet velocity of So-mode and the group velocity dispersion of Ao-mode. Natural diamond is known to be acoustically cubic (m3m). Table 1 shows the stiffness coefficients reported for natural and CVD diamond [1-5]. It is noted that data are grouped into two. Two groups reported 238 and 250 GPa for C_{12} , and two others 125 GPa. Jiang et al. [5] measured the coefficient C_{12} of CVD diamond as 122 GPa by using Brillouin scattering.

Table 1 Reported data for elastic stiffness (C_{11} , C_{12} , C_{44}), anisotropy (η) and density (ρ) of diamond.

	Specimen	C_{11} ,GPa	C_{12} ,GPa	C_{44} ,GPa	η	ρ ,kg/m ³	Method
R.Auld ¹⁾	Natural diamond	1020	250	492	1.28	3512	-
A.Tourlog ²⁾	Natural diamond	1029	238	527	1.33	-	Line-focus Acoustic Microscopy
H.J.McSkimin ³⁾	Natural diamond	1076	125	576	1.21	3512	-
M.H.Grimsditch ⁴⁾	Natural diamond	1076	125	577	1.21	-	Brillouin scattering ($\sim 23^\circ\text{C}$)
X.Jiang ⁵⁾	CVD diamond	1062	122	541	1.15	-	Brillouin scattering

We first attempted to utilize the velocity dispersion of Rayleigh wave. However, Rayleigh wave can only exist in a limited velocity range from 6900 (Rayleigh wave velocity of the substrate) to 8200 m/s (shear wave velocity of the diamond). This suggests that the estimation of stiffness coefficients from the Rayleigh wave was very difficult. Thus, we utilized the Lamb waves measured on the free-standing diamond film.

Figure 2 shows the effects of density (ρ) and Lamé's constants ($\lambda = C_{12}$, $\mu = C_{44}$) on the group velocity dispersion of the Ao-mode Lamb waves of the diamond film. These dispersion curves are computed using the C_{12} and C_{44} reported by Auld [1]. It is noted that λ gives small effect on the dispersion and is difficult to estimate from the Ao-mode. Therefore, we measured the sheet velocity of So-mode Lamb.

Figure 3 shows the method for measuring the Lamb waves. Here, a pulse YAG laser with duration of 5 ns was irradiated on the Au-coated distal plane of the diamond film and monitored by laser interferometer at propagation distances of 14.1 and 15.4 mm. Two of the waveforms detected are shown in (b), from which the group velocity dispersion of Ao-mode Lamb was obtained by wavelet transform (see (c)). The bold solid line in (c) was computed using the properties by Auld (1) for natural diamond. Fine lines are the dispersion curves computed by changing only the value of μ from 0.8 to 1.2 times that obtained by Auld. Data points shown by

x in (c) agrees well with the line computed for 0.8μ .

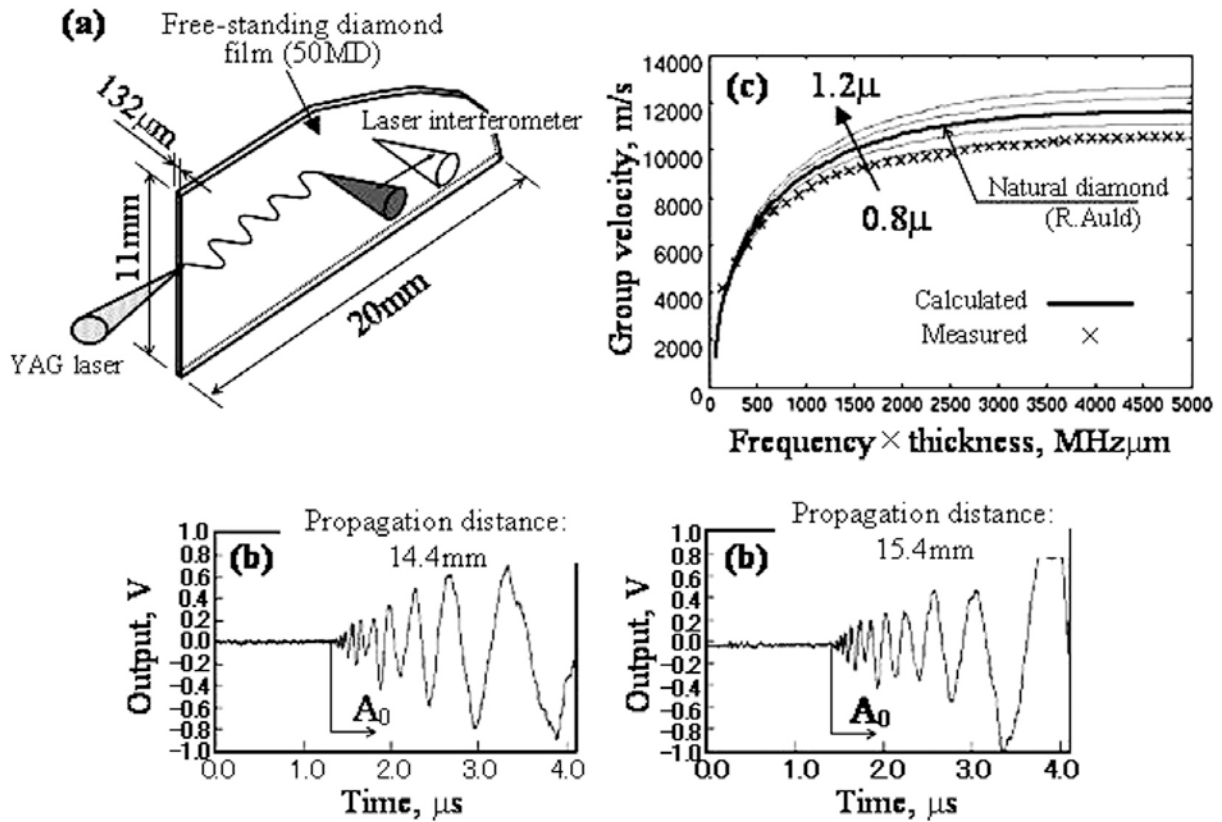


Fig. 3 (a) Method for measuring the Lamb waves. (b) Two waveforms detected. (c) The group velocity dispersion of A_0 -mode Lamb waves obtained by wavelet transform of the detected waves.

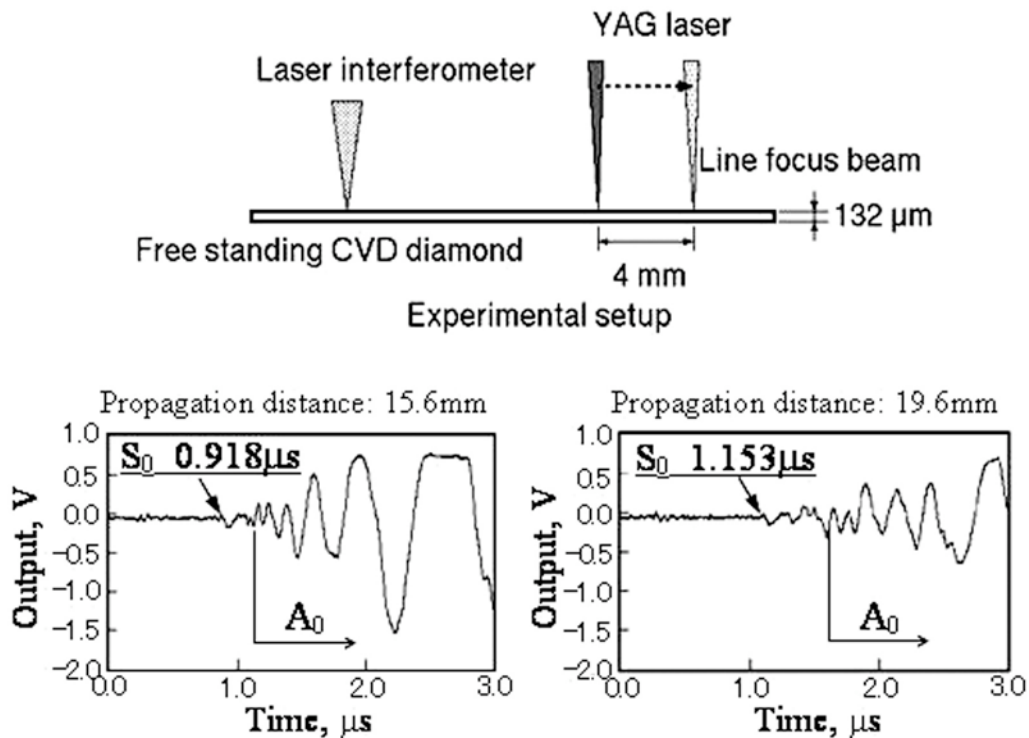


Fig. 4 Method for exciting S_0 -mode Lamb waves and detected wave for 50 FSD film.

Using the Simplex-assisted inverse scheme, we estimated the stiffness coefficients from group velocity dispersion of Ao-Lamb waves. Assuming the density as 3515 kg/m^3 , C_{11} and C_{44} were estimated for the case of $C_{12}=125 \text{ GPa}$ and 250 GPa . For $C_{12}=125 \text{ GPa}$, $C_{11}=941 \text{ GPa}$ and $C_{44}=407 \text{ GPa}$ were obtained, and $C_{11}=1026 \text{ GPa}$, $C_{44}=388 \text{ GPa}$ for $C_{12}=250 \text{ GPa}$. The sheet velocity is computed as $16,200 \text{ m/s}$ for the former case ($C_{12}=125 \text{ GPa}$) and $16,600 \text{ m/s}$ for the later case ($C_{12}=250 \text{ GPa}$).

Next we measured the So-mode Lamb wave using the method shown in the upper part of Fig. 4. A line-focused beam of a high-energy YAG laser was irradiated onto the un-coated diamond film normal to the surface. So-mode Lamb wave was excited by the thermal expansion of the diamond film. Beam position was moved and So-packets detected at the limit distances of 15.6 and 19.6 mm are shown. The sheet velocity was measured as $17,000 \text{ m/s}$ and close to the computed one for $C_{12}=250 \text{ GPa}$. The Rayleigh wave velocity calculated from $C_{12}=250 \text{ GPa}$, $C_{11}=1026 \text{ m/s}$ and $C_{44}=388 \text{ GPa}$ is 9550 m/s and agrees well with $10,000 \text{ m/s}$ measured using an ultrasonic microscope (at 200 MHz). Finally, C_{44} of CVD diamond was estimated to be 80% of that reported by Auld (1) for natural diamond. Accurate determination of the three stiffness coefficients from limited acoustic data is difficult, but we have demonstrated that the elastic properties of CVD-diamond is very close to those of natural diamond and almost isotropic.

Raman spectroscopy is occasionally utilized for the estimation of residual stress. Sharma et al. [6] measured Raman spectra of diamond under static high pressure, and found a linear relation between drift amount (Δn) of the peak from the position under no stress and applied stress (σ), by Eq. (1).

$$\sigma (\text{GPa}) = -0.422 \times \Delta n (\text{cm}^{-1}) \quad (1)$$

We measured residual stress using Raman spectroscopy on the CVD-diamond film (3MD) deposited on WC-Co substrate. Residual stress was measured as -2.2 to -2.4 GPa (in compression).

3. Analyses of AE during Four-Point Bending of Coated Diamond

Experimental Method

We monitored AE signals from diamond films subjected to four-point bending using the equipment as shown in the left of Fig. 5. Distance of the inner span is 73 mm . It is noted the both sides of specimen were rigidly clamped to steel blocks. Fine-structure diamond films (3MD) of $10\text{-}\mu\text{m}$ thickness were deposited on the WC-Co plate of 1 mm thick, 100 mm long and 30 mm wide. Two types of specimen were tested. One is Type-A specimen with the diamond film deposited within 16 mm square at the central portion of the plate. Type-B is the specimen with diamond film deposited over central $60 \text{ mm} \times 30 \text{ mm}$ area. Diamond film of Type-B extended to the areas under the steel blocks. The diamond film was loaded so as to apply both compression and tension. Four AE sensors (PAC Type PICO) were mounted on the corner of $30 \text{ mm} \times 16 \text{ mm}$ rectangle at specimen center as shown in Fig. 5 (right). In case of Type-B, the sensors are on the diamond film. Sensor outputs were amplified 40 dB using NF9913 (NF Circuit Co.), digitized by a fast A/D converter H310 (Autonics Co.) and fed to a personal computer.

Both fracture-type classification and source location were performed using the So-packet of Lamb AE signals. Sheet velocity of WC-Co is as fast as 6600 m/s , and fast sampling interval of 50 ns were used for accurate determination of the arrival time. Amplification of the system was adjusted so as to detect only the first portion of the So-packet.

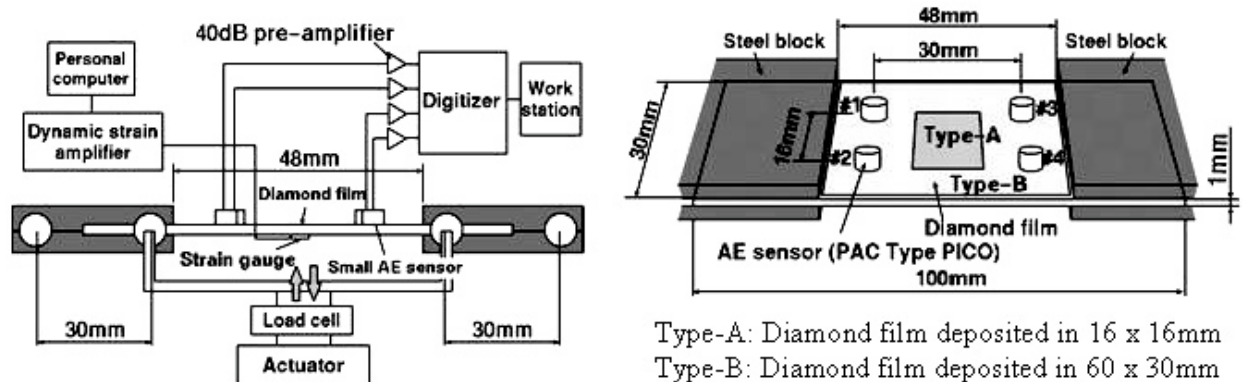


Fig. 5 Experimental setup for AE monitoring during four-point bending of diamond film deposited on WC-Co plate.

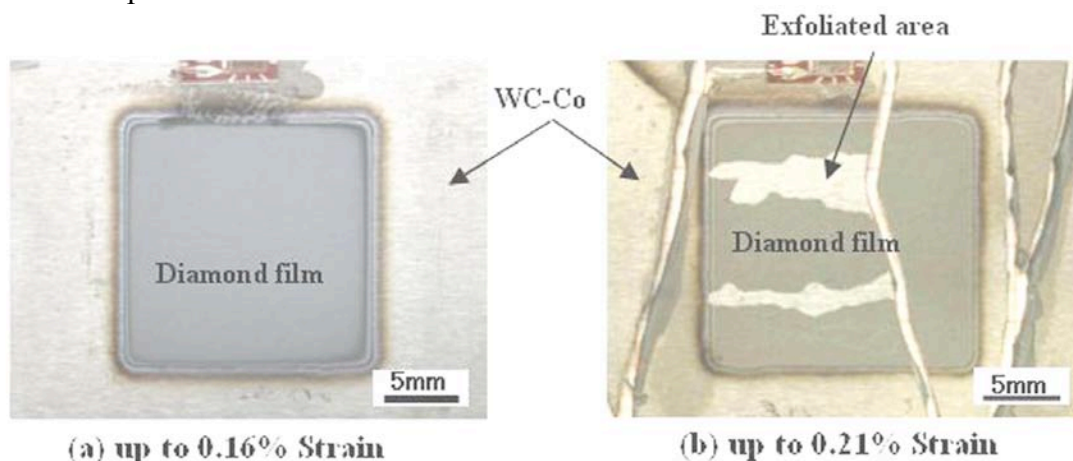


Fig. 6 (a) Surface photograph of Type-A specimen after bending to the surface strain of 0.16%. (b) At 0.21% strain, substrate fractured and diamond film exfoliated in parts.

Results of Type-A specimen with small area diamond film

Diamond films deposited within 16-mm square area were submitted to tensile or compressive bending. No AE was detected for any diamond film below the surface strain of 0.16% and stress of 1 GPa. Only one AE event was detected when the substrate WC-Co suffered unstable fracture at strain of 0.21% (1.56 GPa). This finding was the same when the diamond film is subjected to tension or compression. Figure 6 shows the surface photographs of the diamond film subjected to the surface strain of 0.16% and 0.21%. At 0.16%, no macroscopic or microscopic damages were observed. At the strain of 0.21%, the WC-Co plate sustained several unstable fractures and caused partial exfoliation of diamond film, shown in (b). This demonstrates that the CVD-diamond film deposited in a limited area possesses very high adhesion to the substrate WC-Co.

Results of Type-B Specimen with Large Area Diamond Film

We observed no AE during the tensile bending up to the surface stress of 1 GPa (0.16% strain), which is close to the tensile fracture strength (1.5 GPa) of the substrate. AE sensors were removed from the specimen above the stress of 1 GPa to avoid the sensor damage due to unstable macroscopic fracture of brittle WC-Co. This finding demonstrates that the CVD-diamond film, even if it is coated over wide area, has strong adhesion to the WC-Co substrate under tension. Diamond film was found to be free of any damages after being unloaded as shown in Fig. 7.

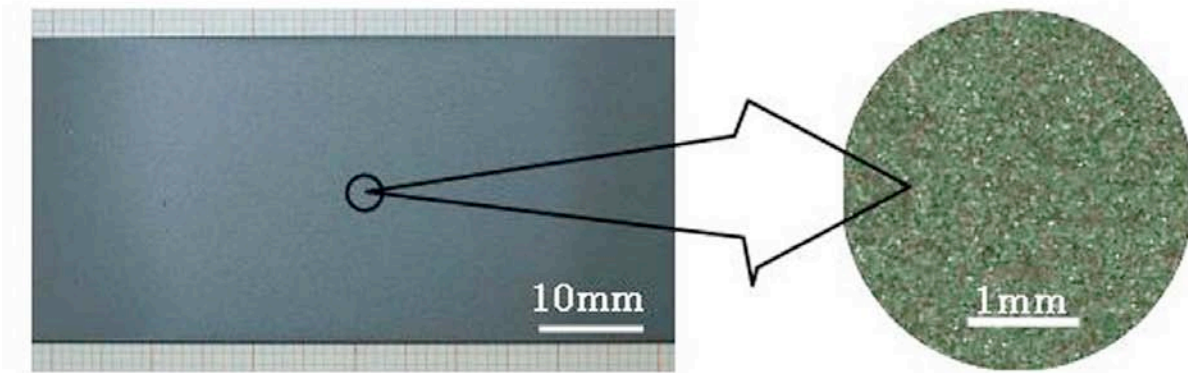


Fig. 7 Surface photograph of the CVD-diamond subjected to bending to surface tensile stress of 1 GPa.

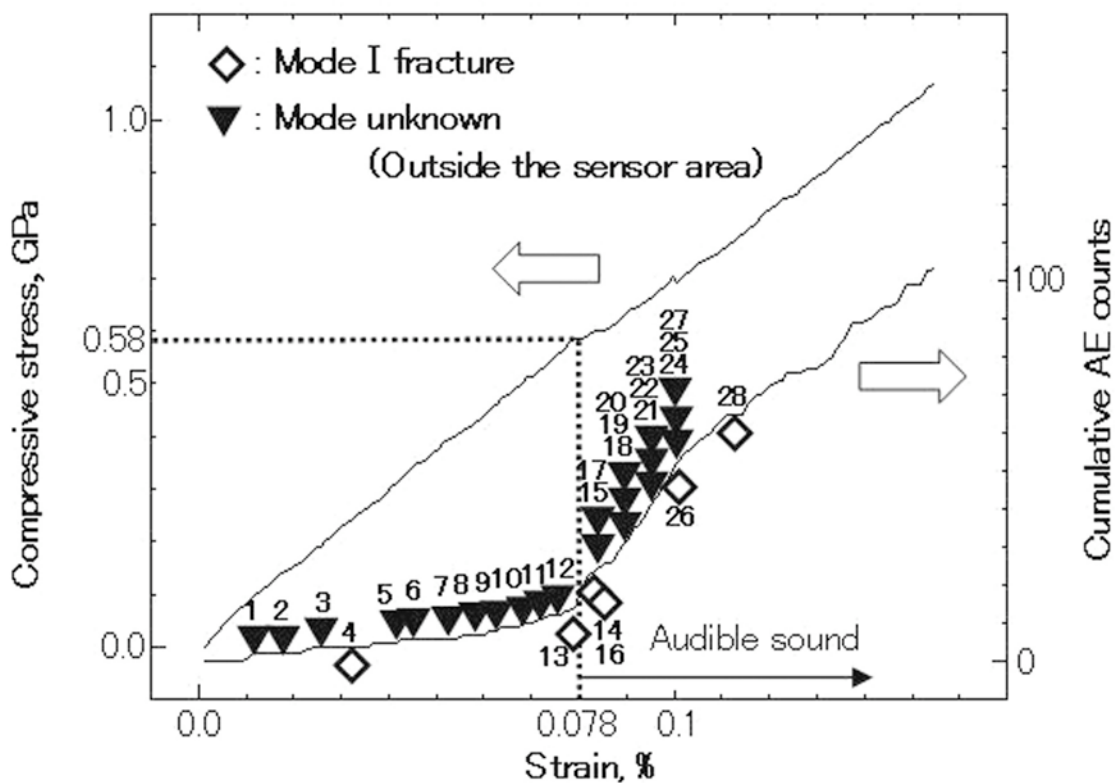


Fig. 8 Compressive stress vs. strain diagram with cumulative AE counts.

Contrary to the high performance of the diamond film under tension, we detected frequent AE signals when the diamond films are subjected to compressive stresses in bending. Figure 8 shows compressive stress vs. strain with cumulative AE counts. AE counts rapidly increased at compressive strains larger than 0.078 % (corresponding to surface stress of 0.58 GPa). Most AE events (event number 1 to 12) detected below 0.078% strain are, as indicated by symbol ▼, located at the edges of steel block (rigid fastening) as shown in Fig. 9. These events are likely to be contact noise. Above 0.078% strain, we heard frequent crack-sounds and simultaneously detected many AE signals. AE events denoted by symbol ▼ with number 17, 18, 22, 23, 25 and 27 were located near Sensors #1, 2 and 3. Further we detected five other AE events (event 13, 14, 16, 26 and 28) designated by symbol ◇. Three of them (13, 14 and 16) at around the surface strain of 0.08% were located along the upper edge of the specimen, but other two (26, 28) de

ected at higher stresses were located inside the monitoring area. It is noted that no AE was located near the specimen center.

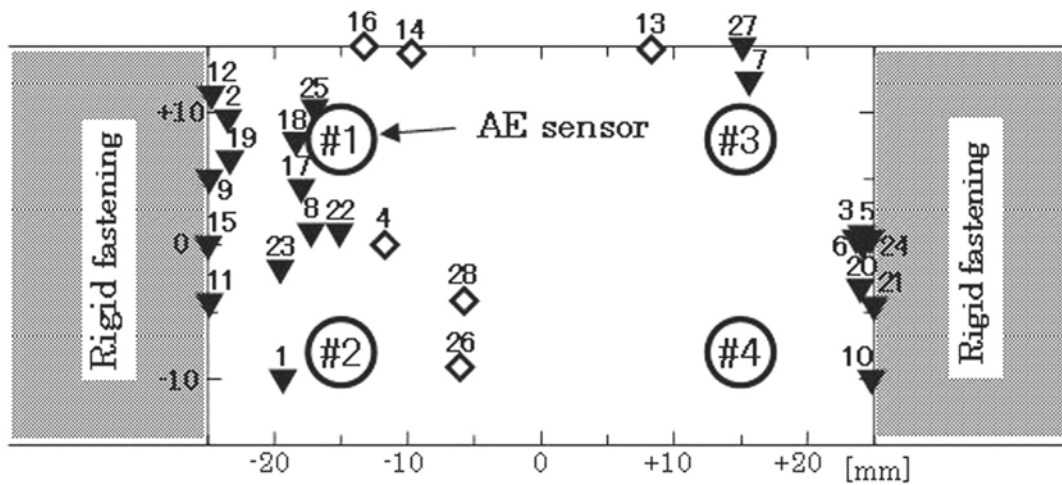


Fig. 9 Source location of AE events detected during compressive bending of WC-Co with large area CVD-diamond film (Type-B specimen).

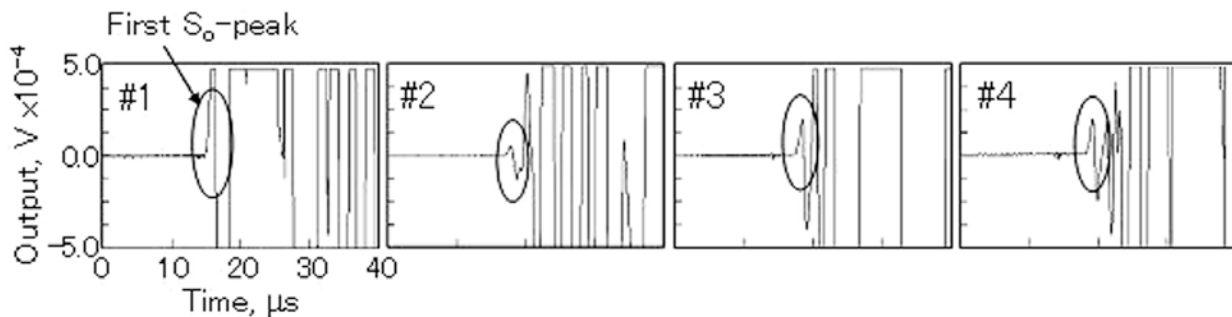


Fig. 10 First portion of the So-packet of Lamb AE signals (\diamond , No. 14) indicating the Mode-I cleavage fracture of the diamond film under compressive bending.

Figure 10 shows Lamb waveform of event No. 14 (\diamond) located near the sensor #1. Polarity of the first So-peak of four sensors is positive, and indicates the Mode-I fracture with crack opening vector parallel to the surface. This radiation characteristic agrees well with those of So-Lamb waves produced by adiabatic expansion of line focused pulse laser (Mode-I fracture with an opening vector parallel to the surface) reported by Sato et al. [7]. Fast rise time of the first So-mode, 0.8 to 0.9 μ s, indicates the fast crack opening of diamond film, while the weak amplitude less than 1 mV shows a small crack volume.

We primarily produced Lamb wave utilizing a 2-mm wide and 5-mm long compression-type PZT element with an opening (expansion) of 8×10^{-6} mm at 1.5 μ s rise time. This simulates the Mode-I decohesion of the film with opening vector in the surface normal direction. We detected strong So-peak of 20 mV with negative polarity. Polarity and peak amplitude of this simulated So-Lamb wave are much different from these observed in Fig. 10. As shown in Fig. 11, exfoliated diamond film are fragmented with sizes from less than 1 mm to a few mm. Thus, the signal \diamond shown in Figs. 8 and 9 are not produced by the large-size Mode-I decohesion (normal to surface) but from small-size Mode-I fracture (in-plane) due to buckling of the diamond film.

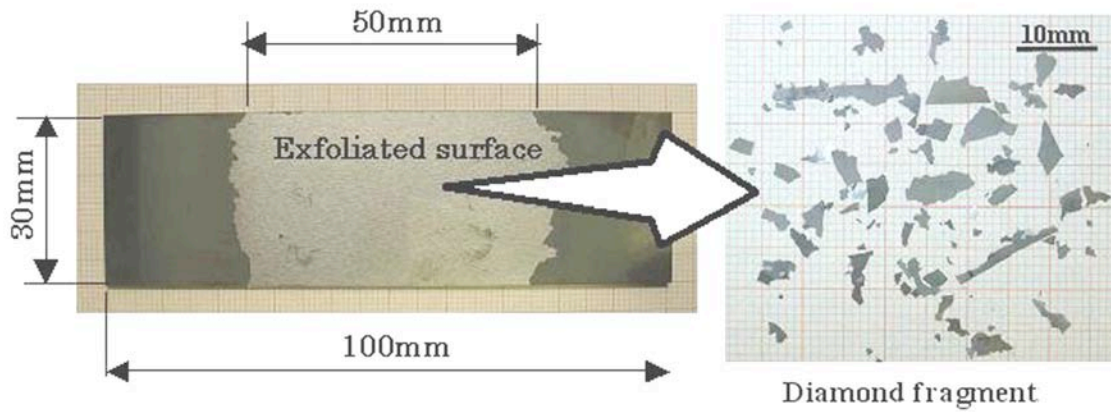


Fig. 11 Fragments of diamond film from WC-Co substrate after being subjected to bending in compression up to 0.75 GPa.

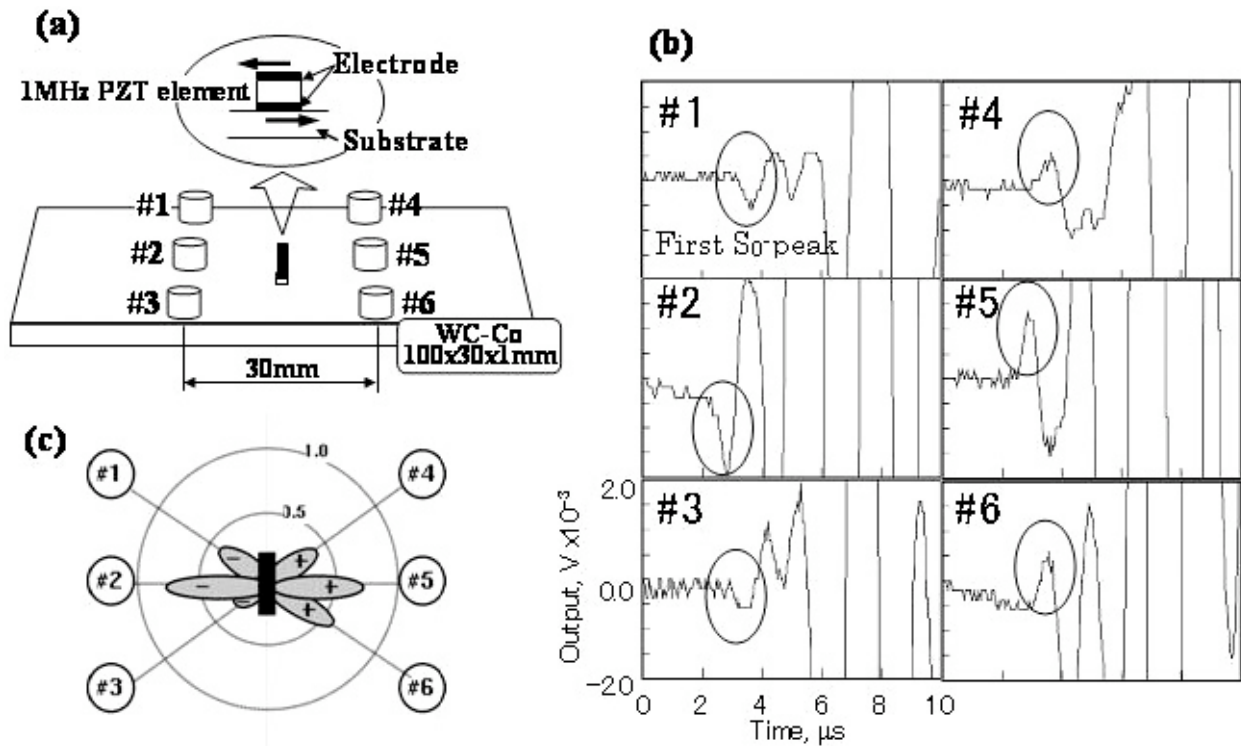


Fig. 12 (a) Method for Mode-II shear fracture simulation. (b) Resultant waveforms. (c) The radiation pattern of the first peak of So-packet of the Lamb waves.

4. Discussion of Interfacial Quality of CVD-Diamond

Some important findings were revealed by this study. These are:

- 1) Large compressive residual stress of -2.3 GPa exists in CVD-diamond films.
- 2) Diamond film deposited in a limited area shows strong adhesion to the substrate under both tensile and compressive bending.
- 3) Diamond film deposited in a large area shows strong adhesion under tension but lower bending strength under compression.

We can assume that the diamond film suffers the first cleavage crack when the actual tensile (or compressive) stress in the film reaches the critical value for fracture. Apparent threshold substrate stress for crack initiation under compression is -0.58 GPa, and 1.56 GPa under tension. Residual stress was measured to be about -2.3 GPa in compression. Consequently actual stress necessary for cleavage cracking is estimated to be -2.9 GPa when the diamond film suffers compression. Now assuming that fracture stress in tension is equal to that of compression, we have to apply 2.9 GPa to cause tensile fracture. This means that 5.2 GPa is needed for the diamond fracture under tensile loading. However, the diamond suffered fracture at 1.56 GPa (much lower than above estimation) when the unstable fracture of the substrate occurred. This lower stress is not for the diamond fracture but for the WC-Co substrate fracture. Above discussion can explain the fact 3) for the diamond film deposited over large area. However, it cannot explain the fact 2). Large difference of the decohesion strength of large area diamond under tensile and compressive loading might be due to shear stress at the diamond/substrate interface. The interfacial shear stress, originated from residual stress and applied loading, distributes over the axial direction of diamond film and has the maximum values near the film edges. The maximum shear stress increases with increasing the area (length) of the diamond film. However, we did not detect AE signals suggesting Mode-II fracture (shear fracture) at the interface. Here, we have to take a look at AE events ▼ in Figs. 8 and 9. As these events are located outside of the sensors, we could not determine the fracture type of these events. Mode-II fracture, simulated by shear-type PZT element rigidly attached on the substrate, shows a characteristic radiation pattern as shown in Fig. 12; i.e., positive polarity in the right area when the discontinuity vector on the substrate surface points to the right, and negative in the left area. This important information, however, cannot be utilized for fracture-type classification since the sources were outside of the four sensors. We are now planning to study the polarity distribution of the signal ▼ using different sensor layout and bending apparatus.

5. Conclusion

We first studied elastic properties of CVD-diamond by laser ultrasonic technique and then the interfacial quality of the film deposited on WC-Co substrate by AE monitoring during tensile or compressive bending. Results are summarized below:

- 1) Elastic stiffness coefficients of the CVD-diamond estimated by the inverse processing of Lamb waves were found to be close to these reported by Auld for natural diamond. Residual stress of the CVD-diamond deposited on WC-Co substrate was measured as -2.2 to -2.4 GPa by Raman spectroscopy.
- 2) AE monitoring during tensile and compressive bending of WC-Co with the diamond film in 16 mm square (Type-A) and over entire surface (Type-B) was attempted to determine the threshold stress to cause micro-fractures and also the fracture types. No AE was detected when the Type-A specimens were subjected to tensile and compressive bending. The CVD-diamond deposited in a limited area shows the superior adhesion strength.
- 3) No AE was detected when the Type-B specimen is subjected to tensile bending. Film damages occurred when the substrate suffered macroscopic unstable fracture at 1.56 GPa.
- 4) Frequent AE signals were monitored from small surface stress when Type-B specimen was subjected to bending in compression. AE signals rapidly increased above the surface strain of -0.078% (-0.58 GPa). Lamb AE signals with small amplitude and fast rise time of So-packet detected above -0.078% strain are diagnosed to be produced by the Mode-I cleavage fracture of the film. Spalling of fragmentary diamond film were observed above -0.078% strain. Damage of diamond film is significantly influenced by the compressive residual stress in the film, but the damage mechanism has not been clarified in detail.

References

- 1) B. A. Auld, "Acoustic Field and Waves in Solids", Wiley-Interscience Publ., (1973), 368.
- 2) A. Tourlog, W. Li and D. Achenbach, Applied Physics Letters, **69** (1996), 3680.
- 3) H. J. McSkimin and W. L. Bond, Physical Review, **105** (1956), 116.
- 4) M. H. Grimsditch and A. K. Ramdas, Physical Review B, **11** (1975), 3139.
- 5) X. Jiang, J. V. Harzer, B. Hillbrands, Ch. Wild and P. Koidl, Applied Physics Letters, **59** (1991), 1055.
- 6) S. K. Sharma, J. of Raman Spectroscopy, **16** (1985), 350.
- 7) T. Sato, M. Takemoto and K. Ono, Japanese Journal of Applied Physics, **38** (1999), 3193.

EVALUATION OF COATED FILM BY LASER-BASED AE-UT TECHNIQUE

M. ENOKI and T. KUSU

Department of Materials Engineering, The University of Tokyo,
7-3-1 Hongo, Bunkyo-ku, Tokyo 113-8656, Japan

Abstract

The method to evaluate the thickness of coated film in steel from backside was investigated in order to apply it to the coal coking in plant pipe. Acoustic emission-ultrasonic testing or AE-UT technique was developed using laser based ultrasonic testing method. Ultrasound in coated specimen was generated by Nd:YAG pulse laser and detected by He-Ne laser interferometer. There were large amplitude signal and small one in experiment. Small signal was identified to be an ultrasound in steel specimen by considering the wave velocity. Wave propagation in coated specimen was also simulated by dynamic finite element method and waveform was analyzed by fast Fourier transfer method. In this experiment generated wave was due to thermal mode by comparing with detected signal and simulated waveform. It was also demonstrated from both experiment and simulation that this non-contact AE-UT technique was effective to evaluate coated film.

Keywords: Acoustic emission, AE-UT, Laser based ultrasonic, Laser interferometer, Wave propagation, Coated film

1. Introduction

Coking is a phenomenon that carbon stacks inside of plant pipe. This coking causes the loss of pressure in pipe and often brings about the stop of operation in plant. Also it gives rise to corrosion inside of pipe, creep rupture and breaking of pipe due to the increase of temperature inside of pipe. It becomes important to establish the inspection method to quantitatively measure the thickness of coking outside of pipe. A contact type AE-UT (acoustic emission-ultrasonic testing) method has been used to predict a thickness of coated film, but it is difficult to apply this technique to coking problem at elevated temperature because a PZT transducer is used in this method. Also this method is not so quantitative to evaluate the thickness of coated film. Recently non-contact type laser based ultrasonic technique has been developed to investigate materials properties and flaws under severe environment or at elevated temperature [1-9]. Also AE signals were successfully detected in several materials tests [10-12]. The purpose of this paper is to establish the non-contact AE-UT method, consists of pulse laser for ultrasonic generation and non-contact detection of simulated AE by laser interferometer, and wave propagation is also simulated by finite element method to quantitatively evaluate the thickness of coking using.

2. Experimental Procedures

Specimens

Stainless (SUS304) plate of 200 by 200 by 5 mm was used for experiments, shown in Fig. 1. Incident point of pulse laser and measuring point by laser interferometer are on a line and also shown in this figure, and the distance between these points were varied to investigate the effect of wave propagation. Simulated coking was made of silicon or polymer rubber with several

thicknesses and 40 mm width. Coated surface was opposite to the both incident and measuring points.

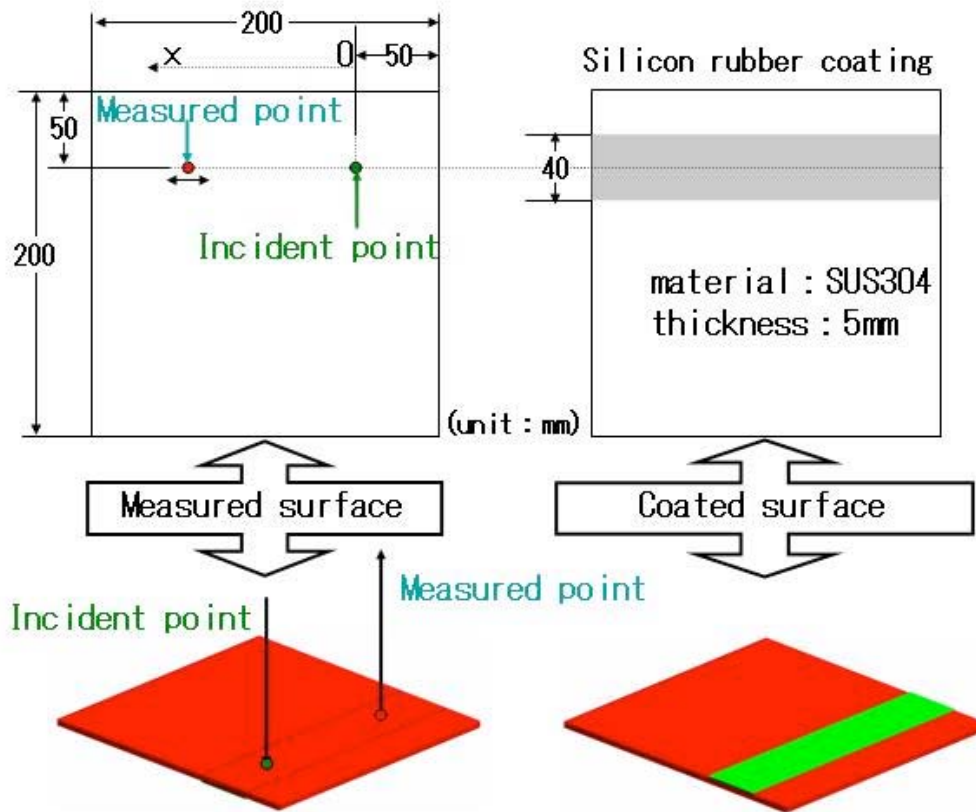


Fig. 1 Geometry of sample with silicon rubber coating, and incident point of laser beam and measured point of surface velocity.

Measuring system

Ultrasound was generated by pulse laser (Nd:YAG, New Wave Research Co.) and wave velocity in the normal direction to the surface was measured by laser interferometer (AT3500, Graphtec Corp.). Waveform was recorded using AE analyzer (DCM-120, JT Tohshi Co.). The block diagram of measuring system was shown in Fig. 2. Spectrum in frequency domain by fast Fourier transform (FFT) was compared with the thickness of coated film to quantitatively predict the thickness. Propagated waveforms in the plates with and without coated film were recorded and analyzed in frequency domain, by varying the distance between input point of pulse laser and output point of laser interferometer.

Wave simulation

Preprocessor eta-FEMB and FEM code (LS-DYNA 3D, Livermore Software Technology) were used to simulate a wave propagation in coated plate with several conditions of specimen size, coated thickness, input/output points, materials properties such as density, Poisson's ratio and Young's modulus, and with some input pulse time function and input mode. Waveform of surface velocity in the normal direction to the surface at the measuring point corresponding to the experimental setup was calculated. Coated thickness was predicted by comparing the detected waveform with simulated waveform.

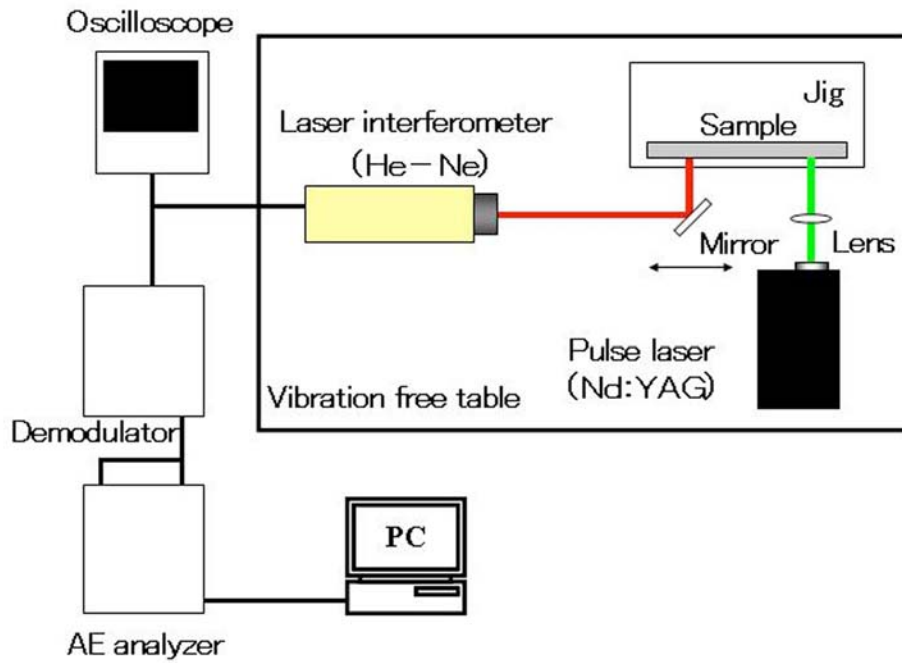


Fig. 2 Schematic diagram of laser AE-UT measuring system.

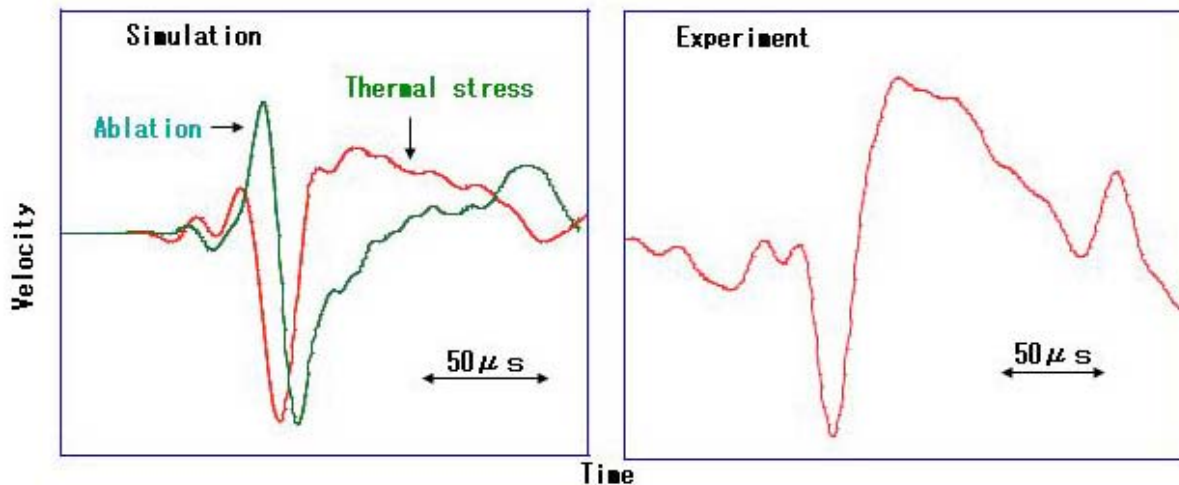


Fig. 3 Effect of incident mode on simulated waveform and experimental one.

3. Results and Discussion

Incidence mode of pulse laser

There are two modes of thermal stress and ablation in the case of generation of elastic wave by the incidence of pulse laser into materials. These modes have different mechanism in the generation of elastic wave. Simulated waveforms with two incidence modes were compared with the detected waveforms by laser interferometer in order to ensure the effectiveness of this simulation and decide the incidence power of laser pulse, shown in Fig. 3. This figure shows that ultrasound was generated nearly in thermal stress mode. Waveforms were calculated with several conditions such as incidence time function and incidence mode for ultrasound generation. Optimal simulation conditions were obtained by comparing with the detected ones.

Visualization of wave propagation

Figure 4 shows an example of visualized wave propagation in the normal velocity to the sur

face, where thermal stress mode was selected as incident condition and coated thickness was 0.75 mm. The left and right side of figure show the results of measuring and coated surface, respectively. It was clearly observed that coated film causes the turbulence in waveform.

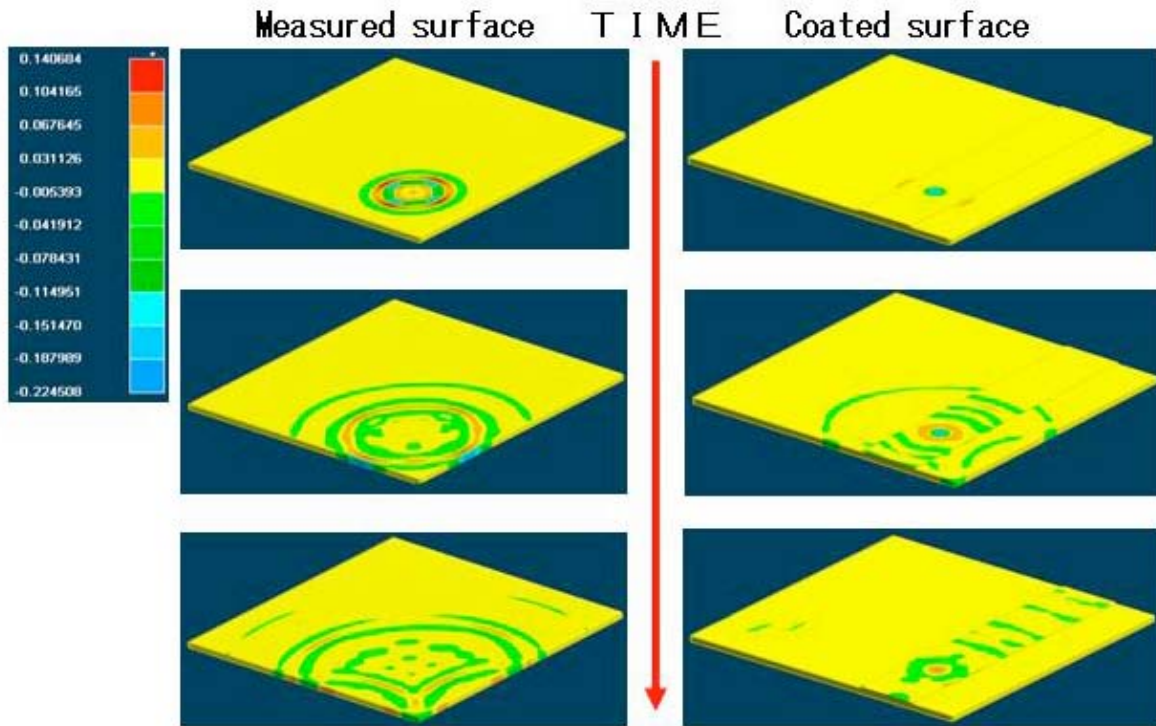


Fig. 4 Visualization of wave propagation in coated sample.

FFT analysis in simulated waveforms

The results of simulated waveforms were shown in Fig. 5, where the distance between incident and measured points was 50 mm and the coated thickness was selected as 0, 0.25 0.50 and 0.75 mm. Arrival of longitudinal wave and the following transverse and surface waves were clearly observed from the figure.

Normalized spectra in frequency domain after FFT were shown in Fig. 6 as a function of coated thickness. The profile around 110 kHz was extended and the difference of power was plotted as a function of coated thickness. Spectra of coated specimen demonstrated the different profile of non-coated ones. It was suggested that this properties was used to quantitatively predict the coated thickness.

FFT analysis in detected waveforms

Figure 7 shows the measured waveforms in the specimens with the coated thickness of 0, 0.41, 0.63 and 0.84 mm. The effect of coated thickness on frequency spectra was also observed in the detected waveforms by laser based AE-UT method, shown in Fig. 8. The similar effect of coated thickness on the difference of power was also found. It demonstrates that this non-contact laser based AE-UT method was effective to predict the coated thickness.

4. Conclusions

1. Simulation of wave propagation by FEM and FFT analysis in the coated plate demonstrates that the laser AE-UT method is effective to predict the coated thickness in steel plate.

2. The measured waveform by laser interferometer was compared with the simulated one, and the generation of ultrasound by the pulse laser in this experiment was identified to be nearly in thermal stress mode.
3. The frequency analysis in the simulated coated specimens is in good agreement with the wave propagation result, and it was demonstrated that the non-contact laser AE-UT method was effective to predict the coking thickness in plant pipe.

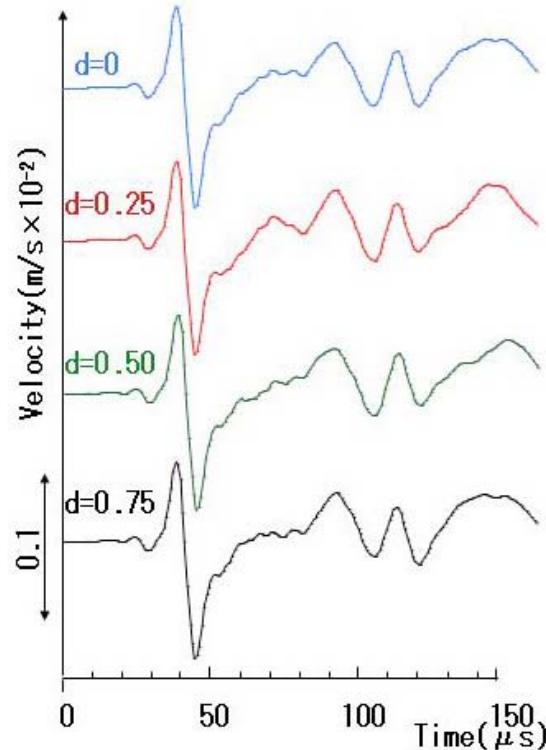


Fig. 5 Simulated waveforms of samples with coating thickness of 0, 0.24, 0.50 and 0.75 mm..

References

- 1) H. Nakano, S. Nagai and H. Imai: *Int. J. Thermophysics*, **8** (1987), 437-480.
- 2) R. J. Dewhurst and O. Shan: *Opt. Laser. Eng.*, **16** (1992), 163-178.
- 3) H. Nakano and S. Nagai: *Jpn. J. App. Phys.*, **32** (1993), 2540-2542.
- 4) H. Nishino, Y. Tsukahara, C. Hideo, Y. Nagata, T. Koda and K. Yamanaka: *Jpn. J. App. Phys.*, **34** (1995), 2874-2878.
- 5) J. P. Monchalain and R. Heon: *Mater. Eval.*, **44** (1996), 1231-1237.
- 6) H. Yamawaki, T. Saito, H. Fukuhara, C. Masuda and Y. Tanaka: *Jpn. J. App. Phys.*, **35** (1996), 3075-3079.
- 7) H. Cho, H. Sato and M. Takemoto: *Jpn. J. App. Phys.*, **35** (1996), 3062-3065.
- 8) C. H. Palmer: *Review of Progress in Quantitative Nondestructive Evaluation*, **5A** (1986), 651-658.
- 9) D. A. Bruttomesso, L. J. Jacobs and R. D. Costley: *J. Eng. Mech.*, **119** (1993), 2303-2316.
- 10) M. Watanabe, P. Chivavibul, H. Mori, M. Enoki and T. Kishi: *J. Jpn. Soc. Non-Destructive Inspection*, **48** (1999) 369-373. (in Japanese)
- 11) M. Watanabe, K. Tomita, M. Enoki and T. Kishi: *J. Jpn. Soc. Non-Destructive Inspection*, **49** (2000) 376-381. (in Japanese)
- 12) M. Enoki, M. Watanabe, P. Chivavibul and T. Kishi: *Sci. Tech. Adv. Mater.*, **1** (2000) 157-165.

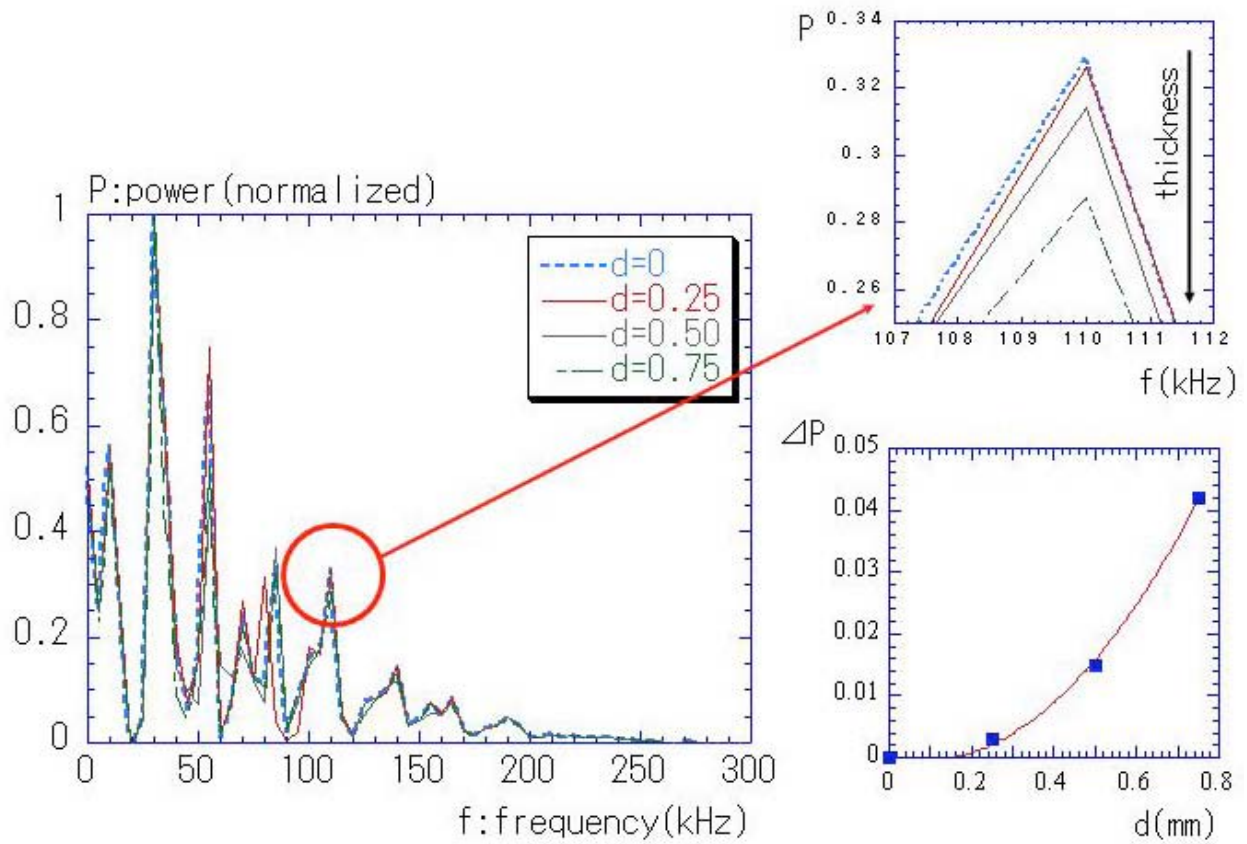


Fig. 6 Results of FFT analysis of simulated waveforms, and relation between power loss and coating thickness.

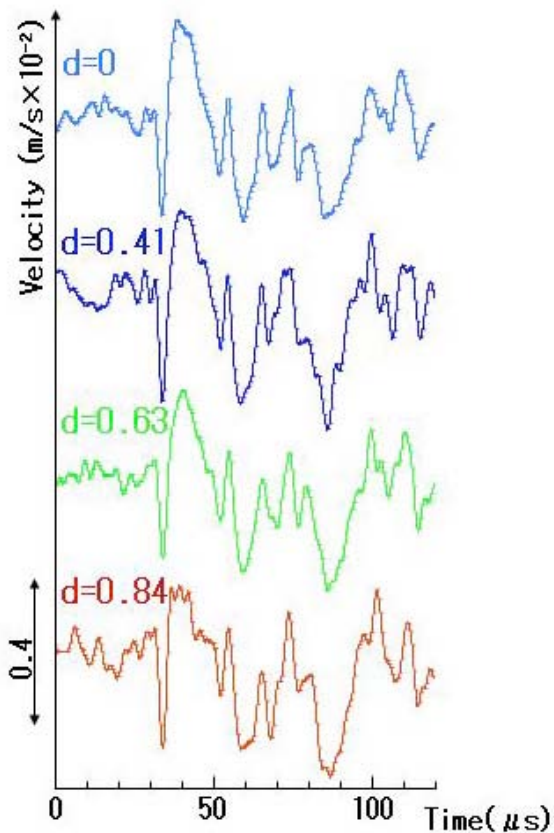


Fig. 7 Measured waveforms of samples with coating thickness of 0.0, 0.41, 0.63 and 0.84 mm.

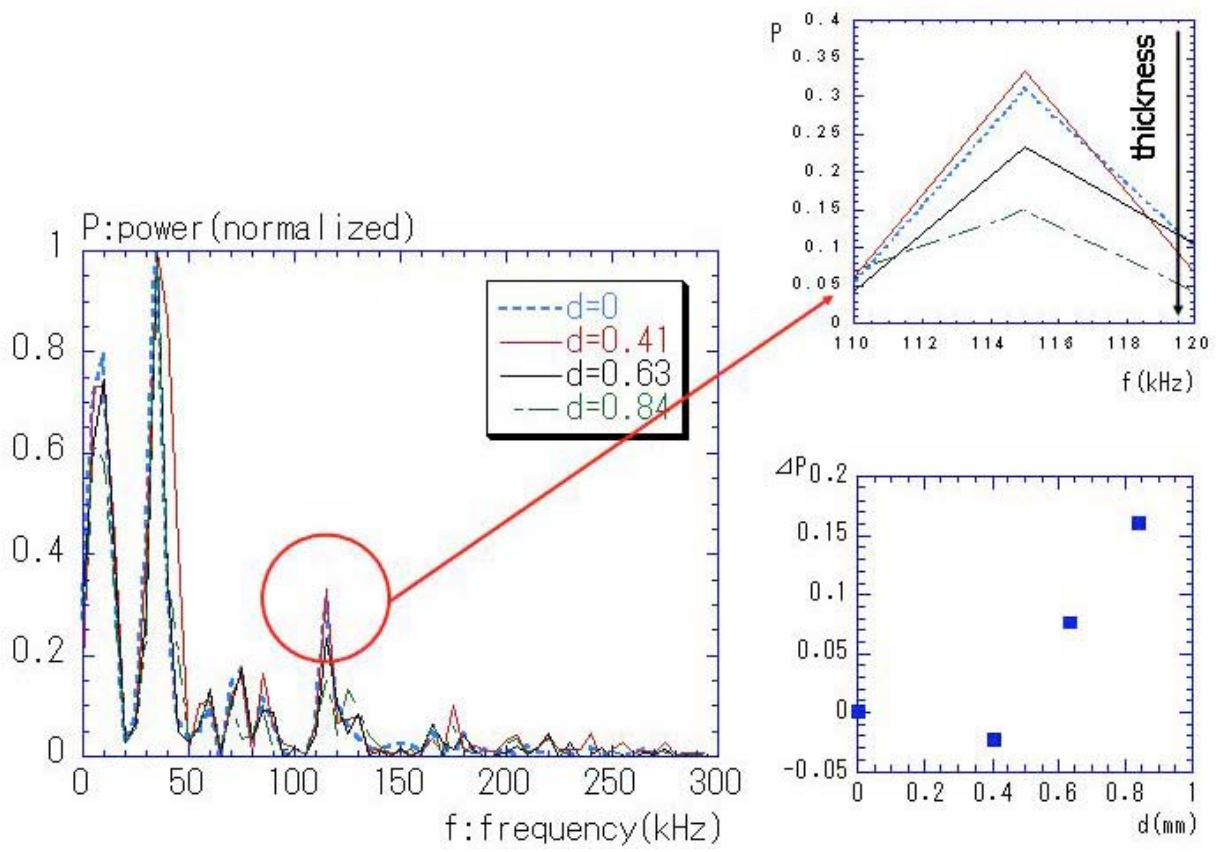


Fig. 8 Results of FFT analysis of measured waveforms, and relation between power loss and coating thickness.

ACOUSTIC EMISSION FROM MICRO-FRACTURE PROCESSES OF BIO-CERAMICS IN SIMULATED BODY ENVIRONMENT

SHUICHI WAKAYAMA, TEPPEI KAWAKAMI, SATOSHI KOBAYASHI,
MAMORU AIZAWA* and AKIRA NOZUE*

Department of Mechanical Engineering, Tokyo Metropolitan University,
Minami-Ohsawa, Hachioji, Tokyo 192-0397, JAPAN

*Department of Mechanical Engineering, Sophia University, Chiyoda, Tokyo 102-8554, JAPAN

Abstract

The micro-fracture processes during four-point bending tests of bio-ceramics were evaluated by acoustic emission technique. Alumina ceramic specimens were used as typical bio-inert ceramic materials. The tests were conducted in simulated body fluid (SBF), air and deionized water. In order to characterize the micro-fracture process, AE signals during tests were detected. In the AE generation pattern, both cumulative AE event and energy started to increase rapidly before the final unstable fracture. It is known that the stress at this critical point, σ_C , corresponds to critical stress for the maincrack formation due to the coalescence of micro-cracks and/or pores. The values of σ_C had similar tendency to the fracture strength, i.e. it decreased in the simulated body environment. However, it is important from the viewpoint of fatigue strength that the decrease in σ_C was significantly larger than the bending strength especially in SBF. Consequently, the critical stress, σ_C , could be used as a new evaluation parameter, which is essential for the long-term reliability of bio-ceramic materials.

Key Words: Bioceramics, Bending test, Micro-fracture process, Maincrack formation, Simulated body fluid

1. Introduction

Ceramics has recently been used as substitute biomaterials because of its high biocompatibility and biosafety; for example, femoral balls in total hip prosthesis, immediate replacement of tooth roots after extractions, of diseased parts of person [1-3]. Since these applications require surgical procedures with severe physical and mental damage to patients, successful application requires a detailed understanding of the time-dependent behavior so that accurate failure prediction and reliability assessment of lifetime can be made under body environment. Therefore, it is necessary to investigate mechanical properties, especially the long-term reliability such as fatigue strength.

We have investigated the micro-fracture processes during bending tests of alumina ceramics using AE technique [4,5]. It was found in the previous study that the main crack was formed due to the propagation and/or coalescence of micro-cracks and became the origin of the final unstable fracture. The critical stress for main crack formation, σ_C , was determined and its properties were also investigated.

The objective of the present study is to establish the method to assess the long-term reliability of ceramics under body environment based on the critical stress concept. Four-point bending tests were carried out in air, deionized water and the simulated body fluid (SBF) in order

to investigate the dependence of micro-fracture process on environments. The micro-fracture process during bending tests was evaluated by AE technique. Especially, the critical stress for maincrack formation was determined and the influence of the environments was investigated.

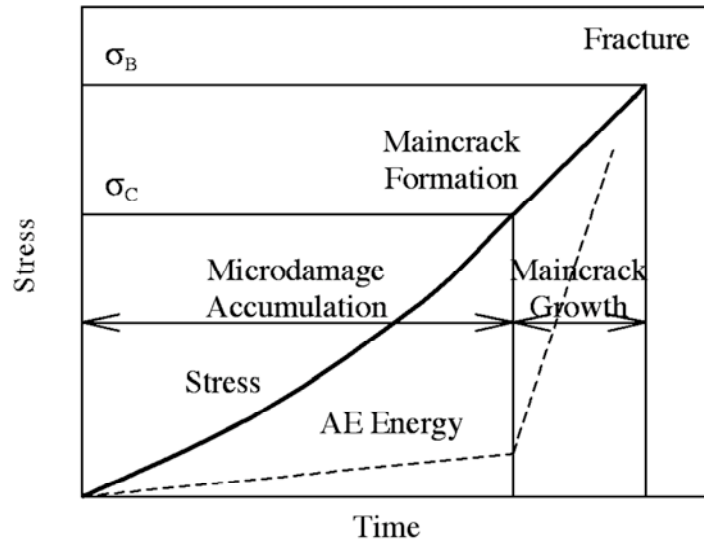


Fig. 1 Schematic representation of the AE behavior during bending tests of ceramics.

2. Critical Stress for Maincrack Formation

The authors carried out four-point bending tests of alumina ceramics and detected AE signals in the previous study [4,5]. Typical AE behavior is schematically shown in Fig. 1. It is important to note that the rapid increase in AE energy was observed before final fracture. Linear location of AE sources showed that the micro-crack sites were distributed widely over the inner span before the point of AE increase and they were concentrated after the point to the location corresponding to final failure. Furthermore, the observation of fracture process using the fluorescent-dye penetrant technique demonstrated that these AE behaviors corresponded to the maincrack formation. Thus, the micro-fracture processes during bending test consist of micro-damage accumulation, maincrack formation and its growth to final fracture. This strongly suggested that the critical stress for the maincrack formation, σ_C , has an essential role for the long-term reliability of bioceramics rather than the bending strength, σ_B .

The values of σ_C were measured under various loading rates. σ_C decreased with decreasing loading rates, which might be the influence of the stress corrosion cracking by water. It was also observed that the water content of specimen decreases the value of σ_C . However, these results were obtained by the bending tests in air. Therefore, the present investigations were carried out under the simulated body environment.

3. Experimental Procedure

Specimens

Two types of alumina ceramics, ADS-11 and SAPPHAL (Toshiba Ceramics Co., Ltd., Japan), were used to examine the influence of purity on fracture behavior. The properties of these materials are presented in Table 1 and the microstructures are shown in Fig. 2. It can be seen in the figure that ADS-11 (purity of 99.5%) has more intergranular glassy phases than SAPPHAL (purity of 99.97%).

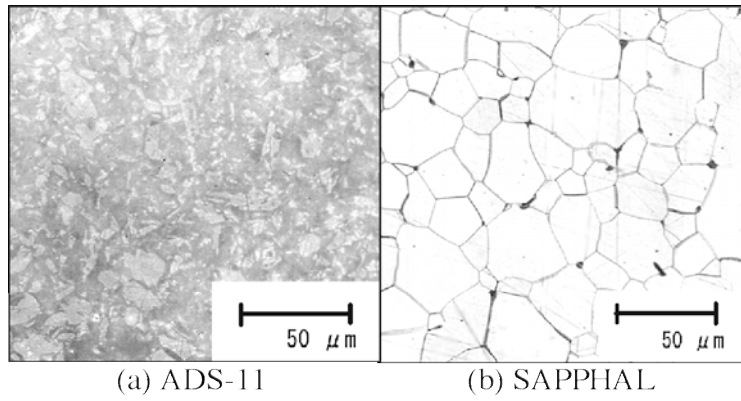


Fig. 2 Microstructure of test materials. (a) ADS-11; (b) SAPPHAL.

Table 1 Material Property

	ADS-11	SAPPHAL
Purity [%]	99.5	99.97
Density [g/cm^3]	3.9	3.99
Grain Size [mm]	6	25
Elastic Modulus [GPa]	360	390
Fracture Toughness [$\text{MPa} \sqrt{\text{m}}$]	4.5	4

The size of a specimen was 3 x 4 x 40 mm. The specimens were cut from sintered blocks by diamond wheel and polished with diamond paste. To minimize the effect of water content on fracture process, specimens were dried in vacuum drying oven at 150°C for 2h.

Bending Tests and AE Measurement

Bending tests were carried out in three environments; air, deionized water and the simulated body fluid (SBF). SBF is an aqueous solution with ion concentrations that were almost equal to those of human blood plasma [6].

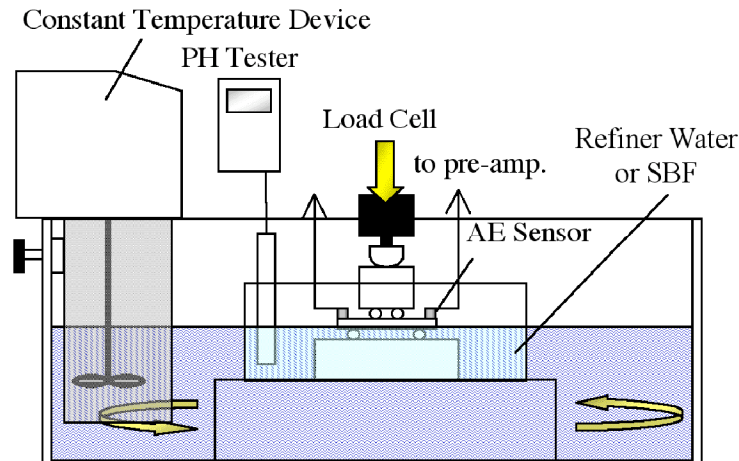


Fig. 3(a) Schematic diagram of bending testing system in water and SBF.

The testing system in water and SBF is shown in Fig. 3(a). Four-point bending tests were conducted with the inner span of 10 mm and the outer span of 30 mm at a loading rate of 0.1 mm/min according to JIS R 1601. Constant temperature device was used to keep the fluid temperature at $36 \pm 1^\circ\text{C}$. In SBF tests, pH tester was also used to monitor the pH balance in order

to maintain the constant condition. The fluid level was controlled so that the lower surface of the specimen was soaked in the fluid during the test. Prior to these tests, the specimens were soaked in each environment and treated in an ultrasonic bath for 30 min. in order to remove the bubbling noise during AE measurement. The bending tests in air were conducted with the same condition except for soaking before tests.

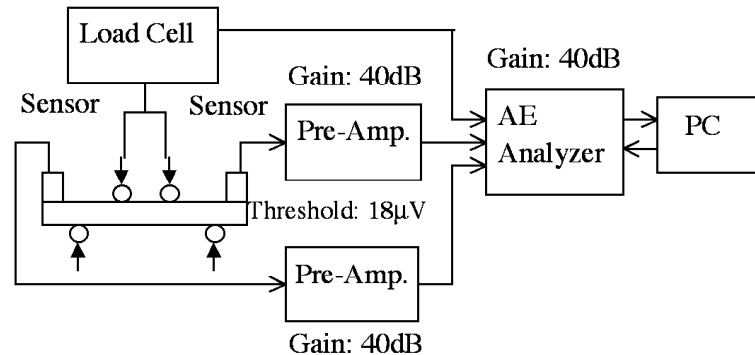


Fig. 3(b) Schematic diagram of AE measurement system.

The AE measuring system is shown in Fig. 3(b). The piezoelectric elements with 3 mm diameter and 3 mm height were used as AE sensors and attached on the top ends of the specimen. The AE signals detected by the two AE sensors were amplified by pre-amplifiers and sent to an AE analyzer. Total gain was 80 dB and threshold level was 18 μV at the input of the pre-amplifiers. The resonant frequency of sensors was 200 kHz and the bandpass filter was used with a range of 100 to 500 kHz.

4. Results and Discussion

Bending Tests and AE Behavior

The microfracture processes during bending tests were characterized using AE technique. Figure 4 shows the typical results of bending tests and AE behavior of during bending tests of ADS-11 in air (Fig. 4(a)) and SBF (Fig. 4(b)), and SAPPHAL in air (Fig. 4(c)) and SBF (Fig. 4(d)). It can be seen in Fig. 4(a) that the point of rapid rise in cumulative AE energy was detected at 370s in air, while the critical point was detected at 330s in SBF (Fig. 4(b)) in spite of nearly equivalent times to final fracture. Observed σ_C is lower in SBF than that in air. The AE behaviors of SAPPHAL (Figs. 4(c) and (d)) have the same tendency, except for larger numbers of AE events, which may be because more signals were emitted due to a larger grain size. Here, observed σ_C is much lower in SBF than that in air.

Figure 5 shows the AE source location as histogram of AE energy for ADS-11 tested in air. It can be seen in the figure that there is a peak of AE sources after the critical point (Fig. 5(b)), but such a peak is not obvious before the critical point (Fig. 5(a)). It is found that the location of the peak of AE sources corresponds to the final fracture. These results demonstrate the main crack formation due to micro-damage (micro-crack) accumulation at the critical point and its growth to final fracture. Hence the critical stress of main crack formation can be determined as the stress at the critical point, or σ_C .

Average values of bending strength, σ_B , and the critical stresses for main crack formation, σ_C , obtained for each environment, are tabulated in Table 2. It was understood that both of σ_B and σ_C decreased in the deionized water and SBF test environments. σ_C is more sensitive than

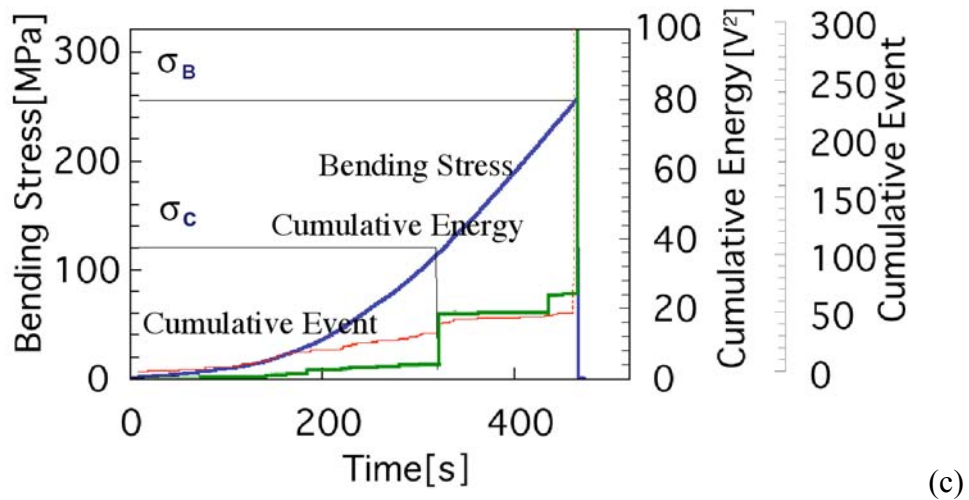
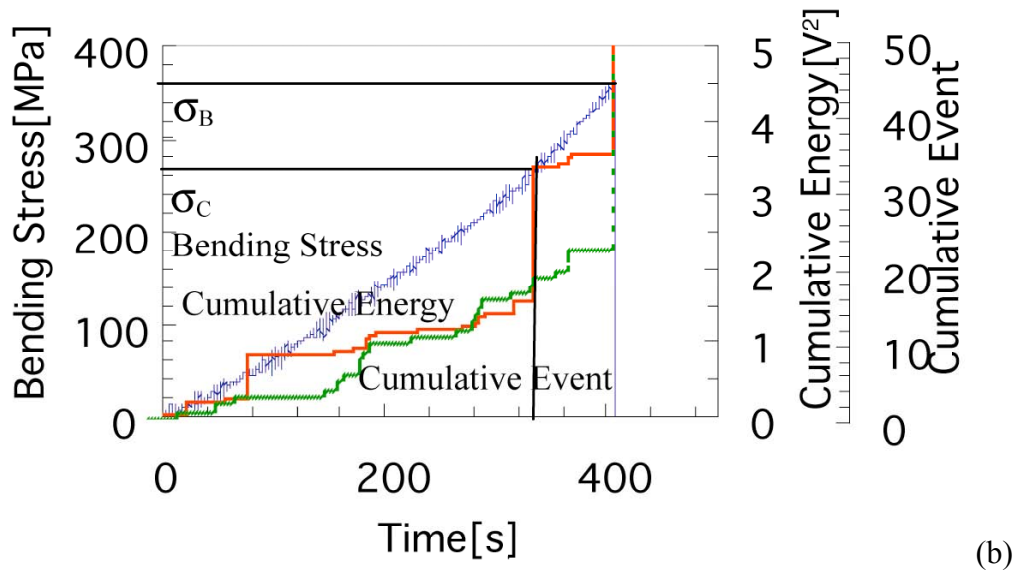
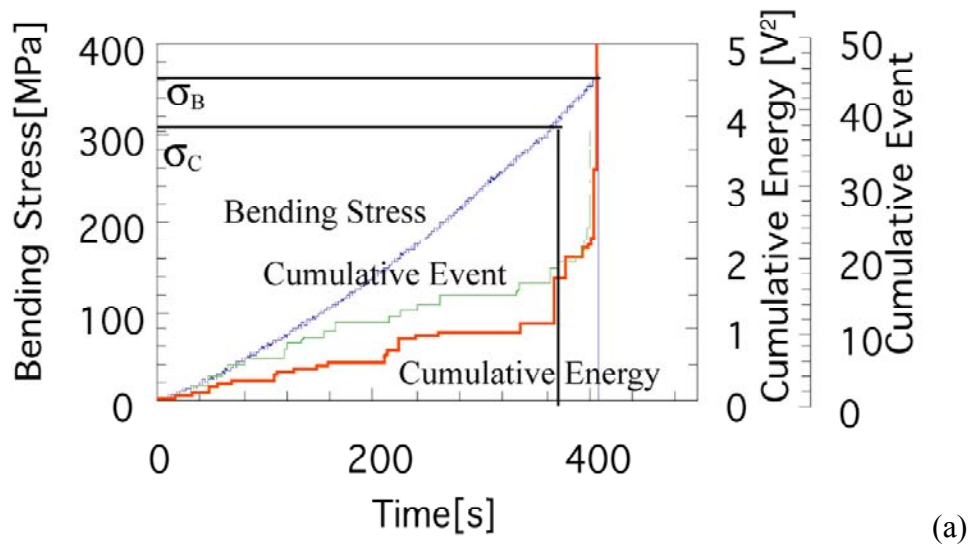


Fig. 4 Bending stress and AE behavior during bending tests. (a) ADS-11 tested in air. (b) ADS-11 tested in SBF. (c) SAPPHAL tested in air.

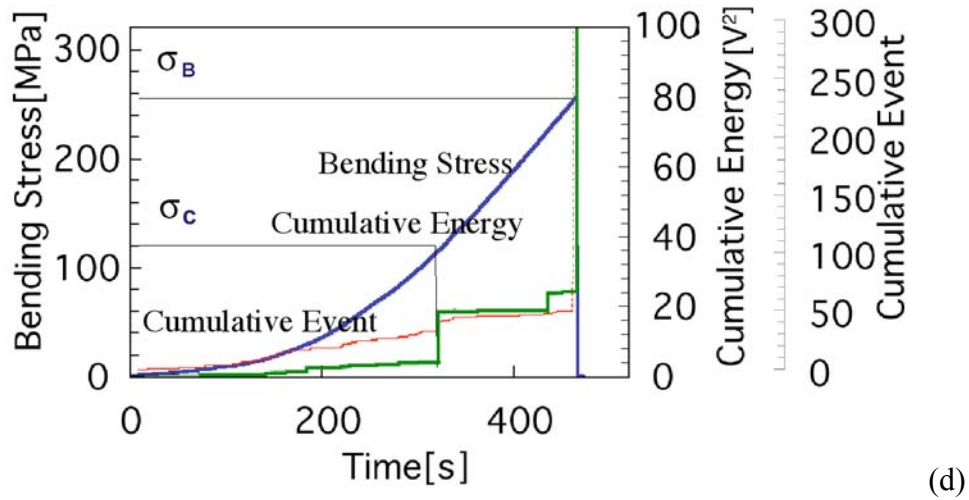


Fig. 4 Bending stress and AE behavior during bending tests. (d) SAPPHAL tested in SBF.

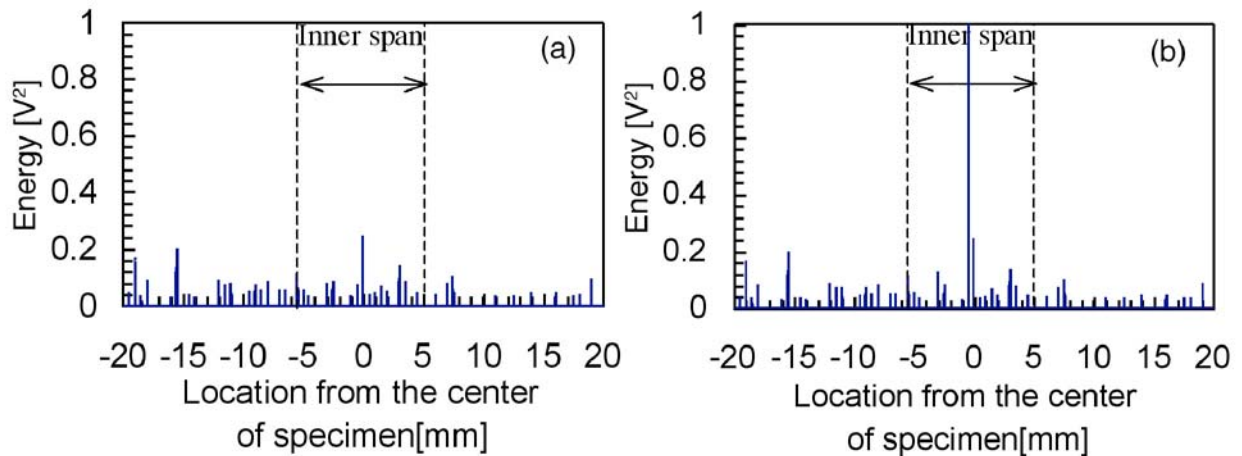


Fig. 5 Results of AE source location during bending test of ADS-11 in air. (a) Before and (b) after the point of rapid increase in AE.

σ_B in these environments. Comparing the values in water and SBF, σ_B and σ_C in SBF are smaller than those in water for ADS-11, but σ_B and σ_C are almost unchanged in water and SBF for SAPPHAL. It is worth noting that, for ADS-11, although the decrease in bending strength is small, σ_C becomes much smaller in deionized water and SBF than in air.

Table 2 Average values of σ_B and σ_C in each environment

		Air	Deionized Water	SBF
ADS-11	Ave. σ_B [MPa] (ratio)	375 (1.00)	361 (0.963)	344 (0.917)
	Ave. σ_C [MPa] (ratio)	244 (1.00)	186 (0.762)	168 (0.689)
SAPPHAL	Ave. σ_B [MPa] (ratio)	280 (1.00)	232 (0.829)	237 (0.846)
	Ave. σ_C [MPa] (ratio)	163 (1.00)	113 (0.693)	116 (0.712)

Surface Observation

The surfaces of several specimens were observed by scanning electron microscopy (SEM) before and after the tests. Figure 6 shows the micrographs of the surfaces of ADS-11. Figure 6(a) shows the surface before loading while those soaked in water and SBF without loading are shown in Figs. 6(b) and (c), respectively. Without loading, the surface morphology changed little with test environment. The micrographs of the surfaces of fractured specimens tested in air, deionized water and SBF are shown in Figs. 6(d), (e) and (f), respectively. In comparison with the surfaces before loading, significant increases in corrosion pores were observed on the surface after the water and SBF tests. Therefore, loading (i.e. tensile stress) is an important factor for corrosion behavior of ceramic materials.

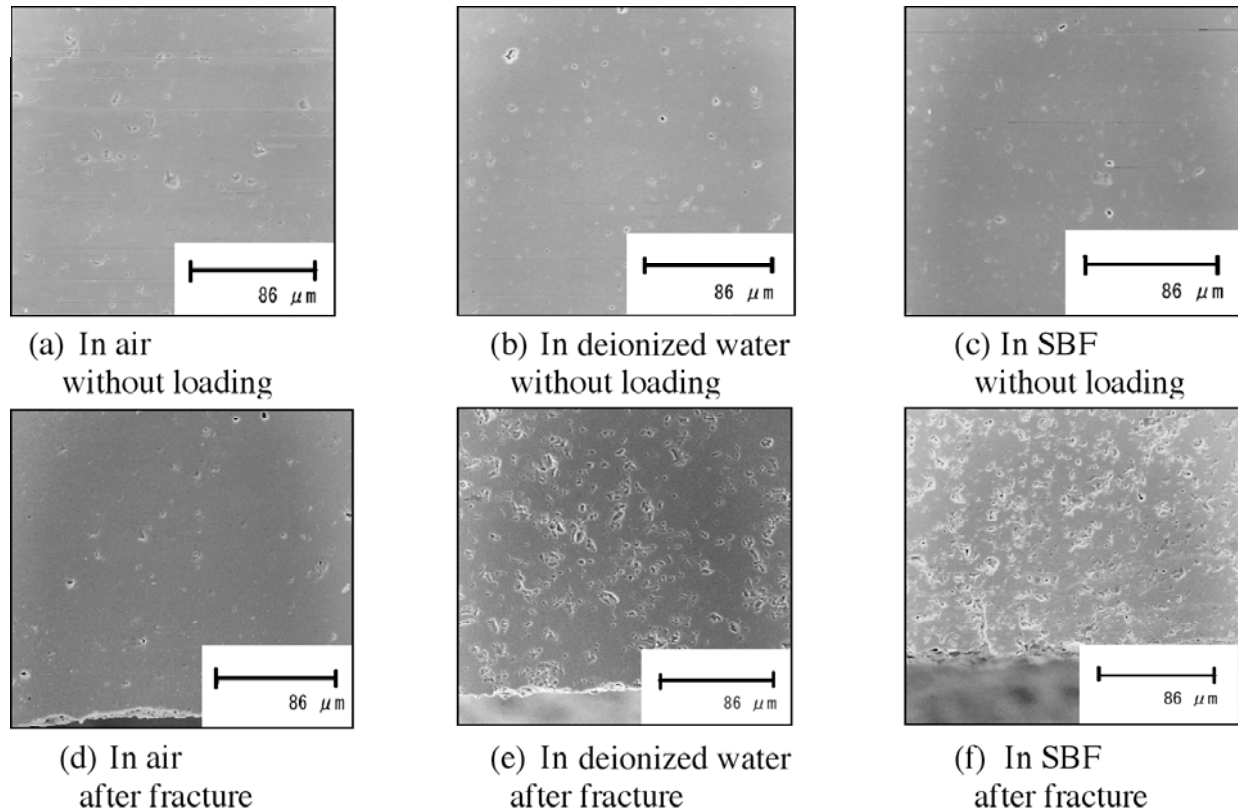


Fig. 6 Micrographs of the surface of specimens (ADS-11).

In the case of SAPPHAL also observed using SEM, however, no remarkable morphological changes of surfaces were observed in any environment. Reduced amounts of intergranular glassy phases in SAPPHAL contributed to this high corrosion resistance, confirming that the difference of purity affects the degree of corrosion of these materials.

Micro-fracture Process during Bending Tests in Environment

The micro-fracture process during bending test in liquids as well as in air consists of micro-damage accumulation, main crack formation and its growth to final fracture. A large number of pores from corrosion were observed on the surface of ADS-11 after loading in water and SBF. It implies that these pores hastened the main crack formation, and decreased the critical stress, σ_C . However, the pores also caused the crack deflection, and the decrease in bending strength, σ_B , was not large.

On the other hand, few pores were observed on the surface of SAPPHAL after fracture. Nevertheless, the decrease in σ_C due to environment was larger than σ_B . Therefore, it appears that the test environment affects the main crack formation rather than final failure. This is consistent with the previous study [4,5].

Since it was reported that the fatigue behavior of ceramics can be characterized by crack growth behavior [7], it is suggested that the main crack formation and growth are dominant in the fatigue fracture. Therefore, main crack formation might be more significant than final fracture for the long-term application. Moreover, the body environments affected σ_C more strongly than σ_B for the materials under mechanical loading, especially for materials with a large amount of intergranular glassy phases. Consequently, it is concluded that the evaluation of the critical stress for maincrack formation σ_C is important for the long-term reliability of bioceramics.

5. Conclusions

Bending tests were carried out in air, deionized water and SBF, and the micro-fracture process during the tests was evaluated by AE technique. Bending strength, σ_B , and critical stress for main crack formation, σ_C , were obtained from the results of these tests. σ_C exhibited significant decrease as compared with σ_B in corrosive environments.

Difference of purity, i.e. the amount of intergranular glassy phase, affected the degree of corrosion in environment as mechanical loading induced a significant increase in corrosion pores in ADS-11, but not in SAPPHAL. Both purity and loading are essential factors for corrosion characteristics of these materials.

The critical stress of main crack formation σ_C is essential factor to evaluate time dependent failure characteristics of ceramics structure used in the human body. Although low strain rate and static fatigue tests of other ceramic materials used as bio-materials will be required, it can be concluded that the evaluation of the main crack formation is one of the most important subject for the long-term reliability.

Acknowledgement

The authors would like to thank Toshiba Ceramics Co., Ltd. for offering materials.

References

- [1] L. L. Hench, J. Am. Ceramic Soc., **81** (7) (1998), 1705-1727
- [2] L. L. Hench and J. Wilson, *An Introduction to Bioceramics*, Advanced Series in Ceramics-Vol. 1, World Scientific, (1993), 1.
- [3] H. Aoki, and S. Tanba, *Bioceramics-Dependent and Clinical Applications*, (in Japanese), Quintessence, (1987), 26.
- [4] S. Wakayama, T. Koji and H. Nishimura, *Progress in Acoustic Emission V*, (1990), 460.
- [5] S. Wakayama, T. Koji and H. Nishimura, *Trans. Japan Soc. Mech. Eng.*, **57**, A (1991), 504.
- [6] T. Kokubo, H. Kushitani, S. Sakka, T. Kitsugi and T. Yamamuro, *J. Biomed. Mater. Res.*, **24** (1990), 721.
- [7] A. G. Evans and S. M. Wiederhorn, *Int. J. Fracture*, **10** (1974), 379.

CORROSION MONITORING IN REINFORCED CONCRETE BY ACOUSTIC EMISSION

MASAYASU OHTSU and YUICHI TOMODA

Kumamoto University, 2-39-1 Kurokami, Kumamoto 860-8555, JAPAN

Abstract

Cracking of concrete due to corrosion of reinforcement is one of critical problems in reinforced concrete (RC) structures. Here, an application of acoustic emission (AE) to corrosion monitoring is studied. In an accelerated corrosion test, AE events are detected continuously. Comparing with permeation of chloride ions, a relationship between chloride concentration and AE activity is clarified. It is demonstrated that the onset of corrosion and nucleation of cracking are readily identified by AE monitoring. Applying SiGMA procedure, generating mechanisms of a surface crack, a spalling crack, and an internal crack due to expansion of corrosive product are studied. The surface crack is nucleated dominantly by tensile cracks. For the spalling crack, both tensile and shear cracks are generated, but the former dominates near a stress-free surface. In contrast, the main mechanism of the internal crack is of shear-crack motion. Based on these findings, a strategy for repairing corroded RC members is discussed.

Key Words: Reinforced concrete; Corrosion of rebars, AE activity due to corrosion, SiGMA analysis

1. Introduction

It is widely recognized in concrete engineering today that concrete structures are not maintenance-free. A variety of activities for maintenance and repair of the concrete structures are ongoing all over the world. According to the Standard Specification for Concrete Structures on Maintenance by the Japan Society for Civil Engineers (JSCE, 2001), six representative mechanisms for concrete deterioration are recognized. These are the deterioration due to salt attack, neutralization, chemical attack, freezing and thawing, alkali-aggregate reaction, and fatigue. Out of these mechanisms, neutralization, chemical attack and alkali-aggregate reaction are actually associated with the transition of chemical contents in concrete. Thus, it is not easy to identify them nondestructively at an early stage of deterioration. Concerning the deterioration due to freezing-thawing and fatigue, it is demonstrated that the rate process analysis of acoustic emission (AE) activity in a compression test of core samples is applicable to estimate the damage degree quantitatively (Ohtsu and Watanabe, 2001).

In reinforced concrete (RC) structures, passive-alkali layer on the reinforcement in concrete is readily broken by ingress of chloride ions. Eventually, salt attack leads to the corrosion of reinforcement. Because almost of all concrete structures are reinforced by reinforcing steel-bars (rebars), the corrosion is presently considered to be the most critical deterioration in concrete structures. A variety of studies have been conducted for nondestructive inspection, nucleation mechanisms, preventive treatments, and repair techniques. As for nondestructive techniques of corrosion inspection, the measurements of half-cell potentials and polarization resistances are developed and commercially available. It is, however, reported that reliability and accuracy are still marginal.

In the present paper, an AE inspection of the corrosion is investigated. This is because in situ AE monitoring techniques have been standardized to estimate the structural integrity of the existing concrete structures (NDIS 2421, 2000; Yuyama et al., 1998). AE techniques have been extensively studied in concrete (Ohtsu, 1989) and are applied to the estimation of corroded members (Yoon et al., 2000). An applicability of AE techniques to monitor the corrosion in RC members is investigated in two tests. During an accelerated corrosion test, AE events are monitored continuously. AE activity is compared with the half-cell potentials for nondestructive evaluation of corrosion and with ingress of chloride ions. Analyzing concentration of chloride ions around rebars, we attempted to quantitatively estimate the onset of corrosion and nucleation of cracking from AE observation. In a crack-expansion test, we simulated crack patterns due to expansion of corrosive product by employing expansive agent. Then, cracking mechanisms of a surface crack, a spalling crack, and an internal crack are identified by applying SiGMA (Simplified Green's functions for Moment tensor Analysis) procedure.

2. Experiments

Mixture proportions of tested concrete are given in Table 1. In the accelerated corrosion test, two types of mixture were employed. The water-to-cement ratios (W/C) were 45 % and 55%. In the crack-expansion test, W/C of concrete was 50%. In all the mixes, sand and gravel were common and the maximum gravel size was 20 mm. Admixture was added to control the slump values and air contents. Compressive strengths were determined at 28 days after moisture-cured in the standard room (20°C). Averaged strengths of three samples were 40.9 MPa for the concrete of W/C = 45 %, 34.6 MPa for W/C = 55% and 39.1 MPa for W/C = 50 %.

In the accelerated corrosion test, reinforced concrete slabs of dimensions 10 cm x 25 cm x 40 cm were made. A sketch of the slab is shown in Fig. 1. The test was conducted as shown in Fig. 2. In a tank, a copper plate was placed at the bottom, and 100 mA electric-current was charged between rebars and the copper plate. To maintain electrical conductivity, the tank was filled with 3% NaCl solution. AE sensors of 50 kHz resonance (RA5; Physical Acoustics Corp.) were placed on the top surface as shown in Fig. 1. Amplification was 40 dB gain in total and the frequency range was set from 10 kHz to 200 kHz. AE hits under accelerated corrosion were detected continuously. After the tests, core samples (see Fig. 1) were taken and crashed. Chloride contents were measured by the potentiometric titration.

Table 1 Mixture proportions of concrete

Test	W/C (%)	Air contents (%)	Slump values (cm)	Unit weight per volume (kg/m ³)			
				Water	Cement	Sand	Gravel
Accelerated test	45	5.2	3.5	175	389	686	1138
	55	6.8	7.7	176	321	741	1179
Crack-expansion test	50	5.5	4.1	162	323	853	1072

In the crack-expansion test, a concrete plate of dimensions 10 cm x 25 cm x 25 cm was made. In order to simulate radial pressure due to corrosion product, expansive agent of dolomite paste was poured into a hole of 30 mm diameter as shown in Fig. 3. The specimen corresponds to a cross-section of a reinforced concrete (RC) member. A 6-channel AE system was employed to record AE waveforms as shown in Fig. 4, and SiGMA analysis was performed from detected waveforms.

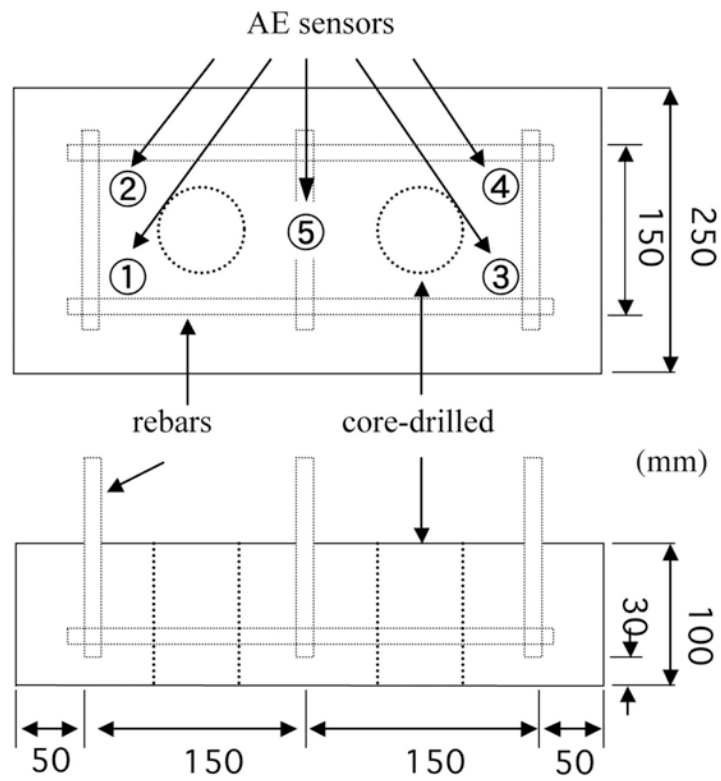


Fig. 1 Sketch of reinforced concrete slab for an accelerated test.

3% NaCl solution

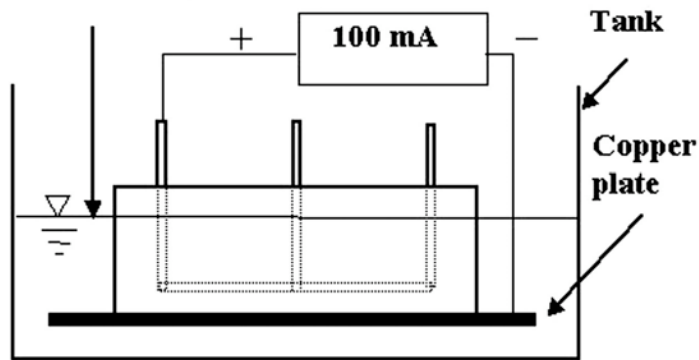


Fig. 2 Accelerated corrosion test.

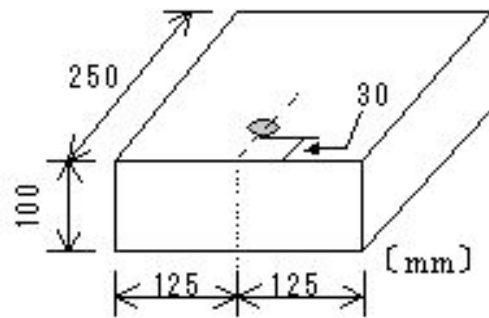


Fig. 3 Specimen in a crack-expansion test.

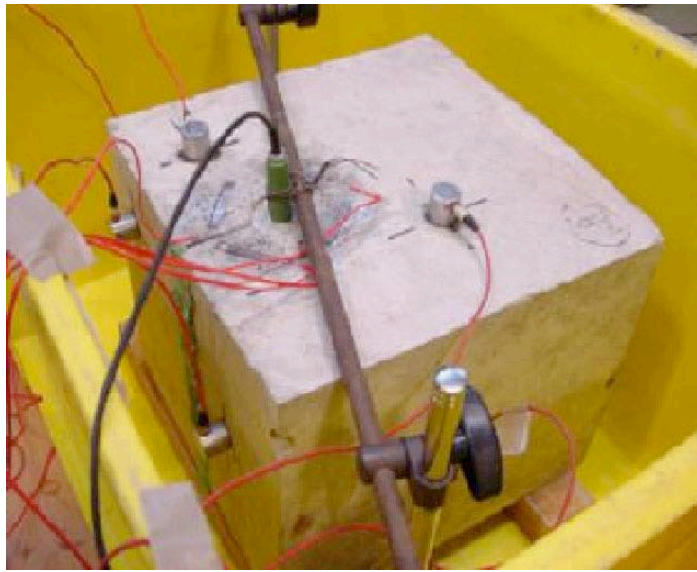


Fig. 4 Setup for the crack-expansion test.

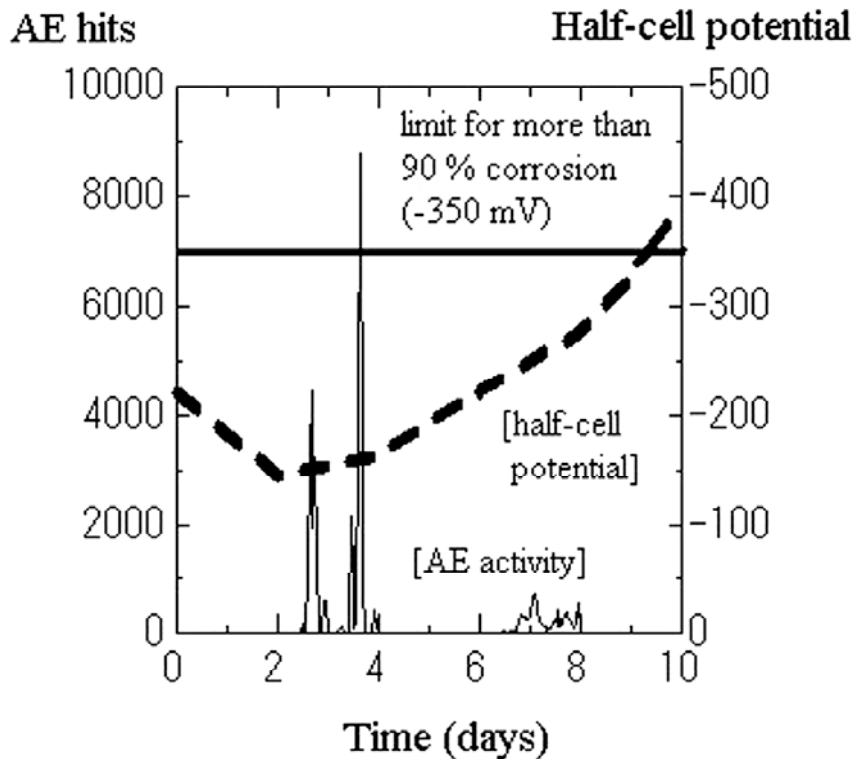


Fig. 5 AE activity and half-cell potential vs. time during accelerated corrosion (W/C=55%).

3. Results and Discussion

Accelerated Corrosion Test

Three specimens were prepared for each W/C ratio, and the chloride contents were measured after accelerated corrosion. For W/C = 45%, core samples were taken at 4 days, 10 days, and 12 days elapsed, while for W/C = 55% at 4 days, 8 days, and 10 days elapsed. These periods are determined from a comparison between AE activity and half-cell potentials. One example in the

specimen of W/C = 55% is given in Fig. 5. High AE activities are observed at two stages of 3 days and 7 days elapsed. For nondestructive evaluation of corrosion, the half-cell potential measurement is normally carried out. From the potentials measured at the surface, the probability of corrosion is estimated as more than 90% when the potentials are lower than -350 mV. As seen in Fig. 5, the potentials start to decrease, around at the first AE activity (finished at 4 days). Then the potential reaches lower than -350 mV after 10 days, following the second AE activity (finished at 8 days). Consequently, the test of one specimen for W/C = 55% was finished at 4 days, and the other was completed at 8 days. The third specimen was conducted up to 10 days. Results in Fig. 5 reveal that AE activities could provide earlier warning than the half-cell potential measurement.

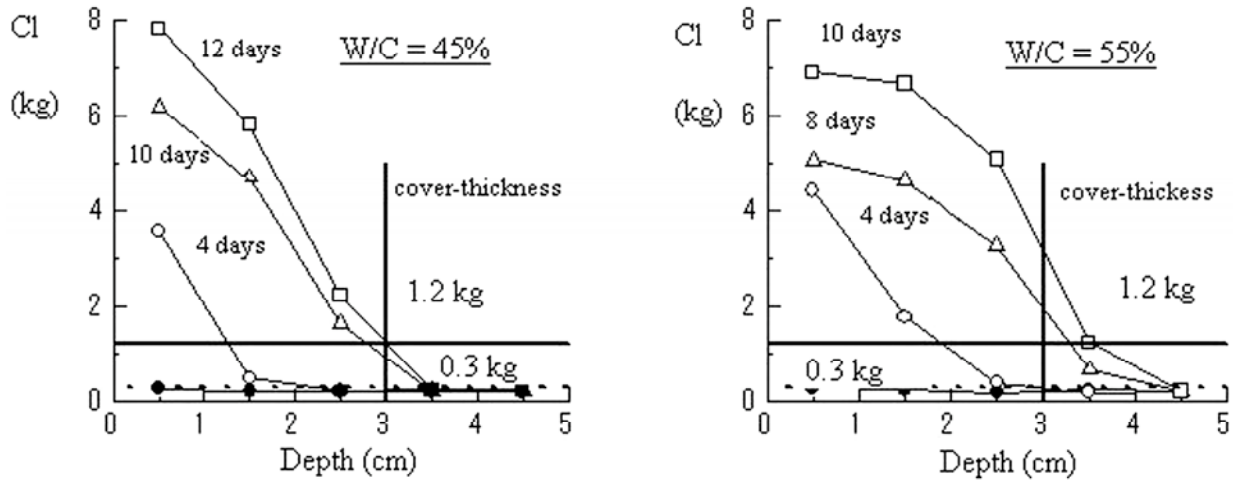


Fig. 6 Distribution of chloride ions in depth.

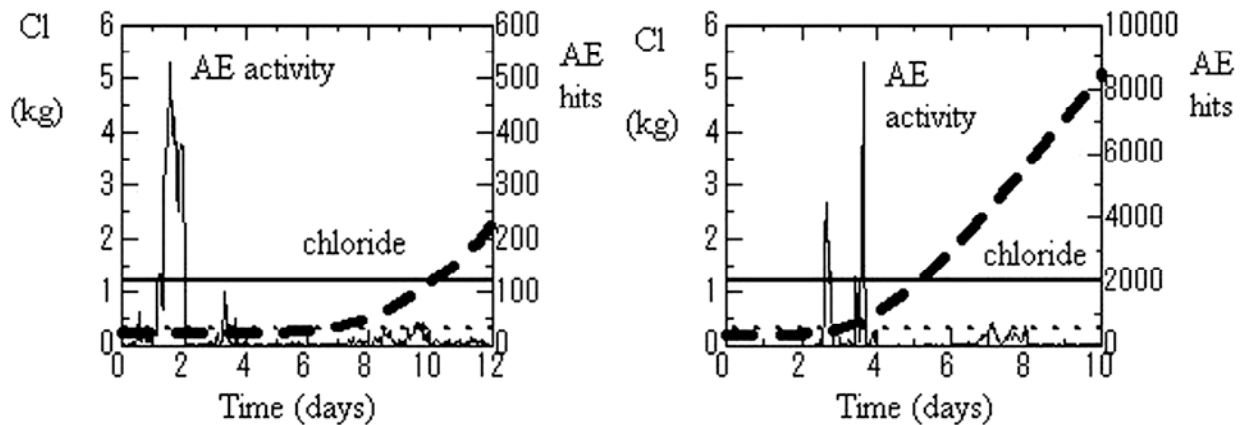


Fig. 7 Comparison between AE activities and chloride contents.

Distribution of chloride contents in depth was determined, and results are given in Fig. 6. At the location of concrete cover, chloride ions per m^3 becomes higher than 1.2 kg after 12 days in a sample with W/C = 45%. In contrast, it reaches over 1.2 kg after only 8 days for W/C = 55%. This is because the permeability increases with an increase in W/C ratio in concrete. According to the Standard Specification (JSCE, 2001), the lower and upper bounds for triggering corrosion are prescribed as 0.3 kg/m^3 and 1.2 kg/m^3 , respectively. Consequently, the amount of chloride contents, $C(t)$, was computed at cover-thickness based on Fick's law,

$$C(t) = C_0 (1 - \text{erf}(x/2[Dt]^{1/2})), \quad (1)$$

where C_0 is the surface concentration, D is diffusion coefficient, t is time and erf is Gauss's error function. Results are compared with AE activities in Fig. 7. Here, chloride contents in concrete were determined first from potentiometric titration. The surface concentration and the diffusion coefficient were estimated by the regression analysis, by fitting the distribution using Eq. 1. Obtained values of the surface concentration, C_0 , and the diffusion coefficient, D , are 10.02 kg/m^3 and $6.05 \times 10^{-8} \text{ cm}^2/\text{sec}$, respectively..

Right after the chloride contents become higher than the lower bound (0.3 kg), the first high AE activity is observed in both cases of $W/C = 45\%$ and 55% . At the stage where the chloride content exceeds the upper bound (1.2 kg), another high AE activity is observed. These results demonstrate that high AE activities of the two stages are observed in the accelerated corrosion test. One is the stage where the chloride content reaches 0.3 kg/m^3 , and the other is the stage where the chloride level becomes higher than 1.2 kg/m^3 in concrete.

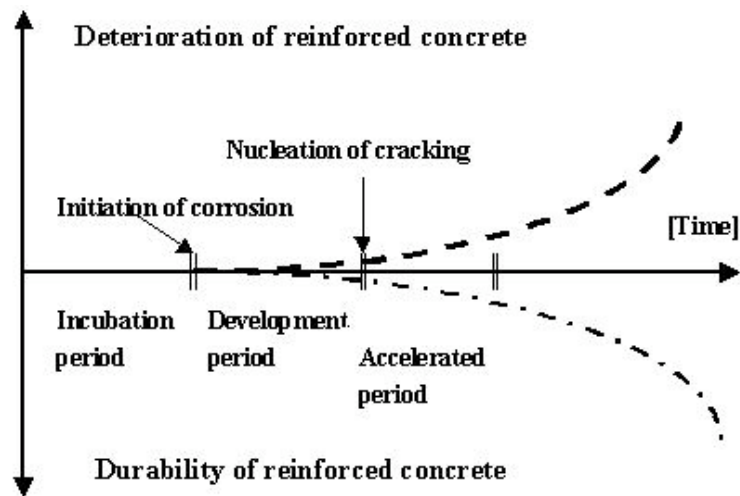


Fig. 8 Deterioration process due to salt attack.

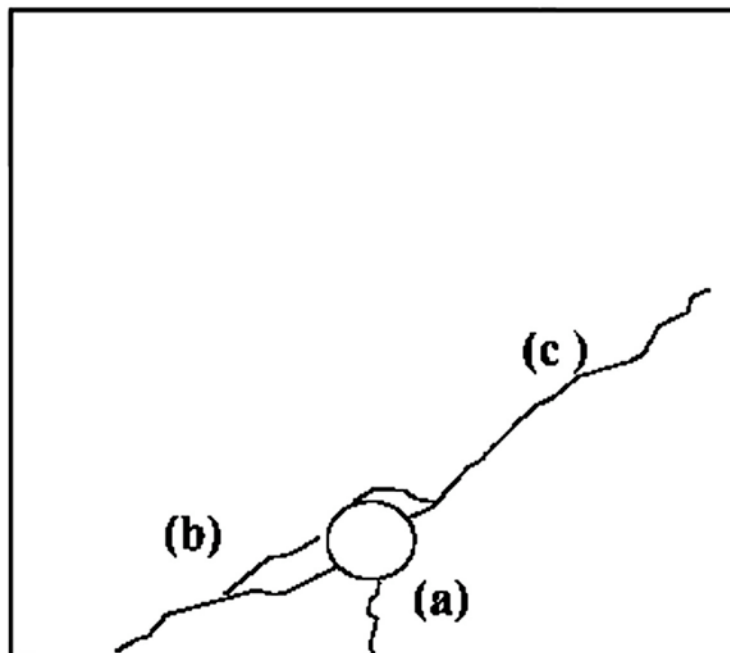


Fig. 9 Crack patterns observed after the test.

These are in remarkable agreement with the deterioration process due to salt attack, which is prescribed in the Standard Specification. According to the process shown in Fig. 8, there exist the first stage for the initiation of corrosion from the incubation to the development period, and the second for the nucleation of cracking from the development period to the accelerated corrosion.

Characterization of Corrosion Cracks by SiGMA

Nucleation of typical corrosion cracks was simulated by employing expansive agent. A hole of 30 mm diameter to represent the rebar location was made at 3 cm depth from the side, corresponding to 3 cm cover-thickness. After casting expansive agent into the hole, surface cracks were observed after two days. During extension of these cracks, AE events were detected by six AE sensors as shown in Fig. 4. After the test, SiGMA analysis was conducted. Three main cracks observed are shown in Fig. 9, which are labeled as crack traces (a), (b), and (c). In reference to the cross-section of a reinforced concrete member this model simulates, crack trace (a) corresponds to a surface crack, which is normally observed as corrosion cracking. Crack trace (b) is commonly observed as a spalling crack due to corrosion. An internal crack (crack trace (c)) is generally not taken into account, because this is inaccessible to usual visual inspection.

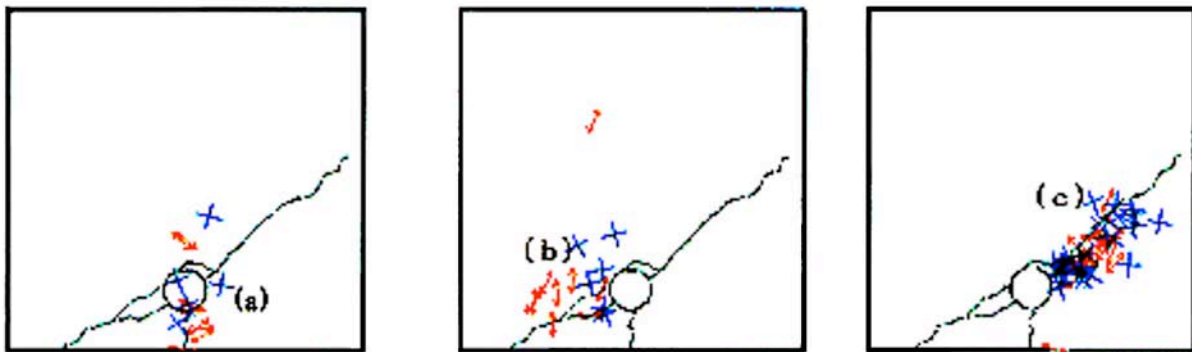


Fig. 10 Results of SiGMA analysis classified in three clusters.

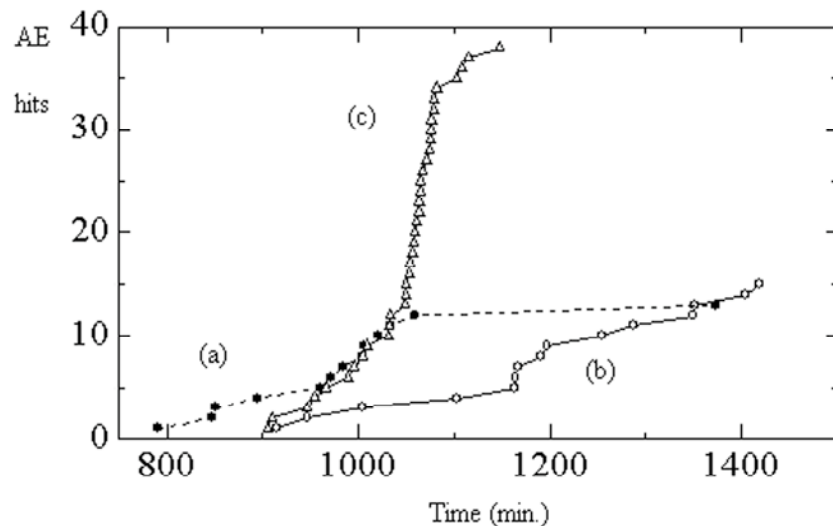


Fig. 11 AE activities during crack nucleation.

AE events analyzed by SiGMA procedure were first located, and then were classified as three clusters responsible for crack traces (a), (b) and (c) from Fig. 9. All the results of SiGMA analysis are plotted in Fig. 10. AE events analyzed are marked with arrow or cross symbols. The arrow symbol represents a tensile crack, and the arrow direction indicates the crack opening direction. Shear cracks are denoted by cross symbols, and their two orientations correspond to the crack motion vector and the crack normal vector, respectively.

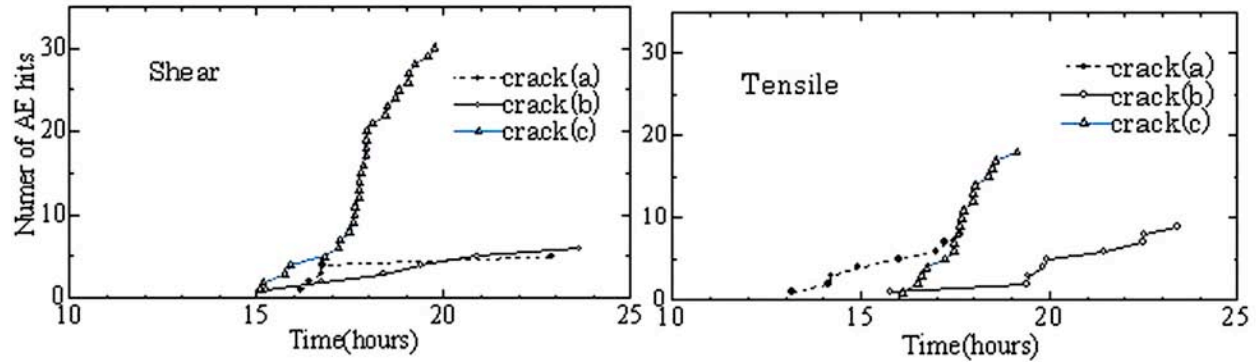


Fig. 12 AE activities classified into shear and tensile cracks.

Concerning crack trace (a), tensile cracks running vertically to the surface are mostly visible from outside. In contrast, shear cracks are not explicitly associated with the extension of surface-breaking cracks. For crack trace (b), tensile cracks are primarily observed at the locations far from the reinforcement or close to the stress-free surface, while shear cracks are mostly observed near the reinforcement. In crack trace (c), tensile and shear cracks are fully mixed up.

In order to elucidate cracking mechanisms on these three crack traces, activities of AE events are plotted in Fig. 11, after classifying into tensile cracks and shear cracks. It is obvious that in the beginning, crack trace (a) is created, followed by crack traces (b) and (c). In Fig. 12, AE events of tensile and shear cracks are separately plotted. It is found that crack trace (a) propagates as the tensile cracks. For both crack traces (b) and (c), tensile cracks are nucleated as well as shear cracks. In particular, activity of shear cracks is higher than that of tensile cracks in the case of crack trace (c). Thus, we find that cracking mechanisms are different, depending on crack traces. The surface crack or trace (a) is first observed due to corrosion and AE events are generated as tensile cracks along the final crack surface. The spalling crack or trace (b) is nucleated as a mixture of tensile and shear cracks. Approaching to the surface, tensile cracks are predominant over shear cracks. The internal crack or trace (c) is generated diagonally to the surface and consists mostly of shear cracks.

In actual practice of visual inspection, the detection of surface and spalling cracks is the main target for inspection. By monitoring the nucleation of tensile cracks by applying SiGMA procedure, it is possible to estimate and predict the extension of these two types of cracking. It is noted that internal cracks could be generated following the surface cracks. This must be taken into account in visual inspection, because the presence of the internal cracks could lead to the loss of durability of an entire structure.

4. Conclusion

In order to inspect the corrosion of rebars nondestructively, practical electro-chemical techniques of the half-cell potential and the polarization resistance have been developed. Because

their reliability and accuracy are still marginal, an application of AE to corrosion cracking is studied. Results obtained are summarized, as follow:

1. In the accelerated corrosion tests, AE occurrence is monitored continuously. Investigating ingress of chloride ions, a relationship with chloride concentration and AE activity is obtained. Right after the chloride contents become higher than 0.3 kg/m^3 , a high AE activity period is observed. Subsequently, at the stage where the chloride contents become higher than 1.2 kg/m^3 , another high AE activity period is observed.
2. Two stages of high AE activities are observed in the accelerated corrosion test, which remarkably correspond to the two stages in the deterioration process due to salt attack. These are the initiation of corrosion from the incubation period to the development and the nucleation of cracking from the development period to the accelerated. This suggests that these two stages are possibly identified by in situ AE monitoring.
3. The corrosion probability by the half-cell potential reaches over 90% after the appearance of these two stages. It confirms that AE monitoring could provide earlier warning of corrosion than the half-cell potential measurement.
4. Applying SiGMA procedure, nucleation mechanisms of a surface crack, a spalling crack, and an internal crack due to the expansion of corrosion product are identified. The surface-breaking crack is nucleated dominantly by tensile cracks. For the spalling crack, both the tensile and the shear cracks are generated. Tensile cracking is dominant near a stress-free surface, but the main mechanisms of the internal crack is of shear-crack motion.
5. In the case of visual inspection, the detection of the surface and spalling cracks is the main target. Monitoring the nucleation of tensile cracks by applying SiGMA procedure, it is possible to estimate and predict the extension of these two types of cracking. It is noted that the internal crack could be generated following the surface crack, and the main mechanism of the internal crack is of shear. Even though the cover concrete and the reinforcement are repaired, this implies that the internal crack may still exist and could result in the loss of durability.

References

- JSCE (2001), Standard Specification for Concrete Structures on Maintenance, Concrete Committee, Japan Society for Civil Engineers.
- JSNDI (2000), Recommended Practice for In-Situ Monitoring of Concrete Structures by Acoustic Emission, NDIS 2421, Japanese Society for Non-Destructive Inspection.
- Ohtsu, M. (1989), "A Review of Acoustic Emission in Civil Engineering with Emphasis on Concrete," *Journal of AE*, **8**(4), 93-98.
- Ohtsu, M., Okamoto, T. and Yuyama, S., (1998), "Moment Tensor Analysis of Acoustic Emission for Cracking Mechanisms in Concrete," *ACI Structural Journal*, **95**(2), 87-95.
- Ohtsu, M. and Watanabe, H. (2001), "Quantitative Damage Estimation of Concrete by Acoustic Emission," *J. Construction and Building Materials*, **15**, 217-224.
- Yoon, D. J., Weiss, W. and Shah, S. P. (2000), "Assessing Damage in Corroded Reinforced Concrete using Acoustic Emission," *J. Engineering Mechanics*, ASCE, **126**(3), 189-194.
- Yuyama, S., Okamoto, T., Shigeishi, T., Ohtsu, M. and Kishi, T. (1999), "A Proposed Standard for Evaluating Structural Integrity of Reinforced Concrete Beams by Acoustic Emission," *Acoustic Emission: Standards and Technology Update*, ASTM STP 1353, 25-40.

EVALUATION OF BOND BEHAVIOR OF REINFORCING BARS IN CONCRETE STRUCTURES BY ACOUSTIC EMISSION

K. IWAKI, O. MAKISHIMA, H. TANAKA, T. SHIOTANI and K. OZAWA*

Research Institute of Technology, Tobishima Corp., Kimagase 5472, Sekiyado, Chiba, 270-0222, Japan. * Graduate School of Frontier Sciences, University of Tokyo
Hongo 7-3-1, Bunkyo, Tokyo, 113-0033, Japan.

Abstract

In reinforced concrete structures, a poor bond between concrete and reinforcements develops when compaction causes insufficient mechanical properties or induces corrosion of steel bars. In order to investigate such bond behavior due to compaction of concrete, concrete walls made of two different conditions of compaction and a wall made of SQC (super quality concrete; high strength and self-compacting concrete) were subjected to pull-out tests of steel bars. In evaluating temporal and spatial evolution of cracking during the pull-out tests, AE measurements are conducted. Attention is paid to mechanical engagement between ribs of steel bars and concrete. Visual observation is also made for the sections of cored samples from the walls, and rifts between steel bars and concrete are measured. The results indicate that lower AE activities around steel bars show the locations of insufficient bond area, where it is also difficult to distribute stress of steel bars to concrete. The bond behavior of a conventional concrete is directly influenced by means of compaction, whereas stable bond behavior irrespective of the compaction is observed in the SQC.

Key Words: Reinforced concrete; Bond behavior; Self-compacting concrete; Compaction; Pull-out test

1. Introduction

In order to construct reliable and durable concrete structures in the field, elaborate effort of compaction of concrete is important since the compaction significantly influences the quality of concrete structures. Contrary to the conventional concrete, self-compacting concrete (SCC) has no requirement for compaction using vibration, and can reduce the initial defects of concrete structures [1]. In reinforced concrete structures, a poor bond between concrete and steel bars develops when compaction causes insufficient mechanical properties or induces corrosion of the steel bars. The SCC can decrease both segregation and bleeding that degrade the quality of interfaces between cement paste and steel bars. Super quality concrete (SQC) is a variety of SCC and has high strength and high durability [2]. The SQC has been developed to design economical concrete structures and reduce the maintenance cost [3]. A preliminary study on bond property of SQC in laboratory tests can be seen in reference [4], and the high performance of bond property was reported in the SQC. However, filling property around steel bars in full-scale structures, namely bond behavior of SQC has not yet been evaluated. Also in conventional concrete, details of bond behavior influenced by conditions of compaction have not so far been studied.

In the present study, the bond behavior influenced by compaction is studied with three full-scale walls, made by three different compaction methods, namely two different compactions of a conventional concrete and SQC (which performs self-compaction). Pull-out tests of the steel bars

embedded in the wall are carried out for the three walls. Acoustic emission (AE) measurement is performed to evaluate temporal and spatial evolution of cracking during the tests. Visual observations of defects are also performed on sections of samples cored from the walls.

2. Experiment

Experimental walls

An SQC mixture (identified as S) and a conventional concrete mixture (identified as N) are shown in Table 1. An experimental wall was cast by the SQC without compaction. Two other walls were cast using N mixture with different conditions of compaction as indicated by N1 and N2. Table 2 shows the three conditions of placement accompanied with compaction. The horizontal movement shows long side direction of the wall. The SQC was deposited at an edge of the wall and allowed to flow 8 m to the other edge without compaction. As shown in Fig. 1, nine high-strength deformed steel bars (USD685) of 25 mm diameter, which were used for pull-out tests, were embedded horizontally in each wall. As shown in Fig. 2, a bond length of each steel bar was 150 mm, whereas the remaining length was isolated. Next to each bar, nine deformed normal-strength steel bars (SD345) of 25 mm diameter were also embedded for visual observation. To evaluate effects of segregation and bleeding, these steel bars were located on three elevations as denoted by upper (U), middle (M) and lower (L) groups consisting of three bars each. In this paper, experimental cases are represented by e.g. “N1-L”, which stands for placing condition: N1 and elevation level: L.

Table 1 Mix proportions of conventional concrete (N) and SQC (S).

Mixture No.	Slump flow (cm)	Slump (cm)	W/C (%)	Max. agg. size (mm)	Unit content (kg/m ³)				
					Cement	Water	Sand	Gravel	Admixture
N	-	12	57.5	20	289 ^{*1}	166	862	982	2.89 ^{*2}
S	65	-	29.6	20	551 ^{*3}	163	813	798	5.79 ^{*4}

*1: Ordinary Portland cement, *2: Water reducer, *3: Low heat Portland cement, *4: Superplasticizer

Table 2 Placement conditions.

Wall No.	Height of a lift	Placing		Compaction	Vibration			Horizontal movement
		Speed	Pitch		Interval	Insert depth	Duration	
N1	40-50 cm	3.0 m/hr	1.5 m	High freq. internal vibrator	50 cm	10 cm into lower layer	5-15 sec	Unavailable
N2	100-150 cm	6.0 m/hr	4.0 m		100 cm	50 cm into lower layer	20-30 sec	Available by vibration
S	Continuous placement	6.0 m/hr	From one point only	None	-	-	-	8.0 m

Pull-out test with AE measurement

The steel bar was pulled out by a center-hole jack after aging 56 days. Averaged compressive strengths of cored samples from walls of N1, N2 and S were 34.8, 36.9 and 85.0 MPa, respectively. During the tests, pull-out load and displacement at the end of the steel bars were measured. Simultaneously, AE measurement was performed with a MISTRAS AE system with eight channels (Physical Acoustics Corp.). AE signals detected by AE sensors of 60 kHz resonance were fed to the system for digital signal processing. Eight AE sensors were placed onto the walls as shown in Fig. 2. Based on in-situ elastic wave velocities, 3D location of AE sources were

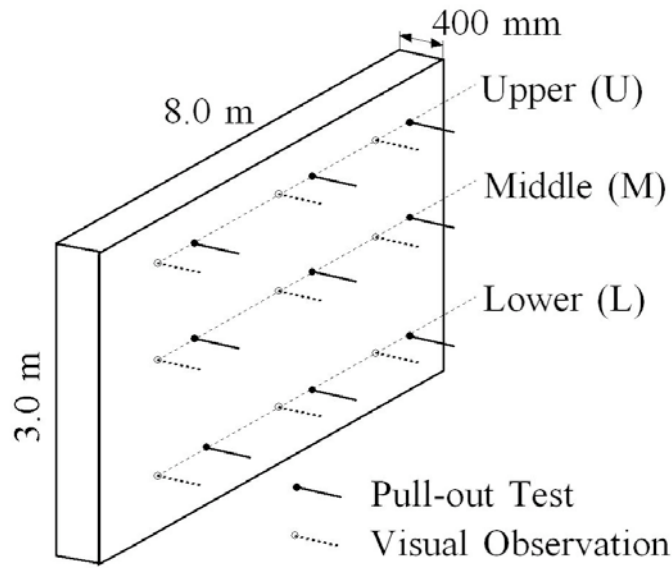


Fig. 1 An experimental wall.

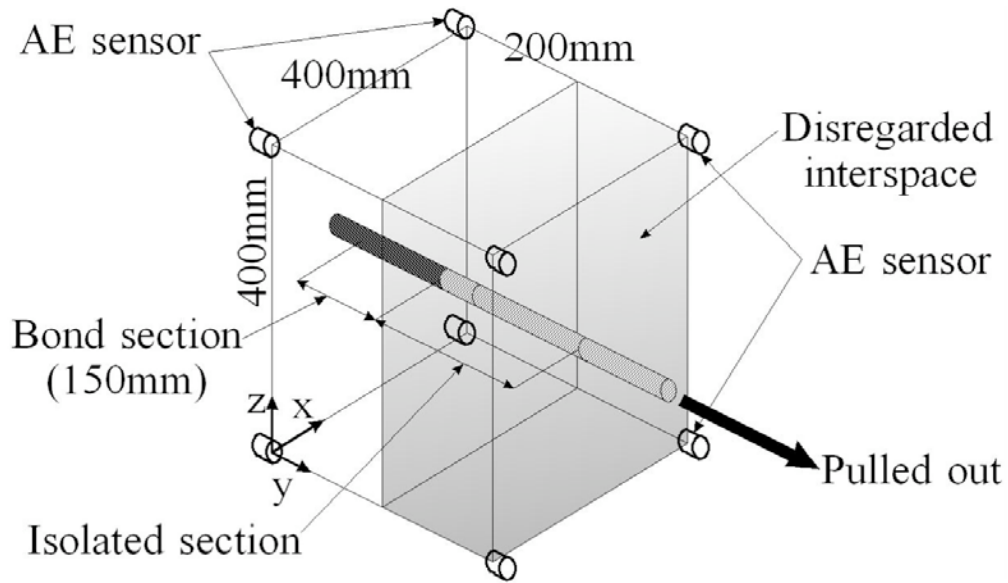


Fig. 2 Location of AE sensors for pull-out tests.

identified using arrival time differences of AE signals. In actual tests, the AE events also appeared in the interspace corresponding to the volume where steel bar was isolated from concrete. The center-hole jack was placed on the surface of the interspace. Thus, the AE signals located within the interspace was disregarded for evaluating cracking behavior.

Visual observation

Figure 3 shows the cored sample of 400 mm length, containing a steel bar. To make two cross sections on the specimen, the both ends of the sample were cut off by 100 mm from the edges. In this way, the two cross sections of each specimen were observed visually. Several voids were found around the steel bar as shown in Fig. 4(a). To quantify the area of voids expediently, the void is represented by a triangle, with the rift length (i.e., base) is a circumference of steel bar exposing to void and the rift height is the maximum distance from the surface of steel bar to the

void edge as shown in Fig. 4(b). Thus, the rift area is readily calculated as a triangle. The rift length and the rift area were used for indices to evaluate bond properties.



Fig. 3 A cored sample including a steel bar.

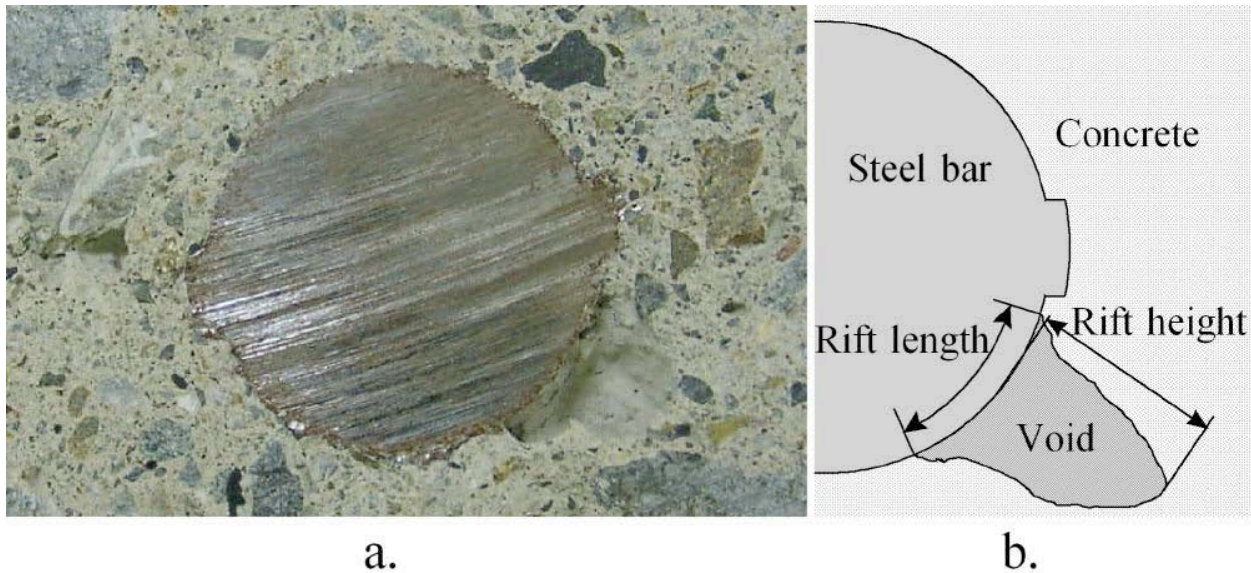


Fig. 4 (a) A cross section of N1-U3. (b) An example of a pair of rift length and rift height for quantifying an observed void.

3. Results and Discussion

Pull-out test with AE measurement

The AE activity in N2-U3 is a typical AE activity of N series and is shown in Fig. 5(a). The AE hit rate shows the rate of total AE hits derived from all channels. The displacement at the end of steel bar and applied load are shown as well in the figure. In both N1 and N2, large slippage of steel bars and intensive AE activity were observed after the peak of load. A typical result of S series is shown in Fig. 5(b) in the same manner as in Fig. 5(a). In the S series, the steel bars yielded in almost all the cases, and the yield point of steel bars corresponded well to the curvature of the load chart. After the yield point, the load increased slightly then ceased to increase. The AE activity continued to be inactive; in fact, rather extremely calm, even when the load reached the yield point. Subsequently, the steel bar started to extend and resulting high AE activity was generated. The extension of steel bar would occur at the bond section, therefore the bar end displacement in Fig. 5(b) was constant. Averaged maximum pull-out loads of N1, N2 and S were 179 kN, 212 kN and 387 kN, respectively. The maximum pull-out loads of S were consistent with the yield strength of high-strength deformed steel bar used. Thus, it is shown that the

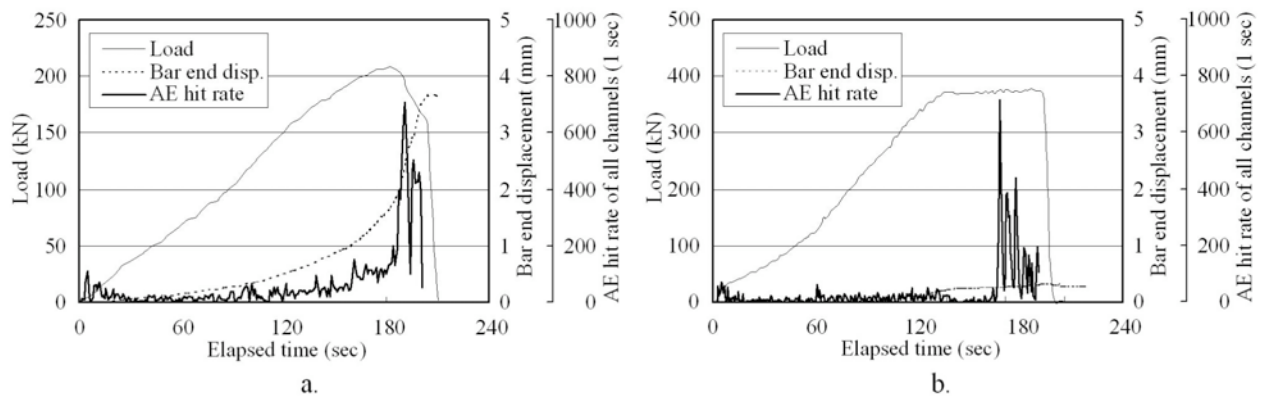


Fig. 5 Loading history, bar end displacement and AE hit rate (a: N2-U3, b: S-M2).

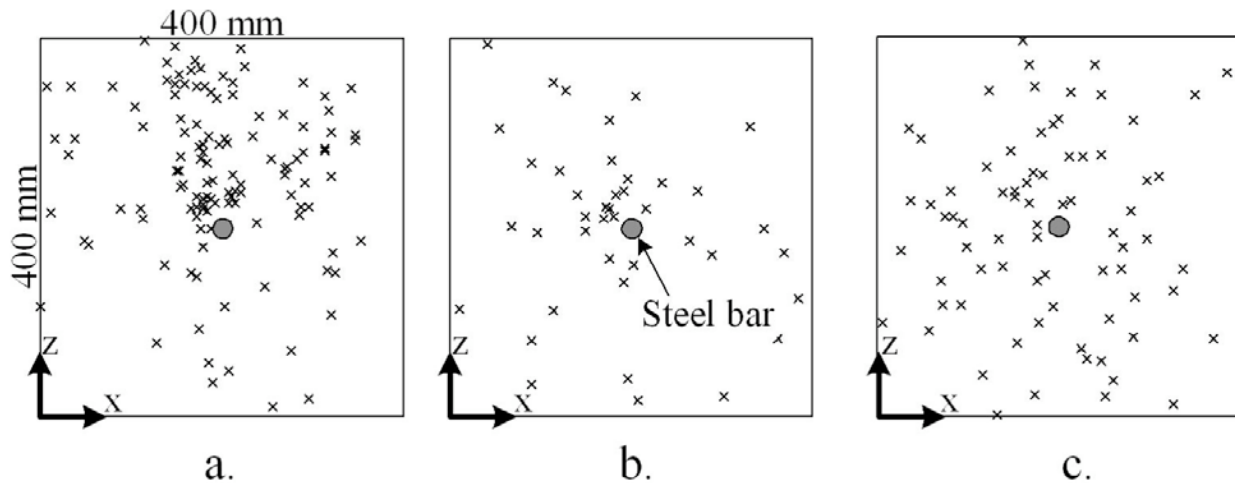


Fig. 6 Front view of AE source locations (a: N1-L1, b: N2-L2, c: S-U1).

bond strength of SQC is high to such an extent that the high-strength steel bar is subjected to yielding.

Three-dimensional AE sources obtained from the experiments are projected to the front surfaces of the walls. Three typical AE source locations in each placing condition are shown in Fig. 6(a- c), in which AE sources are extracted before the peak load only. For N1-L1 shown in Fig. 6(a), AE events were mainly concentrated above the steel bar, whereas AE events of S-U1 were scattered over the monitoring area (see Fig. 6(c)). To evaluate the spatial density of AE events, the monitoring area is divided into radial zones from the center of steel bar. As shown in Fig. 7, 12 slices of 30° each are defined, but we combined two slices in symmetrical positions (e.g., 0 to 30° and 150° to 180°) into a single zone for a total of six zones. AE events, which located in each of the six zones, were averaged in each of the experiments. The average AE events obtained from each series are shown in Fig. 8 in terms of the ranges. It is noted that a negative angle indicates AE events located below the steel bar, while a positive angle shows those above the bar. In N1 series shown in Fig. 8(a), the average AE events below the steel bars were smaller than those above the steel bars. No relationship between located elevations of steel bars and AE events was observed. As for N2 series shown in Fig. 8(b), lower AE activities below the steel bars were also obtained; however, the trend was not so extreme as in N1 series. In N2-U (upper level), the average AE events in the range from -60° to 0° , corresponding to below the side of steel bars, were

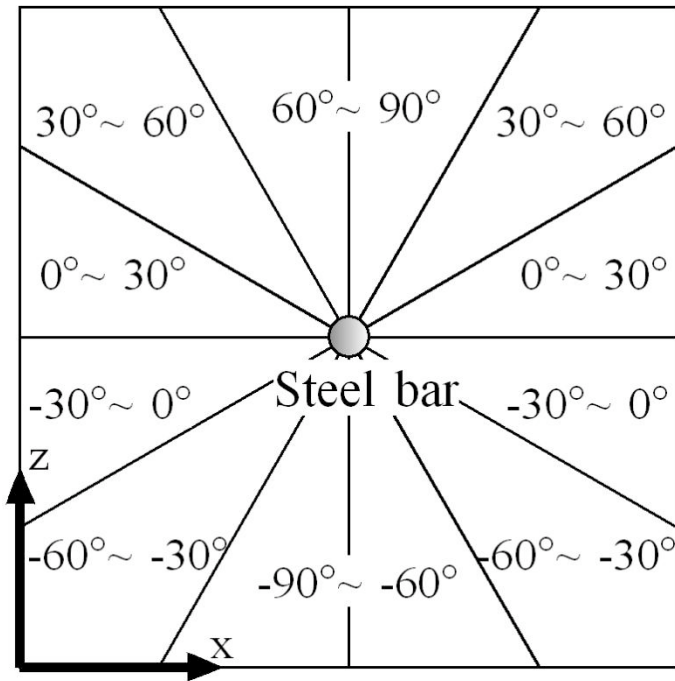


Fig. 7 Radial division of monitoring area.

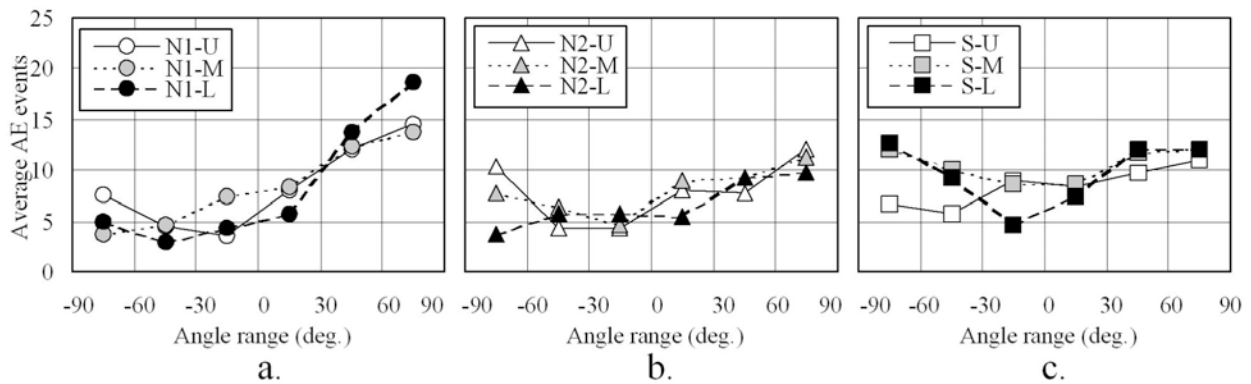


Fig. 8 Average AE events of each angle range (a: N1, b: N2, c: S).

smaller than those in the other ranges. In S series shown in Fig. 8(c), a relatively constant number of AE events were obtained in all zones. This suggests that, AE sources are distributed homogeneously around the steel bars in S series. Especially, the AE activity in S-M (middle level) showed the most well distributed AE activities in all directions. In S-L (lower level), however, smaller average AE events were observed in the range from -30° to 0° corresponding to below the side of steel bars.

To characterize the bond fracture of the pull-out tests, AE parametric analyses were performed. In this study, the initial part of AE waves, important part of an AE waveform for characterizing crack types [5], is employed. We used a parameter of “grade,” describing the initial wave components [6]. The “grade” is defined as the gradient of ascending part of an AE wave- form and is calculated by the AE peak-amplitude (dB) divided by the rise time (μ s). The initial gradient of AE waves is expected to be larger in tensile type fracture, while it becomes smaller for the shear type fracture. Figure 9 shows relationships between the grade and AE source locations angle. In the grade analysis, AE events of either less than 6 AE counts or rise time less than 2μ s were disregarded. In all cases, large grade were not

observed, whereas almost all of the AE events had smaller grade at maximum about 2 dB/ μ s. This implies that the shear fracture was dominant during the pull-out tests.

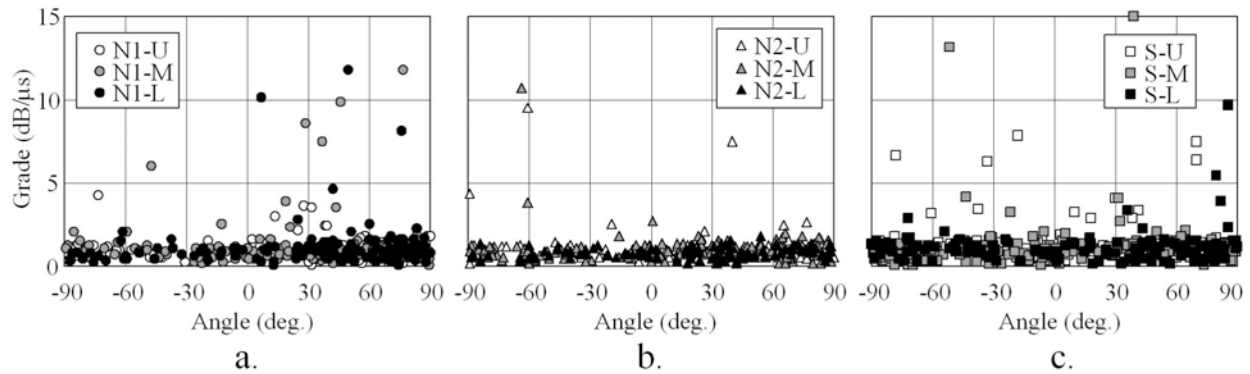


Fig. 9 Relationship between AE location angle and its grade (a: N1, b: N2, c: S).

Bond fracture between concrete and deformed steel bars is reported to be divided into three following modes: 1) local compression at ribs of steel bars, 2) shear motion along connections among the apexes of the ribs and 3) circumferential tension stress due to spreading effect caused by the rib shift [7]. The reason why the shear fracture was dominant during the pull-out tests seems to be the following. The covered concrete surrounding the steel bars was so massive in full-scale walls to avoid generating circumferential tension stress corresponding to Mode III fracture. Consequently, the stress concentrated on mechanical engagement between ribs of steel bars and concrete, corresponding to Mode I and II fracture. Thus, AE activity would be mainly characterized as shear type fracture. AE events, which have large grade values, were obtained in S series rather than in N series. This would be caused by partial shifts of steel bars after the yielding, corresponding to the bond fracture of Mode III.

The mechanical engagement of steel bar ribs with surrounding concrete is essential to distribute stress in the steel bar to the surrounding concrete. Thus, incomplete bonding due to segregation, bleeding and inadequate compaction cause the defective mechanical engagement of steel bar ribs with concrete resulting in insufficient stress distribution. Especially, if there were non-uniformity in the bonding, the stress is intensively distributed only on the sound area, where sufficient connection of steel bars with concrete exists. Consequently, the localized stress results in cracks developing in the sound area. Hence, the angle ranges, in which lower AE activities are observed (see Fig. 8) would be an incomplete bonding area. In this way, it is estimated that there were incomplete bonding below the steel bars in the N1 series because lower AE activities were observed below the steel bars. The same lower AE activity as in the N1 series can be seen in N2-U and S-L, suggesting incomplete bonding below the steel bars. Contrary to those series, S-M showed the uniform AE activities. This implies adequate bonding existed around steel bar in S-M.

Visual observation

With the angle range defined in Fig. 7, the rift lengths are also divided. The averaged rift lengths of each series are shown in Fig. 10. In general, the rift lengths were large at the negative angle, or the zones below a steel bar. Especially in N1-U, very large rift lengths of around 7 mm, which occupied 50% of divided circumference, were observed. Contrary to N1 series, which show large rift lengths in the upper level, there was no obvious difference of rift lengths among elevations in N2 series. In S series, small rift lengths were observed in the upper level. Generally

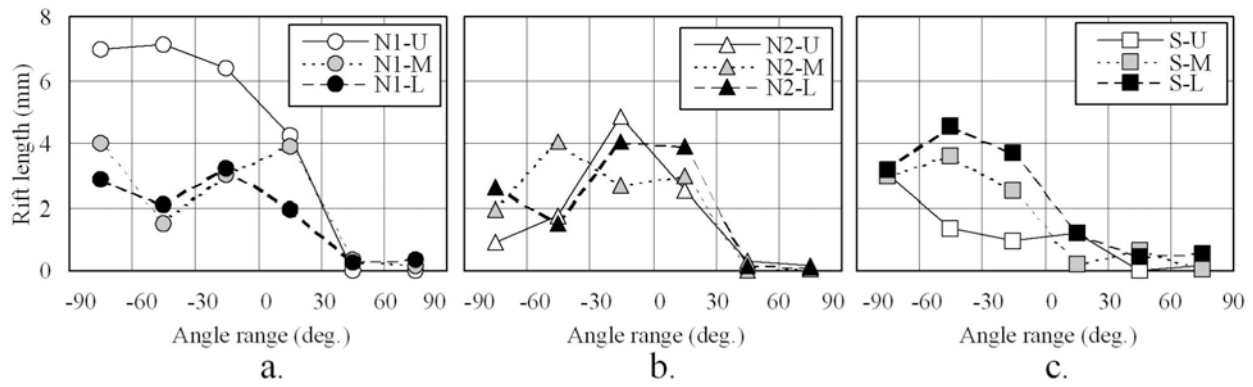


Fig. 10 Rift length of each angle range (a: N1, b: N2, c: S).

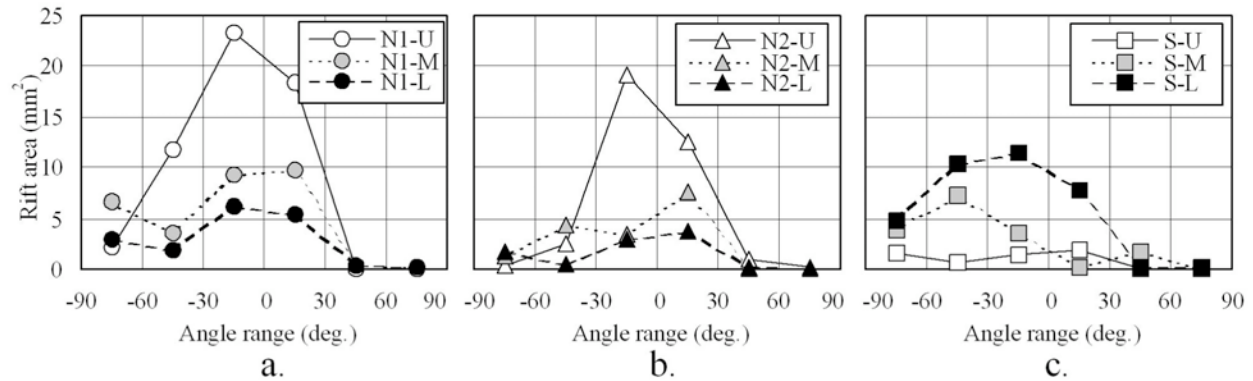


Fig. 11 Rift area of each angle range (a: N1, b: N2, c: S).

in horizontal steel bars, rifts below steel bars are easily developed due to segregation or bleeding, and they become larger as in upper levels of concrete placement. Therefore, the large rift lengths obtained on upper level in N1 series would be caused by segregation or bleeding. These results also suggest that the SQC has a high inhibition effect on segregation.

The averaged rift areas are shown in Fig. 11 as in Figure 10. The rift areas showed the maximum in the range of $\pm 30^\circ$, which was the side of steel bars. Especially in upper level of N series, N1-U and N2-U, very large rift areas around 20 mm^2 were obtained. These large voids on the side of steel bars in N series seemed to develop when the steel bars obstructed the horizontal movement of concrete. Contrary to N series, larger rift areas were observed in the lower level of S series (S-L). The observed voids around steel bars in S series seem to be independent small bubbles due to entrapped air. This would be caused by high viscosity of fresh concrete due to high cement content of SQC.

From these results, the placing condition of N2 was better than that of N1 in this study. Accordingly, it is confirmed that the bond behavior of conventional concrete mixture (N) varies with the conditions of placing and compaction. The rift sizes of S series were smaller than that of N2 series, which is a better placing condition in N series. Thus, it is concluded that the SQC is effective to reduce rifts between concrete and steel bars, even without requirement for the compaction.

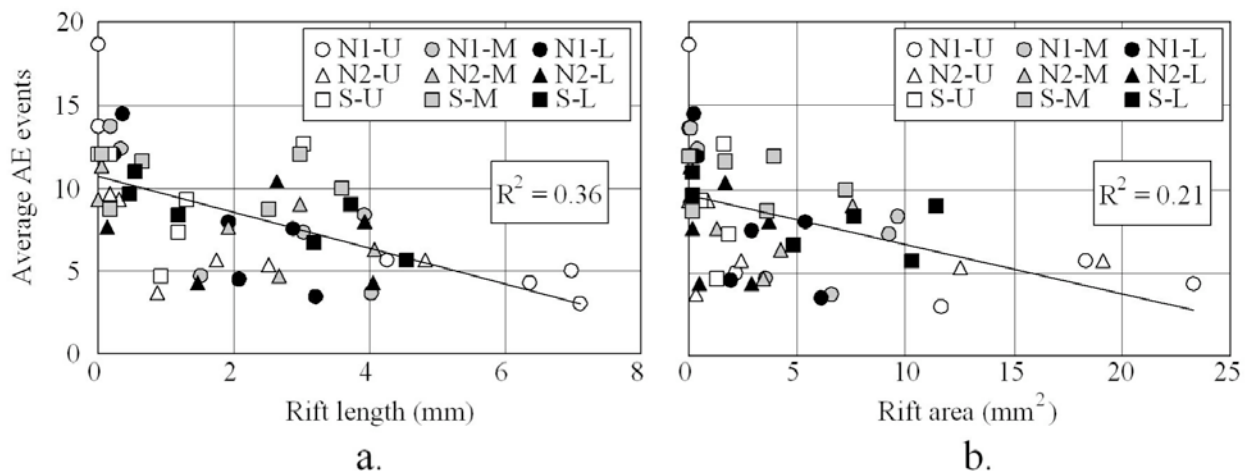


Fig. 12 Relationship between rift sizes and average AE events (a: rift length, b: rift area).

Relation of AE results and visual observation

The AE result shows that the localized lower AE activity around steel bars can be evaluated to have incomplete bonding for stress distribution. For example, below the steel bars of all N1 series and below the steel bars for N2-U and S-L were estimated as the locations where incomplete bonding existed. From visual observations, the larger rift lengths below the steel bars were obtained in all the cases. Especially it was remarkable in N1-U. Also, the large rift areas located on the side of steel bars were observed in N1-U, N2-U and S-L. These results imply that the incomplete bonding estimated by AE measurement is in good agreement with the locations of rift around the steel bars.

Figure 12 shows relationships between the rift sizes and average AE events. Since the AE measurements and the visual observations were conducted separately with different specimens, the correlation coefficients between the rift sizes and AE events have low values. However, it is found that the number of AE events tends to be higher as rift sizes become smaller. This suggests that the higher AE activities showing evolution of cracks can be correlated with adequate stress distribution achieved by enough mechanical engagement of the ribs with concrete.

4. Conclusions

Bond behavior of steel bars was studied using walls cast by the SQC and a conventional concrete. For different conditions of placing and compaction, the bond properties were evaluated by pull-out tests with AE measurements. Comparison was made between AE activities and visual observations of sections on the cored samples. The following findings were obtained:

- 1) AE activities during the pull-out tests can be mainly characterized as shear type fracture, which seems to be caused by concentrated stress on mechanical engagement between ribs of steel bars and concrete.
- 2) The localized lower AE activities around steel bars can be evaluated to have insufficient bond area, where it is difficult to distribute stress of steel bars to surrounding concrete.
- 3) The bond behavior of a conventional concrete is directly influenced by means of compaction; however, stable bond behavior irrespective of the compaction is observed in the SQC. Thus, it becomes clear that the SQC is effective not only for mechanical improvement but also for reduction of bond defects.

Acknowledgements

This research was part of the Millennium Project, 'A study on next-generation construction system using super quality concrete' supported by a grant from Ministry of Education, Culture, Sports, Science and Technology, Japan. The authors would like to express their appreciation to colleagues who contribute to the project.

References

1. H. Okamura, K. Maekawa and K. Ozawa: *High Performance Concrete*, Gihodo Publishing (1993).
2. O. Makishima, H. Tanaka, Y. Itoh, K. Komada and F. Satoh: Evaluation of mechanical properties and durability of super quality concrete, Proc. Intl. Symp. SCC (2001), pp. 475-482.
3. Japan Soc. Civil Engrs.: Design and construction recommendations for self-compacting, high-strength and high-durability concrete structure (2001).
4. H. Yamamoto, T. Mishima, M. Kikuchi and H. Shima: Study on bond characteristics of reinforced concrete structure using super quality concrete, Proc. Intl. Symp. SCC (2001), pp. 491-499.
5. M. Ohtsu, M. Shigeishi, H. Iwase and W. Koyanagi: Deformation of crack location, type and orientation in concrete structures by acoustic emission, Mag. Concrete Res., **43** (1991), 127-134.
6. T. Shiotani, M. Ohtsu, K. Ikeda: Detection and evaluation of AE waves due to rock deformation, Constr. Build. Mater., **15** (2001), 235-246.
7. K. Okada: *Reinforced Concrete Engineering*, Asakura Publishing (1972), pp. 136-142.

DEVELOPMENT OF A NOVEL OPTICAL FIBER SENSOR FOR AE DETECTION IN COMPOSITES

ISAMU OHSAWA, KAZURO KAGEYAMA, YUKIYA TSUCHIDA*
and MAKOTO KANAI

Department of Environmental and Ocean Engineering, Graduate School of Engineering,
The University of Tokyo, Bunkyo, Tokyo 113-8656, Japan. * Now at Technical Research and
Development Institute, Japan Defense Agency, Meguro, Tokyo 153-8630, Japan.

Abstract

A novel AE sensor was developed by using a conventional optical fiber. The principle of the sensor is based on the Doppler-effect in curved optical fiber. A loop-type optical fiber sensor showed excellent sensitivity to elastic wave activity. The basic characteristics of the loop sensor were examined by propagating an elastic wave in a steel plate and detecting it with the sensor. The loop sensor was also used for assessing damage propagation in an adhesive joint in composite structure, and the results showed activity almost similar to that of a PZT AE sensor.

Key Words: Doppler-effect; Optical fiber sensor; Loop sensor; Composite structure

1. Introduction

Composite structures have an important role to play in fields that demand lightweight and energy-saving features. Development of systems to evaluate and assure soundness of structures using health monitoring and non-destructive examinations are needed, and greater attention is being focused on fiber-optic sensors [1]. Various kinds of sensors have been proposed and developed ranging from those that use loss of transmitted beam due to breakage or bending of the optic-fiber itself, to those that use interference or phase difference of light [2].

Optical fiber is light in weight, flexible, and also has good durability, excellent corrosion resistance, high strength and good resistance to electromagnetic noise. The diameter of the optical fiber is very small at about 250 micrometers, therefore, it is easy to set the fiber even on three-dimensional curves and to embed the fiber in composite materials. Thus, optical fiber has good prospects of being used as a sensor for monitoring composite structures [3, 4].

Optical fiber sensors using frequency change characteristics due to the Doppler effect of light transmitted within the optical fiber have the advantage of excellent dynamic behavior over a wide frequency range. However, it is difficult to use this sensor for ultrasonic applications like AE, because its sensitivity is low. By using Laser Doppler Velocimeter (LDV), we examined experimentally the basic characteristics of a straight optical fiber of about 10 cm in length, in which the plastic cladding was peeled off, and used it as a vibration sensor [6]. The straight sensor was also used in tensile tests of GFRP, and the results of this sensor were compared with the results of a conventional resonant-type AE sensor. It was observed that in the straight optical fiber, low amplitude AE data were buried in electric noise due to the low S/N ratio of the fiber. However, it was confirmed that the optical fiber sensor could detect high amplitude AE data, which correspond to high-energy failure of materials, similar to the AE sensor.

Subsequently, the LDV was improved, and it was found that a loop-type optical fiber with a diameter of about 10 mm indicated higher sensitivity than obtained until now and could be used as a high-sensitivity vibration sensor. It was also evident from the results of our studies that no patent or sensor existed that used this method.

Thus, the aim of this research was to clarify and confirm the characteristics of the newly developed optical fiber vibration sensor. Moreover, the application of the sensor to track the inter-laminar failure of polymer composites was also studied as part of this research.

2. Development of a Novel Loop Sensor

Figure 1 shows the schematic of one-turn loop of an optical fiber. This is the simplest loop sensor developed in our work. The loop sensor was affixed carefully on a steel plate with plastic tape. Figure 2 shows a waveform and frequency spectrum, which was emitted by a quasi-AE oscillator and detected by the loop sensor. In this case, no frequency filter was used for the output wave. Figure 3 shows similar results detected by a conventional 150-kHz resonant-type AE sensor. In this case, a bandpass filter of 100 kHz to 300 kHz was used. It was confirmed here that a small loop of optical fiber works well as a vibration sensor, although its output is small. However, when the sensor part of the optical fiber was made straight, waves as shown in Fig. 2 were not detected for the same threshold level. This confirmed that the loop form of the sensor increased the sensitivity of the sensor.

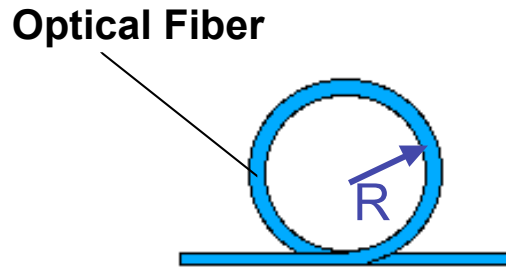


Fig. 1 Loop sensor configuration.

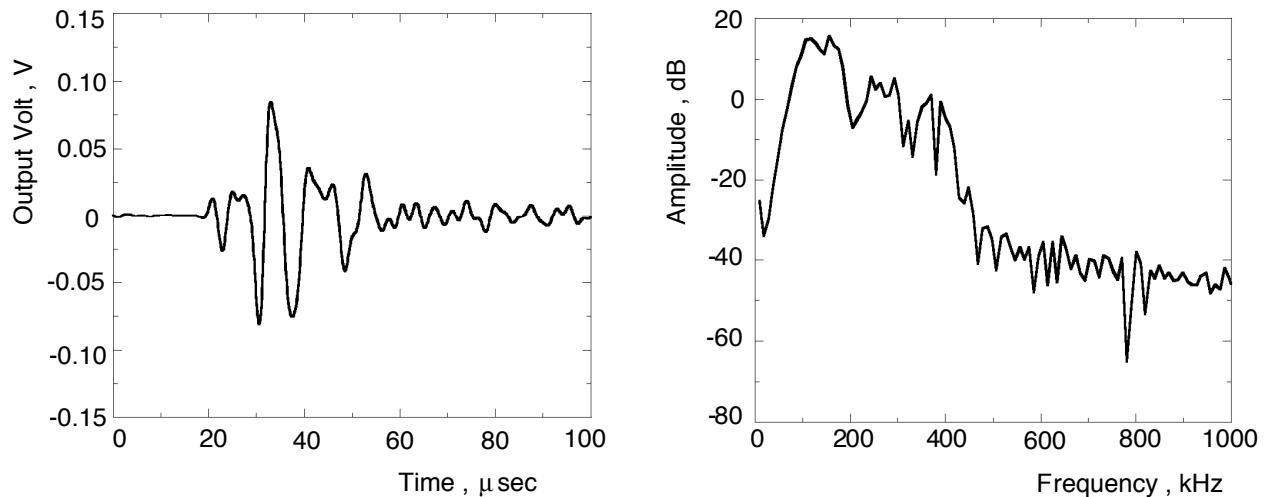


Fig. 2 Signal detected by a loop sensor of $R = 5$.

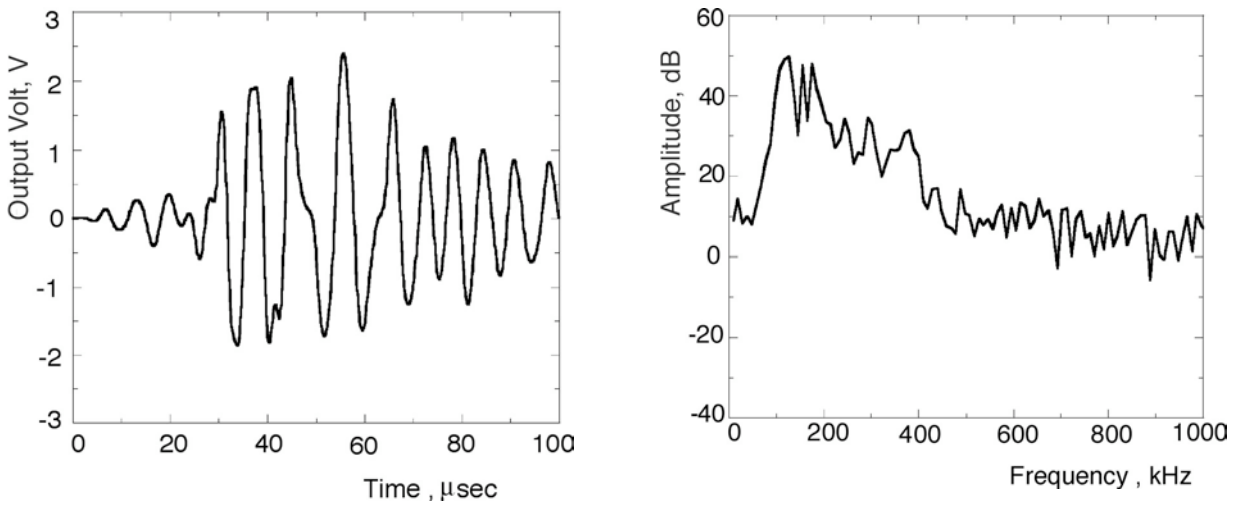


Fig. 3 Signal detected by an AE sensor (R15).

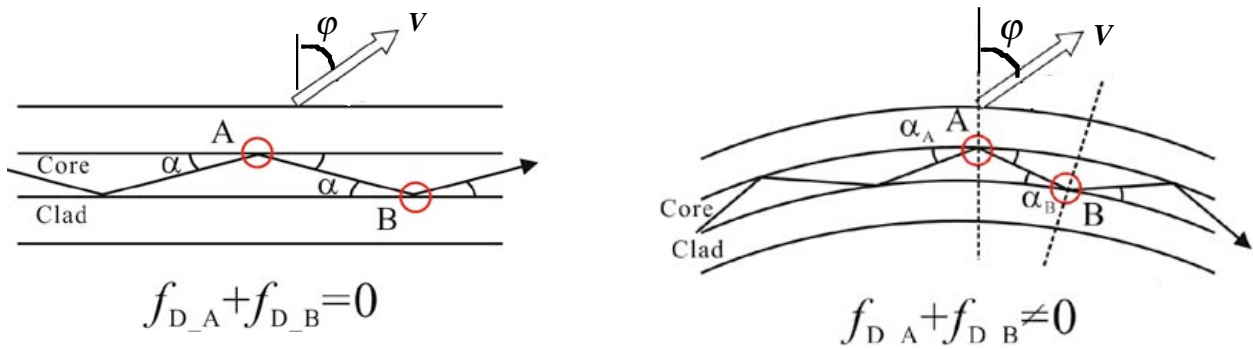


Fig. 4 Doppler effect in a straight and a curved optical fiber

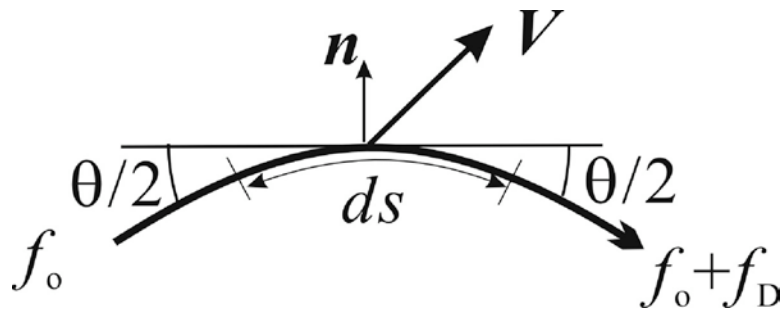


Fig. 5 Propagation model of light in a curved optical fiber,

It was observed that duration of the waveform of the loop sensor was shorter compared to that of the AE sensor waveform. Since the principle of measurement of AE sensor is to use resonant frequency, beats due to resonance probably occurred. In case of a loop sensor, however, a waveform closer to the original waveform was probably detected.

3. Principle of Curved Optical Fiber Sensor

When light with a constant frequency is irradiated on a moving object, the frequency of a reflected light changes. This change in frequency is called Doppler shift or Doppler effect. Light in

a narrow optical fiber is transmitted after being repeatedly reflected from the interface of the core and the cladding. When a straight optical fiber, as shown in Fig. 4, receives some velocity component, the changes in frequency cancel out each other because of symmetry and the Doppler effect does not occur. On the other hand, when a curved optical fiber receives a velocity component, the angles of reflection are different and do not cancel each other out, with the result that the Doppler effect appears. Light in a curved optical fiber is considered to be a single beam as shown in Fig. 5. The Doppler shift df_D that occurs in infinitesimal length ds can be expressed by equation (1). The total Doppler shift f_D for a length L can be obtained by integrating equation (1), and is shown in equation (2).

$$df_D = -\frac{2f_0}{c} \mathbf{V} \cdot \mathbf{n} \sin \frac{d\theta}{2} = -\frac{f_0}{c} \mathbf{V} \cdot \mathbf{n} d\theta \quad (1)$$

$$f_D = -\frac{f_0}{c} \int_L \kappa \mathbf{V} \cdot \mathbf{n} ds \quad (2)$$

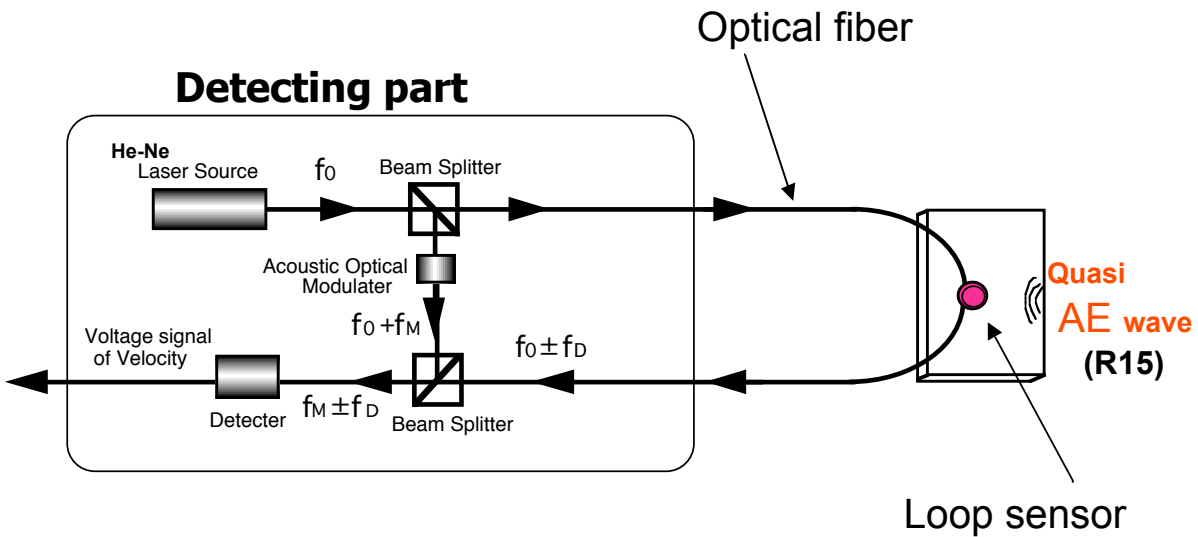


Fig. 6 Sketch showing components of LDV.

3. Principle of Measurement of Laser Doppler Velocimeter

Figure 6 shows the principle of measurement of the Laser Doppler Velocimeter. The He-Ne laser beam of frequency f_0 originating from a light source splits into two routes due to a beam splitter. One route becomes an incident beam on the optical fiber sensor. The sensor part is affixed with the loop type optical fiber. As a result, the frequency of the laser beam from the sensor part shifts to the frequency $f_0 \pm f_D$, which is proportional to the vibration velocity. The other beam is a reference beam, and the length of its light path is unchanged. This is a reference beam with a frequency shift of $f_0 + f_M$ through AOM. The frequency difference $f_M \pm f_D$ is measured by interference of these two beams. Only the Doppler shift frequency component $\pm f_D$ is extracted, and the signal voltage V , corresponding to the vibration velocity in the FM recovery circuit is output from the Doppler effect equation $f = 2v/\lambda$. Here, λ is the wave length (633 nm) of the laser. The detecting instrument used was a modified LV-1100, made by Ono Sokki Instrument Co., Ltd., with a measurable frequency range from 1 Hz to 1.5 MHz.

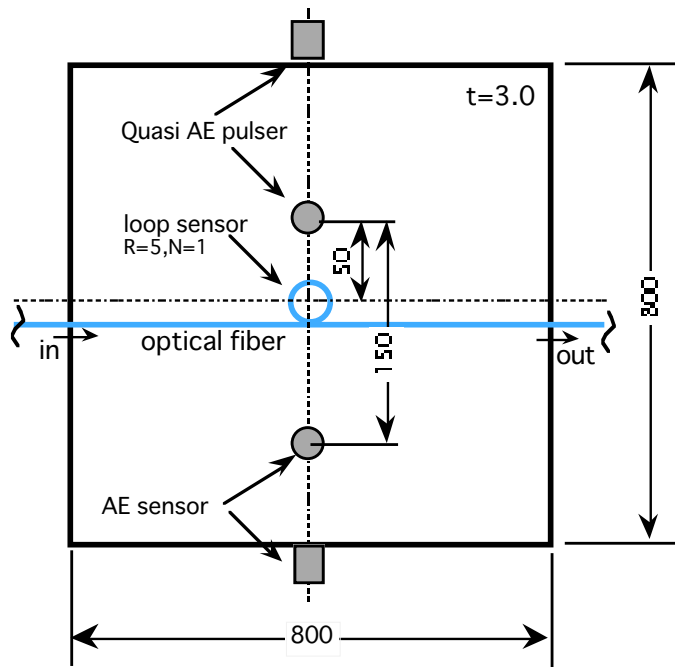


Fig. 7 Experimental setup.

4. Experiment To Evaluate Sensor Characteristics

Experimental Method

Figure 7 shows the setup of the experiment. Quasi-AE waves were generated on a square steel plate 800 mm x 800 mm x 3 mm and waveforms detected by the loop sensor were analyzed. Pulse voltage was applied through quasi-AE waves generated in an oscillator (PAC, C-101-HV) and passed through the AE sensor (PAC-R15, 150 kHz resonant type). The speed of elastic waves through the steel plate was measured as 4,711 m/s via time-of-flight method. Since a 150-kHz resonant-type AE sensor was used for transmission and detection, the frequency of the elastic waves is also considered to be 150 kHz, and thus, its wavelength is 31 mm.

The loop sensor was installed at the center of the steel plate to avoid the effect of reflection at the end faces of the steel plate. The output gain from FLDV was set at 0 dB through a bandpass filter of 100 kHz to 300 kHz. The detected signal was input in the AE system (PAC, MISTRAS) and analyzed using waveform measurement software (PAC, MI-TRA). Simultaneous measurements were carried out using an AE sensor (PAC-R15) at all times and compared with the loop sensor measurements. The signal from the AE sensor was amplified 20 dB, passed through a 100-300 kHz bandpass filter, and AE waveforms were similarly digitized.

Effect of Radius of Curvature R of Sensor Loop

To examine the effect of radius of curvature R , the sensitivity was examined by varying the radius of curvature, taking the number of turns of the loop N as 1. Quasi-AE wave was made to fall on the surface of the steel plate at a distance of 50 mm from the center of the loop.

Figure 8 shows the plots of maximum output voltage (V_{pp}) of each waveform for all values of R tested, where each plot has been determined from the average value of 10 waveforms. The results show that the smaller the value of R , the greater is the value of V_{pp} , and the better is the sensitivity. This is probably because when the radius of the loop is small, the loop can catch the vibrations uniformly. The wavelength was found to be 31 mm, which gives the radius of curva-

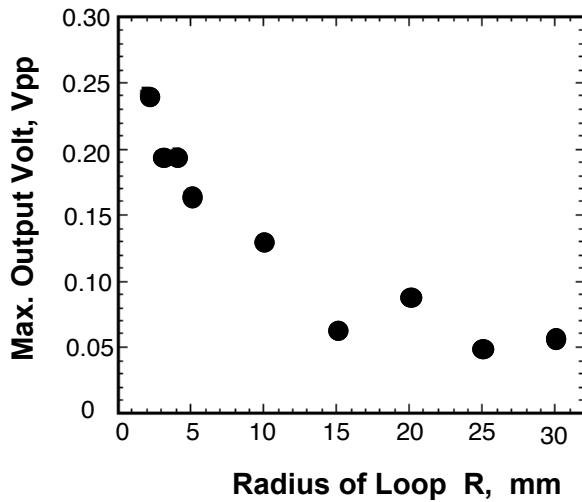


Fig. 8 Relationship between Vpp and R.

ture R as 15 mm. As shown in Fig. 8, the value of output (Vpp) decreases until R = 15 mm, but it remains at an almost constant level after this value. The radius of curvature should be made small in order to realize a small-sized sensor with high sensitivity. However, considering light loss and strength in optical fiber, the lower limit of R is 5 mm.

Effect of the Number of Turns of the Loop

An increase in the number of turns is expected to improve the Doppler effect. Therefore, the effect of the number of turns was examined. As shown in Fig. 9, the number of turns on the outside of the loop was increased and the sensitivity was checked taking the inside radius of the loop sensor as 5 mm. Quasi-AE wave was generated at a distance of 50 mm from the center of the loop. Figure 10 shows the relation between the number of turns and the maximum output voltage (Vpp) of the detected waves. The result shows that Vpp increases in proportion to the number of turns. Furthermore, it was confirmed that the dynamic range also improved with the increase in Vpp.

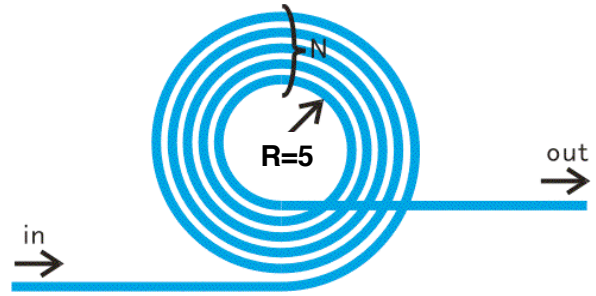


Fig. 9 Configuration of a loop sensor with N turns.

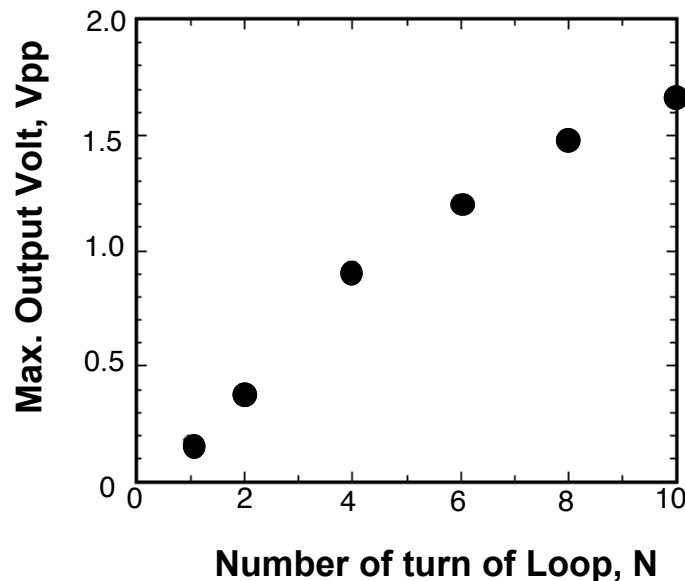


Fig. 10 Relationship between Vpp and number of turns N.

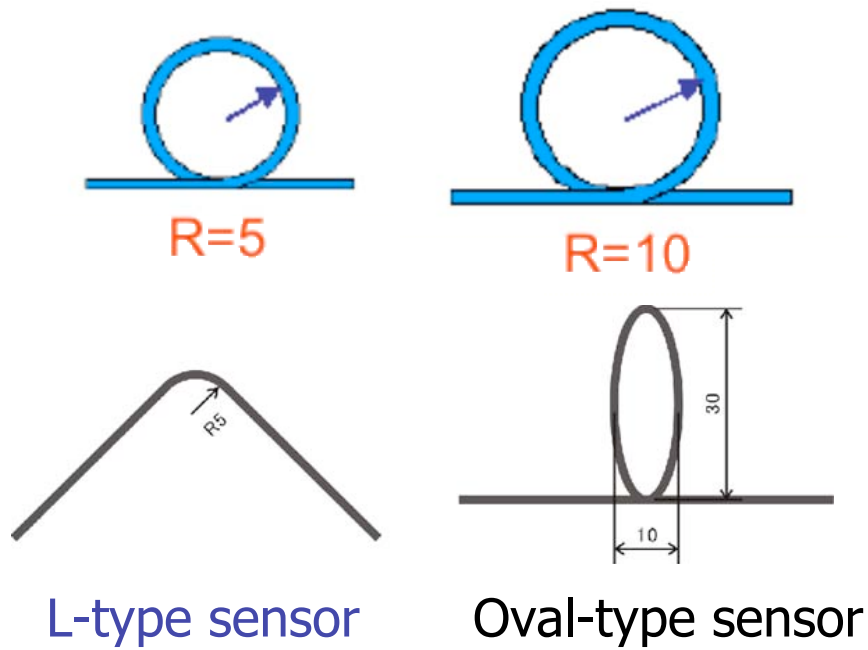


Fig.11 Four kinds of optical-fiber sensors.

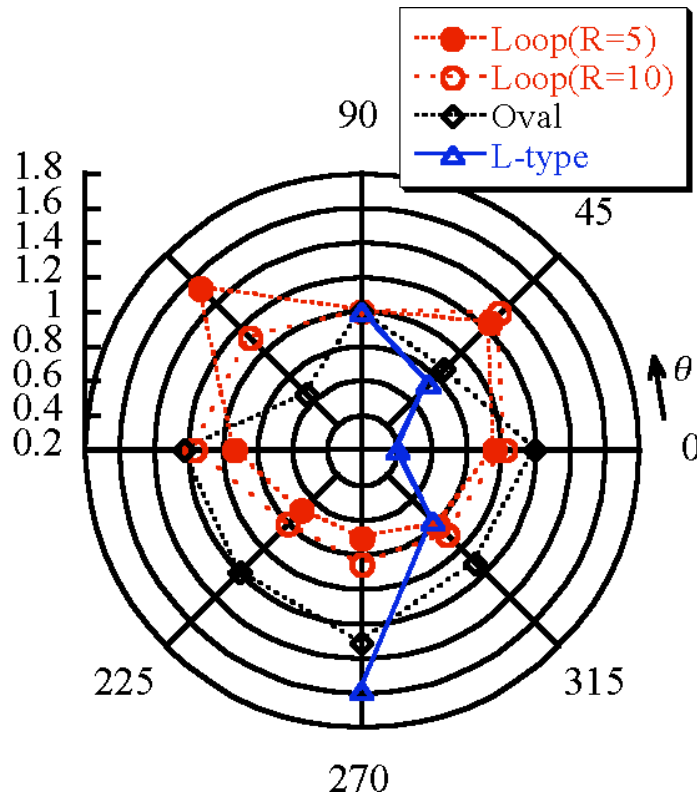


Fig. 12 Directivity dependence on the type of sensor.

Directivity of the Sensor

The sensitivity of the sensor corresponding to its directivity was checked by varying the angle of incidence of quasi-AE on the loop sensor in steps of 45° from 0° to 315° . The experiment was carried out on 4 kinds of sensors: two kinds of sensors with $N=1$, $R = 5$ mm and 10 mm, and

two kinds of L-type and oval-type sensors, as shown in Fig. 11. Figure 12 shows the relationship between angle θ and V_{pp} for all kinds of sensors. Resultant data was normalized taking V_{pp} as 1 for $\theta=90^\circ$. The results showed that there was no distinctive directivity for loop and oval-type sensors, and that the L-type sensor showed excellent directivity at the sensitivity in the 90° direction.

5. Application to Damage Progression Behavior in Composite Materials

Mode-I Interlaminar Damage Progression Experiments

A loop sensor was used to evaluate the interlaminar damage progression behavior of a double cantilever beam (DCB) specimen of uni-directional CFRP (T800H/3900-2). As shown in Fig. 13, a loop sensor ($R=5\text{mm}$, $N=10$) and a small AE sensor (DIGITALWAVE, B1025) with wide frequency range were installed on the specimen. The experiment was carried out according to JIS-K 7086, with pin-loading and by controlling the displacement of crosshead at the speed of 1 mm/min and loading until a maximum crack of 50 mm. Collection of output data and its analysis was performed similar to the basic experiments, using the AE system (PAC, MISTRAS).

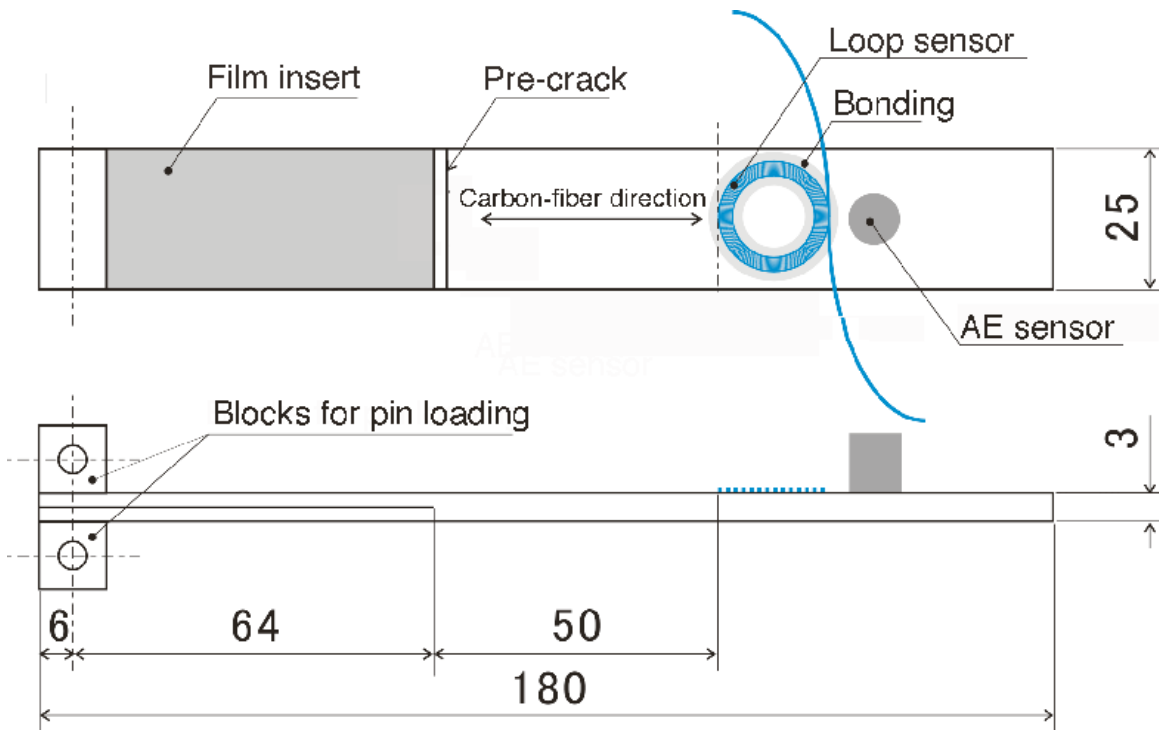


Fig. 13 DCB specimen and location of a sensor.

Figure 14 indicates the measured results and the comparison of the parameters of the loop sensor and an AE sensor, namely, amplitude, energy, event rate and total event. Both figures indicated almost same results, confirming that the loop sensor could detect just like an AE sensor with almost the same sensitivity.

Experiment for Debonding Failure in Adhesive Joint

A large number of adhesive joints are used in composite structures. The loop sensor was used to evaluate the debonding behavior of adhesive joints. Together with the debonding progression, the loop sensor was checked to confirm whether it could be used to evaluate the characteristics of attenuation of incident elastic waves. Joint specimens were fabricated with pre-preg sheets of 3K

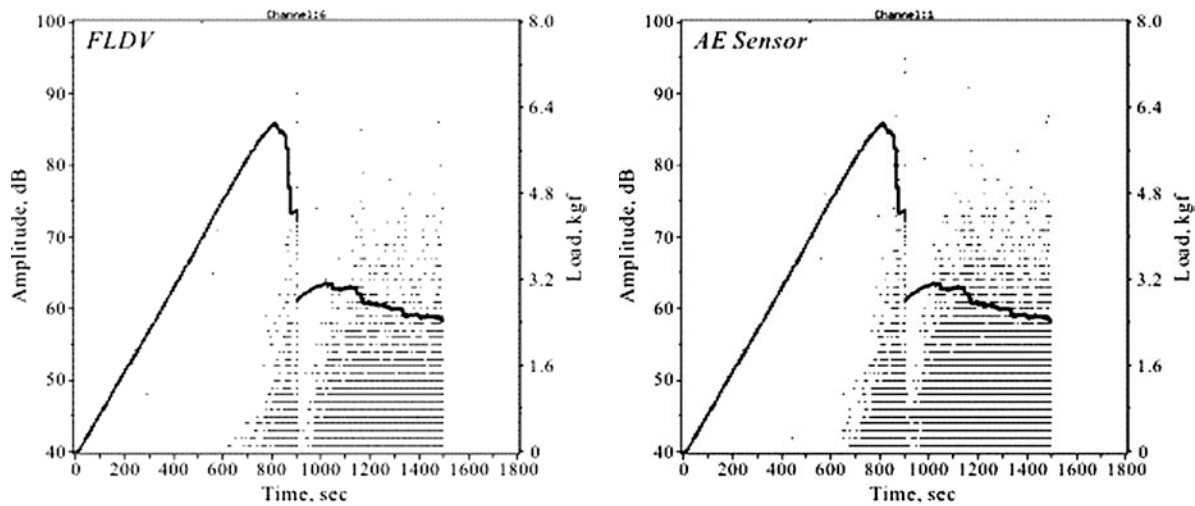


Fig. 14 Resultant AE parameters detected by loop sensor (left) and AE sensor (right),

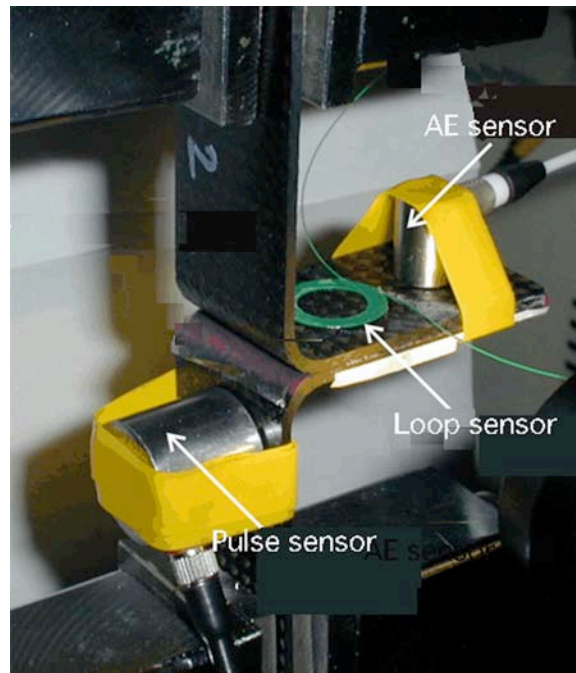


Fig. 15 Adhesive joint specimen and sensor location.

plain-weave fabric, carbon-fiber equivalent to Toray T300 and toughened epoxy resin. A 25- μm thick Teflon film had been inserted into the bonding layer in the specimen as an artificial crack. The laminates were quasi isotropic, and Fig. 15 shows the configuration of the specimens and the sensor locations.

Tensile load was applied with displacement control at the rate of 0.2 mm/min. Experiment of attenuation of propagation was carried out with repetitive unloading each time the crack progressed by 3 mm. Loop sensor with $R=5$, $N=10$ and AE sensor were used. The detection conditions of the AE system were set similar to those in the DCB test. Quasi-AE waves were made incident through the AE sensor (PAC, $R=15$), the attenuated elastic waves that had passed through debonded part were detected by using a loop sensor, and the waveform was recorded and analyzed to evaluate the attenuation of propagation.

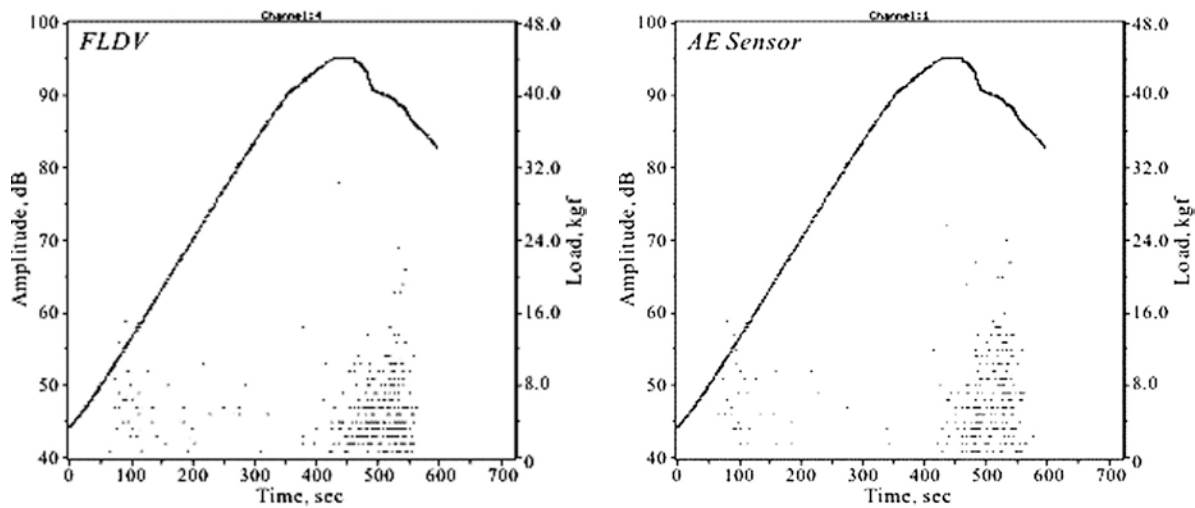


Fig. 16 Results of amplitude distribution detected by loop sensor (left) and AE sensor (right) for crack length of 0 mm to 3.5 mm.

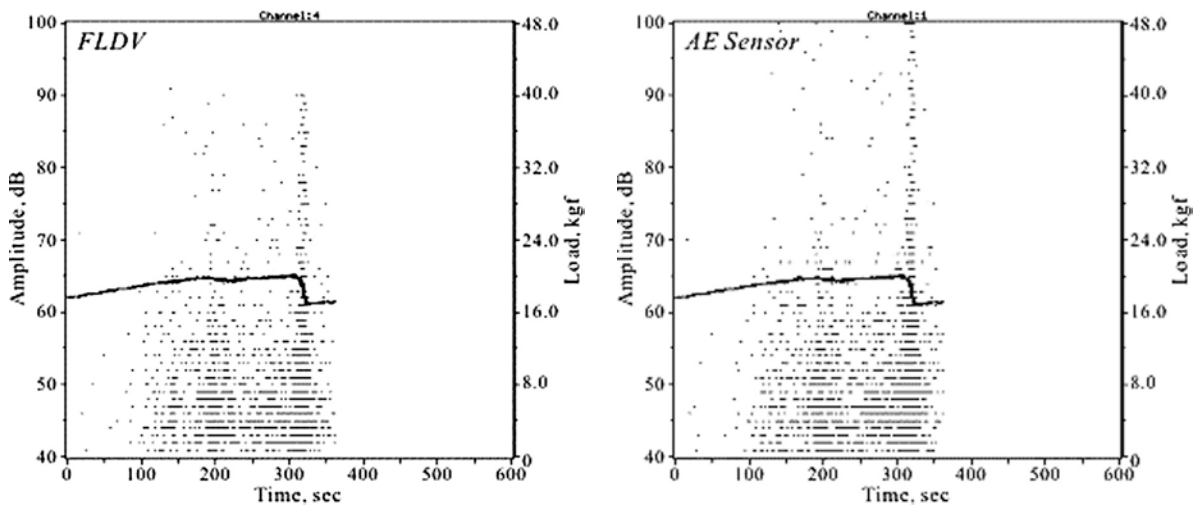


Fig.17 Results of amplitude distribution detected by loop sensor (left) and AE sensor (right) for crack length of 17.5 mm to 20.5 mm.

Figure 16 shows the output results of amplitude distribution from the loop sensor and the AE sensor between 0 mm to 3.5 mm of crack length. Similarly, Fig. 17 shows the amplitude distribution between 17.5 mm to 20.5 mm of crack length. Results for the two sensors indicate almost the same trend and sensitivity, confirming that the loop sensor could detect AE behavior during debonding with high sensitivity.

6. Conclusion

It was verified that the FLDV system and the newly developed optical fiber loop sensor could detect AE activity to the same level as the conventional AE system for interlaminar delamination and debonding failure in adhesive joints of composite materials. The basic characteristics such as the effect of radius of curvature and number of turns of the loop sensor were also clarified. The features of optical fiber sensor as obtained through this research and the future prospects of the sensor are described below.

1. The loop sensor is a vibration sensor with excellent sensitivity comparable to a conventional resonant type AE sensor.
2. S/N ratio can be raised by increasing number of turns.
3. It can detect frequency in the range of a few Hz to 1 MHz.
4. Multi-point measurements are possible with just one fiber.
5. It is possible to build a system incorporating this sensor within another optical fiber sensor system.
6. As optical fibers have low loss of light, a line extending to several kilometers can be measured since losses are small.

References

1. Eric Udd, *Fiber Optic Smart Structures*, John Wiley & Sons, Inc., (1995).
2. T.G. Giallorenzi, A. Bucano, et. al., "Optical fiber Sensor Technology, IEEE J. Quantum Electronics, **QE18** (4) (1982), 626-665.
3. S.G. Pierce, et al., "Surface-bonded and embedded optical fibers as ultrasonic sensors" *Applied Optics*, **35**, (25) (1996), 5191-5197.
4. H. Murayama, K. Kageyama, et al., "Application of health monitoring technology using fiber optic distributed sensors to IACC yachts", *Proc. of the Second Asian-Australasian Conference on Composite Materials*, Vol.2 (2000), 1059-1064.
5. K. Liu, et al., "Damage detection in composites with embedded fiber optic interferometric sensors", *Proc. SPIE*, Vol. 1170 (1990).
6. I. Ohsawa, I. Kimpara, K. Kageyama, et al., "AE detection in composites by using fiber-optic sensor", *Proc. 12th National AE Conference*, (1999), 13-18 (in Japanese).

ACOUSTIC EMISSION EVALUATION OF CORROSION DAMAGES IN BURIED PIPES OF REFINERY

S. YUYAMA and T. NISHIDA*

Nippon Physical Acoustics, Ltd., Okamoto LK Bldg. 8F, Higashi 2-17-10, Shibuya, Tokyo 150-0011 Japan, * Petroleum Refining Engineering Center, Japan Energy Corporation, Ushio 2-1, Kurashiki, Okayama, 712-8588 Japan

Abstract

In order to investigate the applicability of AE method for the evaluation of corrosion damages in buried pipes, systematic tests have been conducted in laboratory and field. Corrosion tests in laboratory showed that steel specimens with thick oxide film generate very strong AE signals with amplitudes over 80 dB during the corrosion process in a salt water. It was also found that signals in a low frequency band (20 – 80 kHz) are mainly produced during the process. Wave propagation tests using pipes under different surface and buried conditions found that source location can be applied to a buried pipe covered with protection film up to 4 m in length. Field AE measurements for 13 buried pipes in service were made in a refinery. Comparison of the AE data and UT thickness measurements and visual inspection demonstrated the potential usefulness of AE technique for evaluation of corrosion damages in buried pipes.

Key Words: Acoustic emission (AE); Attenuation curve; Buried pipe; Corrosion damage; Non-destructive testing (NDT); Refinery

1. Introduction

Corrosion damages of buried pipes have been a significant problem in refinery. Since the pipes are buried, it is difficult to apply such NDT methods as UT, RT, PT, and visual inspection for the damaged areas. Acoustic emission (AE) has been widely used for the evaluation of corrosion damages of tank floor in service, but AE applications in piping have been limited. [1,2] The advantage of the method is that it can evaluate and locate the damages without taking the structure out of service.

In order to investigate the applicability of AE method for the evaluation of corrosion damages in buried pipes, systematic tests have been conducted in laboratory and field. Corrosion tests in laboratory showed that steel specimens with thick oxide film generate AE signals with amplitudes over 80 dB during the corrosion process in a salt water. It was also found that the signals in a low frequency band (20 – 80 kHz) are mainly produced in the process. Wave propagation tests using pipes under different surface and buried conditions found that source location should be applicable to a buried pipe covered with protection film up to 4 m in length. To verify the usefulness of the technique field AE measurements for 13 buried pipes in service were made in a refinery. Comparison of the AE results and UT thickness measurements and visual inspection showed that AE can be a very promising method for evaluation of corrosion damages in buried pipes.

This paper reports results of the systematic tests conducted in laboratory and field, as a research project of Petroleum Energy Center.

2. Test Procedure and Results

AE due to corrosion

Four pieces of small steel specimens were cut out for the tests from a roof of a tank in service (Fig. 1). Three specimens (Nos. 2-4) were covered with thick oxide film on one side. The corrosion product (oxide film) was completely removed from the surface in specimen No. 1. The size was approximately 270 mm long, 35 mm wide and 2 mm thick.

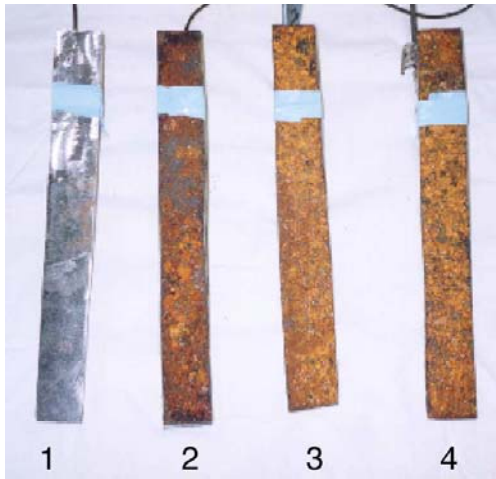


Fig. 1 Specimens before testing.



Fig. 2 Four specimens in 3% salt water (Test 1).

The specimens were immersed in 3% salt water (bottom 9 cm) in order to investigate AE activities due to corrosion, as seen in Fig. 2. Three different types of resonant AE sensors, PAC R3I (30 kHz resonant), R6I (60 kHz) and R15I (150 kHz) were employed for the tests.

In Test 1, an R15I sensor was mounted on each specimen and AE was monitored continuously for 55 days. Figure 3 shows AE amplitude histories and distributions obtained from this test. It is observed that AE signals with high amplitude that reach 80 - 90 dB were produced during the corrosion of the specimens with thick surface oxides (Nos. 2 - 4), while the amplitudes are smaller than 60 dB in specimen No. 1 without thick oxides.

In Test 2, three sensors, one each of R15I, R6I and R3I, were mounted on specimen No. 1 without oxide. AE was monitored continuously for 13 days. Indicated in Fig. 4 are amplitude histories and distributions. The amplitudes are smaller than 60 dB in R15I, while larger amplitudes that reach 70 - 75 dB are detected with R6I and R3I sensors. Number of hits detected by R15I was 40, while it was about 160 in both R6I and R3I. Therefore, it is obvious that signals produced during the corrosion process have a main frequency band in low frequencies (20 - 80 kHz).

Wave propagation tests in pipes

Wave propagation tests were made on several pipes in a plant and model pipes under different conditions (empty, filled with liquid, with and without rust-preventive coating). The pipes are made of carbon steel, 254 mm in diameter of schedule 10B. Other pipes had diameter of 50.4 mm (2B) to 610 mm (20B). These pipes extend much longer than the tested distances in both directions. Four AE sensors with different resonant frequencies (R1.5I (15 kHz), R3I (30 kHz), R6I (60 kHz), and R15I (150 kHz)) were mounted on the pipes to detect AE signals due to pencil-lead breaking. Above-ground pipes (empty and liquid-filled) and simulated buried pipes

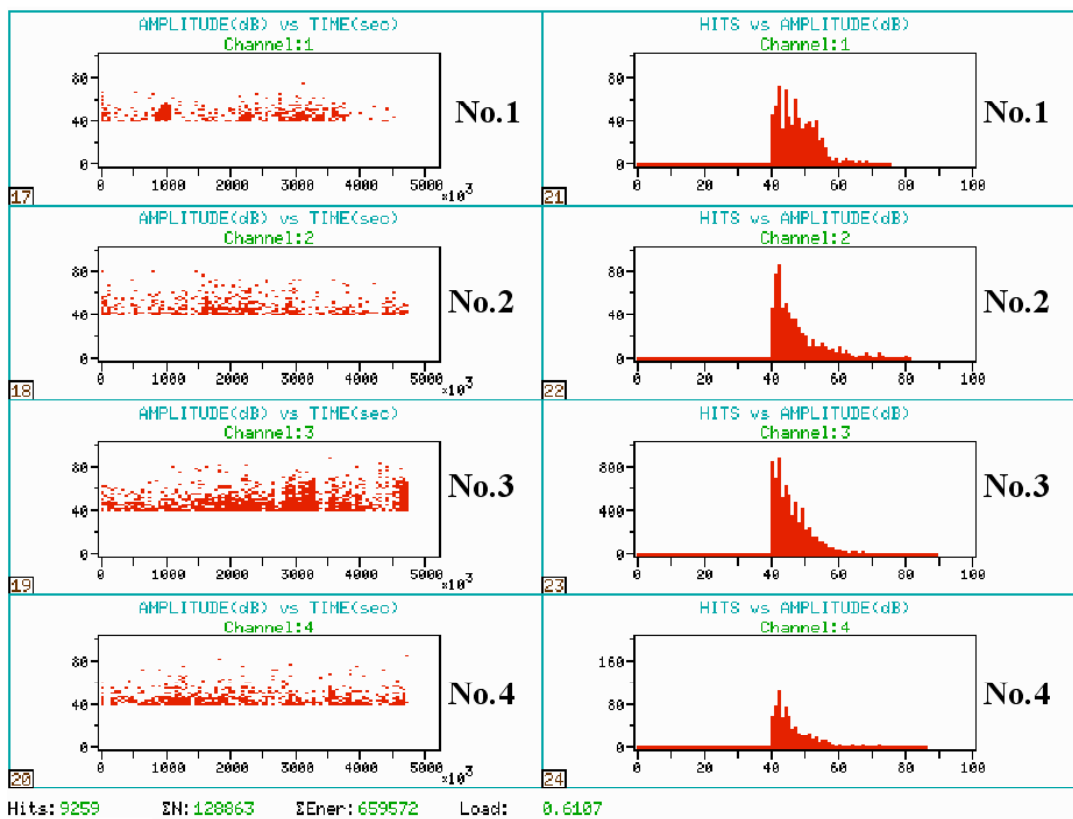


Fig. 3 Results of Test 1 (Amplitude histories and distributions).

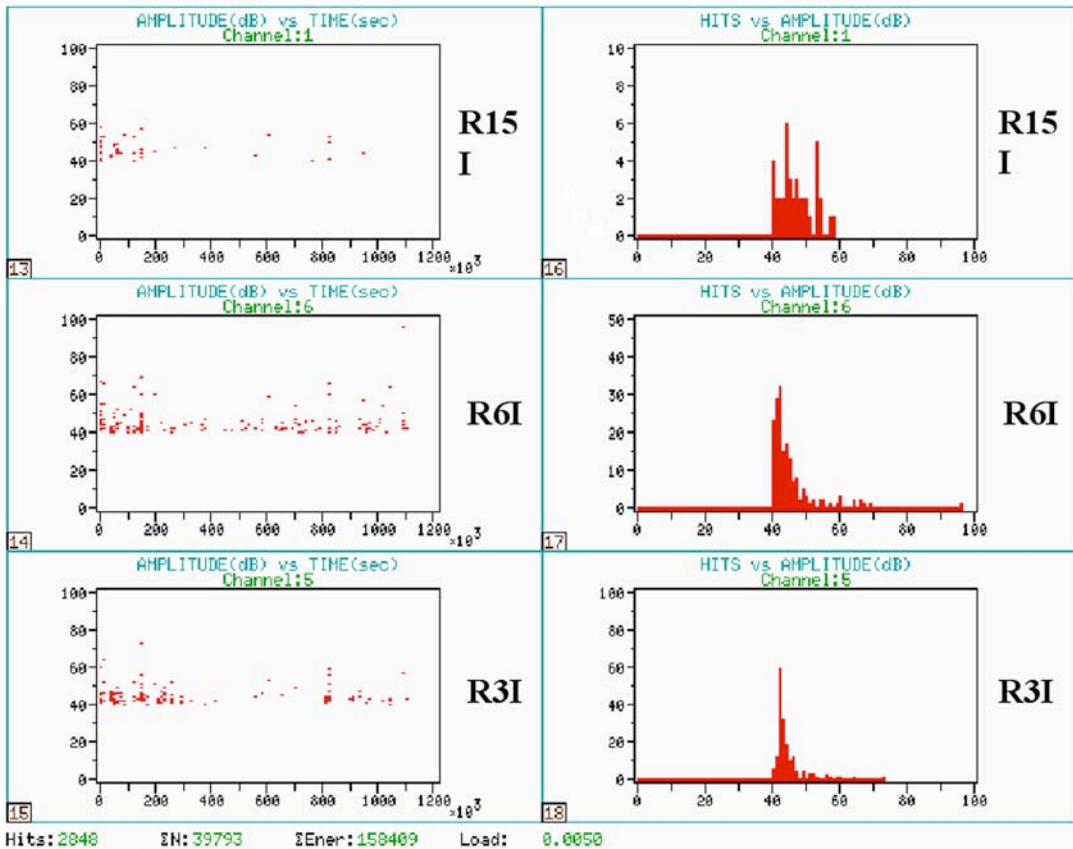


Fig. 4 Results of Test 2 with specimen No. 1 (Amplitude histories and distributions).



Fig. 5 AE sensors mounted on a simulated buried pipe.

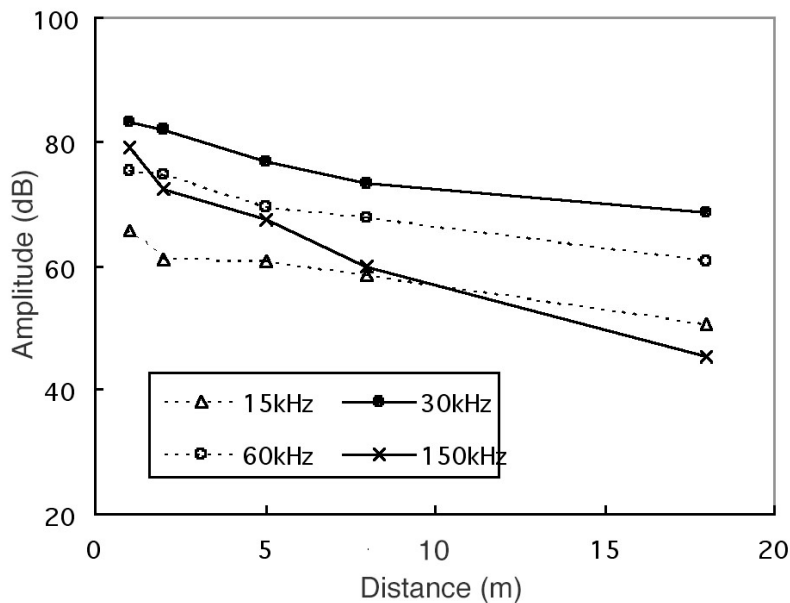


Fig. 6 Attenuation curve on an above-ground empty pipe (pencil-lead break sources).

covered with sandbags were utilized. Shown in Fig. 5 are AE sensors mounted on a simulated buried pipe. Note that they are different from ones listed in Table 1.

Figure 6 gives attenuation curves for A_0 waves in an above-ground empty pipe. AE signals in the high frequency band (R15I) attenuate about 30 dB after traveling 17 m, while it is about 10 - 15 dB in lower frequencies (R6I, R3I, and R1.5I). Shown in Fig. 7 are attenuation curves for an above-ground pipe filled with liquid. The attenuation is slightly greater than that of the empty pipe and the signals attenuate about 10 dB after traveling 8 m.

Attenuation curves of an empty buried pipe without protective film are indicated in Fig. 8. The signals attenuate about 20 dB after traveling 4 m. Shown in Fig. 9 are those of an empty buried pipe covered with protection film. The attenuation is the largest in this case and the signals attenuate almost 30 dB after traveling 4 m. As presented in the previous section, AE signals due to corrosion can give amplitudes of 80 – 90 dB if the surface is covered with thick

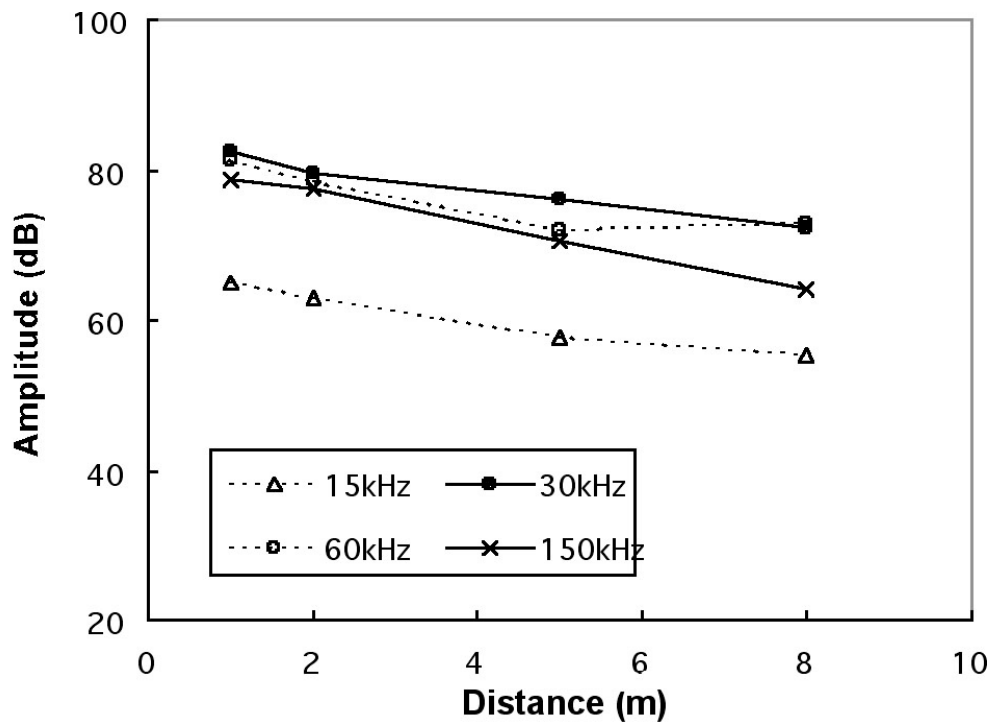


Fig. 7 Attenuation curve on an above-ground pipe filled with liquid (pencil lead breaks).

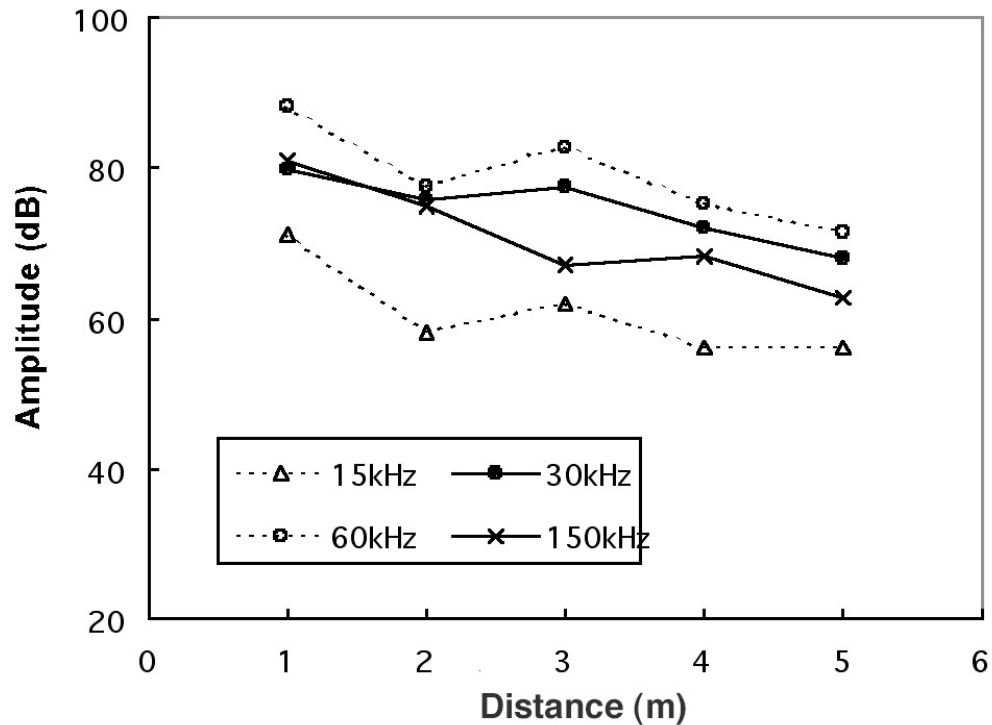


Fig. 8 Attenuation curve of an empty buried pipe without protection film (pencil lead breaks).

oxide film. These signals should be detectable over a conventional threshold voltage at the distance of 4 m from the source, even taking the attenuation during the wave propagation into account. Thus it is concluded that source location should be applicable to a buried pipe covered with protection film up to 4 m in length.

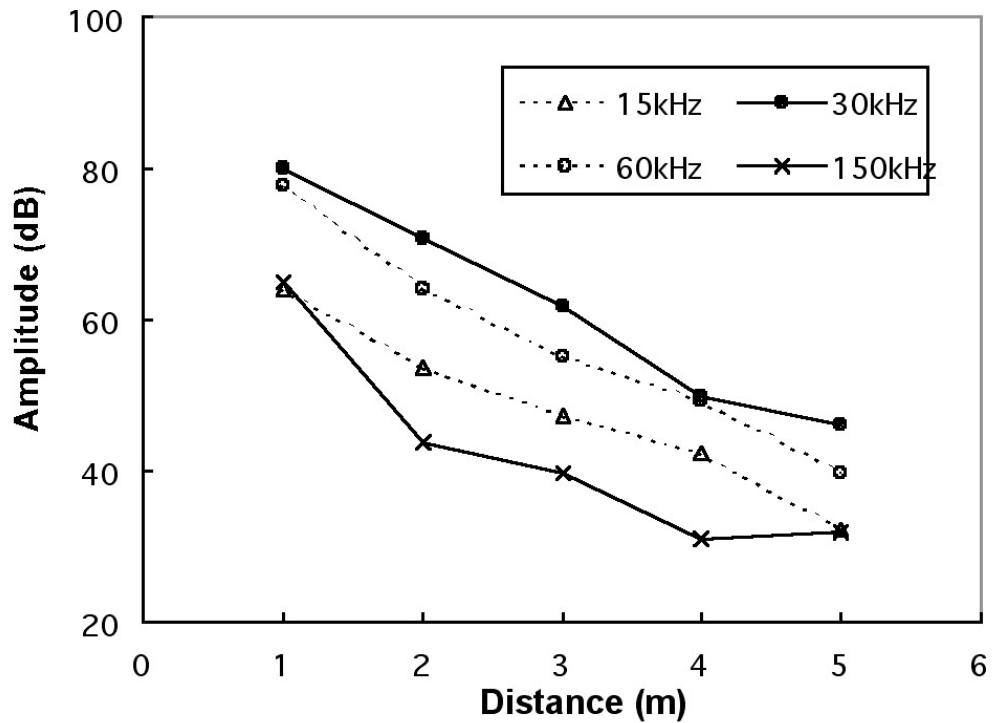


Fig. 9 Attenuation curve of an empty buried pipe covered with protection film (pencil lead breaks).

Field AE measurements for 13 pipes in a refinery

Field AE measurements were made for 13 pipes in a refinery. Listed in Table 1 are pipe numbers, sizes (nominal diameter in inches), liquid inside, and flow (volume) rates. Ten of them (Nos. 02 – 11) are partially buried (about 3 m in length) and three of them (Nos. 12 – 14) are above-ground pipes, steam-heated and insulated. These pipes are shown in Fig. 10.



Fig. 10 Partially buried pipes tested.

Table 1 Tested pipes.

No.	Size	Liquid	Volume rate (kl / h)	Flow rate (cm / s)
02	6B	Desulpherlyzed Naphtha	204	310.1
03	6B	Desulpherlyzed light gasoline	48	73.1
04	6B	Improved gasoline	20	30.5
05	6B	Kerosene	71	108.1
06	6B	Light oil	112	170.6
07	8B	Heavy gasoline	204	174.7
08	2B	Unknown	-	-
09	4B	Cycle oil	51	174.7
10	6B	Light oil	28	42.6
11	6B	Jet fuel	0	0
12	18B	Sub-produced heavy oil	0	0
13	18B	Mid-quality sub-produced heavy oil	0	0
14	24B	Mid-sulphur heavy oil	0	0

AE measurements were made normally for 30 minutes with 30 kHz and 60 kHz sensors mounted on the pipe surface with magnet hold-downs. Both sensors were paired and placed near the both ends of the buried part, spaced 4 m to perform linear source location.

Figure 11 gives test results of pipe 02, obtained with 30 kHz sensors. Number of hits detected by each channel, hit rate history, hit history, amplitude history, source location and event history are indicated. 280 hits are detected by the two sensors. The maximum amplitude exceeds 70 dB. 10 events are located and an event cluster is observed at one side (N side) of the buried zone. Test results obtained with 60 kHz sensors are shown in Fig. 12. 120 hits are detected but only one event is locatable in this case, indicating much less detectability at 60 kHz.

Test results for all the pipes are summarized in Table 2. Number of hits, number of events and comments on the source location are listed with the pipe number and type of sensor. Note that measurements were made in very noisy environments for pipes Nos. 12 – 14 due to high noise resulting from steam leaks.

Comparisons of AE data with UT and visual inspection

UT thickness measurements and visual inspections (VI) were made in order to verify usefulness of the AE data. Listed in Table 3 are comparison of AE results with UT and VI data, giving correlation between them. In pipe No. 2, excellent agreement is obtained between the AE and UT/VI. Both UT and VI observed significant corrosion at the N side of the buried part, corresponding to the location of the AE cluster (source). Small numbers of hits were detected in pipes Nos. 6 – 11, where no significant corrosion was found. Therefore, the correlation between AE and UT/VI is relatively good.

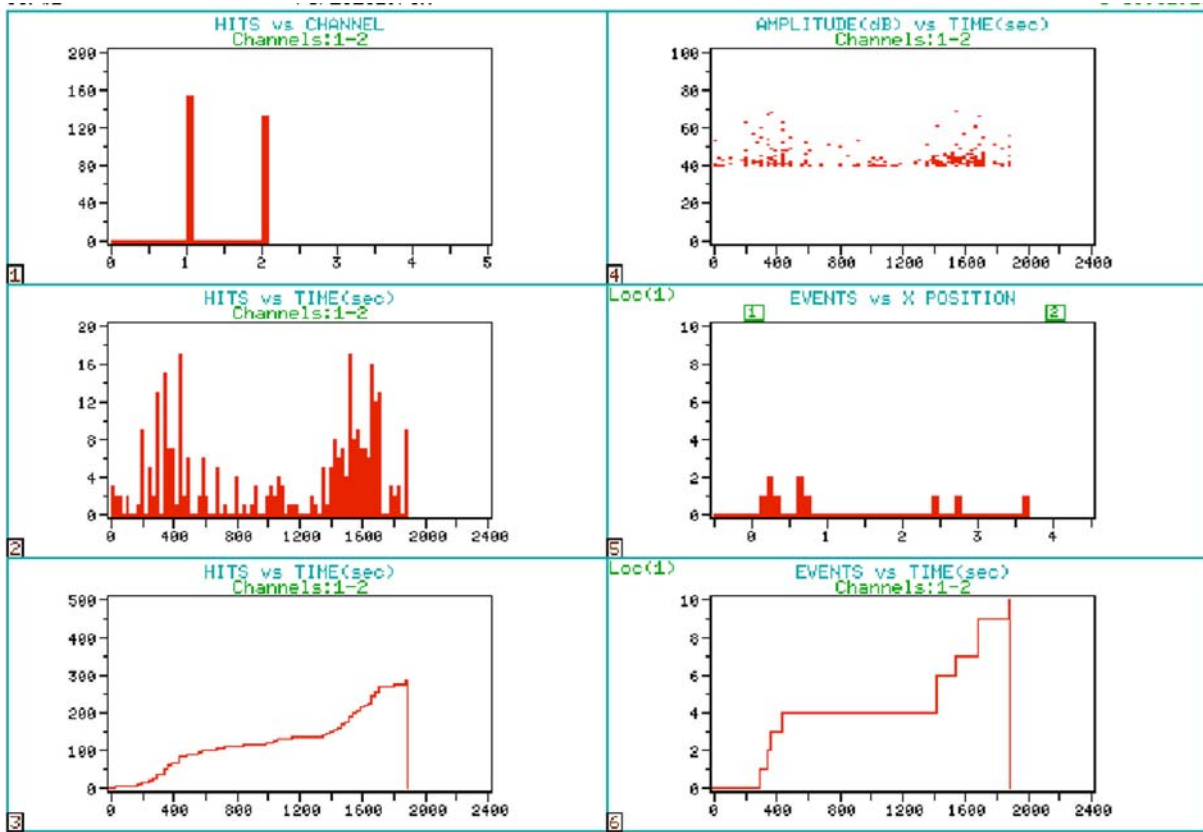


Fig. 11 Test results of pipe 02 (with R3I sensor).

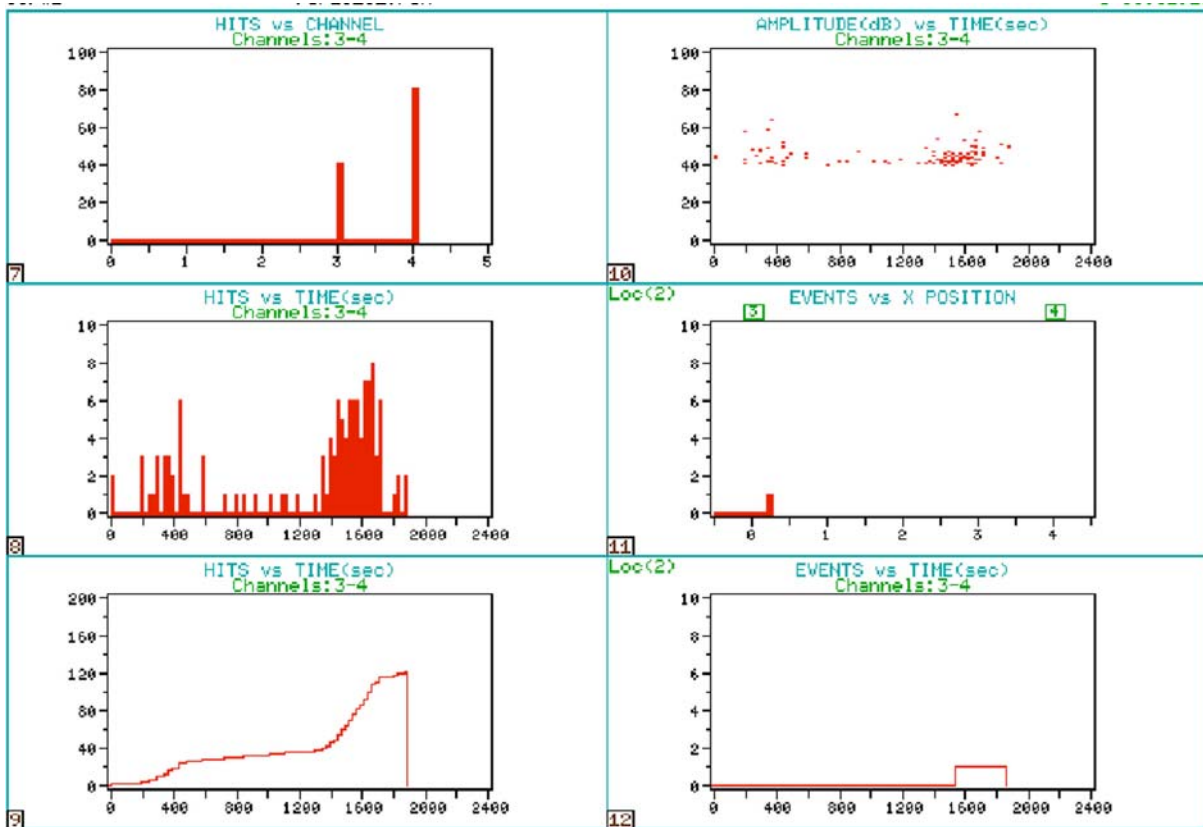


Fig. 12 Test results of pipe 02 (with R6 sensor).

Table 2 Summary of the test results.

No. (sensor)	Flow rate (cm/s)	Number of hits (30 minutes)	Number of events	Source location
02(R3)	310.1	280	10	Left end of the buried part
02(R6)	310.1	120	1	Left end of the buried part
03(R3)	73.1	300	13	Left and right ends of the buried part
03(R6)	73.1	100	0	—
04(R3)	30.5	650	18	Left side of the buried part
05(R3)	108.1	480	45	Widely spread over the buried part
06(R3)	170.6	70	0	-
07(R3)	174.7	90	2	1 event each in the center and left side
08(R3)	-	16	-	-
09(R3)	174.7	120	-	-
10(R3)	42.6	70	-	-
11(R3)	0	36	5	Right end of the buried part
12(R3)	0	700(10 minutes)	220	Peaks in the left and right sides (Vth = 50dB)
13(R3)	0	190(10 minutes)	42	Peaks in the left and right sides (Vth = 50dB)
14(R3)	0	2500(15 minutes)	600	Peaks in the left and right sides
14(R6)	0	190(15minutes)	50	3 peaks in the right side of the buried part

In pipe No. 3, though AE clusters (sources) were found at both sides of the buried part, no significant corrosion was observed. Accordingly, there is no good correlation in this case. In pipes Nos. 4 and 5, it was difficult to obtain meaningful AE data due to unknown continuous noise. A lot of AE signals were detected but there was no significant corrosion on the pipes. In pipes No. 12 – 14, it was also difficult to obtain meaningful AE data due to continuous AE signals resulting from steam leaks.

AE measurement was made under good conditions for eight pipes. Good correlation with UT and VI was observed in seven of them. There was one clear failure in the evaluation. The data obtained from the field measurements thus show that AE can be a promising method for evaluating corrosion damages in buried pipes. However, care must be taken to obtain meaningful data for evaluation. It is obvious that AE measurement must be done under good conditions with low noise.

3. Conclusions

In order to investigate the applicability of AE method for the evaluation of corrosion damages in buried pipes, systematic tests have been conducted in laboratory and field. From the test results, the following conclusions can be drawn:

(1) Corrosion tests in laboratory showed that steel specimens with thick oxide film generate strong AE signals with amplitudes over 80 dB during the corrosion process in salt water. It was also found that the signals with low frequencies (20 – 80 kHz) are mainly produced during the process.

(2) Wave propagation tests using pipes under different surface and buried conditions found that source location can be applied to a buried pipe covered with protection film up to 4 m in length.

(3) AE measurements for 13 pipes in service were made in a refinery. The comparison of the AE results to UT thickness measurements and visual inspections showed the potential usefulness of AE technique for evaluation of corrosion damages in buried pipes.

Table 3 Correlation between AE data and thickness measurement (UT) and visual inspection (VI).

○:Good △:Intermediate ×:Bad

Pipe No.	Thickness measurement(UT)	Visual inspection(VI)	Comments
②	Maximum loss at N side(○)	Significant corrosion at N side (protection film (○))	Significant AE source at N (left) side
③	No significant loss (×)	No significant corrosion (×)	AE source (R3 sensor) at left and right sides, do not agree with UT and VI
④	No loss (×)	No corrosion (×)	Some events due to continuous noises
⑤	No loss (×)	No corrosion (×)	Continuous noises
⑥	No loss (○)	No corrosion (○)	Small hits
⑦	No loss (○)	No corrosion (○)	Small hits
⑧	No loss (○)	No corrosion (○)	Small hits
⑨	No loss (○)	No corrosion (○)	Small hits
⑩	No loss (○)	No corrosion (○)	Small hits
⑪	No loss (○)	No corrosion (○)	Small hits, some events
⑫	No loss (×)	No corrosion (×)	High noises due to steam
⑬	No loss (×)	Small corrosion (△)	AE events corresponds to corrosion
⑭	No loss (×)	No corrosion (×)	High noises due to steam

References

1. ASNT Nondestructive Testing Handbook, 2nd ed., Vol. 5, Acoustic Emission Testing, 1989, p. 166.
2. Long, R.S., Vine, K., Lowe, M.J.S. and Cawley, P. 'Monitoring of acoustic wave propagation in buried water pipes', *Review of Progress in Quantitative NDE*, Vol. 20, D.O. Thompson and D.E. Chimenti (eds), 2001, American Institute of Physics, pp. 1202-1209.

NEW CONCEPT OF AE STANDARD: JIS Z 2342-2002 “METHOD FOR ACOUSTIC EMISSION TESTING OF PRESSURE VESSELS DURING PRESSURE TESTS AND CLASSIFICATION OF TEST RESULTS”

Y. MORI¹, M. SHIWA², M. NAKANO³ AND K. IWAI⁴

¹ Department of Mechanical Engineering, College of Industrial Technology, Nihon University, 1-2-1, Izumi, Narashino, Chiba 275-8575, Japan.

² Tsurumi R&D Center, Japan Power Engineering & Inspection Corp., Yokohama, Japan

³ Chiyoda Advanced Solutions Co., Ltd., Yokohama, Japan

⁴ Showa Electric Laboratory Co., Ltd, Tokyo, Japan

Abstract

Japanese Industrial Standard (JIS) Z 2342 was revised significantly in 2002. The original standard was enacted in 1991 with the title, "Method for acoustic emission testing of pressure vessels during pressure test". The title was also changed, based on NDIS2412 “Acoustic Emission Testing of Spherical Pressure Vessel Made of High Tensile Strength Steel and Classification of Test Results”, which was enacted in 1980. This paper reports the new concept and the contents of the amendment.

Keywords: JIS; NDIS2412; pressure vessels; pressure tests; classification; acoustic emission

1. Introduction

Japanese Industrial Standard (JIS) Z 2342-91 "Method for acoustic emission testing of pressure vessels during pressure test" is a standard enacted in 1991 based on NDIS 2409-79 of the Japanese Society for Non-Destructive Inspection (JSNDI). After ten years, remarkable improvement was made in the performance of AE equipment and the analysis technique. Moreover, the domestic maintenance specifications based on defective permission of a structure have been deregulated with the changing needs of the Japanese society. Establishment of the nondestructive inspection whose cost can be reduced while maintaining dependability was called for, thus changing the environment of AE examination. The revision of JIS Z 2342 was conducted in 2002 in response to this change. In the present revision the method of classification of AE test results was enlarged and the quantitative classification method based on the empirical rule, which can evaluate the structural integrity of the vessels during pressure test, was introduced as a new concept of the new AE standard.

2. Background of the Revision

When creating the JIS draft proposal of 1991 edition, there was NDIS 2412-80 (Acoustic Emission Testing of Spherical Pressure Vessel Made of High Tensile Strength Steel and Classification of Test results), which JSNDI had enacted in 1980 as a domestic standard. NDIS2412 included important new approach embodying the classification of test results by a cumulative AE energy value based on cluster location processing (as it is known today), and the cumulative AE events behavior pattern. These were not in any of various foreign standards at that time (1,2). In 1991, it was proposed to draft a JIS based on this NDIS 2412-80 at the outset. However, with the technical problems of those days, the objection arose as to the validity of large-scale equip-

ment for measurements and the signal analysis of AE. Thus, opinions were divided in the committee with respect to the classification algorithm. Consequently, JIS Z 2342-91, was enacted for the purpose of specifying the AE testing methods in common with ASME and/or ASTM standards without including the advanced contents of the classification scheme (3-8).

In this revision, since the analysis of large-scale AE dataset and the use of complicated parameters for the classification has become feasible by the miniaturization of AE equipment system, improvement in the data acquisition and analysis speed, and increasing of memory size, AE engineers have reached a new understanding of the still valid points of the classification algorithm of NDIS 2412-80. This is aided by experience from the actual results gained in Japan for the past 20+ years. Therefore, in the revised standard, AE testing and the latest techniques of AE analysis are adopted, incorporating the classification method of AE test results, originally used in NDIS 2412-80. The standard title is also modified to reflect this change as " Method for acoustic emission testing of pressure vessels during pressure tests and classification of test results". Additionally, substantial contents have been added in the new standard.

3. Contents of JIS Z 2342-02

This standard consists of the following items.

1. Scope
2. Referenced Documents
3. Terminology
4. Test Preparations
 - 4.1 Preliminary Survey
 - 4.1.1 Materials Characteristics and Weld Characteristics of Vessel
 - 4.1.2 Configuration of Vessel
 - 4.1.3 Pressurization Hysteresis of Vessel
 - 4.1.4 Pressurization Schedule and Pressurization Conditions
 - 4.1.5 Cure of Noise Situation
 - 4.1.6 Others Requirement
 - 4.2 Testing Equipment
 - 4.2.1 AE Sensor
 - 4.2.2 AE Equipment
 - 4.2.3 Simulated AE Source
 - 4.2.4 Continuation Record of Pressure
 - 4.3 Calibration of AE Equipment
 - 4.3.1 AE Sensor Mounting
 - 4.3.2 Calibration
 - 4.4 AE Propagation Characteristics of vessel
 - 4.4.1 Wave Velocity
 - 4.4.2 Attenuation
 - 4.4.3 Source Characteristics of AE
 - 4.5 Sensor Spacing and Location
 - 4.6 Safety
5. Test Procedure
 - 5.1 Sensor Coupling and Circuit Continuity Verification
 - 5.2 Background Noise Check
 - 5.3 Adjustment of AE Threshold Value

- 5.4 Loading Sequence
 - a) Pre-load
 - b) Loading Speed
 - c) Pressurization method
 - d) Stop of pressurization
- 5.5 AE Measurement
- 5.6 Pressure Measurement
- 6. Classification of Test Result
 - 6.1 Source Location based analysis
 - 6.1.1 Arrival Time Differential source Location
 - 6.1.2 Calculation of Relative AE Energy Value
 - 6.1.3 Grouping by Cluster Location
 - 6.1.4 Overall AE Evaluation value
 - 6.1.4.1 Type of Group
 - 6.1.4.2 Class of Group
 - 6.1.4.3 Overall AE Evaluation of Group
 - 6.1.4.4 Output Message
 - 6.2 Zone Location based analysis
 - 6.2.1 Zone Location
 - 6.2.2 AE Energy Value
 - 6.2.3 Overall AE Evaluation value
 - 6.2.3.1 Type of Group
 - 6.2.3.2 Class of Group
 - 6.2.3.3 Overall AE Evaluation of Group
 - 6.2.3.4 Output Message
- 7. Report

4. Outline of JIS Z 2342-02

Scope

This practice covers AE examination of metal pressurized vessels and tanks under pressure or vacuum to determine structural integrity. Moreover, this practice can be applied to the examination performed at the time of periodical inspections without limiting to the examination at the time of product startup. Furthermore, this specification is applicable also online monitoring by AE. The scope of the method of AE examination and the classification of test results specified by this specification is fundamentally applicable not only to metal but also FRP vessels during the proof tests and pneumatic tests. However, by this practice, the scope was specified as a metal container and its pipeline.

AE Sensor

There was no specification about the characteristics of AE sensors to be used in the old documentation. It is covered in NDIS 2109-91 of JSNDI as “Method for absolute calibration of acoustic emission transducers by reciprocity technique”, which was published after establishment of the old documentation. Following this, "NDT Acoustic emission inspection- Secondary calibration of acoustic emission sensors" was published as ISO 12714-99 in 1999. Usually sensitivity of AE sensor was calibrated by one of the methods in these documents at present. Therefore, the present revision prescribed the sensitivity and the frequency band of the AE sensor to be used. Since the calibration result of AE sensor by ISO 12714-99 is almost the same as that of NDIS 2109-91, the revised Standard specified to require the absolute sensitivity by the Rayleigh

wave calibration since it is common to both of them (9,10).

Basic Concept of Classification Method

The classification method of a large-scale structure is aimed to evaluate the crack propagation locally by the stress concentration as a dangerous defect. From several tens of examples of AE inspection during loading of the large-scale pressurized vessels, the following correlation are confirmed between the states of AE and generating defects.

- (1) The possibility of defect existence is high when many burst-type AE signals are generated and their locations are concentrated.
- (2) Generally the instability of defect is judged from the following,
 - a) It is unstable when there are many burst-type AE events.
 - b) It is unstable when the amount of released AE energy from the defect is large.
 - c) It is related to the trend pattern of burst-type AE being generated. The increasing trend during high-pressure application indicates more instability than of the similar pattern at low pressure.

The structural integrity of pressure vessels is evaluated by combining all the burst-type AE phenomena generated from the defective part as a cluster or zone, as shown in Fig. 1. At first, each locally located AE event is combined as a single cluster. Next, "Type" is characterized by an active pattern of AE events in each cluster. "Class" is defined from the activity of each cluster characterized by the combination of a cumulative AE event counts value and a cumulative AE energy value. Furthermore, "Rank", which means the evaluated classification of the defect, is obtained by the combination of "Type" and "Class".

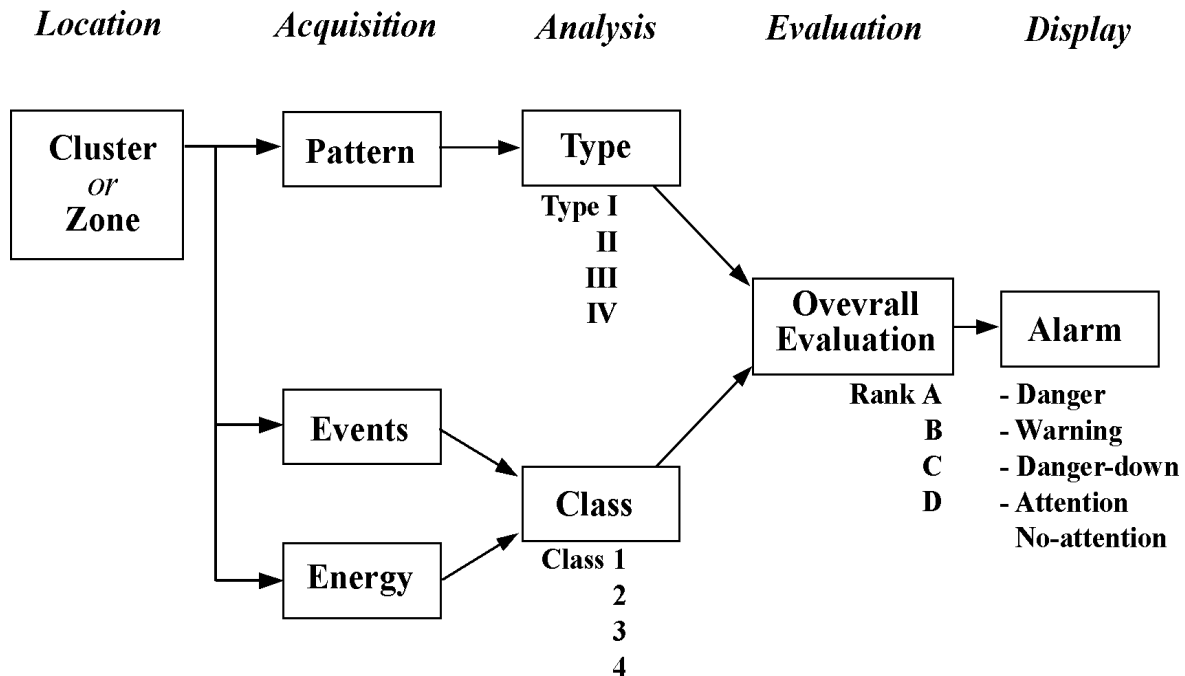


Fig. 1 Evaluation flow chart of JIS Z 2342-2002.

This evaluation can be conducted on-line in real time for every generated AE event by using the algorithm shown later about the cluster, to which the AE event belongs. In an emergency, it can output an alarm signal using the algorithm.

Classification Algorithm (Type, Class and Rank)

It is necessary to conduct the clustering of located events. There are the source location method and zone location method in clustering. Both types of location methods can be used in this practice.

Source Location based analysis

(1) Clustering

A located AE event identified by source location belongs to one cluster. A typical cluster's length R is 5 to 10% of the maximum AE sensor spacing. When an AE event α is identified at position P_1 , cluster A of the radius R centering on P_1 is formed. Next, if an AE event β is identified at position P_2 , which is in the circle of the radius R of cluster A, the AE event β belongs to cluster A. On the other hand, if it is out of the circle of cluster A, the cluster B of the radius R centering on the position of located P_2 will newly be formed. Thus, every located AE events belong to clusters.

(2) "Type" of Cluster

"Type" of cluster is characterized by the combination of cumulative AE event counts ΣN and cumulative AE energy value ΣE . AE energy used here is defined as relative energy. The relative energy is an energy value converted into the generating location of the AE source, and is the value, by which the attenuation by wave propagation distance was corrected. That is, when the peak amplitude V_p^l is detected as the first arrival AE signal at AE sensor position L_1 and distance Δr with the source position L_0 of the located event, the relative energy E_{AE}^R will be calculated by the following equation.

$$E_{AE}^R = (V_p^l)^2 / (\alpha E \times \Delta r) \quad (1)$$

where αE is the attenuation value of AE energy.

(3) "Case" of Cluster

The cluster is classified into one of the following four types, I to IV, according to correlation with cumulative AE energy value ΣE of a cluster, and the present pressure level P_i .

Type I is a type of AE generated throughout various loading levels; AE is sparsely detected over all processes and there is no intensive generation.

Type II is low or intermediate intensive type; AE is detected at low pressure or medium pressure and the generation stops or decreases rapidly in high-pressure region.

Type III is a rapid increase with high-pressure process. AE increases substantially at high pressure.

Type VI is a frequent occurrence type, and AE is detected frequently throughout the pressurization.

The classification of the type I to VI is performed by the following algorithm. Figure 2 shows a relationship between the cumulative AE energy value ΣE and the applied pressure level P . At first, the present pressure value P_i is equally divided into five sections as evaluation pressure. Then, the difference of the cumulative AE energy $\Delta \Sigma E$ of the each evaluation pressure section is obtained as $\Delta \Sigma E_1$ to $\Delta \Sigma E_5$. P_0 is the pressure at the start of evaluation, E_0 is the reference AE energy value for evaluation and is the cumulative AE energy value of Type II and III. E_l is the cumulative energy value for the Type VI.

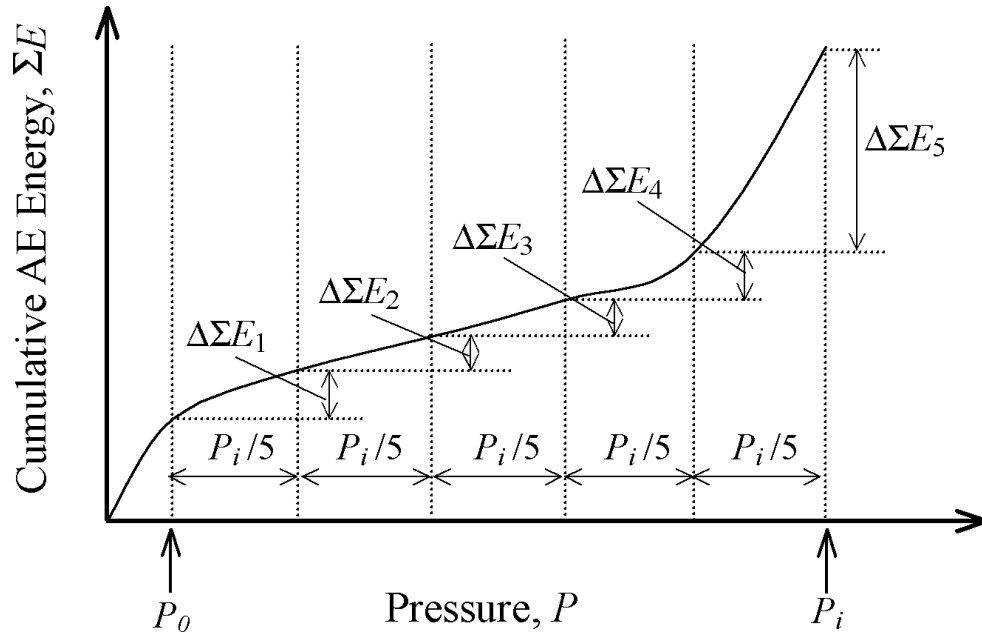


Fig. 2 Classification of “Type” of cluster and/or zone.

$$\Sigma E = \Delta\Sigma E_1 + \Delta\Sigma E_2 + \Delta\Sigma E_3 + \Delta\Sigma E_4 + \Delta\Sigma E_5 \quad (2)$$

$$\text{Type IV : all of } \Delta\Sigma E \geq E_l \quad (3)$$

$$\text{Type III : } (\Delta\Sigma E_4 + \Delta\Sigma E_5) / \Sigma E \geq 70\% \text{ and } \Sigma E \geq E_0 \quad (4)$$

$$\text{Type II : } (\Delta\Sigma E_2 + \Delta\Sigma E_3 + \Delta\Sigma E_4) / \Sigma E \geq 70\% \text{ and } \Sigma E \geq E_0 \quad (5)$$

$$\text{Type II : } (\Delta\Sigma E_1 + \Delta\Sigma E_2) / \Sigma E \geq 70\% \text{ and } \Sigma E \geq E_0 \quad (6)$$

$$\text{Type I : when it is not above any, either} \quad (7)$$

(4) “Class” of Cluster

Clusters are classified into the following class, first to fourth, using the classification diagram of cumulative AE event count ΣN of a cluster, and cumulative AE energy value ΣE . The basic judging diagram is shown in Fig. 3. Note that a user judges and determines classification value of each N and E . Class is judged by correlation of the number of cumulative AE events of each cluster location or the number of cumulative AE events of each zone location, and cumulative AE energy value after the start of measurement. Since the judgment levels $N_1, N_2, N_3, E_1, E_2,$ and E_3 in a classification diagram depend on the condition of cluster location, such as base metal and weld line, these values or ranking are set up based on the prior results by fracture test of specimens and/or AE proof test.

The first class corresponds to the case that depends on a small defect or noise. The second class corresponds to a stable defect or a small defect. The third class corresponds to the tendency of a propagating defect. The fourth class corresponds to the continuous defect propagation under pressure.

Located Cumulative AE Energy, ΣE	E_R				
	\uparrow				
	E_3	2	3	4	4
	E_2	1	2	3	4
E_1	1	1	2	3	
		N_1	N_2	N_3	$\rightarrow N_R$
		Located Cumulative AE Events, N			

Fig. 3. Classification method of “Class” of cluster and/or zone.

(5) “Rank” of Cluster by overall evaluation

The Rank of cluster from A to D is characterized by the Type-m and Class-n as shown in Table 1. Since the Rank changes with location characteristics such as base metal and weld line,

Table 1 Ranking table of overall evaluation value.

Class (n)	1	2	3	4
Type (m)				
I	D	D	C	B
II	D	C	C	B
III	D	C	B	A
IV	C	B	A	A

*Classified as Rank A and B in overall AE evaluation values shall be confirmed for possible flaws by other NDT methods. The AE groups ranked as C and D are not required to be further confirmed for possible flaws.

the matrix of Table 1 is set up based on the prior results by fracture test of specimens and/or AE proof test.

Zone Location based analysis

(1) Clustering

Located AE event carried out by zone location belongs to one of clusters.

(2) “Type” of Cluster

Type of cluster is characterized by combination of cumulative AE event counts ΣN and cumulative AE energy value ΣE . The AE energy used here is defined as AE energy value at sensor position.

(3) “Case” of Cluster

The Case of cluster is the same as that of the case of the source location based analysis.

(4) “Class” of Cluster

The “Class” of cluster is the same as that of the case of the source location based analysis.

(5) “Rank” of Cluster by overall evaluation

The “Rank” of Cluster by overall evaluation is the same as that of the case of the source location based analysis.

Output Message

Output message is given while performing the evaluation of AE classification of the cluster during testing. It provides five levels of output messages according to the change of a rank. When the Rank A continues and ΔP interval is shorter than critical setting-pressure ΔP_c , alarm message of “Danger” is sent. If the Ranks B, C, and D turn into Rank A for the first time and although Rank A continued when the applied pressure rate is low, alarm message of “Warning” is sent.

5. Conclusion

In this significant revision of JIS Z 2342 in 2002, the analysis of complicated AE parameters is adopted for the classification of AE signals detected. The title was also revised to “Method for acoustic emission testing of pressure vessels during pressure tests and classification of test results”. This is made possible with the miniaturization of AE equipment system, improvement in the data acquisition and analysis speed, and increase of memory size. We have recognized the advantages of the classification algorithm of NDIS 2412-80 from the actual AE testing results accumulated in Japan for over 20 years. In revising this standard that was enacted in 1991, the latest AE testing and analysis techniques are adopted, and the classification method of the test results is incorporated. Starting from clustering, an observed set of AE signals are classified into Types I to IV and Classes 1 to 4, which lead to the classification or Rank A to D, with Rank A indicating imminent danger. Cumulative event counts and AE energy are the parameters of importance in this scheme.

References

- 1) NDIS 2412-80: “Acoustic Emission Testing of Spherical Pressure Vessel Made of High Tensile Strength Steel and Classification of Test results”, JSNDI, (1980).
- 2) T. Kishi and Y. Mori: ASTM STP 697, (1979), 131-148.
- 3) ASME Boiler and Pressure Vessel Code Section V article 11: “Nondestructive Examination - Nondestructive Method of Examination - Acoustic Emission Examination of Fiber-Reinforced Plastic Vessels”, ASME.
- 4) ASME Boiler and Pressure Vessel Code Section V article 12: “Nondestructive Examination - Nondestructive Method of Examination - Acoustic Emission Examination of Metallic Vessels During Pressure”, ASME.
- 5) ASME Boiler and Pressure Vessel Code Section V article 13: “Nondestructive Examination - Nondestructive Method of Examination - Continuous Acoustic Emission Monitoring”, ASME.
- 6) ASTM-E1067-96: “Standard Practice for Acoustic Emission Examination of Fiberglass Reinforced Plastic Resin (FRP) Tank/Vessels”, ASTM, (1996).

- 7) ASTM-E1419-96: "Standard Test Method for Examination of Seamless, Gas-Filled, Pressure Vessels Using Acoustic Emission", ASTM, (1996).
- 8) ASTM-E1930-97: "Standard Test Method for Examination of Liquid-Filled Atmospheric and Low-Pressure Metal Storage Tanks Using Acoustic Emission", ASTM, (1997).
- 9) ISO 12713: "NDT-Acoustic emission inspection - Primary calibration of transducers", ISO, (1998).
- 10) ISO 12714: "NDT-Acoustic emission inspection - Secondary calibration of acoustic emission sensors", ISO, (1999).

ACOUSTIC EMISSION CAUSED BY ENVIRONMENTAL EMBRITTLEMENT OF AN Al-Mg-Si ALLOY

KEITARO HORIKAWA, KENICHI YOSHIDA, A. OHMORI and KIYOSHI SAKAMAKI

Department of Mechanical Engineering, Tokushima University

2-1 Minami-josanjima, Tokushima 770-8506, Japan

Abstract

Acoustic emission (AE) due to intergranular fracture was examined in Al-Mg-Si alloys. In T6-aged specimens, concentration of AE event counts appeared at the moment of intergranular fracture as well as at the yielding point. The AE signals associated with the intergranular fracture had its amplitude ranges up to 100 dB. Similar results on the increase in number of AE event counts with high amplitude were also observed when T4-tempered Al-Mg-Si alloys showed intergranular fracture due to hydrogen embrittlement.

Keywords: Al-Mg-Si alloys, Environmental embrittlement, Intergranular fracture, Hydrogen effect

1. Introduction

Automobile manufacturers has been interested in wrought aluminum alloys having excellent mechanical properties for car body panels. Among all the wrought aluminum alloys, 6xxx-series Al-Mg-Si alloys have been widely used due to their good formability, corrosion resistance, spot weldability, and precipitate strengthening after paint-bake cycles [1]. The basic requirement for automotive sheet is to have a good formability so that the panel can be stamped, or preferably increasing their strength when the part is painted and baked. Thus, these alloys combine the good formability of the solution-treated state (T4 temper) with the additional increased strength of the age-hardened state (T6).

However, the formability of the Al-Mg-Si alloys is not enough for the demands of automotive sheets as compared with Al-Mg alloys [2,3]. It was reported recently that T4-tempered Al-Mg-Si alloys containing excess silicon were prone to show intergranular fracture when the alloys were deformed at room temperature: tensile strain rates were very slow ($\sim 10^{-7} \text{ s}^{-1}$) [4] and the bending stress was applied [5]. Thus, suppression of the intergranular fracture would be a vital issue to improve the formability of Al-Mg-Si alloys. In order to comprehend the mechanism of the intergranular fracture in Al-Mg-Si alloys, dynamic observation in the tensile deformation and fracture would be valuable. In the present study, we applied acoustic emission (AE) method to examine the intergranular fracture of Al-Mg-Si alloys. In particular, effects of additional silicon, aging, and strain rate on AE characteristics are examined.

2. Experimental

Materials

Two kinds of Al-Mg-Si alloys were cut from the rolled sheets so that the longitudinal direction of the specimens was perpendicular to the rolling direction (LT). Chemical compositions of the alloys are shown in Table 1. Plate type specimens for the measurement of

Table 1 Chemical composition of Al-Mg-Si alloys [wt.%].

Alloys	Mg	Si	Cu	Fe	Mn	Zn	Al
Balanced	0.70	0.46	0.34	0.03	<0.01	<0.01	Bal.
Excess Si	0.70	0.76	0.34	0.03	<0.01	<0.01	Bal.

AE, having a gage length of 50 mm, width of 25 mm, and thickness of 5-10 mm were prepared. All of the test specimens were solution treated at 510°C for 0.5 h in the furnace and then quenched in water (As-Q). Average grain size of all the specimens after the solution heat treatment was about 250 μm . After the As-Q condition, some of the specimens were kept at room temperature for 7 days (T4) and then aged at 175°C for 0.5 h (BH) or 18 h (T6). Tensile tests were carried out at room temperature, where the relative humidity was about 70%. Ranges of an initial strain rate of the tensile test were from $1.7 \times 10^{-6} \text{ s}^{-1}$ to $1.7 \times 10^{-4} \text{ s}^{-1}$. Mechanical properties were evaluated by measuring values such as 0.2% yield strength, tensile strength (UTS), and elongation. Fracture surfaces were examined with a scanning electron microscope (SEM, Hitachi S-4700). The ratio of the intergranular fracture surface to entire fracture surface was determined from the SEM image.

AE Measurement

Acoustic emission was examined using a two-channel AE system (MISTRAS-2001, Physical Acoustics Corp.) We attached two AE sensors with 200 kHz resonant frequency on the gage part of the test specimen with glue before tensile testing. AE signals were amplified by a total gain of 60 dB and passed through a band-pass filter with the range of 100 to 1200 kHz. The threshold level was 50 dB and the time interval between two sensors was within 10 μs to detect the AE in the deformed region only. Obtained AE data, which consist of number of events, peak amplitude, and root mean square (RMS) voltage, were input to a microcomputer.

Detection of Hydrogen

Hydrogen microprint technique [6] (HMT) with the aid of photographic effect was applied to the Al-Mg-Si alloy with excess silicon deformed 11% at room temperature with an initial strain rate of $1.7 \times 10^{-6} \text{ s}^{-1}$. Before the tensile deformation, the polished specimen was covered with a monolayer of photographic emulsion (Illford L-4 diluted by seven times) by the wire-loop method [7]. After the deformation by 11%, the specimen with the emulsion was developed and then observed together with the microstructure on the specimen surface using SEM with an EDXS attachment.

3. Results and Discussion

As-Q Specimens

Figure 1 shows the effect of excess silicon on AE during the tensile test in the As-Q condition at a strain rate of $1.7 \times 10^{-4} \text{ s}^{-1}$, together with stress versus displacement curves. AE events appeared at the yield point, but no clear AE events could be identified near the fracture point irrespective of the difference in silicon content. Fracture of both Al-Mg-Si alloys with or without excess silicon was entirely transgranular in the As-Q condition. As expected, AE signals due to a sequence of transgranular fracture, namely, void nucleation and growth, and coalescence could not be detected in the present testing condition. The values of 0.2% yield stress were 60 MPa (balanced) and 75 MPa (excess Si), respectively. The difference in the number of AE

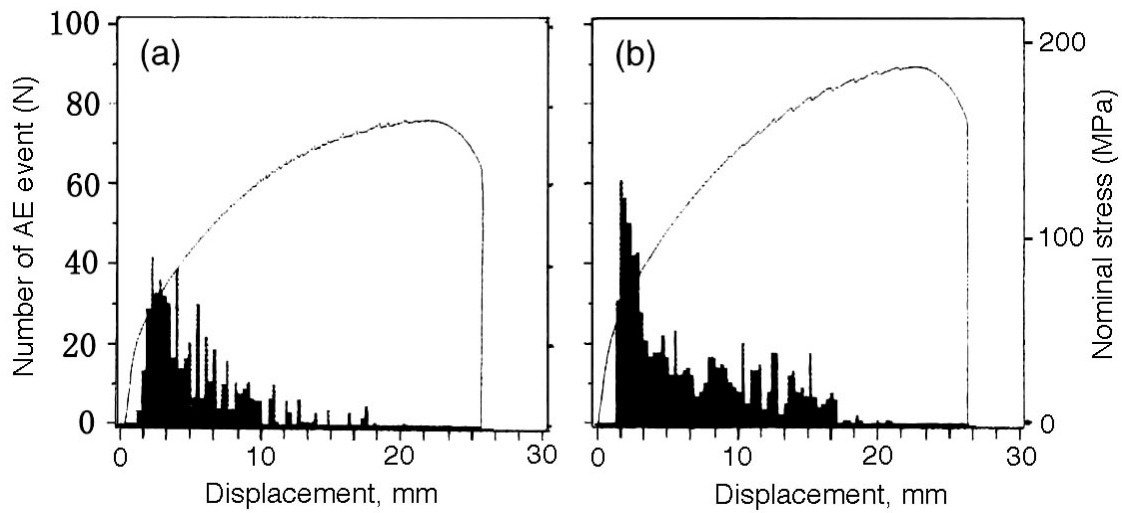


Fig. 1 AE during the tensile test of Al-Mg-Si alloys of (a) balanced and (b) excess-Si in the As-Q condition.

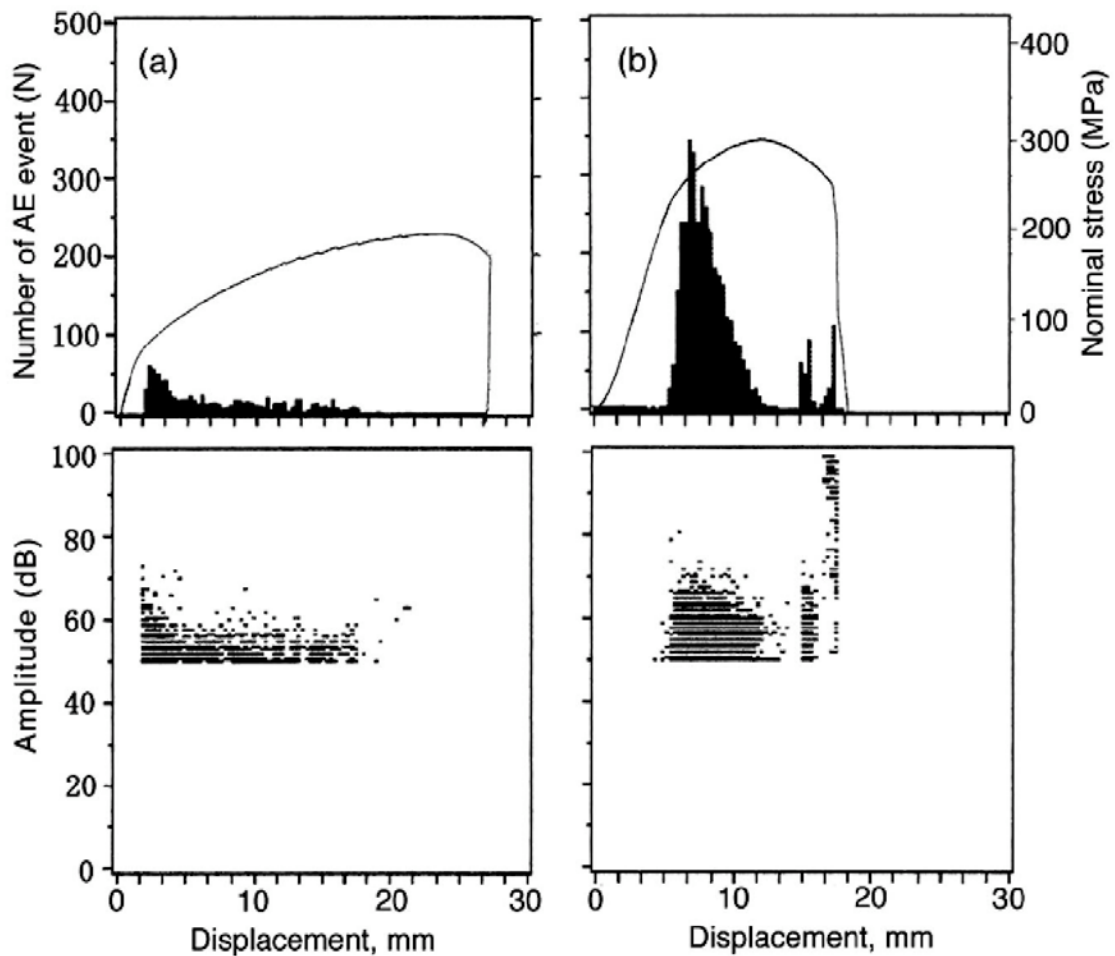


Fig. 2 Effect of aging on AE in an Al-Mg-Si alloy with excess silicon of (a) As-Q and (b) T6-aged.

events at the yield point in the two types of specimens would be due to the difference in solute hardening by silicon in solid solution.

Effect of T6-Aging on AE in Excess-Si Specimens

Effects of T6-aging on AE in the excess-Si specimen tested at an initial strain rate of $1.7 \times 10^{-4} \text{ s}^{-1}$ are shown in Fig. 2. For comparison, the result of AE in the As-Q condition (Fig.1 (b)) is indicated again by changing the scale of vertical axis. AE events in the T6-aged specimen at the yield point have remarkably increased in number as compared with that in the As-Q condition. The maximum of AE events at the yield point in the T6-aged specimen was about six times higher. The value of 0.2% yield stress in the T6-aged specimen was 165 MPa, an increase of 90 MPa over As-Q. The increase in number of AE events at the yield point would be due to the precipitation hardening by β' - Mg_2Si phases reported [8]. In contrast to the As-Q condition, a sudden burst of AE was observed upon fracture in the T6-aged specimen. AE events were also detected at the stage of local deformation before the fracture. The T6-aged specimen showed almost complete intergranular fracture as shown in Fig. 3. The intergranular fracture surfaces covered about 95%. In Fig. 3, GB precipitates and micro-dimples were also visible on the fracture surface.

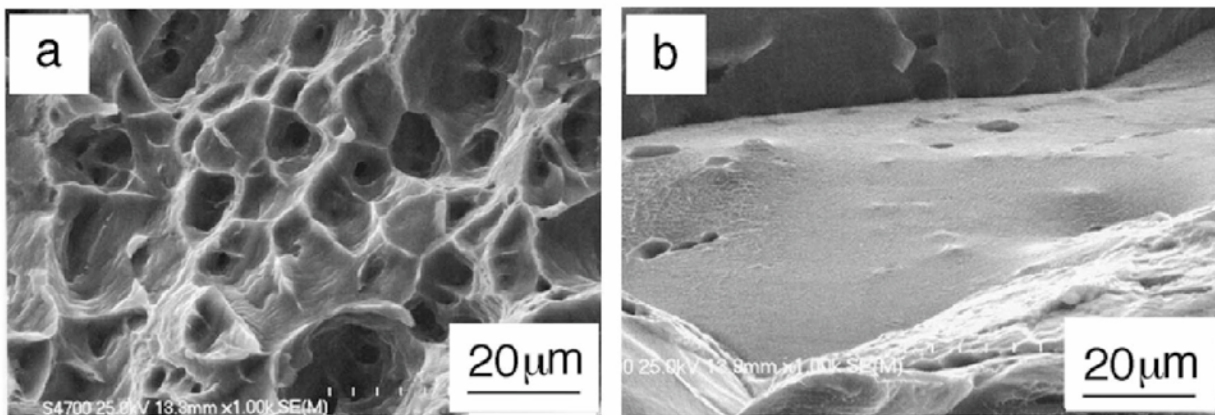


Fig. 3 Fracture surfaces in Al-Mg-Si alloy with excess silicon of (a) As-Q and (b) T6-aged.

Thus, it appears that AE signals detected at the moment of fracture contain the information about a sequence of intergranular fracture, such as crack nucleation, growth, and propagation. The AE signals observed at fracture had high amplitude ranges from 50 to 100 dB. These were higher than those observed at yield (Fig. 3). This suggests that a high AE energy was released from the T6-aged specimen when the intergranular fracture occurred. It is also believed that AE signals observed at the stage of local elongation could represent the information about the initiation and growth of intergranular cracks.

Effect of Strain Rate on AE in BH Specimens

Effect of strain rate on AE during the tensile test in BH specimens is shown in Fig. 4. It was revealed that total elongation decreased when the initial strain rate decreased from $1.7 \times 10^{-4} \text{ s}^{-1}$ to $1.7 \times 10^{-6} \text{ s}^{-1}$, which was in good agreement with the result of Kuramoto et al. [4]. Near the fracture point, a slight increase in number of AE events was observed in both BH specimens tested at both strain rates. The increase in AE amplitude and RMS voltage in the BH specimen tested at the slow strain rate showed that a higher AE energy was released not only at fracture but also at the stage of local deformation, in a similar way as shown in the T6-aged specimen. Intergranular fracture was rarely found on the fracture surface in the BH specimen tested at the strain rate of $1.7 \times 10^{-4} \text{ s}^{-1}$, while fracture morphology in the BH specimen tested at the slow strain rate was a mixture of intergranular and transgranular modes as shown in Fig. 5. The ratio of

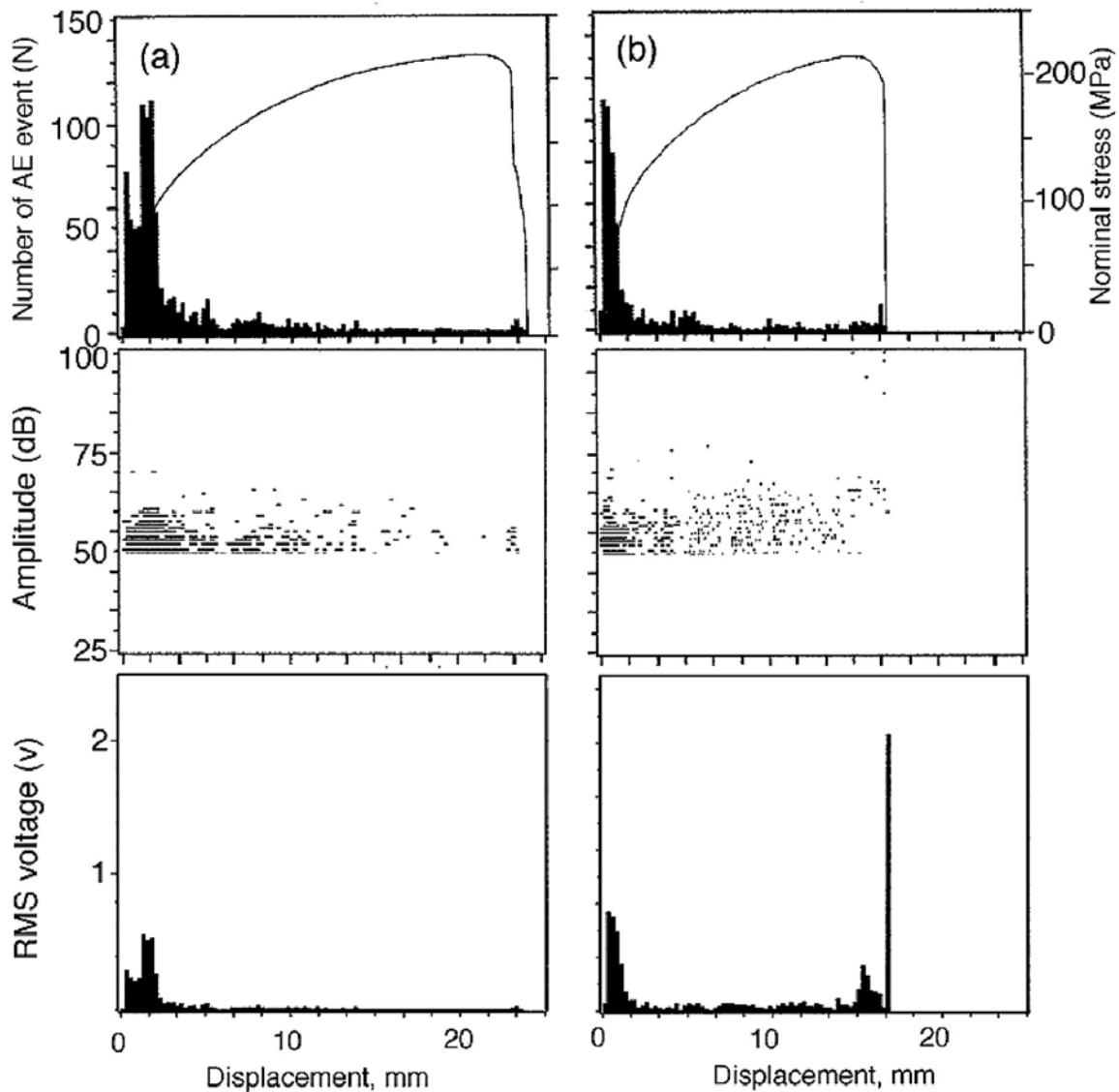


Fig. 4 Effect of strain rate in an Al-Mg-Si (BH) alloy with excess silicon tested at a strain rate of (a) $1.7 \times 10^{-4} \text{ s}^{-1}$ or (b) $1.7 \times 10^{-6} \text{ s}^{-1}$.

intergranular fracture surface to entire fracture surface increased from 0.2% to 8% when the initial strain rate decreased. The intergranular fracture surface in the BH specimen tested at the slow strain rate was distributed preferentially near the surface of the test pieces. This implies that environmental embrittlement occurs in the BH specimen tested at the slow strain rate. At high magnifications, slip steps were frequently visible with micro-dimples on the intergranular fracture surface (Fig. 6). This suggests that matrix slip localization, applying high stress concentration at grain boundaries, would affect the intergranular fracture in the BH specimen tested at the low strain rate. A similar morphology was also reported in an Al-Zn-Mg-Cu alloy [9]. They explained that absorbed hydrogen by the surface reactions between the Al-Zn-Mg-Cu alloy and H_2O are accumulated in the stress field near the crack tip by dislocation motion.

SEM image adjacent to grain boundaries by the HMT method was shown in Fig. 7. Arrangement of silver particles revealed that hydrogen was preferentially located at the grain boundaries. This means that hydrogen introduced from the testing atmosphere was transported to

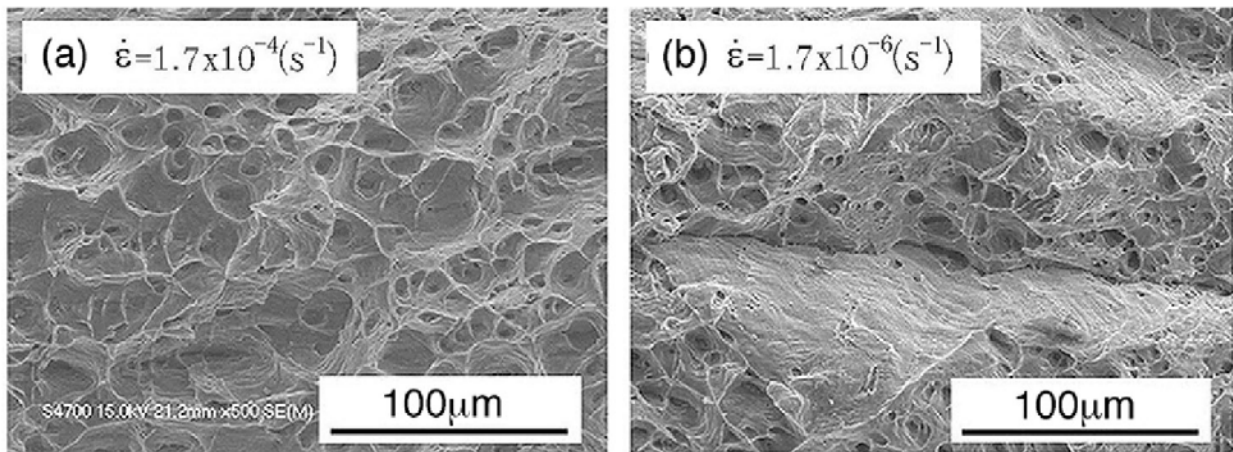


Fig. 5 Fracture surfaces of the Al-Mg-Si (BH) alloy with excess silicon tested at a strain rate: (a) $1.7 \times 10^{-4} \text{ s}^{-1}$, (b) $1.7 \times 10^{-6} \text{ s}^{-1}$.

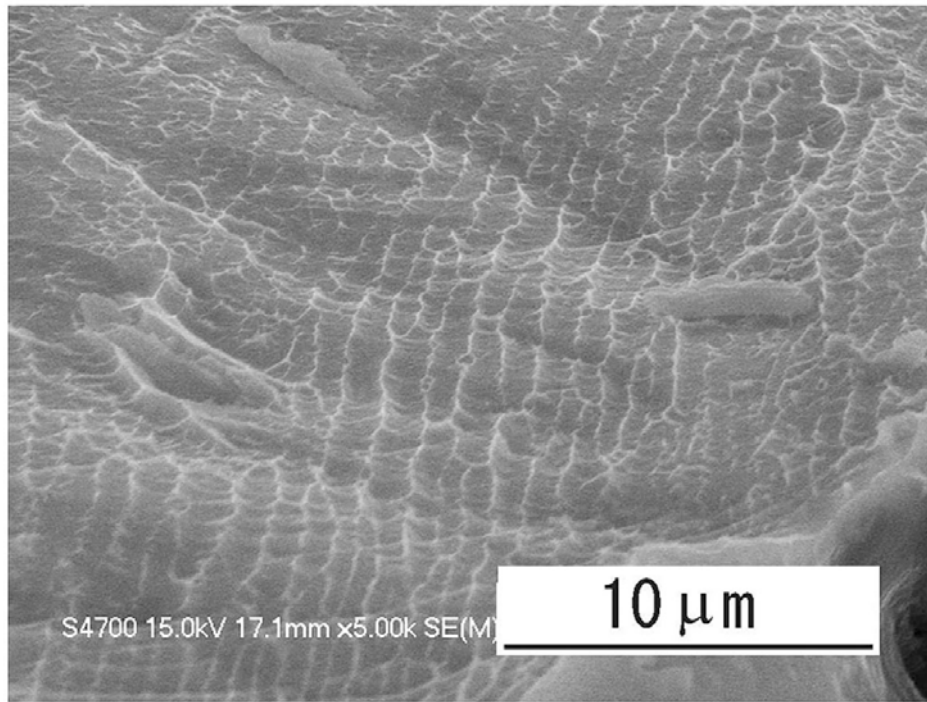


Fig. 6 Magnified image in Fig. 5(b).

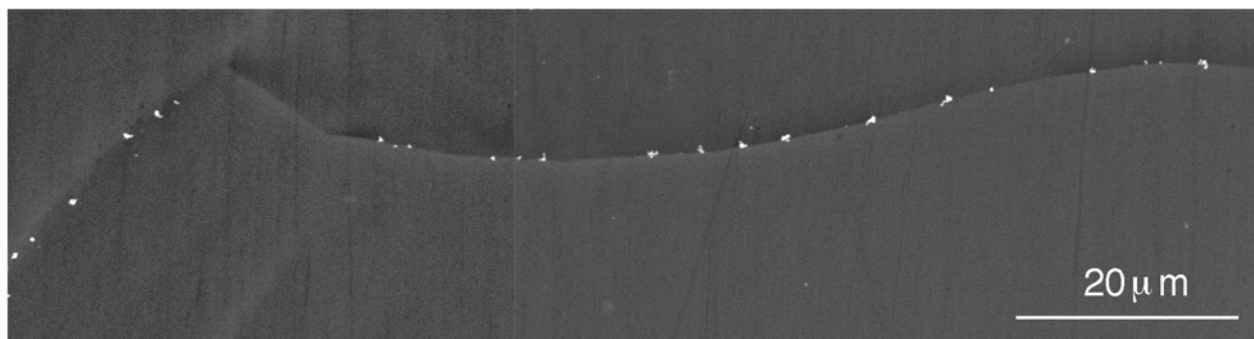


Fig. 7 HMT image of an Al-Mg-Si alloy with excess-Si deformed by 15%. Silver grains representing the position of hydrogen are visible along grain boundaries.

the grain boundaries with a number of gliding dislocations. When the hydrogen concentration at the grain boundaries reaches a certain level during deformation, intergranular cracks would be initiated. Thus, it is concluded that AE signals, detected near the fracture point in the BH specimen tested at the slow strain rate, arise from hydrogen embrittlement.

4. Summary

- (1) In As-Q conditions, no clear AE events caused by the transgranular fracture was identified in Al-Mg-Si alloys irrespective of the difference in silicon content. A single peak of AE event counts was observed at the yield point in both specimens with or without excess silicon.
- (2) In the T6-aged Al-Mg-Si alloy with excess silicon, AE events were observed not only at the yield point but also at the moment of the intergranular fracture. AE signals due to the intergranular fracture had a high amplitude ranges up to 100 dB.
- (3) In the BH specimen tested at a slow strain rate of $1.7 \times 10^{-6} \text{ s}^{-1}$, the increase in AE amplitude and RMS voltage accompanying the decrease in the elongation was observed. The morphology of the near-surface intergranular fracture suggested that AE signals generated near the fracture point are related to hydrogen embrittlement.

Acknowledgements

We wish to thank Branch Research Committee on Physical Metallurgy Related to Grain Boundaries, Japan Institute of Light Metal for providing us with the materials.

References

- [1] S. M. Hirth et al.: Mater. Sci. Engng., **A319-321** (2001), 452.
- [2] J. Saker et al.: Mater. Sci. Forum, **331-337** (2000), 585.
- [3] S. A. Court et al.: Mater. Sci. Engng., **A319-321** (2001), 443.
- [4] S. Kuramoto, M. C. Hsieh and M. Kanno: Abstract of The 101th Conf. Japan Inst. of Light Metals, (2001), p. 243.
- [5] G. Itoh et al.: Abstract of The 100th Conf. Japan Inst. of Light Metals, (2001), p. 349.
- [6] T. E. Perez and J. Ovejero Garcia: Scr. Metall., **16** (1982), p. 161.
- [7] G. V. Prabhu Gaunkar, A. M. Hunts and P. Lacombe: J. Mater. Sci., **11** (1976), 1439.
- [8] G. A. Edwards et al.: Acta Mater., **46** (1998), 3983.
- [9] S. Kuramoto, J. Okahana and M. Kanno: Mater. Trans., **42** (2001), 2140.

QUANTITATIVE STUDY OF ACOUSTIC EMISSION DUE TO LEAKS FROM WATER TANKS

K. MOROFUJI¹, N. TSUI¹, M. YAMADA², A. MAIE², S. YUYAMA³ and Z. W. Li³

¹ Tokyo Gas Co., Ltd., Shin Isogo 34, Isogo, Yokohama, Kanagawa 235-0017, Japan.

² National Research Institute of Fire and Disaster, Nakahara, Mitaka, Tokyo 181-8633, Japan.

³ Nippon Physical Acoustics Ltd., Higashi, Shibuya-ku, Tokyo 150-0011, Japan.

Abstract

Leakage from tank floor can possibly pollute the environment or cause major accidents. To prevent them, acoustic emission (AE) testing has come to the fore as a means of inspecting tanks without taking them out of service. Under the AE method, however, there are almost no data on leakage; the basic characteristics for leakage have not been elucidated. This paper presents the results of a study, using a water tank for fire-fighting, involving the measurement of AE waves generated by leakage of water from small holes made in the bottom, in order to identify the fundamental characteristics and clarify the differences from AE results in the case of corrosion.

Key Words: Acoustic emission; Oil tank; Leak detection; Tank bottom; Tank floor; Corrosion; Location

1. Introduction

Although the number of oil tanks installed in Japan is steadily declining (1), the number of accidents associated with leakage is steadily rising (2). The principal cause of these accidents is deterioration due to factors such as corrosion. Caution is required particularly with large-capacity oil tanks, because leakage from them can assume large proportions if detection is delayed. To prevent such accidents, the law requires all oil tanks with a capacity of at least 1,000 kl to undergo an overhaul inspection at a prescribed interval. In contrast, such overhaul inspections are not legally required for oil tanks with a capacity of less than 1,000 kl; the enterprises in question are to fix overhaul intervals and check them on their own initiative (3). In some cases, leakage of contents from floor is not immediately detected; it is discovered only after being carried by groundwater under the tank foundation into rivers, etc. Such accidents pose major pollution problems.

Regardless of the amount, leakage from the bottom of oil tanks constitutes a serious social obligation of the parties responsible for preserving their safety and imposes a substantial economic burden. Deterioration associated with corrosion is the cause of most such leakage, and its prevention is therefore one of the key tasks of oil tank safety management. In recent years, acoustic emission (AE) testing has been attracting attention as a technology for fulfilling this task. It enables assessment of the damage from corrosion on the tank floor without overhaul (i.e., opening). In Japan, AE testing has been conducted on over 20 tanks (4 - 8), and the country is beginning to acquire its own database for AE testing (6). Nevertheless, data on leakage from tank bottoms are not included in this database, and the fundamental characteristics of AE waves for leakage detection have not been illuminated.

The study that is the subject of this paper was conducted with a tank storing industrial water for firefighting (to be referred to as "water tank"). It consisted of the measurement of AE waves

generated in the event of leakage of water from small holes made in the bottom. Its objective was to ascertain the fundamental characteristics and to clarify the differences from AE waves associated with bottom damage due to corrosion.

2. Experimental Procedures

Test objectives

We deliberately made holes of varying diameters in the floors of the water tank, and detected and analyzed the AE signals from actual leakage in order to identify the marginal hole diameter (measurements) for leakage detection. An additional objective was to collect quantitative data related to the signal energy level, etc.

Test method

Water tank specifications are given in Table 1.

Table 1 Specifications of the water tank used in the study.

Capacity (kl)	Diameter (m)	Height (m)	Content
200	6.7	6.0	Water
Max water Level (m)	Floor board thickness (mm)	Side board thickness (mm)	Years used
5.7	6.0	6.0	24

(1) System: The study applied the system shown in Fig. 1 for detection of AE due to leakage from the tank floor. Three AE sensors (30-kHz resonant) with built-in preamplifiers were installed along the tank circumference at equal intervals and in an equilateral triangle array, 1.2 m above the bottom. For AE measurement and assessment, we utilized the DiSP system manufactured by Physical Acoustics Corp.

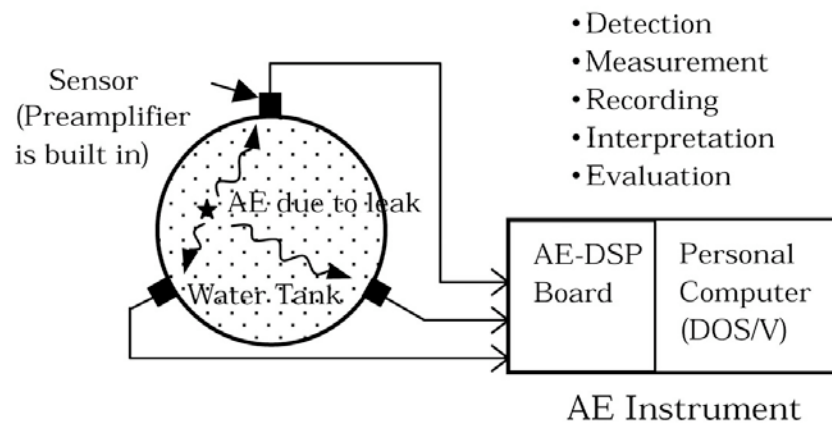


Fig. 1 The system applied in the study.

(2) Fabricated leakage holes: A total of five holes were made to simulate damage resulting in leakage. Based on the diameters of holes discovered in oil tank bottoms thus far, the smallest had a diameter of 1 mm, and the other four were given respective diameters of 3, 5, 7, and 9 mm in order to confirm detection limits. To facilitate the extraction of plugs inserted into the holes from the manhole on top of the tank, the holes were opened under it. Figure 2 shows the hole array.

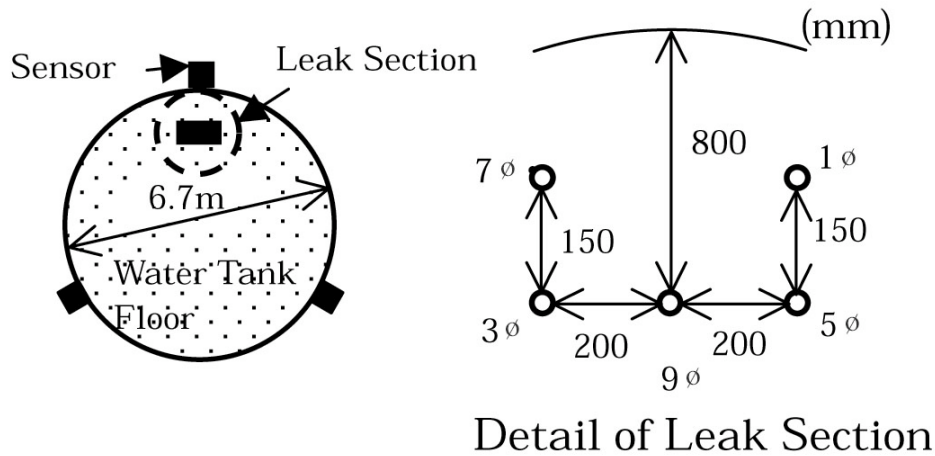


Fig. 2 The hole array.

As for plugs, we used iron wire to plug the 1-mm hole and sheathed copper wire to plug the 3-mm hole. The wires were inserted into the holes and then caulked with putty to seal any interspaces. For the 5-, 7-, and 9-mm holes, plugs were fabricated from silicon rubber caps and forced into the holes. Once the plugs were inserted into the holes, stainless steel wires (with a diameter of 0.3 mm) were attached to them and strung to the manhole at the top. The water level was set at 5.7 m (the full-tank level) in the first AE measurement and 2.0 m (the minimum fluid level of ordinary oil tanks) in the second measurement. After the water was put into the tank, we waited for at least two days before starting the AE measurement, in order to stabilize the water surface.

(3) Test procedure: We first made an AE measurement when there was no leakage, then extracted the plug from the 1-mm hole by pulling the wire attached to it from the top manhole, and measured AE during the resulting leakage. This was followed by plug extraction and AE measurement with the other holes. Therefore, beginning with the 3-mm hole, there was leakage from multiple holes, until all of the holes were finally unplugged.

3. Test Results

(1) 1-mm hole: As shown in Fig. 3, although almost no AE were detected before the plug was extracted from the 1-mm hole, the number of hits rapidly rose once the extraction was made, about 100 s after the start of the test. As used here, the term "number of hits" refers to the number of times that the amplitude of the detected AE waves exceeded the threshold value in one second. The threshold value was 43 dB for leakage from the holes with diameters ranging from 1 to 7 mm, and 60 dB for that from the 9-mm hole.

As for amplitude, a sensor output of 1 μ V was assigned the value of 0 dB. As shown in Fig. 4, we observed the continuous occurrence of AE with the amplitude in the range of 43 - 48 dB, and also detected AE with the amplitude in excess of 60 dB at the maximum. In other words, even for leakage from the 1-mm hole, the number of AE detections was much higher than when there was no leakage, and the energy level increased as shown in Fig. 5. For the energy levels shown in Fig. 5, we used the product of the amplitude of 10 V x duration of 1 ms corresponding to 1,000. From these measurement results, it was concluded that AE testing was fully capable of detecting leakage from holes even with a diameter of 1 mm.

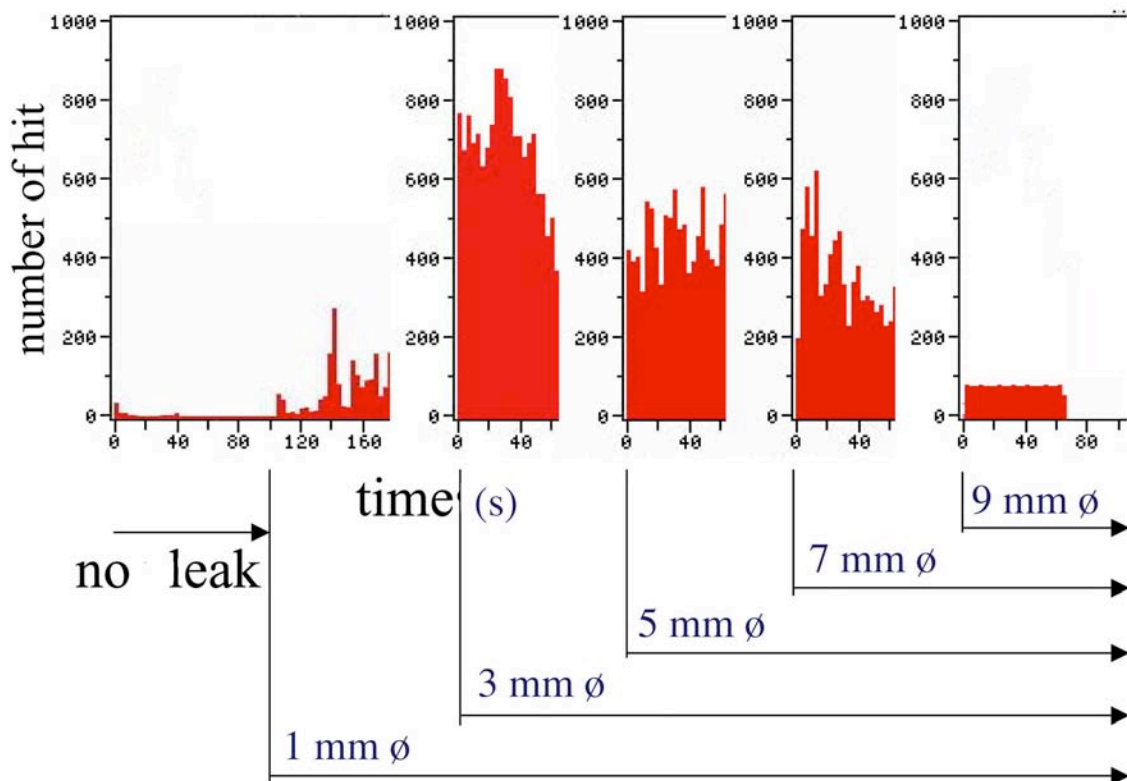


Fig. 3 Hit vs. time of leakage.

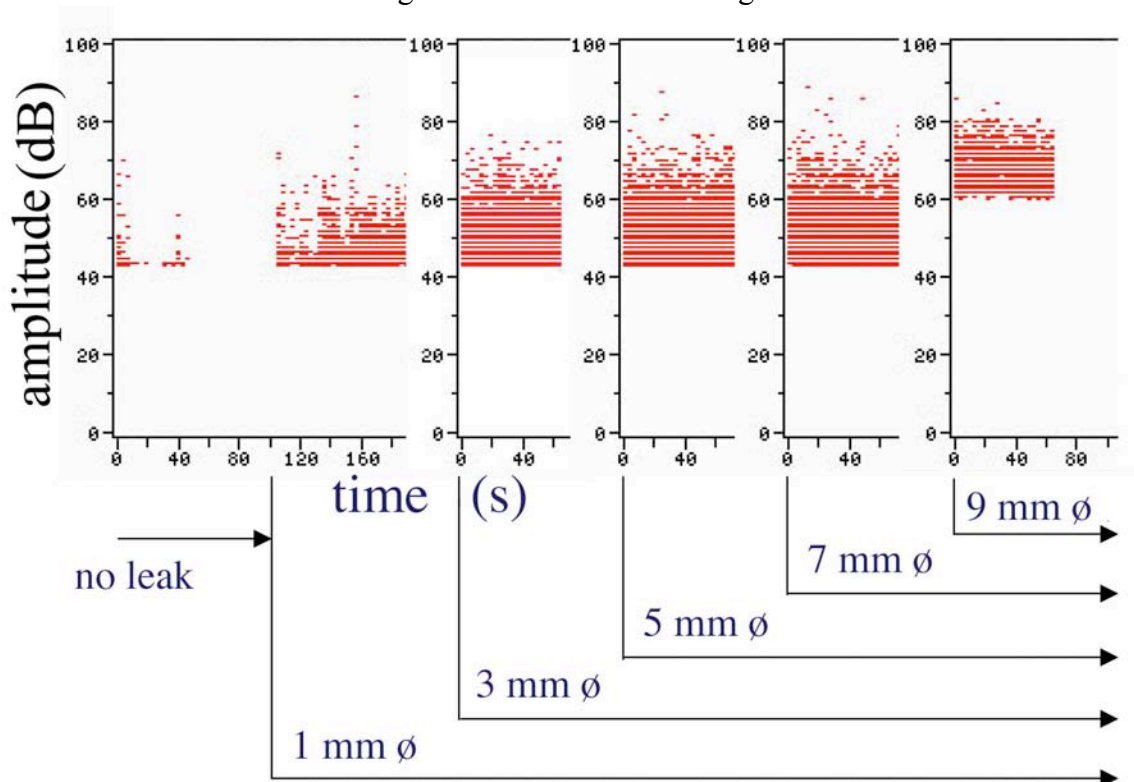


Fig. 4 Amplitude vs. time of leakage.

(2) 3-mm hole: When the plug in the 3-mm hole was extracted after leak monitoring of the 1-mm hole, the level of AE activity increased markedly. Numerous AE with amplitude in the range of

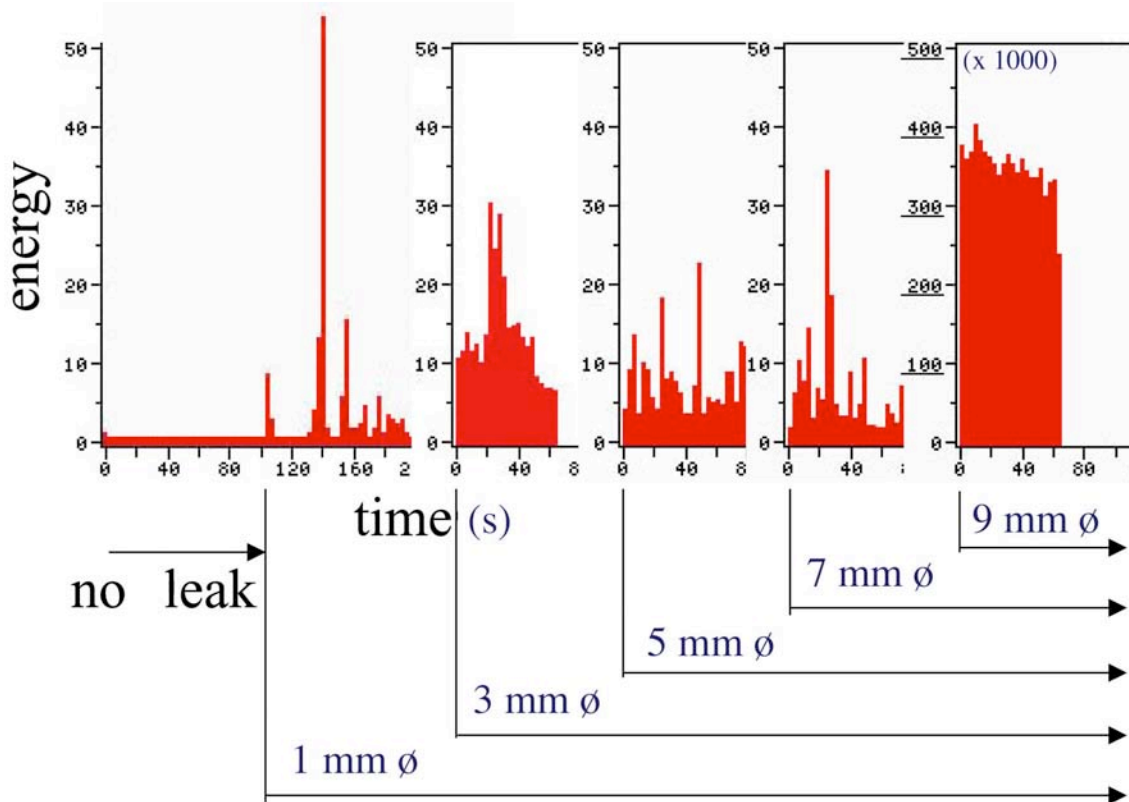


Fig. 5 Energy vs. time of leakage.

43 - 60 dB were detected in succession and made it very easy to detect leakage. In contrast, the number of hits declined, because the AE amplitude continuously exceeded the threshold value.

(3) 5-mm and larger holes: Next, we extracted the plugs from the holes with larger diameters, one after the other. AE with large amplitudes in the range of 80 - 90 dB occurred in large numbers and made leakage detection extremely easy. When the plug in the 9-mm hole was finally extracted, there arose many bursts of large-amplitude AE. These had a very high energy level, as shown in Fig. 5. On this occasion, we verified the existence of a large quantity of leakage at the tank bottom.

Leakage location ranging

Figure 6 shows the results of a ranging of the plane location of the AE signals detected for the 1-mm hole. Figure 7 presents 3D expressions of the integrated values for the number of AE hits detected. As is clear from these figures, the occurrence of AE signals was concentrated in the vicinity of the hole. This suggests the possibility of making an assessment to determine the leakage locations to a certain degree. As shown in Fig. 8, on the other hand, it was not possible to range the location for the 5-mm hole, because of the continuous AE waveform. Figure 9 shows the AE waveform obtained for leakage from the 9-mm hole. It can be seen that the location cannot be ranged because of the continuous occurrence of large-amplitude AE waves. Therefore, it may be concluded that ranging is possible to a certain extent in the case of leakage from a small hole with a diameter of about 1 mm but not in that of leakage from larger holes.

Implications

Figures 3 - 5 showed that the AE waves measured from the leakage were clearly different from those occurring when there was no leakage. Figure 10 shows an example of AE waveforms

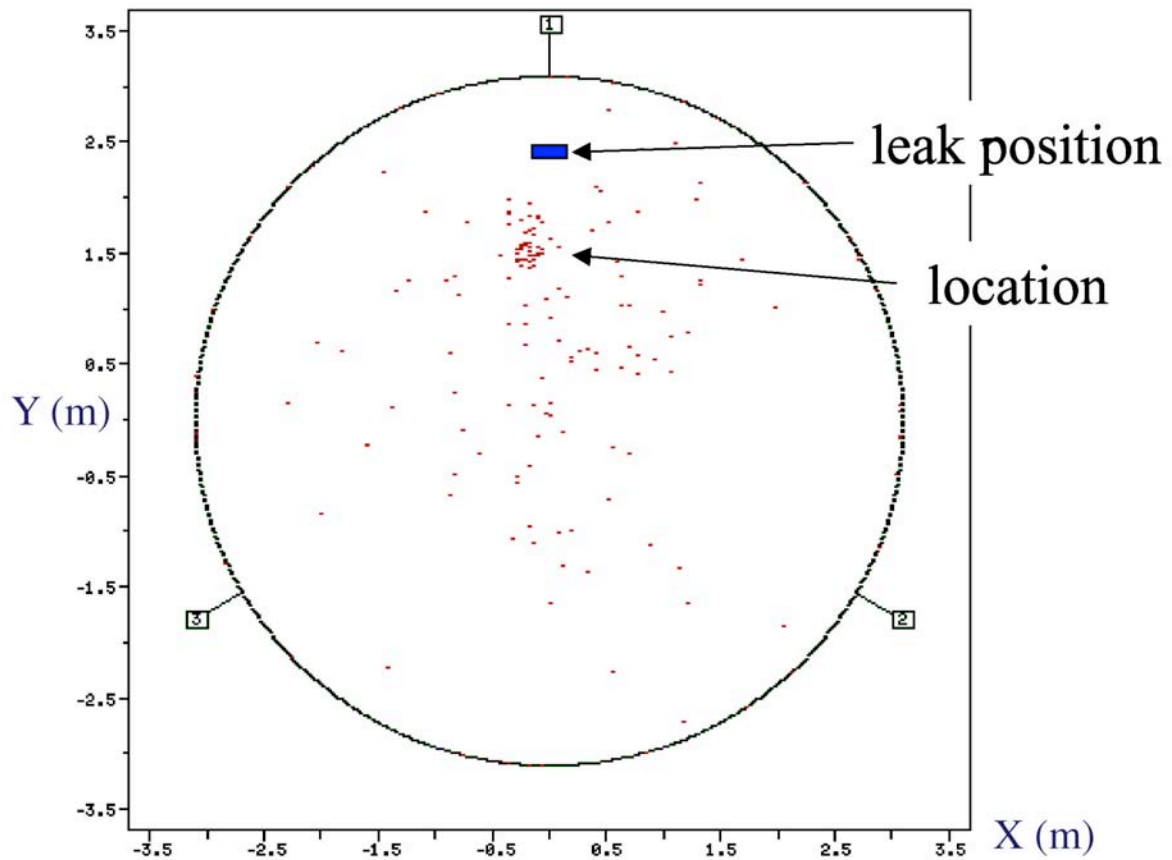


Fig. 6 Floor location plot; plan view (1 mm ϕ).

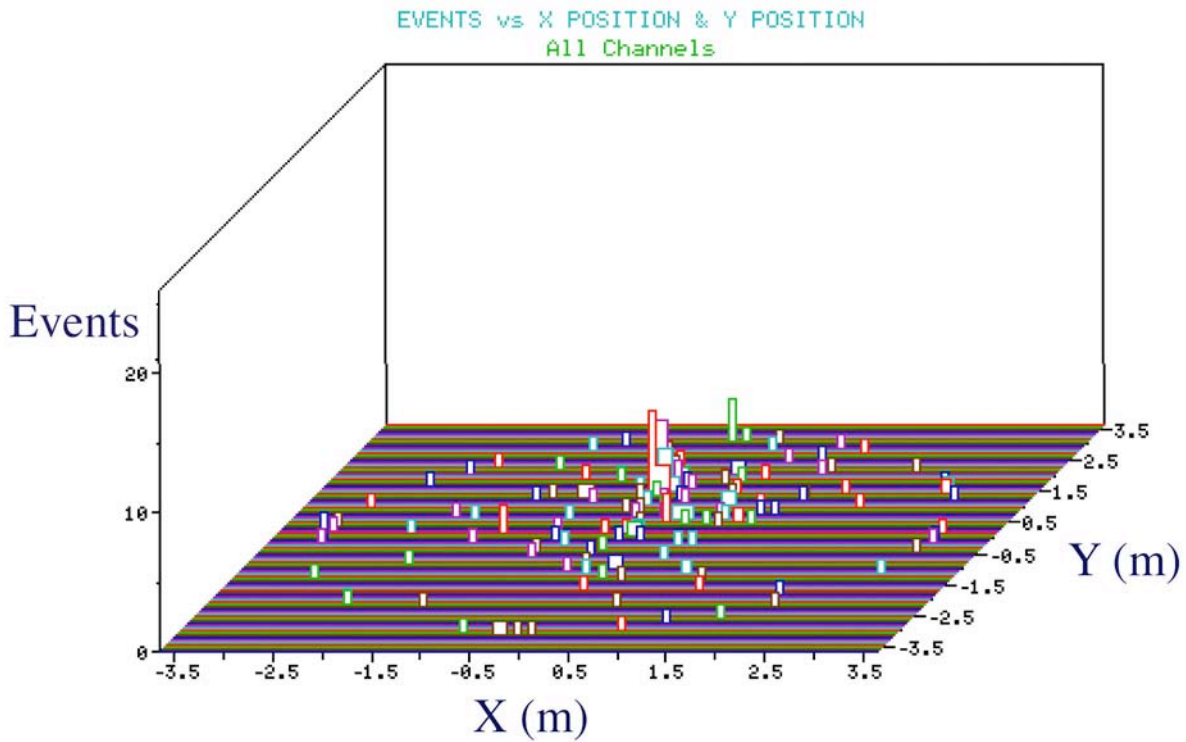


Fig. 7 Floor location plot; 3D view (1 mm ϕ).

detected as a result of corrosion. Whereas the AE waveforms due to corrosion began to attenuate in about 1 ms, those due to leakage occurred on a continuous basis, as shown in Fig. 9. Figure 11

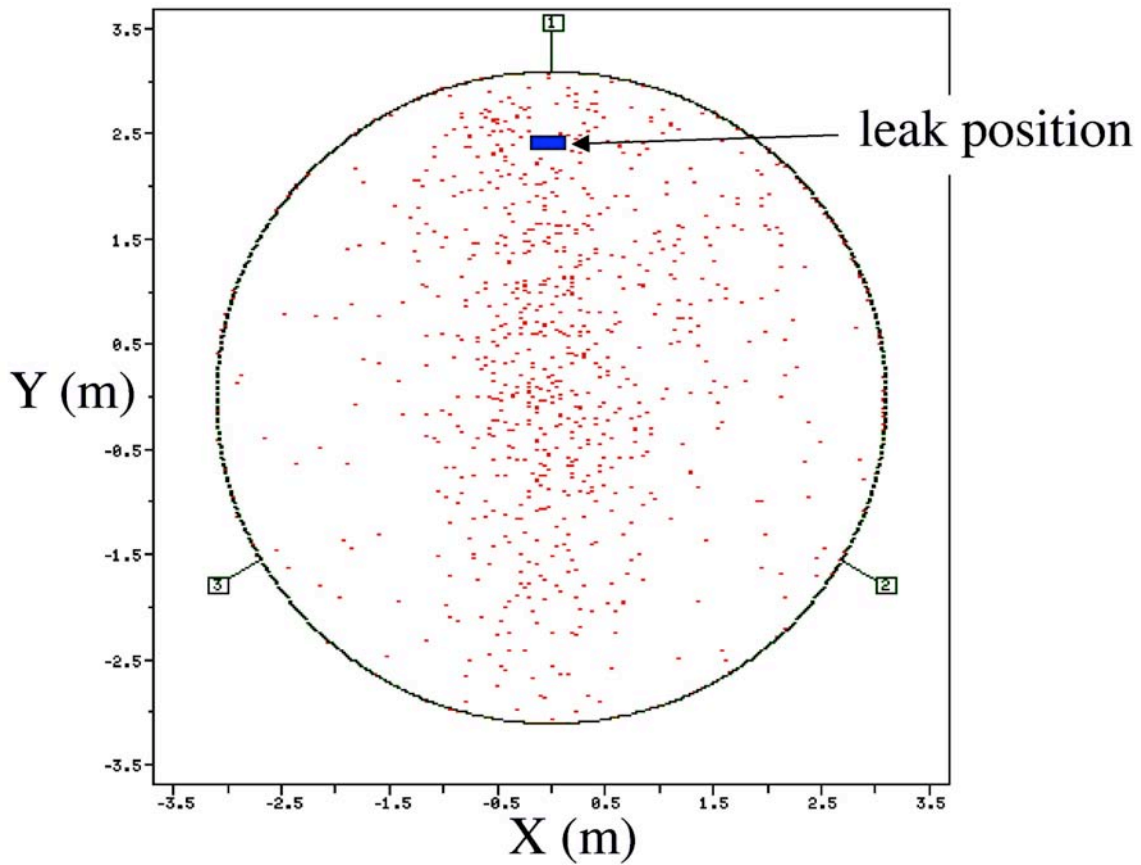


Fig. 8 Floor location plot; plan view (5 mm ϕ).

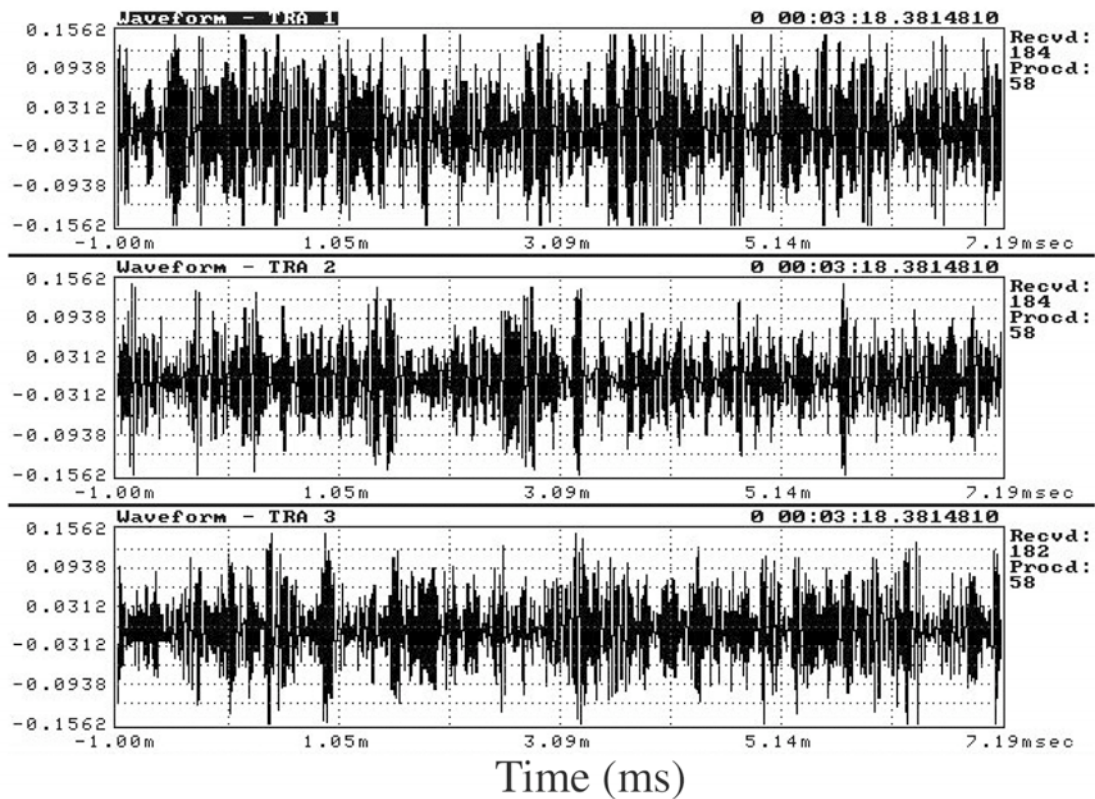


Fig. 9 Example of the waveforms in case of 9 mm ϕ hole.

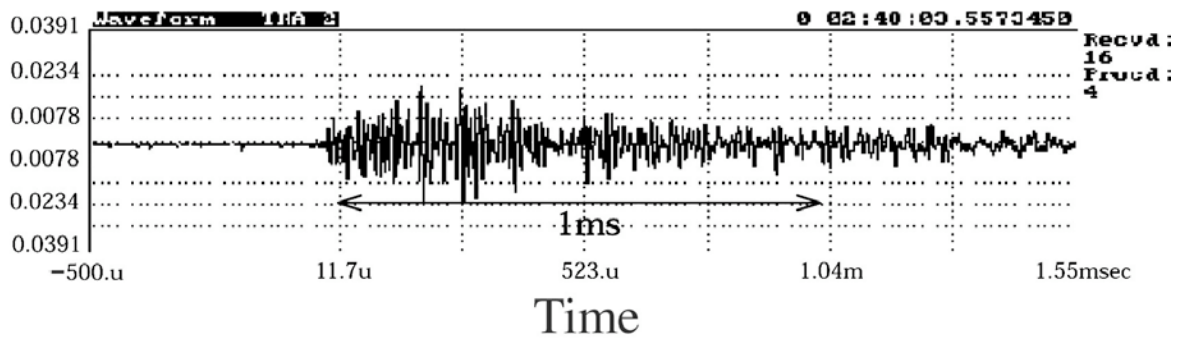


Fig. 10 Example of AE waveform due to corrosion.

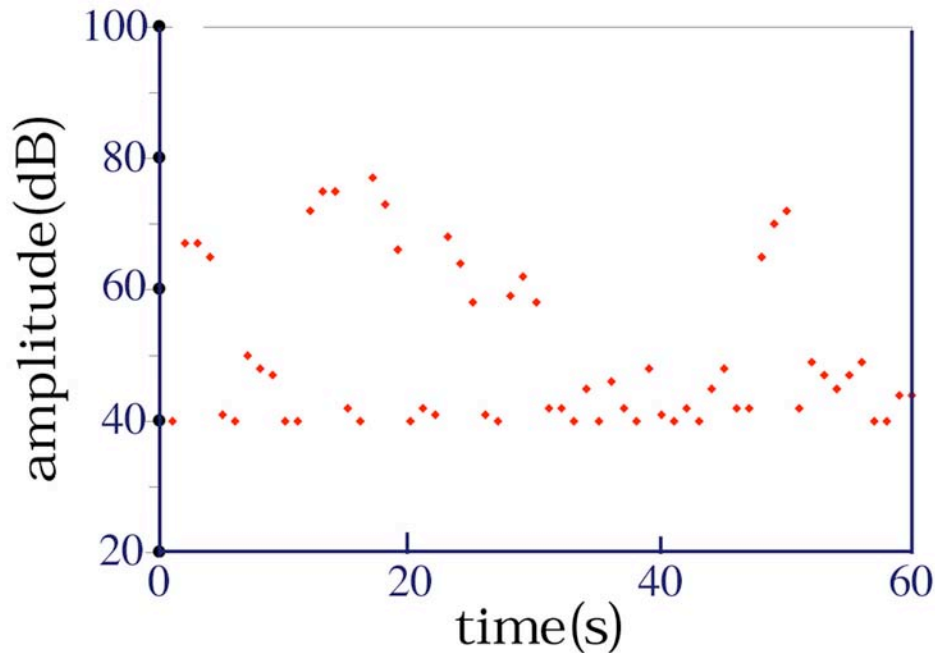


Fig. 11 Examples of AE amplitude occurring due to corrosion.

shows the change over time in the AE amplitude obtained in the AE testing for assessment of the degree of floor corrosion before extraction of the hole plugs. Whereas the amplitude in AE due to corrosion was detected only sporadically, that due to leakage was detected continuously. These differences provide the basis for a clear distinction between corrosion and leakage in AE testing.

Table 2 presents the relationship between the hole diameters and the AE signal amplitudes obtained in the testing. The results indicate that, in the case of small-scale tanks with a diameter of about 10 m (equivalent to non-specified tanks with a capacity of less than 1,000 kl), it would be fully possible to detect leakage from holes with a diameter of about 1 mm through an AE testing and also to specify the leakage location to a certain extent. Even considering the AE wave propagation attenuation in the stored contents (9), detection of leakage is estimated to be possible in large-scale tanks with a diameter of about 80 m, provided that the leakage holes are at least 5 - 7 mm in diameter.

An overseas study presents the results of an AE test for leakage from a diesel oil tank in which a hole with a diameter of 1 mm was detected in the floor (10). In this case, the epoxy coating on the tank interior had been damaged in certain places, with the result of progressive local corrosion and the occurrence of pinholes. The leakage was confirmed by regular AE

Table 2 Relationship between hole diameter and amplitude.

Diameter of leak hole	Amplitude (dB) (water level 2.0m)	Amplitude (dB) (water level 5.7m)
1 mm \varnothing	43~48	43~48
3 mm \varnothing	43~50	43~60
5 mm \varnothing	43~55	43~70
7 mm \varnothing	43~60	43~70
9 mm \varnothing	43~60	Max 90

testing, and the study described herein provides corroboration for the possibility of leak detection noted by the overseas study. Particular importance is attached to leakage detection in other countries. France and the United Kingdom are strongly recommending AE testing as a method for detection of leakage from tanks. The aforementioned recommended procedure for AE application was prepared in France. In the United States, AE testing is conducted for the purpose of preventing the occurrence of major accidents due to leakage in states with stricter environmental regulations.

This study was the first to make a quantitative analysis of the possibilities of detection of leakage from tanks through AE testing. It furnishes data that are applicable for judgments and assessments regarding leakage detection in future AE testing of tanks.

4. Conclusion

The study consisted of AE measurements related to artificial leakage from the floor of a water tank and examination of the implications of the measurement results. It showed that a clear distinction could be drawn between AE due to leakage and that due to corrosion. Furthermore, it also confirmed that AE testing would be fully capable of detecting leakage from holes with a diameter of about 1 mm in small-scale tanks with a diameter of about 10 m (equivalent to non-specified tanks with a capacity of less than 1,000 kl). In addition, it brought to light prospects for specification of the leakage location to a certain extent.

Even taking account of the attenuation of AE wave propagation in the stored contents, leakage is thought to be detectable in large-scale tanks with a diameter of about 80 m, provided that the leakage holes are at least 5 - 7 mm in diameter. It is hoped that the study results will provide a standard for judgments about leakage in AE testing.

Acknowledgement

The authors are deeply indebted to Mr. Shigeo Konno of the Technology and Environment Department in the Petroleum Association of Japan for his precious advice and cooperation regarding the promotion of this study.

References

- 1) "Annual Reports of Statistical Tables related Hazardous Material Establishments", Fire and Disaster Management Agency, (2000), pp. 12.

- 2) "Annual Reports of Accidents related Hazardous Material Establishments", Fire and Disaster Management Agency, (1998)-(2000).
- 3) "Technical Standard Guide for Aboveground Storage Tank", Hazardous Material Safety Techniques Association, (2001).
- 4) "Research Report on Corrosion Monitoring Technique for Bottom Plates of Oil Storage Tank by AE Method", Technical Report of NRIFD, No. 52 (2001).
- 5) High Pressure Institute of Japan, "Research Committee Report on Diagnosis and Preservation Technology for large crude oil Tanks", (1998)-(2000) (in Japanese).
- 6) High Pressure Institute of Japan, "Research Committee Report on Optimized Method in Global Diagnosis and Internal Inspections of Large Crude Oil Tanks" (2001) (in Japanese).
- 7) Engineering Advancement Association of Japan, Report on Development of Evaluation Technology in Storage Facilities in Refineries", (2001), (2002) (in Japanese).
- 8) T. Amano, H. Nakamura, M. Tagami, "Development of Inspection Technology for Corrosion Damage of Tank Floor by AE Method", IIC Review No. 25 (2001), p. 6, (in Japanese).
- 9) I. Morita, H. Nakamura, M. Tagami, "Fundamental examination of AE corrosion detection in oil storage tank floors", J. High Pressure Institute of Japan, **40** (2002), 31.
- 10) Phillip T. Cole, Peter J. Van De Loo, "Listen to Your Storage Tank to Improve Safety and Reduce Cost", *Acoustic Emission-Beyond the Millennium*, Kishi, T., Ohtsu, M., and Yuyama, S. editors, Elsevier (2000), p. 169.

EFFECT OF PINHOLE SHAPE WITH DIVERGENT EXIT ON AE CHARACTERISTICS DURING GAS LEAK

K. YOSHIDA, Y. AKEMATSU, K. SAKAMAKI and K. HORIKAWA

Faculty of Engineering, The University of Tokushima
2-1 Minami-josanjima, Tokushima 770-8506, Japan

Abstract

AE technology has been applied to gas leak detection and inspection. However, it is difficult to detect and inspect the gas leak consistently because measured AE waveforms are different from leak pressures and shapes of leak parts. In this report effects of the stepwise and straightforward pinholes on AE characteristics during gas leaking were discussed. When the pressure reached to about 0.11 MPa in the case of the stepwise pinholes, AE amplitude tends to go up and down, the peak at about 150 kHz was observed. It was found to be easy to detect gas leak from the stepwise pinholes, as compared with the straightforward pinholes.

Key Words: Gas leak; AE waveforms; FFT

1. Introduction

The leak detection for piping faces many challenges. Problems mainly consist of the necessity of many processes for the inspection and difficulty to inspect a gas pipe placed under ground. Acoustic emission monitoring as one of the well-established nondestructive technologies may be put to practical use in future for the leak detection technology. However, the method has not been used widely to monitor the gas leak from pipes. Even if there is no defect before operation or some defects are too small to detect during inspection, various defects occur or develop under operation because of temperature, pressure, and environmental condition and become so large that these cannot be neglected. In recent work, it was reported that the characteristic frequency of AE due to gas leak was 10 kHz [1]. However, there are no reports on AE source. If the AE source is identified, it is expected that the method advances. In this study, AE characteristics were investigated at the frequency of more than 100 kHz.

2. Experimental Procedures

A pipe specimen was 20 mm in outer diameter and 150 mm in length and designated as SGP20A. The pipes were reduced to wall thickness of 0.6 to 2.0mm to obtain a flat surface and to attach an AE sensor. The surface was mechanically polished to #1000 mesh, and a pinhole was made in the wall. The diameters of the straight pinhole were 0.3 mm, 0.5 mm and the stepwise pinholes in these diameters were made to obtain divergent profiles. The overall view of the apparatus used in the experiment is illustrated in Fig. 1. V1 and V2 valves controlled the pressure. An AE sensor with resonant frequency of 100 kHz was placed at 10 mm from the pinhole to detect leak signal. The test pressure was varied from 0.10 MPa to 0.30 MPa. The total gain of detected signal was 60 dB through a band-pass filter of 100 to 1200 kHz. Threshold level was 40 dB that corresponded to 100 μ V at the preamplifier input voltage. AE signals were detected continuously from 0.10 MPa to 0.30 MPa. Compressed air flow was stabilized through the pre-flow pipe of 1000 mm length. If the energy release process due to air leak changes, the

detected AE activity will probably also changes. When AE is generated near the pinhole, continuous-type signals are obtained [2]. In order to clarify the energy release due to air leak, mean amplitude was numerically calculated from the digitized AE waveform and represents the relative energy release due to air leak. On the other hand, the frequency spectrum of the AE waveform due to air leak is expected to clarify the behavior of AE sources in detail [3].

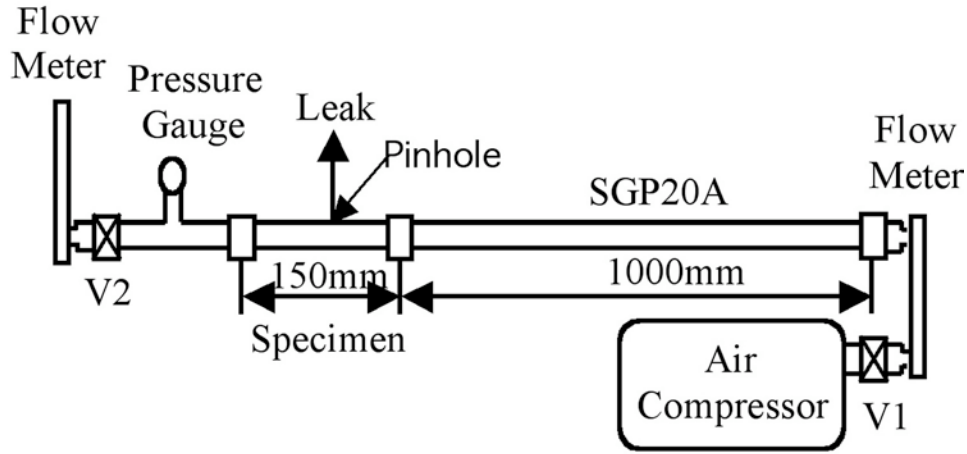


Fig. 1 Schematic view of experimental setup.

3. Results and Discussion

Typical AE waveforms detected during leak at the pressure of 0.10 MPa to 0.30 MPa with the pinhole diameter of 0.3 mm and the wall thickness of 1.00 mm are shown in Fig. 2. The waveform at the pressure of 0.10 MPa stands for electrical noise of the system. The amplitude increases with increase of the pressure and increases rapidly, when the pressure increases from 0.20 MPa to 0.30 MPa. It is also observed that the high frequency components become dominant. The higher the pressure, the more air volume flows through the pinhole. Therefore, Mach number that designates the ratio of the flow velocity to the sound velocity can reach unity in the cross-sectional area in steady flow [4]. Based on the assumption that the pinhole is a converging nozzle, the critical pressure, at which the flow velocity reaches the sound velocity was calculated by equation below, where P_1 is the pressure in pipe, ρ_1 is the air density in pipe, P_2 is the ambient pressure, ρ_2 is the ambient air density, A is the pinhole area, ω_2 is the flow velocity and κ is equilibrium constant [5]. When P_2 is 0.10 (MPa), ρ_1 and ρ_2 are 2.65 and 1.20 (kg/m^3), κ is 1.4, ω_2 is 343.7 (m/s), respectively, and the critical pressure becomes 0.22 (MPa).

$$\rho_2 A \omega_2 = A \sqrt{2 \frac{\kappa}{\kappa - 1} P_1 \rho_1 \left(\frac{\rho_2}{\rho_1} \right)^2 \left[1 - \left(\frac{P_2}{P_1} \right)^{(\kappa - 1)/\kappa} \right]}$$

When the pipe pressure is over the critical value of 0.22 MPa, expansion wall (namely, shock cell outside the pinhole) occurs and screech tones are also generated. The screech tones are known to indicate feedback loops driven by the large-scale instability waves of the airflow [6].

The relations between the pressure of released air and the mean AE amplitude from 0.3 mm and 0.5 mm diameter straight pinholes, and 0.2 mm and 0.8 mm depth stepwise pinholes are shown in Fig. 3 to Fig. 6, respectively. The mean AE amplitude increases monotonically with increase of the pressure to 0.22 MPa as shown in Fig. 3. When the pressure exceeds 0.22 MPa,

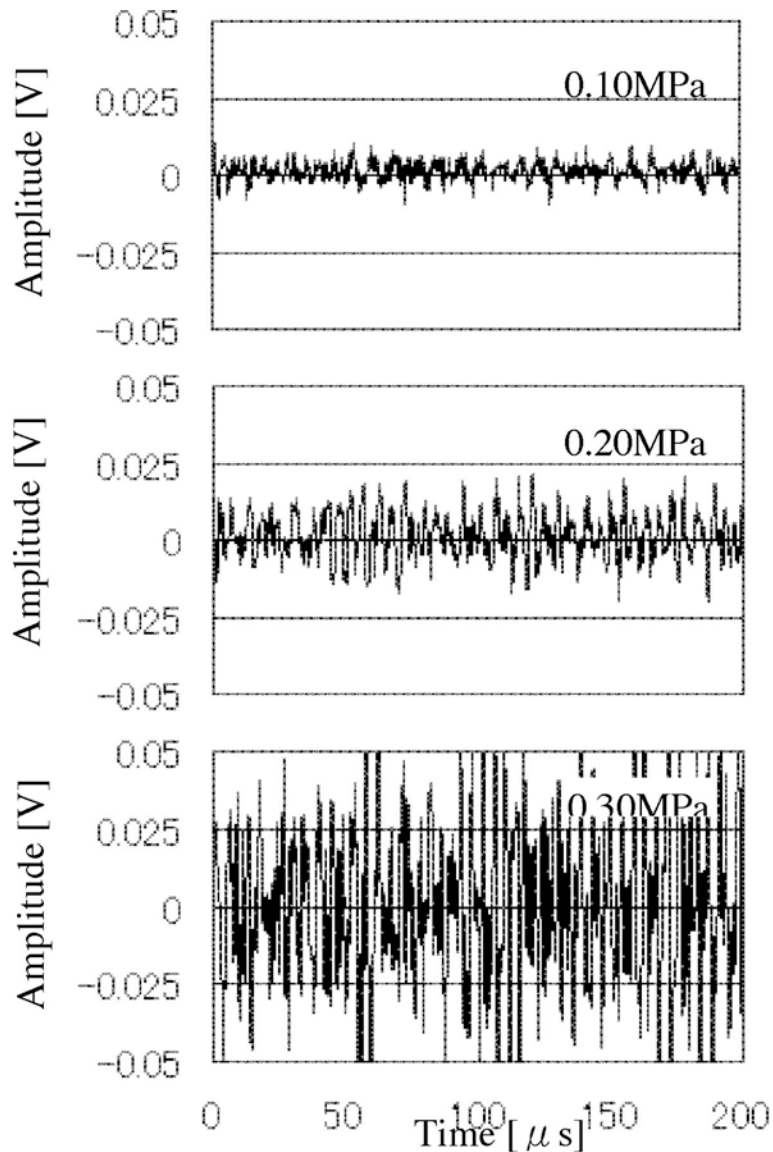


Fig. 2 Typical AE waveforms detected during leak at pressures of 0.10 MPa, 0.20 MPa and 0.30 MPa with pinhole diameter of 0.3 mm and wall thickness of 1.00 mm.

the mean amplitude increases as well and continues to fluctuate with an increase of the pressure. This characteristic is consistent with AE waveforms shown in Fig. 2. In 0.5-mm pinhole, the amplitude also increases with increase of the pressure as shown in Fig. 4. When the pressure is over 0.22 MPa, the amplitude also continues to oscillate wildly. Actually, the ranges of amplitudes broadened starting at 0.18 MPa. We believe that this active AE behavior depends on the generation of screech tones.

With a stepwise pinhole of 0.2 mm depth, the amplitude starts to jump as the pressure reaches 0.11 MPa as shown in Fig. 5. When the pressure is above this range, the mean amplitude increases monotonically with increase of the pressure. This is similar to Fig. 3. However, when the pressure is over 0.22 MPa, the amplitude continues to increase gradually without large changes seen in Fig. 3. If a pinhole is shallow stepwise, it is believed that the expansion wall becomes difficult to form because of the large-scale instability of the airflow. This is quite different in deep stepwise pinhole. Here, the amplitude fluctuated very strongly starting at the

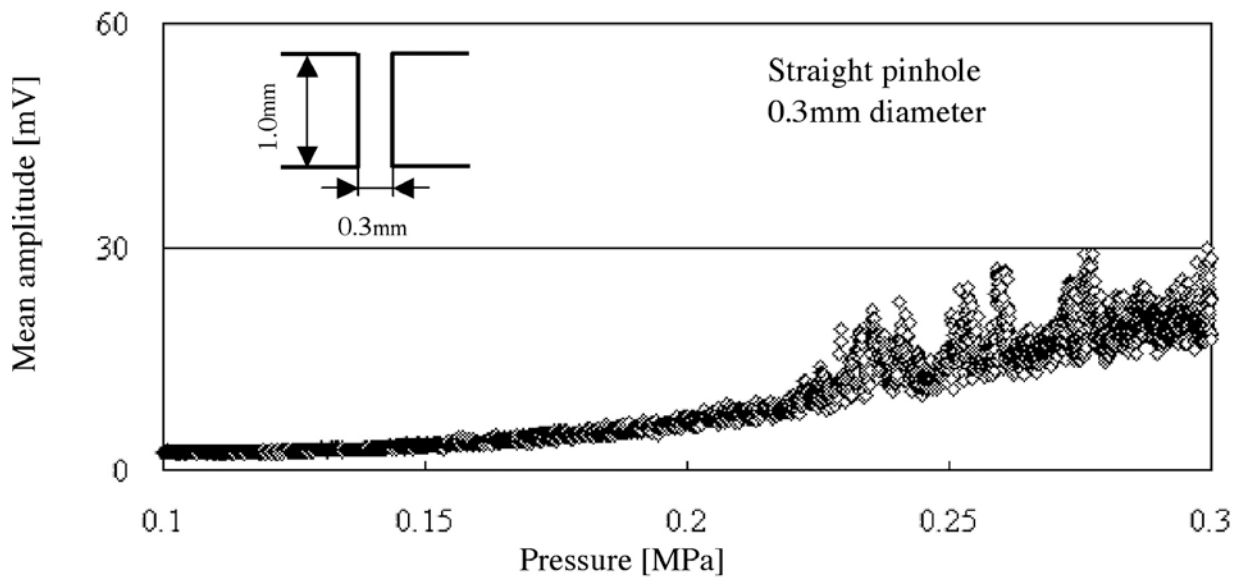


Fig. 3 Relation between the pressure of released air and the mean AE amplitude from 0.3 mm diameter straight pinhole.

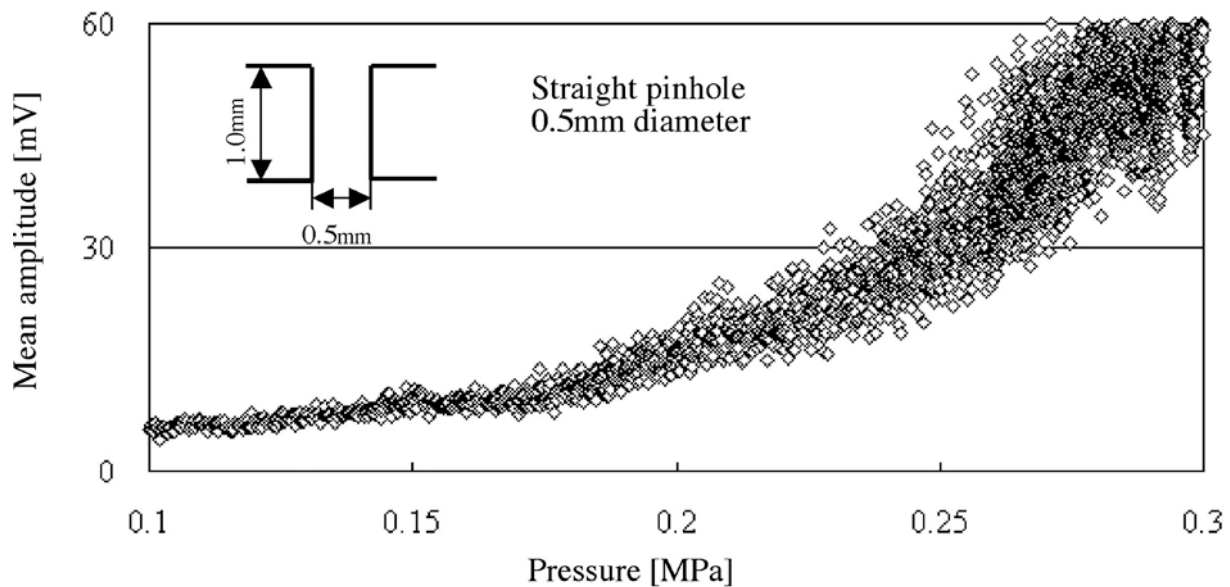


Fig. 4 Relation between the pressure of released air and the mean AE amplitude from 0.5 mm diameter straight pinhole.

pressure of 0.11 MPa and especially at 0.15 MPa as shown in Fig. 6. When the pressure is over 0.15 MPa, the amplitude continues to increase gradually, but still oscillating over a broad range. The mean AE amplitude is supposed to become unstable before the pressure was over the critical value. It is apparent that the simple theory does not apply and the mechanism of AE generation in the stepwise pinholes is different from that in the straight pinhole (shown in Fig. 5 and Fig. 6).

The mean AE amplitude from the stepwise pinhole, whose depth is 0.8 mm, is larger than that from the shallow stepwise pinhole. The amplitude seems to be quite unstable and results from turbulent flow and vortex increase. Four frequency spectra of detected AE waveforms at the pressure of 0.30 MPa are shown in Fig. 7. The power spectrum near 400 kHz is higher than

that near 150 kHz in the straight pinhole but the power spectrum near 150 kHz is higher than any other power spectrum in the stepwise pinhole. We propose a model as shown in Fig. 8 to explain a part of the experimental results.

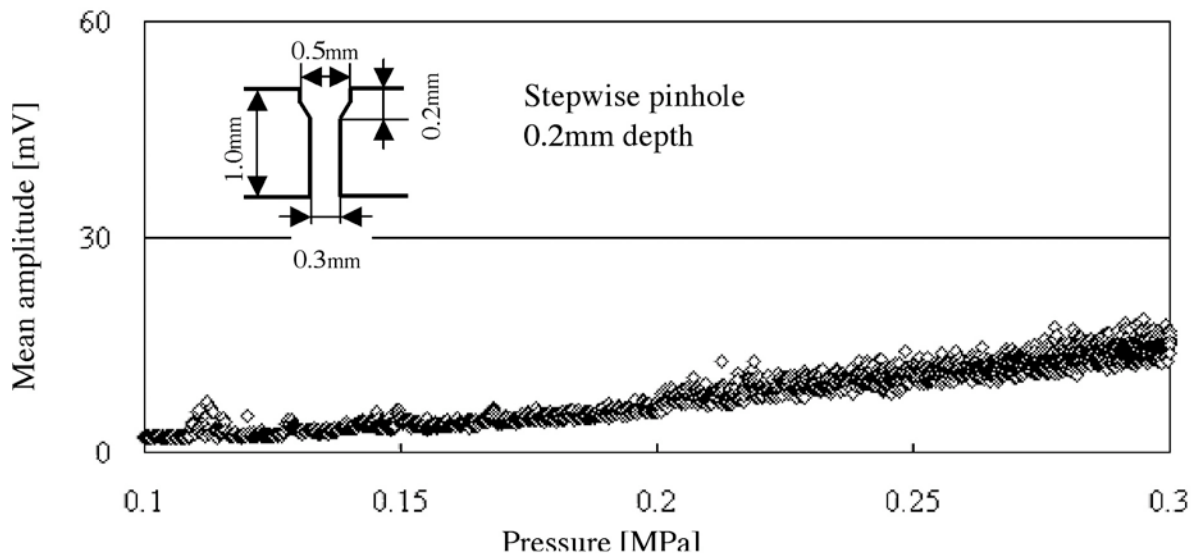


Fig. 5 Relation between the pressure of released air and the mean AE amplitude from a stepwise pinhole whose depth is 0.2 mm

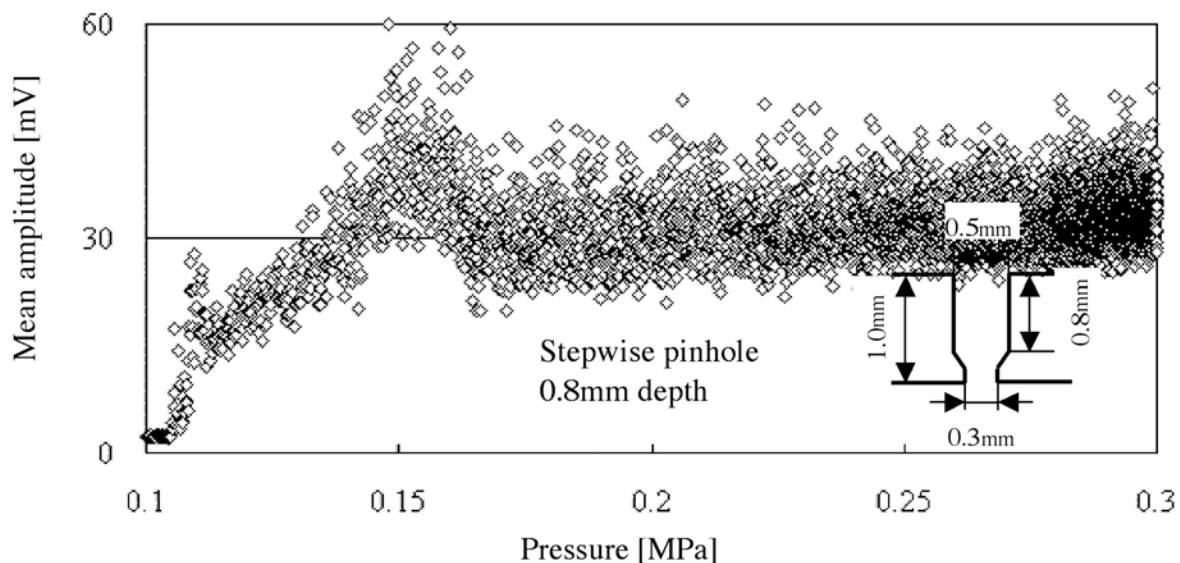


Fig. 6 Relation between the pressure of released air and the mean AE amplitude from a stepwise pinhole whose depth is 0.8 mm

The leak air flows to adhere to one side of the wall at 0.11 MPa as shown in Fig. 8. In the range of 0.11 MPa to 0.15 MPa, strong turbulent flow and vortex appear along the pinhole wall because of remarkable stepwise effect. When the pressure is over 0.15 MPa, it is expected that the stepwise effect along the pinhole wall diminishes somehow because of increase of air flow.

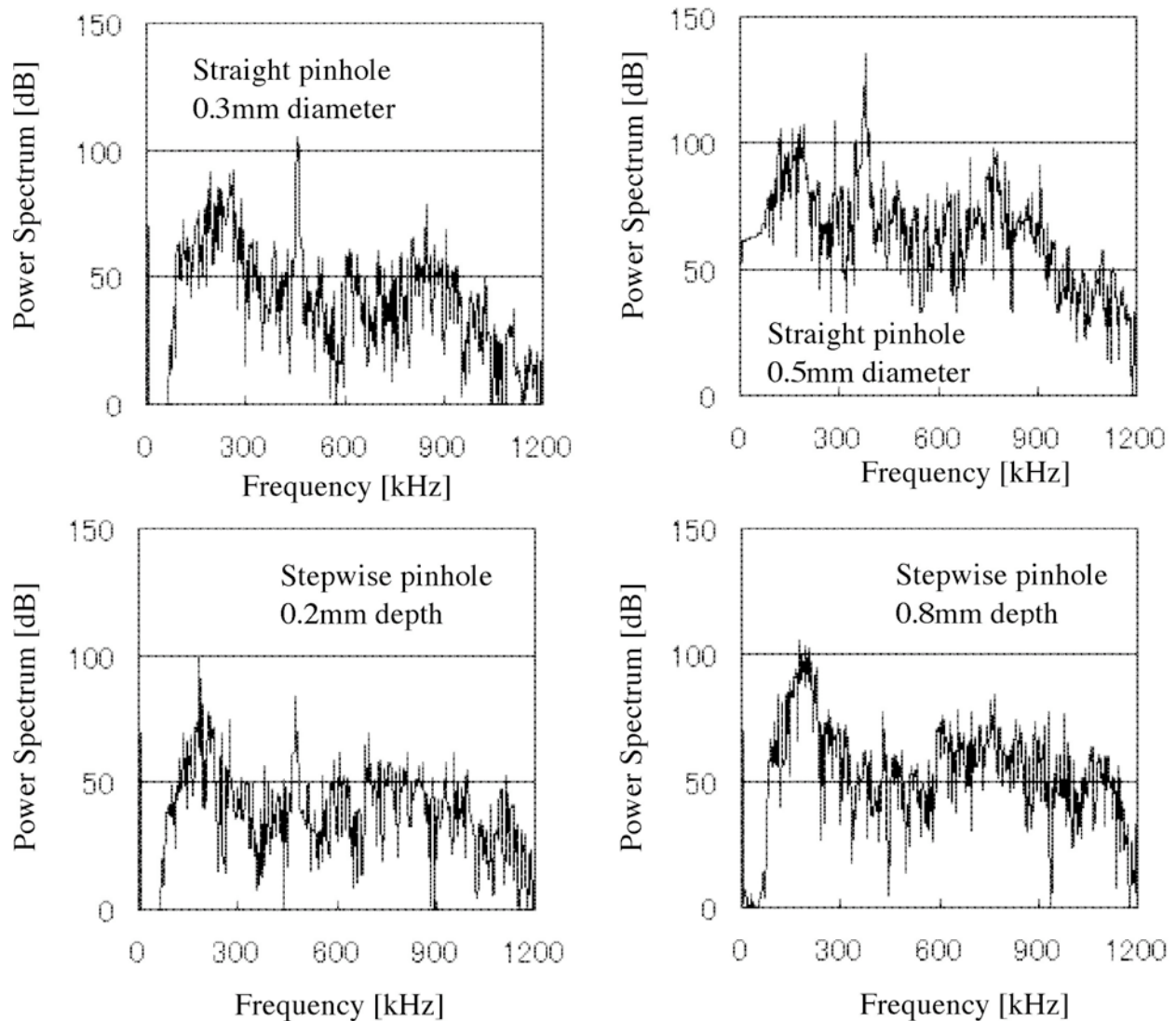


Fig. 7 Frequency spectra of detected AE waveforms at the pressure of 0.30 MPa from Fig. 3 to Fig. 6

4. Conclusion

Detection and inspection of AE during gas leak from pipes with straight and stepwise pinholes have been investigated within the frequency range of 100 kHz to 1200 kHz. Results obtained are as follows:

1. In stepwise pinholes, the mean AE amplitude starts to fluctuate when the pressure reaches 0.11 MPa.
2. With the stepwise depth increasing, the mean AE amplitude increases and airflow becomes unstable.
3. In stepwise pinholes, the power spectrum near 150 kHz is higher than any other zones of power spectrum.

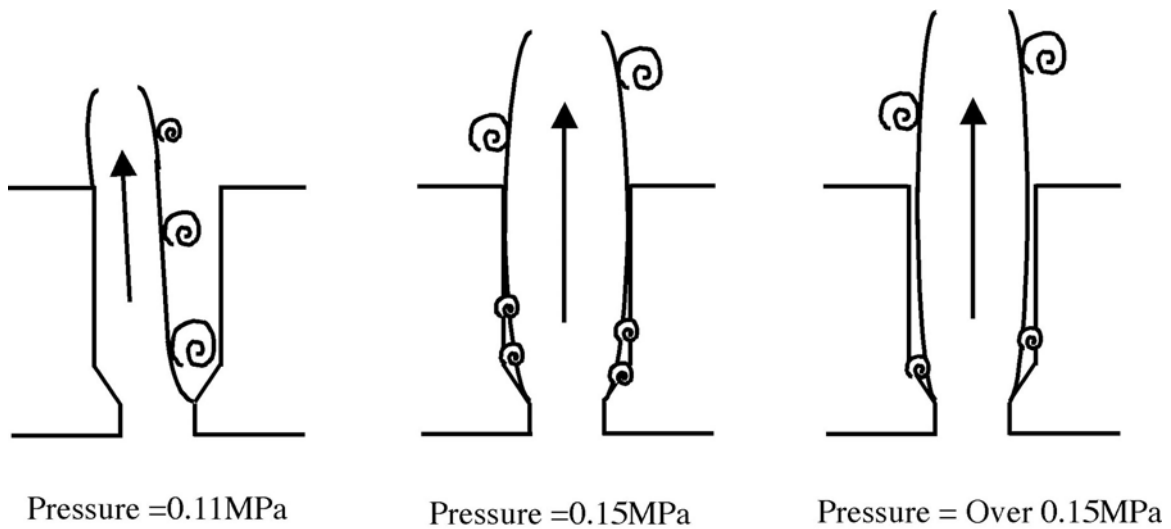


Fig. 8 Schematic model of the AE source.

References

- 1) M. Kotani et al.: Acoustic Characteristic of Leakage Sound and Detection of the Sound Under Noisy Environment; *SICE*, **35** (4) (1999), 554-559.
- 2) M. Ohtsu: *Characteristics and Theory of Acoustic Emission*; Morikita Publ. Co., (1988), p. 36.
- 3) T. Ankyoin and M. Nakajima: *How to Use FFT*; Akiba Publ. Co., (1987), p. 11.
- 4) T. Ichikawa: *Hydrodynamics, Fluid Mechanics*; Corona Publ. Co., (1981), p. 127.
- 5) H. Ohashi: *Fluid Mechanics I*; Corona Publ. Co., (1996), pp. 6-20.
- 6) Young-Kill Yu et al: Screech Tone Noise and Mode Switching in Super Swirling Jets; *AIAA* **36** (11) (1998), 1968-1974.

OPERATION MONITORING OF ROLL COVER BY ACOUSTIC EMISSION

JUHA MIETTINEN and PEKKA SALMENPERÄ

Laboratory of Machine Dynamics, Tampere University of Technology

P.O. Box 589, FIN-33101, Tampere, Finland

Abstract

The growth of line-speeds and the demand of high-quality products in process industry have increased the importance of on-line operation monitoring of processes. The operation monitoring of rotating components in process industry is typically carried out by an automatically operating on-line monitoring system. Sensors attached to bearing housings monitor the vibration behavior of the running. The operation monitoring system usually collects also process data like temperature, pressure, loading and torque or power of drive motors. Advanced systems like neural network or expert monitoring systems can find out causalities between the vibration and process data. These causalities can be used for fault diagnostics or automatic or supervised control of the machine.

This paper describes an acoustic emission measurement system that is used for operation monitoring of the cover of rotating rolls in line contact. The developed monitoring system is installed in a pilot roll station. The pilot roll station corresponds to a soft calendar or a soft coating unit of a commercial paper machine. The paper describes the operation monitoring system and presents measurement results of some running conditions. The running conditions simulate cover damage and a situation where acoustic emission can be used in control of the running.

1. Introduction

Cylindrical rolls in rolling contact are typically used in paper machines and in steel mills. In steel mills usually un-covered steel rolls are used. In paper machine sections, like in calendars and coating units, soft roll applications are common. In these cases the rolls typically have polymer cover with thickness of 10 – 20 mm. The reason for the use of soft-covered rolls is the larger contact area that can be achieved by the soft cover. The production speeds have risen, especially in paper machinery. Higher line speeds create growing requirements for the running stability of the machine.

A new trend is to build the production lines complete integrated. In paper-making process this means the integration all the sections of the machine in a single line. This sets high requirements for the reliability of process and increases the importance of operation monitoring.

When sensors are mounted strictly to machine parts, we can achieve the greatest accuracy in measurement of running parameters and of process variables concerning this component. Transfer of the measurement data from rotating machine parts requires wireless data transfer solutions. In the case of rotating rolls in contact, acoustic emission (AE) is generated by deformation of the cover, micro-sliding between the contacting surfaces and crack nucleation and growth in the cover. The cover can loosen locally from the casing of the roll. This causes frictional micro-movement between the cover and the casing that generates acoustic emission.

The operation monitoring system for polymer cover of rotating rolls is installed in a pilot roll station at Tampere University of Technology. The system consists of measurement computer on the roll, of a wireless LAN bus for data transfer from the rotating measurement computer to the analysis computer and of the user interface implemented with LabVIEW™ development environment.

2. Acoustic Emission Sources in Roll Contact

Acoustic emission generated by the contact of rotating rolls can be used in fault diagnostics of the cover and in control of the running of the rolls. A typical and very serious failure mechanism in soft covers starts when a detrimental dirt particle adheres on the surface of the cover. The particle causes a local, strongly deformed place on the cover. This deformation generates local heat, so called “hot spot”, and the thermal expansion can destroy the cover by cracking it. Sometimes the cracking can be like explosion. The clean cover can also locally loosen from the surface of the casing of the roll. This generates friction and heat that destroy the cover.

The dominating phenomena in the soft cover in normal running are depending on the material of the cover and on the contact and running parameters. The acoustic emission generated by these normal running phenomena can be used in control of the running parameters like contact line load, relative driving moment share between the rolls or the sliding in closing process of the roll contact and the stability of the running of the rolls. An unstable running condition of the rolling contact is a resonance vibration caused by time delay of the elastic deformation of the cover [1, 4-6].

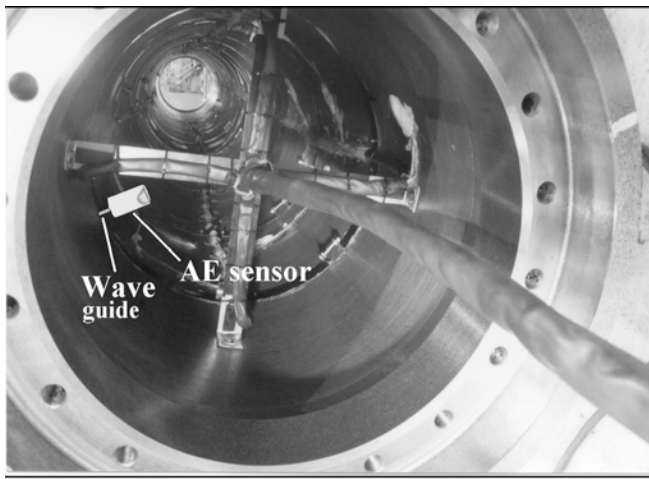
Acoustic emission can be generated by many other mechanisms than mentioned above. This can make it difficult to monitor the phenomenon under consideration. Acoustic emission can be generated from pressure vessels of air and hydraulics systems, from welding, from mechanical impacts, from fretting and from sliding contacts. These effects can disturb AE measurement especially in field environment. If the AE sensor is fitted inside a rotating roll, disturbances arise mainly from the support bearings of the rolls [2].

3. Measuring System

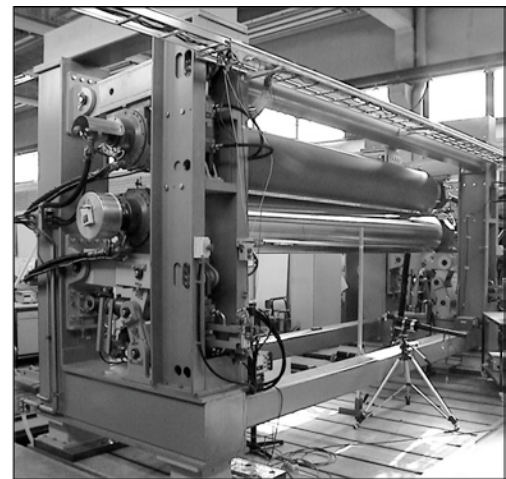
In the pilot roll station, one of the rolls is coated with soft polymer cover and the other roll is un-coated hard roll. The width of the line contact of the rolls is 4.4 m. The AE sensor is situated inside the hard roll because the covered roll is heated by hot water. Because of the heat and in order to get reliable fitting of the sensor on the inner surface of the casing a wave-guide is used. The sensor is piezo-electric resonance sensor. In Fig. 1 the pilot roll station and the acoustic emission sensor inside the non-covered roll are shown.

3.1 Measuring device

The measuring device is assembled on the shaft end of the hard roll, see Fig. 2. The AE measuring device contains an analog filter having central frequency of 200 kHz and band-width of one octave, a 46-db amplifier and an A/D converter with sampling rate of 1 MHz. The measurement principle is AE count rate, and the measurement unit also contains variable threshold level. The size of the unit is large due to other measurement facilities, like acceleration and strain gauge measurements. The power supply for amplifier is fed via sliding rings.



a)



b)

Fig. 1. a) AE sensor inside the lower, non-covered roll. b) The pilot roll station.

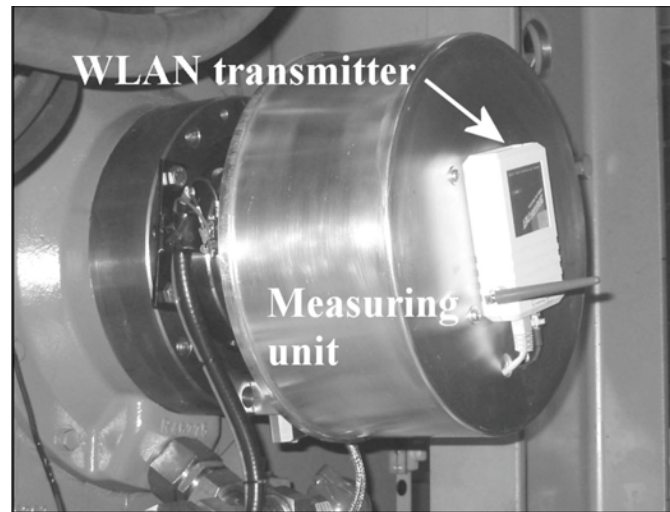


Fig. 2. The measurement device on the end of the lower roll.

3.2 Wireless data transfer and user interface

The measurement data is transferred with wireless LAN Ethernet connection from the measurement computer to the analysis computer that is located in the control room. The wireless transfer distance is about 10 m. The link is in accordance with the standard IEEE802.11, and has the carrier frequency of 2.4 GHz [7]. The WLAN transmitter is fitted on the box of the measuring device, see Fig. 2.

The AE count method reduces the amount of the transferred data to the level suitable for the capacity of the wireless connection. The measurement unit calculates the AE count rates and transfers them as packets to the analysis computer. The AE packets are analyzed in the analysis computer as a pulse queue that indicates changes of the AE on the circle of the roll. The roll is equipped with a pulse encoder that makes it possible to position the pulse count packet. If the measurement result contains many pulse bars the measurement result shows like a continuous line. This can be noticed from the graphs of the measurement results presented later in the text. In Fig. 3 the principle of the AE data acquisition and wireless measurement data transfer of the roll station are shown.

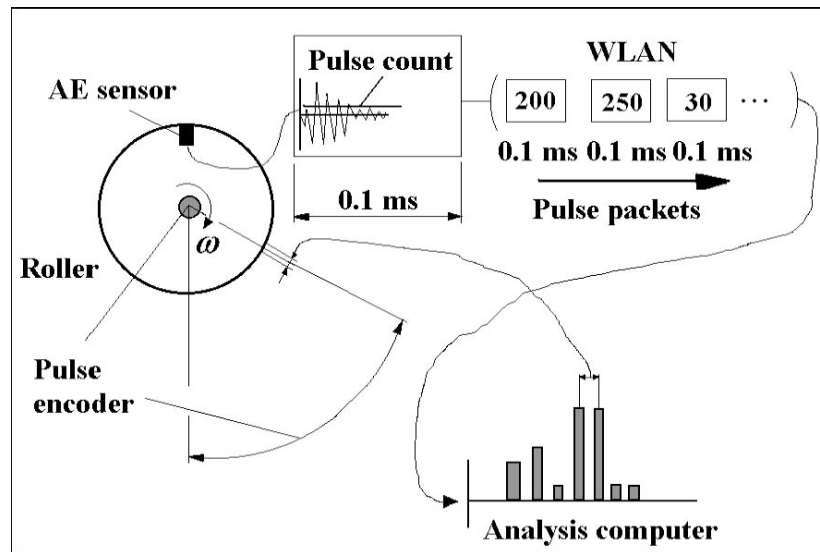


Fig. 3. The principle of the AE data acquisition and wireless measurement data transfer from the rotating roll to the analysis computer.

The measurement computer in the roll uses RT-Linux™ operating system. The data communication is also implemented with Linux™ operating system. In transferring the AE pulse count packets with WLAN, the UDP (User Datagram Protocol) protocol is used to send time-stamped packets in 0.1-1000 ms intervals. The UDP protocol is faster than TCP protocol, because it uses transfer mechanism of the net's lower layers when TCP builds its transfer mechanism over these layers [3]. The reason to use of the UDP protocol in this application is the real-time demands. The definition of a real-time system is when a control value is given as an input, with a 100% assurance the output comes during a certain time. The definition does not specify the length of the time. The laboratory measurement analysis system can be considered as a so-called soft real-time system with a real-time delay of 1000 ms maximum.

The user interface is implemented with LabVIEW™ development environment. From the interface it is possible to adjust the threshold level for AE count, to adjust the sampling rate of the AE count packets and total measurement time. With the "Configure" function the configuration of the measurement is transferred to the measurement computer in the rotating roll. The measurement result is saved on the hard disc of the analysis computer for further analysis. The user interface is shown in Fig. 4.

4. Experiments

The operation monitoring system has been tested with a simulated cover fault condition and two running conditions where the AE can be used in control of the running of the rolls. At first the system was calibrated for adjusting the suitable threshold level. The test conditions were following:

simulated fault condition

- two pieces of paper on the surface of the hard roll

control condition

- chance of the line load in the roll contact and
- resonance-running condition caused by the delay of the relaxation of the roll soft cover.

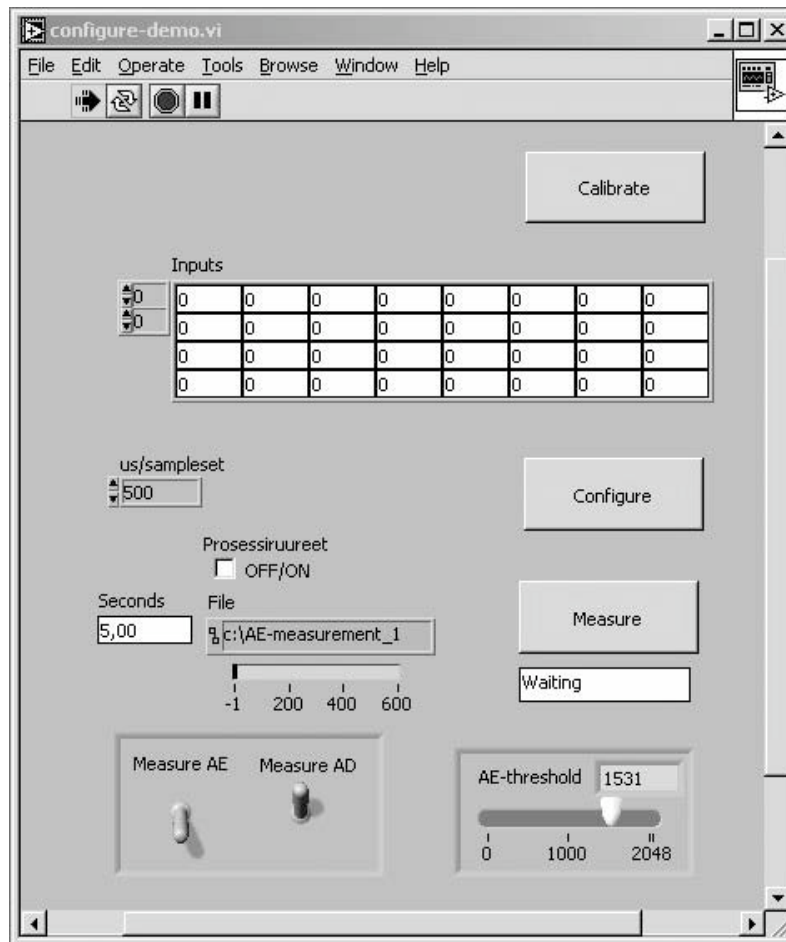


Fig. 4. The user interface of the acoustic emission monitoring system. “Measure AE” is AE measurement. “Measure AD” and “Inputs” are associated to other measurements.

The sampling rate in all measurements was 2 kHz that corresponds the sampling time of 500 μ s. In the measurement results the “AE activity” shown in the figures means the number of AE counts per 500 μ s. Because the “AE activity” is proportional to the rotational speed of the rolls, depending on the AE count method, the rotational speed of the rolls was stable during individual measurement.

5. Results and Discussion

5.1 Calibration of the measurement system

The basic construction of a piezoelectric sensor is simple and reliable. However, bad measurement cables, bad cable connectors or incorrect mounting of the sensor can cause errors in measurements. Great care must be used in the case when the sensor is installed inside the roll. If the fitting of the sensor or the cables are incorrect it is impossible to repair the installation without removing the roll from the machine. In this investigation the absolute values of the AE activity was not under examination, so the calibration of the sensor was not such an important element. The condition of the measurement system was confirmed by testing the measurement chain before and after measurements. In these tests a spring-loaded impulse peak was used. The impulse was focused on the end flange of the roll where the AE sensor was situated. Another method could be the "Pencil Lead Break" method according to ASTM standard number E 976-

84. One calibration measurement result is shown in Fig. 5. There are five impulses given during a 10-s period.

The impulse is rather sharp compared to the phenomena that generate acoustic emission in rolling contact of the test rolls. However, the threshold level was adjusted to suit the measurements with the impulse tests. In these measurements the rolls were not contacting each other but rotating slowly.

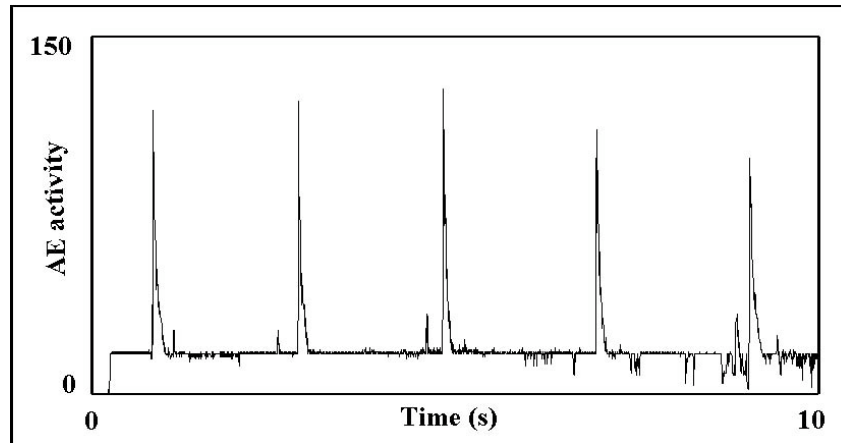


Fig. 5. Measurement result of one calibration test.

5.2 *Two pieces of paper on the surface of the hard roll*

This measurement simulates the conditions when there is a contaminant particle attached on the surface of the cover or on the surface of the hard roll. A situation like this is also found if the cover is locally loosening from the surface of the roll casing. The measurement result is shown in Fig. 6.

The highest peaks in the Fig. 6a indicate the time when the paper pieces pass the line contact zone. The paper pieces were round with diameter of 10 mm and thickness of 0.2 mm. In the figure the points of the passing time of the paper pieces are marked. The distance of the paper pieces were 620 mm on the circle of the roll. Rotational frequency of the hard roll is 3.55 Hz, diameter of the hard roll is 524 mm and line load is 18 kN/m. The time differences correspond the location of the paper pieces.

5.3 *The chance of the line load in the roll contact*

The rolls are designed with crowning for nominal line load of 15 kN/m. With that line load the pressure in the contact is designed to be even. In the measurements the line load was changed from 10 kN/m to the value of 20 kN/m. The AE result of the influence of the line load is shown in Fig. 7. With larger line load the hard roll penetrates deeper inside the soft cover. This increases the deformation of the cover, the length of the contact zone and micro sliding. These phenomena generate increasing level of acoustic emission. From the measurement result shown in Fig. 7, it can be seen that there is a delay of about 5 s in the line load control system before the line load starts to rise.

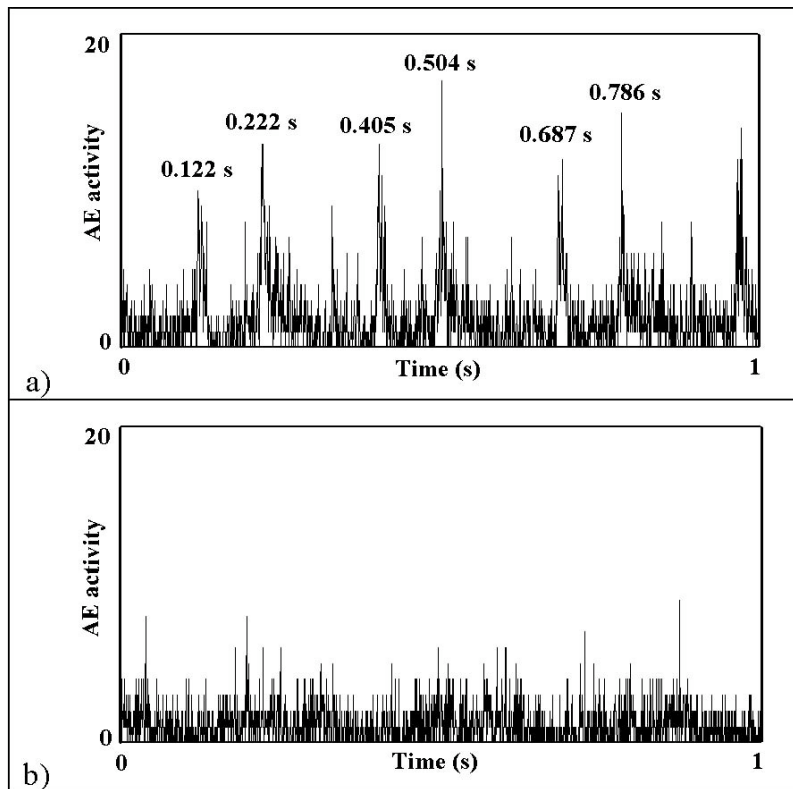


Fig. 6. a) Result of the measurement “two pieces of paper on the surface of the hard roll”. b) The measurement result when the papers were removed.

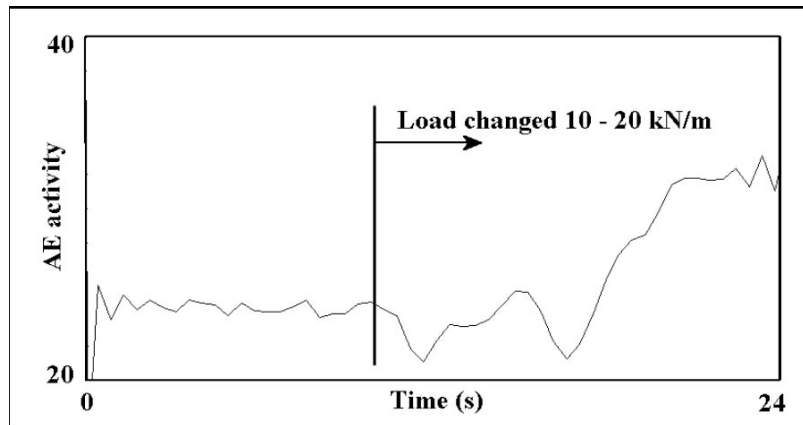


Fig. 7. Measurement result of the influence of the line load on the acoustic emission.

Furthermore there is some fluctuation in the line load control circuit just after the control command. The result is strongly filtered therefore the graph looks smooth. By calibrating the AE level to correspond the line load, it is possible to use the AE level for direct measurement of the line load in the contact.

5.4 The resonance-running condition

The resonance condition caused by the relaxation time delay is especially harmful running condition of the contacting rolls. This kind of resonance condition occurs when the rotational

speed of the rolls is such that the cover has not enough time to relax from the deformation that has exerted on it in the contact zone. The condition is at worst when the resonance frequency is an integer multiple of the roll rotational frequency. In that kind of resonance condition the rolls are vibrating relative against each other. This means that the line load is changing in the frequency of the resonance. This phenomenon generates AE like the change of the line load. The result of the resonance condition is shown in Fig. 8.

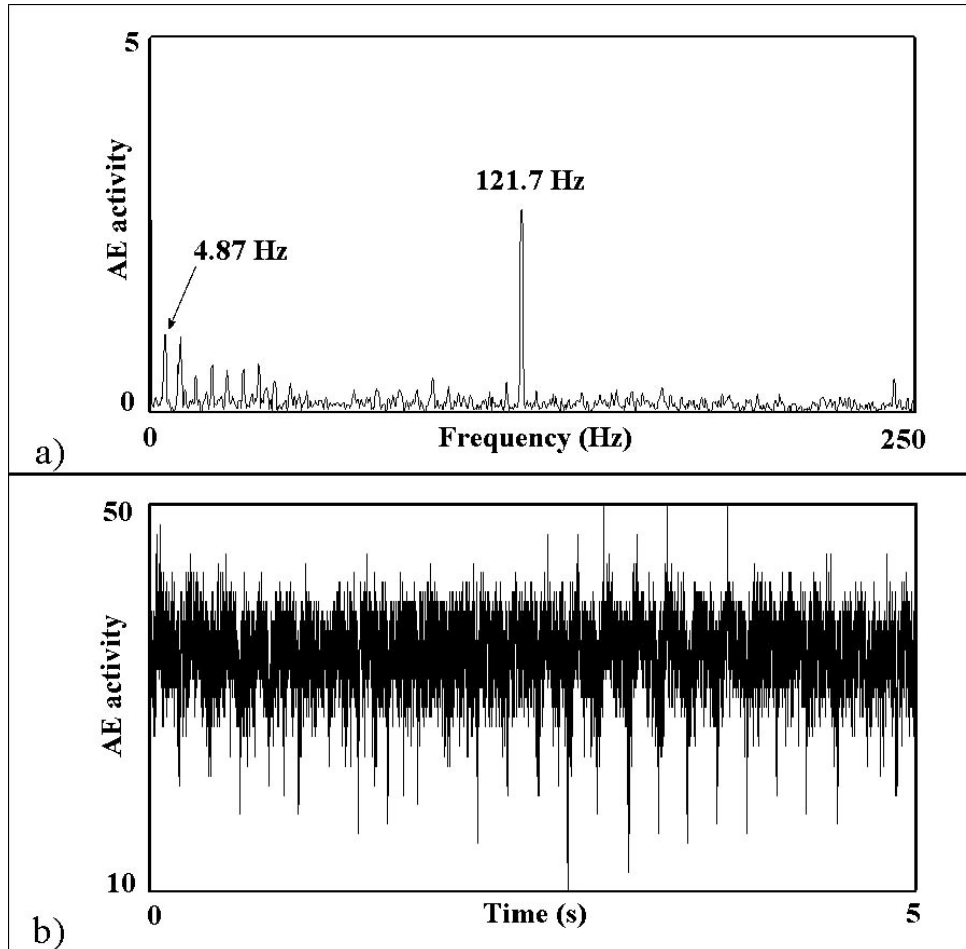


Fig. 8. Result of the measurement of the resonance condition. a) Frequency spectrum of AE count signal. b) The time signal of AE count. Line load is 18 kN/m.

From the frequency spectrum of the AE count result it can be detected the rotational frequency 4.87 Hz of the covered roll and its several harmonic components. The resonance frequency 121.7 Hz and its first harmonic component also can be seen clearly from the spectrum. The resonance frequency is exactly 25 times the rotational frequency of the covered roll. This tells us that the resonance is caused by the delay phenomena of the cover. The resonance condition can be eliminated by changing the rotational frequency so that it is not an integer fraction of the frequency of 121.7 Hz.

6. Conclusions

This paper presents a wireless on-line AE monitoring system of the cover of rotating rolls. The monitoring system is implemented in a pilot roll station of Laboratory of Machine Dynamics at Tampere University of Technology.

The tests have shown that the AE count method is a suitable method for wireless measurement data transfer of the AE signal. The AE count method has also the advantage that it is like a “triggered” signal that makes it possible to position the AE source on the circle of the roll cover. The disadvantage of the AE count method is that the AE count rate depends on the rotational frequency of the roll.

The methods used in control of the line load of contacting rolls in industry environment typically are based on indirect measurement methods. The line load is calculated for example from the hydraulic pressures according the geometry of the loading system. With the AE measurement system presented in here it is possible to monitor the line load of the contact direct. The tests have also shown that with the measurement system it is possible to detect contaminants, which are on the surface of the rolls.

The resonance running condition caused by the delay of the deformation of roll cover is a harmful phenomenon. It stresses the mechanical constructions and lowers the quality of the product. The AE measurement can be used in adaptive control of the roll rotational frequency. The goal in this kind of control is to drive the rolls in a certain driving window where the vibrations are at an acceptable level.

Acknowledgements

The authors are grateful for the financial and technical support from the following companies and institutions: National Technology Agency (Tekes) in Finland, the Finnish companies Metso Paper Inc, Metso Automation Oy, ABB Oy, M-real Oyj, Bosch-Rexroth Oy, Microteam Oy and Acutest Oy.

References

1. Chinn, F., "Dynamic Instability of Poly Covered Press Rolls". Pulp & Paper Canada, **100**, (1), 1999. 11-14.
2. Miettinen, J., Leinonen, P. Monitoring of Contaminants in a Grease Lubricated Rolling Bearing by Acoustic Emission in Field Environment. In: Proceedings of the 2nd COST 516 Tribology Symposium. Antwerpen, Mol. (editors J. Meneve and K. Vercammen), Flemish Institute for Technological Research. 1999. ISBN 90-5857-001-0. pp. 243-252.
3. Reilly, T. J., Networked Vibration Testing and Analysis, Sound and Vibration, March 2002. pp. 14-17.
4. Taylor, James. I. "The Vibration Analysis Handbook" Vibration Consultants Inc, Tampa FL, 1994. 360 p. ISBN 0-9640517-0-2.
5. Vinicki, J., Barring Induced Vibration, "Sound and Vibration", 2001, **35**, (9). 26-28.
6. Yuan, L. "Analysis of Delay Phenomena in Roll Dynamics" Tampere University of Technology, Publications 397, Doctoral Thesis, 2002, ISBN 925-15-0916-3. 132 p.
7. IEEE 802.11 WLAN standard. www.ieeexplore.ieee.org.

The 16th International Acoustic Emission Symposium IAES 16

November 12 –15, 2002
Industrial Memorial Hall of Tokushima University

Tuesday, November 12

Materials

Non-destructive Evaluation of High Temperature Creep Damage Using AE Method: *Y. Yokono (Non-Destructive Inspection Co. Ltd.)*

Micro-Cracking and Breakdown of Kaiser Effect in Ultra High Strength Steels: *H. Cho (Tohoku University), K. Fukaura (Himeji Institute of Technology) and K. Ono (University of California, Los Angeles)*

Effect of Boron Additives on Acoustic Emission Behaviour during Tensile Deformation of Ni-Al Intermetallic Compounds: *K. Yoshida, K. Horikawa and K. Sakamaki (Tokushima University)*

Impact Damage Threshold of CFRP Laminates and Acoustic Emission from Impact and Fracture: *Y. Mizutani (National Space Development Agency of Japan), K. Ono (University of California, Los Angeles) and M. Takemoto (Aoyama Gakuin University)*

Evaluation of Bending Fatigue Damage for FRP Laminates with Acoustic Emission - Application of Wavelet Transform -: *M. Takuma and N. Shinke (Kansai University)*

Characterization of Paperboard Deformation by AE: *S. Suzuki, Y. Fukuzawa, S. Nagasawa (Nagaoka University of Technology), H. Sakayori (Koutou Carving Co.) and I. Katayama (Katayama Steel Rule Die Co. Ltd.)*

Micro-Fracture Process during Bending Tests of Bio ceramics in Simulated Body Environment Evaluated by Acoustic Emission: *S. Wakayama, T. Kawakami, S. Kobayashi (Tokyo Metropolitan University), M. Aizawa and A. Nozue (Sophia University)*

Detection of Micro-Cracking in PZT Ceramics Using Pattern Recognition of Acoustic Emission Signals: *S. P. M. Rao (Osmania University, India)*

Fracture Toughness Test and AE Analysis of Ceramics Using Indentation Method: *A. Yonezu, T. Ogawa and M. Takemoto (Aoyama Gakuin University)*

Evaluation of Micro-Fracture Process of Graphite Material by Acoustic Emission: *S. Nambu and M. Enoki (The University of Tokyo)*

Thin Film & Coating

Acoustic Emission from Atmospheric Rust Fracture: *M. Takemoto, T. Sogabe, K. Matsuura (Aoyama Gakuin University) and K. Ono (University of California, Los Angeles)*

Acoustic Property of CVD-Diamond Film and Acoustic Emission Analysis for Integrity Evaluation: *R. Ikeda, Y. Hayashi and M. Takamoto (Aoyama Gakuin University)*

Evaluation of Coated Film by Laser AE-UT Technique: *M. Enoki and T. Kusu (The University of Tokyo)*

Evaluation of Micro-Fracture Criterion during Thermo-Mechanical Test of Ceramic Coating: *K. Nozawa, M. Enoki (The University of Tokyo) and K. Tomita (Industrial Technology Center of Fukui Prefecture)*

Development of In-Process Monitoring System for Coatings Using Laser AE Technique: *S. Nishinoiri, M. Enoki (The University of Tokyo) and K. Tomita (Industrial Technology Center of Fukui Prefecture)*

Wednesday, November 13

Concrete

Corrosion Cracking in Reinforced Concrete by Acoustic Emission: *M. Ohtsu and Y. Tomoda (Kumamoto University)*

Evaluation of Bond Behavior of Reinforcing Bars in Concrete Structures by Acoustic Emission: *K. Iwaki, O. Makishima, T. Shiotani and K. Ozawa (Tobishima Corporation)*

Non-Destructive Inspection of Pre-stressed Concrete Containment: *G. Muravin, E. Osterberg and L. Lezvinsky (Margan Physical Diagnostics Ltd., Israel)*

Acoustic Emission in Fatigue Process of Steel-Concrete Composite Slabs: *T. Ito (Kawada Industries Co. Ltd.), M. Shigeishi and M. Ohtsu (Kumamoto University)*

Classification of Cracking in Concrete Structures by Acoustic Emission: *M. Uchida (Taiheiyo Cement Corporation), N. Tsuji (Taiheiyo Consultant Corporation) and M. Ohtsu (Kumamoto University)*

Sensor & Data Analysis

Acoustic Emission Sensors of RFNC-VNIIEF: *A. A. Bazhenov, O. Yu. Vititnev, S. A. Kamyshev, M. K. Smirnov and V. I. Yarovikov (Russian Federal Nuclear Center – VNIIEF, Russia)*

A Fiber-Optic Micro-Sensor for Acoustic Emission Measurement Fabricated by Micro-Machining: *M. Shiga, G. Suzuki, M. Yamada, M. Kitahara and H. Niitsuma (Tohoku University)*

Development of A Novel Optical Fiber Sensor for AE Detection in Composites: *I. Osawa, K. Kageyama, Y. Tsuchida and M. Kanai (The University of Tokyo)*

Development of AE Monitoring System Using Optical Fibers: *T. Matsuo and M. Takemoto (Aoyama Gakuin University)*

Updating of AE-SIGMA Analysis: 3D Visualization of AE Moment Tensor Solutions on the Internet: *M. Shigeishi and M. Ohtsu (Kumamoto University)*

Free Tools for Dispersion Curve Display, Wavelet Transform and the Overlay of Both Analysed Waveforms from Resonant Sensors in Known Source Distances: *H. Vallen, J. Vallen (Vallen-System GmbH, Germany)*

How to Measure the Maximum Data Acquisition rate of Modern AE-Equipment: *H. Vallen, J. Forker (Vallen-System GmbH, Germany)*

Structure & Monitoring

Acoustic Emission Evaluation of Corrosion Damages in Buried Pipe of Refinery: *S. Yuyama (Nippon Physical Acoustics Ltd.) and T. Nishida (Japan Energy)*

Evaluation of The Use of Acoustic Emission Technology to Reveal Flaws with Small Stress Intensity in High Energy Piping and to Determine Their Type and Danger Level: *B. Muravin, E. Turkel and G. Muravin (Margan Physical Diagnostics Ltd., Israel)*

The Dislocation Mechanisms of Creep Development in High Pressure and High Temperature Pipes and Possibility of Creep Revealing by Associated Acoustic Emission: *G. Muravin, V. Finkel and L. Lezvinsky (Margan Physical Diagnostics Ltd., Israel)*

Identification and Evaluation of Clusters of Acoustic Emission Events Observed near Excavations in a Mine: *T. Spies (Federal Institute for Geosciences and Natural Resources, Germany) and J. Eisenblätter (Gesellschaft für Materialprüfung und Geophysik mbH, Germany)*

Study on The Applicability of Train-Induced Secondary Acoustic Emission for Non-Destructive Inspection of Structures: *Xiu Luo, H. Haya, T. Inaba (Railway Technical Research Institute), T. Shiotani and Y. Nakanishi (Tobishima Corporation)*

Acoustic Emission Evaluation of Tank Floor Condition: *S. Yuyama (Nippon Physical Acoustics Ltd.), M. Yamada (National Research Institute of Fire and Disaster), K. Sekine (Yokohama National University), S. Kitsukawa (High Pressure Institute of Japan) and H. Maruyama (National Oil Corporation of Japan)*

Review of JIS 2342-2002 " Method for Acoustic Emission Testing of Pressure Vessels during Pressure Tests and Classification of Test Results ": *Y. Mori (Nihon University), M. Shiwa (Japan Power Engineering & Inspection Corporation), M. Nakano (Chiyoda Advanced Solutions Co., Ltd.) and K. Iwai (Showa Electric Laboratory Co., Ltd.)*

Thursday, November 14

Materials

Conformation of Precipitate Cracking as A Source of Acoustic Emission: *T. Stuch and S. H. Carpenter (University of Denver)*

Acoustic Emission Accompanied by Grain Boundary Embrittlement of An Al-Mg-Si Alloy:

K. Horikawa, A. Ohmori, K. Yoshida and K. Sakamaki (Tokushima University)

Evaluation of Serration Stress Drop Behavior of Al-Mg Alloy by Acoustic Emission: *T. Egi, Y. Obata and Y. Mori (Nihon University)*

Acoustic Emission Source Location and Signal Processing for the Detection of Fatigue Damage in Thin Aluminum Structures: *Oh-Yang Kwon, Yong-Kyu Kang and Sung-Jin Kim (Inha University, Korea)*

Rock & Stone

Collapsing Method for Delineation of Structures inside AE Cloud Associated with Compression Test of Salt Rock Specimen: *H. Moriya, S. Mochizuki, H. Niitsuma, M. Ishimoto (Tohoku University), G. Manthei, J. Eisenblatter (Gesellschaft für Materialprüfung und Geophysik mbH, Germany), and R. H. Jones (ABB-OFFshore Systems, UK)*

Evaporation Induced Acoustic Emission in Porous Materials: *T. Shiotani (Tobishima Corporation), J Bisschop (Delft University of Technology, The Netherland) and J. G. M. Mier (Institute for Building Materials, Switzerland)*

Acoustic Emission and Deformation of Rock under Compression: *Y. Imaizumi, T. Nagano, T. Furue (Kyushu Electric Power Co., Inc.), T. Ebuchi, M. Maeda, M. Shindo, T. Imanaka (Non-Destructive Inspection Co., Ltd.), Y. Mori, A. Hosogi (Nihon University), T. Tamari and S. Tawaki (Kyusyu Environmental Evaluation Association)*

Application of Stress Inversion Methods using Moment Tensors of Acoustic Emission Events Obtained during Hydraulic Fracturing Tests in Salt Rock: *G. Manthei (Gesellschaft für Materialprüfung und Geophysik mbH, Germany)*

Friday, November 15

Diagnosis & Evaluation

Process Monitoring of Submerged-Arc Cladding by Acoustic Emission: *Shan-Ping Lu, Tae-Bum Kim and Oh-Yang Kwon (Inha University, Korea)*

Acoustic Emission in Bending Fatigue Process of Super-Carburized Spur Gear Teeth: *K. Miyachika, Yin-Ling Zeng, T. Koide, C. Namba, T. Hayashi (Tottori University), K. Tsubokura (Matsue National College of Technology), S. Oda (Fukuyama University) and Y. Kanayama (Izumo Murata Manufacturing Co., Ltd.)*

Quantitative Studies of Acoustic Emission due to Leaks from Above Ground Water Tank: *K. Morofuji, M. Tsuji (Tokyo Gas Co., Ltd.), M. Yamada, A. Maie (National Research Institute of Fire and Disaster) and S. Yuyama (Nippon Physical Acoustics Ltd.)*

Effect of Pinhole Shape with Divergent Exit on AE Characteristics during Gas Leak: *Y. Akematsu, K. Yoshida, K. Horikawa and K. Sakamaki (Tokushima University)*

Detection of Shaft-Seal Rubbing in Large-Scale Power Generation Turbines using Acoustic Emission; Case Study: *D. Mba (Cranfield University, UK)*

Collision Tests Simulated the Solid Particle Erosion and Damage on the Nozzle and Blade of a Steam Turbine by AE Technique: *M. Maeda (Non-Destructive Inspection Co., Ltd.), T. Furue (Kyushu Electric Power Co., Ltd.)*

On a Feasibility of AE Monitoring to the Performance of a Steam Turbine: *T. Furue, M. Shimizu, Y. Imaizumi (Kyushu Electric Power Co., Ltd.), M. Maeda, T. Yoshiara and T. Imanaka (Non-Destructive Inspection Co., Ltd.)*